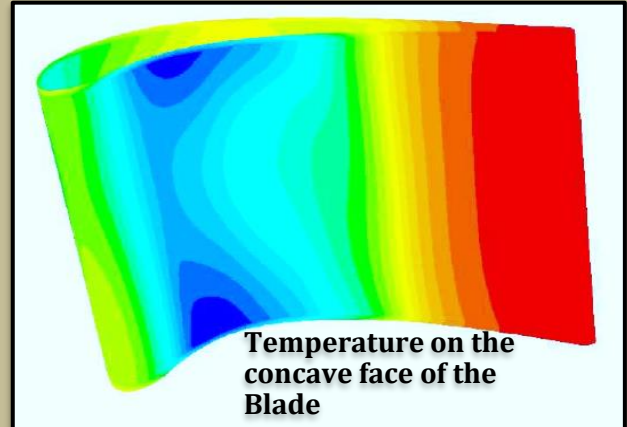
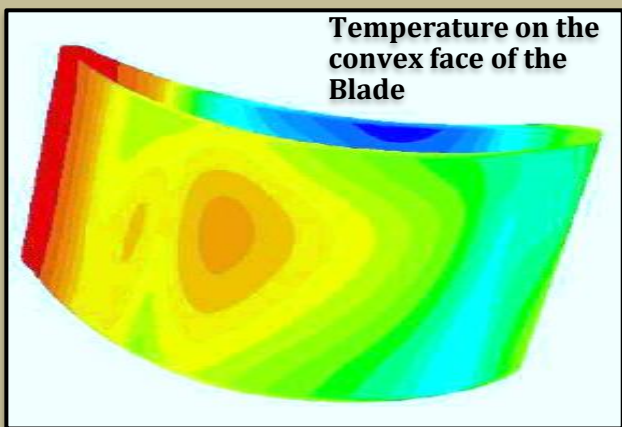
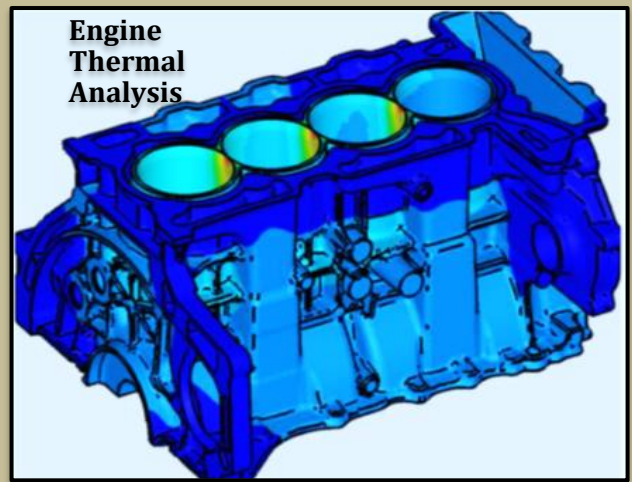
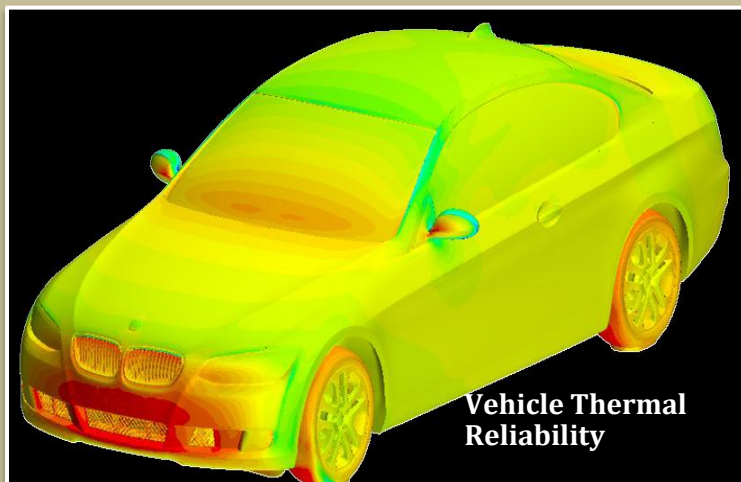
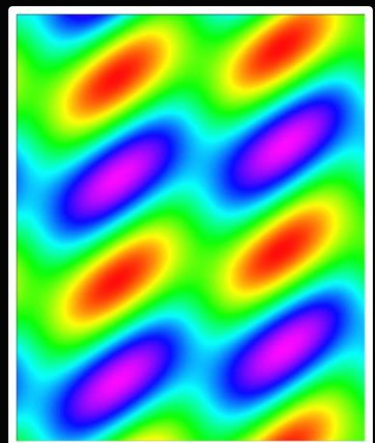


# Classical & Numerical Heat Transfer

Edited :  
Ideen Sadrehaghghi, Ph.D.



<b>1</b>	<b>Introduction.....</b>	<b>20</b>
1.1	Preliminaries.....	20
1.2	Methods and Nature of Prediction.....	20
1.2.1	Experimental Investigation.....	20
1.2.2	Calculation .....	21
1.3	Choice of Prediction Method .....	22
1.4	Basic Heat Transfer Modes .....	22
1.4.1	Conduction .....	22
1.4.2	Convection.....	23
1.4.3	Radiation.....	24
<b>2</b>	<b>Classical Heat Transfer .....</b>	<b>25</b>
2.1	Preliminaries.....	25
2.2	The General Transport Equation.....	25
2.3	Energy Equation .....	26
2.4	Newton's 2 <sup>nd</sup> Law and Momentum Equation.....	26
2.5	Time-Averaged Equations for Turbulent Flow.....	27
2.6	Turbulence-Kinetic-Energy Equation.....	27
2.7	Modes of Heat Transfer .....	27
2.7.1	Physical Perspectives of Conduction .....	27
2.7.2	Convection Phenomena .....	29
2.7.2.1	Convection Types .....	30
2.7.2.2	Free (Natural) Convection .....	31
2.7.2.3	Mixed Convection.....	31
2.7.3	Dimensionless Parameters .....	33
2.7.4	Convection vs. Conduction .....	33
2.7.5	Radiation.....	33
2.7.5.1	Radiation Properties.....	34
2.7.5.2	Radiation Models.....	35
2.8	Phase Transition.....	35
2.9	Conjugate Heat Transfer (CHT).....	36
2.10	Coupling & De-Coupling of Governing Equations.....	37
2.11	Mass Transfer .....	38
2.11.1	Mass Transfer by Diffusion .....	38
2.11.2	Mixture Composition .....	38
2.11.3	Fick's Law of Diffusion .....	39
2.11.4	Mass Diffusivity.....	40
2.11.5	Nonstationary Media - Absolute and Diffusive Species Fluxes .....	40
2.12	The Definition of Entransy and Entransy Dissipation .....	41
2.12.1	Entransy Analysis in Conduction Heat Transfer.....	44
<b>3</b>	<b>Discretization Methods.....</b>	<b>45</b>
3.1	The Structure of the Discretization Equation.....	45
3.2	Methods of Deriving the Discretization Equations .....	45
3.2.1	Taylor-Series Formulation (Finite Difference - FD).....	45
3.2.2	Variational Formulation.....	46
3.2.3	Method of Weighted Residuals .....	46
3.2.4	Control-Volume Formulation (CV).....	47

3.3	Consequence of Various Discretization Schemes .....	48
3.3.1	The Upwind Treatment.....	48
3.3.2	Numerical Diffusion .....	49
3.3.3	Other Remedies .....	49
3.3.4	The General Discretization Form.....	50
3.3.5	Another Point of View in regard to Spatial Discretization.....	51
<b>4</b>	<b>Numerical Methods for Solving Conduction (Diffusion) Equation .....</b>	<b>52</b>
4.1	One Dimensional Steady Conduction.....	52
4.2	Unsteady One-Dimensional Conduction.....	53
4.2.1	Explicit, Crank-Nicolson and Fully Implicit Schemes.....	55
4.2.1.1	Explicit Scheme .....	55
4.2.1.2	Crank-Nicolson Scheme.....	56
4.2.1.3	Fully Implicit Scheme.....	56
4.3	Discretization Equation for 2D .....	57
4.4	Discretization Equation for 3D .....	57
4.5	Solution of the Algebraic Equations .....	58
4.5.1	Gauss-Seidel Point-by-Point Method .....	58
4.5.2	A Line-by-Line Method .....	59
4.5.3	Other Iterative Methods.....	59
4.5.3.1	Over-Relaxation and Under-Relaxation.....	59
4.6	Convection and Diffusion.....	60
4.7	General Convection & Diffusion Equation .....	60
4.7.1	Steady One-Dimensional Convection and Diffusion.....	61
4.7.1.1	A Preliminary Derivation .....	61
4.7.1.2	Discussion .....	62
4.7.1.3	The Upwind Scheme.....	63
4.7.1.4	The Exact Solution .....	63
4.7.1.5	Implications .....	63
4.7.2	False Diffusion .....	64
4.7.2.1	The Common View of False Diffusion.....	64
4.7.2.2	Proper View of False Diffusion .....	65
<b>5</b>	<b>Flow Field Calculation (Convection) .....</b>	<b>67</b>
5.1	Difficulty in Estimating Pressure.....	67
5.2	Vorticity-Based Methods.....	67
5.3	Pressure-Gradient Term .....	68
5.4	Representation of the Continuity Equation.....	69
5.4.1	A Remedy; Staggered Grid.....	69
5.5	Momentum Equations.....	70
5.6	Pressure and Velocity Corrections.....	72
5.6.1	Pressure-Correction Equation .....	72
5.6.2	SIMPLE Algorithm .....	73
5.6.3	The Relative Nature of Pressure .....	73
5.7	Revised Algorithm of SIMPLER .....	74
5.8	2D Parabolic Flow.....	75
5.9	3D Parabolic Flow.....	76
5.9.1	Partially Parabolic Flows .....	76

<b>6 Case Studies for Numerical Heat Transfer .....</b>	<b>78</b>
<b>6.1 Case Study 1 – Heat Transfer in Axisymmetric Stagnation Flow on Thin Cylinders.....</b>	<b>78</b>
6.1.1 Basic Equations .....	78
6.1.2 Results and Discussions .....	79
<b>6.2 Case Study 2 – Computation of Heat Transfer in Linear Turbine Cascade.....</b>	<b>80</b>
6.2.1 Numerical Methods .....	81
6.2.2 Mesh Generation .....	81
6.2.3 Heat Transfer Results for 2D & 3D.....	82
6.2.4 Experimental Data .....	83
6.2.5 Effects of Turbulence.....	84
<b>6.3 Case Study 3 - DNS of Heat Transfer of the Flow Over a Cylinder at Re = 200 and 1000 .....</b>	<b>85</b>
6.3.1 Introduction.....	85
6.3.2 Computational details .....	85
6.3.3 Results .....	86
6.3.4 Conclusion .....	88
6.3.5 References .....	88
<b>6.4 Case Study 4 - Unsteady Conjugate Heat Transfer Modeling.....</b>	<b>90</b>
6.4.1 Introduction & Background .....	90
6.4.2 Time Scale Analysis and Problem Statement .....	91
6.4.3 Baseline Flow and Conduction Solver .....	92
6.4.3.1 Flow Equations and Discretization .....	92
6.4.3.2 Conduction Equation for Solid Domain.....	93
6.4.3.3 Verification for Convection Heat Transfer.....	94
6.4.4 Frequency-Domain Unsteady Conduction Model and Analysis .....	94
6.4.5 Fluid-Solid Interface.....	96
6.4.5.1 Discrete Interface Condition.....	96
6.4.5.2 Semi-Analytical Interface Condition.....	97
6.4.5.3 Case Analysis for Fluid-Solid Interface.....	99
6.4.6 Coupled Unsteady Conjugate Method .....	101
6.4.6.1 Further Modeling Considerations.....	101
6.4.6.2 Proposed Method.....	101
6.4.6.3 Case Study for Coupled Conjugate Method .....	102
6.4.7 Concluding Remarks .....	107
6.4.8 References .....	107
<b>6.5 Case 5 - Fluid-Structure Interaction (FSI) of a Hot Flexible Thin Plate Inside an Enclosure .....</b>	<b>110</b>
6.5.1 Nomenclature.....	110
6.5.2 Introduction.....	111
6.5.3 Problem Definition and Mathematics .....	113
6.5.4 Numerical Solution, Grid Independence Test, and Verifications .....	116
6.5.4.1 Numerical Solution .....	116
6.5.4.2 Grid Independence Test .....	116
6.5.4.3 Verification .....	117
6.5.5 Results and Discussion.....	119
6.5.6 Conclusion .....	121
6.5.7 References .....	122
<b>6.6 Case Study 6 - Different Turbulence Models Simulations of a Vortex Tube .....</b>	<b>125</b>
6.6.1 Introduction .....	125

6.6.2	Mathematical & Geometry Models.....	127
6.6.3	Governing Equations .....	127
6.6.4	Boundary Conditions and Solver .....	128
6.6.5	Results and Discussions .....	129
6.6.5.1	Pressure Distribution.....	129
6.6.5.2	Tangential Velocity Distribution.....	131
6.6.5.3	Axial Velocity .....	133
6.6.5.4	Radial Velocity .....	134
6.6.6	Temperature Field .....	134
6.6.7	Streamline Field.....	135
6.6.8	Conclusion .....	135
6.6.9	References .....	136
6.7	Case Study 7 - Highly-Resolved LES of Turbulent Convective Flow Along A PWR Rod Bundle .....	138
6.7.1	Introduction.....	138
6.7.2	Modelling.....	139
6.7.2.1	Highly-Resolved LES.....	140
6.7.2.2	The Filtered LES Equations .....	140
6.7.2.3	SGS Modeling.....	140
6.7.3	Problem Description .....	141
6.7.4	Problem Setup .....	142
6.7.4.1	Computational Domain, Boundary Conditions & Mesh .....	142
6.7.4.2	Initial Conditions & Simulations Parameters.....	143
6.7.5	Flow Structures Results .....	144
6.7.5.1	Time Averaged Results .....	146
6.7.5.2	Energy Spectra Results .....	147
6.7.5.3	Global Parameters Results .....	148
6.7.6	Conclusions.....	149
6.7.6.1	Conflict of Interest.....	150
6.7.6.2	Acknowledgements .....	150
6.7.7	References .....	150
6.8	Case Study 8 – 2D Evaluation of Combined Delaunay Triangulation and Remeshing for Finite Element Analysis of Conductive Heat Transfer.....	152
6.8.1	Abstract .....	152
6.8.2	Nomenclature.....	152
6.8.3	Introduction.....	154
6.8.4	Finite Element Thermal Analysis .....	154
6.8.4.1	Governing Differential Equations and Boundary Conditions .....	154
6.8.4.2	Finite Element Equations.....	155
6.8.5	Delaunay Triangulation For Thermal Analysis .....	156
6.8.5.1	Concept and Algorithms Survey .....	156
6.8.5.2	Mesh Generation Procedure .....	157
6.8.5.3	Automatic Node Creation Procedure .....	157
6.8.5.4	Mesh Smoothing.....	159
6.8.6	Adaptive Remeshing Technique .....	159
6.8.6.1	Element Size Determination.....	160
6.8.6.2	Adaptive Mesh Regeneration.....	161
6.8.7	Algorithm Evaluation .....	161

6.8.7.1 Steady-State Heat Conduction In A Square Plate Subjected To A Highly Localized Surface Heating.....	162
6.8.7.2 The Transient Heat Conduction In A Long Plate Subjected To A Moving Heat Source	
163	
6.8.8 Conclusions.....	168
6.8.9 Acknowledgements .....	168
6.8.10 References .....	168
6.9 Case Study 9 – 3D Heat Transfer for Hypersonic Flow Using Shock Wave/Boundary-Layer Interactions with Wall-Modeled LES (WMELS).....	170
6.9.1 Introduction.....	171
6.9.2 LES Governing Conservation Equations.....	171
6.9.2.1 LES Wall Model Based on Equilibrium Boundary Layer Approximations .....	172
6.9.3 Numerical Methods .....	174
6.9.4 Double-Finned Problem Definition and Computational Setup .....	175
6.9.5 Results and Discussion.....	176
6.9.5.1 WMLES with Semi-Local Scaling Based Damping Function .....	176
6.9.5.1.1 Overall Statistics .....	176
6.9.5.1.2 Data Analyses in x-z and x-y Planes.....	178
6.9.5.2 WMLES with Van Driest Scaling Based Damping Function.....	183
6.9.6 Conclusions.....	185
6.9.7 Acknowledgments .....	185
6.10 Case Study 10 - Comparison of Steady and Unsteady RANS Heat Transfer Simulations of Hub and End all of a Turbine Blade Passage .....	186
6.10.1 Introduction .....	186
6.10.2 Computational Method .....	188
6.10.3 Boundary Conditions .....	189
6.10.4 Results and Discussion.....	190
6.10.5 Heat Transfer Comparison With Open Literature .....	197
6.10.6 Comparison of Casing Heat Flux With [Epstein et al.].....	198
6.10.7 Comparison of Hub Heat Transfer With Tallman et al. ....	198
6.10.8 Conclusions.....	199
<b>7 Heat Transfer Applications in Automotive Engineering.....</b>	<b>200</b>
7.1 Background.....	200
7.1.1 Case Study 1 – Simulation of Windshield De-Icing .....	200
7.1.2 Meshing .....	201
7.1.3 Velocity Contours and Convection De-Icing .....	201
7.1.4 Effect of Turbulence Modeling .....	202
7.2 Powertrain.....	202
7.3 Powertrain Cooling .....	203
7.3.1 Engine Cooling Block.....	203
7.3.1.1 System Component: Radiator.....	204
7.3.1.2 System Component: Fans .....	205
7.4 Case-Study 2 - Cooling Jacket Design.....	206
7.4.1 Cooling Jacket Geometry.....	206
7.4.2 Design Objectives .....	206
7.4.3 Meshing .....	208
7.5 Electric Powertrains .....	208

7.5.1	Battery Electric Vehicles .....	208
7.5.2	Mild Hybrid Electric Vehicles .....	208
7.6	Internal Combustion Engine (ICE).....	209
7.6.1	Abnormal Combustion Phenomena .....	210
7.6.2	Methods for Dynamic Mesh Motion .....	211
7.6.2.1	Automatic Mesh Motion .....	211
7.6.3	Valve Closure Problem.....	212
7.6.4	Physics .....	212
7.6.5	Case Study 3 - An Original Approach To Address 3D Automatic Meshing For Internal Combustion Engine (ICE) Simulation Using Hybrid Body Fitted Grid and Embedded Remeshing Process	212
7.6.5.1	Introduction and Background.....	212
7.6.5.2	Hybrid IFP-C3D Combustion Solver .....	213
7.6.5.2.1	Mesh Generation.....	213
7.6.5.2.2	Parallelism .....	214
7.6.5.3	Automatic Mesh Generation Procedure .....	214
7.6.5.4	Cylinder Multi-Cycle Engine Simulation .....	216
7.6.5.5	Conclusion .....	217
7.7	Case Study 4 - Predicting Surface Temperature of the Exhaust System .....	218
7.7.1	Heat Transfer Methodology .....	218
7.7.1.1	Conduction .....	218
7.7.1.2	Convection.....	219
7.7.2	Exhaust System.....	220
7.7.3	Method Development and Setup .....	221
7.7.4	CFD Coupling.....	221
7.7.5	Thermal Model Development .....	222
7.7.5.1	Characterization of the Manifold .....	222
7.7.5.2	Case Study 4.1 – Exhaust Manifold with Transient BC Velocity and Temperature .....	224
7.7.5.2.1	Input data .....	224
7.7.5.2.2	CFD Simulation Set-up.....	224
7.7.5.2.3	Running CFD Simulation .....	224
7.7.6	Characterization of the Turbocharger .....	224
7.7.7	Characterization of the Catalytic Converter .....	225
7.7.8	Characterization of the Exhaust Pipe and Flex-Pipe.....	225
7.7.9	Results and Discussion.....	225
7.7.10	Validation.....	226
<b>8</b>	<b>Heat Exchangers .....</b>	<b>228</b>
8.1	Case Study – Steady Heat Transfer in Fin and Tube Heat Exchanger.....	228
8.1.1	Problem Formulation.....	228
8.1.2	Performance Parameters .....	229
8.1.2.1	Reynolds Number .....	230
8.1.2.2	Fanning friction factor-f.....	230
8.1.2.3	Colburn j-factor .....	230
8.1.2.4	Pressure Drop .....	230
8.1.3	Classification of Heat Exchangers .....	231
8.1.3.1	Fin & Tube Heat Exchangers.....	232

8.1.3.2	Oval Tube.....	233
8.1.4	Governing Equations and Numerical Schemes.....	234
8.1.5	Boundary Conditions .....	234
8.1.6	Grid Independence Study .....	235
8.1.7	Flow Characteristic .....	235
8.1.7.1	Velocity Observations.....	235
8.1.7.2	Kinetic Energy k distribution.....	235
8.1.8	Characteristics of Heat Transfer .....	236
8.1.9	Choice of different Turbulence Modelling as available in OpenFOAM <sup>®</sup> .....	237
8.1.10	Turbulence Modeling.....	237
8.1.11	Comparison of Friction Factor .....	238
8.1.12	Comparison of Colburn j-Factor .....	238
8.1.13	Conclusion .....	239
<b>9</b>	<b>HVAC in Building and Related Issues .....</b>	<b>240</b>
9.1	Thermal Analysis in Buildings.....	240
9.2	Ventilation Analysis .....	241
9.2.1	Numerical Simulations of the Effect of Outdoor Pollutants on Indoor Air Quality of Buildings next to a street canyon .....	241
9.3	HVAC & Environmental Issues .....	242
9.3.1	Introduction to Air-Conditioning Processes .....	243
9.3.1.1	Heating .....	243
9.3.1.2	Cooling.....	243
9.3.1.3	Humidifying .....	243
9.3.1.4	De-Humidifying.....	243
9.3.1.5	Cleaning .....	243
9.3.1.6	Ventilating .....	244
9.3.1.7	Air Movement.....	244
9.3.2	The Role of CFD In HVAC System Optimization .....	244
9.3.2.1	Why Use CFD Analysis in HVAC Design.....	244
9.3.2.1.1	Performance Prediction .....	244
1.1.1.1.1	Provides Key HVAC Design Parameter Information .....	244
1.1.1.1.2	Using CFD For Validation/Optimization of HVAC Design Parameters.....	244
1.1.1.1.3	Modification Of Malfunctioning HVAC Systems.....	245
9.3.3	Case Study 1 - Aircraft Hangar Fire & Smoke Model.....	245
9.3.3.1	Results .....	246
9.3.4	Case Study 2 - CFD Modeling Approach for HVAC Systems Analysis .....	246
9.3.4.1	Modeling and Simulation Approach.....	247
9.3.4.2	Results and Discussion.....	248
9.3.5	Case Study 3 - Investigation of the Natural Ventilation of Wind Catchers with Different Geometries in Arid Region Houses .....	248
9.3.5.1	Abstract .....	248
9.3.5.2	Introduction.....	249
9.3.5.2.1	Thermal Comfort .....	249
9.3.5.2.2	Natural Ventilation.....	249
9.3.5.2.3	Wind-Driven Natural Ventilation.....	250
9.3.5.3	Mathematical Modelling of the Problem .....	250

9.3.5.3.1	Governing Equations .....	250
9.3.5.3.2	Wind Catchers Between Past, Present and Future .....	251
9.3.5.4	Numerical Simulation of External Airflows Around A Tower-House System .....	252
9.3.5.4.1	Geometry and Dimension .....	253
9.3.5.4.2	Meshting .....	254
9.3.5.4.3	Boundary Conditions .....	254
9.3.5.5	Results and Discussion.....	254
9.3.5.5.1	Analysis of the Internal Airflow in Ventilated Spaces .....	256
9.3.5.5.2	Effect of the Opening Position on Internal Airflow .....	259
9.3.5.6	Conclusion .....	259
9.3.5.7	References.....	260
<b>10</b>	<b>Cooling Data Centers.....</b>	<b>264</b>
10.1	Preliminaries.....	264
10.1.1	Air-Based Cooling.....	264
10.1.2	Liquid-Based Cooling .....	264
10.1.3	Evaporative Cooling .....	264
10.1.4	What Are Some New Data Center Cooling Systems and Innovations? .....	267
10.2	Case Study 1 - Smart Cooling of Data Centers .....	268
10.2.1	Motivation .....	268
10.2.2	Static Smart Cooling .....	269
10.2.3	Dynamic Smart Cooling .....	271
10.2.4	Smart Cooled Data Center Concept.....	272
10.2.5	Construction of The Smart Data Center .....	274
10.2.6	Work Underway To Develop The Control Systems .....	275
10.2.7	Summary & Conclusions .....	275
10.3	Case Study 2 - Performance Assessment of Cooling Systems for Data Centers with New Thermal Metric.....	277
10.3.1	Introduction .....	277
10.3.2	Indexes for Assessing Data Center Cooling .....	278
10.3.2.1	Return Heat Index (RHI) and Supply Heat Index (SHI).....	278
10.3.2.2	Rack Cooling Index (RCI) .....	279
10.3.2.3	Return Temperature Index (RTI) .....	280
10.3.3	Introducing a New Index for Assessment of Data Center Cooling .....	280
10.3.4	Development of Numerical Model and Calculation of CCI for Different Configuration of Data Center .....	281
10.3.4.1	Governing Equations .....	281
10.3.4.2	Boundary Condition and Inlet .....	282
10.3.4.3	Validation of the Model.....	282
10.3.4.4	Modeling and Problem Description .....	283
10.3.4.5	Detailed Room Summary of Marand PC Data Center and Introducing Alternative Models	283
10.3.5	Results .....	284
10.3.5.1	Investigated Temperature Points .....	284
10.3.5.2	Assessing the Performance and Cooling Efficiency.....	285
10.3.5.2.1	Group 1: Models 11–14.....	285
10.3.5.2.2	Group 2: Models 5–10.....	286
10.3.5.2.3	Group 3: Models 1–4 and 15 .....	286

10.3.6	Numerical Calculation of CCI .....	287
10.3.7	Conclusion .....	287
10.4	Case Study 3 - Load Capacity and Thermal Efficiency Optimization of a Research Data Center Using Computational Modeling.....	289
10.4.1	Introduction and Literature Survey .....	290
10.4.2	Method .....	292
10.4.3	Results .....	294
10.4.4	Conclusions.....	296
<b>11</b>	<b>Heat Transfer in Semiconductor Industry .....</b>	<b>298</b>
11.1	Brief Description of Semiconductor Devices .....	298
11.2	Thermal Management in Semiconductors.....	299
11.2.1	Can You Really Fry an Egg on a CPU?.....	300
11.3	Case Study 1 - Thermal Analysis on Micro-Electronic Heat Sink by CFD using Rectangular and Trapezoidal Fin Arrays.....	301
11.3.1	Abstract .....	301
11.3.2	Introduction.....	301
11.3.2.1	Optimal Heat Sink in Micro-Electronic Cooling System.....	301
11.3.2.2	Need of Optimization .....	302
11.3.3	Numerical Analysis .....	303
11.3.4	Methodology .....	303
11.3.4.1	Design Procedure for Rectangular Array of Fin Heat Sink Model .....	303
11.3.4.2	Design Procedure for Trapezoidal Array of Fin Heat Sink Model.....	304
11.3.5	Governing Equations .....	305
11.3.6	Results and Discussion.....	305
11.3.6.1	Trapezoidal Heat Sink .....	305
11.3.6.2	Graphical Representation of Temperature .....	305
11.3.6.2.1	Heat Transfer Coefficient (H) .....	305
11.3.6.2.2	Nusselt Number.....	305
11.3.6.2.3	Heat Transfer Rate .....	305
11.3.6.2.4	Temperature vs. Efficiency .....	305
11.3.7	Conclusions.....	305
11.3.8	References .....	307
11.4	Case Study 2 - CFD Analysis of Convective Heat Transfer from Inverted Trapezoidal Plate Fin Array .....	308
11.4.1	Abstract .....	308
11.4.2	Introduction.....	308
11.4.3	Numerical Analysis .....	309
11.4.3.1	Computational Mesh.....	309
11.4.3.2	CFD Simulation Approach.....	310
11.4.3.3	Boundary Conditions .....	310
11.4.3.4	CFD Post Processing .....	311
11.4.4	Result and Discussion .....	311
11.4.4.1	Variation of Heat Transfer Coefficient with Re .....	311
11.4.4.2	Variation of Nu with Re .....	311
11.4.4.3	Variation of Pressure Drop with Re.....	312
11.4.5	Conclusions.....	312
11.4.6	References .....	312

11.5 Case Study 3 - The Optimal Design of Heat Sinks: A Review.....	314
11.5.1 Abstract .....	314
11.5.2 Introduction.....	314
11.5.3 Heat Sink Classification.....	315
11.5.3.1 Pin Fin Heat Sink.....	315
11.5.3.1.1 Optimal Pin Fin Heat Sink under Natural Convection .....	315
11.5.3.1.2 Optimal Pin Fin Heat Sink under Forced Convection .....	316
11.5.3.2 Flat Fin Heat Sink.....	319
11.5.3.2.1 Optimal Flat Fin Heat Sink under Natural Convection .....	319
11.5.3.2.2 Optimal Flat Fin Heat Sink under Force Convection .....	321
11.5.3.3 Micro-channel Heat Sink .....	324
11.5.3.4 Topology Optimized Heat Sink .....	327
11.5.4 Conclusions.....	328
11.5.5 References .....	329

## List of Tables

Table 3.1 Summary of the Spatial Discretization Schemes Considered in the Present Study .....	51
Table 6.1 Percentage Errors in Calculated Unsteady Wall Temperature .....	96
Table 6.2 Literature review summary of the natural convection heat transfer in an enclosure .....	<b>Error! Bookmark not defined.</b>
Table 6.3 Grid testing for $\tilde{N}\mathbf{u}$ , $\sigma_{\max}$ and T at different grid sizes for fixed point 1 (P1), $Ra = 10^6$ , $\gamma = 90^\circ$ and $Pr = 6.2$ .....	115
Table 6.4 Properties of the fluid and flexible wall of the Küttler and Wall's problem [52].....	116
Table 6.5 Working Condition Used By Different Experiments (length unit: mm) .....	131
Table 6.6 Outlet temperature under different models .....	134
Table 6.7 Reference operating conditions for PSBT tests [3] .....	141
Table 6.8 Test case 2 operating flow conditions .....	142
Table 6.9 Grid Properties Used For The LES And For The Highly-Resolved LES .....	143
Table 6.10 Test Case 2 Operating Flow Conditions.....	149
Table 6.11 Grid parameters inside the turbulent boundary layer upstream of the double fins ...	176
Table 7.1 CAF influence in the surface temperature prediction.....	223
Table 7.2 Wind Tunnel Test.....	225
Table 8.1 Geometric Parameter of Heat Exchanger .....	229
Table 9.1 Grid information of the simulation cases .....	253
Table 9.2 External total pressure (Pa) and pressure coefficients of the models under investigation .....	255
Table 9.3 Airflow velocities (m/s) inside the ventilated space with different wind speeds: $V_{wind} = 1, 2, 3, 5, 6$ and $10 \text{ m/s}$ .....	258
Table 10.1 Dimensions of Hall and Thermal Load of Equipment – Courtesy of Norouzi-Khangah et al.].....	283
Table 10.2 Comparing 11, 12, 13 and 14 Models – Courtesy of [Norouzi-Khangah et al.] .....	285
Table 10.3 Comparing 5,-10 Models – Courtesy of [Norouzi-Khangah et al.] .....	286
Table 10.4 Comparing 1, 2, 3, 4 and 15 Models – Courtesy of [Norouzi-Khangah et al.].....	286
Table 10.5 Values of Indexes – Courtesy of [Norouzi-Khangah et al.].....	287
Table 10.6 Ranking of Models According to the CCI index.....	287
Table 10.7 Nomenclature.....	289
Table 10.8 Optimal Design Operating Point.....	296
Table 11.1 Meshing Details .....	309

## List of Figures

Figure 6.17 Radial temperature distribution (cylinder) .....	96
Figure 6.18 Harmonic temperature distribution (1D slab): (a) in phase harmonic component A, and (b) out-phase harmonic.....	96
Figure 6.19 Fluid-solid domain interface .....	97
Figure 6.20 Temperature Amplitude Corner Solution: (a) Semi-Analytical BC and (b) Finite-Difference BC .....	99
Figure 6.21 Heat Transfer in Corner Region: (a) Normal Flux only and (b) Normal and Tangential Fluxes.....	99
Figure 6.22 Radial temperature harmonics .....	100
Figure 6.23 Unsteady Heat Flux in Time (With and Without Unsteady) .....	100
Figure 6.24 Mesh-dependence of wall temperature: (a) 100 Hz and (b) 1000 Hz .....	101
Figure 6.25 Cooled blade configuration (subject to Incoming hot streak).....	102
Figure 6.26 Computational Mesh (Conjugate Solution).....	102
Figure 6.27 Instantaneous Unsteady Total Temperatures (Inlet Total Temperature Amplitude , $A_T = 0.2$ ) .....	103
Figure 6.28 Solution Convergence Characteristic: (a) Heat Flux.....	103
Figure 6.29 Time averaged surface heat flux: (a) 10% and (b) 20% hot streak amplitudes.....	104
Figure 6.30 Total Temperature Contours (Steady Versus Time Averaged).....	105
Figure 6.31 Instantaneous Stream-Traces: (a) Hot and (b) Cold portion Impinging.....	105
Figure 6.32 Impinging hot and cold flow patterns .....	106
Figure 6.33 Time traces of fluid temperatures: (a) 10% and (b) 20% hot streak amplitudes .....	106
Figure 6.34 Schematic of the Physical Model .....	<b>Error! Bookmark not defined.</b>
Figure 6.35 A comparison between the results of the present study and [52]. .....	116
Figure 6.36 Grid-points Distribution for a Grid Size $G5 = 3879$ Elements.....	117
Figure 6.37 The time history of the non-dimensional temperature at the denoted point for the present work and [54].....	118
Figure 6.38 A comparison of the Temperature field from work conducted by Turan et al. [53] and the present prediction .....	117
Figure 6.39 A comparison between the temperature fields of (a): the current numerical study and (b): the experimental work performed by Calcagni et al. [55] .....	118
Figure 6.40 Variations of the Unsteady streamlines for various dimensionless time ( $\tau$ ) at fixed point 1 (P1), $Ra = 10^6$ , $\gamma = 90^\circ$ , $Pr = 6.2$ , and $E = 5 \times 10^{10}$ .....	119
Figure 6.41 Variations of the Unsteady isotherms for various dimensionless time ( $\tau$ ) at fixed point 1 (P1), $Ra = 10^6$ , $\gamma = 90^\circ$ , $Pr = 6.2$ , and $E = 5 \times 10^{10}$ .....	120
Figure 6.42 Variations of the steady streamlines and isotherms for various fixed point locations (P1–P3) at $Ra = 10^6$ , $\gamma = 45^\circ$ , $Pr = 6.2$ , and $E = 5 \times 10^{10}$ .....	121
Figure 6.43 Airflow in a Vortex Tube .....	125
Figure 6.44 Schematic Diagram of Gao's Experimental Setup.....	126
Figure 6.45 Side view of vortex tube. A-A: cross section at the entrance of the nozzle; B-B: the distance from the cross section of .....	127
Figure 6.46 Static Pressure Distribution of A-A Cross Section With Different Turbulence Models .....	129
Figure 6.47 Static Pressure Distribution of D-D Cross Section With Different Turbulence Models (M/S).....	130
Figure 6.48 Tangential Velocity Distribution of D-D Cross Section With Different Turbulence Models (m/s) .....	131
Figure 6.49 Comparison of The Dimensionless Tangential Velocity .....	132
Figure 6.50 Axial Velocity Distribution Of D-D Cross Section With Different Turbulence Models (M/S).....	133
Figure 6.51 The Diagram of The Viscous-Shear Theory.....	133

Figure 6.52 Radial velocity distribution of D-D cross section with different turbulence models (m/s).....	134
Figure 6.53 Total temperature distribution of D-D cross section with different turbulence models(K).....	135
Figure 6.54 Instantaneous streamlines for the vortex tube in D-D plane.....	136
Figure 6.55 Computational Domain: Dimensions & B.C. s.....	142
Figure 6.56 Medium (Left) And Fine (Right) Grids For LES (X-Y). Arrows Show 0 And 45 Degrees Segments.....	143
Figure 6.57 Frictional velocity evolution with non-dimensional time.....	144
Figure 6.58 Fine (Left) Vs. Medium (Right) Grid: Instantaneous Velocities And Temperature Contours.....	<b>Error! Bookmark not defined.</b>
Figure 6.59 Fine (Left) Vs. Medium (Right) Grid: Instantaneous Cross-Sectional Velocities And Temperature Contours.....	144
Figure 6.60 Fine vs. medium resolutions: Instantaneous (a and c) and time averaged (b and d) cross-sectional velocities and temperature contours .....	145
Figure 6.61 Time averaged cross-sectional shear-stress and secondary-flow intensity ( $ \tilde{U}\tilde{V}=u_0v_0 $ ) contours.....	146
Figure 6.62 Fine vs. medium resolutions (scaled domain for illustration): Instantaneous .....	146
Figure 6.63 Mean velocity profiles across the subchannel ( $0^\circ$ & $45^\circ$ ) compared to the DNS of Eggels et al. [20]. .....	147
Figure 6.64 Mean Temperature Profiles Across The Subchannel At Various Streamwise Locations .....	147
Figure 6.65 Low-frequency PSD of U, V and W at various locations ( $z/L = 0.55, 80$ and $95$ ).....	148
Figure 6.66 Low- & high-frequency PSD of W velocity at various locations ( $z/L = 0.55, 80$ and $95$ ). .....	149
Figure 6.67 Delaunay triangulation dual of Voronoi diagram for a given set of points .....	156
Figure 6.68 Calculation of the nodal distribution values.....	158
Figure 6.69 Mesh refinement with automatic node creation scheme (Algorithm II ) and Delaunay triangulation (Algorithm I).....	159
Figure 6.70 Mesh refinement and smoothing for a lug with holes geometry .....	160
Figure 6.71 Governing differential equation, boundary conditions, and temperature contours .	162
Figure 6.72 Plate temperature and surface heating distributions along a diagonal direction of the plate.....	163
Figure 6.73 Uniform refined meshes and their temperature solution contours for a plate subjected to a highly localized surface heating.....	164
Figure 6.74 Adaptive meshes and their temperature solution contours for a plate subjected to a highly localized surface heating .....	165
Figure 6.75 Comparison of the exact temperature solution and the predicted temperatures from the third nonadaptive and adaptive meshes.....	166
Figure 6.76 Flow-chart for generating adaptive mesh movement to capture transient temperature response in a structure .....	167
Figure 6.77 Problem statement for transient thermal analysis of a plate subjected to a moving heat source .....	168
Figure 6.78 The Geometry Parameters and the Computational Coordinate System.....	174
Figure 6.79 Computational geometry and mesh sketch for the double-fin simulations: (a) the overview of the computational geometry; (b,c,d) the zoom-in views of the Voronoi mesh distributions (70M total mesh elements).....	175
Figure 6.80 (a) Time- and spanwise-averaged Mach number contour on the wall-normal x-y plane and (b) the instantaneous streamwise velocity distribution on the wall-parallel x-z plane of $y/L_r =$	

0:3616. In panel (b), the high-speed region is associated with the oblique shock wave originating from the leading edge of the flat plate at $x/L_r = 0$ .....	177
Figure 6.81 Time and Spanwise Averaged Distributions of (a) Mach number, (b) Density, and (c) Streamwise Velocity at $x/L_r = 162$ . The blue and red lines denote the results from WMLES and experiment [23], respectively .....	178
Figure 6.82 Time- and spanwise-averaged distributions of (a) density and (b) streamwise velocity at $x/L_r = 162$ . The fine grid denotes the mesh with parameters given in Table 5.9. The resolutions of the medium and coarse grids are 50% and 70% coarser than that of the fine grid.....	178
Figure 6.83 Distribution of the time-averaged $y_+$ at the first off-wall cell centers. For facilitating the presentation, only the data over the flat plate and one vertical fin are shown.....	179
Figure 6.84 (a) Instantaneous Surface Heat Flux Distribution, (b) Time-Averaged Surface Heat Flux Distribution, (c) Time-Averaged Pressure Distribution, and (d) Time-Averaged Surface Shear Stress Distribution. The location of the double-shock intersection based on the inviscid theory is around the midpoint of the two fin shoulders. For facilitating the presentation, only the data over the flat plate and one vertical fin are shown.....	180
Figure 6.85 Streamwise Distributions of The Time-Averaged (a) Surface Pressure and (b) Surface Heat Flux On The Flat Plate at $y/L_r = 0$ and $z/L_r = 0$ . The green lines and the red dots denote the results from the WMLES simulation and the experiment, respectively. The location.....	181
Figure 6.86 Distributions of the Time-Averaged (a) Surface Pressure and (b) Surface Heat Flux on the Flat Plate at $y/L_r = 0$ . The location of the double-shock intersection based on the inviscid theory is also shown in the plots. Also shown is the shock impingement location around .....	181
Figure 6.87 Included in this figure are the R.M.S statistics of the (a) Pressure, (b) Temperature and (c) Streamwise Velocity Fluctuations. These statistics are projected to the plate surface from the first off-wall cell centers. ....	182
Figure 6.88 Spanwise distributions of (a) the time-averaged surface pressure at the streamwise station $x/L_r = 187.5$ and (b) the time averaged surface heat flux at the streamwise station $x/L_r = 185.8$ . The green lines, the blue lines and the red symbols denote the data from the WMLES with the semi-local scaling, the WMLES with the van Driest scaling, and the experiment, respectively.....	184
Figure 6.89 Streamwise distributions of the time-averaged (a) surface pressure and (b) surface heat flux on the flat plate at $y/L_r = 0$ and $z/L_r = 0$ . The green lines, the blue lines and the red symbols denote the data from the WMLES with the semi-local scaling, the WMLES with van Driest scaling, and the experiment, respectively.....	184
Figure 6.90 Distribution of the time-averaged pressure on the flat-plate surface at $y/L_r = 0$ . The location of the double-shock intersection based on the inviscid theory is also shown in the plot. The result reported in this plot is from WMLES with van Driest scaling based damping function .....	185
Figure 6.91 Grid on the Solid Surfaces of the Geometry .....	188
Figure 6.92 (a) Casing surface mesh showing multiblock structure and (b) hub surface mesh showing multiblock structure .....	189
Figure 6.93 Total temperature ( $T_0$ ) and total pressure ( $P_0$ ) at the blade inlet .....	189
Figure 6.94 Instantaneous and time-averaged „dashed... hub surface.....	191
Figure 6.95 Instantaneous and time-averaged (dashed) hub heat transfer distribution for a wake passing .....	192
Figure 6.96 Time-Averaged Casing Pressure.....	193
Figure 6.97 Time-Averaged Hub Pressure.....	193
Figure 6.98 Difference in hub pressure distribution between the time-averaged and steady results .....	193
Figure 6.99 Difference in casing pressure distribution between the time-averaged and steady results .....	194
Figure 6.100 Time-averaged casing adiabatic wall temperature.....	194
Figure 6.101 Time-averaged hub adiabatic wall temperature.....	195



Figure 8.9	Contours of Turbulent Kinetic Energy $\kappa$ Using SST $\kappa-\omega$ Model in Different Inlet Velocities.....	236
Figure 8.10	Collaboration Between Flow Direction and Temperature Streamlines.....	236
Figure 8.11	Colburn $j$ -factor against Reynolds number for different Inlet Airflow Velocities and Flow Models.....	238
Figure 9.1	Effect of window loading in outdoor pollutants .....	242
Figure 9.2	Pollution between two buildings separated by a street.....	242
Figure 9.3	Impact of Window Opening Percentage (WOP) on indoor air quality .....	242
Figure 9.4	Study for HVAC Design of an Aircraft Hangar.....	245
Figure 9.5	Building Schematic with Internal Configuration .....	246
Figure 9.6	Post Processing of Results .....	247
Figure 9.7	Vertical wind profile speed (for an open space, roughness class = 0.5, roughness length = 0.0024 m, $u_r = 3 \text{ m/s}$ , $z_r = 10 \text{ m}$ ) .....	250
Figure 9.8	Types of the wind-driven natural ventilation.....	250
Figure 9.9	Yazd traditional wind-catcher for: (a) house ventilation and (b) water cooling .....	251
Figure 9.10	Schematic diagram of the modern wind catcher .....	252
Figure 9.11	Malqaf at Al-Jawhara house in Cairo, Egypt with outside and inside view of the device .....	252
Figure 9.12	House of Muhib Ad-Din equipped with Malqaf, Cairo [33].....	253
Figure 9.13	(a) Takhtabush in an old Egyptian house and (b) New model is based on the geometry and position of Takhtabush.....	253
Figure 9.14	Boundary conditions for the external flow around a tower-house system.....	254
Figure 9.15	Total external pressure (Pa) with $V_{\text{wind}} = 3 \text{ m/s}$ .....	255
Figure 9.16	External streamline of airflow around the structures (tower and house).....	256
Figure 9.17	Total internal pressure (Pa) with $V_{\text{wind}} = 3 \text{ m/s}$ .....	256
Figure 9.18	Internal airflow velocities and streamlines for the four studied models with $V_{\text{wind}} = 3 \text{m/s}$ .....	257
Figure 9.19	Internal total pressure (Pa) for three window positions: (a) down, (b) middle and (c) top ( $V_{\text{wind}} = 3 \text{ m/s}$ ).....	258
Figure 10.1	Cold or Hot Air Containment - Source: Submer .....	265
Figure 10.2	Liquid Baaed Cooling - Source: data center frontier .....	266
Figure 10.3	An Evaporated Cooling - Source: Condair .....	266
Figure 10.4	Typical Data Center Configuration .....	269
Figure 10.5	Provisioned CRACs .....	270
Figure 10.6	Smart Data Center Conceptual Sketch.....	273
Figure 10.7	Schematic of the Smart Data Center.....	274
Figure 10.8	Data Center Control Diagram.....	275
Figure 10.9	Air Re-Circulation and By-Pass in Data Center Racks – Courtesy of J. Cho, B. S. Kim	281
Figure 10.10	Numerical Model of Thermometer of Marand-PC Data Center – Courtesy of [Norouzi-Khangah et al.] .....	282
Figure 10.11	A Sample of Modeled Data Center – Courtesy of [Norouzi-Khangah et al.] .....	283
Figure 10.12	Thermal Assessed Points of Model – Courtesy of [Norouzi-Khangah et al.].....	285
Figure 10.13	Optimization Methodology Flowchart .....	291
Figure 10.14	VSORC full Hot Aisle Containment Layout. The "X" .....	292
Figure 10.15	Flow Rate Effect on Max Inlet Temperature .....	294
Figure 10.16	Supply Temperature Effect on Maximum Inlet.....	295
Figure 10.17	Minimization of Total Power Using Factorial Analysis .....	296
Figure 11.1	Illustrates the various classes of conductors .....	298
Figure 11.2	Modern Semiconductor.....	299
Figure 11.3	Thermal Management of Semiconductor (courtesy of Mentor CFD) .....	299

Figure 11.4	An Example of an Egg Frying on a CPU .....	300
Figure 11.5	Rectangular Heat Sink Model.....	301
Figure 11.6	Cross-Section of Three Types of Fins .....	302
Figure 11.7	Design for Rectangular array of fin heat sink model.....	303
Figure 11.8	Design for Trapezoidal array of fin heat sink model.....	304
Figure 11.9	Meshed model of the Trapezoidal Heat Sink.....	304
Figure 11.10	Graphical Representation of Temperature Vs. Heat Transfer Rates.....	306
Figure 11.11	Meshing Details.....	310
Figure 11.12	Temperature Contour at $Re = 4000$ and $Q=125$ W .....	311
Figure 11.13	Heat Transfer coefficient vs. Reynolds No. at $Q = 125$ W .....	311
Figure 11.14	Nusselt No. Vs Reynolds No. at $Q= 125$ W.....	312
Figure 11.15	Pressure drop Vs Reynolds's No. at $Q= 125$ W .....	312
Figure 11.16	Schematic of a pin fin configuration [29] .....	315
Figure 11.17	The modified pin fin heat sinks with (a) 1 degree (b) 2 degree and (c) 3 degree of expansion [30] .....	316
Figure 11.18	The structure and design of the heat sink [31] .....	316
Figure 11.19	The various numbers and locations of perforation in pin fin heat sink [33] .....	317
Figure 11.20	Fins with circular, diamond and elliptical perforation shapes [36].....	317
Figure 11.21	Geometries and dimensions of the different fins [37] .....	318
Figure 11.22	Design and dimensions of (a) plate-fin heat sink and (b) cross-fin heat sink [49]..	319
Figure 11.23	Schematics configurations of the heat sinks [54] .....	320
Figure 11.24	Fins with different geometries: (a) trapezoidal, (b) rectangular and (c) triangular [57] .....	321
Figure 11.25	Triangular fin with different perforations shapes [57] .....	321
Figure 11.26	Plat fin (a) without notch (b) with circular notch (c) with triangular notch [60]....	322
Figure 11.27	Designs and dimensions of the fins [63].....	322
Figure 11.28	Different fin orientation for vertical plates fin heat sink [65] .....	323
Figure 11.29	The geometrical model (a) non-fillet profile (b) fillet profile [71] .....	324
Figure 11.30	Various Geometrical cross-sections for micro-channel heat sink. (a) Rectangular, (b) inverse trapezoidal, (c) triangular bottom, (d) trapezoidal bottom, (e) W shape, (f) varied width rectangular, and (g) semi-oval [77] .....	325
Figure 11.31	Schematic diagrams: (a) parallel-channel design; (b) cross-channel design [81]...	326
Figure 11.32	Schematic of the DL-MCHS with different micro-channel cross-sectional shapes: (a) triangular; (b) rectangular; (c) circular; (d) trapezoidal; (e) reentrant shaped [86].....	327
Figure 11.33	3D topology optimized heat sink with volume fraction (a) 0.19 (b) 0.23 (c) 0.27 (d) 0.31 [89] .....	327

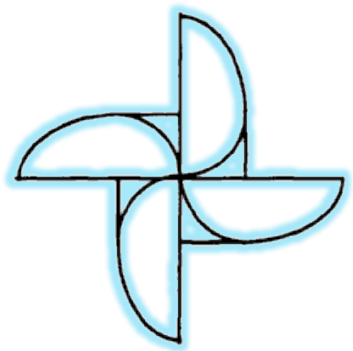
---

## Contributors

---

- Cornelie Revnic, Teodor Gros, An, and Ioan Pop, "Heat Transfer In Axisymmetric Stagnation Flow On Thin Cylinders", *Studia Univ. "Babes,-Bolyai", Mathematica*, Volume LV, Number 1, March 2010.
- Kalitzin, G. & Iaccarino G., "End wall heat transfer computations in a transonic turbine cascade", XVII Congresso nazionale sulla trasmissione del calore, U.I.T, Ferrara, 1999.
- Sovani, Sandeep: "CFD Applications in the Automotive Industry", Fluent Inc. 2006.

- B.Réveillé, N.Gillet, J.Bohbot, O.Laget, "An original approach to address 3D automatic meshing for internal combustion engine simulation using hybrid body fitted grid and embedded remeshing process", IFP Energies Nouvelles, Fr.
- A., M., Hansen, "CFD simulation of a fin-and-tube heat exchanger", Master of Science Thesis Computational Chemical Engineering, Group for Chemical Fluid Flow Processes Aalborg University Esbjerg, Neils Bohrs Vej 8, DK-6700 Esbjerg, Nov. 2008.
- R. Mahu, F. Popescu and I.V. Ion, "CFD Modeling Approach for HVAC Systems Analysis", Chem. Bull. "POLITEHNICA" Univ. (Timisoara), Volume 57(71), 2, 2012.
- Wang, Chi-Chuan; Chang, Yu-Juei; Hsieh, Yi-Chung; Lin, Yur-Tsai. "Sensible heat and friction characteristics of plate fin-and-tube heat exchangers having plane fins", International Journal of Refrigeration, Vol. 19, No. 4 (1996) pp. 223-230.
- Sauer, Harry J. Jr., Ronald H. Howell, William J. Coad. 2001. "Principles of Heating, Ventilating, and Air Conditioning", Atlanta: ASHRAE.
- Robert McDowall, P. Eng. "Fundamentals of HVAC Systems", Butterworth-Heinemann publications, ISBN-10: 0-12-372497-X, 2006.
- Begoña León Moya, "Fluid and Thermodynamic Under-hood Simulations", Thesis for the Degree of Master of Science, Lund University.
- Cornelia Revnic, Teodor Gros, An, and Ioan Pop, "Heat Transfer In Axisymmetric Stagnation Flow On Thin Cylinders", Studia Univ. "Babes,-Bolyai", Mathematica, Volume LV, Number 1, March 2010.
- Suhas V. Patankar, "Numerical Heat Transfer and Fluid Flow", Mc Graw Hill Book Company, 1980.
- Mentor Graphics, What They Didn't Teach You in School About Heat Transfer, white paper.
- Bakker, Ander, "Applied Computational Fluid Dynamics", Lecture 13 - Heat Transfer, 2002-2006.
- F.P., Incropera, D.P., DeWitt, T,L, Bergman, A,S, Lavine, "Fundamentals of Heat and Mass Transfer", 6<sup>th</sup> edition, John Wiley and Sons, 2007.F.P., Incropera, D.P., DeWitt, T,L, Bergman, A,S, Lavine, "Fundamentals of Heat and Mass Transfer", 6<sup>th</sup> edition, John Wiley and Sons, 2007.
- R.K.Agrawal, 'A third-order accurate upwind scheme for Navier- Stokes at high Reynolds numbers', AIAA 81-0112, (1981).
- Kalitzin, G. & Iaccarino G., "Computation of heat transfer in a linear turbine cascade", Center for turbulence Research Annual Research Briefs, 1999.
- R.Courant, E.Isaacson & M.Rees, 'On the solution of non-linear hyperbolic differential equations by finite differences', Comm. Pure Appl. Maths, 5, p243, (1952).
- P.H.Gaskell and A.K.C.Lau, "Curvature-compensated convective transport: SMART, a new boundedness-preserving transport algorithm ", Int. J. Num. Meth. Fluids, Vol.8, p617, (1988).
- J. E.Fromm, 'A method for reducing dispersion in convective difference schemes', J. Comp. Phys., Vol.3, (1968).
- C. Hirsch, 'Numerical computation of internal and external flows', Computational Methods for Inviscid and Viscous Flows, Vol.2,Wiley Inter science, (1990).
- B. Koren, 'A robust upwind discretization method for advection, diffusion and source terms', Numerical Methods for Advection-Diffusion Problems, Ed. C. B. Vreugdenhil & B. Koren, Vieweg, Braunschweig, p117, (1993).
- Robert S. L. Christoph G. Helmut, Schneider, Helwig Hauser, H., Hagen, H., "Visual Analysis and Exploration of Fluid Flow in a Cooling Jacket".
- J. Gu and Z. Gan, *Entransy in Phase-Change Systems*, Springer Briefs in Thermal Engineering and Applied Science, 2014
- S.A.M. Mehryan a, Ammar Alsabery b,c, Alireza Modir d, Ehsan Izadpanahi d, Mohammad Ghalambaz



# 1 Introduction

## 1.1 Preliminaries

Heat, like most things, prefers the path of least resistance. But it is not welcomed everywhere. Sometimes, heat is the enemy, such as in the design of consumer electronics, where powerful chips are squeezed into tighter and tighter quarters. Heat generated by an electronic product needs to be removed from its enclosure so that the heat does not accumulate and damage the internal components. For smart phones, the ingenious designers have even taken into account that our body can act as heatsinks; while you use the phone, the heat is transferred out by conduction through the contact to your body. Heat and its behavior are complex. Rules of thumb are often used to visualize the heat path for design or physical prototypes; but knowing how heat is traveling, at what speed and where it will go, is difficult. This is why today's design-centric software for modeling and simulation using computational fluid dynamics (CFD) is integral to understanding heat flow and channeling it correctly without having to build and test as many expensive and time-consuming physical prototypes<sup>1</sup>.

Heat transfer is the exchange of thermal energy between physical systems. It is the science that seeks to predict the energy transfer that may take place between material bodies as a result of a temperature difference. The rate of heat transfer is dependent on the temperatures of the systems and the properties of the intervening medium through which the heat is transferred. The three fundamental modes of heat transfer are **conduction**, **convection** and **radiation**. Heat transfer, the flow of energy in the form of heat, is a process by which a system's internal energy is changed, hence is of vital use in applications of the First Law of Thermodynamics. Conduction is also known as diffusion, not to be confused with diffusion related to the mixing of constituents of a fluid<sup>2</sup>. The direction of heat transfer is from a region of high temperature to another region of lower temperature, and is governed by the Second Law of Thermodynamics. Heat transfer changes the internal energy of the systems from which and to which the energy is transferred. Heat transfer will occur in a direction that increases the entropy of the collection of systems. Heat transfer ceases when thermal equilibrium is reached, at which point all involved bodies and the surroundings reach the same temperature. Thermal expansion is the tendency of matter to change in volume in response to a change in temperature<sup>3</sup>.

## 1.2 Methods and Nature of Prediction

The prediction of behavior in a given physical situation consists of the values of the relevant variables governing the processes of interest. Let us consider a particular example. In a combustion chamber of a certain description, a complete prediction should give us the values of velocity, pressure, temperature, concentrations of the relevant chemical species, etc., throughout the domain of interest; it should also provide the shear stresses, heat fluxes, and mass flow rates at the confining walls of the combustion chamber. The prediction should state how any of these quantities would change in response to proposed changes in geometry, flow rates, fluid properties, etc. Prediction of heat transfer and fluid-flow processes can be obtained by two main methods: **Experimental investigation** and **Theoretical calculation**. We shall briefly consider each and then compare the two.

### 1.2.1 Experimental Investigation

The most reliable information about a physical process is often given by actual measurement. An experimental investigation involving full-scale equipment can be used to predict how identical copies

<sup>1</sup> Mentor Graphics, What They Didn't Teach You in School About Heat Transfer, white paper.

<sup>2</sup> From Wikipedia, the free encyclopedia.

<sup>3</sup> Paul A., Tipler; Gene Mosca (2008), "Physics for Scientists and Engineers, Volume 1 (6th Ed.)", Worth Publishers. pp. 666-670. ISBN 1-4292-0132-0.

of the equipment would perform under the same conditions. Such full-scale tests are, in most cases, prohibitively expensive and often impossible. The alternative then is to perform experiments on small-scale models. The resulting information, however, must be extrapolated to full scale, and general rules for doing this are often unavailable. Further, the small-scale models do not always simulate all the features of the full-scale equipment; frequently, important features such as combustion or boiling are omitted from the model tests. This further reduces the usefulness of the test results. Finally, it must be remembered that there are serious difficulties of measurement in many situations, and that the measuring instruments are not free from errors<sup>4</sup>.

### 1.2.2 Calculation

A theoretical prediction works out the consequences of a *mathematical model*, rather than those of an actual physical model. For the physical processes of interest here, the mathematical model mainly consists of a set of differential equations. If the methods of classical mathematics were to be used for solving these equations, there would be little hope of predicting many phenomena of practical interest. A look at a classical text on heat conduction or fluid mechanics leads to the conclusion that only a tiny fraction of the range of practical problems can be solved in closed form. Fortunately, the development of **numerical methods** and the availability of large digital computers hold the promise that the implications of a mathematical model can be worked out for almost any practical problem. Suppose that we wish to obtain the temperature field in the domain shown. It may be sufficient to know the values of temperature at discrete points of the domain. One possible method is to imagine a grid that fills the domain, and to seek the values of temperature at the grid points. We then construct and solve algebraic equations for these unknown temperatures. The simplification inherent in the use of algebraic equations rather than differential equations is what makes numerical methods so powerful and widely applicable.

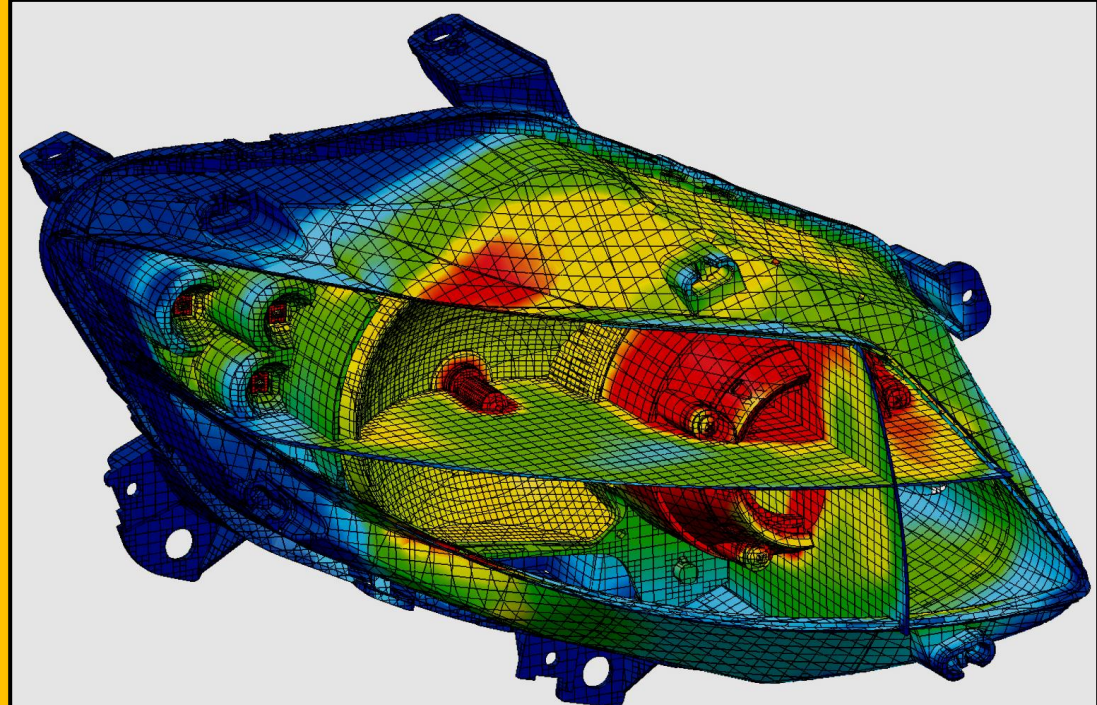


Figure 1.2.1 SmartCells Technology Provides Accurate Analysis Results (Courtesy of FloEFD)

<sup>4</sup> Suhas V. Patankar, "Numerical Heat Transfer and Fluid Flow", McGraw Hill Book Company, 1980.

### 1.3 Choice of Prediction Method

This discussion about the relative merits of computer analysis and experimental investigation is not aimed at recommending computation to the expense of experiment. An appreciation of the strengths and weaknesses of both approaches is essential to the proper choice of the appropriate technique. There is no doubt that experiment is the only method for investigating a new basic phenomenon. In this sense, experiment leads and computation follows. It is in the synthesis of a number of interacting known phenomena that the computation performs more efficiently. Even then, sufficient validation of the computed results by comparison with experimental data is required. On the other hand, for the design of experimental apparatus, preliminary computations are often helpful, and the amount of experimentation can usually be significantly reduced if the investigation is supplemented by computation. An optimal prediction effort should thus be a judicious combination of computation and experiment. The proportions of the two ingredients would depend on the nature of the problem, on the objectives of the prediction, and on the economic and other constraints of the situation<sup>5</sup>. The starting point of any heat-transfer numerical analysis is to define the overall boundary conditions of the problem including the selection of material properties. Once a project is created and the boundary conditions applied, the model needs to be meshed, that is, a computational grid has to be built. Developing a mesh is one of those skills that was left up to CFD specialists<sup>6</sup>. (see [Figure 1.2.1](#)).

### 1.4 Basic Heat Transfer Modes

Heat transfer is the physical act of thermal energy being exchanged between two systems by dissipating heat. Temperature and the flow of heat are the basic principles of heat transfer. The amount of thermal energy available is determined by the temperature, and the heat flow represents movement of thermal energy. On a microscopic scale, the kinetic energy of molecules is the direct relation to thermal energy. As temperature rises, the molecules increase in thermal agitation manifested in linear motion and vibration. Regions that contain higher kinetic energy transfer the energy to regions with lower kinetic energy. Simply put, heat transfer can be grouped into three broad categories: conduction, convection, and radiation. (see [Figure 1.4.1](#)).

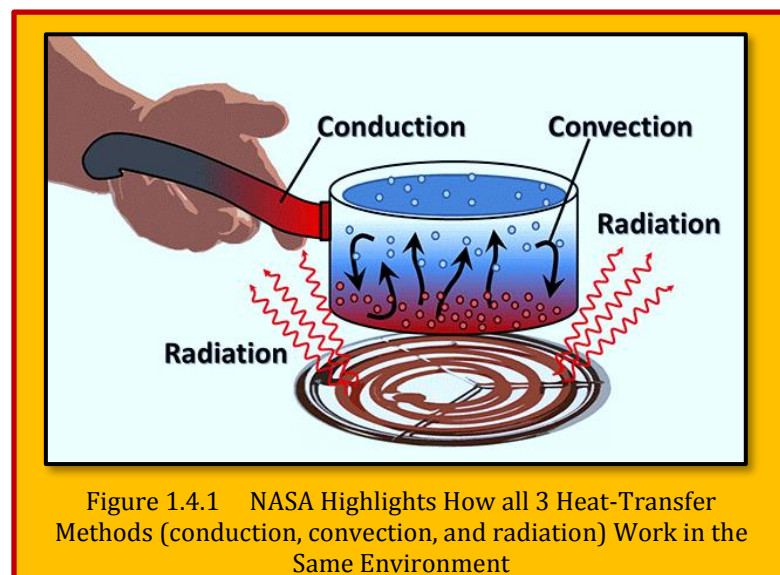


Figure 1.4.1 NASA Highlights How all 3 Heat-Transfer Methods (conduction, convection, and radiation) Work in the Same Environment

#### 1.4.1 Conduction

Conduction transfers heat via direct molecular collision. An area of greater kinetic energy will transfer thermal energy to an area with lower kinetic energy. Higher-speed particles will collide with slower speed particles. The slower-speed particles will increase in kinetic energy as a result. Conduction is the most common form of heat transfer and occurs via physical contact. Examples would be to place your hand against a window or place metal into an open flame. Cross-section and path of travel both play an important part in conduction. The greater the size and length of an object,

<sup>5</sup> See Previous.

<sup>6</sup> Mentor Graphics, What They Didn't Teach You in School About Heat Transfer, white paper.

the more energy that's required to heat it. And the greater the surface area that's exposed, the more heat is lost. Smaller objects with small cross-sections have minimal heat loss. Physical properties determine which materials transfer heat better than others. Specifically, the thermal conductivity coefficient dictates that a metal material will conduct heat better than cloth when it comes to conduction.

#### 1.4.2 Convection

When a fluid, such as air or a liquid, is heated and then travels away from the source, it carries the thermal energy along. This type of heat transfer is called convection. The fluid above a hot surface expands, becomes less dense, and rises. At the molecular level, the molecules expand upon introduction of thermal energy. As temperature of the given fluid mass increases, the volume of the fluid must increase by same factor. This effect on the fluid causes displacement. As the immediate hot air rises, it pushes denser, colder air down. A space heater is a classic convection example (see [Figure 1.4.2](#)) . As the space heater heats the air surrounding it near the floor, the air will increase in temperature, expand, and rise to the top of the room. This forces down the cooler air so that it becomes heated, thus creating a convection current.

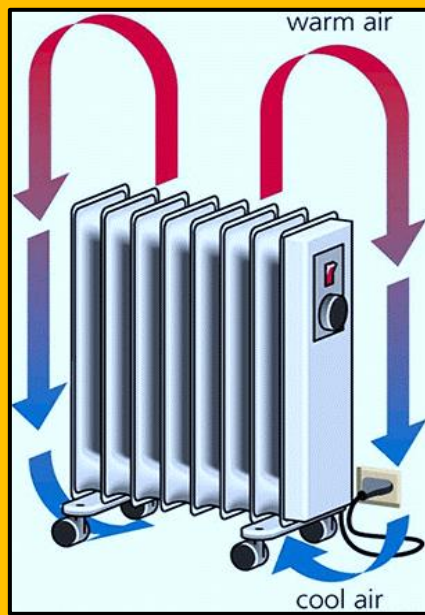


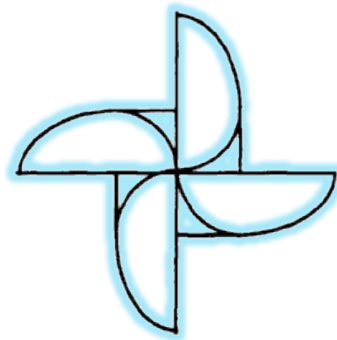
Figure 1.4.2 An Space Heater as Prime Example of Convection



Figure 1.4.3 Typical Solar Panel (Courtesy of Solar City)

### 1.4.3 Radiation

Thermal radiation generates from the emission of electromagnetic waves. These waves carry the energy away from the emitting object. Radiation occurs through a vacuum or any transparent medium (either solid or fluid). Thermal radiation is the direct result of random movements of atoms and molecules in matter. Movement of the charged protons and electrons results in the emission of electromagnetic radiation. All materials radiate thermal energy based on their temperature. The hotter an object, the more it will radiate. The sun is a clear example of heat radiation that transfers heat across the solar system. At normal room temperatures, objects radiate as infrared waves. The temperature of the object affects the wavelength and frequency of the radiated waves. As temperature increases, the wavelengths within the spectra of the emitted radiation decrease and emit shorter wavelengths with higher-frequency radiation. Solar cell or photovoltaic cell, converts the energy of light into electricity via the photovoltaic effect. Light is absorbed and excites the electron to a higher energy state and the electric potential is produced by the separation of charges. Efficiency of solar panels has risen in recent years. In fact, those currently being produced by SolarCity, a company co-founded by Elon Musk, are at 22%. Emissivity is defined as an object's effectiveness in emitting energy as thermal radiation. It is the ratio, at a given temperature, of the thermal radiation from a surface to the radiation from an ideal black surface as determined by the Stefan-Boltzmann law. (see [Figure 1.4.3](#)).



## 2 Classical Heat Transfer

### 2.1 Preliminaries

The heat transfer is concerns with conservation of Energy Equation, where there is a temperature gradient. While, the CFD is all about applying techniques from mathematics to address the operators involve with governing equations of fluid motions, heat transfer is more about understanding the physics. Basically, one is math and the other is engineering physics. In majority of applications, the flow is coupled in nature, therefore, the energy and momentum equations has to be solved simultaneously. The Typical design problems involve the determination of overall heat transfer coefficient, e.g. for a car radiator; temperature profile in a system, e.g. in a gas turbine; Temperature distribution (related to thermal stress), e.g. in the walls of a spacecraft; Temperature response in time dependent heating/cooling problems, e.g. engine cooling, or how fast does a car heat up in the sun and how is it affected by the shape of the windshield (see [Figure 2.1.1](#)).

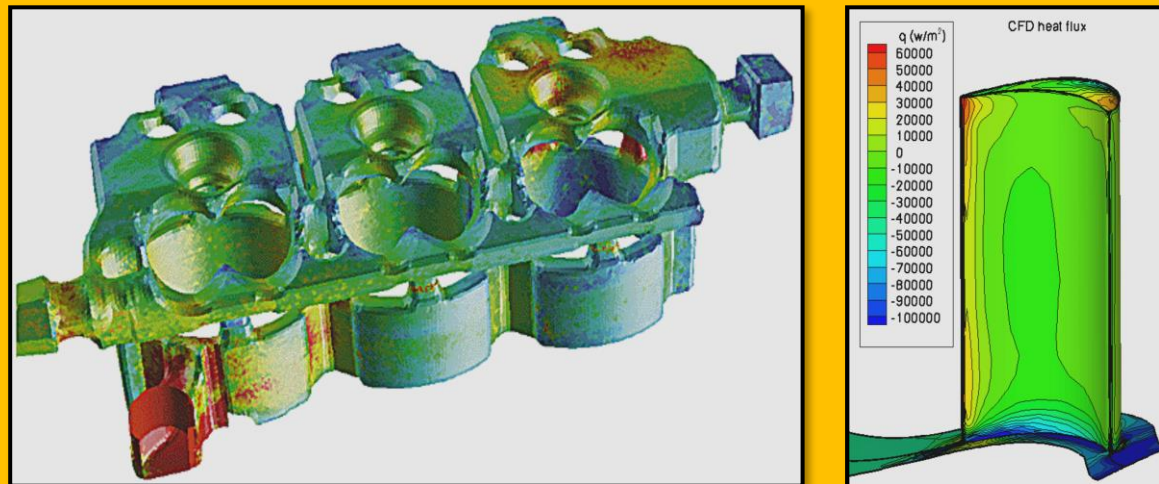


Figure 2.1.1 Heat Transfer Effects in Cooling Jacket and Turbine Blade

### 2.2 The General Transport Equation

This brief journey through some of the relevant differential equations has indicated that all the dependent variables of interest here seem to obey a generalized conservation principle. If the dependent variable is denoted by  $\varphi$ , the general differential equation is

$$\underbrace{\frac{\partial}{\partial t}(\rho\varphi)}_{\text{Transient}} + \underbrace{\nabla(\rho u\varphi)}_{\text{Convection}} = \underbrace{\nabla \cdot (\Gamma_\varphi \nabla \varphi)}_{\text{Diffusion}} + \underbrace{S_\varphi}_{\text{Source}}$$

[Eq. 2.2.1](#)

where  $\Gamma$  is the diffusion coefficient, and  $S$  is the source term where they are specific to a particular meaning of  $\varphi$ . The four terms in the general differential equation are the unsteady term, the convection term, the diffusion term, and the source term. The dependent variable  $\varphi$  can stand for a variety of different quantities, such as the mass fraction of a chemical species, the enthalpy or the temperature, a velocity component, the turbulence kinetic energy, or a turbulence length scale. Accordingly, for each of these variables, an appropriate meaning will have to be given to the diffusion coefficient  $\Gamma$  and the source term  $S$ . "Not all diffusion fluxes are governed by the gradient of the relevant variable. The use of  $\text{div}(\Gamma \text{ grad } \varphi)$  as the diffusion term does not, however, limit the general

equation to gradient-driven diffusion processes. Whatever cannot be fitted into the nominal diffusion term can always be expressed as a part of the source term; in fact, the diffusion coefficient  $\Gamma$  can even be set equal to zero if desired. A gradient-diffusion term has been explicitly included in the general equation because most dependent variables do require a prominent diffusion term of this nature. The density appearing in above equation may be related, via an equation of state, to variables such as mass fraction and temperature. These variables and the velocity components obey the general differential equation<sup>7</sup>. Further, the flow field should satisfy an additional constraint, namely, the mass conservation or the continuity equation, which is

$$\frac{\partial \rho}{\partial t} + \nabla \cdot (\rho \mathbf{u}) = 0 \quad \text{Eq. 2.2.2}$$

### 2.3 Energy Equation

The energy equation in its most general form contains a large number of influences. Since we are primarily interested in the form rather than in the details of the equation, it will be sufficient to consider some restricted cases<sup>8</sup>. For a steady low-velocity flow with negligible viscous dissipation, the energy equation can be written as

$$\underbrace{\frac{\partial(\rho C_p T)}{\partial t}}_0 + \frac{\partial}{\partial x_j} \left( \rho C_p u_j T - k \frac{\partial T}{\partial x_j} \right) = \underbrace{\frac{\partial p}{\partial t} + u_j \frac{\partial p}{\partial x_j} + \tau_{ij} \frac{\partial u_j}{\partial x_j}}_0$$

**Eq. 2.3.1**

where  $k$  is the thermal conductivity,  $T$  is the temperature. The term  $\text{div}(k \text{ grad } T)$  represents the influence of conduction heat transfer within the fluid, according to the *Fourier law* of conduction. The steady heat-conduction situation, in tensor notation, is obtained by setting the velocity  $u_j$  to zero; thus,

$$\nabla \cdot (k \nabla T) = 0 \quad \text{Eq. 2.3.2}$$

Constant  $k$  yields to

$$\nabla^2 T = 0 \quad \text{Eq. 2.3.3}$$

### 2.4 Newton's 2<sup>nd</sup> Law and Momentum Equation

The differential equation governing the conservation of momentum for a Newtonian fluid can be written along similar lines; however, the complication is greater because both shear and normal stresses must be considered and because the Stokes viscosity law is more complicated "than Fick's law or Fourier's law. With  $u$  denoting the velocity vector,  $P$  is the pressure, and  $g$  is the body force, we write the corresponding momentum equation as

$$\rho \frac{D \mathbf{u}}{Dt} = \rho \mathbf{g} - \nabla P + \nabla \cdot \boldsymbol{\tau}_{ij} \quad , \quad \boldsymbol{\tau}_{ij} = \mu \left( \frac{\partial u_i}{\partial x_j} + \frac{\partial u_j}{\partial x_i} \right) - \frac{2}{3} \mu \delta_{ij} \frac{\partial u_k}{\partial x_k}$$

or

$$\frac{\partial(\rho u_i)}{\partial t} + \frac{\partial}{\partial x_j} (\rho u_i u_j + P \delta_{ij} - \tau_{ij}) = \rho g_i \quad \text{Eq. 2.4.1}$$

<sup>7</sup> Suhas V. Patankar, " Numerical Heat Transfer and Fluid Flow", Mc Graw Hill Book Company, 1980.

<sup>8</sup> See Previous.

## 2.5 Time-Averaged Equations for Turbulent Flow

Turbulent flows are commonly encountered in practical applications. It is the time-mean behavior of these flows that is usually of practical interest. Therefore, the equations for unsteady laminar flow are converted into the time averaged equations for turbulent flow by an averaging operation in which it is assumed that there are rapid and random fluctuations about the mean value. The additional terms arising from this operation are the so-called Reynolds stresses, turbulent heat flux, turbulent diffusion flux, etc. To express these fluxes in terms of the mean properties of the flow is the task of a turbulence model. Many turbulence models employ the concept of a turbulent viscosity or a turbulent diffusivity to express the turbulent stresses and fluxes. The result is that the time averaged equations for turbulent flow have the same appearance as the equations for laminar flow, but the laminar exchange coefficients such as viscosity, diffusivity, and conductivity are replaced by effective (i.e., laminar plus turbulent) exchange coefficients. From a computational viewpoint, a turbulent flow within this framework is equivalent to a laminar flow with a rather complicated prescription of viscosity. (The same idea is applicable to non-Newtonian flows, which can be thought of as flows in which the viscosity depends on the velocity gradient.)

## 2.6 Turbulence-Kinetic-Energy Equation

The currently popular “**two-equation models**” of turbulence [Launder and Spalding, 1972, 1974] employ, as one of the equations, the equation for the kinetic energy  $k$  of the fluctuating motion, which reads

$$\frac{\partial}{\partial t}(\rho k) + \nabla \cdot (\rho u k) = \nabla \cdot (\Gamma_k \nabla k) + G - \rho \varepsilon \quad \text{Eq. 2.6.1}$$

where  $\Gamma_k$  is the diffusion coefficient for  $k$ ,  $G$  is the rate of generation of turbulence energy, and  $\varepsilon$  is the kinematic rate of dissipation. The quantity  $G - \rho \varepsilon$  is the net source term in the equation. A similar differential equation governs the variable  $\varepsilon$ .

## 2.7 Modes of Heat Transfer

There are three modes of heat transfer, namely, **Conduction**, **Convection** and **Radiation**. In most practical situations, they appear in combination<sup>9</sup>.

### 2.7.1 Physical Perspectives of Conduction

At mention of the word conduction, we should immediately conjure up concepts of atomic and molecular activity, for it is processes at these levels that sustain this mode of heat transfer. Conduction may be viewed as the transfer of energy from the more energetic to the less energetic particles of a substance due to interactions between the particles<sup>10</sup>. The physical mechanism of conduction is most easily explained by considering a gas and using ideas familiar from your thermodynamics background. Consider a gas in which there exists a temperature gradient and assume that there is no bulk, or macroscopic, motion. The gas may occupy the space between two surfaces that are maintained at different temperatures, as shown in **Figure 2.7.1**. We associate the temperature at any point with the energy of gas molecules in proximity to the point. This energy is related to the random translational motion, as well as to the internal rotational and vibrational motions, of the molecules. Higher temperatures are associated with higher molecular energies, and when neighboring molecules collide, as they are constantly doing, a transfer of energy from the more

<sup>9</sup> Bakker, Ander, “Applied Computational Fluid Dynamics”, Lecture 13 - Heat Transfer, 2002-2006.

<sup>10</sup> F.P., Incropera, D.P., DeWitt, T.L., Bergman, A.S., Lavine, “Fundamentals of Heat and Mass Transfer”, 6<sup>th</sup> edition, John Wiley and Sons, 2007.

energetic to the less energetic molecules must occur. In the presence of a temperature gradient, energy transfer by conduction must then occur in the direction of decreasing temperature.

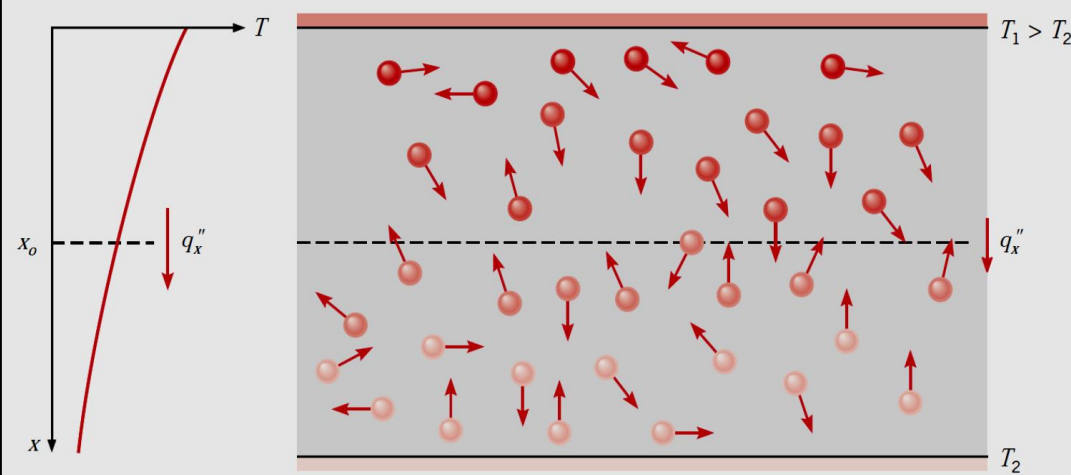


Figure 2.7.1 1D Heat Transfer by Conduction (Diffusion of Energy)

This would even be true in the absence of collisions, as is evident from [Figure 2.7.1](#). The hypothetical plane at is constantly being crossed by molecules from above and below due to their random motion. However, molecules from above are associated with a larger temperature than those from below, in which case there will be a net transfer of energy in the positive  $x$  direction. Collisions between molecules enhance this energy transfer. We may speak of the net transfer of energy by random molecular motion as a diffusion of energy. The situation is much the same in liquids, although the molecules are more closely spaced and the molecular interactions are stronger and more frequent. Similarly, in a solid, conduction may be attributed to atomic activity in the form of lattice vibrations. The modern view is to ascribe the energy transfer to lattice waves induced by atomic motion. In an electrical nonconductor, the energy transfer is exclusively via these lattice waves; in a conductor it is also due to the translational motion of the free electrons. Examples of conduction heat transfer are multitude. The exposed end of a metal spoon suddenly immersed in a cup of hot coffee will eventually be warmed due to the conduction of energy through the spoon. On a winter day there is significant energy loss from a heated room to the outside air. This loss is principally due to conduction heat transfer through the wall that separates the room air from the outside air. It is possible to quantify heat transfer processes in terms of appropriate rate equations. These equations may be used to compute the amount of energy being transferred per unit time. For heat conduction, the rate equation is known as [\*Fourier's law\*](#). For the one-dimensional plane wall shown in [Figure 2.7.2](#), having a temperature distribution  $T(x)$ , the rate equation is expressed as the heat flux  $q_x$  ( $\text{W/m}^2$ ) is the heat transfer rate in the  $x$  direction per unit area perpendicular to the direction of transfer, and it is proportional to the temperature gradient,  $dT/dx$ , in this direction. The parameter  $k$  is a transport property known as the thermal conductivity ( $\text{W/m K}$ ) and is a characteristic of the

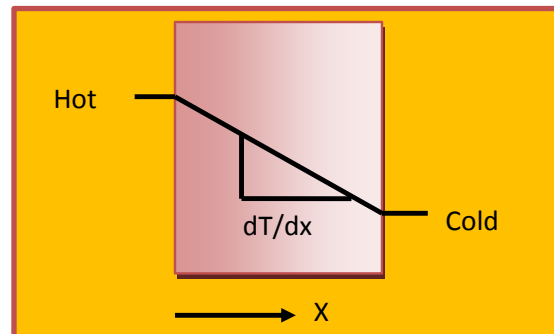


Figure 2.7.2 Conduction Heat Transfer on a Slab

wall material. The minus sign is a consequence of the fact that heat is transferred in the direction of decreasing temperature. Under the steady-state conditions shown in [Figure 2.7.2](#), where the temperature distribution is linear, the temperature gradient may be expressed as and the heat flux is then

$$q_{\text{con}} = -kA\nabla T \quad \text{Eq. 2.7.1}$$

Where  $k(x, y, z, T)$  is the thermal conductivity of medium. [Figure 2.7.2](#) depicts a conduction heat transfer on a slab.

## 2.7.2 Convection Phenomena

The convection heat transfer mode is comprised of two mechanisms. In addition to energy transfer due to random molecular motion (diffusion), energy is also transferred by the bulk, or macroscopic, motion of the fluid<sup>11</sup>. This fluid motion is associated with the fact that, at any instant, large numbers of molecules are moving collectively or as aggregates. Such motion, in the presence of a temperature gradient, contributes to heat transfer. Because the molecules in the aggregate retain their random motion, the total heat transfer is then due to a superposition of energy transport by the random motion of the molecules and by the bulk motion of the fluid. It is customary to use the term convection when referring to this cumulative transport and the term advection when referring to transport due to bulk fluid motion. We are especially interested in convection heat transfer, which occurs between a fluid in motion and a bounding surface when the two are at different temperatures. Consider fluid flow over the heated surface of [Figure 2.7.3](#). A consequence of the fluid surface interaction is the development of a region in the fluid through which the velocity varies from zero at the surface to a finite value  $u_\infty$ , associated with the flow. This region of the fluid is known as the hydrodynamic, or velocity, boundary layer. Moreover, if the surface and flow temperatures differ, there will be a region of the fluid through which the temperature varies from  $T_s$  at  $y = 0$  to  $T_\infty$  in the outer flow. This region, called the **thermal boundary layer**, may be smaller, larger, or the same size as that through which the velocity varies. In any case, if  $T_s > T_\infty$  convection heat transfer will occur from the surface to the outer flow.

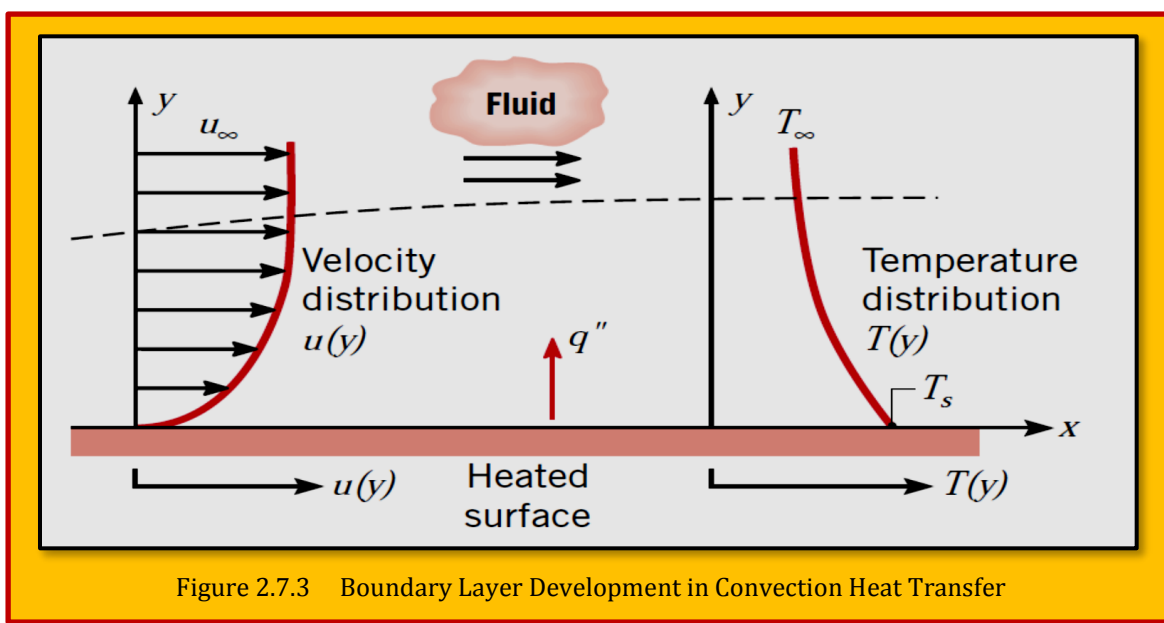


Figure 2.7.3 Boundary Layer Development in Convection Heat Transfer

<sup>11</sup> F.P., Incropera, D.P., DeWitt, T.L, Bergman, A.S, Lavine, "Fundamentals of Heat and Mass Transfer", 6<sup>th</sup> edition, John Wiley and Sons, 2007.

The convection heat transfer mode is sustained both by random molecular motion and by the bulk motion of the fluid within the boundary layer. The contribution due to random molecular motion (diffusion) dominates near the surface where the fluid velocity is low. In fact, at the interface between the surface and the fluid ( $y = 0$ ), the fluid velocity is zero and heat is transferred by this mechanism only. The contribution due to bulk fluid motion originates from the fact that the boundary layer grows as the flow progresses in the  $x$  direction. In effect, the heat that is conducted into this layer is swept downstream and is eventually transferred to the fluid outside the boundary layer. Appreciation of boundary layer phenomena is essential to understanding convection heat transfer. It is for this reason that the discipline of fluid mechanics will play a vital role in our later analysis of convection. The rate of heat transfer,  $q$ , can be written in the form of Newton's law of cooling as

$$q_{\text{cov}} = hA(T_s - T_\infty)$$

#### Eq. 2.7.2

As the input speed of air increases, the change in temperature increases, and the shape of the temperature profile narrows to thinner region.

#### 2.7.2.1 Convection Types

Convection heat transfer may be classified according to the nature of the flow. We speak of **forced convection** when the flow is caused by external means, such as by a fan, a pump, or atmospheric winds. As an example, consider the use of a fan to provide forced convection air cooling of hot electrical components on a stack of printed circuit boards; or flow over warm body as depicted in **Figure 2.7.4**. In contrast, for **free (natural) convection** the flow is induced by buoyancy forces, which are due to density differences caused by temperature variations in the fluid (see **Figure 2.7.5**). An example is the free convection heat transfer that occurs from hot components on a vertical array of circuit boards. Air that makes contact with the components experiences an increase in temperature and hence a reduction in density. Since it is now lighter than the surrounding air, buoyancy forces induce a vertical motion for which warm air ascending from the boards is replaced by an inflow of cooler ambient air. While we have presumed pure forced convection and pure natural convection, conditions corresponding to **mixed (combined) force and natural convection** may exist. For example if the velocities associated with the flow of are small and/or buoyancy forces are large, a secondary flow that is comparable to the imposed forced flow could be induced. In this case, the buoyancy-induced flow would be normal to the forced flow and could have a significant effect on convection heat transfer from the components. An example would of mixed convection would result if a fan were used to force air upward between the circuit boards, thereby assisting the buoyancy flow, or downward, thereby opposing the buoyancy flow. We have described the convection heat transfer mode as energy transfer occurring within a fluid due to the combined effects of conduction and bulk fluid motion. Typically, the energy that is being transferred is the sensible, or internal thermal, energy of the fluid. However, there are convection processes for which there is, in addition, latent heat exchange. This latent heat exchange is generally associated with a phase change between the liquid and vapor states of

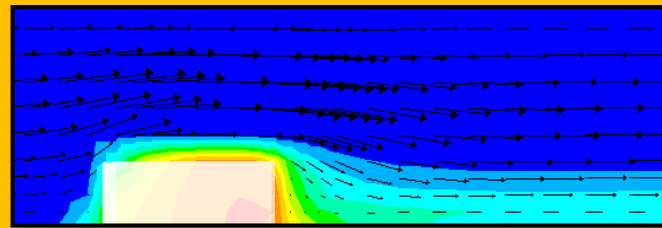


Figure 2.7.4 Cold flow Pass a Warm Body (Forced Convection)

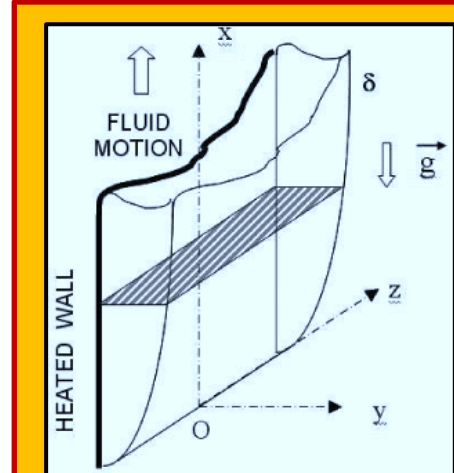


Figure 2.7.5 Velocity and Temperature in a Heated Vertical Wall

the fluid. Two special cases of interest in this text are **boiling** and **condensation**. For example, convection heat transfer results from fluid motion induced by vapor bubbles generated at the bottom of a pan of boiling water or by the condensation of water vapor on the outer surface of a cold water pipe. Regardless of the particular nature of the convection heat transfer process, the appropriate rate equation is of the form as described before.

### 2.7.2.2 Free (Natural) Convection

For low-speed flow or free convection where gravity forces are comparable to inertia and viscous forces, and cannot be neglected. There is a significant density changes due to temperature changes. In that case,

$$\rho = \rho_{\infty} + \Delta\rho \approx \rho_{\infty}(1 - \beta\Delta T), \quad \beta = -\frac{1}{\rho} \left( \frac{\partial \rho}{\partial T} \right)_p$$

now the Navier - Stoke equation becomes :

Eq. 2.7.3

$$\rho_{\infty} \frac{D\mathbf{u}_i}{Dt} \approx -\nabla p - \rho_{\infty} g[1 + \beta(T - T_{\infty})] + \nabla \cdot \tau_{i,j} \quad i, j = 1, 3$$

Where we written the viscous terms in the short form for convenience, and  $\beta$  is coefficient of thermal expansion. The subscripts ( $\infty$ ) denotes the free stream conditions. This is fundamental to the study of low-speed or natural convection problems. Together with Energy equation (coupled of course) they form a set of equation for natural convection to be solved. Laminar free convection problem on a vertical wall (see [Figure 2.7.5](#)) has been plentifully investigated considering constant wall heat flux or wall temperature. Let us consider 2D, incompressible with constant properties, and non-negligible source terms (buoyancy) as:

$$\begin{aligned} \frac{\partial u}{\partial x} + \frac{\partial v}{\partial y} &= 0, \quad u \frac{\partial u}{\partial x} + v \frac{\partial v}{\partial y} = g_x \beta(T - T_{\infty}) + v \frac{\partial^2 u}{\partial y^2} \\ \text{B.C.} \quad u(x, 0) &= v(x, 0) = u(x, \infty) = 0 \\ u \frac{\partial T}{\partial x} + v \frac{\partial T}{\partial y} &= \alpha \frac{\partial^2 T}{\partial y^2} \quad \text{subject to B.C.} \quad T(x, 0) = T_w(x), T(x, \infty) = T_{\infty} = \text{constant} \end{aligned}$$

### Eq. 2.7.4

As a natural convection, the analysis of buoyancy-driven flow between eccentric annulus cylinders is a problem which currently receives considerable attention from researchers such as [Hazar and Abbasian]<sup>12</sup>. Examples are the design of furnaces, in the operation of solar collectors, which contribute to energy losses minimization to increase collector efficiency, nuclear reactor insulation, the determination of the requirements for aircraft cabin insulation are just to name the few.

### 2.7.2.3 Mixed Convection

Mixed convection, occurs when natural convection and forced convection mechanisms act together to transfer heat. This is also defined as situations where both pressure forces and buoyant forces interact. How much each form of convection contributes to the heat transfer is largely determined by the flow, temperature, geometry, and orientation. The Combined forced and natural convection can be generally described in one of three ways:

<sup>12</sup> Mohammad Ali Hazar, Ali Akbar Abbasian, "Numerical analysis of the natural convection in horizontal cylindrical annuli", International Academic Journal of Science and Engineering Vol. 3, No. 5, 2016, pp. 68-76.

- The first case is when natural convection aids forced convection. This is seen when the buoyant motion is in the same direction as the forced motion, thus enhancing the heat transfer. An example of this would be a fan blowing upward on a hot plate. Since heat naturally rises, the air being forced upward over the plate adds to the heat transfer.
- The second case is when natural convection acts in the opposite way of the forced convection. Consider a fan forcing air upward over a cold plate. In this case, the buoyancy force of the cold air naturally causes it to fall, but the air being forced upward opposes this natural motion, keeping the cool air hovering around the cold plate. This, in turn, diminishes the amount of heat transfer.
- The third case is referred to as transverse flow. This occurs when the buoyant motion acts perpendicular to the forced motion. (see [Figure 2.7.6](#)). This enhances fluid mixing, and enhances the heat transfer. An example of this is air flowing horizontally over a hot or cold pipe. This can encourage phase changes, which often creates a very high heat transfer coefficient. For example, steam leaving a boiler can pass through a pipe that has a fan blowing over it, cooling the steam back to a saturated liquid that all.

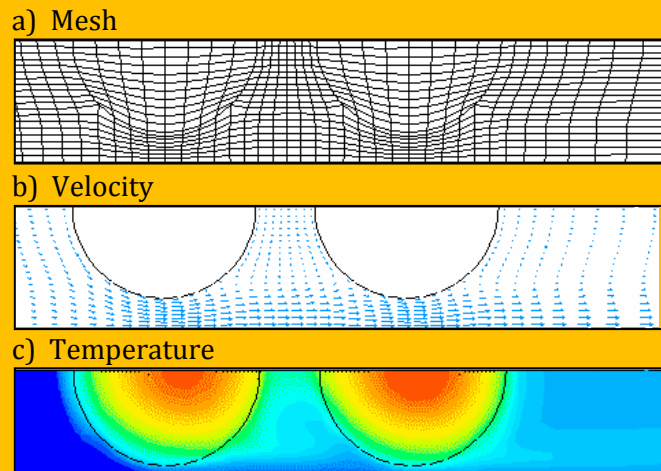


Figure 2.7.6 a) Mesh b) Velocity vectors c) Temperature contours

Cases of combined forced and natural convection is often seen in very-high-power-output devices where the forced convection is not enough to dissipate all of the heat necessary. At this point, combining natural convection with forced convection will often deliver the desired results. Examples of these processes are nuclear reactor (cooling towers) technology and some aspects of electronic cooling<sup>13</sup>.

$$Nu = \frac{h_c L}{k} \quad \text{Convective heat transfer Coefficient}$$

$$Pe = \frac{\rho V L c_p}{k} = Re Pr \quad \text{Ratio of heat transfer by convection to conduction used in forced}$$

$$St = \frac{h_c}{\rho V c_p} = \frac{Nu}{Re Pr} \quad \text{Ratio of heat transfer at surface to that transported by fluid}$$

$$Pr = \frac{\mu c_p}{k} = \frac{\nu}{\alpha} \quad \text{Ratio of momentum to thermal diffusion}$$

$$Ra = Gr Pr = \frac{g \Delta \rho L^3}{\mu \alpha} = \frac{g \beta \Delta T L^3}{\nu \alpha}$$

<sup>13</sup> From Wikipedia, the free encyclopedia.

### 2.7.3 Dimensionless Parameters

To refresh, the important dimensionless parameters are described above.

### 2.7.4 Convection vs. Conduction

In a body of fluid that is heated from underneath its container, conduction and convection can be considered to compete for dominance. If heat conduction is too great, fluid moving down by convection is heated by conduction so fast that its downward movement will be stopped due to its buoyancy, while fluid moving up by convection is cooled by conduction so fast that its driving buoyancy will diminish. On the other hand, if heat conduction is very low, a large temperature gradient may be formed and convection might be very strong. The **Rayleigh number (Ra)** is the product of the **Grashof** and **Prandtl** numbers. It is a measure which determines the relative strength of conduction and convection. The Rayleigh number can be understood as the ratio between the rate of heat transfer by convection to the rate of heat transfer by conduction; or, equivalently, the ratio between the corresponding timescales (i.e. conduction timescale divided by convection timescale), up to a numerical factor. This can be seen as follows, where all calculations are up to numerical factors depending on the geometry of the system. The buoyancy force driving the convection is roughly  $g\Delta\rho L^3$ , so the corresponding pressure is roughly  $g\Delta\rho L$ . In steady state, this is canceled by the shear stress due to viscosity, and therefore roughly equals  $\mu V/L = \mu / T_{\text{conv}}$ , where  $V$  is the typical fluid velocity due to convection and  $T_{\text{conv}}$  the order of its timescale. The conduction timescale, on the other hand, is of the order of  $T_{\text{cond}} = L^2 / \alpha$ . Convection occurs when the Rayleigh number is above 1,000–2,000.

### 2.7.5 Radiation

Thermal radiation is energy emitted by matter that is at a nonzero temperature. Although we will focus on radiation from solid surfaces, emission may also occur from liquids and gases. Regardless of the form of matter, the emission may be attributed to changes in the electron configurations of the constituent atoms or molecules. **The energy of the radiation field is transported by electromagnetic waves (or alternatively, photons).** While the transfer of energy by conduction or convection requires the presence of a material medium, radiation does not. In fact, radiation transfer occurs most efficiently in a vacuum. Consider radiation transfer processes for the surface of **Figure 2.7.7**. Radiation that is emitted by the surface originates from the thermal energy of matter bounded by the surface, and the rate at which energy is released per unit area ( $\text{W/m}^2$ ) is termed the surface emissive power  $E$ . There is an upper limit to the emissive power, which is prescribed by the Stefan-Boltzmann law

$$E_b = \sigma T_s^4 \quad \text{Eq. 2.7.5}$$

where  $T_s$  is the absolute temperature (K) of the surface and  $\sigma$  is the Stefan-Boltzmann constant ( $5.67 \times 10^{-8} \text{ W/m}^2\text{K}$ ). Such a surface is called an ideal radiator or blackbody. The heat flux emitted by a real surface is less than that of a blackbody at the same temperature and is given by

$$q_{\text{rad}} = \sigma A(T_1^4 - T_2^4) \quad \text{Eq. 2.7.6}$$

Where  $\sigma$  is Stephan-Boltzmann constant,  $T_1$  is the temperature of the black body and  $T_2$  is the surface temperature of the closure. It is in effect the transfer of energy by electromagnetic waves between surfaces with different temperatures, separated by a medium that is at least partially transparent to the (infrared) radiation. Radiation is especially important at high temperatures, and for black bodies. It is easy to envision cases in which all three modes of heat transfer are present, as in **Figure 2.7.8**. In this case the heat conducted through the plate is removed from the plate surface by a combination of convection and radiation. An energy balance would give

$$-\frac{dA}{dy} \left. \frac{dT}{dy} \right|_{\text{wall}} = hA(T_w - T_\infty) + F_e F_G \sigma A (T_w^4 - T_s^4) \quad \text{Eq. 2.7.7}$$

where  $F_e$  is the emissivity function, and  $F_G$  is the geometric "view factor" function, and  $T_s$  = temperature of surroundings  $T_w$  = surface temperature  $T_\infty$  = fluid temperature To apply the science of heat transfer to practical situations, a thorough knowledge of all three modes of heat transfer must be obtained.

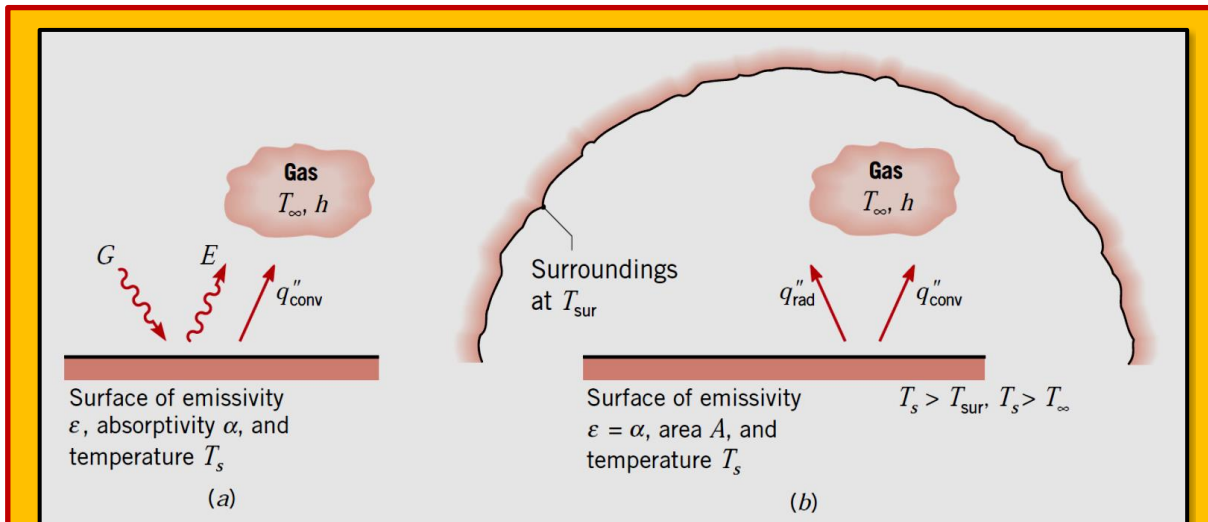


Figure 2.7.7 Radiation Exchange: (a) at a surface and (b) between a surface and large surroundings

### 2.7.5.1 Radiation Properties

When radiant energy strikes a material surface, part of the radiation is reflected, part is absorbed, and part is transmitted, as shown in **Figure 2.7.9**. We define the reflectivity  $\rho$  as the fraction reflected, the absorptivity  $\alpha$  as the fraction absorbed, and the transmissivity  $\tau$  as the fraction transmitted<sup>14</sup>. Thus

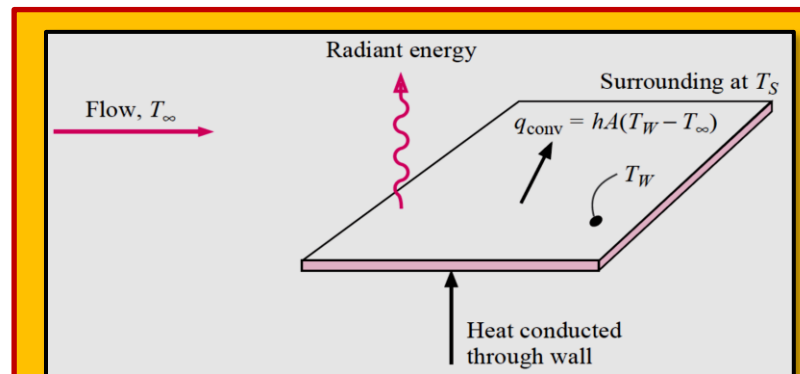


Figure 2.7.8 Combination of Conduction, Convection, and Radiation Heat Transfer

$$\rho + \alpha + \tau = 1$$

$$\text{Eq. 2.7.8}$$

<sup>14</sup> F.P., Incropera, D.P., DeWitt, T.L, Bergman, A.S, Lavine, "Fundamentals of Heat and Mass Transfer", 6<sup>th</sup> edition, John Wiley and Sons, 2007.

Most solid bodies do not transmit thermal radiation, so that for many applied problems the transmissivity may be taken as zero. Two types of reflection phenomena may be observed when radiation strikes a surface. If the angle of incidence is equal to the angle of reflection, the reflection is called **specular**. On the other hand, when an incident beam is distributed uniformly in all directions after reflection, the reflection is called **diffuse**. Note that a specular reflection presents a mirror image of the source to the observer. No real surface is either specular or diffuse. An ordinary mirror is quite specular for visible light, but would not necessarily be specular over the entire wavelength range of thermal radiation. Ordinarily, a rough surface exhibits diffuse behavior better than a highly polished surface. Similarly, a polished surface is more specular than a rough surface. The influence of surface roughness on thermal radiation properties of materials is a matter of serious concern and remains a subject for continuing research. The emissive power of a body  $E$  is defined as the energy emitted by the body per unit area and per unit time<sup>15</sup>.

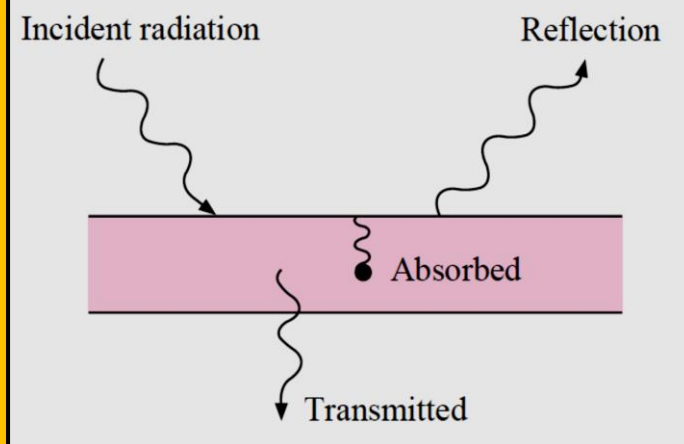


Figure 2.7.9 Effects of incident radiation

#### 2.7.5.2 Radiation Models

There are different models to provide radiation with or without participating mediums. For participating media problem, a network of patches or beams definitions to build view factors. This uses a CFD volume mesh to facilitate the calculation, hence all patches must lie within or on the surface of the enclosing CFD mesh<sup>16</sup>. **The Discrete Transfer Radiation Model (DTRM)** and **Discrete Ordinates (DO)** Radiation Model, are two of the chief investigators in radiation. You should include radiative heat transfer in your simulation when the radiant heat flux,  $q_{rad}$  is large compared to the heat transfer rate due to convection or conduction. Typically this will occur at high temperatures where the fourth-order dependence of the radiative heat flux on temperature implies that radiation will dominate<sup>17</sup>. For details of each model and their respective advantages and limitations, please refer to<sup>18</sup>.

## 2.8 Phase Transition

Phase transition or phase change, takes place in a thermodynamic system from one phase or state of matter to another one by heat transfer. Phase change examples are the melting of ice or the oiling of water. The Mason equation explains the growth of a water droplet based on the effects of heat transport on evaporation and condensation. Types of phase transition occurring in the four fundamental states of matter, include:

- **Solid** - Deposition, freezing and solid to solid transformation.
- **Gas** - Boiling/evaporation, recombination/deionization, and sublimation.

<sup>15</sup> J. P. Holman, "Heat Transfer", 10<sup>th</sup> edition, The Mc Grow Hills companies.

<sup>16</sup> CD-Adapco® Methodology, Star-CD Version 4.02, 2006.

<sup>17</sup> FLUENT 6.3 User's Guide

<sup>18</sup> See previous.

- **Liquid** - Condensation and melting/fusion.
- **Plasma** - Ionization.

A prime example is liquids like water, in three phases of **Boiling**, **Condensation** and **Melting**. Boiling occurs when the boiling point of a substance is the temperature at which the vapor pressure of the liquid equals the pressure surrounding the liquid<sup>19</sup> and the liquid evaporates resulting in an abrupt change in vapor volume. Condensation is when a vapor is cooled and changes its phase to a liquid and the Melting is a physical process that results in the phase transition of a substance from a solid to a liquid.

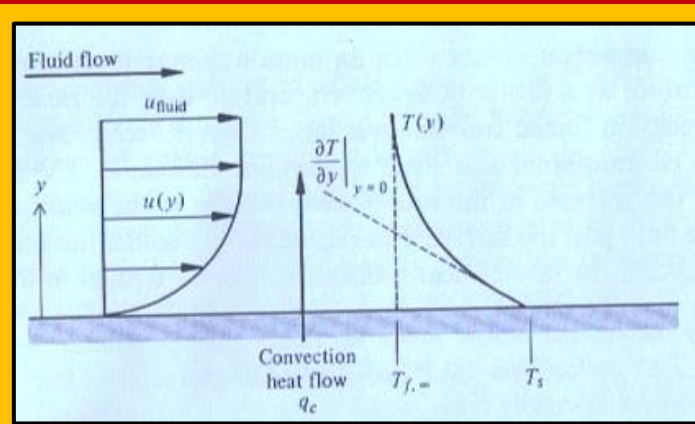


Figure 2.8.1 Relationship Between Conduction and Convection at the Wall

## 2.9 Conjugate Heat Transfer (CHT)

Conjugate heat transfer refers to ability to compute conduction of heat through solids, coupled with convective heat transfer in fluids. Either the solid zones, or fluid zones or both may contain the heat source. Coupled boundary zones are available for wall regions. Another example is 2D heat exchanger/condenser, where the velocity vectors and temperature contours are shown in [Figure 2.7.6](#). [Figure 2.9.1](#) shows the temperature profile for coolant flowing over fuel rods that generate heat. [Figure 2.8.1](#) shows a heated plate cooled by a stream of air flowing over it with corresponding velocity and temperature B.L. distribution. The velocity,  $u(y)$ , decreases in the direction toward the surface as the result of viscose forces. Since the velocity of the fluid layer adjacent to the wall is zero, the heat transfer per unit area between the surface and this fluid must be by conduction alone.

$$\frac{q}{A} = -k \frac{\partial T}{\partial y} \Big|_{y=0} = h (T_s - T_\infty) \quad \text{Eq. 2.9.1}$$

Although this viewpoint suggest that the process can be viewed as conduction, the temperature gradient as the surface,  $(dT/dy)_{y=0}$ , is determined by the rate at which the fluid farther from the wall can transport the energy into the main stream. Thus the temperature gradient at the wall depends on the flow field, with higher velocities able to produce larger temperature gradients and higher rate of heat transfer. At the same time, however, the thermal conductivity of the fluid plays a role, as an example, the value of  $k$  for water is an order of magnitude larger than that of air. Thus convection heat transfer coefficient for water is larger than of air.<sup>20</sup>

<sup>19</sup> David. E. Goldberg (1988), "3,000 Solved Problems in Chemistry (1st ed.)", McGraw-Hill. ISBN 0-07-023684-4. Section 17.43, page 321.

<sup>20</sup> Laboratory for Product and Process Design, LPPD-Project 12/31/04.

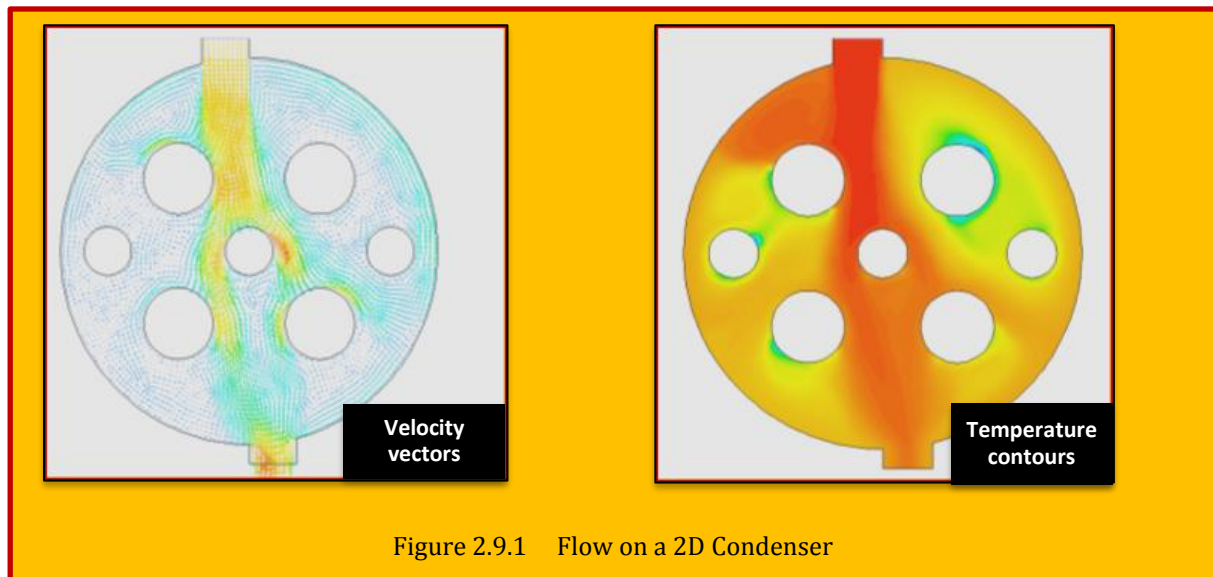


Figure 2.9.1 Flow on a 2D Condenser

## 2.10 Coupling & De-Coupling of Governing Equations

The partial governing PDE are coupled and nonlinear, but there are exceptions. Remembering the energy equation as,

$$\rho C_p \frac{DT}{Dt} = \frac{Dp}{Dt} + \nabla \cdot (k \nabla T) + \varphi \quad \text{where} \quad \varphi = \tau_{ij} \frac{\partial u_i}{\partial x_j} \text{ and } i, j = 1, 3 \quad \text{Eq. 2.10.1}$$

Now if the ratio of a typical pressure difference to the absolute pressure is small compared to ratio of a typical temperature difference to the absolute temperature. The perfect gas law  $p=\rho RT$  or  $dp/p=dp/\rho=dT/T$  show that effect of pressure change on the temperature is small; this is the case of low speed flows. Also, at low speed flows the dissipation term  $\varphi$  will be small since it is proportional to the square of a typical velocity. Therefore, for low speed flows we can neglect the pressure work and dissipation term,

$$\rho C_p \frac{DT}{Dt} = \nabla \cdot (k \nabla T) \quad \text{Eq. 2.10.2}$$

For a steady, constant property, without flow (i.e., conduction), the energy equation reduces to

$$\nabla^2 T = 0 \quad \text{Eq. 2.10.3}$$

Which is the celebrated **Laplace equation** and linear in nature. Analytical solutions to the transient heat conduction for a 2D rectangular fin, with general boundary conditions is obtained by the principle of **separation variables** [Kung]<sup>21</sup>. In the analysis, the partial differential equation is directly transformed into ordinary differential equation. The closed form transient temperature distribution and the heat transfer rate are generalized for a linear combination of the product of Fourier series and exponential function.

<sup>21</sup> Kuang Yuan Kung, "Transient Analysis of Two-Dimensional Rectangular Fin With Various Surface Heat Effects", Mechanical Engineering Department, Nanya Institute Of Technology, Taiwan.

## 2.11 Mass Transfer

Mass transfer deals with situations in which there is more than one component present in a system; for instance, situations involving chemical reactions, dissolution, or mixing phenomena. A simple example of such a **multicomponent** system is a **binary** (two component) solution consisting of a solute in an excess of chemically different solvent. Mass transfer can result from several different phenomena. There is a mass transfer associated with convection in that mass is transported from one place to another in the flow system. This type of mass transfer occurs on a macroscopic level and is usually treated in the subject of fluid mechanics. When a mixture of gases or liquids is contained such that there exists a concentration gradient of one or more of the constituents across the system, there will be a mass transfer on a microscopic level as the result of diffusion from regions of high concentration to regions of low concentration. In this chapter we are primarily concerned with some of the simple relations that may be used to calculate mass diffusion and their relation to heat transfer. Nevertheless, one must remember that the general subject of mass transfer encompasses both mass diffusion on a molecular scale and the bulk mass transport that may result from a convection process<sup>22-15</sup>. Not only may mass diffusion occur on a molecular basis, but accelerated diffusion rates will also occur in turbulent-flow systems as a result of the rapid-eddy mixing processes, just as these mixing processes created increased heat transfer and viscous action in turbulent flow. Although beyond the scope of our discussion, it is well to mention that mass diffusion may also result from a temperature gradient in a system; this is called **thermal diffusion**. Similarly, a concentration gradient can give rise to a temperature gradient and a consequent heat transfer. These two effects are termed **coupled phenomena** and may be treated by the methods of irreversible thermodynamics<sup>23</sup>.

### 2.11.1 Mass Transfer by Diffusion

Consider a chamber in which two different gas species at the same temperature and pressure are initially separated by a partition. If the partition is removed, both species will be transported by diffusion. **Figure 2.11.1** shows the situation as it might exist shortly after removal of the partition. A higher concentration means more molecules per unit volume, and the concentration of species A (light dots) decreases with increasing  $x$ , while the concentration of B increases with  $x$ . Since mass diffusion is in the direction of decreasing concentration, there is net transport of species A to the right and of species B to the left. The physical mechanism may be explained by considering the imaginary plane shown as a dashed line at  $x_0$ . Since molecular motion is random, there is equal probability of any molecule moving to the left or the right. Accordingly, more molecules of species A cross the plane from the left (since this is the side of higher A concentration) than from the right. Similarly, the concentration of B molecules is higher to the right of the plane than to the left, and random motion provides for *net* transfer of species B to the left. Of course, after a sufficient time, uniform concentrations of A and B are achieved, and there is no *net* transport of species A or B across the imaginary plane. Mass diffusion occurs in liquids and solids, as well as in gases. However, since mass transfer is strongly influenced by molecular spacing, diffusion occurs more readily in gases than in liquids and more readily in liquids than in solids. Examples of diffusion in gases, liquids, and solids, respectively, include nitrous oxide from an automobile exhaust in air, dissolved oxygen in water.

### 2.11.2 Mixture Composition

Throughout this chapter we will be concerned with the transfer of mass in mixtures. A mixture consists of two or more chemical constituents (*species*), and the amount of any species  $i$  may be quantified in terms of its *mass density*  $\rho_i$  (kg/m<sup>3</sup>) or its *molar concentration*  $C_i$  (kmol/m<sup>3</sup>). The mass

<sup>22</sup> Frank P. Incropera , David P. Dewitt, Theodore L. Bergman, Adrienne S. Lavine, "Fundamentals of Heat and Mass Transfer", Sixth Edition, John Wiley & Sons, ISBN-13: \*978-0-471-45728-2 (cloth)-ISBN-10: 0-471-45728-0 (cloth), 2006.

<sup>23</sup> J. P. Holman, "Heat Transfer", 10<sup>th</sup> edition, McGraw-Hill Companies, ISBN 978-0-07-352936-3, 2010.

density and molar concentration are related through the species molecular weight,  $M_i$  (kg/kmol), and mole fraction  $x_i$  such that

$$\rho_i = M_i C_i \quad , \quad \rho = \sum_i \rho_i \quad , \quad \sum_i m_i = 1 \quad , \quad \sum_i x_i = \sum_i \frac{C_i}{C} = 1 \quad \text{Eq. 2.11.1}$$

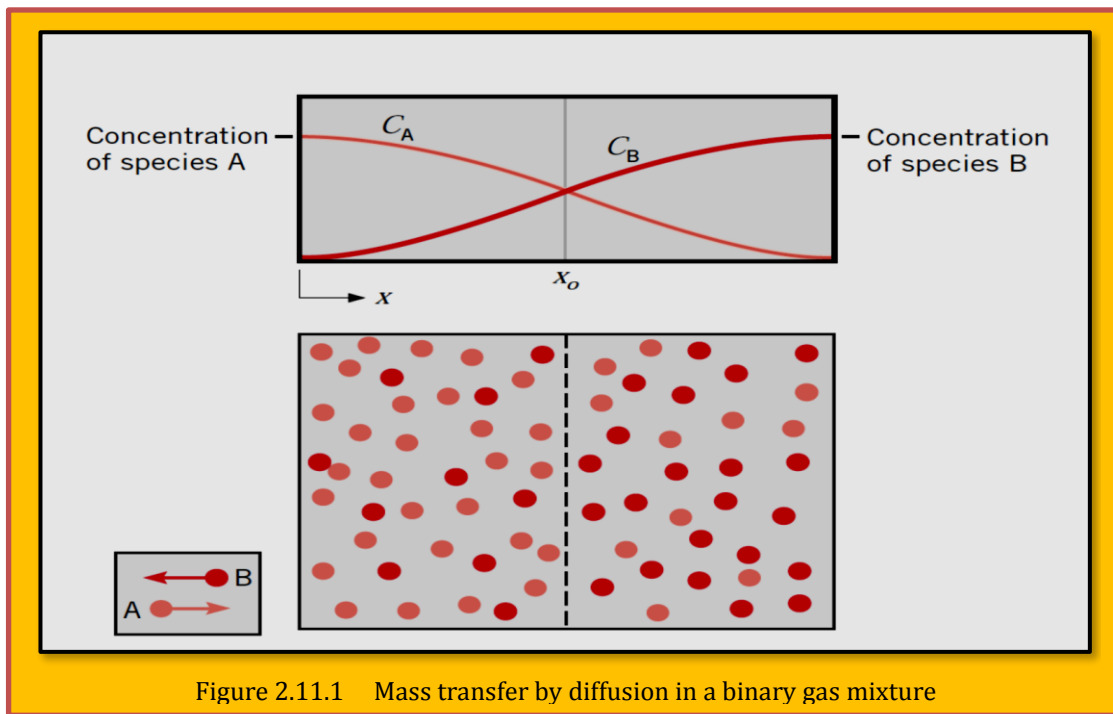


Figure 2.11.1 Mass transfer by diffusion in a binary gas mixture

### 2.11.3 Fick's Law of Diffusion

Since similar physical mechanisms are associated with heat and mass transfer by diffusion, it is not surprising that the corresponding rate equations are of the same form. The rate equation for mass diffusion is known as **Fick's law**, and for the transfer of species A in a **binary mixture** of A and B, it may be expressed in vector form as

$$\mathbf{j}_A = -\rho D_{AB} \nabla m_A \quad \text{or} \quad \mathbf{J}_A = -CD_{AB} \nabla x_A \quad \text{Eq. 2.11.2}$$

The form of these expressions is similar to that of Fourier's law. Moreover, just as Fourier's law serves to define one important transport property, the thermal conductivity, Fick's law defines a second important transport property, namely, the **binary diffusion coefficient** or **mass diffusivity,  $D_{AB}$** . The quantity  $j_A$  (kg/s.m<sup>2</sup>) is defined as the diffusive mass flux of species A. It is the amount of A that is transferred by diffusion per unit time and per unit area perpendicular to the direction of transfer, and it is proportional to the mixture mass density,  $\rho = \rho_A + \rho_B$  (kg/m<sup>3</sup>), and to the gradient in the species mass fraction,  $m_A = \rho_A/\rho$ . The species flux may also be evaluated on a molar basis, where  $J_A$  (kmol/s.m<sup>2</sup>) is the diffusive molar flux of species A. It is proportional to the total molar concentration of the mixture,  $C = C_A + C_B$  (kmol/m<sup>3</sup>), and to the gradient in the species mole fraction,  $x_A = C_A/C$ . The foregoing forms of **Fick's law** may be simplified when the total mass density  $\rho$  or the total molar concentration  $C$  is a constant.

#### 2.11.4 Mass Diffusivity

Considerable attention has been given to predicting the mass diffusivity  $D_{AB}$  for the binary mixture of two gases, A and B. Assuming ideal gas behavior, kinetic theory may be used to show that

$$D_{AB} \approx P^{-1} T^{3/2} \quad \text{Eq. 2.11.3}$$

where  $T$  is expressed in kelvins. This relation applies for restricted pressure and temperature ranges and is useful for estimating values of the mass diffusivity at conditions other than those for which data are available. [Bird et al.]<sup>24</sup> provide detailed discussions of available theoretical treatments and comparisons with experiment. For binary liquid solutions, it is necessary to rely exclusively on experimental measurements. For small concentrations of A (the solute) in B (the solvent),  $D_{AB}$  is known to increase with increasing temperature. The mechanism of diffusion of gases, liquids, and solids in solids is extremely complicated and generalized theories are not available. Furthermore, only limited experimental results are available in the literature<sup>25</sup>.

#### 2.11.5 Nonstationary Media - Absolute and Diffusive Species Fluxes

We have seen that diffusion mass transfer is similar to conduction heat transfer and that the diffusive fluxes are analogous to the heat flux as expressed by *Fourier's law*. If there is bulk motion, then, like heat transfer, mass transfer can also occur by advection. Unlike conduction heat transfer, however, the diffusion of a species always involves the movement of molecules or atoms from one location to another. In many cases, this molecular scale motion results in bulk motion. In this section we define the total or **absolute flux** of a species, which includes both diffusive and advective components. The absolute mass (or molar) flux of a species is defined as the total flux relative to a fixed coordinate system. To obtain an expression for the absolute mass flux, consider species A in a binary mixture of A and B. The absolute mass flux is related to the species absolute velocity by  $n''_A = \rho_A v_A$ . A value of  $v_A$  may be associated with any point in the mixture, and it is interpreted as the average velocity of all the A particles in a small volume element about the point. An average, or aggregate, velocity may also be associated with the particles of species B, in which case  $n''_B = \rho_B v_B$ . A **mass-average velocity for the mixture** may then be obtained from the requirement that  $v = m_A v_A + m_B v_B$ . It is important to note that we have defined the velocities ( $v_A, v_B, v$ ) and the fluxes ( $n''_A, n''_B, n''$ ) as **absolute quantities**. That is, they are referred to axes that are fixed in space. The mass-average velocity  $v$  is a useful parameter of the binary mixture, for two reasons. First, it need only be multiplied by the total mass density to obtain the total mass flux with respect to fixed axes. Second, it is the mass-average velocity which is required in the equations expressing conservation of mass, momentum, and energy such as those presented. We may now define the **mass flux of species A relative to the mixture mass average velocity** as

$$\begin{aligned} n''_A &= -\rho D_{AB} \nabla m_A + m_A (n''_A + n''_B) \\ n''_B &= -\rho D_{AB} \nabla m_B + m_B (n''_A + n''_B) \\ \text{and molar average velocity of the mixture } v^* &= x_A v_A + x_B v_B \end{aligned} \quad \text{Eq. 2.11.4}$$

Readers should consult details using any Heat and Mass Transfer text books such as excellent discussion on<sup>26-19</sup>.

<sup>24</sup> Bird, R. B., W. E. Stewart, and E. N. Lightfoot, "Transport Phenomena", 2<sup>nd</sup> ed. Wiley, New York, 2002.

<sup>25</sup> Frank P. Incropera , David P. Dewitt, Theodore L. Bergman, Adrienne S. Lavine, "Fundamentals of Heat and Mass Transfer", 6<sup>th</sup> Edition, John Wiley & Sons, 2006.

<sup>26</sup> Bird, R. B., W. E. Stewart, and E. N. Lightfoot, "Transport Phenomena", 2<sup>nd</sup> ed. Wiley, New York, 2002.

## 2.12 The Definition of Entransy and Entransy Dissipation<sup>27</sup>

The **entransy is a new developed parameter that is effective in optimization of heat transfer**. It can be used as an evaluation of the transport ability of heat. Here, based on the energy conservation equation, the entransy balance equations for heat conduction and convective heat transfer are developed. The entransy dissipation extreme principle is developed. This extreme principle can be concluded into the minimum thermal resistance principle defined by entransy dissipation. [Guo et al.]<sup>28</sup> found that all transport processes contain two different types of physical quantities due to the existing irreversibility: the conserved ones and the non-conserved ones, and the loss or dissipation in the non-conserved quantities can then be used as the measurements of the irreversibility in the transport process. Taking an electric system as an example, although both the electric charge and the total energy are conserved during an electric conduction, the electric energy, However, is not conserved and it is partly dissipated into the thermal energy form due to the existence of the electrical resistance. Consequently, the electrical energy dissipation rate is often regarded as the irreversibility measurement in the electric conduction process. Similarly, for a viscous fluid flow, both the mass and the momentum of the fluid, transported during the fluid flow, are conserved, whereas the mechanical energy, including both the potential and kinetic energies, of the fluid is turned partially into the thermal energy form due to the viscous dissipation.

As a result, the mechanical energy dissipation is a common measure of irreversibility in a fluid flow process. The above two examples show that the mass, or the electric quantity, is conserved during the transport processes, while some form of the energy associated with them is not. This loss or dissipation of the energy can be used as the measurement of irreversibility in these transport processes. However, an irreversible heat transfer process seems to have its own particularity, for the heat energy always remains constant during transfer and it does not appear to be readily clear what the non-conserved quantity is in a heat transfer process. Based on the analogy between electrical and heat conductances, [Guo et al.]<sup>29</sup> made a comparison between electrical conduction and heat conduction as shown in<sup>30</sup>.

It could be found in the table that there is no corresponding parameter in heat conduction for the electrical potential energy in a capacitor, and hence they defined an equivalent quantity, G, that corresponds to the electrical potential energy in a capacitor, which is called "entransy." They further derived **Eq. 2.12.1** according to the similar procedure of the derivation of the electrical potential energy in a capacitor. Entransy was originally referred to as the heat transport potential capacity in an earlier paper by the [Guo et al.]<sup>31</sup>.

$$G = \frac{1}{2} QT \text{ [JK]}$$

### Eq. 2.12.1

where Q is,  $m c_v T$ , the thermal energy or stored heat in a body at constant volume kept at temperature T. It is equivalent to potential electrical energy in a capacitor, which makes a current (heat flow) between two objects connected with a resistance together at two different potential levels. It is also

<sup>26</sup> Frank P. Incropera , David P. Dewitt, Theodore L. Bergman, Adrienne S. Lavine, "Fundamentals of Heat and Mass Transfer", 6<sup>th</sup> Edition, John Wiley & Sons, 2006.

<sup>27</sup> J. Gu and Z. Gan, *Entransy in Phase-Change Systems*, Springer Briefs in Thermal Engineering and Applied Science, 2014.

<sup>28</sup> Guo J, Xu M, Cheng L (2009) *The application of field synergy number in shell-and-tube heat exchanger optimization design*. Appl Energy 86: 2079–2087

<sup>29</sup> See Previous.

<sup>30</sup> Guo Z, Zhu H, Liang X (2007) *Entransy—A physical quantity describing heat transfer ability*. Int J Heat Mass Transfer 50:2545–2556

<sup>31</sup> See Previous.

possible to explain a heat transfer process through the analogy as depicted in **Figure 2.12.1**. **Entransy represents the heat transfer ability of an object**. It possesses both the nature of “energy” and the transfer ability. If an object is put in contact with an infinite number of heat sinks that have infinitesimally lower temperatures, the total quantity of “potential energy” of heat, whose output can be  $(1/2)QT$ . [Biot] suggested a similar concept in the derivation of the differential conduction equation using the variation method. [Eckert and Drake]<sup>32</sup> pointed out that, [Biot] in a series of papers beginning in 1955, formulated from the ideas of irreversible thermal dynamics, a variational equivalent of the heat conduction equation that constituted a thermodynamically analogy to Hamilton’s principle in mechanics and led to a Lagrangian formulation of the heat conduction problem in terms of generalized coordinates.

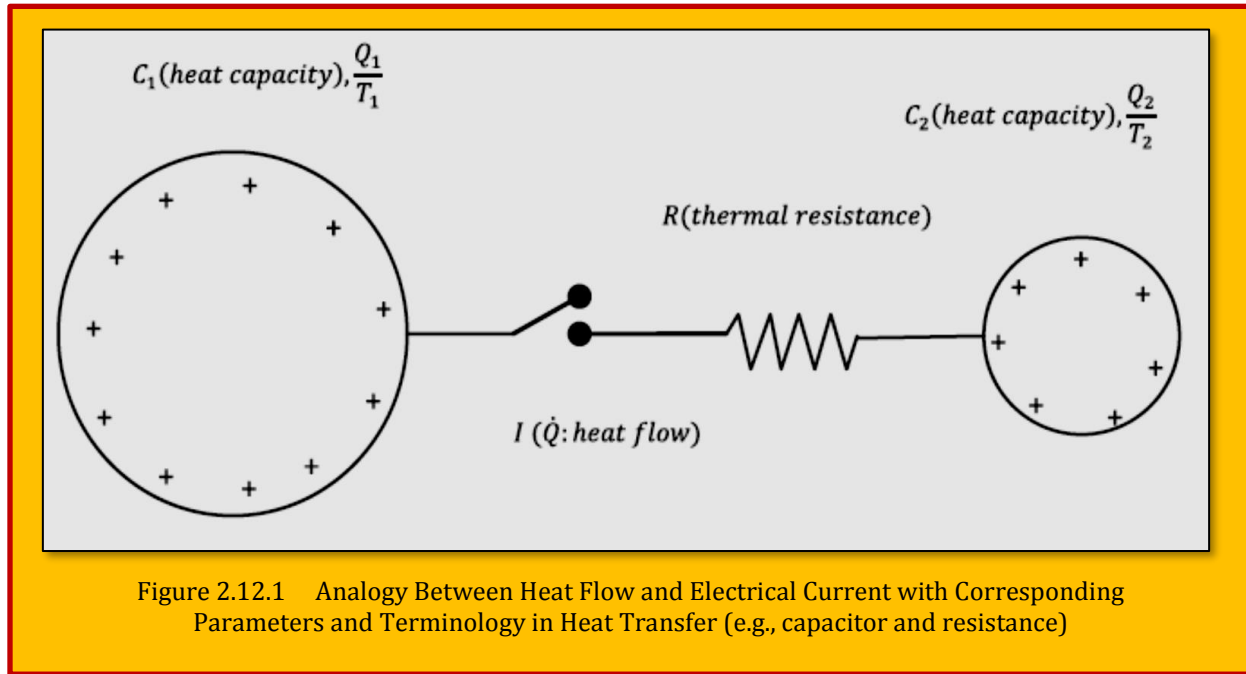


Figure 2.12.1 Analogy Between Heat Flow and Electrical Current with Corresponding Parameters and Terminology in Heat Transfer (e.g., capacitor and resistance)

[Biot] defines a thermal potential as  $E = 1/2 \iiint_Q c T^2 dV$ . The thermal potential “E” plays a role analogous to a potential energy. However, [Biot] did not further explain the physical meaning of thermal potential and its application was not found later except in the approximate solutions of anisotropic conduction problems. Accompanying the electric charge, the electric energy is transported during electric conduction. Similarly, along with the heat, the entransy is transported during heat transfer too. Furthermore, when a quantity of heat is transferred from a high temperature to a low temperature, the entransy is reduced and some of it is dissipated during the heat transport. The lost entransy is called entransy dissipation. Entransy dissipation is an evaluation of the irreversibility of heat transport ability. For a transient heat conduction process without any heat transfer with ambient environment, the thermal energy conservation equation can be expressed as

$$\rho c_p \frac{\partial T}{\partial t} = \nabla \cdot (k \nabla T)$$

### Eq. 2.12.2

where  $q$ ,  $c_p$ ,  $k$  are density, constant pressure, specific heat and thermal conductivity, respectively. The entransy equilibrium equation can be obtained by multiplying both sides by temperature  $T$ :

<sup>32</sup> Eckert ERG, Drake RM (1959) *Heat and mass transfer*. McGraw-Hill Inc, New York

$$\rho c_p T \frac{\partial T}{\partial t} = \nabla \cdot (T k \nabla T) - k |\nabla T|^2$$

### Eq. 2.12.3

where the left side represents the time variation of the entransy stored per unit volume, the first term on the right side is the entransy transfer from one object to another associated with heat transfer, while the second term is the local entransy dissipation rate due to heat conduction. This is similarly like electric energy dissipation during an electric conduction process or mechanical energy dissipation during mechanical moving process. Since electrical energy and mechanical energy dissipations are both irreversibility measure of their respective process, entransy dissipation rate is hence a measure of the irreversibility in heat transfer process and can be written as

$$\dot{G} = k |\nabla T|^2$$

### Eq. 2.12.4

In a similar manner, the thermal energy conservation equation for a steady-state convective heat transfer process with no heat source can be expressed,

$$\rho c_p U_f \cdot (\nabla T) = \nabla \cdot (k \nabla T)$$

### Eq. 2.12.5

where  $U_f$  is the velocity vector of the fluid. Similarly, the entransy equilibrium equation for the convective heat transfer can be derived by multiplying both sides by temperature  $T$ ,

$$U_f \cdot \nabla \left( \frac{\rho c_p T^2}{2} \right) = \nabla \cdot (k T \nabla T) - k |\nabla T|^2$$

### Eq. 2.12.6

The left side of this equation express the entransy transferred associated with the fluid particles motion, while the right side of this equation is in the same form as the heat conduction process, which include the entransy diffusion within the fluid due to temperature gradient and the local entransy dissipation rate. By integrating Eq. 2.12.6 over the entire domain, transforming the volume integral to the surface integral on the domain boundary, and ignoring the heat diffusion in the flow direction at both inlets and outlets, we can obtain

$$\left( \frac{1}{2} \rho c_p \dot{V} T^2 \right)_{out} - \left( \frac{1}{2} \rho c_p \dot{V} T^2 \right)_{in} = \iint_{\Gamma} \vec{n} \cdot k T \nabla T \, dA + \underbrace{\iiint_{\Omega} k |\nabla T|^2 \, dV}_{\dot{G}}$$

### Eq. 2.12.7

where the first term on the left side describes the entransy flowing out of the domain, while the second term is the entransy flowing into the domain. On the right side, the first term indicates the entransy flow rate induced by heat transfer through the domain boundary, while the second term can be viewed as the total entransy dissipation rate  $\dot{G}$ . Similar to electrical resistance, the entransy dissipation-based thermal resistance of a heat exchanger is defined a

$$R_{ex} = \frac{\dot{G}}{Q^2}$$

### Eq. 2.12.8

where  $R_{ex}$  is the entransy dissipation-based thermal resistance,  $\dot{G}$  is the entransy dissipation rate

during the heat transfer process and  $Q$  is the total heat transfer rate.

### 2.12.1 Entransy Analysis in Conduction Heat Transfer

The conduction heat transfer equation with no heat source available in a domain is

$$\rho c_v \frac{\partial T}{\partial t} = \nabla \cdot (k \nabla T)$$

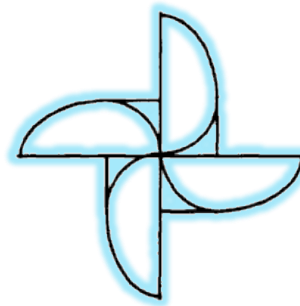
**Eq. 2.12.9**

By multiplying both sides by  $T$ , the entransy equation is

$$\rho c_v T \frac{\partial T}{\partial t} = \nabla \cdot (T k \nabla T) - k |\nabla T|^2 \quad \text{or} \quad \frac{dG}{dt} = -\nabla \cdot \dot{G} - G_\varphi$$

**Eq. 2.12.10**

where  $G$  is entransy density,  $1/2 \rho c_v T^2$ ,  $G_\varphi$  is entransy dissipation as  $K(\bar{v}T)^2$ , and  $\dot{G}$  is entransy flux. The presence of temperature gradient to the power of two in local entransy dissipation resembles viscose dissipation term in entropy generation in fluid flow, which is similar to electrical dissipation. For all these squared terms, energy should be paid (consumed) to maintain the corresponding flow (e.g., heat or mass). For instance, to maintain a viscous flow, pumping power should be provided to have the fluid flowing. For heat transfer, energy should be delivered to maintain the heat flow as there is always a resistance present and entransy dissipation. It looks like a connecting concept between heat transfer and thermodynamics and furthermore between different energy and heat transfer modes<sup>33</sup>.




---

<sup>33</sup> J. Gu and Z. Gan, *Entransy in Phase-Change Systems*, Springer Briefs in Thermal Engineering and Applied Science, 2014.

### 3 Discretization Methods

In focusing attention on the values at the grid points, *we have replaced the continuous information contained in the exact solution of the differential equation with discrete values.* We have thus discretized the distribution of  $(p, l)$  and it is appropriate to refer to this class of numerical methods as discretization methods. The algebraic equations involving the unknown values go at chosen grid  $Q$  points, which we shall now name the discretization equations, are derived from the differential equation governing  $\varphi$ . In this derivation, we must employ some assumption about how  $\varphi$  varies between the grid points. Although this “profile” of  $\varphi$  could be chosen such that a single algebraic expression suffices for the whole calculation domain, it is often more practical to use piecewise profiles such that a given segment describes the variation of  $\varphi$  over only a small region in terms of the  $\varphi$  values at the grid points within and around that region. Thus, it is common to subdivide the calculation domain into a number of subdomains or elements such that a separate profile assumption can be associated with each subdomain. In this manner, we encounter the discretization concept in another context. The continuum calculation domain has been discretized. It is this systematic discretization of space and of the dependent variables that makes it possible to replace the governing differential equations with simple algebraic equations, which can be solved with relative ease.

#### 3.1 The Structure of the Discretization Equation

A discretization equation is an algebraic relation connecting the values of  $\varphi$  for a group of grid points. Such an equation is derived from the differential equation governing  $\varphi$  and thus expresses the same physical information as the differential equation. That only a few grid points participate in a given discretization equation is a consequence of the piecewise nature of the profiles chosen. The value of  $\varphi$  at a grid point thereby influences the distribution of  $\varphi$  only in its immediate neighborhood. As the number of grid points becomes very large, the solution of the discretization equations is expected to approach the exact solution of the corresponding differential equation. This follows from the consideration that, as the grid points get closer together, the change in  $\varphi$  between neighboring grid points becomes small, and then the actual details of the profile assumption become unimportant. For a given differential equation, the possible discretization equations are by no means unique, although all types of discretization equations are, in the limit of a very large number of grid points, expected to give the same solution. The different types arise from the differences in the profile assumptions and in the methods of derivation.

Until now we have deliberately refrained from making reference to finite-difference and finite-element methods. Now it may be stated that these can be thought of as two alternative versions of the discretization method, which we have described in general terms. The distinction between the finite-difference method and the finite-element method results from the ways of choosing the profiles and deriving the discretization equations. The method that is to be the main focus of attention in this book has the appearance of a finite-difference method, but it employs many ideas that are typical of the finite-element methodology. To call the present method a finite-difference method might convey an adherence to the conventional finite-difference practice. For this reason, we shall refer to it simply as a discretization method.

#### 3.2 Methods of Deriving the Discretization Equations

For a given differential equation, the required discretization equations can be derived in many ways. Here, we shall outline a few common methods and then indicate a preference.

##### 3.2.1 Taylor-Series Formulation (Finite Difference - FD)

The usual procedure for deriving finite-difference equations consists of approximating the derivatives in the differential equation via a truncated Taylor series. Let us consider the grid points shown in **Figure 3.2.1**. For grid point 2, located midway between grid points 1 and 3 such that

$$\varphi_1 = \varphi_2 - \Delta x \left( \frac{d\varphi}{dx} \right)_2 + \frac{1}{2} (\Delta x)^2 \left( \frac{d^2\varphi}{dx^2} \right)_2 - \dots \quad \text{Eq. 3.2.1}$$

and  $\varphi_3 = \varphi_2 - \Delta x \left( \frac{d\varphi}{dx} \right)_2 + \frac{1}{2} (\Delta x)^2 \left( \frac{d^2\varphi}{dx^2} \right)_2 - \dots$

Truncating the series just after the third term, and adding and subtracting the two equations, we obtain

$$\left( \frac{d\varphi}{dx} \right)_2 = \frac{\varphi_3 - \varphi_1}{2\Delta x}, \quad \left( \frac{d^2\varphi}{dx^2} \right)_2 = \frac{\varphi_1 - 2\varphi_2 + \varphi_3}{(\Delta x)^2} \quad \text{Eq. 3.2.2}$$

The substitution of such expressions into the differential equation leads to the finite-difference equation. The method includes the assumption that the variation of  $\varphi$  is somewhat like a polynomial in  $x$ , so that the higher derivatives are unimportant. This assumption, however, leads to an undesirable formulation when, for example, exponential variations are encountered. The Taylor-series formulation is relatively straightforward but allows less flexibility and provides little insight into the physical meanings of the terms (Patankar, 1980)<sup>34</sup>.

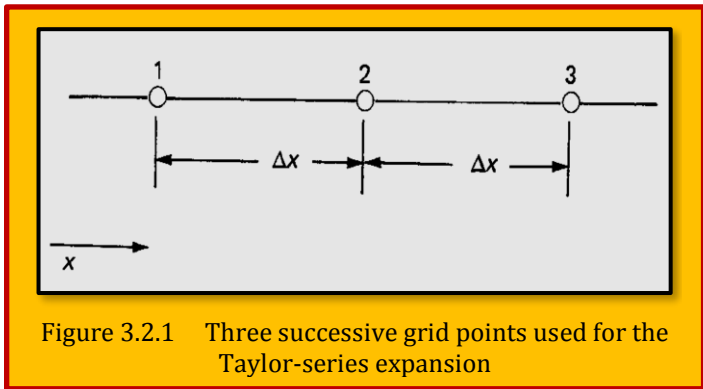


Figure 3.2.1 Three successive grid points used for the Taylor-series expansion

### 3.2.2 Variational Formulation

Another method of obtaining the discretization equations is based on the calculus of variations. To understand the method fully, the reader should have sufficient knowledge of this branch of calculus. However, a general appreciation of the main ingredients of the formulation is all that is needed for the present purposes. The calculus of variations shows that solving certain differential equations is equivalent to minimizing a related quantity called the functional. This equivalence is known as a *Variational* principle. If the functional is minimized with respect to the grid-point values of the dependent variable, the resulting conditions give the required discretization equations. The Variational formulation is very commonly employed in finite-element methods for stress analysis, where it can be linked to the virtual-work principle. In addition to its algebraic and conceptual complexity, the main drawback of this formulation is its limited applicability, since a Variational principle does not exist for all differential equations of interest.

### 3.2.3 Method of Weighted Residuals

A powerful method for solving differential equations is the method of weighted residuals, which is described in detail by Finlayson (1972). The basic concept is simple and interesting. Let the differential equation be represented by

$$L(\varphi) = 0 \quad \text{Eq. 3.2.3}$$

<sup>34</sup> Patankar, S. V. (1980). *Numerical Heat Transfer and Fluid Flow*. Mc Graw Hill Book Company.

Further, let us assume an approximate solution  $\bar{\varphi}$  that contains a number of undetermined parameters, for example,

$$\bar{\varphi} = a_0 + a_1 x + a_2 x^2 + \dots + a_m x^m \quad \text{Eq. 3.2.4}$$

the  $a$ 's being the parameters. The substitution of  $\bar{\varphi}$  into the differential equation leaves a residual  $R$ , defined as

$$R = L(\varphi) \quad \text{Eq. 3.2.5}$$

We wish to make this residual small in some sense. Let us propose that

$$\int W R dx = 0 \quad \text{Eq. 3.2.6}$$

where  $W$  is a weighting function and the integration is performed over the domain of interest. By choosing a succession of weighting functions, we can generate as many equations as are required for evaluating the parameters. These algebraic equations containing the parameters as the unknowns are solved to obtain the approximate solution to the differential equation. Different versions of the method (known by specific names) result from the choice of different classes of weighting functions. The method was very popular in boundary-layer analysis before the finite-difference method nearly replaced it. However, a connection with the finite-difference method, or rather with the discretization method, can be established if the approximate solution  $\varphi$ , instead of being a single algebraic expression over the whole domain, is constructed via piecewise profiles with the grid-point values of  $\varphi$  as the unknown parameters. Indeed, much of the recent development of the finite-element technique is also based on piecewise profiles used in conjunction with a particular weighted-residual practice known as the **Galerkin method**. The simplest weighting function is  $W = 1$ . From this, a number of weighted-residual equations can be generated by dividing the calculation domain into subdomains or control volumes, and setting the weighting function to be unity over one subdomain at a time and zero everywhere else. This variant of the method of weighted residuals is called the subdomain method or the control-volume formulation. It implies that the integral of the residual over each control volume must become zero. Since we shall adopt the control-volume approach in this book, a more detailed discussion is desirable, which now follows.

### 3.2.4 Control-Volume Formulation (CV)

Often elementary textbooks on heat transfer derive the finite-difference equation via the Taylor-series method and then demonstrate that the resulting equation is consistent with a heat balance over a small region surrounding a grid point. We have also seen that the control-volume formulation can be regarded as a special version of the method of weighted residuals. The basic idea of the control-volume formulation is easy to understand and lends itself to direct physical interpretation. The calculation domain is divided into a number of non-overlapping control volumes such that there is one control volume surrounding each grid point. The differential equation is integrated over each control volume. Piecewise profiles expressing the variation of  $\varphi$  between the grid points are used to evaluate the required integrals. The result is the discretization equation containing the values of  $\varphi$  for a group of grid points. The discretization equation obtained in this manner expresses the conservation principle for  $\varphi$  for the finite control volume, just as the differential equation expresses it for an infinitesimal control volume. Indeed deriving the control-volume discretization equation by integrating the differential equation over a finite control volume is a rather roundabout process. The most attractive feature of the control-volume formulation is that the resulting solution would imply that the integral conservation of quantities such as mass, momentum, and energy is exactly satisfied

over any group of control volumes and, of course, over the whole calculation domain. This characteristic exists for any number of grid points not just in a limiting sense when the number of grid points becomes large. Thus, even the coarse-grid solution exhibits exact integral balances. When the discretization equations are solved to obtain the grid-point values of the dependent variable, the result can be viewed in two different ways. In the finite-element method and in most weighted-residual methods, the assumed variation of  $\varphi$  consisting of the grid-point values and the interpolation functions (or profiles) between the grid points is taken as the approximate solution. In the finite-difference method, however, only the grid-point values of  $\varphi$  are considered to constitute the solution, without any explicit reference as to how  $\varphi$  varies between the grid points. This is akin to a laboratory experiment where the distribution of a quantity is obtained in terms of the measured values at some discrete locations without any statement about the variation between these locations. In our control-volume approach, we shall also adopt this view. We shall seek the solution in the form of the grid-point values only. The interpolation formulas or the profiles will be regarded as auxiliary relations needed to evaluate the required integrals in the formulation. Once the discretization equations are derived, the profile assumptions can be forgotten. This viewpoint permits complete freedom of choice in employing, if we wish, different profile assumptions for integrating different terms in the differential equation. To make the foregoing discussion more concrete, we shall now derive the control-volume discretization equation for a simple situation (Patankar, 1980).

### 3.3 Consequence of Various Discretization Schemes

In all finite-volume CFD codes for which cell-center values of variables are stored, the question arises: what value should be ascribed to the fluid which crosses the cell face? In the diagram below, (**Figure 3.3.1**), values of the variable  $\varphi$  are known for the cell centers W, P and E; but what is the value of  $\varphi$  in the fluid at face w, which travels from cell W to cell P, or from P to W? The answer is given to this question influences the balance equations for both cell W and cell P.

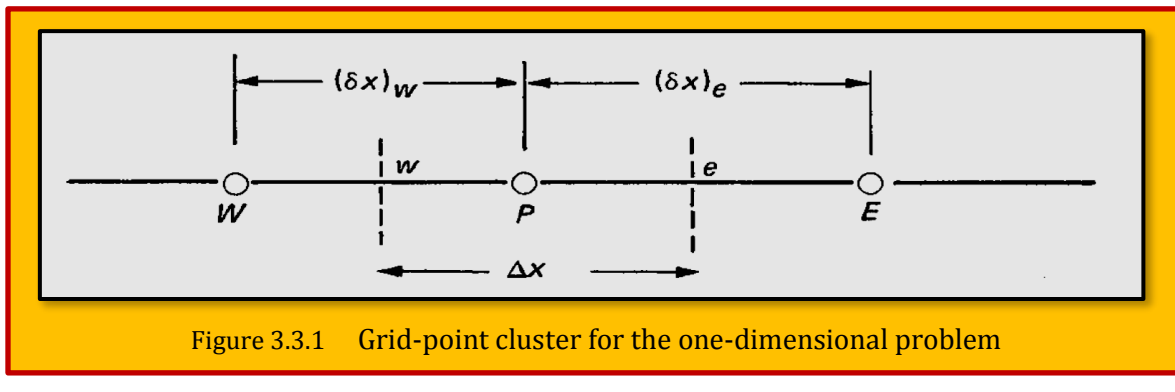


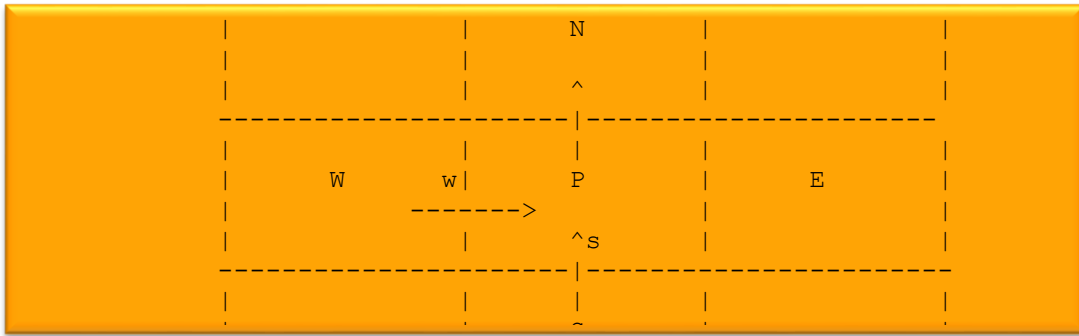
Figure 3.3.1 Grid-point cluster for the one-dimensional problem

#### 3.3.1 The Upwind Treatment

The obvious answer according to on-line *PHOENICS*<sup>®</sup> software is the one which ensures fairly good solution, i.e.,  $\varphi_w = \varphi_W$  when the flow is from W to P, but  $\varphi_P$  when the flow is from P to W. In other words,  $\varphi_w$  equals the  $\varphi$  on the *UPWIND* side of the cell face. This, or rather the so-called "*hybrid*" variant of it, is what is used in other scheme is switched on by the user. The hybrid variant uses the upwind scheme only when the Peclet number (normal-to-face velocity times inter-node distance divided by diffusivity) exceeds 2.0. Otherwise, the arithmetic average of  $\varphi_W$  and  $\varphi_P$  is taken. The two schemes are called respectively the "*Upwind Discretization Scheme*" (**UDS**) and the "*hybrid discretization scheme*". (See **Figure 3.3.1**).

### 3.3.2 Numerical Diffusion

However, there is an objection: when the flow direction is diagonal to the grid, cell P receives fluid from both the west and the south cells and so takes up an intermediate value. This intermediate value is then passed on to cell N; and so on. The result is that physically-present discontinuities become "smeared" by the numerical procedure<sup>35</sup>.



### 3.3.3 Other Remedies

Many means have been proposed for reducing the magnitude of this effect, which for obvious reasons is called "numerical diffusion" or "false diffusion". Some, such as Raithby's "*skew-upwind scheme*" address directly the influence of the diagonality of the flow. Another such method, which is available is the "*conservative low-dispersion algorithm*" (CLDA), which is rather successful as seen if **Figure 3.3.2 (b)**. Other authors have sought to find formulae for cell-face values in simpler ways, involving only the  $\varphi$  values on either side of the face, and one still farther upstream. Following the jargon of the specialist literature, they are called the "*higher-order schemes*"<sup>36-37</sup>.

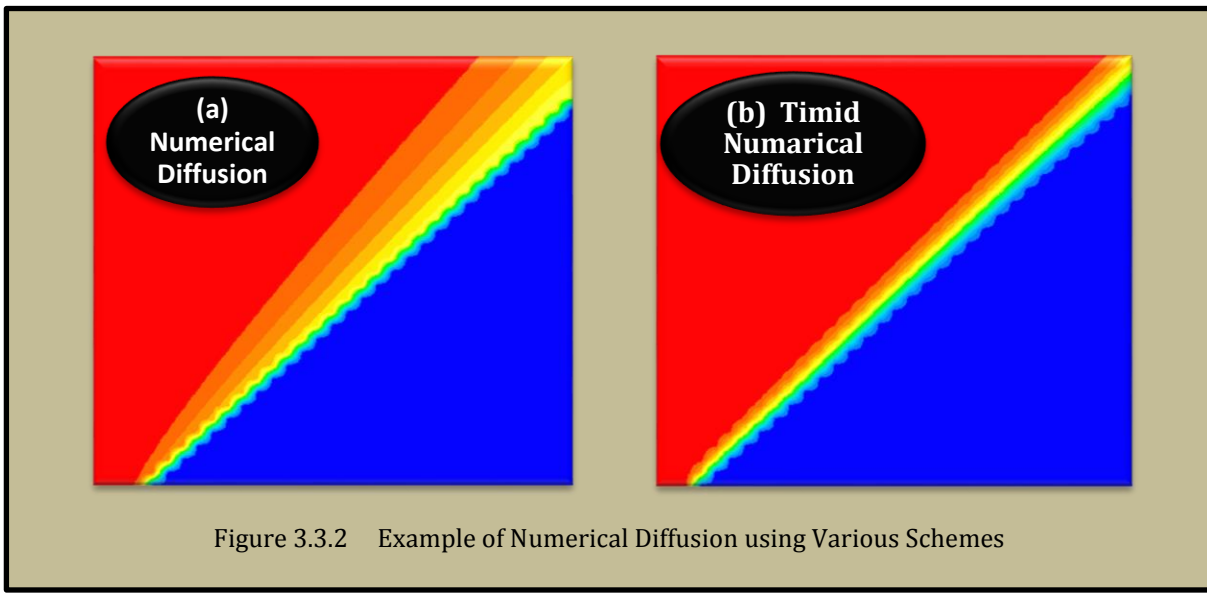


Figure 3.3.2 Example of Numerical Diffusion using Various Schemes

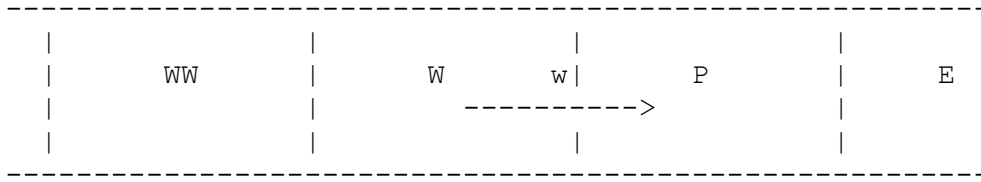
<sup>35</sup> R.K.Agrawal, 'A 3<sup>rd</sup> order accurate upwind scheme for Navier- Stokes at high Reynolds numbers', AIAA 81-0112, (1981).

<sup>36</sup> R.Courant, E.Isaacson & M.Rees, 'On the solution of non-linear hyperbolic differential equations by finite differences', Comm. Pure Appl. Maths, 5, p243, (1952).

<sup>37</sup> P.H.Gaskell and A.K.C.Lau, "Curvature-compensated convective transport: SMART, a new boundedness-preserving transport algorithm", Int. J. Num. Meth. Fluids, Vol.8, p617, (1988).

### 3.3.4 The General Discretization Form

All of the formulae will be expressed in terms of the face value,  $\varphi_w$ , and the cell-center values  $\varphi_{ww}$ ,  $\varphi_w$  and  $\varphi_p$ , thus:



$$\varphi_w = \varphi_w + \frac{B(r, k)}{2} (\varphi_w - \varphi_{ww}) \quad , \quad B(r, k) = \frac{1}{2} [(1+k)^r - (1-k)]$$

$$\text{and } r = \frac{\varphi_p - \varphi_w}{\varphi_w - \varphi_{ww}} \quad (.)$$

#### Eq. 3.3.1

It is assumed that the flow is from left to right. Thus W is on the upwind side of P, and WW is on the upwind side of W. If the flow direction were reversed,  $\varphi_E$  would be involved instead of  $\varphi_{ww}$ <sup>38</sup>. The schemes are divided in two group of **Linear** and **Nonlinear** ones. It is left when k is defined in each schemes. For **linear schemes** we have :

- UDS - upwind difference  $B(r, k) = 0$
- CDS - central difference  $B(r, k) = r$
- LUS - linear-upwind  $K = -1$
- QUICK - quadratic upwind  $K = 0.5$
- FROMM - Fromm's upwind scheme  $K = 0$
- CUS - cubic upwind scheme  $K = 0.3333$

the **nonlinear** ones can be expressed as <sup>39 - 40</sup>:

- SMART bounded QUICK  $B(r, k) = \text{Max}(0, \min(2*r, 0.75*r+0.25, 4))$
- KOREN  $B(r, k) = \text{Max}(0, \min(2*r, 2*r/3 + 1/3, 2))$
- VANL1 (or MUSCL)  $B(r, k) = \text{Max}(0, \min(2*r, 0.5 + 0.5*r, 2))$
- HQUICK harmonic QUICK  $B(r, k) = 2*(r+|r|)/(r+3)$
- OSPRE  $B(r, k) = 3*(r^{**2} + r)/\{2.*(r^{**2} + r + 1)\}$
- VANL2 (or VANLH)  $B(r, k) = (r + |r|)/(r + 1)$
- VANALB  $B(r, k) = (r^{**2} + r)/(r^{**2} + 1)$
- MINMOD  $B(r, k) = \text{Max}(0, \min(r, 1))$
- SUPBEE  $B(r, k) = \text{Max}(0, \min(2*r, 1), \min(r, 2))$
- UMIST bounded QUICK  $B(r, k) = \text{Max}(0, \min(2*r, 0.25 + 0.75*r, 0.75 + 0.25*r, 2))$
- HCUS  $B(r, k) = 1.5*(r + |r|)/(r + 2)$
- CHARM bounded QUICK  $B(r, k) = r*(3r + 1)/(r + 1)^{**2} \text{ for } r > 0 \quad B(r) = 0. \text{ for } r \leq 0$

<sup>38</sup> J. E .Fromm, 'A method for reducing dispersion in convective difference schemes', J. Comp. Phys., Vol.3, (1968).

<sup>39</sup> C. Hirsch, 'Numerical computation of internal and external flows', Computational Methods for Inviscid and Viscous Flows, Vol.2,Wiley Inter science, (1990).

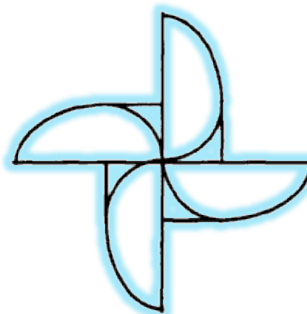
<sup>40</sup> B. Koren, 'A robust upwind discretization method for advection, diffusion and source terms', Numerical Methods for Advection-Diffusion Problems, Ed. C. B. Vreugdenhil & B. Koren, Vieweg, Braunschweig, p117, (1993).

### 3.3.5 Another Point of View in regard to Spatial Discretization

Another interesting study performed by Taegee Mina al eta.<sup>41</sup> is to study the effect of discretization schemes for the convection term in the constitutive equation on numerical solutions of viscoelastic fluid flows. Testing is done a temporally evolving mixing layer, a two-dimensional vortex pair interacting with a wall, and a fully developed turbulent channel flow are selected as test cases, and eight different discretization schemes are considered. Among them, ***the first-order upwind difference scheme (UD) and artificial diffusion scheme (AD)***, which are commonly used in the literature, show most stable and smooth solutions even for highly extensional flows. However, the stress fields are smeared too much by these schemes and the corresponding flow fields are quite different from those obtained by higher-order upwind difference schemes. Among higher-order upwind difference schemes investigated in this study, a third-order ***Compact Upwind Difference scheme (CUD3)*** with locally added AD shows stable and most accurate solutions for highly extensional flows even at relatively high Weissenberg numbers. The results of their study is presented in **Table 3.3.1**. Among higher-order upwind difference schemes, ***MCUD3*** shows stable and most accurate solutions even at relatively high Weissenberg numbers. Therefore, MCUD3 is recommended for the spatial discretization of the convection term in the constitutive equation in the numerical simulations of highly extensional flows.

Schemes	Order of Accuracy	Stencil size	Dissipative Error
1 <sup>st</sup> order upwind difference scheme (UD)	1	3	Yes
2 <sup>nd</sup> order central difference scheme (CD)	2	3	No
3 <sup>rd</sup> order upwind difference (LUDS)	2	5	Yes
Artificial Diffusion scheme (AD)	2	3	Yes
3 <sup>rd</sup> upwind difference scheme (QUICK)	3	5	Yes
4 <sup>th</sup> accurate compact scheme (COM4)	4	3	No
3 <sup>rd</sup> compact upwind difference scheme (CUD3)	3	3	Yes
(CUD3 with local AD) (MCUD3)	2-3	3	Yes

Table 3.3.1 Summary of the Spatial Discretization Schemes Considered in the Present Study



<sup>41</sup> Taegee Mina, Jung Yul Yoo, Haecheon Choi, "Effect of spatial discretization schemes on numerical solutions of viscoelastic fluid flows", J. Non-Newtonian Fluid Mech. 100 (2001) 27–47.

## 4 Numerical Methods for Solving Conduction (Diffusion) Equation

### 4.1 One Dimensional Steady Conduction

Let us consider steady one-dimensional heat conduction governed by

$$\frac{d}{dx} \left( k \frac{dT}{dx} \right) + S = 0$$

#### Eq. 4.1.1

where  $k$  is the thermal conductivity,  $T$  is the temperature, and  $S$  is the rate of heat generation per unit volume. To derive the discretization equation, we shall employ the grid-point cluster shown in **Figure 3.3.1**. We focus attention on the grid point  $P$ , which has the grid points  $E$  and  $W$ , as its neighbors. ( $E$  denotes the east side, i.e., the positive  $x$  direction, while  $W$  stands for west or the negative  $x$  direction.) The dashed lines show the faces of the control volume; their exact locations are unimportant for the time being. The letters  $e$  and  $w$  denote these faces. For the one-dimensional problem under consideration, we shall assume a unit thickness in the  $y$  and  $z$  directions. Thus, the volume of the control volume shown is  $\Delta x \cdot 1.1$ . Integrating **Eq. 4.1.1** over the control volume, we get

$$\left( k \frac{dT}{dx} \right)_e - \left( k \frac{dT}{dx} \right)_w + \int_w^e S dx = 0 \quad \text{Eq. 4.1.2}$$

If we evaluate the derivatives  $dT/dx$  the resulting equation will be

$$\begin{aligned} \frac{k_e(T_E - T_P)}{(\delta x)_e} - \frac{k_w(T_P - T_W)}{(\delta x)_w} + \bar{S} \Delta x &= 0 \quad \text{or} \\ a_p T_p &= a_E T_E + a_w T_w + B \end{aligned} \quad \text{Eq. 4.1.3}$$

where  $a_E = \frac{k_e}{(\delta x)_e}$  ,  $a_w = \frac{k_w}{(\delta x)_w}$  ,  $a_p = a_E + a_w$  ,  $B = \bar{S} \Delta x$

where  $\bar{S}$  is the average value of  $S$  over the control volume. This equation represents the standard form in which we shall write our discretization equations. The temperature  $T_p$  at the central grid point appears on the left side of the equation, while the neighbor-point temperatures and the constant  $b$  form the terms on the right side. As we shall see later, the number of neighbors increases for two- and three dimensional situations. In general, it is convenient to think of

$$\begin{aligned} \frac{k_e(T_E - T_p)}{(\delta x)_e} - \frac{k_w(T_p - T_W)}{(\delta x)_w} + \bar{S} \Delta x &= 0 \quad \text{or} \\ a_p T_p &= a_E T_E + a_w T_w + B \end{aligned} \quad \text{Eq. 4.1.3}$$

where  $a_E = \frac{k_e}{(\delta x)_e}$  ,  $a_w = \frac{k_w}{(\delta x)_w}$  ,  $a_p = a_E + a_w$  ,  $B = \bar{S} \Delta x$

as having the form

$$a_p T_p = \sum_{nb} a_{nb} T_{nb} + B$$

#### Eq. 4.1.4

where the subscript nb denotes a neighbor, and the summation is to be taken over all the neighbors. Before we proceed to develop the basic rules, we shall give some attention to the source term S in **Eq. 4.1.1**. Often, the source term is a function of the dependent variable T itself, and it is then desirable to acknowledge this dependence in constructing the discretization equation. We can, however, formally account for only a linear dependence because, as we shall see later, the discretization equations will be solved by the techniques for linear algebraic equations. *The procedure for “linearizing” a given S-T relationship will be discussed in the next*. Here, it is sufficient to express the average value S as

$$\bar{S} = S_C + S_p T_p \quad \text{Eq. 4.1.5}$$

where  $S_C$  stands for the constant part of S, while  $S_p$  is the coefficient of  $T_p$ . (Obviously,  $S_p$  does not stand for S evaluated at point P). The appearance of  $T_p$  reveals that, in expressing the average value S, we have presumed that the value  $T_p$  prevails over the control volume; in other words, the stepwise profile has been used. With the linearized source expression, the discretization equation would still look like **Eq. 4.1.4**. The new set is

$$a_p T_p = a_E T_E + a_W T_W + B$$

where  $a_E = \frac{k_e}{(\delta x)_e}$ ,  $a_W = \frac{k_w}{(\delta x)_w}$ ,  $a_p = a_E + a_W - S_p \Delta x$ ,  $B = S_C \Delta x$

#### Eq. 4.1.6

The foregoing introductory discussion provides sufficient background to allow the formulation of the basic rules that our discretization equations should obey, to ensure physical realism and overall balance. Forgoing, we have made certain basic decisions about the type of discretization method to be developed. The discussion has been given in terms of temperature T as the dependent variable. This was done simply for conceptual convenience. The convection term in the general differential equation requires special formulation. The remaining three terms are dealt with in the framework of heat conduction<sup>42</sup>.

## 4.2 Unsteady One-Dimensional Conduction

With reference to the general differential equation for  $\phi$ , we have now seen, at least in the one-dimensional context, how to handle the diffusion term and the source term. Here, we turn to the unsteady term and temporarily drop the source term, since nothing new needs to be said about it. Thus, we seek to solve the unsteady one-dimensional heat-conduction equation

$$\rho c_p \frac{\partial T}{\partial t} = \frac{\partial}{\partial x} \left( k \frac{\partial T}{\partial x} \right) \quad \text{Eq. 4.2.1}$$

---

<sup>42</sup> Suhas V. Patankar, "Numerical Heat Transfer and Fluid Flow", McGraw Hill Book Company, 1980.

Further, for convenience, we shall assume  $\rho c_p$  to be constant. (it was shown how the heat conduction equation could be modified to take account of the variable specific heat  $c_p$ ) Since time is a one-way coordinate, we obtain the solution by marching in time from a given initial distribution of temperature. Thus, in a typical “time step” the task is this: Given the grid-point values of  $T$  at time  $t$ , find the values of  $T$  at time  $t + \Delta t$ . The “old” (given) values of  $T$  at the grid points will be denoted by  $T_{P}^0$ ,  $T_E^0$ ,  $T_W^0$ , and the “new” (unknown) values at time  $t + \Delta t$  by  $T_P^1$ ,  $T_E^1$ ,  $T_W^1$ . The discretization equation is now derived by integrating the above mentioned over the control volume shown in **Figure 3.3.1** and over the time interval from  $t$  to  $t + \Delta t$ . Thus,

$$\rho c_p \int_w^e \int_t^{t+\Delta t} \frac{\partial T}{\partial t} dt dx = \int_t^{t+\Delta t} \int_w^e \left( k \frac{\partial T}{\partial x} \right) dx dt \quad \text{Eq. 4.2.2}$$

where the order of the integrations is chosen according to the nature of the term. For the representation of the term  $dT/dt$ , we shall assume that the grid-point value of  $T$  prevails throughout the control volume. Then

$$\rho c_p \int_w^e \int_t^{t+\Delta t} \frac{\partial T}{\partial t} dt dx = \rho c_p \Delta x (T_P^1 - T_P^0) \quad \text{Eq. 4.2.3}$$

Following our steady-state practice for  $k aT/dx$ , we obtain  $t + \Delta t$

$$\rho c_p \Delta x (T_P^1 - T_P^0) = \int_t^{t+\Delta t} \left[ \frac{k_e (T_E - T_P)}{(\delta x)_e} - \frac{k_w (T_P - T_W)}{(\delta x)_w} \right] dt$$

#### **Eq. 4.2.4**

It is at this point that we need an assumption about how  $T_p$ ,  $T_E$ , and  $T_w$  vary with time from  $t$  to  $t + \Delta t$ . Many assumptions are possible, and some of them can be generalized by proposing  $t + \Delta t$

$$\int_t^{t+\Delta t} T_P dt = [f T_P^1 + (1-f) T_P^0] \Delta t \quad \text{Eq. 4.2.5}$$

where  $f$  is a weighting factor between 0 and 1. Using similar formulas for the integrals of  $T_E$  and  $T_W$ , we derive from **Eq. 4.2.4**

$$\begin{aligned} \rho c_p \frac{\Delta x}{\Delta t} (T_P^1 - T_P^0) &= \\ f \left[ \frac{k_e (T_E^1 - T_P^1)}{(\delta x)_e} - \frac{k_w (T_P^1 - T_W^1)}{(\delta x)_w} \right] + (1-f) \left[ \frac{k_e (T_E^0 - T_P^0)}{(\delta x)_e} - \frac{k_w (T_P^0 - T_W^0)}{(\delta x)_w} \right] \end{aligned}$$

#### **Eq. 4.2.6**

While rearranging this, we shall drop the superscript 1, and remember that  $T_p$ ,  $T_E$ ,  $T_w$  henceforth stand for the new values of  $T$  at time  $t + \Delta t$ . The result is:

$$a_p T_p = a_E [f T_E + (1-f) T_E^0] + a_w [f T_w + (1-f) T_w^0] + [a_p^0 - (1-f)a_E - (1-f)a_w] T_p^0$$

$$a_E = \frac{k_e}{(\delta x)_e}, \quad a_w = \frac{k_w}{(\delta x)_w}, \quad a_p^0 = \frac{\rho c_p \Delta x}{\Delta t}, \quad a_p = f a_E + f a_w + a_p^0$$

**Eq. 4.2.7**

#### 4.2.1 Explicit, Crank-Nicolson and Fully Implicit Schemes

For certain specific values of the weighting factor  $f$ , the discretization equation reduces to one of the well-known schemes for parabolic differential equations. In particular,  $f = 0$  leads to the explicit scheme,  $f = 0.5$  to the Crank-Nicolson scheme, and  $f=1$  to the fully implicit scheme. We shall briefly discuss these schemes and finally indicate the fully implicit scheme as our preference. The different values  $f$  can be interpreted in terms of the  $T_p \sim t$  variations shown in **Figure 4.2.1**.

##### 4.2.1.1 Explicit Scheme

The explicit scheme essentially assumes that the old value  $T_p^0$  prevails throughout the entire time step except at time  $t + \Delta t$ . The fully implicit scheme postulates that, at time  $t$ ,  $T$  suddenly drops from  $T_p^0$  to  $T_p^1$  and then stays at  $T_p$  over the whole of the time step; thus the temperature during the time step is characterized by  $T$ , the new value. The Crank-Nicolson scheme assumes a linear variation of  $T_p$ . At first sight, the linear variation would appear more sensible than the two other alternatives. Why then would we prefer the fully implicit scheme? The answer will emerge very shortly. **For the explicit scheme ( $f=0$ ) :**

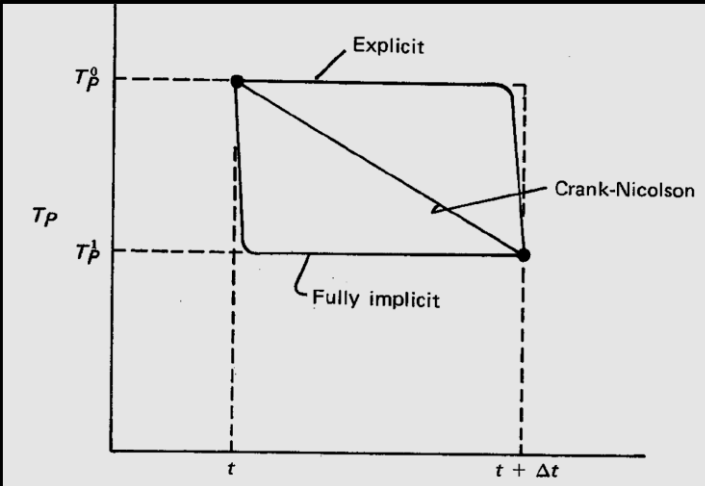


Figure 4.2.1 Variation of Temperature with Time for Three Different Schemes

$$a_p T_p = a_E T_E^0 + a_w T_w^0 + (a_p^0 - a_E - a_w) T_p^0 \quad \text{Eq. 4.2.8}$$

This means that  $T_p$  is not related to other unknowns such as  $T_E$  or  $T_w$ , but it is explicitly obtainable terms of the known temperatures  $T_p$ ,  $T_E$ ,  $T_w$ . This is why the scheme is called explicit. Any scheme with **f Not equal 0** would be implicit; that is,  $T_p$  would be linked to the unknowns  $T_E$  and  $T_w$ , and the solution of a set of simultaneous equations would be necessary. The convenience of the explicit scheme in this regard is, however, offset by a serious limitation. For uniform conductivity and  $\Delta x = (\delta x)_e = (\delta x)_w$ , this condition can be expressed as

$$\Delta t < \frac{\rho c_p (\Delta x)^2}{2k}$$

**Eq. 4.2.9**

If this condition is violated, physically unrealistic results could emerge, because the negative coefficient implies that a higher  $T_{P0}$  results in a lower  $T_P$ .

**Eq. 4.2.9** is the well-known stability criterion for the explicit scheme. It is interesting to note that we have been able to derive this from physical arguments based on one of our basic rules. The troublesome feature about condition (

**Eq. 4.2.9**) is that, as we reduce  $\Delta x$  to improve the spatial accuracy, we are forced to use a much smaller  $\Delta t$ .

#### 4.2.1.2 Crank-Nicolson Scheme

The Crank-Nicolson scheme is usually described as unconditionally stable. An inexperienced user often interprets this to imply that a physically realistic solution will result no matter how large the time step, and such a user is, therefore, surprised to encounter oscillatory solutions. The “stability” in a mathematical sense simply ensures that these oscillations will eventually die out, but it does not guarantee physically plausible solutions. In our framework, this behavior is easy to explain. For  $f = 0.5$ , the coefficient of  $T_{P0}$  in

**Eq. 4.2.9** becomes average of  $a_0 - (a_E + a_W)/2$ . For uniform conductivity and uniform grid spacing, this coefficient can be seen to be  $\rho c_p \Delta x / \Delta t - k / \Delta x$ . Again, whenever the time step is not sufficiently small, this coefficient could become negative, with its potential for physically unrealistic results. The seemingly reasonable linear profile in **Figure 4.2.1** is a good representation of the temperature-time relationship for only small time intervals. Over a larger interval, the intrinsically exponential decay of temperature is akin to a steep drop in the beginning, followed by a flat tail. The assumptions made in the fully implicit scheme are thus closer to reality than the linear profile used in the Crank-Nicolson scheme, especially for large time steps.

#### 4.2.1.3 Fully Implicit Scheme

If we require that the coefficient of  $T_{P0}$  in

**Eq. 4.2.9** must never become negative, the only constant value of  $f$  that ensures this is 1. Thus, the **fully implicit scheme ( $f = 1$ )** satisfies our requirements of simplicity and physically satisfactory behavior. It is for this reason that we shall adopt the fully implicit scheme. It must be admitted that for small time steps the fully implicit scheme is; not as accurate as the Crank-Nicolson scheme. Again, the reason can be seen from **Figure 4.2.1**. The temperature-time curve is nearly linear for small time intervals. It is tempting to seek a scheme that combines the advantages of both schemes and shares the disadvantages of neither. Indeed, this has been done, and the result, called the exponential scheme, has been described by [Patankar and Baliga (1978)]. That scheme is somewhat complicated and it's not included here. Here we record the fully implicit form of

**Eq. 4.2.9**. In doing so, we shall introduce the linearized source term, which we had temporarily dropped. The result is:

$$a_P T_P = a_E T_E + a_W T_W + b$$

$$a_E = \frac{k_e}{(\delta x)_e} , \quad a_W = \frac{k_w}{(\delta x)_w} , \quad a_P^0 = \frac{\rho c_p \Delta x}{\Delta t} , \quad b = S_C \Delta x + a_P^0 T_P^0$$

$$a_P = a_E + a_W + a_P^0 - S_P \Delta x$$

#### Eq. 4.2.10

It can be seen that, as  $\Delta t \rightarrow \infty$ , this equation reduces to our steady-state discretization equation. The main principle of the fully implicit scheme is that the new value  $T_P$  prevails over the entire time step. Thus, if the conductivity  $k_p$  depended on temperature, it should be iteratively recalculated from  $T_P$ , exactly as in our steady-state procedure. Other aspects of the steady-state procedure, such as boundary conditions, source-term linearization, and the TDMA, are also equally applicable to the

unsteady situation.

### 4.3 Discretization Equation for 2D

A portion of a two-dimensional grid is presented in **Figure 4.2.1**. For the grid point P, points E and W, are its x-direction neighbors, while N and S (denoting north and south) are the y-direction neighbors. The control volume around P is shown by dashed lines. Its thickness in the z direction is assumed to be unity. The nomenclature introduced in **Figure 3.3.1** for distances  $\Delta x$ ,  $(\delta x)_e$ , is to be extended to two dimensions here. The question of the actual location of the control-volume faces in relation to the grid points is still left open. Locating them exactly midway between the neighboring grid points is an obvious possibility, but other practices can also be employed, some of which will be discussed earlier. Here we shall derive discretization equations that will be applicable to any such practice.

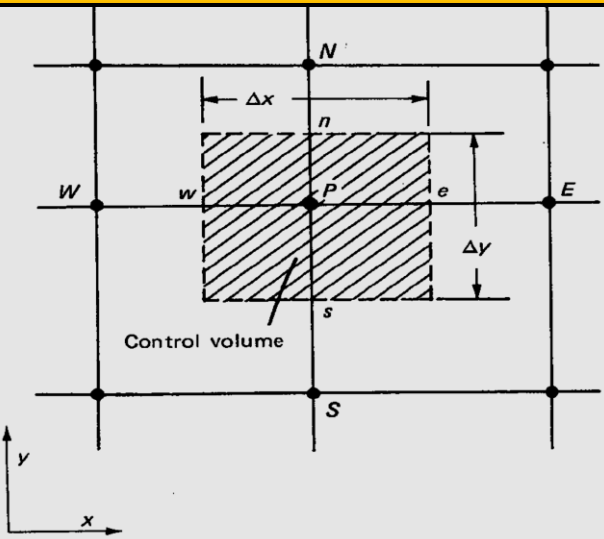


Figure 4.2.1 Control Volume for two dimensional

$$\rho c_p \frac{\partial T}{\partial t} = \frac{\partial}{\partial x} \left( k \frac{\partial T}{\partial x} \right) + \frac{\partial}{\partial y} \left( k \frac{\partial T}{\partial y} \right) + S \quad \text{Eq. 4.3.1}$$

We have seen how to calculate the heat flux  $q_e$  at the control-volume face between P and E. We shall assume that  $q_e$ , thus obtained, prevails over the entire face of area  $\Delta y$ . 1. Heat flow rates through the other faces can be obtained in a similar fashion. In this manner, the differential equation situation (like above) can be instantly turned into the discretization equation:

$$a_P T_P = a_E T_E + a_W T_W + a_N T_N + a_S T_S + b \quad (.)$$

$$\text{where } a_E = \frac{k_e \Delta y}{(\delta x)_e}, \quad a_W = \frac{k_w \Delta y}{(\delta x)_w}, \quad a_N = \frac{k_n \Delta x}{(\delta y)_n}, \quad a_S = \frac{k_s \Delta x}{(\delta y)_s},$$

$$a_P^0 = \frac{\rho c_p \Delta x \Delta x}{\Delta t}, \quad b = S_C \Delta x \Delta y + a_P^0 T_P^0$$

$$a_P = a_E + a_W + a_N + a_S + a_P^0 - S_P \Delta x \Delta y$$

#### Eq. 4.3.2

The product  $\Delta x \Delta y$  is the volume of the control volume.

### 4.4 Discretization Equation for 3D

Finally, we add two more neighbors T and B (top and bottom) for the z direction to complete the three-dimensional configuration. For details readers should consult excellent discussion in (Patankar, 1980).

## 4.5 Solution of the Algebraic Equations

It should be noted that, while constructing the discretization equations, we cast them into a linear form but did not assume that a particular method would be used for their solution. Therefore, any suitable solution method can be employed at this stage. It is useful to consider the derivation of the equations and their solution as two distinct operations, and there is no need for the choices in one to influence the other. In a computer program, the two operations can be conveniently performed in separate sections, and either section can be independently modified when desired. So far, we have obtained the multidimensional discretization equations by a straightforward extension of the one-dimensional situation. One procedure that cannot so easily be extended to multiple dimensions is the tridiagonal matrix algorithm (TDMA). Direct methods (i.e., those requiring no iteration) for solving the algebraic equations arising in two- or three-dimensional problems are much more complicated, and require rather large amounts of computer storage and time. For a linear problem, which requires the solution of the algebraic equations only once, a direct method may be acceptable; but the alternative, then, is iterative methods for the solution of algebraic equations. These start from a guessed field of  $T$  (the dependent variable) and use the algebraic equations in some manner to obtain an improved field.

Successive repetitions of the algorithm finally lead to a solution that is sufficiently close to the correct solution of the algebraic equations. Iterative methods usually require very small additional storage in the computer, and they are especially attractive for handling nonlinearities. In a nonlinear problem, it is not necessary or wise to take the solution of the algebraic equations to final convergence for a fixed set of coefficient values. With a given set of these values, a few iterations of each equation-solving algorithm are sufficient before the updating of the coefficients is performed. It seems that, in general, there should be a certain balance between the effort required to calculate the coefficients and that spent on solving the equations. Once the coefficients are calculated, we must perform sufficient iterations of the equation solver to extract substantial benefit from the coefficients, but it is unwise to spend an excessive amount of effort on solving equations that are based on only tentative coefficients. There are many iterative methods for solving algebraic equations, but we shall describe only two methods; the first will set the background, and the second is recommended for use.

### 4.5.1 Gauss-Seidel Point-by-Point Method

The simplest of all iterative methods is the Gauss-Seidel method in which the values of the variable are calculated by visiting each grid point in a certain order. Only one set of  $T$ 's is held in computer storage. In the beginning, these represent the initial guess or values from the previous iteration. As each grid point is visited, the corresponding value of  $T$  in the computer storage is altered as follows: If the discretization equation is written as

$$a_p T_p = \sum_{nb} a_{nb} T_{nb} + b \quad \text{Eq. 4.5.1}$$

where the subscript nb denotes a neighbor point, then  $T_p$  at the visited grid point is calculated from

$$T_p = \frac{\sum_{nb} a_{nb} + T_{nb}^* + b}{a_p} \quad \text{Eq. 4.5.2}$$

where  $T^*$  stands for the neighbor-point value present in the computer storage. For neighbors that have already been visited during the current iteration,  $T^*$ , is the freshly calculated value; for yet o-

be-visited neighbors,  $T^*$ , is the value from the previous iteration. In any case,  $T^*$ , is the latest available value for the neighbor-point temperature. When all grid points have been visited in this manner, one iteration of the Gauss-Seidel method is complete. A major disadvantage of the otherwise attractive Gauss-Seidel method is that its convergence is too slow, especially when a large number of grid points are involved. The reason for the slowness is easy to understand; the method transmits the boundary-condition information at a rate of one grid interval per iteration.

#### 4.5.2 A Line-by-Line Method

A convenient combination of the direct method (TDMA) for one-dimensional situations and the **Gauss-Seidel** method can now be formed. We shall choose a grid line (say, in the y direction), assume that the T's along the neighboring lines (i.e., the x- and z-direction neighbors of the 5 points on the chosen line) are known from their "latest" values, and solve for the T's along the chosen line by the TDMA. We shall follow this procedure for all the lines in one direction and repeat the procedure, if desired, for the lines in the other direction(s).

#### 4.5.3 Other Iterative Methods

A commonly used line-by-line method known as *ADI (Alternating-Direction Implicit)*. Another iterative technique for solving multidimensional discretization equations is the *Strongly Implicit Procedure* described by Stone (1968). A detailed study of these methods is left to the interested reader.

##### 4.5.3.1 Over-Relaxation and Under-Relaxation

In the iterative solution of the algebraic equations or in the overall iterative scheme employed for handling nonlinearity, it is often desirable to speed up or to slow down the changes, from iteration to iteration, in the values of the dependent variable. This process is called over relaxation or under relaxation, depending on whether the variable changes are accelerated or slowed down. Over relaxation is often used in conjunction with the Gauss-Seidel method, the resulting scheme being known as Successive Over-Relaxation (SOR). With the line-by-line method, the use of over relaxation is less common. Under relaxation is a very useful device for nonlinear problems. It is often employed to avoid divergence in the iterative solution of strongly nonlinear equations. There are many ways of introducing over relaxation or under relaxation. Some practices will be described here. We shall work with the general discretization equation of the form

$$T_p = \frac{\sum_{nb} a_{nb} + T_{nb}^* + b}{a_p} \quad \text{Eq. 4.5.3}$$

If we add  $T_p^*$  and subtract to RHS, we have

$$T_p = T_p^* + \frac{\sum_{nb} a_{nb} + T_{nb}^* + b}{a_p} - T_p^* \quad \text{Eq. 4.5.4}$$

where the contents of the parentheses represent the change in  $T_p$  produced by the current iteration. This change can be modified by the introduction of a relaxation factor  $\beta$ , so that

$$T_p = T_p^* + \beta \left( \frac{\sum_{nb} a_{nb} + T_{nb}^* + b}{a_p} - T_p^* \right)$$

Eq. 4.5.5

$$\text{or } \frac{a_p}{\beta} T_p = \sum_{nb} \beta_{nb} T_{nb} + b + (1 - \beta) \frac{a_p}{\beta} T_p^*$$

At first, it should be noted that, when the iterations converge, that is,  $T_p$  becomes equal to  $T_p^*$ , it implies that the converged values of  $T$  do satisfy the original equation. Any relaxation scheme, of course, must possess this property; the final converged solution. When the relaxation factor is between 0 and 1, its effects is *under-relaxation*; that is, the values of  $T_p$  stay closer to  $T_p^*$ . For a very small value of  $\beta$ , the changes in  $T_p$  become very slow. When  $a$  is greater than 1, *over-relaxation* is produced. There are no general rules for choosing the best value of  $\beta$ . The optimum value depends upon a number of factors, such as the nature of the problem, the number of grid points, the grid spacing, and the iterative procedure used. Usually, a suitable value of  $a$  can be found by experience and from exploratory computations for the given problem. There is no need to maintain the same value of  $\beta$  during the entire computation. The value can be changed from iteration to iteration. Indeed, it is permissible, though not very convenient, to choose a different value of  $a$  for each grid point.

## 4.6 Convection and Diffusion

So far, in the guise of heat conduction, we have seen how to formulate the discretization equation from the general differential equation containing the unsteady term, the diffusion term, and the source term. The previous description in terms of temperature  $T$  and conductivity  $k$  can easily be recast in terms of the general variable  $\varphi$  and its diffusion coefficient  $\Gamma$ . The only omission has been the convection term, which we shall now include. We have also dealt with the methods of solving the algebraic equations; as long as the addition of the convection term does not alter the form of the discretization equation, the same methods continue to apply. The convection is created by fluid flow. Our task is to obtain a solution for  $\varphi$  in the presence of a given flow field (i.e., the velocity components and the density). How we know the flow field is a question we do not ask at this stage. It could have come from experiment, be given as an analytical solution, be obtained by the method described later or simply be guessed. The origin of the flow-field information is immaterial here. Having somehow acquired the flow field, we wish to calculate the temperature, concentration, enthalpy, or any such quantity that is represented by the general variable.

Although convection is the only new term introduced here, its formulation is not very straightforward. The convection term has an inseparable connection with the diffusion term, and therefore, the two terms need to be handled as one unit. This is why the words "convection and diffusion" forms; other terms can also be present, but, only in the background. It should be remembered that the word diffusion is used here in a generalized sense. It is not restricted only to the diffusion of a chemical species caused by concentration gradients. The diffusion flux due to the gradient of the general variable  $\varphi$  is  $\Gamma \partial \varphi / \partial x_i$ , which, for specific meanings of  $\varphi$  would represent chemical-species diffusion flux, heat flux, viscous stress, etc.

## 4.7 General Convection & Diffusion Equation

The general differential equation contains the term  $(\partial / \partial x_i)(\Gamma \partial \varphi / \partial x_i)$ , which is designated as the diffusion term. Actually, this expression denotes the sum of three terms for the three coordinate directions, yet it is convenient to refer to them collectively as the diffusion term. The same is true of

the convection term, which is  $(\partial/\partial x_j)(\rho u \varphi)$ . Since the given flow field must satisfy the continuity equation

$$\frac{\partial \rho}{\partial t} + \frac{\partial}{\partial x_j}(\rho u_j) = 0$$

#### Eq. 4.7.1

the general differential equation is given by **Error! Reference source not found.** From this form of the equation, it follows that, for given distributions of  $\rho$ ,  $u_j$ ,  $\Gamma$ , and  $S$ , any solution  $\varphi$  and its variant ( $\varphi$  plus a constant) would both satisfy the above equation.

#### 4.7.1 Steady One-Dimensional Convection and Diffusion

As in the last chapter, much can be learned from consideration of the simplest possible case. Here we shall consider a steady one-dimensional situation in which only the convection and diffusion terms are present. The governing differential equation is

$$\frac{d}{dx}(\rho u \varphi) = \frac{d}{dx}\left(\Gamma \frac{d\varphi}{dx}\right) \quad \text{Eq. 4.7.2}$$

where  $u$  represents the velocity in the  $x$  direction. Also, the continuity equation becomes

$$\frac{d}{dx}(\rho u) = 0 \quad \text{or} \quad \rho u = \text{constant} \quad \text{Eq. 4.7.3}$$

Similar procedures can be used for 2 or 3 dimensional flows. For example for a unsteady two dimensional flow

$$\frac{\partial}{\partial t}(\rho \varphi) + \frac{\partial J_x}{\partial x} + \frac{\partial J_y}{\partial y} = S$$

where  $J_x = \rho u \varphi - \Gamma \frac{\partial \varphi}{\partial x}$  and  $J_y = \rho v \varphi - \Gamma \frac{\partial \varphi}{\partial y}$  Eq. 4.7.4

And  $u$  and  $v$  denotes the velocities in  $x$  and  $y$  direction which can be easily integrated over the control volume.

##### 4.7.1.1 A Preliminary Derivation

Integration of **Eq. 4.7.1** over the control volume shown in **Figure 4.7.1** gives

$$(\rho u \varphi)_e - (\rho u \varphi)_w = \left( \Gamma \frac{d\varphi}{dx} \right)_e - \left( \Gamma \frac{d\varphi}{dx} \right)_w$$

#### Eq. 4.7.5

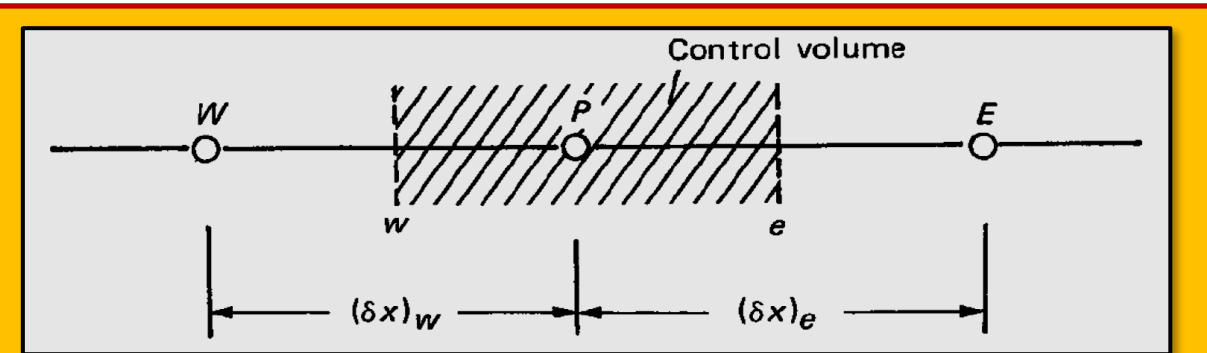


Figure 4.7.1 Typical grid point cluster

For the convection term, the same choice of profile would at first seem natural. The factor 1/2 arises from the assumption of the interfaces being midway; some other interpolation factors would have appeared for differently located interfaces. Now, [Eq. 4.7.5](#) can be written as

$$\frac{1}{2}[(\rho u)_e(\varphi_E + \varphi_P) - (\rho u)_w(\varphi_E + \varphi_P)] = \frac{\Gamma_e(\varphi_E + \varphi_P)}{(\delta x)_e} - \frac{\Gamma_w(\varphi_E + \varphi_P)}{(\delta x)_w}$$

**Eq. 4.7.6**

where the values of  $\Gamma_e$  and  $\Gamma_w$  are to be obtained as before. To arrange the equation more compactly, we define two new symbols F and D, as follows:

$$F = \rho u \quad , \quad D = \frac{\Gamma}{\delta x} \quad \text{Eq. 4.7.7}$$

Both have the same dimensions; F indicates the strength of the convection (or flow), while D is the diffusion conductance. It should be noted that, whereas D always remains positive, F can take either positive or negative values depending on the direction of the fluid flow. With the new symbols, the discretization equation becomes:

$$a_P \varphi_P = a_E \varphi_E + a_W \varphi_W$$

where  $a_E = D_e - \frac{F_e}{2}$  ,  $a_W = D_w + \frac{F_w}{2}$  ,  $a_P = D_e + \frac{F_e}{2} + D_w - \frac{F_w}{2}$

**Eq. 4.7.8****4.7.1.2 Discussion**

- Since by continuity  $F_e = F_w$ , we do get the property  $a_P = a_E + a_W$ . Further, it is interesting to note from [Eq. 4.7.8](#) that the discretization equation has this property only if the flow field satisfies continuity, just as Eq. (5.3) can be derived from Eq. (5.2) only if the continuity equation is satisfied.
- The discretization Eq. 4.7.6 represents the implications of the piecewise-linear profile for (b). This form is also known as the *central-difference scheme* and is the natural outcome of a Taylor-series formulation.

- The above formulation prone to produce unrealistic results. This is why all the early attempts to solve convective problems by the central-difference scheme were limited to low Reynolds numbers (i.e., to low values of F/D). Since the foregoing preliminary formulation has resulted in an unacceptable discretization equation, we must seek better formulations. Some such possibilities are described in the following subsections.

#### 4.7.1.3 The Upwind Scheme

A well-known remedy for the difficulties encountered is the upwind scheme, which is also known as the upwind-difference scheme, the upstream-difference scheme, the donor-cell method, etc. It was first put forward by Courant, Isaacson, and Rees (1952). The upwind scheme recognizes that the weak point in the preliminary formulation is the assumption that the convected property  $\varphi_e$  at the interface is the average of ( $\varphi_E$  and  $\varphi_P$ , and it proposes a better prescription. The formulation of the diffusion term is left unchanged, but the convection term is calculated from the following assumption that the value of  $\varphi$  at an interface is equal to the value of  $\varphi$  at the grid point on the upwind side of the face. Thus,

$$\varphi_e = \varphi_P \quad \text{if} \quad F_e > 0 \quad , \quad \varphi_e = \varphi_E \quad \text{if} \quad F_e < 0 \quad \text{Eq. 4.7.9}$$

The value of  $\varphi_w$  can be defined similarly.

#### 4.7.1.4 The Exact Solution

Fortunately, the governing equation (5.4) can be solved exactly if Peclet number (P) is taken to be constant [pu is already constant, as given by Eq. (5.5)]. If a domain  $0 < x < L$  is used, with the boundary condition

$$\frac{\varphi - \varphi_0}{\varphi_L - \varphi_0} = \frac{\exp(Px/L) - 1}{\exp(p) - 1} \quad \text{B.C.s } \begin{cases} x = 0 \rightarrow \varphi = \varphi_0 \\ x = L \rightarrow \varphi = \varphi_L \end{cases} \quad \text{Eq. 4.7.10}$$

where  $P = \frac{\rho u L}{\Gamma}$

It can be seen that P is the ratio of the strengths of convection and diffusion. The nature of the this exact solution can be understood from [Figure 4.7.2](#) where the  $\varphi \sim x$  variation has been plotted for different values of the Peclet number. In the limit Of zero Peclet number, we get the pure-diffusion (or conduction) problem, and the  $\varphi \sim x$  variation is linear. When the flow is in the positive x direction (i.e., for positive values of P), the values of  $\varphi$  in the domain seem to be more influenced by the upstream value ( $\varphi_0$ ). For a large positive value of P, the value of  $\varphi$  remains very close to the upstream value  $\varphi_0$  over much of the domain. The picture is reversed for negative values of P. When the fluid flows in the negative x direction,  $\varphi_L$  becomes the upstream value, which dominates the values of  $\varphi$  in the domain. For a large negative P, the value of  $\varphi$  over most of the region is very nearly equal to  $\varphi_L$ .

#### 4.7.1.5 Implications

For constructing the discretization equation, we can now obtain guidance from [Figure 4.7.2](#) regarding the appropriate  $\varphi \sim x$  profile between grid points.

- It is easy to see why our preliminary derivation failed to give a satisfactory formulation. The  $\varphi \sim x$  profile is far from being linear except for small values of P.

- When  $P$  is large, the value of ( $\phi$  at  $x = L/2$  (the interface) is nearly equal to the value of  $\phi$  at the upwind boundary. This is precisely the assumption made in the upwind scheme; but there it is used for  $\phi_L$  all values of  $P$ , not just for large values.
- When  $P$  is large,  $d\phi/dx$  is nearly zero at  $x=L/2$ . Thus, the diffusion is almost absent.

The upwind scheme always calculates the diffusion term from a linear  $\phi \sim x$  profile and thus overestimates diffusion at large values of  $P$ . If the discretization equation were to be obtained directly from the exact solution shown in **Figure 4.7.2**, the resulting scheme would not have any of these defects. Other noticeable schemes are the **exponential**, **hybrid** and **the power law** schemes.

#### 4.7.2 False Diffusion

Here, we shall discuss a topic that has caused considerable controversy, confusion, and misunderstanding among the practitioners of numerical analysis. There is something called "**false diffusion**" which is quite commonly misinterpreted, but which, in its proper meaning, represents a major weak point of most convection-diffusion formulations.

##### 4.7.2.1 The Common View of False Diffusion

It is very common to encounter, in the literature, statements such as the central-difference scheme has second-order accuracy, while the upwind scheme is only first-order accurate; or the upwind scheme causes severe false diffusion. The implication is that the central-difference scheme is better than the upwind scheme. It is true that from a Taylor-series expansion one can show that the central-difference scheme has a truncation error of the order of  $(\Delta x)^3$ , while the upwind scheme has an error of the order of  $(\Delta x)^2$ . However, since the  $\phi \sim x$  variation arising in the convection-diffusion problem is exponential, a truncated Taylor series ceases to be a good representation of it for anything but extremely small values of  $\Delta x$  (or, rather, of the corresponding Peclet number). At larger values of  $\Delta x$ , which is all one can afford in most practical problems, the Taylor-series analysis is misleading; there, as we have seen, it is the upwind scheme that gives more reasonable results than the central-difference scheme. If we compare the coefficients for the central-difference and upwind schemes, it can be shown that the upwind scheme is equivalent to replacing  $\Gamma$  in the central-difference scheme with  $\Gamma + \rho u \delta x / 2$ . In other words, the upwind scheme seems to augment the true diffusion coefficient  $\Gamma$  by a fictitious (and hence false) diffusion coefficient  $\rho u \delta x / 2$ . This introduction of an artificial diffusion coefficient is then considered to be inaccurate, a wrong representation of reality.

Again, the trouble in the argument lies in assuming the central-difference scheme as accurate and standard (or the underlying Taylor-series expansion as reliable) and then viewing the upwind scheme from this frame of reference. In this manner, one would discover some false diffusion even in the exponential scheme, which is the exact solution itself. On the other hand, the theory presented in this chapter leads to the conclusion that the so-called false diffusion coefficient  $\rho u \delta x / 2$  is indeed a desirable addition at large Peclet numbers, for it actually tends to correct the wrong implications that would otherwise follow from the central-difference scheme. There is no doubt that, for very small Peclet numbers, the central-difference scheme is more accurate than the upwind scheme. This has already been shown in a number of diagrams; and favored schemes such as the exponential, the hybrid, and the power-law scheme indeed conform to the central-difference scheme at very low

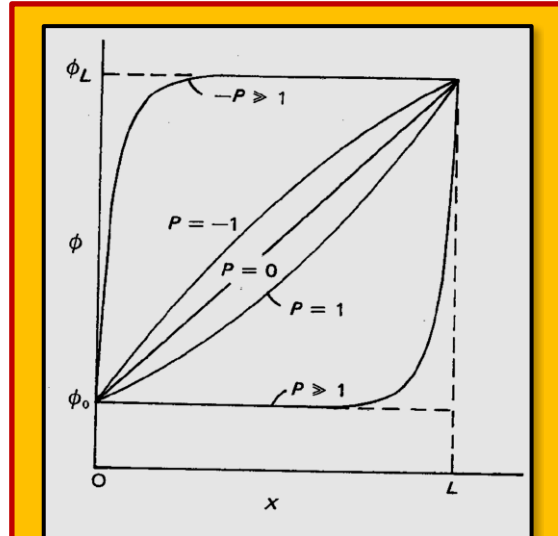


Figure 4.7.2 Exact solution for one-dimensional convection-diffusion problem

Peclet numbers. In any case, the question of false diffusion is never serious at low Peclet numbers, because then the real diffusion is quite large by comparison. It is for large Peclet numbers that the matter of false diffusion attains importance. There the central-difference scheme has little to offer, and all the other schemes that we have considered show almost identical behavior. It is for this reason that our remaining discussion will concentrate on very large Peclet numbers and on the upwind scheme; however, the conclusions will be equally applicable to the exponential, hybrid, and power-law schemes.

#### 4.7.2.2 Proper View of False Diffusion

Having seen that the common view of false diffusion is indeed misleading, we now turn to what can be truly described as false diffusion. The first thing to recognize is that false diffusion is a multidimensional phenomenon; it has absolutely no counterpart in steady one-dimensional situations. (Unsteady one-dimensional situations do suffer from a kind of false diffusion; we shall, however, confine our attention to steady situations). To visualize what is correctly meant by false diffusion, let us consider the situation shown in **Figure 4.7.3**.

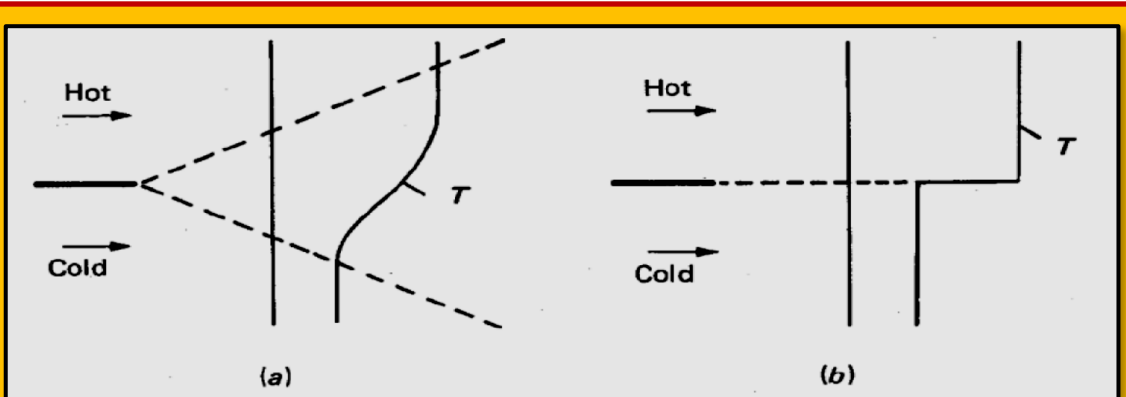


Figure 4.7.3 Temperature Distributions in the Presence or Absence of Diffusion

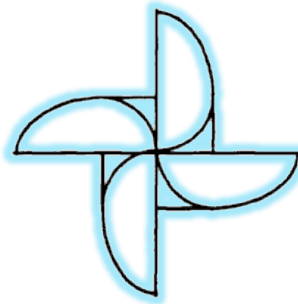
Two parallel streams of equal velocity but unequal temperatures come in contact. If the diffusion coefficient  $\Gamma$  is nonzero, a mixing layer will form in which the temperature gradually changes from the higher value to the lower one, and the cross-stream width of this layer will grow in the downstream direction. If, on the other hand, the diffusion coefficient  $\Gamma$  were zero, no mixing layer would form and the temperature discontinuity would persist in the stream wise direction. The best situation for observing false diffusion is the one in which the real diffusion is set to zero. If the numerical solution for the  $\Gamma = 0$  case produces a smeared temperature profile (which is characteristic of a nonzero  $\Gamma$ ), we can conclude that the numerical scheme entails false diffusion. For  $\Gamma = 0$ , the central-difference scheme would lead to  $a_p = 0$ . Therefore, the usual iterative methods for solving the algebraic equations cannot be used. If an attempt is made to solve the equations by a direct method, then either a unique solution is not found

or the solutions turn out to be highly unrealistic. A numerical solution of a differential equation consists of a set of numbers from which the distribution of the dependent variable  $\varphi$  can be constructed. In this sense, a numerical method is akin to a laboratory experiment, in which a set of instrument readings enables us to establish the distribution of the measured quantity in the domain under investigation. The numerical analyst and the laboratory experimenter both must remain content with only a finite number of numerical values as the outcome, although this number can, at least in principle, be made large enough for practical purposes. Let us suppose that we decide to represent the variation of  $\varphi$  by a polynomial in  $x$ ,

$$\varphi = a_0 + a_1 x + a_2 x^2 + \dots + a_m x^m$$

Eq. 4.7.11

and employ a numerical method to find the finite number of coefficients  $a_0, a_1, a_2, \dots, a_m$ . This will enable us to evaluate  $\varphi$  at any location  $x$  by substituting the value of  $x$  and the values of the  $a$ 's into Eq. 4.7.11. This procedure is, however, somewhat inconvenient if our ultimate interest is to obtain the values of  $\varphi$  at various locations. The values of the  $a$ 's are, by themselves, not particularly meaningful, and the substitution operation must be carried out to arrive at the required values of  $\varphi$ . This leads to the following thought: *Why not construct a method that employs the values of  $\varphi$  at a number of given points as the primary unknowns?* Indeed, most numerical methods for solving differential equations do belong in this category, and therefore we shall limit our attention to such methods. Thus, a numerical method treats as its basic unknowns the values of the dependent variable at a finite number of locations (called the grid points) in the calculation domain. The method includes the tasks of providing a set of algebraic equations for these unknowns and of prescribing an algorithm for solving the equations.



## 5 Flow Field Calculation (Convection)

### 5.1 Difficulty in Estimating Pressure

Previously, we formulated the procedure for solving the general differential equation. However, except in some very special circumstances, it is not possible to specify the flow field; rather, we must calculate the local velocity components and the density field from the appropriate governing equations. The velocity components are governed by the momentum equations, which are particular cases of the general differential equation for  $\varphi$  (with  $\varphi = u, \Gamma = \mu$ , and so on). Thus, we are tempted to conclude that we already have developed the method for solving the momentum equations, thereby getting the velocity field. Where, then, is the difficulty? If the nonlinearity of the momentum equations appears to be a difficulty, we only have to remind ourselves that, while treating heat conduction, we saw **how to handle non-linearity by iteration**. In particular, the convection coefficient  $\rho u$  being a function of the dependent variable of the momentum equation is no different from the conductivity  $k$  being a function of the temperature  $T$ . Starting with a guessed velocity field, we could iteratively solve the momentum equations to arrive at the converged solution for the velocity components.

**The real difficulty in the calculation of the velocity field lies in the unknown pressure field.** The pressure gradient forms a part of the source term for a momentum equation. Yet, there is no obvious equation for obtaining pressure. For a given pressure field, it is true, there is no particular difficulty in solving the momentum equations. But, the way to determine the pressure field seems rather obscure. The pressure field is indirectly specified via the continuity equation. When the correct pressure field is substituted into the momentum equations, the resulting velocity field satisfies the continuity equation. This indirect specification, however, is not very useful for our purposes unless we attempt a direct solution of the whole set of the discretization equations resulting from the momentum and continuity equations. Since we have preferred iterative methods of solving the discretization equations even for a single dependent variable, the direct solution for the entire set of velocity components and pressure seems out of the question.

### 5.2 Vorticity-Based Methods

The difficulty associated with the determination of pressure has led to methods that eliminate pressure from the governing equations. Thus, in two dimensions, the elimination of pressure from the two momentum equations by cross differentiation leads to a vorticity-transport equation. This, when combined with the definition of a stream function for steady two-dimensional situations, is the basis of the well-known "**stream-function/vorticity method**". The stream-function/vorticity method has some attractive features. The pressure makes no appearance, and, instead of dealing with the continuity equation and two momentum equations, we need to solve only two equations 1 to obtain the stream function and the vorticity. Some of the boundary conditions can be rather easily specified: When an external irrotational flow lies adjacent to the calculation domain, the boundary vorticity can conveniently be set equal to zero. There are, however, some major disadvantages to the stream-function[vorticity method. The value of vorticity at a wall is difficult to specify and is often the cause of trouble in getting a converged solution. The pressure, which has been so cleverly eliminated, frequently happens to be an important desired result or even an intermediate outcome required for the calculation of density and other fluid properties. Then, the some methods, especially those dealing with compressible flows, regard the density  $\rho$  as the dependent variable of the continuity equation and then extract the pressure from it via an equation of state. This approach is, however, inapplicable to constant density or incompressible flows. In such situations, it is the effect of pressure on velocity, and not on density, that is of primary importance. effort of extracting pressure from vorticity offsets the computational savings obtained otherwise. But, above all, the major shortcoming of the method is that it cannot easily be extended to three-dimensional situations, for

which a stream function does not exist. Since most practical problems are three-dimensional, a method that is intrinsically restricted to two dimensions suffers from a serious limitation.

For three dimensions, an approach based on vorticity uses six dependent variables, namely, the three components of the vorticity vector and the three components of the velocity-potential vector [Aziz and Hellums (1967)]. Thus, the complexity is actually greater than that of treating the three velocity components and pressure directly. Also, the vorticity vector and the velocity-potential vector involve concepts that are harder to visualize and interpret than the meanings of the velocity components and pressure. In keeping with our desire to formulate physically meaningful approaches, we seek a method that uses the so-called *primitive variables*, namely the velocity components and pressure. Thus the main task in this chapter is to convert the indirect information in the continuity equation into a direct algorithm for the calculation of pressure. A few minor difficulties arise, which we shall discuss before we begin this task.

### 5.3 Pressure-Gradient Term

If we begin to construct the discretization form of the x-direction momentum equation for the one-dimensional situation shown in [Figure 5.3.1](#), the only new feature is the representation of the term  $dp/dx$  integrated over the control volume. The resulting contribution to the discretization equation is the pressure drop  $p_w - p_e$ , which is the net pressure force exerted on the control volume of unit cross-sectional area. To express  $p_w - p_e$  in terms of the grid-point pressures, we may assume a piecewise-linear profile for pressure. Further, if the control-volume faces e and w, are chosen to lie midway between the respective grid points, we have

$$p_w - p_e = \frac{p_w + p_p}{2} - \frac{p_p + p_e}{2} = \frac{p_w - p_e}{2} \quad \text{Eq. 5.3.1}$$

This assumption is made here only for algebraic convenience. When the control volume faces are not midway, the difficulties being discussed here do not go away, but appear in a less clear form. Thus, the assumption of midway faces is not a cause of the difficulties, but makes the discussion easy to follow. This means that the momentum equation will contain the pressure difference between two alternate grid points, and not between adjacent ones. The implication is that the pressure is, in effect, taken from a coarser grid than the one actually employed. This would tend to diminish the accuracy of the solution. But, there is another implication that is far more serious. It can be best seen from [Figure 5.3.1](#), where a pressure field is proposed in terms of the grid-point values of pressure. Such a zig-zag field cannot be regarded as realistic; but, for any grid point P, the corresponding  $P_w - P_e$  can be seen to be zero, since the alternate pressure values are everywhere equal. Thus, the devastating sequence is that such a wavy pressure field will be felt like a uniform pressure field by the momentum equation.

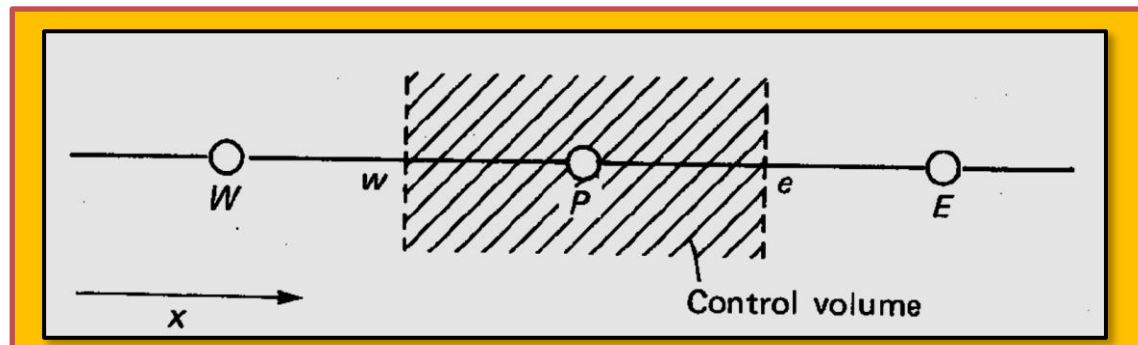


Figure 5.3.1 Three-point grid cluster

The difficulty can be seen more dramatically in a two-dimensional situation. Just as the x-direction momentum is influenced by  $P_w - P_E$ , the y-direction momentum is affected by  $P_S - P_N$  *then the pressure  $P_P$  has no role to play.* With this in mind, we can conclude that the pressure field, which is made up of four arbitrary values of pressure arranged in a checkerboard pattern, would produce no pressure force in the x or y direction. Thus, a highly non-uniform pressure field would be treated as a uniform pressure field by the particular discretized form of the momentum equations. Should such pressure fields arise during the iterative solution procedure, there would be nothing to stop them from being preserved till convergence, since the momentum equations would be oblivious to their presence. It is easy to imagine that the three-dimensional situation would allow an even more complex pattern, which the momentum equations would still interpret as a uniform pressure field. If a certain smooth pressure field is obtained as a solution, any number of additional solutions can be constructed by adding a checkerboard pressure field to that solution. The momentum equations would remain unaffected by this addition, since the checkerboard field implies zero pressure force. A numerical method that allows such absurd solutions is certainly undesirable.

## 5.4 Representation of the Continuity Equation

A similar kind of difficulty arises when we try to construct the discretization form of the continuity equation. For the steady one-dimensional constant density situation, the continuity equation is simply

$$\frac{du}{dx} = 0 \quad , \quad u_E - u_W = 0 \quad \text{Eq. 5.4.1}$$

Thus, the discretized continuity equation demands the equality of velocities at alternate grid points and not at adjacent ones. *A consequence is that velocity fields of the type wavy which are not at all realistic, do satisfy the discretized continuity equation.* In two- and three-dimensional situations, similar patterns for all the velocity components can be created. They will satisfy the continuity equation but can hardly be accepted as reasonable or meaningful solutions. These difficulties must be resolved before a numerical method involving the velocity components and pressure can be formulated. In the literature, some methods can be found that pay no special attention to these difficulties. There, the possible unrealistic solutions are avoided by some special treatment at the boundaries, by over specification of the boundary conditions, by under relaxation with respect to a smooth initial guess, or by good fortune. But most such methods would accept pressure and velocity fields of the type shown here as satisfactory solutions, and, in absence of special tricks, there is always the danger of arriving at such solutions.

Before we proceed to describe a way out of these difficulties, it is interesting to note that the troublesome hurdles in numerical analysis seem to . be associated with the first derivatives. The second derivative is always well behaved and creates no difficulties. On the other hand, all the complications encountered can be attributed to the first derivative representing the convection term and here, the first derivatives of pressure (in the momentum equations) and of velocity (in the continuity equation) cause considerable nuisance.

### 5.4.1 A Remedy; Staggered Grid

The difficulties described so far can be resolved by recognizing that we do not have to calculate all the variables for the same grid points. We can, if we wish, employ a different grid for each dependent variable. Of course, we would not exercise this freedom if there were no benefit to be derived. But, in the case of the velocity components, there is a significant benefit to be obtained by arranging them on grids that are different from the grid used for all other variables. The benefit is that the difficulties described previously will totally disappear. Such a displaced or "staggered" grid for the velocity components was first used by Harlow and Welch (1965) in their MAC method and has been used in

other methods developed by Harlow and co-workers. It forms the basis of the SIVA procedure of Caretto, Curr, and Spalding (1972) and the *SIMPLE* procedure of Patankar and Spalding (1972a). In the staggered grid, the velocity components are calculated for the points that lie on the faces of the control volumes. Thus, the x-direction velocity  $u$  is calculated at the faces that are normal to the x direction. The locations for  $u$  are shown in [Figure 5.5.1](#) by short arrows, while the grid points (hereafter called the main grid points) are shown by small circles; the dashed lines indicate the control-volume faces. It will be noticed that, with respect to the main grid points, the  $u$  locations are staggered only in the x direction. In other words, the location for  $u$  lies on the x-direction link joining two adjacent main grid points. Whether the  $u$  location is exactly midway between the grid points depends upon how the control volumes are defined. The  $u$  location must lie on the control-volume face, irrespective of whether the latter happens to be midway between the grid points. It is easy to see how the locations for the velocity components  $P$  and  $W$  are to be defined. A corresponding three dimensional pattern can be imagined in a straightforward manner. An immediate consequence of the staggered grid is that the mass flow rates across the control-volume faces can be calculated without any interpolation for the relevant velocity component.

However, this feature, although it offers some convenience in setting up the general discretization equation is not an important advantage of the staggered grid. The important advantages are twofold. For a typical control volume (shown shaded in [Figure 5.5.1](#)) it is easy to see that the discretized continuity equation would contain the differences of adjacent velocity components, and that this would prevent a wavy velocity field, such as the one for pressure, from satisfying the continuity equation. In the staggered grid, only "reasonable" velocity fields would have the possibility of being acceptable to the continuity equation. The second important advantage of the staggered grid is that the pressure difference between two adjacent grid points now becomes the natural driving force for the velocity component located between these 3 grid points. Consequently, pressure fields such would no longer be felt as uniform pressure fields and could not arise as possible solutions. ***The difficulties described can thus be attributed to the practice of calculating all variables for the same grid points. With the staggered grid, these difficulties are entirely eliminated.*** This freedom from difficulties has its own price. A computer program based on the staggered grid must carry all the indexing and geometric information about the locations of the velocity components and must perform certain rather tiresome interpolations. But the benefits of the staggered grid are well worth the additional trouble.

## 5.5 Momentum Equations

We again remind the reader that, if the pressure field is given, the solution of the momentum equations can be obtained by employing the formulation completed previously for the general variable  $\varphi$ . In the momentum equation,  $\varphi$  stands for the relevant velocity component, and  $P$  and  $S$  are to be given their appropriate meanings. The adoption of the staggered grid does make the discretized momentum equations somewhat different from the discretization equations for the other  $\varphi$ 's that are calculated for the main grid points. But this difference is one of detail and not of essence. It arises from the use of staggered control volumes for the momentum equations. A staggered control volume for the x-momentum equation is shown in [Figure 5.5.1](#). If we focus attention on the locations for  $u$  only, there is nothing unusual about this control volume. Its faces lie between the point  $e$  and the corresponding locations for the neighbor  $u$ 's. The control volume is, however, staggered in relation to the normal control volume around the main grid point  $P$ .

The staggering is in the x direction only, such that the faces normal to that direction pass through the main grid points  $P$  and  $E$ . This layout realizes one of the main advantages of the staggered grid: The difference  $P_p - P_E$  can be used to calculate the pressure force acting on the control volume for the velocity  $u$ . The calculation of the diffusion coefficient and the mass flow rate at the faces of the  $u$  control volume shown in [Figure 5.5.1 \(left\)](#) would require an appropriate interpolation; but

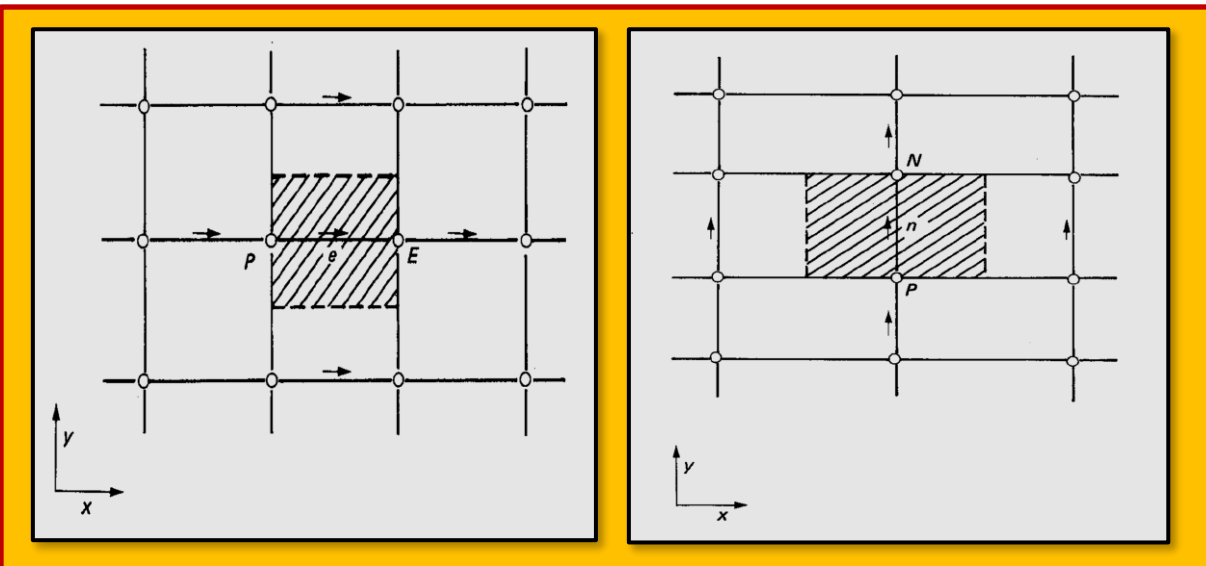


Figure 5.5.1 Control Volume for  $u$  (left) and  $v$  (right)

essentially the same formulation as described before would be applicable. The resulting discretization equation can be written as

$$a_e u_e = \sum a_{nB} u_{nB} + B + (P_p - P_E) A_e$$

Eq. 5.5.1

Here the number of neighbor terms will depend on the dimensionality of the problem. For the two dimensional situation in **Figure 5.5.1**, four  $u$  neighbors are shown outside the control volume; for a three dimensional case, six neighbor  $u$ 's would be included. The neighbor coefficients account for the combined convection-diffusion influence at the control-volume faces. The term  $B$  is defined in the same manner, but the pressure gradient is not included in the source-term quantities  $S_C$  and  $S_p$ . The pressure gradient gives rise to the last term in Eq. 5.5.1. Since the pressure field is also to be ultimately calculated, it would be inconvenient to bury the pressures in the momentum source term. The term  $(p_p - p_E)A_e$  is the pressure force acting on the  $u$  control volume,  $A_e$  being the area on which the pressure difference acts. For two dimensions,  $A_e$  will be  $\Delta_x$ , while in the three-dimensional case,  $A$  will stand for  $\Delta_y \Delta_z$ . The momentum equations for the other directions are handled in a similar manner. **Figure 5.5.1 (right)** shows the control volume for the  $y$ -direction momentum equation; it is staggered in the  $y$  direction. The discretization equation for  $u''$  can be seen to be

$$a_e v_e = \sum a_{nB} v_{nB} + B + (P_p - P_N) A_n \quad \text{Eq. 5.5.2}$$

where  $(P_p - P_N)A_n$  is the appropriate pressure force. For the three-dimensional case, a similar equation for the velocity component  $w$  can be written. The momentum equations can be solved only when the pressure field is given or is somehow estimated. Unless the correct pressure field is employed, the resulting velocity field will not satisfy the continuity equation. Such an imperfect velocity field based on a guessed pressure field  $p^*$  will be denoted by  $u^*, u^*, w^*$ . This "starred" velocity field will result from the solution of the following discretization equations:

$$\begin{aligned}
 a_e u_e^* &= \sum a_{nB} u_{nB}^* + B + (P_p^* - P_E^*) A_e \\
 a_e v_n^* &= \sum a_{nB} v_{nB}^* + B + (P_p^* - P_E^*) A_n \\
 a_e w_t^* &= \sum a_{nB} w_{nB}^* + B + (P_p^* - P_E^*) A_t
 \end{aligned}$$

Eq. 5.5.3

In these equations, the velocity components and pressure have been given the superscript (\*). The location t, it can be noted, lies on the z-direction grid line between the grid points P and T.

## 5.6 Pressure and Velocity Corrections

Our aim is to find a way of improving the guessed pressure  $p^*$  such that the resulting starred velocity field will progressively get closer to satisfying the continuity equation. Let us propose that the correct pressure  $p$  is obtained from

$$P = P^* + P'$$

### Eq. 5.6.1

where  $p'$  will be called the pressure correction. Next, we need to know how the velocity components respond to this change in pressure. The corresponding velocity corrections  $u'$ ,  $v'$ ,  $w'$  can be introduced in a similar manner:

$$u = u^* + u' , \quad v = v^* + v' , \quad w = w^* + w'$$

### Eq. 5.6.2

At this point, we shall boldly decide to drop the term summation from the equation. An extensive discussion of this action will be presented in<sup>43</sup>. For the time being, it is best to pay no attention to this move or to regard it simply as a computational convenience. The result is

$$u_e = u_e^* + d_e (P'_p - P'_E) \quad \text{where } d_e = \frac{A_e}{a_e} \quad \text{Eq. 5.6.3}$$

This will be called the velocity-correction formula, which can also be written as This shows how the starred velocity  $u$ : is to be corrected in response to the pressure corrections to produce  $u_e$ . The correction formulas for the velocity components in other directions can be written similarly. Thus, we now have all the preparation needed for obtaining a discretization equation for  $p'$ . It is to this task that we now turn.

### 5.6.1 Pressure-Correction Equation

We shall now turn the continuity equation into an equation for the pressure correction. For the purpose of this derivation, we shall assume that the density  $\rho$  does not directly depend on pressure. The derivation is given here for the three dimensional situation where the one- and two-dimensional forms can easily be obtained. We shall integrate this over the shaded control volume (Only a two-dimensional View is shown for convenience). The same control volume, it will be remembered, was used for deriving the discretization equation for the general variable  $\varphi$ . We shall now turn the continuity equation into an equation for the pressure correction. For the purpose of this derivation, we shall assume that the density  $\rho$  does not directly depend on pressure. The derivation is given here for the three dimensional situation where the one- and two-dimensional forms can easily be

<sup>43</sup> Suhas V. Patankar, "Numerical Heat Transfer and Fluid Flow", Mc Graw Hill Book Company, 1980.

obtained. We shall integrate this over the shaded control volume shown in **Figure 5.5.1** (Only a two-dimensional view is shown for convenience). The same control volume, it will be remembered, was used for deriving the discretization equation for the general variable  $\varphi$ . For the integration of the term  $d\rho/dt$ , we shall assume that the density  $\rho_p$  prevails over the control volume. Also, a velocity component such as  $u_e$  located on a control-volume face will be supposed to govern the mass flow rate for the whole face. In conformity with the fully implicit practice, the new values of velocity and density (i.e., those at time  $t + \Delta t$ ) will be assumed to prevail over the time step; the old density  $\rho_0^p$  (i.e., the one at time  $t$ ) will appear only through the term  $d\rho/dt$ . With these decisions, the integrated form of continuity becomes

$$\frac{(\rho_p - \rho_0^p)\Delta x\Delta y\Delta z}{\Delta t} + [(\rho u)_e - (\rho u)_w]\Delta y\Delta z + [(\rho u)_n - (\rho u)_s]\Delta x\Delta z + [(\rho u)_t - (\rho u)_b]\Delta x\Delta y = 0 \quad (.)$$

substitute for all the velocity components the expressions given by the velocity-correction formulas we obtain, after rearrangement, the following discretization equation for  $P'$ . Since the values of the density at 0 will normally be available only at the main grid points, the interface densities such as  $P_e$  may be calculated by any convenient interpolation. Whatever the method of interpolation, the value of  $P_e$  must be consistently used for the two control volumes to which the interface belongs.

### 5.6.2 SIMPLE Algorithm

The procedure that we are developing for the calculation of the flow field has been given the name SIMPLE, which stands for *Semi-Implicit Method for Pressure-Linked Equations*. The procedure has been described in [ Patankar and Spalding (1972)]. The sequence of events as follows:

1. Guess the pressure field  $P^*$ .
2. Solve the momentum equations, such to obtain  $u^*, v^*, w^*$
3. Solve the  $P'$  equation.
4. Calculate  $P$  by adding  $P'$  to  $P^*$ .
5. Calculate  $u, v, w$  from their starred values using the velocity-correction formula.
6. Solve the discretized equation for other  $\varphi$ 's (such as temperature, concentration, and turbulence quantities) if they influence the flow field through fluid properties, source terms, etc.
7. Treat the corrected pressure  $P$  as a new guessed pressure  $P''$ , return to step and repeat the whole procedure until a converged solution is obtained.

### 5.6.3 The Relative Nature of Pressure

The foregoing description of the  $P'$  boundary conditions leads to a subtle but important issue. Let us consider a constant-density steady situation, in which the normal velocities are given at all boundary locations. Since no boundary pressure is specified and all the boundary coefficients such as  $a_E$  will be zero, the  $P'$  equation is left without any means of establishing the absolute value of  $P'$ . The situation, however, presents no real difficulty. For such a problem (in which the density is unaffected by pressure), the absolute value of pressure and hence of pressure correction-is not relevant at all; only differences in pressure are meaningful, and these are not altered by an arbitrary constant added to the  $P'$  field. Pressure is then a relative variable, not an absolute one. If the absolute value of  $P'$  is not unique, would the computations converge at all? Fortunately, an iterative method of solving the algebraic equations does converge to a solution, the absolute value of which is decided by the initial guess. A direct method, however, would encounter a singular matrix and refuse to give a solution. The remedy then is to arbitrarily assign the value of  $P'$  in one control volume and solve the  $P'$  equations for the remaining control volumes. The same technique can be used in an iterative method,

but letting  $P'$  seek its own level gives faster convergence than insisting on a definite value at a certain point.

Another way of looking at the indeterminate  $P'$  field is to note that the continuity equations for all the control volumes do not represent a linearly independent set. Since, in a properly specified problem, the given boundary velocities must satisfy overall mass conservation, the continuity equation for the last control volume does not convey any information that is not already contained in the continuity equations for all other control volumes. Thus, even if one of the control-volume equations is discarded (and the value of  $P'$  is prescribed there), the resulting corrected velocity field would satisfy continuity for all control volumes. In many problems, the value of the absolute pressure is much larger than the local differences in pressure that are encountered. If the absolute values of pressure were used for  $p$ , round-off errors would arise in calculating differences like  $P_p - P_E$ . It is, therefore, best to set  $P = 0$  as a reference value at a suitable grid point and to calculate all other values of  $p$  as pressures relative to the reference value. Similarly, before the  $p'$  equation is solved during each iteration, it is useful to start from  $P' = 0$  as the guess for all points, so that the solution for  $P'$  does not acquire a large absolute value. When the pressure at some boundary points is specified, or when the density depends on pressure, the indeterminacy of the pressure level does not arise.

## 5.7 Revised Algorithm of SIMPLER

The SIMPLE algorithm has been extensively used and has served well. For example, all the fluid-flow calculations to be presented were performed using this algorithm. However, in attempts to improve its rate of convergence, a revised version has been worked out. It is called SIMPLER, which stands for SIMPLE Revised. The approximation introduced in the derivation of the  $P'$  equation (the omission of the summation term) leads to rather exaggerated pressure corrections, and hence under relaxation becomes essential. Since the influence of the neighbor point velocity corrections is removed from the velocity-correction formula, the pressure correction has the entire burden of correcting the velocities, and this results into a rather severe pressure-correction field. In : most cases, it is reasonable to suppose that the pressure-correction equation does a fairly good job of correcting the velocities, but a rather poor job of correcting the pressure. *If we employ the pressure-correction equation only for the task of correcting the velocities and provide some other means of obtaining an improved pressure field, we construct a more efficient algorithm. This is the essence of SIMPLER.*

Although the pressure equation and the pressure-correction equation are almost identical, there is one major difference: No approximations have been introduced in the derivation of the pressure equation. Thus, if a correct velocity field were used to calculate the pseudo velocities, the pressure equation would at once give the correct pressure. The revised algorithm consists of solving the pressure equation to obtain the pressure field and solving the pressure-correction equation only to correct the velocities. The sequence of operations can be stated as:

1. Start with a guessed velocity field.
2. Calculate the coefficients for the momentum equations and hence calculate  $u$ ,  $v$ ,  $w$  from equations by substituting the values of the neighbor velocities  $u_{nb}$ .
3. Calculate the coefficients for the pressure equation (6.30), and solve it to obtain the pressure.
4. Treating this pressure field as  $p^*$ , solve the momentum equations to obtain  $u^*, v^*, w^*$ .
5. Calculate the mass source  $b$  [Eq. (6.23h)] and hence solve the  $p'$  equation.
6. Correct the velocity field, but do not correct the pressure.
7. Solve the discretization equations for other  $\varphi$ 's if necessary.
8. Return to step 2 and repeat until convergence.

In SIMPLE, a guessed pressure field plays an important role. On the other hand, SIMPLER does not use guessed pressures, but extracts a pressure field from a given velocity field. If the given velocity

field happens to be the correct velocity field, then the pressure equation in SIMPLER will produce the correct pressure field, and there will be no need for any further iterations. If, on the other hand, the same correct velocity field and a guessed pressure field were used to start the SIMPLE procedure, the situation would actually deteriorate at first. The use of the guessed pressure would lead to starred velocities that would be different from the given correct velocities. Then, the approximations in the  $P'$  equation would produce incorrect velocity and pressure fields at the end of the first iteration. Convergence would take many iterations, despite the fact that we did have the correct velocity field at the beginning. Furthermore, the relative nature of the pressure discussed could have been described by reference to the pressure equation. Although SIMPLER has been found to give faster convergence than SIMPLE, it should be recognized that one iteration of SIMPLER involves more computational effort. First, the pressure equation must be solved in addition to all the equations solved in SIMPLE; and second, the calculation of  $u, v, w$  represents an effort for which there is no counterpart in SIMPLE. However, since SIMPLER requires fewer iterations for convergence, the additional effort per iteration is more than compensated by the overall saving of effort.

## 5.8 2D Parabolic Flow

When a steady two-dimensional flow has one one-way space coordinate, it is called a two-dimensional parabolic flow. (See [Figure 5.8.1](#)). Such a flow has a predominant velocity in the one-way, and hence the convection always dominates the diffusion in that coordinate. It is this feature that imparts the one-way character to the stream wise direction. Obviously, no reverse flow in that direction would be acceptable. A further requirement arises from the influence of pressure. It was indicated that pressure normally exerts two-way (or elliptic) influences. For the stream wise coordinate to be treated as one-way, the pressure variations in the cross-stream direction must be regarded as negligible. Examples of two-dimensional parabolic flows are plane or axisymmetric cases of boundary

layers on walls, duct flows, jets, wakes, and mixing layers. The solution for such situations is obtained by starting with a known 'distribution of 45 at an upstream station and marching in the stream wise direction. For every forward step, the distribution in the cross-stream coordinate is calculated at one stream wise station. The solution of the momentum and continuity equations presents no special problem. The stream wise pressure gradient is assumed to be known. With this pressure gradient, the stream wise momentum equation is solved to yield the stream wise velocity. The cross-stream velocity is then calculated from the continuity equation. The pressure gradient for external flows comes from the pressure field in the external irrotational stream outside the boundary layer. For confined flows, overall mass conservation across the duct cross section is used to adjust the stream wise pressure gradient. No counter part of SIMPLE or SIMPLER is needed for two-dimensional parabolic flows. The calculation method described therein uses a dimensionless stream function as the cross-stream coordinate, which provides a convenient way of expanding and contracting the width of the calculation domain in conformity with changes in the thickness of the boundary layer.

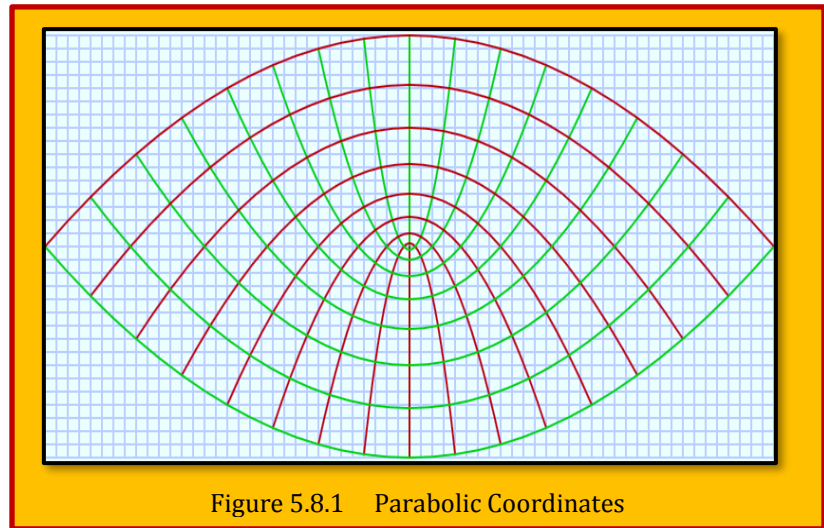


Figure 5.8.1 Parabolic Coordinates

## 5.9 3D Parabolic Flow

If in a steady three-dimensional flow there exists one one-way coordinate, the flow can be characterized as a three-dimensional parabolic flow. Again, the conditions under which a space coordinate becomes one-way are the existence of a predominant unidirectional velocity in that coordinate; hence, negligible diffusion and absence of reverse flow in that direction; and negligible pressure variations in the cross-stream plane. Examples of three-dimensional parabolic situations are similar to their two-dimensional counterparts. The boundary layer over a skewed airfoil, the flow in a duct of rectangular cross section, and a jet issuing from a noncircular orifice are all three-dimensional parabolic flows. Although the apparent difference between the two and three-dimensional parabolic situations is slight, the solution procedure needed for three dimensional parabolic problems is far more complex than that for two dimensional parabolic flows. The reason is that, after the stream wise velocity has been calculated from the stream wise momentum equation, the two cross-stream velocities cannot be obtained from the continuity equation alone. To determine how the flow distributes itself in the two cross-stream directions, both cross-stream momentum equations must be solved. The two-dimensional parabolic procedure, on the other hand, does not employ the cross-stream momentum equation.

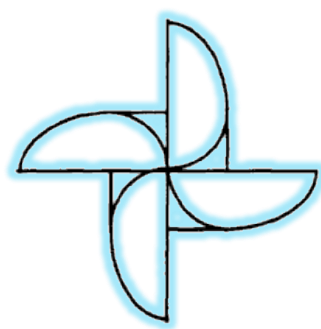
Because of the direct reference to cross-stream momentum equations, an assumption about pressure, which goes unnoticed in the procedure for two-dimensional parabolic flows, comes to the forefront in the three dimensional parabolic procedure. This assumption is that the stream wise velocity is influenced by a cross-sectional mean pressure  $\bar{P}$ , while the cross stream velocities are "driven" by a pressure variation  $P$  over the cross section<sup>44</sup>. This pressure "decoupling" is essential to the use of a parabolic procedure. For external flows, the stream wise variation of  $\bar{P}$  is obtained from the surrounding irrotational stream. In confined flows, the  $\bar{P}$  variation is adjusted to satisfy overall mass conservation over the duct cross section. In a given forward step, once the stream wise velocity has been obtained with the appropriate stream wise gradient of  $\bar{P}$ , the problem of calculating the two cross-stream velocities and the cross-sectional pressure distribution is almost identical to a two-dimensional elliptic problem, which can be solved by the use of *SIMPLE* or *SIMPLER*.

### 5.9.1 Partially Parabolic Flows

In some practical situations there exists a predominant flow direction, and yet the cross-stream pressure variation is not negligible. Thus, the pressure decoupling employed in the parabolic procedures is not appropriate for such flows. In all other respects, the solution can be obtained by marching from the upstream end of the domain to the downstream end, but the downstream effects are transmitted upstream via pressure. Such situations are called *partially parabolic*. Highly curved ducts, a jet in a cross stream, ducts with a rapid change of cross section, and rotating passages are examples of partially parabolic situations. The basic concept of this class of flows was presented by Pratap and Spalding (1975, 1976). In the partially parabolic calculation procedure, the pressure field is stored for the entire calculation domain, while all other variables are stored for only one or two marching stations. For a given pressure field, the marching procedure is employed just as in the fully parabolic situation, while an improved pressure field is obtained from a pressure-correction equation or a pressure equation. Many repetitions of the marching procedure are needed before a converged solution is obtained. Compared with the fully elliptic procedure, the fully parabolic procedure offers savings in both computer time and computer storage. The partially parabolic procedure saves storage, but the savings in computer time may not be appreciable.

---

<sup>44</sup> The cross-sectional pressure  $P$  could be regarded as a perturbation over the mean pressure. For the flow to be treated as parabolic, the pressure perturbation over a cross section should be small so that, in the stream wise momentum equation, no significant error is introduced by the use of the mean pressure instead of the actual local pressure.



## 6 Case Studies for Numerical Heat Transfer

### 6.1 Case Study 1 – Heat Transfer in Axisymmetric Stagnation Flow on Thin Cylinders

**Authors :** Cornelia Revnic, Teodor Grosan, and Ioan Pop

**Affiliations :** Studia University

**Title of Paper :** Heat Transfer in Axisymmetric Stagnation Flow on Thin Cylinders

**Citation :** (REVNIC, GROSAN, & POP, 2010)<sup>45</sup>

The Navier-Stokes and energy equations for the steady laminar incompressible flow past a row of circular cylinders at constant temperature are solved numerically. Prime attention was focused on how heat transfer characteristics are affected by variation of Reynolds number. The study was limited to Reynolds number ranging from 1 to 100 and the Prandtl number has been fixed to a value equal to 1. For different values of above parameters streamlines, isotherms and the local Nusselt number has been determined. The problem investigated by (REVNIC, GROSAN, & POP, 2010) the problem of cooling by forced convection of a row of circular cylinders is numerically studied. Namely, flow and heat transfer characteristics are determined for different values of the Reynolds number, keeping the Prandtl number constant ( $\text{Pr} = 1$ ). The value of the Reynolds number is consider to be in the range  $1 \leq \text{Re} \leq 100$  and the viscous dissipation is negligible small.

#### 6.1.1 Basic Equations

Consider the steady two-dimensional forced convection flow over a circular cylinders' row of radius  $R$  placed in a viscous fluid of ambient temperature  $T_{\text{infin}}$  and velocity  $U_{\text{infin}}$ . It is assumed that the distance between the cylinders is  $2R$  and that the temperature of the cylinders is constant  $T_w$  ( $T_w > T_{\text{infin}}$ ). The mathematical model is given by continuity, Navier-Stokes and energy equations:

$$\begin{aligned} \frac{\partial u}{\partial x} + \frac{\partial u}{\partial y} &= 0 \\ u \frac{\partial u}{\partial x} + v \frac{\partial u}{\partial y} &= -\frac{1}{\rho} \frac{\partial p}{\partial x} + v \left( \frac{\partial^2 u}{\partial x^2} + \frac{\partial^2 u}{\partial y^2} \right) \\ u \frac{\partial v}{\partial x} + v \frac{\partial v}{\partial y} &= -\frac{1}{\rho} \frac{\partial p}{\partial y} + v \left( \frac{\partial^2 v}{\partial x^2} + \frac{\partial^2 v}{\partial y^2} \right) \\ \rho c_p \left( u \frac{\partial T}{\partial x} + v \frac{\partial T}{\partial y} \right) &= k \left( \frac{\partial^2 T}{\partial x^2} + \frac{\partial^2 T}{\partial y^2} \right) \end{aligned} \quad \text{Eq. 6.1.1}$$

where  $x$  and  $y$  are the Cartesian co-ordinate along the horizontal and vertical direction, respectively,  $u$  and  $v$  are the velocity components along  $x$  and  $y$ -axes,  $p$  is the pressure,  $T$  is the temperature,  $k$  is the thermal diffusivity of the viscous fluid,  $\rho$  is the fluid density and  $c_p$  is the specific heat at constant pressure.

<sup>45</sup> Revnic, C., Grosan, T., & Pop, I. (2010). *Heat Transfer In Axisymmetric Stagnation Flow*. Studia Univ. "Babes,-Bolyai", Mathematica.

### 6.1.2 Results and Discussions

The full Navier-Stokes and energy equations with the corresponding boundary conditions were numerically solved. The model is solved for  $T_{\infty} = 281K$  and  $T_w = 400K$ . We use the following discretization: standard for pressure, SIMPLE for pressure-velocity coupling and power-law for momentum and energy equations. The stop residual were  $1e^{-4}$  for continuity and velocity while for energy the value  $1e^{-6}$  was used. Also the under-relaxation method has been used, the under-relaxation factor was 0.3 for the pressure and 0.7 for the momentum equation. To examine the effect of the Reynolds number, the streamlines, isotherms and local Nusselt number are calculated with isotherms are provided in **Figure 6.1.1**. It is noticed that for larger values of the Reynolds number the vortex region increases. Further we notice that the maximum value of the streamline function

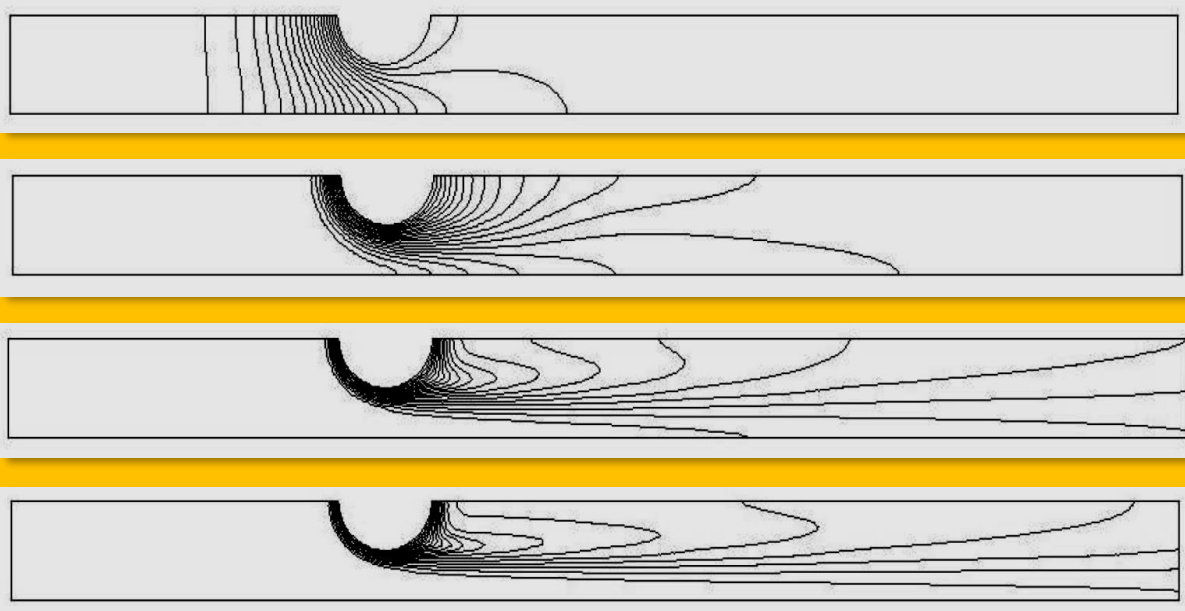


Figure 6.1.1 Evolution of Isotherms for  $Re=1, 10, 50, 100$

increases with the increase of the Reynolds number. Therefore, the cooling of the cylinders is more efficient for large values of the Reynolds number. The variation of the local Nusselt number around the cylinder is shown in [Revnic, et al.]<sup>46</sup>. It is evident that the local Nusselt number sharply increases as the value of the Reynolds number increases, and then gradually decreases with the increases of the angle. In addition we notice that for  $Re = 50$  and  $Re = 100$  the graphs of the local Nusselt numbers change their shapes due to recirculation of the fluid.

<sup>46</sup> Cornelia Revnic, Teodor Grosan, and Ioan Pop, "Heat Transfer In Axisymmetric Stagnation Flow On Thin Cylinders", Studia Univ. "Babes,-Bolyai", Mathematica, Volume LV, Number 1, March 2010.

## 6.2 Case Study 2 – Computation of Heat Transfer in Linear Turbine Cascade

**Authors :** Georgi Kalitzin & Gianluca Iaccarino

**Affiliations :** Center for Turbulence Research Annual Research Briefs 1999

**Title of Paper :** Computation of Heat Transfer in Linear Turbine Cascade

**Citation :** (Kalitzin & Iaccarino, 1999)

**Bibliography :** Kalitzin, G., & Iaccarino, G. (1999). Computation of heat transfer in a linear turbine cascade. Center for Turbulence Research Annual Research Briefs.

The efficiency of a turbine increases in general with an increase of the temperature of the working gas which was investigated by (Kalitzin, & Iaccarino, 1999)<sup>47</sup>. This gas temperature may well exceed the melting temperature of the metal walls. Locally high heat transfer can lead to an excessive temperature and high thermal stresses in the walls, causing an early fatigue of the high pressure turbine components. Thus, the design of these components requires accurate evaluation of heat transfer at the walls (**Figure 6.2.1**). The prediction of heat transfer at the end wall and the blade surface requires simulation of the viscous interaction between the boundary layer approaching the blade and that developing on the blade itself. Secondary flows, horseshoe type vortices, and strong turbulence generate complex end wall heat transfer distributions with several local maxima

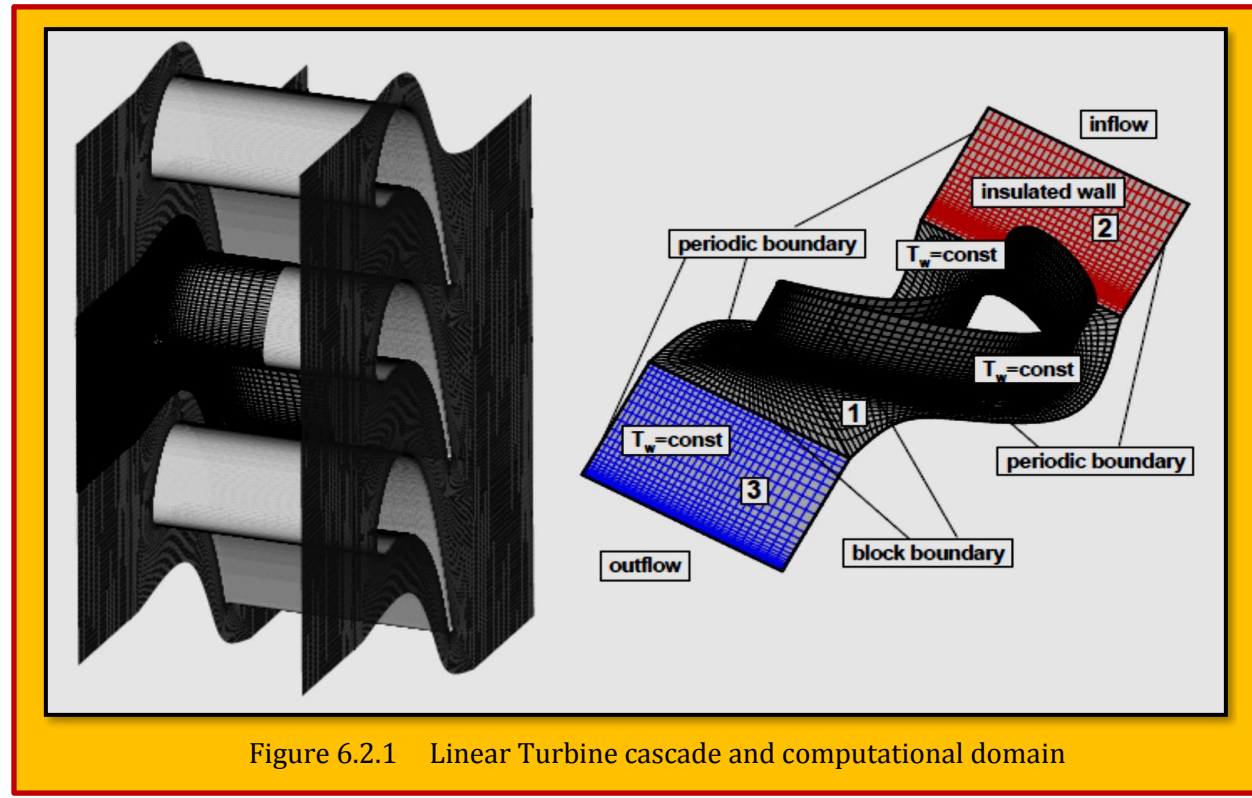


Figure 6.2.1 Linear Turbine cascade and computational domain

occurring at the end wall and the blade surface. Accurate prediction of these peaks is crucial for the design of the turbine cooling system. **The objective of the present work is to use this database to evaluate the influence of turbulence models on the accuracy of heat transfer predictions in**

<sup>47</sup> Kalitzin, G. & Iaccarino G., "End wall heat transfer computations in a transonic turbine cascade", XVII Congresso nazionale sulla trasmissione del calore, U.I.T, Ferrara, 1999.

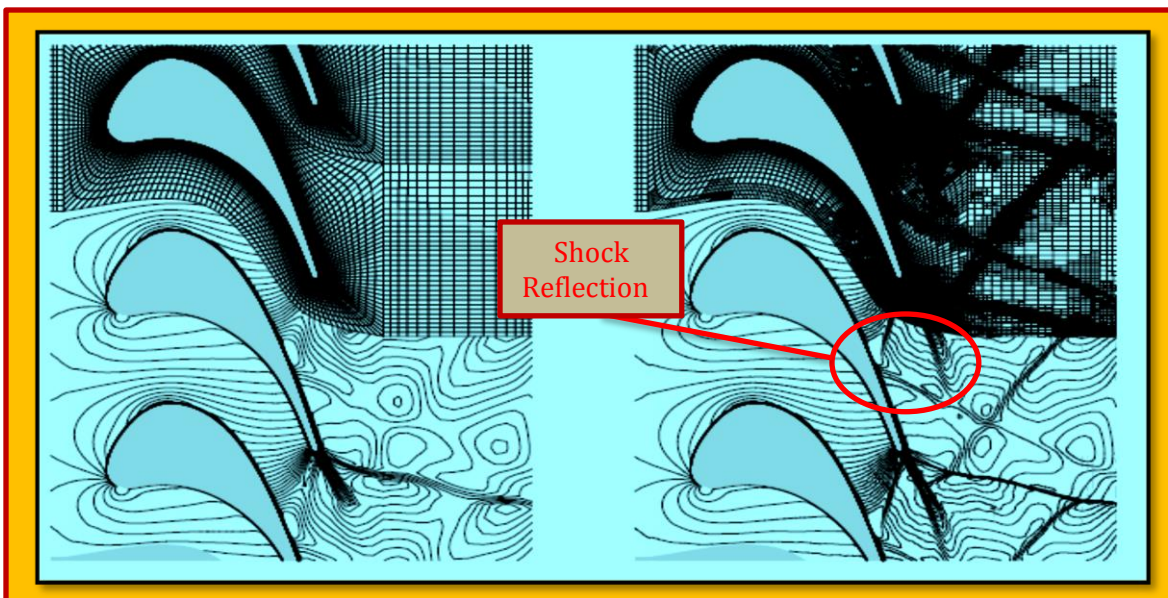
**complex three-dimensional flows in turbine geometries.** The sensitivity of the heat transfer coefficient prediction to the turbulence model used is analyzed using two different models: the *Spalart-Allmaras* one equation model and Durbin's four equation  $v2-f$  model. The use of two different flow solvers, the NASA research code CFL3D and the commercial package FLUENT®, increases confidence in the results and allows the elimination of effects related to the numerical discretization of the equations.

### 6.2.1 Numerical Methods

The present results have been computed using two different RANS flow solvers: the NASA code *CFL3D* and the commercial software *Fluent®* is a compressible, finite-volume code for multi-block structured grids. The mean flow fluxes are computed with the Roe flux difference splitting scheme. Turbulence models are solved segregated from the mean flow in an elimination of effects related to the numerical discretization of the equations. The *CFL3D* is a compressible, finite-volume code for multi-block structured grids. Turbulence models are solved segregated from the mean flow in an implicit manner using three-factored Approximate Factorization. The  $v2-f$  model has been implemented in this code in an implicit manner. The resulting linear algebraic system is solved with a three or two-factored Approximate Factorization scheme. *Fluent®* solves the time-dependent RANS equations on structured and unstructured meshes using a control-volume-based technique; the diffusion terms are discretized using a second-order central-difference scheme while a second-order upwind scheme is employed for the convective terms. An Euler implicit discretization in time is used in combination with a Newton-type linearization of the fluxes. The resulting linear system is solved using a point Gauss-Seidel scheme in conjunction with an algebraic multi-grid method. The additional equations for the turbulent quantities are solved in a segregated fashion using a 1<sup>st</sup> or 2<sup>nd</sup> order upwind discretization scheme with explicit boundary conditions.

### 6.2.2 Mesh Generation

The large scale linear cascade investigated in the experiments consists of twelve blades with an axial chord of 10.7 cm. A part of the cascade is shown in **Figure 6.2.2 A**. The high blade count of the cascade ensures good periodicity. This allows us to consider only one blade and only the region between end wall and symmetry plane in the computations. The actual computational domain is shown in **Figure 6.2.2 B**. The block boundaries of the structured 3-block mesh and the boundary conditions used are highlighted in the Figure 6.2.1. An O-mesh topology around the blade has been



chosen to ensure a high quality mesh near the blade surface. The two-dimensional mesh consisting of  $48 \times 192$  cells has been generated through simple geometric interpolation. After generating the outer boundary as an arbitrary line between two blades and distributing lines connecting the outer boundary with the blade, O-lines have been interpolated using a stretching function. The three-dimensional mesh has been generated by copying the described 2D grid in the span-wise direction and clustering the grid points at the end-wall. Two meshes, mesh A and mesh B, have been generated with 40 and 52 cells span-wise, respectively. All block dimensions have been chosen to contain factors of the power 2 to exploit multi-grid. The mesh has been transformed into an unstructured mesh for the flow computations with *Fluent*<sup>®</sup>. The multi-block decomposition disappears for an unstructured solver. The height of the first cell above the wall has an average  $y^+$  value of about 1. The height has been adjusted after initial computation.

### 6.2.3 Heat Transfer Results for 2D & 3D

In the simulation of three-dimensional flow, the computational grid is often a compromise between a desired resolution and computational accuracy. In two dimensions, however, it is easier to carry out a complete grid sensitivity study. With this objective in mind, the flow in the symmetry plane has been computed in a two-dimensional plane. The structured grid or default mesh, for this report is shown in **Figure 6.2.2(A)**. It is the same used at each span wise location in the three-dimensional calculations. It contains 11008 cells. The unstructured grid, shown in **Figure 6.2.2(B)** is obtained through successive refinement in regions with high pressure gradients and large strain rates like shock waves, boundary layers, and wakes. This mesh contains 71326 cells. The Mach contours plotted for both grids show a very complex shock wave pattern in the wake of the blades. The accelerating flow within the passage generates an oblique shock wave on the pressure side of a blade (see red circles in **Figure 6.2.2**). This shock is reflected on the suction side of the successive blade. It then interacts with the viscous wake of the blade from which it originated. Partly due to reflection in pressure BC. Somehow the new development by ANSYS<sup>®</sup> claims that *Average Pressure Specification at Pressure Boundary* which allows the exit pressure to vary across the boundary, but maintains an average equivalent to the specified exit pressure value<sup>48</sup>. It also claims that it is less reflective than previous

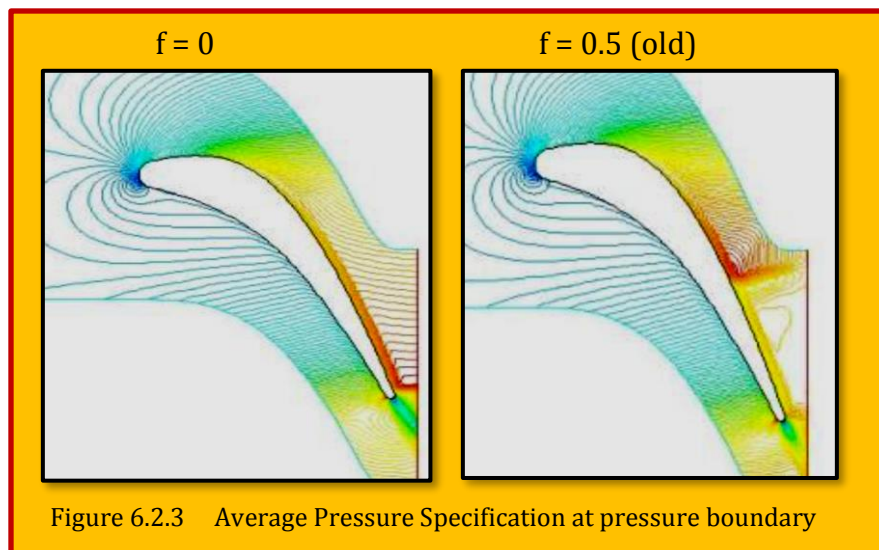


Figure 6.2.3 Average Pressure Specification at pressure boundary

version with improved results. The Pressure blending factor 'f' (default value 0.0) may need to change  $f > 0.0$  in cases where stability is degraded. For  $f = 0$  recovers the fully averaged pressure, and  $f = 1$  recovers the specified pressure. The results of this improvement displayed in **Figure 6.2.3**. A second shock wave is generated on the suction side near the trailing edge. The default mesh does not resolve the shock wave the wake. Only the two shocks at the trailing edge are clearly visible. The heat transfer at the wall depends significantly on the thermal conductivity of the fluid. The effect of using a constant thermal conductivity at reference temperature is demonstrated with the *FLUENT*<sup>®</sup>

<sup>48</sup> Ansys Fluent<sup>®</sup> 16.0 Preview 4.

results reported in the same figure. The overall Stanton number is under-predicted. This explains the difference observed between the *FLUENT* and *CFL3D* Stanton number distributions at the end wall reported. It has to be noted that the constant thermal conductivity is the default option in. The pressure distributions on blade and end-wall are not very sensitive to the grid resolution and inflow profile for the case considered. Both flow solvers predicted a reasonable agreement with the experiment as reported in. We note, however, that the pressure distribution on the blade and the shock structure is sensitive to the treatment of the periodic boundary since it is located relatively close to the blade surface. In this paper we will focus primarily on the analysis of the heat transfer distribution, on the dependence of the Stanton number distribution on inflow profile and grid resolution.

#### 6.2.4 Experimental Data

The experimental data for the end-wall show some interesting features that will help to differentiate the predictive capabilities of the models tested (**Figure 6.2.4**). The horseshoe vortex generated by the rolling up of the incoming boundary layer enhances the wall heat transfer, and its structure is clearly visible in the higher Stanton number (Region A). A second distinct heat transfer peak is measured near the stagnation point (Region A). Within the passage, four additional interesting features are present: the first is a localized peak in the Stanton number related to the impingement of the suction-side leg of the horseshoe vortex on the blade surface (Region B). The second feature is the presence of a shock wave on the pressure side near the trailing edge that increases the heat

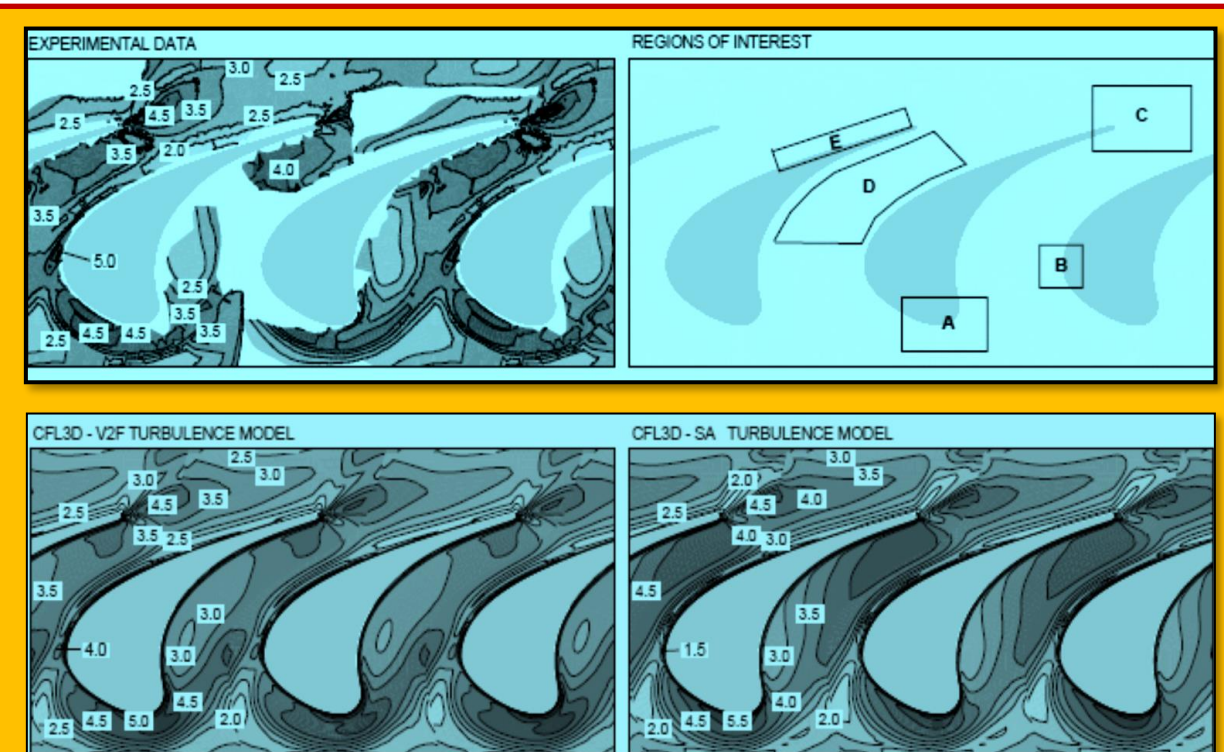


Figure 6.2.4 Stanton Number Distribution on End-Wall

transfer on the end wall (Region C). Third, there is a gradual increase of heat transfer at the end wall which is related to the acceleration of the fluid in the passage (Region D). And finally, the presence of a corner vortex on the suction side of the blade (Region E) is indicated in experiments by a low heat transfer region. In the wake, a very sharp peak in the Stanton number is measured just downstream of the trailing edge (Region C). The numerical predictions of the Stanton number show most of the features observed in the experiments but, in general, fail to predict the quantitative heat transfer on

the end wall correctly.

### 6.2.5 Effects of Turbulence

The increased heat transfer beneath the horseshoe vortex is captured by both turbulence models. The *S-A* model seems to spread this high Stanton number region and shift it towards the suction side. Spreading of the horseshoe vortex is related to the turbulence generation in the vortex shear layer. The *v2-f* model tends to produce a thinner vortex. The secondary peak on the suction side (Region B), which is related to the stagnation of high temperature fluid convected by the horseshoe vortex, is predicted by both models. The *v2-f* model predicts a higher value for the Stanton number. The *S-A* model predicts slightly larger values for the gradual increase in heat transfer within the passage (Region D). The trailing edge peak (Region C) and the low heat transfer region on the suction side of the blade (Region E) are reproduced by both models. A quantitative comparison of the heat transfer on the blade surface is shown for three stations in **Figure 6.2.5** for the *v2-f* and *S-A* model, respectively. The heat transfer in the stagnation region, the location where *span* is 0, is accurately predicted by both models at 25% and 50% span (solid line). Both stations are located outside of the incoming boundary layer specified at the inlet. The station at 10% span, however, is located well inside of this boundary layer, and both models over-predict the heat transfer here by 25%.

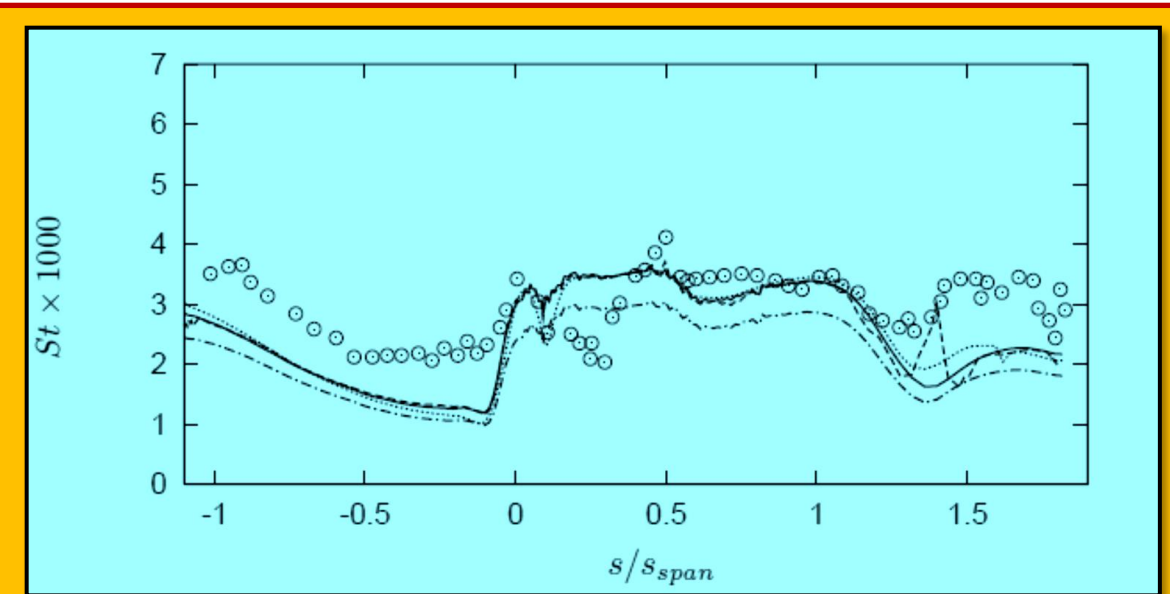


Figure 6.2.5 Stanton number Distribution on Blade Surface for 2D Grid

The higher heat transfer indicates that the turbulence intensity is too high at this location. This observation is supported by a computation in which the turbulence levels inside the end wall boundary layer have been reduced by setting the turbulence quantities at the inlet to a uniform value corresponding to 25% turbulent intensity (dotted line). This lowers the Stanton number in the stagnation region to the value measured in the experiments. In addition, it delays the transition on the upper surface of the blade. The *S-A* model shows a large sensitivity to the reduced boundary layer turbulence across the entire span on the pressure side. The heat transfer on the pressure side of the blade is consistently under-predicted at each station by both models. The same has been observed for the 2D computation shown in **Figure 6.2.5**. At this stage it is not clear whether this is due to the specification of the inlet conditions or the turbulence model<sup>49</sup>.

<sup>49</sup> Kalitzin, G. & Iaccarino G., “Computation of heat transfer in a linear turbine cascade”, Center for turbulence Research Annual Research Briefs, 1999.

### 6.3 Case Study 3 - DNS of Heat Transfer of the Flow Over a Cylinder at Re = 200 and 1000

*Authors :* Palkin, V Ryzhenkov and R Mullyadzhanov

*Appeared in :* Journal of Physics, Conference Series 1382 (2019) 012028

*Source:* doi:10.1088/1742-6596/1382/1/012028

We, [Palkin et al.]<sup>50</sup>, perform a simulations of the flow over a cylinder to study the influence of the thermal boundary conditions on the Nusselt number distribution. The result show very good agreement with some data from the literature. The total Nusselt number for the constant heat flux (CHF) boundary condition is higher for some 15% than for the constant wall temperature (CWT) condition for both  $Re < 200$  and 1000.

#### 6.3.1 Introduction

Heat transfer and forced convection of the flow over a cylinder has been the subject of many numerical and experimental studies representing a canonical bluff body configuration. The drag and lift forces acting on the body due to periodic formation and shedding of typical large-scale vortices lead to flow-induced vibrations and can cause serious structural damages. Effective cost-beneficial control methods of flow-induced drag and lift reduction and heat transfer enhancement require prior understanding of the flow and its vortical dynamics. This case featuring multiple regimes depending on the Reynolds number  $Re$  has been thoroughly studied by many authors [1, 2]. For  $Re < 150$  the flow is steady and two-dimensional, in the range  $150 < Re < 300$  the laminar transitional regime is observed and at  $300 < Re < 10000$  the wake becomes irregular and three-dimensional with laminar turbulent transition occurring in the separated shear layer.

An important issue concerning the heat transfer is the influence of thermal boundary conditions on the wall which usually comes down to the constant wall temperature (CWT) or constant heat flux (CHF) condition. There are a number of extensive reviews about the cylinder heat transfer focusing on various effects [3, 4]. Despite a large amount of studies on this flow configuration, even for relatively low Reynolds numbers, the existing data are significantly scattered. It can partially be explained by differences in parameters like freestream turbulence level, blockage and duct channel aspect ratio, boundary conditions on the cylinder or flow features like low-frequency modulations in irregular flow regime [5-7], which affect both the flow dynamics and heat transfer from the wall. [Boulos & Pei] reported that the total Nusselt number differs within 10-20% between CWT and CHF for  $Re = 5300$ .

The difference between peak values of the wall heat flux for CWT and CHF was found to be around 50% at  $Re = 80000$  reported by [Papell] and confirmed by other authors [10]. The scatter is also present for higher  $Re = 140000$  [11]. Widely accepted correlations are usually constructed based on the data with different parameters (aspect ratio, turbulence level etc) [12]. In the present paper we investigate the heat transfer with CHF and CWT boundary conditions by means of direct numerical simulations to analyze this issue.

#### 6.3.2 Computational details

We perform direct numerical simulations (DNS) of the uniform flow over a cylinder with a heated wall with a relatively fine spatial resolution. The Reynolds number corresponds to 200 and 1000 with the Prandtl number equal to 0.71 (air). For  $Re = 200$  the flow is laminar with unsteady von Karman vortex street, while at  $Re = 1000$  the flow is substantially three-dimensional and laminar-turbulence transition occurs in separated shear layer. To compare with data from the literature for  $Re = 200$  we use a two-dimensional setup while for  $Re = 1000$  the geometry is three-dimensional with the computational domain representing a box with  $25D \times 20D \times 6D$  in  $x \times y \times z$  directions as shown in

<sup>50</sup> Palkin, V Ryzhenkov and R Mullyadzhanov, "DNS of Heat Transfer of the Flow Over a Cylinder at Re = 200 and 1000", Journal of Physics, Conference Series 1382 (2019) 012028.

**Figure 6.3.1.** A circular cylinder with diameter  $D$  is located at the origin  $x = 0, y = 0$ . The inflow boundary is taken at  $x = -10D$ , while the outflow is  $x = 15D$  downstream. At the side boundaries  $|y| = 10D$  zero normal velocity condition is imposed and periodic boundaries are set alongside the cylinder at  $z = 0$  and  $6D$  with  $L = 6D$  being the length of the cylinder. For the temperature field either constant heat flux (CHF) or constant wall temperature (CWT) condition is used on the cylinder wall, where the Nusselt number can be defined representing a non-dimensional heat flux.

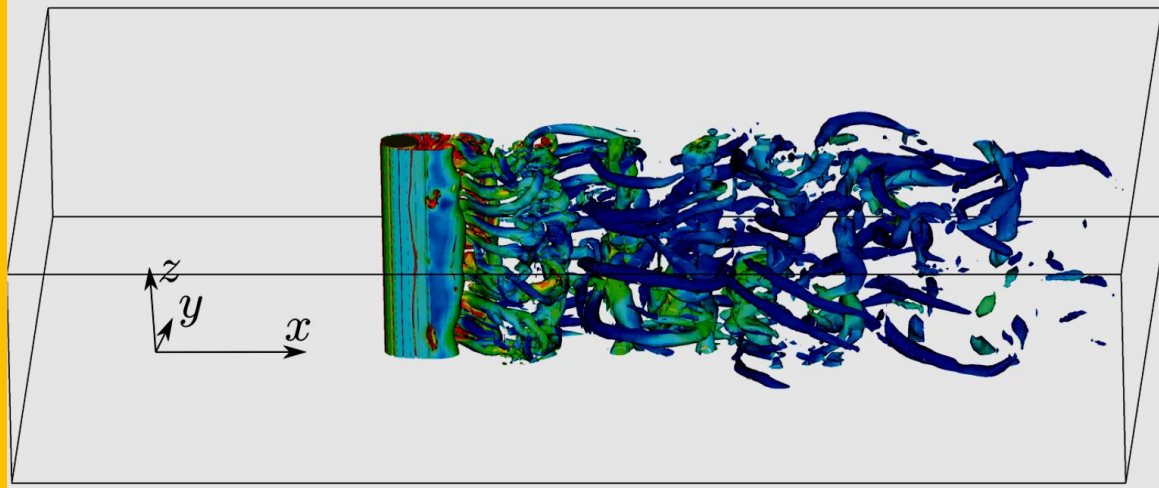


Figure 6.3.1 Computational domain, coordinate system (placed in the center of the cylinder) and iso-surfaces of the instantaneous  $Q$ -criterion for  $Re = 1000$  and CWT boundary condition colored with the non-dimensional temperature field  $T$  in the range  $[0; 0.25]$ .

We use the computational code Nek5000 featuring semi-implicit third-order time integration scheme and spatial discretization based on the spectral-element method (SEM). The Navier–Stokes equations are discretized in space with the use of the Galerkin approximation with 8th-order Lagrange polynomial interpolants based on the Gauss–Lobatto–Legendre points for both the velocity and pressure fields (PN–PN formulation). In circumferential direction alongside the cylinder we use 24 spectral elements for both Reynolds numbers and 12 spectral elements are used in z-direction for  $Re = 1000$ . In total the mesh consists of 0.25 and 16 mln points for  $Re = 200$  and  $Re = 1000$ , respectively.

### 6.3.3 Results

The surface of the instantaneous  $Q$  - criterion presented in **Figure 6.3.1** shows a turbulent three-dimensional flow behind the cylinder similar to experimental observations [2] with attached recirculation zone and periodic vortex shedding.

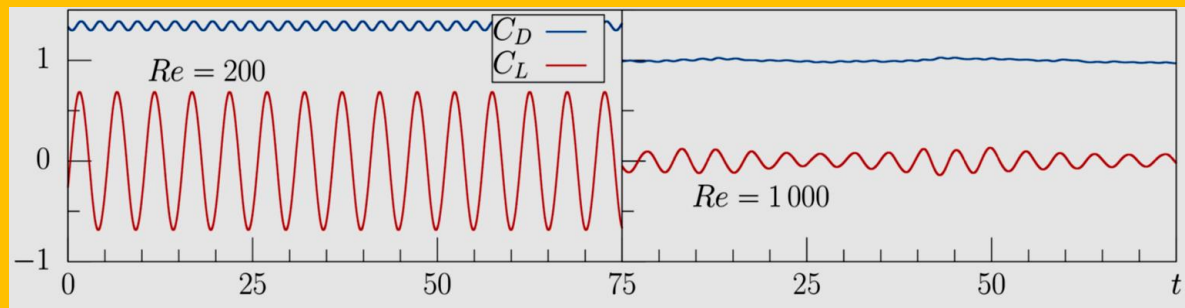


Figure 6.3.2 Time history of the drag and lift coefficient  $C_D = F_x/(L D \rho U^2/2)$ ,  $C_L = F_y/(L D \rho U^2/2)$ , where  $F_x$  and  $F_y$  are the total forces acting on the cylinder.

The time history of the drag and lift coefficients is shown in [Figure 6.3.2](#) demonstrating a sinusoidal signal for  $Re = 200$ , while for  $Re = 1000$  it is somehow modulated. The period of lift coefficient corresponds to the Strouhal number  $St = 0.19$  for  $Re = 200$  matching the results of Bouhairie & Chu [[13](#)]. For  $Re = 1000$  the shedding period corresponds to  $St = 0.219$  and this value is within a good agreement to other authors [[1,13-15,18](#)]. The mean drag coefficient  $C_D = 1.34$  for  $Re = 200$  while [[Piñol & Grau](#)] found the value of 1.27. For  $Re = 1000$  the drag coefficient is significantly lower with  $C_D = 0.99$  since the recirculation zone is elongated, which falls in the scatter of the data from the literature [[14,17-19](#)].

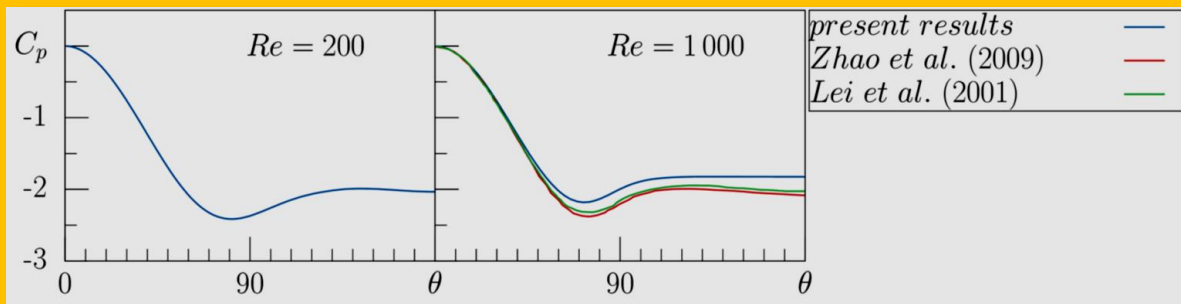


Figure 6.3.3 Circumferential Pressure Coefficient Distribution along the cylinder surface  $C_p = (p - p_s)/(D\rho U^2/2)$ . Red line – data from Zhao et al. [17], green – Lei et al. [18]

The pressure distribution along the wall is presented in [Figure 6.3.3](#) in comparison with the literature data [[17, 18](#)] for  $Re = 1000$ . As the separation point moves upstream with the increase of  $Re$ , the pressure minimum shifts from the angle  $\theta = 80$  to 71 degrees assuming  $\theta = 0$  is the frontal point. The difference between present and reference data is likely to be caused by the mesh resolution, which is 0.73 and 0.4 mln points in [[17](#)] and [[18](#)]. The time-averaged streamwise velocity field together with streamlines is shown in [Figure 6.3.4](#). The data from the literature [[17, 18](#)] feature a secondary recirculation zone attached to the cylinder surface, which is a footprint of the low numerical resolution [[5, 7](#)].

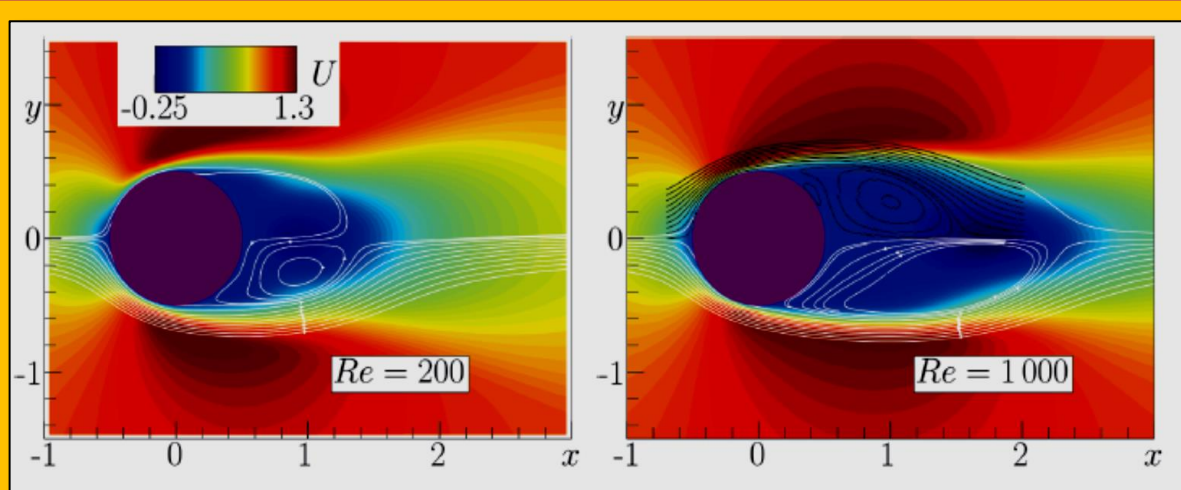


Figure 6.3.4 White Streamlines Correspond to the Time-Averaged Velocity field together with a streamwise component contours for  $Re = 200$  and  $Re = 1000$ . Black streamlines correspond to the data from Zhao et al. [17].

The Nusselt number circumferential distribution is plotted in [Figure 6.3.5](#) against the reference data [13, 20–21] normalized by the peak  $Nu$  value. Nusselt profile for  $Re = 200$  and CWT boundary condition is in rather good agreement with [Bouhairie & Chu] data, although the peak value is slightly higher. For  $Re = 1000$ , the Nusselt number at focal point is in agreement with the reference data,

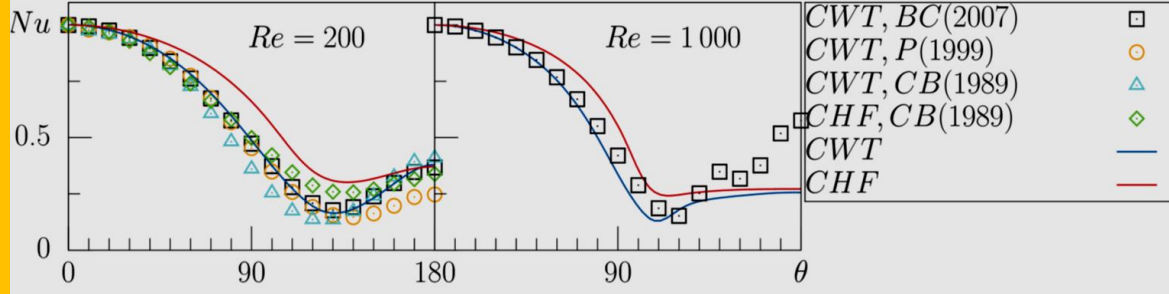


Figure 6.3.5 Circumferential Time-Averaged Nusselt Number Distribution on the Cylinder Wall corresponding to CWT/CHF normalized by the peak value. Left:  $Re = 200$ ,  $Nu_{\max} = 12.65$  [13], 14.69 [20], 16.46/16.75 [21], 14.0 [22], 13.4 [23] and 13.41 with the present calculations. Right:  $Re = 1000$ ,  $Nu_{\max} = 29.43$  [13], 31.3 [22], 30.0 [23] and 30.00 with the present calculations

however after the separation point they start to diverge, which is likely to be caused by two-dimensional approach applied in [13]. The overall Nusselt number is 7.43/8.59 and 15.27/17.42 corresponding to CWT/CHF for  $Re = 200$  and 1000, respectively, while reported value in [24] is 6.58 and 14.3 for  $Re = 200$  and 1000 correspondingly.

### 6.3.4 Conclusion

We performed Direct numerical simulations of the flow over a cylinder to study the influence of the thermal boundary conditions on the distribution of the Nusselt number. The results are in good agreement with the data from the literature. However for  $Re = 1000$  the reference data obtained by a two-dimensional approach [13] show some deviations after the separation point. Generally the total Nusselt number for the constant heat flux (CHF) boundary condition is higher for some 15% than for the constant wall temperature (CWT) condition for the considered cases.

### 6.3.5 References

- [1] Roshko A 1954 *NACA TN 3169*
- [2] Williamson C 1988 *Phys. Fluids* 31 3165–8
- [3] Zukauskas A 1972 *Adv. Heat Transf.* 8 116–33
- [4] Morgan V 1975 *Adv. Heat Transf.* 11 199–264
- [5] Lehmkuhl O, Rodríguez I, Borrell R and Oliva A 2013 *Phys. Fluids* 25 (8) 085109
- [6] Peng S, Wang H, Zeng L and He X 2019 *Exp. Therm. Fluid Sci.* 109 109877
- [7] Palkin E, Mulyadzhanov R, Hadžiabdić M and Hanjalić K 2016 *Flow Turbul. Comb.* 97 1017–46
- [8] Boulos M and Pei D 1974 *Int. J. Heat Mass Transf.* 17 (7) 767–83
- [9] Papell S 1981 *NASA report*
- [10] Baughn J and Saniei N 1991 *J. Heat Transf.* 113 (4)
- [11] Hadžiabdić M, Palkin E, Mulyadzhanov R and Hanjalić K 2019 *Int. J. Heat Fluid Flow* 79108441
- [12] Churchill S and Bernstein M 1977 *J. Heat Transf.* 99 (2) 300–6
- [13] Bouhairie S and Chu H 2007 *J. Fluid Mech.* 570 177–215
- [14] Mittal S 2001 *Phys. Fluids* 13 177–91
- [15] Norberg C 1994 *J. Fluid Mech.* 258 287
- [16] Piñol S and Grau F 1998 *Numerical Heat Transf., Part A: Application*. 34 313–30

- [17] Zhao M, Cheng L and Zhou T 2009 *J. Fluids Struct.* 25 831–47
- [18] Lei C, Cheng L and Kavanagh K 2001 *Computer Methods in Appl. Mech. and Engineer.* 190 2909–23
- [19] Szechenyi E 1975 *J. Fluid Mech.* 70 529–42
- [20] Patnaik B, Narayana P and Seetharamu K 1999 *Int. J. Heat Mass Transf.* 42 (18) 3495–507
- [21] Chun W and Boehm R 1989 *Num. Heat Transf.* 151(1) 101-122
- [22] Squire H 1938 *Modern Developm. Fluid Dyn.* 631–2
- [23] Frossling N 1958 *Tech. Rep.* 1432
- [24] Eckert E and Drake R 1972 *Analysis Heat Mass Transfer*

## 6.4 Case Study 4 - Unsteady Conjugate Heat Transfer Modeling<sup>51</sup>

**Authors :** L. He and M. L. G. Oldfield

**Original Appearance :** Transactions of the ASME, 031022-12 / Vol. 133, JULY 2011

**Source:** <http://turbomachinery.asmedigitalcollection.asme.org/>

**Citation :** He, L., and Oldfield, M. L. G. (November 29, 2010). "Unsteady Conjugate Heat Transfer Modeling." ASME. J. Turbomach. July 2011; 133(3): 031022. <https://doi.org/10.1115/1.4001245>

The primary requirement for high pressure turbine heat transfer designs is to predict blade metal temperature [[He](#) and [Oldfield](#)]. There has been a considerable recent effort in developing coupled fluid convection and solid conduction (conjugate) heat transfer prediction methods. They are, however, confined to steady flows. In the present work, a new approach to conjugate analysis for periodic unsteady flows is proposed and demonstrated. First, a simple model analysis is carried out to quantify the huge disparity in time scales between convection and conduction, and the implications of this for steady and unsteady conjugate solutions. To realign the greatly mismatched time scales, a hybrid approach of coupling between the time-domain fluid solution and frequency-domain solid conduction is adopted in conjunction with a continuously updated Fourier transform at the interface. A novel semi-analytical harmonic interface condition is introduced, initially for reducing the truncation error in finite-difference discretization. More interestingly, the semi analytical interface condition enables the unsteady conjugate coupling to be achieved without simultaneously solving the unsteady temperature field in the solid domain.

This unique feature leads to a very efficient and accurate unsteady conjugate solution approach. The fluid and solid solutions are validated against analytical solutions and experimental data. The implemented unsteady conjugate method has been demonstrated for a turbine cascade subject to inlet unsteady hot streaks.

### 6.4.1 Introduction & Background

Gas turbine designers strive for ever higher turbine inlet temperatures for performance improvement. The current levels are already significantly higher than the turbine blade material melting temperature. As such, turbine blade cooling technology plays a key role in modern gas turbine development. The essential element of an adequate design system is to be able to predict the temperature distribution in blades. This involves convection heat transfer in the fluid part in the passage and conduction heat transfer in the solid part. The conjugate convection conduction modeling is important not only to blade heat transfer, but also to aerothermal performance prediction in general. A fluid only solution can become untenable, due to the uncertain boundary condition for the energy equation when the surface temperature is unknown. There were considerable research efforts in developing and applying methods to account for the coupling between the fluid and solid parts [[1-6](#)].

Conventionally, the blade metal temperature prediction is based on the surface convection heat transfer coefficient and the recovery temperature calculated from a fluid solution CFD, which are then used as the boundary conditions for conduction analysis FEA. The basic assumption is the linear relation between the heat flux and the driving temperature difference. Also, the definition of the local recovery temperature neglects the upstream heat transfer history (e.g., the cooling of upstream boundary layer fluid). Improvement in accuracy can be achieved by further iterations between the fluid solution and FEA [[5,7](#)]. These types of loosely coupled conjugate methods are attractive as a natural extension of the conventional uncoupled methods, and can take advantage of the extensively developed solid conduction analysis capabilities \_e.g., variable material properties etc. in well-

<sup>51</sup> L. He and M. L. G. Oldfield, "Unsteady Conjugate Heat Transfer Modeling", *Journal of Turbomachinery*, JULY 2011, Vol. 133 / 031022-1.

established FEA codes.

Alternatively, fully coupled conjugate models, in which both fluid and solid parts are solved simultaneously using the same CFD solver, were developed [8,9]. It may be argued that, in comparison with the loosely coupled model, the fully coupled conjugate model should be more accurate, as neither the heat transfer coefficient nor the recovery temperature needs to be used. The fully coupled approach should also be more efficient, because of the simultaneous rather than iterative coupling. This potential advantage in computational efficiency can be quantified if the convergence of the conduction solution by the CFD solver is compared with that for the uncoupled fluid solution. This leads to the need to appreciate a more general issue in conjugate heat transfer modeling: the disparity in the time scales between the solid conduction and the fluid convection.

#### 6.4.2 Time Scale Analysis and Problem Statement

Consider a HP blade passage operated at a typical transonic flow condition. If the inlet stagnation temperature is given a sudden rise, the temperature disturbance will be largely propagated downstream at the local flow velocity. For an average flow velocity of 300 m/s with a blade row dimension of 0.1 m, the exit stagnation conditions will show the signature of the inlet disturbance in about 0.0003 s. On the other hand, a thermocouple on the blade surface will show that the blade temperature will change much more slowly and will take about 5–10 s to achieve the major part of the temperature change between the initial and the final states. This simply indicates that the ratio of time scales between the solid conduction and fluid convection is around 10,000.

What is the impact of this time scale disparity on the computational efficiency of a conjugate heat transfer solution? For the extensively developed and widely used time-marching approach [10,11], the convergence rate depends on how fast one can propagate (drive) the initial transient disturbances out of the computational domain. Given the total time scales required for the disturbances to be driven out of the domain by either convection or conduction, the computational time will thus depend on the size of the time step. Consider a simple 1D model system for a convective fluid property  $f$  and temperature  $T$

Time Scale Analysis and Problem Statement. Consider a HP blade passage operated at a typical transonic flow condition.

If the inlet stagnation temperature is given a sudden rise, the temperature disturbance will be largely propagated downstream at the local flow velocity. For an average flow velocity of 300 m/s with a blade row dimension of 0.1 m, the exit stagnation conditions will show the signature of the inlet disturbance in about 0.0003 s. On the other hand, a thermocouple on the blade surface will show that the blade temperature will change much more slowly and will take about 5–10 s to achieve the major part of the temperature change between the initial and the final states. This simply indicates that the ratio of time scales between the solid conduction and fluid convection is around 10,000.

What is the impact of this time scale disparity on the computational efficiency of a conjugate heat transfer solution? For the extensively developed and widely used time-marching approach [10,11], the convergence rate depends on how fast one can propagate (drive) the initial transient disturbances out of the computational domain. Given the total time scales required for the disturbances to be driven out of the domain by either convection or conduction, the computational time will thus depend on the size of the time step. Consider a simple 1D model system for a convective fluid property  $f$  and temperature  $T$

$$\text{Convection : } \frac{\partial f}{\partial t} + V \frac{\partial f}{\partial x} = 0 \quad , \quad \text{Conduction : } \frac{\partial f}{\partial t} - \alpha \frac{\partial^2 T}{\partial x^2} = 0$$

**Eq. 6.4.1**

Here, for simplicity, the system is discretized using the forward explicit discretization in time, the upwind one-sided difference for the first order spatial differential in the convection equation, and the central difference for the second order differential in the conduction equation. Taking the same mesh spacing  $\Delta x$  for both domains,  $t_f, t_s$  as the steps for the fluid and solid domains, respectively, it

can be shown from a numerical stability analysis that

$$\text{Fluid Domain (CFL Number)} = \frac{\Delta t_f V}{\Delta x} < 1$$

$$\text{Solid Domain (Fourier Number)} = \frac{\Delta t_s \alpha}{\Delta x^2} < 0.5$$

#### **Eq. 6.4.2**

For example, consider a case with a convection speed of  $V = 300$  m/s, solid material of steel (specific heat 465 J/kg K, density 7800 kg/m<sup>3</sup>, thermal conductivity 54 W/m K). The mesh spacing is taken to be 0.001 m. Then, interestingly, the ratio of time steps between the two domains becomes

$$\frac{\Delta t_s}{\Delta t_f} \approx 10000$$

#### **Eq. 6.4.3**

Hence, although a conduction process is by a factor of 10,000 slower than a convection one, a similar ratio also exists for the time steps in the corresponding domains, as controlled by the numerical stability. The number of time steps required for convergence of the conjugate computations would thus remain largely the same for both domains. For a typical conjugate HT configuration, the number of mesh points is dominated by that in the fluid part [9]. The total computing time required for a simultaneously coupled conjugate analysis should therefore be comparable to that for an uncoupled steady flow solution. This can be used as a reference point when comparing the computational efficiency.

It is apparent now that the domain dependent time steps lead to a complete loss of time consistency. The approach as it stands is, therefore, only applicable to steady flows. The huge disparity in time scales in the two domains become very acute for unsteady conjugate heat transfer problems. A typical time scale of interest is the blade passing period. This should be comparable to the convection time over one blade passage. Now two very different requirements need to be satisfied. On one hand, the time step needs to be small enough to warrant the time accuracy of an unsteady flow solution. As a reference point, a typical second order scheme should need at least 20 points per period to resolve one harmonic. 200 steps or so per period will typically be required to resolve higher harmonics. On the other hand, the time scale to be covered for the conduction part will be a factor of 10,000, longer than that for the convection. Therefore, for a time-domain unsteady conjugate HT analysis, one will have to march 2,000,000 time steps simply in order to keep the basic time consistency.

The present work is motivated by the need to address this acute mismatch of time scales between the solid conduction and the typical periodic flow unsteadiness in HP turbines. In the following sections, the baseline CFD solver will first be briefly described and an extension made to steady conjugate HT analysis. A frequency-domain conduction model will be introduced to address the mismatched time scales for unsteady CHT. The outcome of the conduction analysis, in conjunction with a new unsteady interface condition, leads to a proposed approach to unsteady conjugate HT prediction. Finally, a case study will be presented.

### 6.4.3 Baseline Flow and Conduction Solver

#### 6.4.3.1 Flow Equations and Discretization

The present work is based on a 3D Navier–Stokes solver [12], developed mainly for turbomachinery unsteady flow [13], and aeromechanics applications [14]. The turbulence stress terms are closed by the Spalart–Allmaras [15] one equation model. The flow equations are spatially discretized in a structured multiblock mesh. The semi discrete flow equations for a mesh cell can be simply written as

$$\frac{\partial \mathbf{U}}{\partial t} = \mathbf{R}(\mathbf{U})$$

#### Eq. 6.4.4

where  $\mathbf{U}$  is a six-element vector with the standard conservative flow variables and the turbulent eddy variable. The right hand side contains the flux terms formulated using the second order cell center based finite volume with the second and fourth order numerical damping. The discretized equations are solved by marching in the pseudo time  $\tau$  using the four stage Runge-Kutta scheme. For the steady flow solution, the time  $t$  in Eq. 6.4.3 is effectively replaced by  $\tau$ . For time-accurate unsteady flow computations, the physical temporal term is approximated by a second order implicit discretization [16]. For a given physical time step  $\Delta t$ , Eq. 6.4.3 for the current time step  $n$  becomes

$$\left( \frac{\partial \mathbf{U}}{\partial \tau} \right)^n + \frac{\mathbf{U}^n - 2\mathbf{U}^{n-1} + 0.5^{n-2}}{\Delta t} = \mathbf{R}(\mathbf{U}^n)$$

#### Eq. 6.4.5

As the time accuracy is not required in the pseudo time-marching to drive  $\partial \mathbf{U} / \partial \tau$  to zero at  $n$ , all the acceleration techniques for steady flows can be directly used. Here, local time stepping and multigrid are employed. On solid blade/end-wall surfaces, either the log-law or the nonslip wall condition is applied. At the inlet, stagnation parameters and flow angles are specified. At the exit, the pitch wise mean static pressure at each spanwise section is specified and the local upstream-running characteristic is formulated to drive the pitch wise average pressure to the specified value, while the local pitch wise nonuniformity is determined by the downstream-running characteristics.

#### 6.4.3.2 Conduction Equation for Solid Domain.

The energy equation for the solid domain has almost the same form as that for the fluid, zeroing all velocity terms. The semi discrete form of the energy equation for a hexahedral mesh cell is

$$\frac{\partial T}{\partial \tau} = \frac{k}{\rho c} \frac{1}{\Delta V} \sum_{m=1}^6 \left( \frac{\partial T}{\partial y} A_x + \frac{\partial T}{\partial y} A_y + \frac{\partial T}{\partial x} A_z \right)_m$$

#### Eq. 6.4.6

The time derivative is only for pseudo time here. The physical time term will be dealt with later in 6.4.4. Thus, Eq. 6.4.6 is for a steady problem only. The directional differentials of temperature on each face of the mesh cell are evaluated using the Gauss theorem on an auxiliary volume surrounding the face [17]. The equation is simultaneously time-marched with the fluid equations. As mentioned earlier, it is essential that local time stepping is used. The time step size is given by

$$\Delta \tau < C_t \frac{\rho c}{k} \left( \frac{\Delta V}{|A_x| + |A_y| + |A_z|} \right)^2$$

#### Eq. 6.4.7

where  $C_t$  is a constant equivalent to the mesh spacing based Fourier number and is typically taken to be 0.2 in the present calculations. It should be pointed out that solid material properties ( $\rho, c, k$ ) in Eq. 6.4.6 can be easily updated as a function of local temperature at each step during the time marching.

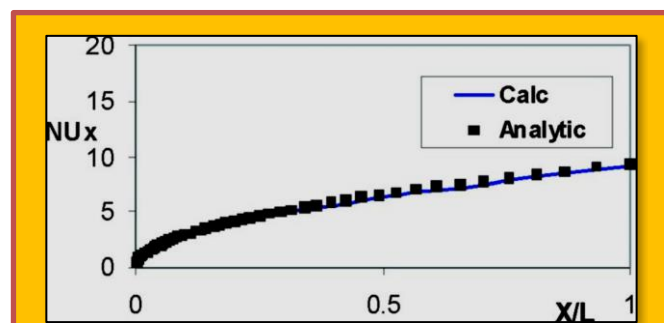


Figure 6.4.1 Nusselt number for Flat Plate Laminar Boundary Layer

#### 6.4.3.3 Verification for Convection Heat Transfer

The baseline CFD method has been verified for various turbomachinery aerodynamic and aeromechanical test cases, but not for heat transfer cases in the past. The capability of the method to predict convection heat transfer is first verified for a flat plate laminar boundary layer. The surface Nusselt number distribution is shown in [Figure 6.4.1](#). A more realistic test case is for a transonic turbine stage (MT1), for which experimental heat transfer data are available [18]. The midspan section is taken for a quasi-3D computation. The mesh is shown in [Figure 6.4.2](#), and the isentropic Mach number distribution on the blade is shown in [Error! Reference source not found.](#). Heat transfer calculations are carried out with a specified inlet total temperature of 444 K, as in the experiment, and a wall temperature of 300 K. The calculated surface Nusselt number distribution is compared with the corresponding experimental data [18].

Overall, the calculated results compare well with the experiment data [Error! Reference source not found.](#). Particular attention is drawn to the suction surface. The lower measured heat transfer coefficient in the region from the leading edge up to 50% axial chord indicates a possible laminar region, followed by a transition. This is completely missed by a fully turbulent solution, also shown in [Figure 6.4.4](#), while a better comparison is achieved by tripping a turbulent transition around 40% axial chord. This highlights the importance of a transition model in heat transfer prediction. The solid conduction solution is verified for a cylinder subject to specified temperatures at the inner and outer surfaces [Figure 6.4.5](#). The computed radial temperature distribution is compared with the analytical solution, giving an excellent agreement, as shown in [Figure 6.4.6](#).

#### 6.4.4 Frequency-Domain Unsteady Conduction Model and Analysis

The overall approach adopted to address the mismatched convection/conduction time scales for the periodically unsteady problems is to solve the unsteady conduction in a frequency domain. This will remove the need for the time-accurate integration in the time domain for the extremely slow solid conduction process, and enable all the solution

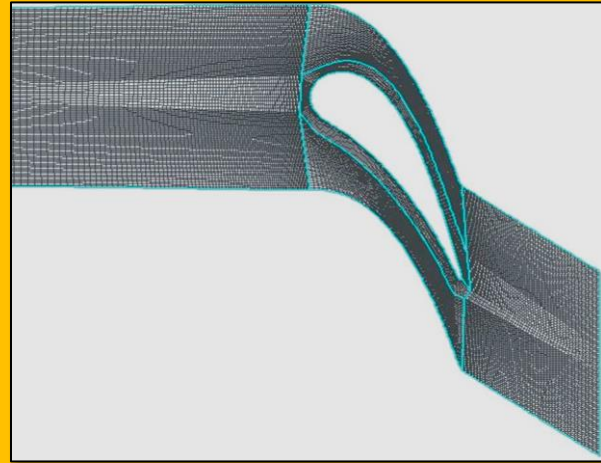


Figure 6.4.2 Computational mesh for a transonic NGV

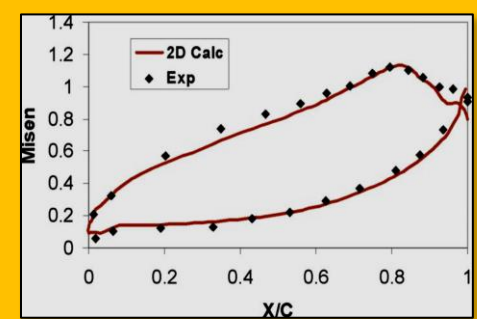


Figure 6.4.3 Surface Pressure Distribution (NGV, MT1)

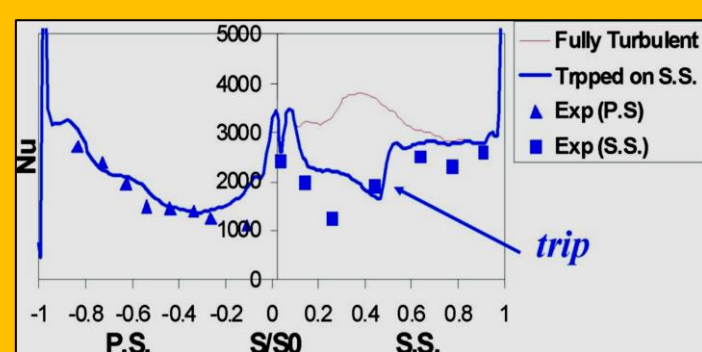


Figure 6.4.4 Surface Nu Distribution (NGV, MT1)

acceleration techniques for steady flows to be employed. An unsteady temperature in the solid domain can be decomposed into a time-mean part, and the Nth order Fourier harmonics at a fundamental frequency  $\omega$ ,

$$T = T_0 + \sum_{n=1}^N A_n \cos(n\omega t) + B_n \sin(n\omega t)$$

#### Eq. 6.4.8

The time-mean part can be calculated separately [Eq. 6.4.6](#), using material properties, which may vary with temperature. Calculation of the Fourier harmonics is most conveniently done by assuming that the metal properties are independent of temperature fluctuations (i.e., taking the material property values from the time-mean part). The unsteady conduction equations are then linear, the time mean  $T_0$  will be the same as the steady value, and each harmonic can be considered separately. The time dependent counterpart of the conduction equation [Eq. 6.4.6](#) can be expressed as

$$\frac{\partial T}{\partial t} = R_s(T)$$

#### Eq. 6.4.9

For a pair of harmonic coefficients A and B

$$-\omega A \sin(\omega t) + \omega B \cos(\omega t) = R_s[A \cos(\Omega t) + B \sin(\omega t)]$$

#### Eq. 6.4.10

Balancing the sine and cosine terms by taking [Eq. 6.4.10](#) at  $\omega t = 0$  deg and  $\omega t = 90$  deg, respectively [14], and introducing the pseudo time  $\tau$ , gives

$$\frac{\partial A}{\partial \tau} = R_s(A) - \omega B \quad , \quad \frac{\partial B}{\partial \tau} = R_s(B) + \omega A$$

#### Eq. 6.4.11

The harmonic coefficients of the unsteady temperatures are time independent. Hence, [Eq. 6.4.11](#) can be efficiently solved by using the steady flow methods. Effectively, one unsteady solution retaining one harmonic now becomes equivalent to two steady state solutions. This real-number harmonic model is implemented with relatively small modifications of the baseline steady conduction solver, as described in 6.4.3.2. A first verification is for unsteady conduction across a 1D plane slab with a specified harmonic temperature at one surface and zero at the other. The material properties chosen are those for steel. The driving temperature amplitude is 100 K. The harmonic temperature distribution is shown in [Figure 6.4.7](#). Also shown is the analytical solution [19], giving a good agreement.

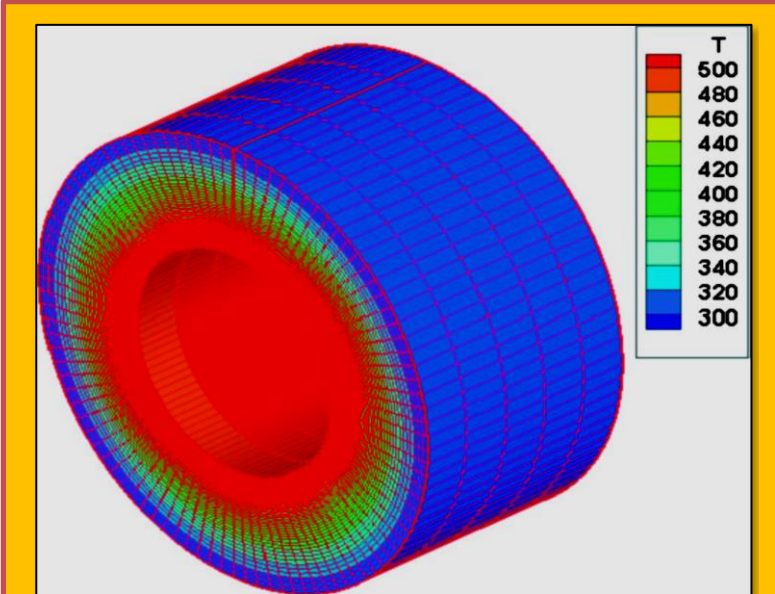


Figure 6.4.5 Mesh for steady conduction (cylinder)

The 1D unsteady conduction across a slab also provides a simple but effective case to demonstrate the mesh dependence for unsteady conduction, compared with the steady counterpart. The small penetration at high frequency leads to high local truncation errors. For a given unsteady wall heat flux, the errors in the calculated unsteady wall temperatures are compared with the analytical solution [19].

**Table 6.4.1** gives the results for three different mesh densities at the same frequency (1000 Hz). The maximum error for the coarsest mesh is about 60%. On the other hand, the steady heat flux is completely mesh independent. Given the range of the frequencies relevant to turbine blade heat transfer, it can be seen that a computational mesh generated for a steady conjugate heat transfer solution will most unlikely be suitable for an unsteady one.

## 6.4.5 Fluid-Solid Interface

### 6.4.5.1 Discrete Interface Condition

The physical requirements for an interface condition are, first, to satisfy energy conservation (the same heat flux across the interface) and second, a temperature continuity (the same wall temperature seen from both sides). Consider an interface between the fluid and solid computational domains, as shown in **Figure 6.4.8**. For given temperatures at interior points (taking the **total** temperature for the fluid side), the two physical requirements can be met by

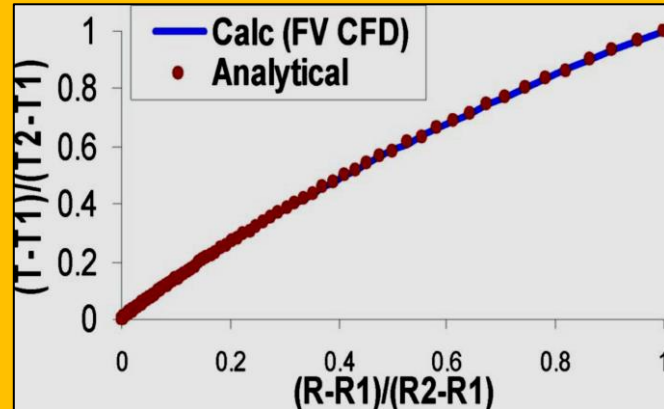


Figure 6.4.6 Radial Temperature Distribution (cylinder)

	10 Points	20 Points	100 Points
Error to analytical solution	60%	25%	2%

Table 6.4.1 Percentage Errors in Calculated Unsteady Wall Temperature Amplitudes for Three Mesh Densities

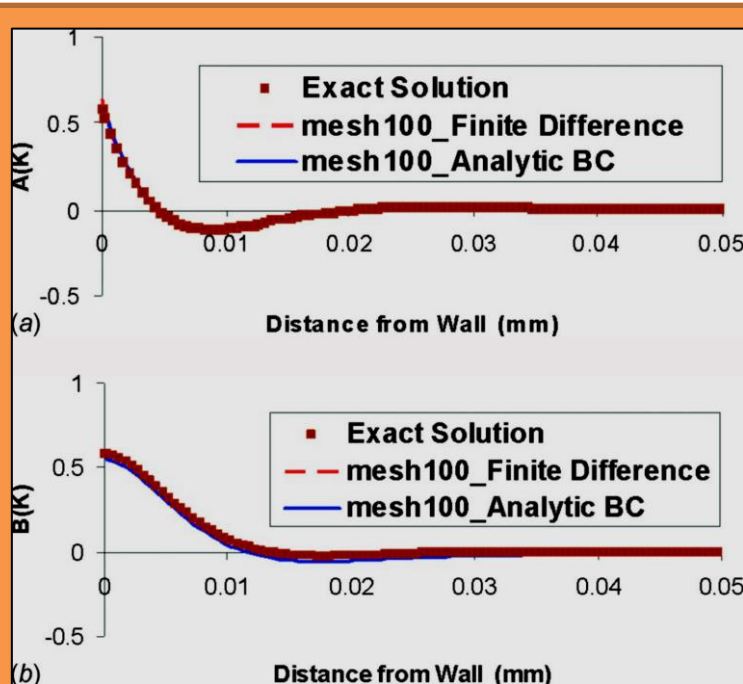


Figure 6.4.7 Harmonic temperature distribution (1D slab): (a) in phase harmonic component A, and (b) out-phase harmonic component B

$$T_w = \frac{T_s(k_s/\Delta x_s) + T_f(k_f/\Delta x_f)}{\frac{k_s}{\Delta x_s} + \frac{k_f}{\Delta x_f}}$$

**Eq. 6.4.12**

For a 1D steady conduction, **Eq. 6.4.12** is the exact analytical relation at the interface. For unsteady conduction, it is an approximation, as the unsteady temperature distribution will be in general nonlinear along a distance from the wall. The unsteady energy conservation means that both the time-mean and unsteady parts of heat flux need to be balanced. In terms of the real-number harmonic coefficients A and B, the unsteady heat flux balance can be approximated by one-sided finite difference

$$\begin{aligned}\frac{k_f}{\Delta x_f}(A_w - A_f) &= \frac{k_s}{\Delta x_s}(A_s - A_w) \\ \frac{k_f}{\Delta x_f}(B_w - B_f) &= \frac{k_s}{\Delta x_s}(B_s - B_w)\end{aligned}$$

**Eq. 6.4.13**

These determine the harmonic wall temperature ( $A_w, B_w$ ), once the fluid and solid harmonic temperatures in the interior points are given, similarly to that for the time-mean wall temperature, using **Eq. 6.4.12**. For HP turbines, a thermal barrier coating (TBC) is typically applied. As TBC layers are very thin, with thicknesses typically less than mesh spacing **Figure 6.4.8**, the TBC effects can be conveniently included by adding the corresponding thermal conduction resistance to the flux calculation. Then the wall temperature is calculated by finite difference. Again, similarly to the simple non-TBC situations, this TBC treatment is accurate for steady cases, but subject to truncation errors for unsteady cases.

#### 6.4.5.2 Semi-Analytical Interface Condition.

The preliminary analysis of unsteady conduction has indicated a strong mesh dependence for the frequency range of interest **Table 6.4.1**. This has motivated an effort to seek a more accurate method to treat the wall boundary in the solid domain. The very small penetration depth \_even smaller if TBC is used\_ for the frequencies of practical interest leads to the consideration of making use of the 1D analytical solutions for unsteady conduction, which has been extensively used in heat transfer experiments [20,21]. In this section, a complex number notation is used here for temporal harmonics for the sake of simple expressions. In the frequency-domain, the solid surface temperature and heat flux harmonics are directly linked. For a semi-infinite domain, this is expressed as

$$\hat{q}_s = \sqrt{i\omega} \sqrt{\rho c k} \hat{T}_s$$

**Eq. 6.4.14**

For a thin slab of thickness  $\delta_1$  (e.g., TBC) with properties denoted with subscript "1," connected to a semi-infinite domain with properties denoted with subscript "2," the relation becomes

$$\hat{q}_s = \sqrt{i\omega} \sqrt{\rho_1 c_1 k_1} \frac{(1+a)e^\delta - (1-a)e^{-\delta}}{(1+a)e^\delta + (1-a)e^{-\delta}} \hat{T}_s$$

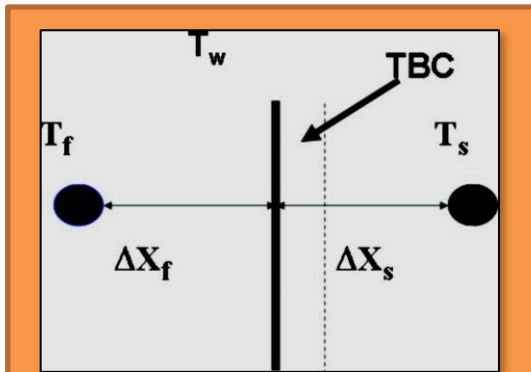
**Eq. 6.4.15**

Figure 6.4.8 Fluid-solid domain interface

where  $\delta = \sqrt{\delta_1 i \omega / \alpha_1}$ ,  $\alpha_1 = k_1 / (\rho_1 c_1)$ , and  $a = \sqrt{(\rho c k)_2 / (\rho c k)_1}$ . The advantage of using the analytical relation can be easily seen in the previous test case of wall temperature calculations in **Table 6.4.1**. For a given heat flux harmonic at the surface, the wall temperature harmonic can now be analytically given, and hence, always exact, regardless of the mesh density. Now the question is, how can this kind of analytical relation be employed to serve the fluid-solid domain interface treatment? Writing a common form for **Eq. 6.4.14** and **Eq. 6.4.15** as

$$\hat{q}_s = \hat{C}_{Tq} \cdot \hat{T}_s$$

#### **Eq. 6.4.16**

$T_q$  is a complex number, dependent on only the solid domain properties, and can be regarded as a "temperature-to-flux transfer function." For the harmonic flux balance  $\hat{q}_f = \hat{q}_s$ , the analytical relation **Eq. 6.4.16** can be used to represent the solid part to avoid the high mesh dependence. Substituting  $T_s$  by  $T_w$  in **Eq. 6.4.16** as required by the temperature continuity and using the finite difference for the fluid heat flux  $\hat{q}_f$ , gives a semi-analytical interface condition for wall temperature harmonic in a complex number form

$$\hat{T}_w = \frac{\hat{T}_f \left( \frac{k_f}{\Delta x_f} \right)}{\left( \frac{k_f}{\Delta x_f} \right) + C_{Tq}}$$

#### **Eq. 6.4.17**

This semi-analytical method can also be used in a more general form when the heat flux harmonic on the fluid side is expressed as a convection heat transfer coefficient,  $\hat{q}_f = h(T_f - T_w)$

$$\hat{T}_w = \frac{h \hat{T}_f}{h + C_{Tq}}$$

#### **Eq. 6.4.18**

A common issue regarding the semi-infinite conduction model is how restrictive the 1D model is. First, it should be emphasized that the condition is only used locally between the mesh point adjacent to the wall and the wall itself. The simple curvature effect is corrected with an extra curvature radius  $r_c$  related term [22] being added in the transfer function

$$(\hat{C}_{Tq})_c = \hat{C}_{Tq} - \frac{k\sigma}{2r_c}$$

#### **Eq. 6.4.19**

where  $\sigma = 1$  for a cylinder and  $\sigma = 2$  for a sphere. An interesting and relevant case to consider is for a sharp corner ( $r_c=0$ ). For simplicity, the surrounding fluid is assumed to provide a constant harmonic heat flux  $\hat{q}$  on the boundaries **Figure 6.4.10-a**. The finite-difference condition **Eq. 6.4.13** can capture the corner effect without a problem, but a direct application of the 1D semi-analytical condition **Eq. 6.4.15** would lead to a constant boundary harmonic temperature. This is a seemingly unrealistic solution, as the corner heating (or cooling) would physically result in a locally higher (or lower) temperature, even on the boundary surface. The problem lies in that a boundary itself will be subject to heat transfer, not only in the normal direction, but also in the tangential direction **Figure 6.4.10-b**. The latter has so far been missed if one simply applies **Eq. 6.4.16** directly.

Because of the linear nature of the conduction equation in the solid domain, one can rectify the problem by superimposing two 1D solutions along the two boundaries forming the corner. This can be easily implemented by recognizing that the normal heat flux  $q_n$  on one boundary would be the tangential heat flux  $q_t$  on the other boundary **Error!**

**Reference source not found.-b.**

This simple linear superposition has been successfully tested. A corner heating example is shown in [Figure 6.4.9](#). In this case, both boundaries around the corner are subject to a constant harmonic flux. The corner temperature amplitude should be doubled because of the corner heating/cooling effect. The superimposed corner solution with the semi-analytical condition [Figure 6.4.9-a](#) resolves the corner heating very well, in excellent agreement with a reference solution using the finite difference condition [Figure 6.4.9-b](#).

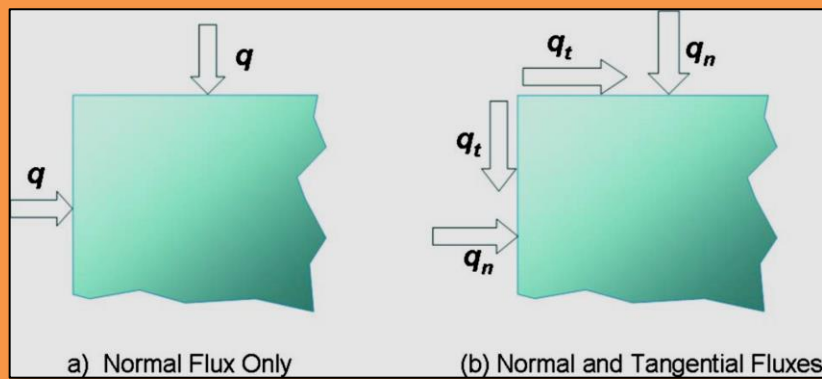


Figure 6.4.10 Heat Transfer in Corner Region: (a) Normal Flux only and (b) Normal and Tangential Fluxes

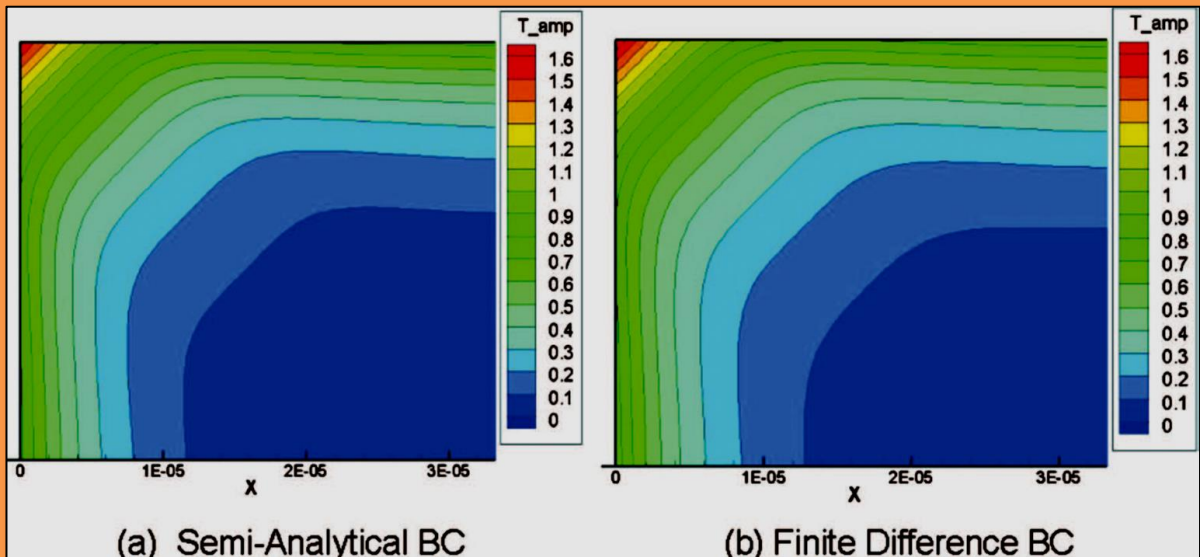


Figure 6.4.9 Temperature Amplitude Corner Solution: (a) Semi-Analytical BC and (b) Finite-Difference BC

#### 6.4.5.3 Case Analysis for Fluid-Solid Interface.

A case study has been carried out to gain some insight for a configuration with some of the characteristics of a cooled turbine blade leading edge. A two-layer cylinder is considered. It consists of an inner layer \_Nickel, thickness 1 mm\_ and an outer "TBC" layer (modeled by Kapton, thickness 0.1 mm). The steady boundary conditions are the specified temperatures: 300 K at the inner boundary ( $r_i = 1$  mm) and 400 K at the outer boundary ( $r_o = 2.1$  mm). The unsteady boundary

conditions at the outer (hot) boundary are a specified heat transfer coefficient (HTC) of 1000 W/m<sup>2</sup> K and a harmonic fluid driver temperature ( $T^{\wedge} = 100$  K). At the inner (cold) boundary, the harmonic temperature is specified to be zero, assuming that the penetration depth is smaller than the total two layer thickness. The overall penetration depth dependence on frequency is clearly indicated in [Figure 6.4.11](#), in which the radial temperature harmonic distributions are shown for three frequencies. The penetration depth is well within the TBC thickness (0.1 mm) once the frequency is above 100 Hz.

Note that for the present cases, the heat flux harmonic remains largely the same at different frequencies for the given HTC and driver fluid temperature harmonic. Thus, the unsteady temperature gradient at the wall is largely the same. Nevertheless, there will have to be a much higher mesh dependence of the solution at high frequencies due to the much reduced penetration depth. This mesh-dependent behavior in terms of surface temperature harmonics can be seen in [Figure 6.4.13](#).

The advantage of the semi-analytical condition is evident, with the temperature harmonic being completely mesh independent (HTC and fluid driver temperature harmonic would fix the unsteady wall temperature [Eq. 6.4.18](#), and thus, the unsteady heat flux). It is noted that the unsteady variation in surface temperature has not been included in previously published conjugate analyses. One would naturally ask, how much difference would the inclusion of unsteady wall temperature make? The effect of neglecting the unsteady variation in wall temperature on the calculated heat flux is illustrated in [Figure 6.4.12](#) for the lowest frequency considered (10 Hz). Clearly, the wall heat flux amplitude is considerably overpredicted. The semi-analytical relation [Eq. 6.4.14](#) gives a 45 deg phase lag of the wall temperature, relative to the heat flux.

Given this relatively small phase difference, neglecting the unsteady wall temperature should lead to an overprediction of the unsteady component of heat flux. The extent of the overprediction depends on both frequency and HTC. A typical value of  $HTC = 3000$  W/m<sup>2</sup> K, gives a 33% overprediction of unsteady heat flux at 10 Hz; an 18% overprediction at 100 Hz, and a 6% overprediction at 1000 Hz. It is worthwhile noting that a typical periodic unsteadiness relevant to HP turbine blades would be the blade passing frequency of the order of 1000 Hz. HP turbine blades may also be subject to lower frequencies, e.g., those due to combustor instabilities of the order of 100 Hz. An example of even

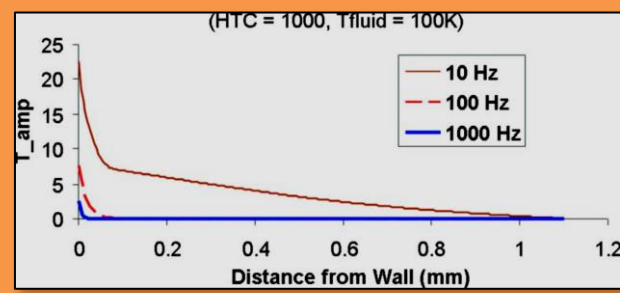


Figure 6.4.11 Radial temperature harmonics

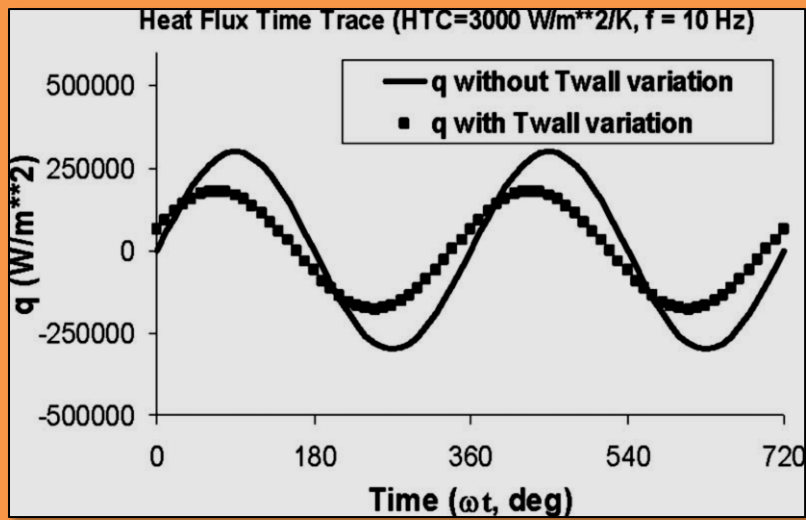


Figure 6.4.12 Unsteady Heat Flux in Time (With and Without Unsteady Wall Temperature)

lower frequencies is that due to a self-excited un-axisymmetric vortical flow structure in a rotor disk cavity. As the pattern circumferentially slips relatively to the rotor disk at about 10% of the rotation speed [23], the frequency should be of the order of 10 Hz.

#### 6.4.6 Coupled Unsteady Conjugate Method

##### 6.4.6.1 Further Modeling Considerations

The unsteady conduction analysis presented above reveals some important features, which will need to be taken into account when developing a coupled unsteady conjugate method. It is clear that unsteady conduction will have a qualitatively different mesh requirement, far more demanding, compared with that for a steady problem. An adequately accurate

unsteady conjugate solution will be expensive, even if the frequency-domain conduction analysis would, as intended, be able to avoid the difficulty, due to the completely mismatched time scales. Putting it simply, one would like to avoid solving an unsteady temperature field in the solid domain. It is also clear that, for the solid domain, what matters most is the unsteady temperature on the surface. This is not only because the maximum temperature fluctuation occurs on the surface, but also because the unsteady wall temperature, once known, will completely determine the whole unsteady temperature field. Interestingly, the new semi-analytical interface condition [Eq. 6.4.16](#) and [Eq. 6.4.17](#) means that for a given unsteady fluid driver temperature at a mesh point adjacent to the surface, one can get the unsteady wall temperature [Eq. 6.4.17](#), and hence, the unsteady heat flux [Eq. 6.4.16](#). Effectively, the unsteady surface temperature can be obtained without solving the unsteady conduction problem in the solid domain.

##### 6.4.6.2 Proposed Method

The observations and findings so far lead to the proposal of the following method for unsteady conjugate heat transfer prediction.

**Fluid part.** To be solved by an unsteady nonlinear CFD solver, providing unsteady fluid driver temperatures at all mesh points adjacent to solid boundaries. Any current URANS or LES solver can be used directly for this task.

**Solid part.** To be solved only as a steady conduction problem, providing a “steady” solid temperature field (noting that for a linear problem, the time-averaged temperature will be the same as a steady one).

**Fluid-solid interface.** The unsteady fluid (driver) temperatures are Fourier-transformed. The time-averaged fluid temperature and the steady solid temperature are coupled to find the time-averaged

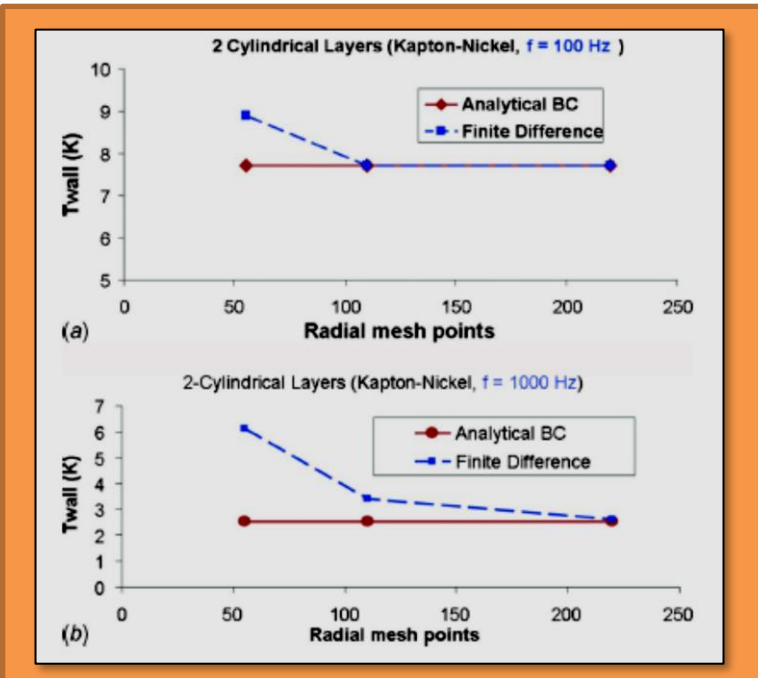


Figure 6.4.13 Mesh-dependence of wall temperature: (a) 100 Hz and (b) 1000 Hz

wall temperatures using the steady interface treatment [Eq. 6.4.12](#).

The harmonic fluid temperature is used to find the harmonic wall temperature by the semi-analytic interface condition [Eq. 6.4.16](#) and [Eq. 6.4.17](#). It should be mentioned that the Fourier transform was used in nonlinear time-domain unsteady turbomachinery flow modeling [24,25]. For unsteadiness with a known fundamental frequency, the Fourier harmonic updating during a time-marching solution can be accelerated by a “partial substitution,” i.e., utilizing the existing Fourier coefficients in the Fourier summation [24]. A continuous updating can be achieved as a result of the partial substitution [25]. This technique is also adopted in the present work for the Fourier transform of the fluid temperatures at mesh points adjacent to wall surfaces.

Finally, it should be added that once the unsteady wall temperatures are obtained as part of the coupled conjugate solution, one can run a completely separate unsteady conduction solution (with an appropriate mesh) for the solid domain, if the detailed unsteady temperature field is required.

#### 6.4.6.3 Case Study for Coupled Conjugate Method

The above unsteady conjugate method has been implemented with fluid and solid solvers, which have been separately validated, as described in the previous sections. A conjugate case has been generated for testing and demonstrating the method. The nozzle guide vane (NGV) blade geometry of the MT1 stage is modified by adding two internal cooling passages (illustrated in [Figure 6.4.14](#) and [Figure 6.4.15](#)). The thickness of the blade metal (Nickel) layer between the external and internal surfaces is about 5% of the chord length. The external surface is covered by TBC (Kapton) of thickness 0.1 mm. The cooling effect is simulated by specifying the temperature of the internal channel surface to give a compatible hot gas/coolant temperature ratio. In this case, the internal surface temperature of 300 K is chosen to give a gas/coolant temperature ratio of around 1.5.

The computational results presented are from the analysis for a quasi-3D configuration, taken from the midspan section of the MT1 NGV blade. Although this is an NGV, rather than a rotor, it is convenient as a well-documented test case [18] and will serve to demonstrate the new technique. The steady flow conditions are the same as in the case presented in [6.4.3.3](#) with an inlet Mach number of 0.3 and an exit Mach number of 0.9. The computational mesh

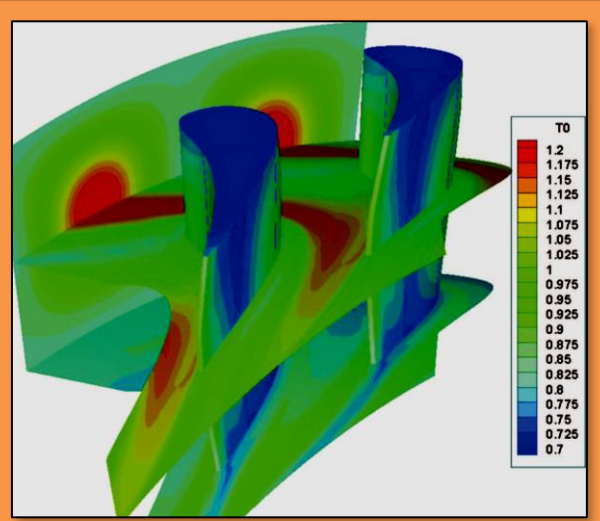


Figure 6.4.14 Cooled blade configuration (subject to Incoming hot streak)

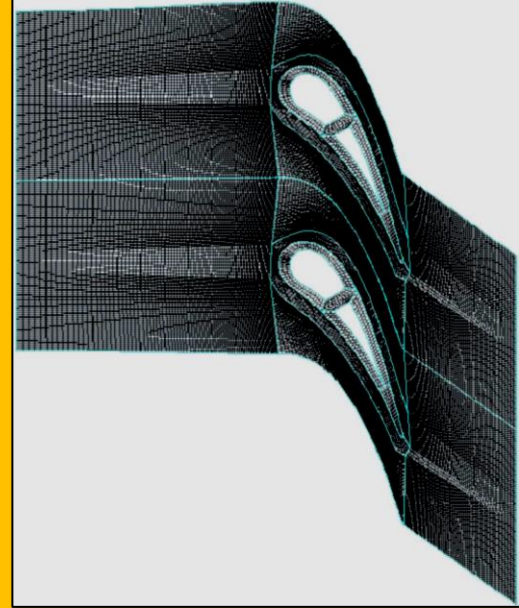


Figure 6.4.15 Computational Mesh (Conjugate Solution)

for the 2D section has ten blocks of 24,400 mesh points in total. The mesh distribution is dominated by the fine resolution required for the fluid domain ([Figure 6.4.16](#)). Periodically unsteady flow disturbances are generated by a specified harmonic unsteady total temperature variation in time at the inlet plane of the form

$$T_t = \bar{T}_t \left[ 1 + A_T \cos\left(\omega t + 2\pi \frac{y}{y_{HS}}\right) \right]$$

#### [Eq. 6.4.20](#)

This corresponds to a circumferential traveling unsteady hot streak disturbance, as seen in a rotor frame. The mean total temperature is the same as that used in the steady solution. The total pressure variation in the hot streak is neglected. The inlet flow [Figure 6.4.14](#) Cooled blade configuration (subject to Incoming hot streak) angle harmonic variation included corresponds to the hot streak velocity perturbations for a given temperature amplitude  $A_T$  [Eq. 6.4.20](#). The hot streak pitch is taken to be two blade pitches, i.e., the hot streak/blade count is 1.2 ([Figure 6.4.16](#)). The frequency is taken to be 1000 Hz.

These unsteady parameters, together with the inlet mean flow velocity, give an angle of about 60 deg between the hot streak and the axial direction. This is comparable to that of the calculated unsteady hot streaks for the MT1 rotor blades [26]. With regard to the unsteady conjugate heat transfer, the first point to note is that the proposed time/frequency-domain coupled method converges well for the present transonic flow case. The fluid part is solved by the dual-time stepping scheme described in 6.4.3.1 with 100 physical time steps per period. At each physical time step, 60 sub iterations are carried out by pseudo time marching. [Figure 6.4.17](#) shows the convergence history of the coupled conjugate solution. The

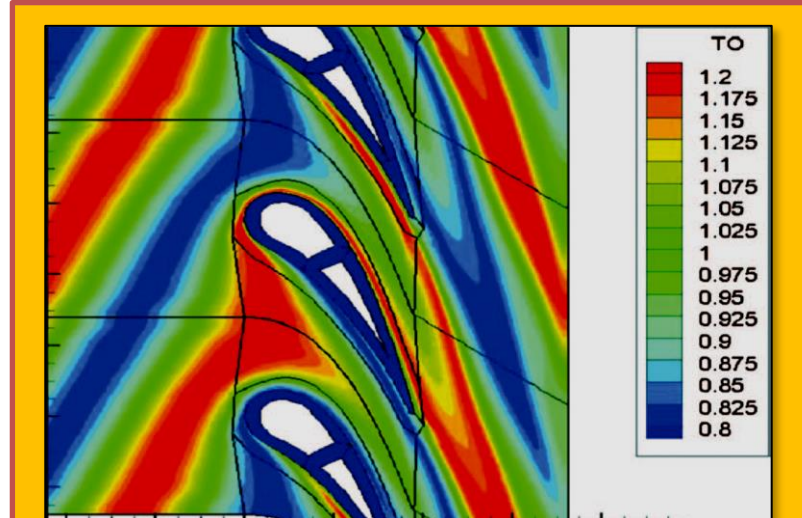


Figure 6.4.16 Instantaneous Unsteady Total Temperatures (Inlet Total Temperature Amplitude ,  $A_T = 0.2$ )

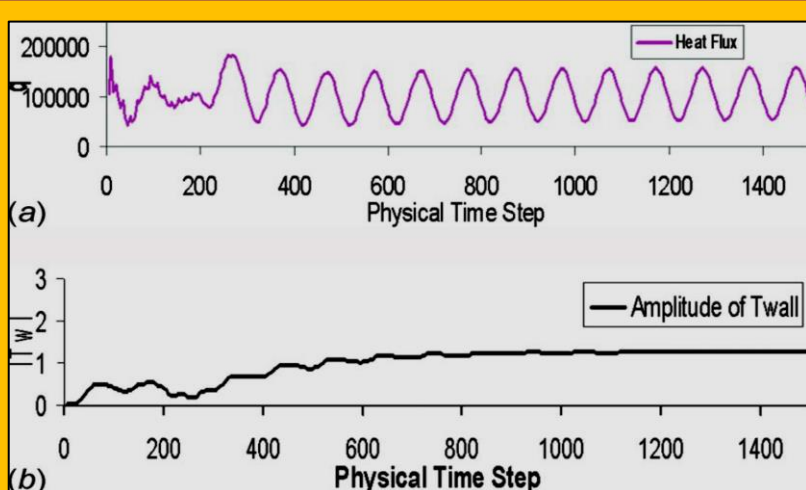


Figure 6.4.17 Solution Convergence Characteristic: (a) Heat Flux (time-domain fluid solution) and (b) Harmonic Wall Temperature amplitude (frequency-domain solution)

time-domain fluid solution is indicated by the heat flux time history on the fluid side at a point near the blade leading edge (**Figure 6.4.17-a**). Apparently, a periodic state is reached after about 5 periods, once the initial transients are driven out of the domain. For the solid domain, the maximum residual of the steady conduction solution is dropped by four orders of magnitude after 500 time steps. A very useful indication of the convergence of this hybrid coupled method is the change in the surface harmonic temperature. The time history of the harmonic amplitude of the wall temperature at the leading edge point is also plotted, again showing that the solution is largely converged after 5–6 periods (**Figure 6.4.17-b**). These time history results demonstrate the intended convergence characteristics.

In terms of the impact of including the unsteady wall temperature, calculations are conducted with and without the harmonic part of the unsteady wall temperature included. The solution without the harmonic wall temperature overpredicts the heat flux by a maximum of 5%. This level of error in predicting the unsteady heat flux in this high frequency is qualitatively in line with the result for a simple cylindrical configuration (sec. 6.4.5.3).

A practically more relevant question is whether or not the periodic unsteadiness would affect the time-averaged performance. An interesting observation in this hot streak case is that there seems to be a strong nonlinear influence of the unsteadiness on the time-averaged heat transfer. This is illustrated in **Figure 6.4.18**, in which 20% hot streak amplitudes the time-averaged surface heat flux distributions are shown for two hot streak amplitudes,  $A_T = 0.1$  and  $0.2$  (see **Eq. 6.4.20**, respectively. Overall, the shape of the distributions shows a high heat transfer around the leading edge, and a roughly flat distribution for the front part of both surfaces. The relatively sudden increase in heat transfer on the suction surface at around 65% axial chord is due to the tripped transition. The level of the heat flux drops quickly toward the trailing edge, largely due to the trailing edge portion of the blade being farther away from the cooling channel in this model (thus, a relatively higher local wall temperature). For the 10% hot streak amplitude (**Figure 6.4.18-a**), the time averaged value is largely the same as the steady one. However, when the amplitude is increased to 20% (**Figure 6.4.18-b**), the time averaged heat flux is markedly lower than the steady one over both the suction and pressure surfaces. To rule out the mesh dependence of this observed feature, a further numerical test is carried out at a higher mesh density with a doubled mesh resolution in the near wall fluid region. The results from the refined mesh also consistently show that the time-averaged heat flux is similarly lower than the steady one.

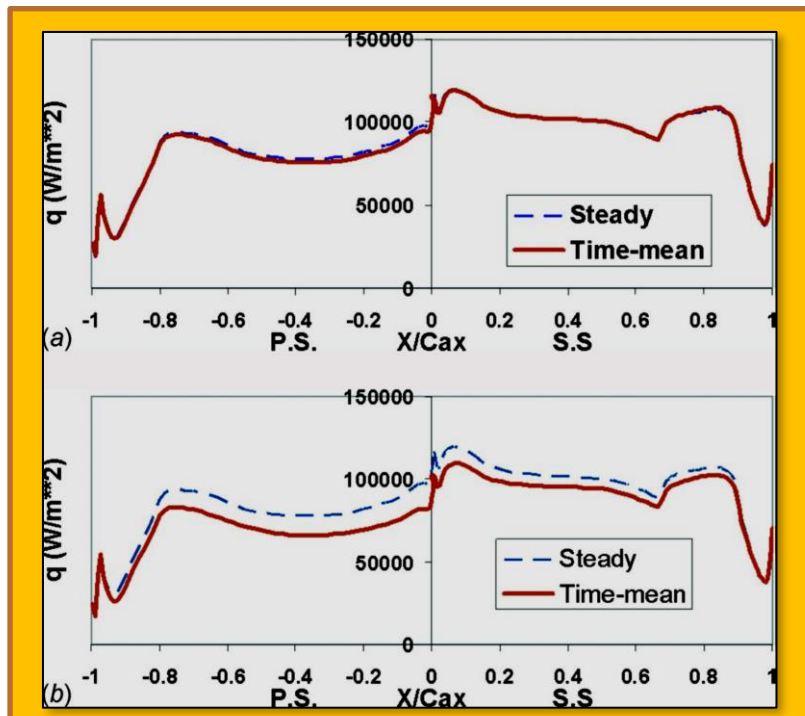


Figure 6.4.18 Time averaged surface heat flux: (a) 10% and (b) 20% hot streak amplitudes

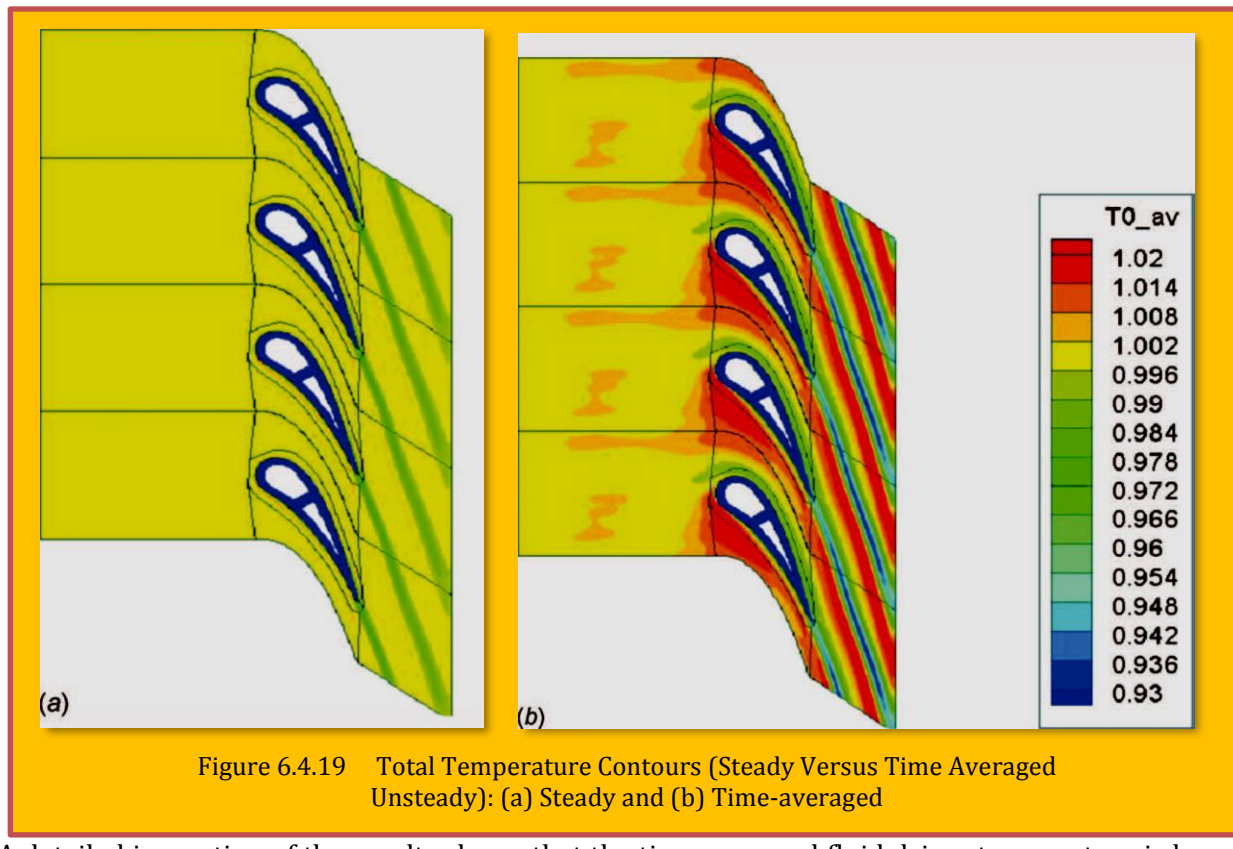


Figure 6.4.19 Total Temperature Contours (Steady Versus Time Averaged Unsteady): (a) Steady and (b) Time-averaged

A detailed inspection of the results shows that the time averaged fluid driver temperature is lower than that of the steady case. It is well known that hot streaks can migrate hot fluid from the suction surface to the pressure surface \_i.e., the “preferential heating” [27]. It is also known that the unsteady potential field associated with blade row interaction can result in a hot streak oscillation, which leads to different hot streak residence times (thus different time-averaged total temperatures) in different locations [28]. These are, however, all kinematic mechanisms, leading to a redistribution of the total temperature in the blade passage. In the present case, a nonuniform total temperature field due to the unsteady kinematics is also observed (**Figure 6.4.19**).

But it seems that neither of these two total temperature redistribution mechanisms offers an

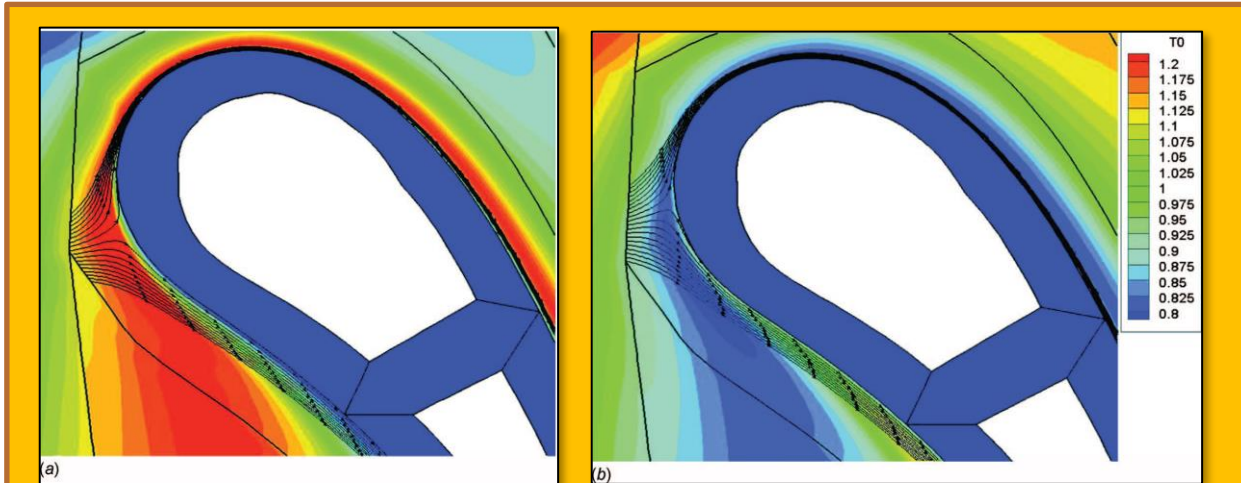


Figure 6.4.20 Instantaneous Stream-Traces: (a) Hot and (b) Cold portion Impinging

explanation for the lower driver temperature on both surfaces. It is noted that the maximum difference between the time averaged and the steady values is around the blade leading edge (**Figure 6.4.18-b**). The question then is whether a cold portion of fluid in a hot streak will have a higher impinging capability, and thus, to be closer to the wall than a hot portion. This can be indicated by stream-traces, based on the instantaneous velocities around the leading edge at two instants in time. One is at the instant when the hot portion impinges the leading edge (**Figure 6.4.20-a**), and the other is when the cold portion impinges the leading edge (**Figure 6.4.20-b**). The stream-traces do illustrate a higher incidence when the hot portion hits the blade, as expected. The comparison of the stream traces around the stagnation regions between the two instants does seem to indicate that the cold portion can get closer to the blade than the hot one.

One possible explanation then arises from consideration of the momentum normal to the hot streak. In the relative frame of reference fixed to the moving hot streak, the tangential velocity along the streak will be higher in the hot portion than in the cold portion, but the normal velocity should be the same for both hot and cold portions. When a hot streak approaches the leading edge, it is distorted\_bent and stretched, shown in **Figure 6.4.16** by the local steady pressure field, in addition to the unsteady pressure field due to the hot streak and blade interaction. The distorted hot streak tends to wrap up around the leading edge (**Figure 6.4.20**) while impinging onto the blade surface. Thus, locally, the hot streak becomes largely parallel to the wall. Then the difference in the impingement onto the wall between a hot portion of the streak (**Figure 6.4.20-a**) and the cold portion (**Figure 6.4.20-b**) may be attributed to the corresponding momentums normal to both the streak and the wall surface.

Assume that the local static pressure field is largely the same for both the hot and cold fluid impingements. The flow pattern of the hot fluid impingement can then be compared with that of the cold one, as indicated in **Figure 6.4.21**. The impinging fluid will be diverted to flow tangentially, when its normal momentum is exhausted by the local normal pressure gradient. Now, also assume that, similar to a straight hot streak, the local normal velocity of the deformed streak remains largely the same for both hot and cold portions (i.e., both hot and cold fluids

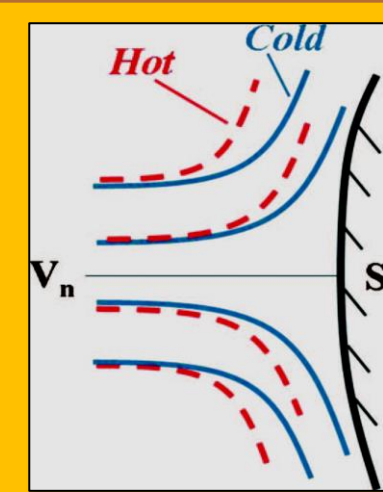


Figure 6.4.21 Impinging hot and cold flow patterns

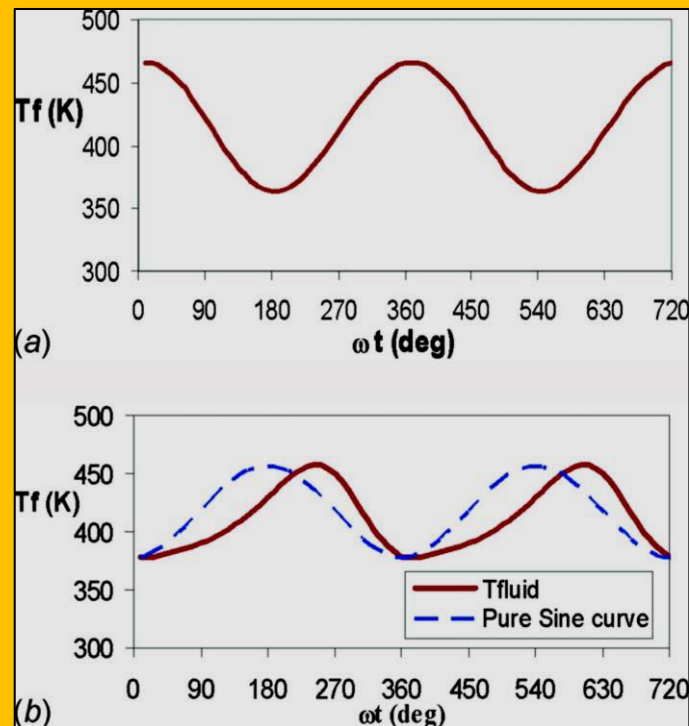


Figure 6.4.22 Time traces of fluid temperatures: (a) 10% and (b) 20% hot streak amplitudes

approach the surface with the same normal velocity,  $V_n$ ). It then follows that the normal momentum will solely depend on the density, which is approximately inversely proportional to the temperature. Consequently, given the same static pressure field (e.g., the same pressure gradient along the stream line leading to the stagnation point "S"), the cold portion should be able to impinge closer to the surface, because of its higher approaching momentum. Furthermore, the cold fluid penetrating to the region closer to the wall will be convected downstream at a slower velocity. Additionally, as the flow is convected around the blade, the hot and cold streaks will be accelerated by the same pressure field and will thus have similar Mach numbers. Their temperature differences will thus cause the cold fluid to move more slowly than the hot fluid. This slower convection of the colder fluid corresponds to a longer residence time for the cold portion than the hot portion. Therefore, both the deeper penetration of the cold fluid and the prolonged residence time should lead to an enhanced cooling. These are nonlinear effects, thus, the time-averaged result is different from the steady counterpart. The enhanced cooling effect can be seen in [Figure 6.4.22](#). The figure shows the time traces of temperature at a mesh point near the leading edge for two different hot streak amplitudes. For the 10% amplitude ([Figure 6.4.22-a](#)), the time trace is of an almost pure sinusoidal shape, a good indication of a linear behavior. However, at the 20% amplitude ([Figure 6.4.22-b](#)), a clearly non-sinusoidal shape is seen, with an enhanced contribution from the cooler part of the cycle. In terms of the time-averaged temperature, the time trace at 10% amplitude, despite having a lower minimum temperature, gives a higher average by 3.2 K than that at 20% amplitude.

#### 6.4.7 Concluding Remarks

There is a huge time scale disparity between fluid convection and solid conduction. For steady conjugate solutions, this does not have a detrimental influence on the computational efficiency of standard time-domain CFD solvers due to the use of local time stepping. However, it becomes extremely problematic if a conjugate solution is sought for unsteady flow with time scales relevant to HP turbine blades. The issue is addressed in the present work by introducing a frequency-domain unsteady conduction model, to realign the greatly mismatched time scales. The unsteady conduction analysis reveals that there will be a qualitatively different spatial meshing requirement for the unsteady conduction compared with the steady one.

Use of the frequency-domain analytical relation between the heat flux and wall temperature is shown to be very effective in reducing the truncation errors in finite-difference discretization at the wall boundary. For all the cases analyzed, the results show that the neglect of the unsteady component of the wall temperature will lead to an overprediction of the magnitude of unsteady heat flux. For a frequency typical of blade passing unsteadiness, the overprediction will be around 5% or less, but the errors increase considerably at lower frequencies.

The analytical relationship for the solid part is combined with the discrete treatment for the fluid part to form a new semi analytical interface condition. This new interface treatment enables a coupled unsteady conjugate solution to be obtained without simultaneously solving the unsteady temperature field in the solid domain. A new hybrid conjugate heat transfer approach is subsequently developed. At the interface, a continuously updated Fourier transform is carried out to enable the coupling between the two domains both for the time-averaged temperatures by the standard interface condition and for the harmonic part by the semi-analytical interface condition. The proposed method has been implemented and demonstrated in a time-marching finite volume CFD solver. The main ingredients for the coupled conjugate heat transfer have been validated against well-established experimental data and analytical solutions. A case study for a turbine blade row subject to unsteady hot streaks is conducted, and the results indicate a strong nonlinear influence of unsteadiness on time-averaged heat transfer for a large hot streak amplitude, resulting to a lower time-averaged heat transfer compared with the steady value.

#### 6.4.8 References

- [1] Bohn, D., Bonhoff, B., and Schonborn, H., 1995, "[Combined Aerodynamic and Thermal Analysis](#)

- of a Turbine Nozzle Guide Vanes,"* ASME Paper No. GT 95-108.
- [2] Han, Z. X., Dennis, B. H., and Dulikravich, G. S., 2000, "Simultaneous Prediction of External Flow-Field and Temperature in Internal Cooled 3D Turbine Blade Material," ASME GT 2000-GT-253.
- [3] Garg, V. K., 2002, "Heat transfer Research on Gas Turbine Airfoils at NASA GRC," Int. J. Heat Fluid Flow, 23\_2, pp. 109–136.
- [4] York, W. D., and Leylek, J. H., 2003, "3-Dimensional Conjugate Heat transfer Simulation of an Internally Cooled Gas Turbine Vane," ASME Paper No. GT-2003-38551.
- [5] Heidmann, J. D., Kassab, A. J., Divo, E. A., Rodrigaez, F., and Stienthorsson, E., 2003, "Conjugate Heat Transfer Effects on a Realistic Film-Cooled Turbine Vane," ASME Paper No. GT-2003-38553.
- [6] Verstraete, T., Alsalihi, Z., and Van den Braemhussche, R., 2007, "Numerical Study of Heat Transfer in Micro Gas Turbines," ASME J. Turbomachinery, 129\_4, pp. 835–841.
- [7] Amaral, S., Verstraete, T., Van den Braemhussche, R., and Arts, T., 2008, "Design and Optimization of Internal Cooling Channels of a HP Turbine Blade, Part 1, Methodology," ASME Paper No. GT2008-51077.
- [8] Starke, C., Janke, E., Hofer, T., and Lengani, D., 2008, "Comparison of a Conventional Thermal Analysis of a Turbine Cascade to a Full Conjugate Heat Transfer Computation," ASME Paper No. GT2008-51151.
- [9] Goormans-Francke, C., Carabin, G., and Hirsch, Ch., 2008, "Mesh Generation for Conjugate Heat Transfer Analysis of a Cooled High Pressure Turbine Stage," ASME Paper No. GT2008-50660.
- [10] Denton, J. D., 1992, "The Calculation of Three-Dimensional Viscous Flow Through Multistage Turbomachine," ASME J. Turb., 114\_1, pp. 18–26.
- [11] Arnone, A., 1994, "Viscous Analysis of Three-Dimensional Rotor Flow Using a Multi-Grid Method," ASME J. Turbo., 116\_3, pp. 435–445.
- [12] He, L., 2000, "3D Navier-Stokes Analysis of Rotor-Stator Interactions in Axial flow Turbines," Proc. Inst. Mech. Eng., Part A, 214, pp. 13–22.
- [13] He, L., Chen, T., Wells, R. G., Li, Y. S., and Ning, W., 2002, "Analysis of Rotor-Rotor and Stator-Stator Interferences in Multi-Stage Turbomachines," ASME J. Turbo., 124\_4, pp. 564–571.
- [14] He, L., 2008, "Harmonic Solution of Unsteady Flow Around Blade With Separation," AIAA J., 46\_6, pp. 1299–1307.
- [15] Sparlart, P. R., and Allmaras, S. R., 1992, "A One-equation Turbulence Model for Aerodynamic Flows," AIAA Paper No. 92-0439.
- [16] Jameson, A., 1991, "Time-Dependent Calculations Using Multi-Grid, With Applications to Unsteady Flows Past Airfoil and Wings," AIAA Paper No. 91-1596.
- [17] He, L., 1993, "New Two-Grid Acceleration Method for Unsteady Navier-Stokes Calculations," J. Prop. Power, 9\_2, pp. 272–280.
- [18] Chana, K. S., Povey, T., and Jones, T. V., 2003, "Heat Transfer and Aerodynamics of Intermediate Pressure Nozzle Guide Vane With and Without Inlet Temperature Non-Uniformity," ASME Paper No. GT 2003-38466.
- [19] Carslaw, H. S., and Jaeger, J. C., 1959, *Conduction of Heat in Solids*, 2nd ed., Oxford University Press, Oxford, UK.
- [20] Schultz, D. L., and Jones, T. V., 1973, "Heat Transfer Measurement in Short Duration Facilities," Paper No. AGARD AG-165.
- [21] Doorly, J. E., and Oldfield, M. L. G., 1987, "The Theory of Advanced Multi-Layer Thin Film Heat Transfer Gauges," Int. J. Heat Mass Transfer, 30\_6, pp. 1159–1168.
- [22] Buttsworth, D. R., and Jones, T. V., 1997, "Radial Conduction Effects in Transient Heat Transfer Experiments," Aeronaut. J., 101\_2215, pp. 209–212.
- [23] Owen, J. M., 2007, "Thermodynamic Analysis Of Buoyancy-Induced Flow in Rotating Cavities," ASME Paper No. GT2007-27387.
- [24] He, L., 1992, "Method of Simulating Unsteady Turbomachinery Flows With Multiple Perturbations," AIAA J., 30\_11, pp. 2730–2735.

- [25] Gerolymos, G. A., Michon, G. J., and Neubauer, J., 2002, "*Analysis and Application of Chorochronic Periodicity in Turbomachinery Rotor/Stator Interaction Computations*," *J. Prop. Power*, 18.
- [26] He, L., Menshikova, V., and Haller, B. R., 2007, "*Effect of Hot-Streak Counts on Turbine Blade Heat Load and Forcing*," *J. Propul. Power*, 23\_6, pp. 1235–1241.
- [27] Kerrebrock, J. L., and Mikolajczak, A. A., 1970, "*Intra-Stator Transport of Rotor Wakes and Its Effect on Compressor Performance*," *ASME J. Eng. Gas Turbines Power*, 92\_4, pp. 359–370.
- [28] Shang, T., and Epstein, A. H., 1997, "*Analysis of Hot Streak Effects on Turbine Rotor Heat Load*," *ASME J. Turbulence*, 119\_3, pp. 544–553.

## 6.5 Case 5 - Fluid-Structure Interaction (FSI) of a Hot Flexible Thin Plate Inside an Enclosure

**Authors:** S.A.M. Mehryan, Ammar Alsabery, Alireza Modir, Ehsan Izadpanahi, and Mohammad Ghalambaz.

**Title :** Fluid-structure interaction of a hot flexible thin plate inside an enclosure

**Appeared in :** International Journal of Thermal Sciences 153 (2020) 106340

**Source :** <http://www.elsevier.com/locate/ijts>

**Citation :** S.A.M. Mehryan, Ammar Alsabery, Alireza Modir, Ehsan Izadpanahi, Mohammad Ghalambaz, Fluid-structure interaction of a hot flexible thin plate inside an enclosure, International Journal of Thermal Sciences, Volume 153, 2020, 106340, ISSN 1290-0729, <https://doi.org/10.1016/j.ijthermalsci.2020.106340>.

(<https://www.sciencedirect.com/science/article/pii/S1290072919312542>)

This study aims to assess the **natural convection heat transfer** in a square cavity wherein the buoyancy-induced flow is generated by a thin flexible heater-plate inside the cavity [[Mehryan et al.](#)]. The vertical walls of the cavity are cold and the horizontal walls are adiabatic. The thin hot plate is assumed to be isothermal and fixed at an alterable point in the middle of the cavity with different inclination angles. To analysis the **Fluid-Structure Interaction (FSI)**, the finite element method along with the **Arbitrary Lagrangian-Eulerian (ALE) technique** is employed. Isotherms and streamlines, as well as the average Nusselt number, the dimensionless temperature in the cavity, and the maximum applied stress on the flexible plate, are studied. The results are presented as a function of Rayleigh number, Prandtl number, inclination angle, and different positions of the fixed point. The outcomes indicate the importance of the inclination angle and the position of the fixed point of the hot plate. The plate experiences significantly large values of stress when it is mounted horizontally. In the case of a plate fixed at its top, the highest stress occurs with an inclination angle of 40°. In contrast, the lowest stress is associated with the plate when it is positioned vertically.

### 6.5.1 Nomenclature

Latin Symbols
ds Solid Displacement Vector
E Dimensionless Elasticity Modulus
Et Young's Modulus
Fv Dimensionless Body Force
g Gravitational acceleration
l Plate length
L Cavity size
Nu Nusselt number
Pr Prandtl number
P1, P2, P3 Fixed points
Ra Rayleigh number
t Time
tp Thin plate thickness
T Temperature
u Fluid velocity vector
W Moving coordinate velocity

x, y Cartesian coordinates
Greek Symbols
$\alpha$ Thermal diffusivity
$\beta$ Thermal expansion coefficient of fluid
$\gamma$ Inclination angle
$\nu f$ Kinematic viscosity
$\rho$ Density
$\sigma$ Stress tensor
$\tau$ Dimensionless time
Subscripts
c Cold
f Fluid
h Hot
p Plate
R Property ratio of the solid to the fluid
s Solid
Superscripts
* Dimensional parameters

### 6.5.2 Introduction

Natural convection inside an enclosure has been investigated comprehensively due to its prime importance in heat transfer engineering applications such as electronic cooling [1], solar collectors [2], energy storage systems [3], and heat exchangers [4,5]. A heated fluid moves upward due to the density reduction which results in fluid circulation inside enclosed spaces [6]. Based on the entities temperature in enclosures, natural convection can be classified into two main categories. The first type occurs when the temperature difference between individual entities in the enclosure itself induces natural convection [7]. The second type is when the inner object has a different temperature with the enclosure, which results in heat transfer between the inner object and the enclosure. The inner objects influence the flow circulation in the enclosure [8,9]. Natural convection in cavities without inner objects have been widely investigated in the past decades, including the nanofluids [10], hybrid nanofluids [11], nano encapsulated phase change suspensions [12–14], and porous media [15,16]. There are also many studies regarding the boundary layer heat transfer of nanofluids [17], and nano encapsulated phase change suspensions [18].

Currently, the interest has shifted to complex cavities with internal obstacles such as complex cylinders [19] or rectangular shape obstacles [20] inside the cavities. Zhang et al. [6] numerically studied the natural convection in a circular enclosure with an inner flat plate located asymmetrically about the center of the cylinder. The surface of the enclosure was kept cold while the plate had a high temperature. Wang et al. [21] explored the natural convection in a square cavity with a vertical thin isolated plate near the walls of the enclosure for three typical Rayleigh numbers. They studied the effect of the inner plate position and found a good agreement between their numerical results with the flow visualization.

[Altac and Kurtul [8] numerically studied the natural convection in a tilted rectangular cavity, containing a vertical thin isothermal hot plate. The tilt angle and Rayleigh numbers were in the range of 0–90° and 10<sup>5</sup> to 10<sup>7</sup>, respectively. The results showed an increase in the average Nusselt number with rise of the tilt angles up to 22.5°, and then, it decreased for all Ra numbers. Shi and Khodadadi [22] investigated the effect of a conductive thin fin on the wall of a square cavity at seven different locations and different aspect ratios. In fluid-structure interaction (FSI) problems, the interaction of a moving or deformable structure with a surrounding or internal fluid flow is studied. FSI occurs in many physical phenomena and has wide applications in engineering problems such as ocean energy converters [23,24], airplane wings stability [25], and wind turbine blades [26]. Due to the vital importance and broad application of FSI in engineering problems and especially in heat transfer, it has received significant attention in recent years. Considering natural convection inside enclosures, the effects of fluid-structure interaction on the heat transfer rate and flow domain have been investigated in limited studies [27–32]. The complexity of the physics and time-consuming nature of calculations, as well as the limitation of computational hardware in the past, made the numerical analysis of these problems inconvenient. The effect of thermal buoyancy on the vortex-induced vibration (VIV) of a flexible mounted circular cylinder is numerically investigated in Ref. [33]. Thermal control as a method for VIV suppression is implemented in Ref. [34].

Fluid-solid interaction in a cavity has been studied in two main cases when one or more walls of the enclosure considered to be flexible [35,36] or existence of a flexible membrane or plates inside the enclosure that influence the heat transfer and fluid behavior in the cavity [28,37,38]. Different industrial applications can be mentioned for these two configurations, such as enclosures with an internal electronic board or enclosures which employed thermal conductive plates for partitioning different electronic units [36]. Chemical reactors or batteries, where plates and membranes should separate different chemical fluids, can be considered as another industrial application of fluid-solid interaction in a cavity [28]. The comparisons of the average Nusselt number of the flexible walls and rigid walls in the enclosure in Refs. [35,36] confirm the significant effect of the flexible walls on the heat transfer rate inside a cavity.

Reference	Type of enclosure	Inner Object
[9]	Square	Corrugated conducting block
[10]	Elliptic	elliptic
[8]	Tilted square	Plate
[11]	Square	Rectangle
[12,13]	Square	-
[14]	Circle	Circle
[15]	Square	-
[16]	Incinerator shape	Rectangular wavy heater block
[19]	Square	Wavy circular heater
[20]	Square	Square
[21]	Square	Plate
[22]	Square	Porous fin
[28,29]	Square	Thin flexible partition
[30,31]	Square	Circle
[32]	Square	Flexible fin
[27,35]	Lid driven square cavity	Flexible bottom wall
[36]	Square-Filled with porous medium	Flexible vertical wall
[28]	Square cavity divided into two triangle part	Flexible diagonal membrane
[37]	Square	Oscillating Elastic fin
[38]	Square	Flexible vertical membrane
[39]	Square	Hot flexible plate

Studied parameter	Method
Entropy generation	FVM
Nanofluids	FVM
Tilt angle and Ra Number	FVM
Hybrid nanofluid	FEM
Nano-Encapsulated Phase Change Materials suspension	FEM
Location of inner circle	FEM
Porous media and location of heated boundaries	FEM
Magnetic field and Rayleigh number	FVM
Magnetic field and Rayleigh number	Control Volume-FEM
Nanofluids and porous media	FDM
Plate location near walls	FVM
Fin inclination angle and location	FEM
Flexibility of the partition	FEM
Flexibility of wall	FEM
Oscillation of flexible fins	
Profile of the flexible bottom wall	FEM- FSI
Porosity, elasticity of the flexible wall	FEM-FSI
Stiffness of the membrane	FEM-FSI
Oscillation amplitude and frequency	FEM-FSI
Magnetic field orientation	FEM-FSI
The elasticity modulus, the height and length of the plate.	FEM-FSI

Table 6.5.1 Literature review summary of the natural convection heat transfer in an enclosure

[Al-Amiri and Khanafer [35] reported a 9.4% difference between the Nusselt number of a cavity with

a rigid bottom wall and a cavity with a flexible bottom wall, which is a function of Reynolds number and increases by increasing Reynolds number. In the case of free convection with a flexible sidewall which was reported in Ref. [36], the maximum Nusselt number of the cavity increased 13.6% in comparison with the case of rigid sidewalls. It was also reported that the flexibility of the sidewall improves the Nusselt number and heat transfer rate. Hence, the heat transfer rate in a cavity with a flexible sidewall is better than a cavity with rigid walls. In the case of natural convection in enclosures with flexible partitions [28,29,38], flexible walls [30,31], or flexible fins [37,39], the heat transfer rate enhanced when the flexibility of the partitions or fins increased. An augmentation in the flexibility of the membrane increases its deformation following the flow pattern, which leads to a considerable rise in the heat transfer inside the cavity. On the other hand, a more rigid partition creates resistance to the flow movement and consequently, declines the heat transfer rate. Most of the studies available in the literature only have focused on vertical or horizontal rigid partitions in heat transfer applications, while in various real-world situations, the inner plate can be flexible. A summary of the heat transfer studies in a cavity with inner objects or flexible walls is presented in [Error! Reference source not found.](#)

Flexible heat spreader for cooling of electronic components [40,41], flexible heat exchangers for medical micro-heat exchangers [43] are examples of such systems. The flexibility of the internal partition affects the heat transfer and flow inside the enclosure which requires the analysis of the fluid-structure interaction for calculating the heat transfer and studying the geometry of the partition. In our previous study [39], the effect of the flexibility of a thin plate on the natural convection heat transfer was addressed while the plate was mounted horizontally and fixed at its center. In Ref. [39] we focused on the flexibility of the plate fixed at its center to study the heat transfer and induced stresses in it. In Ref. [39], we learned that the flexibility and interaction between the fluid and structure notably affect the thermal behavior of the cavity and the induced stresses in the plate. However, not only the flexibility of the plate (addressed in Ref. [34]) but also the clamping location of the plate (the mechanical boundary condition for fixing of the plate) and the mounting angle of a plate could be important parameters on the thermal and mechanical behavior of the cavity and the baffle. To the best of authors' knowledge, the effect of the inclination angle of a flexible hot plate on the natural heat transfer inside a cavity has not been addressed before. In this study, a comprehensive numerical investigation is provided on natural convection heat transfer in a square cavity containing an internal flexible hot thin-plate. The plate is fixed at three different locations in a wide range of inclination angles to assess the effects of the flexibility of the plate and the location of the fixed point on the heat transfer and flow characteristics.

### 6.5.3 Problem Definition and Mathematics

A square 2D enclosure with an inclined flexible plate, shown in **Figure 6.5.1**, is considered as the geometry of the study. The vertical bounds of the square, having the length of  $L^*$ , are kept at the constant temperature of  $T^*c$ , and the horizontal walls are adiabatic. The thin heater plate

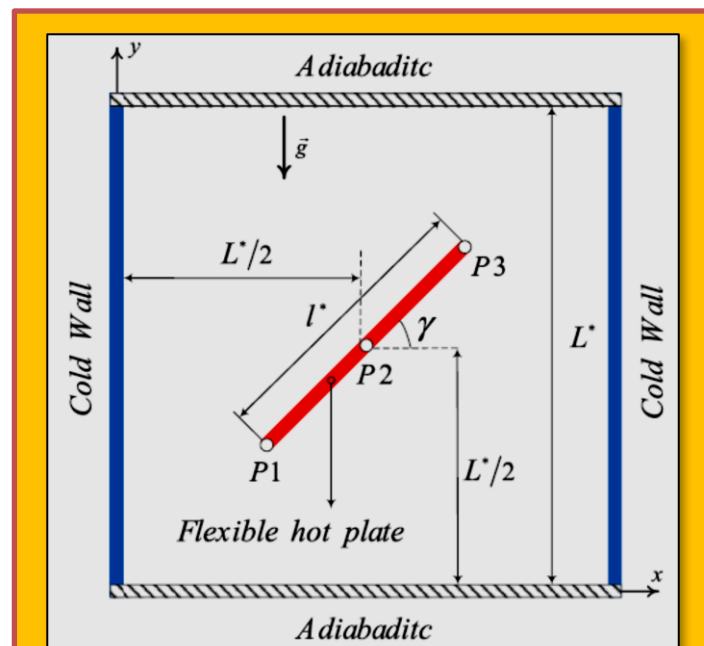


Figure 6.5.1 Schematic of the Physical Model

has the thickness of  $t^*p$  and is isothermal with the higher temperature of  $T^*h$ . The inclination angle of the plate with respect to the horizontal line is considered as  $\gamma$ . All of the solid walls of the cavity and the walls of the flexible plate are impervious against the mass diffusion. The flexible heater can be fixed at one of the three points depicted in **Figure 6.5.1** (P1, P2 or P3). The flow of the fluid inside the enclosure is simulated as laminar, incompressible and Newtonian. The governing equations are introduced in Ref. [39] and can be transformed into a non-dimensional form by considering the cavity size as the characteristic length, and  $\alpha_f = L^*$  as a reference with the same dimension as the velocity. The governing equations of [39] can be transformed into a non-dimensionalized form by utilizing the non-dimensional varying parameters presented below:

$$\begin{aligned} \mathbf{d}_s &= \frac{\mathbf{d}_s^*}{L_s} , \quad \boldsymbol{\sigma} = \frac{\boldsymbol{\sigma}^*}{E_\tau} , \quad \tau = \frac{t\alpha_f}{L^{*2}} , \quad (x, y, l, t_p) = \frac{x^*, y^*, l^*, t_p^*}{L^*} , \quad \mathbf{u} = \frac{\mathbf{u}^* L^*}{\alpha_f} \\ \mathbf{w} &= \frac{\mathbf{w}^* L^*}{\alpha_f} , \quad p = \frac{p^* L^{*2}}{\rho_f \alpha_f} , \quad T = \frac{T^* - T^*}{T_h^* - T_c^*} \end{aligned}$$

### Eq. 6.5.1

where the fluid velocity vector and the moving coordinate velocity are denoted as  $\mathbf{u}^*$  and  $\mathbf{w}^*$ , respectively. Fluid pressure and the fluid/solid temperature are denoted as  $P^*$  and  $T^*$ , respectively. Here, the density is  $\rho$  and thermal diffusivity is  $\alpha_f$ . The subscripts  $f$  and  $s$  represent the fluid and the solid. The tensor and vector fields are denoted in bold. The non-dimensional equations describing the thermal and dynamic behavior of the fluid in the *Arbitrary Lagrangian-Eulerian (ALE)* formulation are listed below:

$$\begin{aligned} \nabla \cdot \mathbf{u} &= 0 \\ \frac{\partial \mathbf{u}}{\partial \tau} + (\mathbf{u} - \mathbf{w}) \cdot \nabla \mathbf{u} + \nabla p - \text{Pr} \nabla^2 \mathbf{u} - \text{PrRa} T_j &= 0 \\ \frac{\partial T}{\partial \tau} + (\mathbf{u} - \mathbf{w}) \cdot \nabla T - \nabla^2 T &= 0 \end{aligned}$$

### Eq. 6.5.2

The governing non-dimensional equations for the energy and structural displacement of the flexible thin plate can be expressed as **Eq. 6.5.3**. Here,  $\boldsymbol{\sigma}$ ,  $\mathbf{d}_s$ , and  $\mathbf{F}_v$  are denoted as the stress tensor, the solid displacement vector, and the applied body force, respectively.

$$\frac{\partial^2 \mathbf{d}_s}{\partial \tau^2} + \rho_R E \nabla \boldsymbol{\sigma} - \rho_R E \nabla \mathbf{F}_v = 0$$

### Eq. 6.5.3

The non-dimensional constant parameters that appeared above are as follows:

$$Ra = \frac{g \beta (T_h^* - T_c^*) L^{*3}}{v_f \alpha_f} , \quad \text{Pr} = \frac{v_f}{\alpha_f} , \quad E = \frac{E_\tau L^{*2}}{\rho_f \alpha_f^2} , \quad \mathbf{F}_v = \frac{(\rho_f - \rho_s) L^* g}{E_\tau} , \quad \rho_R = \frac{\rho_f}{\rho_s}$$

### Eq. 6.5.4

where  $v_f$  is the kinematic viscosity of the fluid,  $\beta$  is the volumetric thermal expansion coefficient, and  $g$  is the gravitational acceleration. Here, it is assumed that  $\rho_f = \rho_s$ . Therefore,  $\rho_R = 1$  and  $\mathbf{F}_v = 0$ . Taking into consideration the no-slip condition in the interface of the fluid at the solid, the boundary conditions in the dimensionless coordinates can be referred to below: At the surfaces of the flexible plate:

$$T = 1, \quad \frac{\partial \mathbf{d}_s}{\partial \tau} = \mathbf{u}, \quad \sigma \cdot \mathbf{n} = -p \mu_f \nabla \mathbf{u}$$

**Eq. 6.5.5**

At the vertical walls:

$$T = 0, \quad u = v = 0$$

**Eq. 6.5.6**

At the horizontal walls:

$$\frac{\partial T}{\partial y} = 0, \quad u = v = 0$$

**Eq. 6.5.7**

The points  $P1-P3$  are fixed points with zero solid-velocity at both  $x$  and  $y$  directions as:

$$\frac{\partial \mathbf{d}_s}{\partial t} = 0$$

**Eq. 6.5.8**

At the beginning of the natural convection, the fluid is motionless, and its temperature is the average of the thin plate ( $T^*h$ ) and cold temperatures of vertical walls ( $T^*c$ ). The physical coupling of the fluid domain and the structure (plate) is through the boundary condition of **Eq. 6.5.5**. The fluid interacts with the plate through the surface forces and induces tensions in the plate. The induced tensions in the plate lead to the deformation of the plate. Consequently, the plate deformation changes the geometry of the plate and affects fluid hydrodynamic and heat transfer. As the interaction of the fluid, heat transfer, and the structure are fully coupled, any changes in the hydrodynamic, heat transfer or the structure would affect all of the physics and equations, simultaneously. To measure the heat transfer rate through the flexible heater, the average Nusselt number is defined as **Eq. 6.5.9** where  $n$  and  $s$  are respectively the normal-direction and the tangential-direction with the surface of the flexible plate.

$$\overline{Nu} = \frac{1}{2(1 + t_p)} \int_{H \text{ of plate}} \left. \frac{\partial T}{\partial n} \right|_{\text{on the hot plate}} ds$$

Grid size	Number of elements (Fluid domain)	Number of elements (Flexible plate)	$\overline{Nu}$	$\sigma_{max}$	$T$
G1	2274	72	14.038	5.76E+08	0.33515
G2	2490	72	14.146	5.77E+08	0.33527
G3	2830	72	14.149	5.78E+08	0.33532
G4	3444	72	14.154	5.81E+08	0.33554
G5	3810	69	14.155	5.82E+08	0.3356
G6	5423	89	14.155	5.82E+08	0.3356
G7	5687	99	14.156	5.82E+08	0.3356
G8	7145	223	14.157	5.83E+08	0.3355

Table 6.5.2 Grid testing for  $\overline{Nu}$ ,  $\sigma_{max}$  and  $T$  at different grid sizes for fixed point 1 (P1),  $Ra = 10^6$ ,  $\gamma = 90^\circ$  and  $Pr = 6.2$

### Eq. 6.5.9

#### 6.5.4 Numerical Solution, Grid Independence Test, and Verifications

##### 6.5.4.1 Numerical Solution

The governing equations, Eq. 6.5.2 - Eq. 6.5.3 with the stated boundary conditions, are numerically solved. Due to the fluid-solid interaction inside the cavity and heat transfer at the interface of fin and fluid, a finer grid is utilized at the boundary interfaces to increase the numerical accuracy of the solution. Arbitrary Lagrangian-Eulerian (ALE) method is employed to model the motion of structure in the fluid domain [44]. The governing equations are first written in a weak form and then integrated over the domain of solution to produce the residual equations. Then, the residual equations are iteratively solved by the Newton method utilizing a *PARallel DIrect SOLver (PARDISO)* [45–47] with a Newtonian damping factor of 0.8 and a residual error  $O(10^{-6})$ . This method is discussed in detail in the early works of [48,49], and recent works of [50,51].

##### 6.5.4.2 Grid Independence Test

Grid-independence tests are performed to ensure that the results are independent of the number of mesh elements. For this purpose, the  $\tilde{\text{Nu}}$ ,  $\sigma_{\max}$  and T for point 1 (P1) at  $\text{Ra} = 10^6$ ,  $\gamma = 90^\circ$  and  $\text{Pr} = 6.2$  are examined for five different mesh sizes. The number of utilized elements for the fluid domain and the structure domain (flexible plate) are reported in Table 6.5.2 for various mesh sizes. The results, which are tabulated in Table 6.5.2, confirm that the grid size of case 5 (G5) is the most suitable mesh considering the precision and computing time. Hence the mesh of case 5 with 3879 elements is

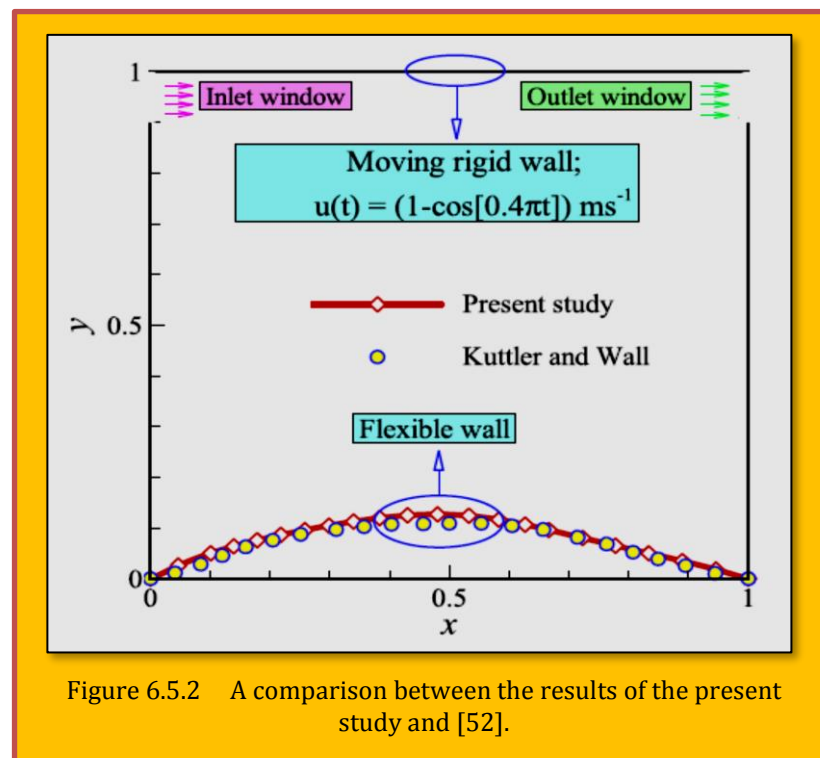


Figure 6.5.2 A comparison between the results of the present study and [52].

Properties	Flexible wall	Fluid
Kinematic viscosity ( $\nu_f$ )	–	$0.01 \text{ m}^2/\text{s}$
Density ( $\rho$ )	$500 \text{ kg/m}^3$	$1 \text{ kg/m}^3$
Poisson's ratio ( $\nu_z$ )	0.0	–
Young's modulus ( $E_z$ )	$250 \text{ N/m}^2$	–
Thickness	0.002 m	–

Table 6.5.3 Properties of the fluid and flexible wall of the Küttler and Wall's problem [52]

selected throughout this research. Grid-points and elements-distribution are shown in **Figure 6.5.3** for different fixed points of case 5.

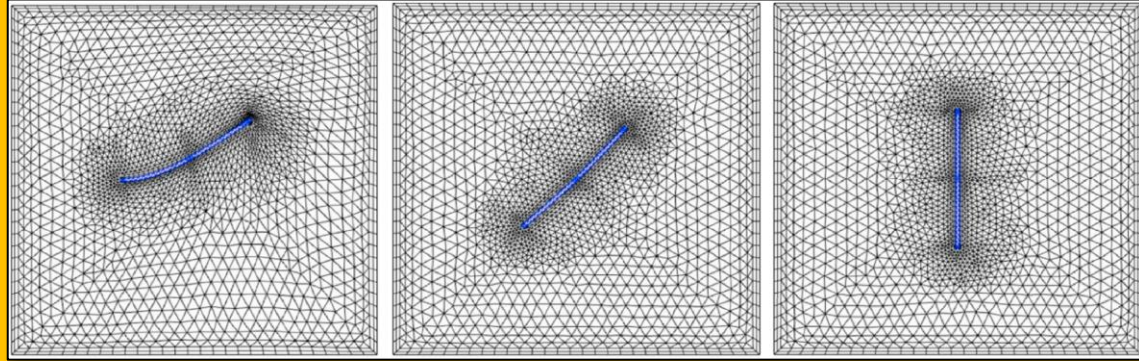


Figure 6.5.3 Grid-points Distribution for a Grid Size G5 = 3879 Elements.

#### 6.5.4.3 Verification

Comparisons with the selective results of the available literature are conducted to check the verification of the utilized numerical methodology and the modeling. As a validation of the FSI code, Kütter and Wall's study [52] has been investigated. They considered a lid-driven square cavity with a flexible bottom wall. The top wall of the cavity was driven at a velocity of  $(1 - \cos(0.4\pi t))$  m/s. On the other hand, two free openings were placed at top of the vertical walls. Horizontal oscillation of the lid excites the fluids and inside the enclosure and induces a vortex. As a result, the interaction between the fluid and flexible lower wall alters the shape of the bottom. This change in the shape of the flexible bottom wall was computed over time. **Table 6.5.3** reports the thermophysical properties of flexible wall and the fluid inside the cavity, which were employed in Ref. [52]. **Figure 6.5.2** depicts a comparison of the results of the current work with [52] for the flexible wall's deformation after  $t = 7.5$  s. The comparison shows that there is a desirable agreement between the results. To validate the natural convection heat transfer in the cavity, the study of [Turan et al. [53]] has been investigated. [Turan et al. [53]] studied the free heat transfer in a square cavity with the top and bottom insulated walls while the right and the left walls were at hot and cold temperatures. For a case of Newtonian fluid with  $\text{Pr} = 1000$  and  $\text{Ra} = 10^5$ , a comparison between the isotherms of the present study and those of [53] is reported in . As it can be observed, the results are in excellent agreement. As a transient heat transfer case, a comparison between the results of the present study and [Xu et al. [54]] are depicted in **Figure 6.5.5**.

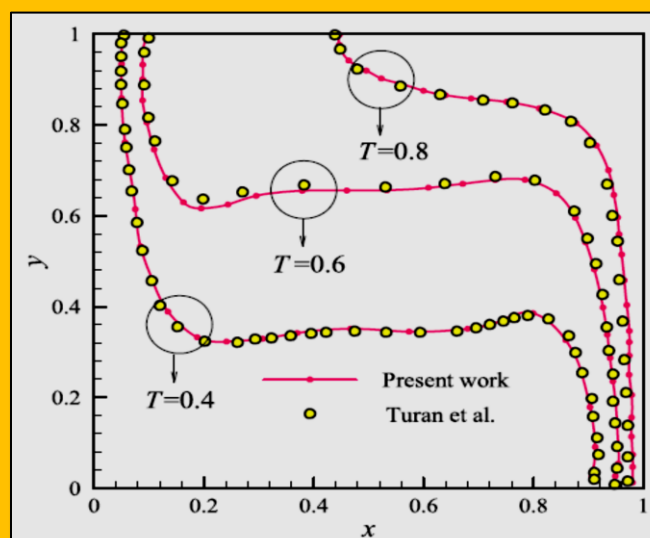


Figure 6.5.4 A comparison of the Temperature field from work conducted by Turan et al. [53] and the present prediction

The schematic of the studied problem by [Xu et al. [54]] is illustrated clearly in **Figure 6.5.5**. As specified in **Figure 6.5.5**, the dimensionless temperature at a certain point ( $x = 0.0083$  and  $y = 0.375$ , assuming the coordinate system at the center of the enclosure) is selected for the comparison. The results computed in the present work are compared with the results given in Ref. [54] for a case when  $\text{Ra} = 9.2 \times 10^8$  and  $\text{Pr} = 6.63$ . As shown in **Figure 6.5.5**, the results of the current work are in good agreement with [Xu et al. [54]]. The present study is further validated through a comparison between its temperature field and the temperature field reported in the experimental work conducted by [Calcagni et al. [55]]. Calcagni et al. [55] experimentally studied an enclosure filled by air in which the horizontal walls were isothermally cooled by means of circulating thermostatic liquid. The upper wall was adiabatic and the bottom of the enclosure was partially maintained at a constant high temperature using a thermostatic bath. In this comparison,  $\text{Ra} = 1.836 \times 10^5$  and  $\text{Pr} = 0.71$ . The matching observed in **Figure 6.5.6** between the results of current work and [Calcagni et al. [55]] confirms the correctness of the present solution. According to the conducted verifications, the provided code can confidently be used to reach the correct and accurate results.

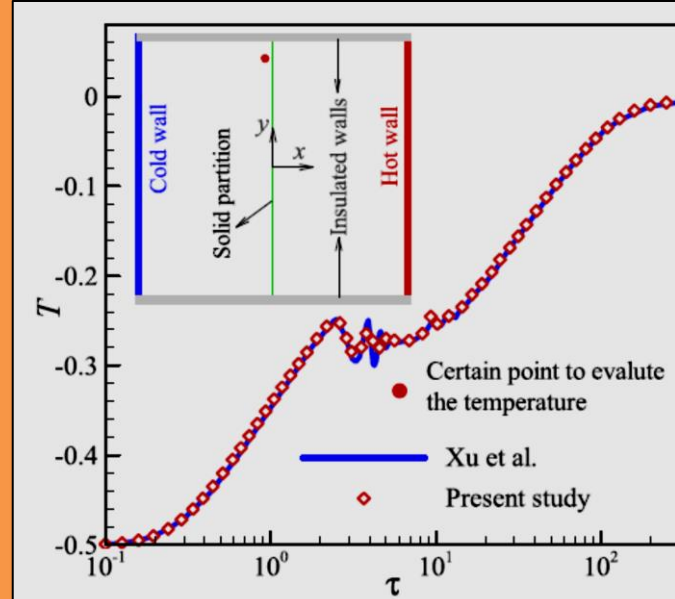
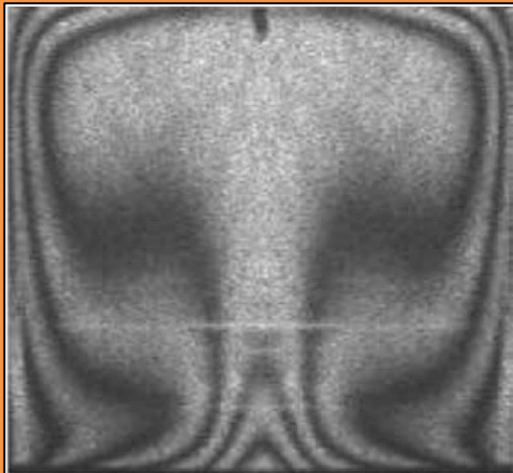
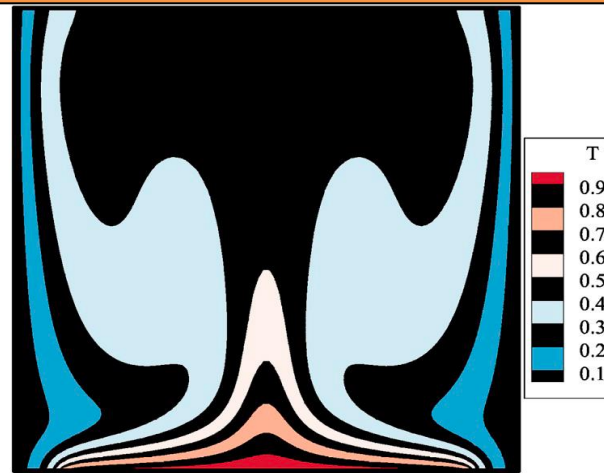


Figure 6.5.6 The time history of the non-dimensional temperature at the denoted point for the present work and [54]



(a)



(b)

Figure 6.5.5 A comparison between the temperature fields of (a): the current numerical study and (b): the experimental work performed by Calcagni et al. [55]

### 6.5.5 Results and Discussion

In the current section, the streamlines, isotherms, average Nusselt number, maximum stress on the flexible plate, and average dimensionless temperature are presented for different cases. The considered non-dimensional parameters in this study are as follows: fixed point location (P1 (fixed point 1), P2 (fixed point 2), P3 (fixed point 3)), Rayleigh number ( $10^3 \leq Ra \leq 10^6$ ), the inclination angle of the flexible heated plate ( $0^\circ \leq \gamma \leq 90^\circ$ ), Prandtl number ( $Pr = 0.71$  (air), 6.2 (water) and 13.4 (seawater)), and the flexible plate stiffness (elasticity modulus) ( $10^9 \leq E \leq 10^{14}$ ). Other parameters such as non-dimensional body force ( $F_v = 0$ ), the density ratio ( $\rho_R = 1$ ), and the plate thickness ( $t_P = 0.01$ ) remained unchanged in all simulations.

**Figure 6.5.7** shows the streamlines when the plate is fixed at P1 for  $Ra = 10^6$ ,  $\gamma = 90^\circ$ ,  $Pr = 6.2$  and  $E = 5 \times 10^{10}$  at different dimensionless time steps. The fluid motion reaches a steady-state condition at  $\tau = 0.06$ . Due to the temperature difference of the vertical walls of the cavity and the inner plate, a clockwise vortex and a counterclockwise vortex are formed in the right and the left sides of the cavity,

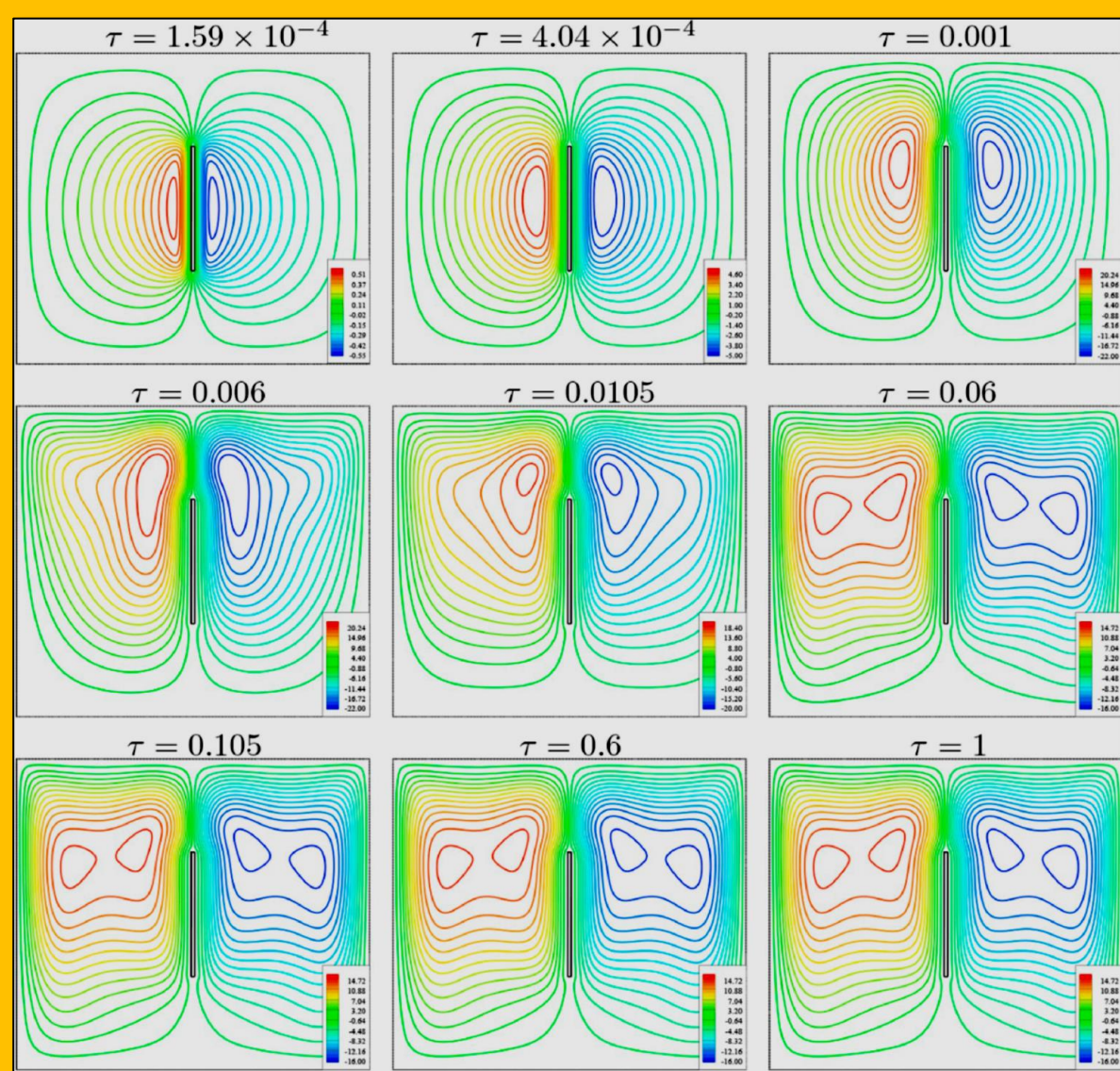


Figure 6.5.7 Variations of the Unsteady streamlines for various dimensionless time ( $\tau$ ) at fixed point 1 (P1),  $Ra = 10^6$ ,  $\gamma = 90^\circ$ ,  $Pr = 6.2$ , and  $E = 5 \times 10^{10}$ .

respectively. At low values of time, the density of streamlines is high in vicinity of the hot plate compared with the other regions, indicating the start of the fluid flow ( $\tau \leq 10^{-3}$ ). At  $\tau \leq 6 \times 10^{-3}$  the streamlines gained strength, and the cells moved toward the top wall of the cavity. The buoyancy-induced flow strengthens as time elapses. As time evolves to  $\tau = 0.06$ , streamlines get a double-eye circulation motion on each side of the enclosure. From  $\tau = 0.06$  to  $\tau = 1$ , the streamlines do not experience a noticeable change which can be considered as the steady-state condition of the fluid flow.

**Figure 6.5.8** illustrates the transient development of the isothermal contours of the fluid for the same parameters of **Figure 6.5.7** at different time steps. Initially, at  $\tau = 1.59 \times 10^{-4}$ , pure conduction occurs around the plate. At  $\tau = 0.001$ , buoyancy induced flow starts to transfer heat from the plate to the medium above the plate. The isotherms distributed moderately in the upper section of the enclosure at dimensionless time  $\tau = 0.006$ . At  $\tau = 0.0105$ , isotherms are starting to align in a horizontal form and fully develop as time passes. At higher time steps, dense isotherms can be

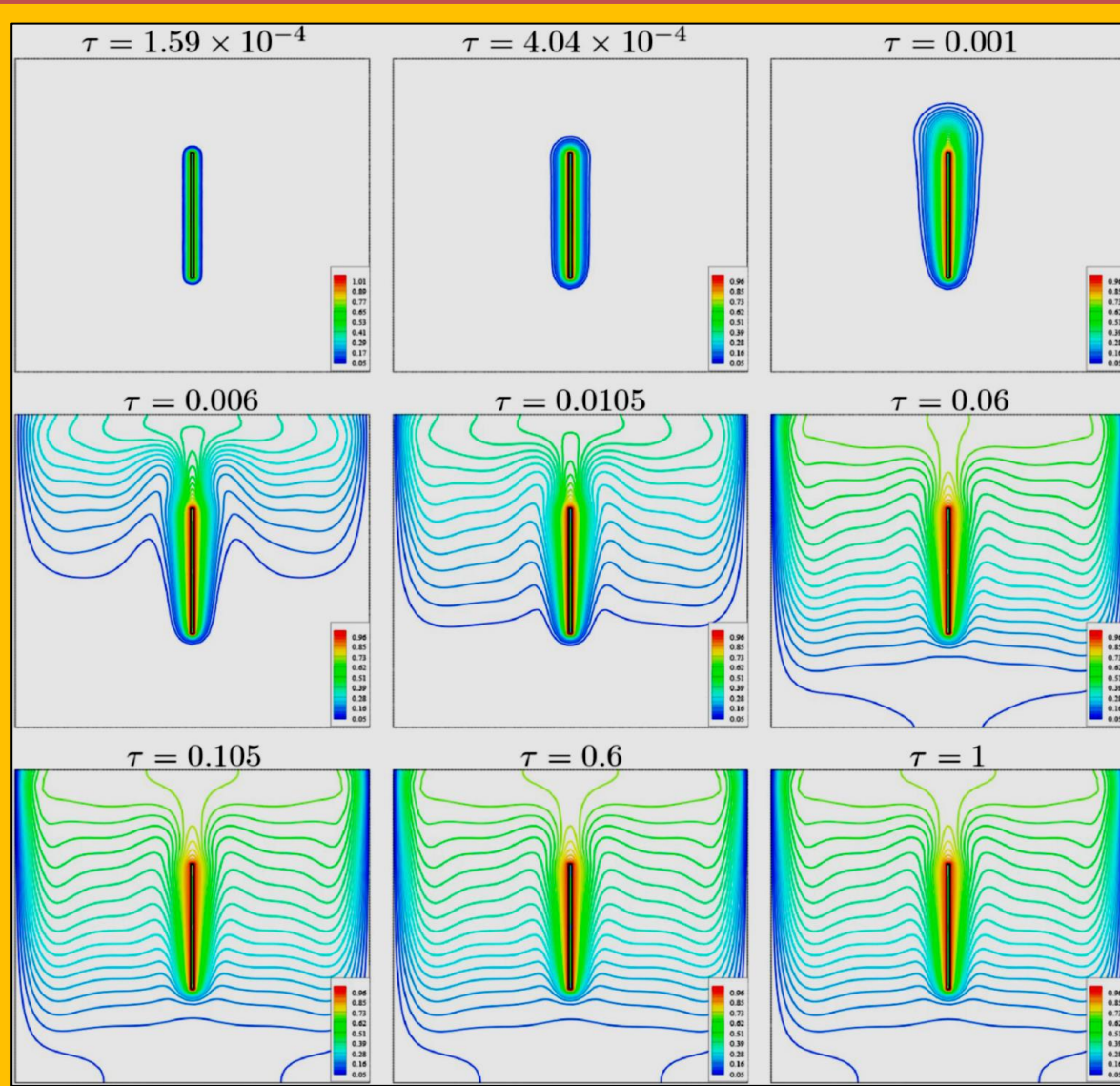


Figure 6.5.8 Variations of the Unsteady isotherms for various dimensionless time ( $\tau$ ) at fixed point 1 (P1),  $Ra = 10^6$ ,  $\gamma = 90^\circ$ ,  $Pr = 6.2$ , and  $E = 5 \times 10^{10}$

observed close to the hot plate and vertical walls. **Figure 6.5.8** indicates that at the steady-state situation, the isotherms compress and extend vertically close to vertical walls and the hot plate in the cavity.

**Figure 6.5.9** shows the steady-state contours of isotherms and streamlines for various fixed points when  $\gamma = 45^\circ$ ,  $\text{Ra} = 10^6$ ,  $\text{Pr} = 6.2$  and  $E = 5 \times 10^{10}$ . The flexible hot plate experiences a substantial deformation when the fixed point is P3. This is caused by the buoyancy force exerted at the free bottom of the plate. It can be seen that the heater has the least deformation for the fixed point P2. The deformation of the plate leads to a change in the pattern of the streamlines and consequently, the heat transfer. The horizontal isotherms in the cavity indicate that the convection is the main heat transfer mechanism in the middle part of the cavity.

Similar results are obtained for different Ra number and the results are presented in [[Mehryan et al](#)] and a parametric study of involving various angles of the flexible heated plate ( $\gamma$ ) and Pr number has been done. For a complete presentation of the results, users are encourage to consult the work by [[Mehryan et al](#)].

## 6.5.6 Conclusion

Natural convection heat transfer in a 2D square cavity with a flexible hot plate in the center was studied numerically for different pertinent parameters. The plate is considered as an elastic body which undergoes large deformations, hence the fluid-structure interaction analysis was required to include the deformation of the plate. Vertical bonds of the wall were kept at a constant temperature, and the horizontal walls were adiabatic. The isothermal hot plate was fixed at one point (each end or the center of the plate) with different inclination angles with respect to the horizontal line. The results are discussed in terms of Nusselt number, Maximum stress on the plate, free tip displacement of the plate, and the average temperature plots as well as isotherms and streamline contours. The numerical results lead to the following conclusions:

- The location of the fixed point and the inclination angle significantly affect the heat transfer and fluid motion inside the cavity.
- The flexible plate experiences the lowest deformation and tension when fixed at its center (P2).
- The maximum stress on the flexible plate and its deformation are minimal at  $\gamma = 90^\circ$  for all fixed points, at different Ra, and Pr numbers.
- For the fixed-points of P1 and P2, decreasing the inclination leads to a considerable increase in the maximum value of the stress on the hot plate and the maximum stress occurred when

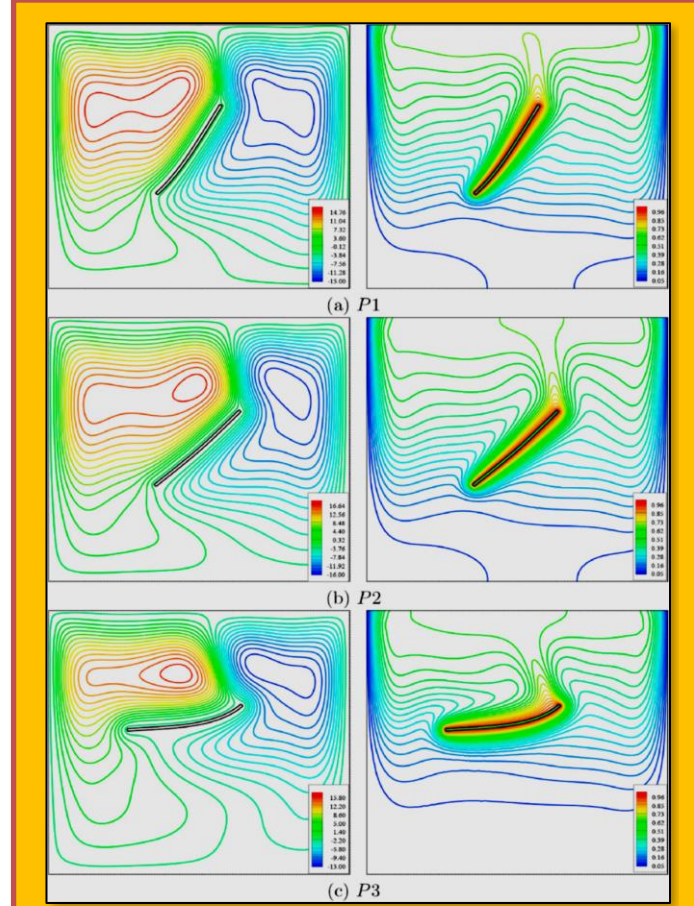


Figure 6.5.9 Variations of the steady streamlines and isotherms for various fixed point locations (P1–P3) at  $\text{Ra} = 10^6$ ,  $\gamma = 45^\circ$ ,  $\text{Pr} = 6.2$ , and  $E = 5 \times 10^{10}$

$\gamma = 0^\circ$ , while  $\gamma \approx 40^\circ$  is the critical inclination angle with a peak tension and minimum average Nusselt number when the plate is fixed at P3.

- When the fixed point is P1 and  $Ra = 10^6$ ,  $\gamma = 45^\circ$  and  $Pr = 6.2$ , the increase of the flexibility of the plate increases the heat transfer and reduces the internal tensions in the plate. However, a flexible plate shows larger deformations. As a result, a flexible plate shows a better heat transfer compared to a rigid plate.

### 6.5.7 References

- [1] A. Al-Amiri, K. Khanafer, J. Bull, I. Pop, *Effect of sinusoidal wavy bottom surface on mixed convection heat transfer in a lid-driven cavity*, Int. J. Heat Mass Tran. 50 (2007) 1771–1780.
- [2] M. Rahman, H.F. €Oztop, A. Ahsan, M. Kalam, Y. Varol, *Double-diffusive natural convection in a triangular solar collector*, Int. Comm. Heat Mass Tran. 39 (2012) 264–269.
- [3] S. Lorente, A. Bejan, J. Niu, Phase change heat storage in an enclosure with vertical pipe in the center, Int. J. Heat Mass Tran. 72 (2014) 329–335.
- [4] F. Garoosi, F. Hoseaninejad, M.M. Rashidi, Numerical study of natural convection heat transfer in a heat exchanger filled with nanofluids, Energy 109 (2016) 664–678.
- [5] S. Yarmohammadi, K. Mohammadzadeh, M. Farhadi, H. Hajimiri, A. Modir, Multi-objective optimization of thermal and flow characteristics of R-404A evaporation through corrugated tubes, J. Energy Storag. 27 (2020), 101137.
- [6] W. Zhang, Y. Wei, X. Chen, H.-S. Dou, Z. Zhu, *Partitioning effect on natural convection in a circular enclosure with an asymmetrically placed inclined plate*, Int. Comm. Heat Mass Tran. 90 (2018) 11–22.
- [7] M.C. Ece, E. Büyük, *Natural-convection flow under a magnetic field in an inclined rectangular enclosure heated and cooled on adjacent walls*, Fluid Dynm. Res. 38 (2006) 564.
- [8] Z. Altaç, €O. Kurtul, *Natural convection in tilted rectangular enclosures with a vertically situated hot plate inside*, Appl. Therm. Eng. 27 (2007) 1832–1840.
- [9] T. Tayebi, A.J. Chamkha, *Entropy generation analysis during MHD natural convection flow of hybrid nanofluid in a square cavity containing a corrugated conducting block*, Int. J. Num. Methods Heat Fluid Flow 30 (3) (2019) 1118–1136.
- [10] T. Tayebi, A.J. Chamkha, M. Djezzar, *Natural convection of CNT-water nanofluid in an annular space between confocal elliptic cylinders with constant heat flux on inner wall*, Sci. Iran. 26 (2019) 2770–2783.
- [11] M. Ghalambaz, A. Doostani, E. Izadpanahi, A.J. Chamkha, *Conjugate natural convection flow of Ag-MgO/water hybrid nanofluid in a square cavity*, J. Therm. Anal. Calorim. (2019) 1–16.
- [12] M. Ghalambaz, A.J. Chamkha, D. Wen, *Natural convective flow and heat transfer of Nano-Encapsulated Phase Change Materials (NEPCMs) in a cavity*, Int. J. Heat Mass Tran. 138 (2019).
- [13] A. Hajjar, S. Mehryan, M. Ghalambaz, *Time periodic natural convection heat transfer in a nano-encapsulated phase-change suspension*, Int. J. Mech. Sci. 166 (2020), 105243.
- [14] S. Mehryan, M. Ghalambaz, L.S. Gargari, A. Hajjar, M. Sheremet, *Natural convection flow of a suspension containing nano-encapsulated phase change particles in an eccentric annulus*, J. Energy Storag. 28 (2020), 101236.
- [15] M. Ghalambaz, A. Tahmasebi, A. Chamkha, D. Wen, *Conjugate local thermal non-equilibrium heat transfer in a cavity filled with a porous medium: analysis of the element location*, Int. J. Heat Mass Tran. 138 (2019) 941–960.
- [16] M. Hashemi-Tilehnoee, A. Dogonchi, S.M. Seyyedi, A.J. Chamkha, D. Ganji, *Magnetohydrodynamic natural convection and entropy generation analyses inside a nanofluid-filled incinerator-shaped porous cavity with wavy heater block*, J. Therm. Anal. Calorim. (2020) 1–13.
- [17] Z. Rashed, S. Ahmed, M.A. Sheremet, *MHD buoyancy flow of nanofluids over an inclined plate immersed in uniform porous medium in the presence of solar radiation*, J. Mech. 35 (2019) 563–576.

- [18] M. Ghalambaz, T. Grosan, I. Pop, *Mixed convection boundary layer flow and heat transfer over a vertical plate embedded in a porous medium filled with a suspension of nano-encapsulated phase change materials*, J. Mol. Liq. 293 (2019), 111432.
- [19] A. Dogonchi, T. Tayebi, A.J. Chamkha, D. Ganji, *Natural convection analysis in a square enclosure with a wavy circular heater under magnetic field and nanoparticles*, J. Therm. Anal. Calorim. 139 (2020) 661–671.
- [20] A.I. Alsabery, M.A. Ismael, A.J. Chamkha, I. Hashim, *Effect of nonhomogeneous nanofluid model on transient natural convection in a non-Darcy porous cavity containing an inner solid body*, Int. Comm. Heat Mass Tran. 110 (2020), 104442.
- [21] Q. Wang, M. Yang, W. Tao, *Natural convection in a square enclosure with an internal isolated vertical plate*, W€arme-und Stoff€bertragung 29 (1994) 161–169.
- [22] X. Shi, J. Khodadadi, *Laminar natural convection heat transfer in a differentially heated square cavity due to a thin fin on the hot wall*, J. Heat Tran. 125 (2003) 624–634.
- [23] A. Modir, M. Kahrom, A. Farshidianfar, *Mass ratio effect on vortex induced vibration of a flexibly mounted circular cylinder, an experimental study*, Int. J. Marine Energy 16 (2016) 1–11.
- [24] A. Modir, N. Goudarzi, *Experimental investigation of Reynolds number and spring stiffness effects on vortex induced vibrations of a rigid circular cylinder*, Eur. J. Mech. B Fluid 74 (2019) 34–40.
- [25] H. Golparvar, S. Irani, M.M. Sani, *Experimental investigation of linear and nonlinear aeroelastic behavior of a cropped delta wing with store in low subsonic flow*, J. Braz. Soc. Mech. Sci. Eng. 38 (2016) 1113–1130.
- [26] M. Sayed, T. Lutz, E. Kr€amer, S. Shayegan, R. W€uchner, *Aeroelastic analysis of 10 MW wind turbine using CFD-CSD explicit FSI-coupling approach*, J. Fluid Struct. 87 (2019) 354–377.
- [27] K. Khanafer, *Comparison of flow and heat transfer characteristics in a lid-driven cavity between flexible and modified geometry of a heated bottom wall*, Int. J. Heat Mass Tran. 78 (2014) 1032–1041.
- [28] E. Jamesahar, M. Ghalambaz, A.J. Chamkha, *Fluid-solid interaction in natural convection heat transfer in a square cavity with a perfectly thermal-conductive flexible diagonal partition*, Int. J. Heat Mass Tran. 100 (2016) 303–319.
- [29] M. Ghalambaz, S. Mehryan, M.A. Ismael, A. Chamkha, D. Wen, *Fluid-structure interaction of free convection in a square cavity divided by a flexible membrane and subjected to sinusoidal temperature heating*, Int. J. Num. Methods Heat Fluid Flow (2019), <https://doi.org/10.1108/HFF-12-2018-0826>.
- [30] A. Alsabery, F. Selimefendigil, I. Hashim, A. Chamkha, M. Ghalambaz, *Fluid-structure interaction analysis of entropy generation and mixed convection inside a cavity with flexible right wall and heated rotating cylinder*, Int. J. Heat Mass Tran. 140 (2019) 331–345.
- [31] A.I. Alsabery, H. Saleh, M. Ghalambaz, A.J. Chamkha, I. Hashim, *Fluid-structure interaction analysis of transient convection heat transfer in a cavity containing inner solid cylinder and flexible right wall*, Int. J. Numer. Methods Heat Fluid Flow 9 (2019) 3756–3780.
- [32] E. Jamesahar, M. Sabour, M. Shahabadi, S. Mehryan, M. Ghalambaz, *Mixed convection heat transfer of nanofluids in a cavity with two oscillating flexible fins: a Fluid-Structure Interaction (FSI) approach*, Appl. Math. Model. 82 (2020) 72–90.
- [33] H. Garg, A.K. Soti, R. Bhardwaj, *Vortex-induced vibration of a cooled circular cylinder*, Phys. Fluids 31 (2019) 83608.
- [34] H. Wan, S.S. Patnaik, *Suppression of vortex-induced vibration of a circular cylinder using thermal effects*, Phys. Fluids 28 (2016), 123603.
- [35] A. Al-Amiri, K. Khanafer, *Fluid-structure interaction analysis of mixed convection heat transfer in a lid-driven cavity with a flexible bottom wall*, Int. J. Heat Mass Tran. 54 (2011) 3826–3836.
- [36] K. Khanafer, *Fluid-structure interaction analysis of non-Darcian effects on natural convection in a porous enclosure*, Int. J. Heat Mass Tran. 58 (2013) 382–394.
- [37] M. Ghalambaz, E. Jamesahar, M.A. Ismael, A.J. Chamkha, *Fluid-structure interaction study of natural convection heat transfer over a flexible oscillating fin in a square cavity*, Int. J. Therm. Sci. 111 (2017) 256–273.

- [38] S. Mehryan, M. Ghalambaz, M.A. Ismael, A.J. Chamkha, *Analysis of fluid-solid interaction in MHD natural convection in a square cavity equally partitioned by a vertical flexible membrane*, J. Magn. Magn Mater. 424 (2017) 161–173.
- [39] S.M.H. Zadeh, S. Mehryan, E. Izadpanahi, M. Ghalambaz, *Impacts of the flexibility of a thin heater plate on the natural convection heat transfer*, Int. J. Therm. Sci. 145 (2019), 106001.
- [40] Aurongzeb DM, Coolidge D, Thompson RC, inventors; Dell Products LP, assignee. *Flexible heat spreader with differential thermal conductivity*. United States patent US 10,088,878. 2018 Oct 2. <https://patents.google.com/patent/US10088878B2/en>.
- [41] Qiu B, Guo X, Raupp JC, Ahrens M, Pidwerbecki D, Lofland SJ, Daskalakis GH, Yee SL, MacDonald M, inventors; Intel Corp, assignee. *Flexible heat spreader*. United States patent US 9,980,412. 2018 May 22. <https://patents.google.com/patent/US9980412B2/en>.
- [42] Fletcher RD, Chen Y, inventors; Coolhead Tech Inc, assignee. *Flexible heat exchangers for medical cooling and warming applications*. United States patent US 7,077,858. 2006 Jul 18. <https://patents.google.com/patent/US7077858B2/en>.
- [43] R.C. Sekol, T.J. Rinker, D. Chakraborty, J.A. Abell, *Mechanically conformable micro-heat exchangers and methods for use in thermal management of target components*, in: Google Patents, 2019.
- [44] J.C. De Los Reyes, S. Gonzalez Andrade, *A combined BDF-semismooth Newton approach for time-dependent Bingham flow*, Numer. Methods Part. Differ. Eq. 28 (2012) 834–860.
- [45] O. Schenk, K. G€artner, *Solving un symmetric sparse systems of linear equations with PARDISO*, Future Generat. Comput. Syst. 20 (2004) 475–487.
- [46] P. Wriggers, *Nonlinear Finite Element Methods*, Springer Science & Business Media, 2008.
- [47] F. Verbosio, A. De Coninck, D. Kourounis, O. Schenk, *Enhancing the scalability of selected inversion factorization algorithms in genomic prediction*, J. Comp. Sci. 22 (2017) 99–108. [48] C.W. Hirt, A.A. Amsden, J. Cook, *An arbitrary Lagrangian-Eulerian computing method for all flow speeds*, J. Comp. Phys. 14 (1974) 227–253.
- [49] T.J. Hughes, W.K. Liu, T.K. Zimmermann, *Lagrangian-Eulerian finite element formulation for incompressible viscous flows*, Comp. Methods Appl. Mech. Eng. 29 (1981) 329–349.
- [50] J.N. Reddy, D.K. Gartling, *The finite element method in heat transfer and fluid dynamics*, 3rd Edition, CRC Press Taylor & Francis Group, 2010. <https://www.crcpress.com/The-Finite-Element-Method-in-Heat-Transfer-and-Fluid-Dynamics/Reddy-Gartling/p/book/9781420085983>.
- [51] M.h. Souli, D.J. Benson, *Arbitrary Lagrangian Eulerian and Fluid-Structure Interaction: Numerical Simulation*, John Wiley & Sons, 2013.
- [52] U. K€ttler, W.A. Wall, *Fixed-point fluid-structure interaction solvers with dynamic relaxation*, Comp. Mech. 43 (2008) 61–72.
- [53] O. Turan, A. Sachdeva, N. Chakraborty, R.J. Poole, *Laminar natural convection of power-law fluids in a square enclosure with differentially heated side walls subjected to constant temperatures*, J. Non-Newtonian Fluid Mech. 166 (2011) 1049–1063.
- [54] F. Xu, J.C. Patterson, C. Lei, *Heat transfer through coupled thermal boundary layers induced by a suddenly generated temperature difference*, Int. J. Heat Mass Tran. 52 (2009) 4966–4975.
- [55] B. Calcagni, F. Marsili, M. Paroncini, *Natural convective heat transfer in square enclosures heated from below*, Appl. Therm. Eng. 25 (2005) 2522–2531.

## 6.6 Case Study 6 - Different Turbulence Models Simulations of a Vortex Tube

**Authors :** Zhuohuan Hu , Rui Li , Xin Yang , Mo Yang , and Yuwen Zhang

**Citation :** Zhuohuan Hu, Rui Li, Xin Yang, Mo Yang & Yuwen Zhang (2020) Numerical simulation for three-dimensional flow in a vortex tube with different turbulence models, *Numerical Heat Transfer, Part A: Applications*, 77:2, 121-133, DOI: [10.1080/10407782.2019.1688024](https://doi.org/10.1080/10407782.2019.1688024)

Three-dimensional flow in a vortex tube with straight nozzle was investigated numerically [Hu et al.]<sup>52</sup>. Four different turbulence models, **Spalart-Allmaras**, **Standard  $k - \epsilon$** , **SST  $k - \omega$**  and **Realizable  $k - \epsilon$**  were proposed to replicate the flow in the vortex tube. The simulation results of pressure, temperature and velocity field were compared with the experimental data based on dimensionless analysis. It was found that the sudden gas expansion in the vortex chamber causes a pressure drop. The secondary circulations phenomena were observed and identified. Furthermore, the friction between the gas and wall surface and the energy transfer between different laminar flows are the main factors of energy separation in the vortex tube. The realizable  $k - \epsilon$  model predicts energy separation better than other models studied in this research.

### 6.6.1 Introduction

Researches on vortex tubes started from discovery of the “**vortex tube effect**” by Ranque, a French metallurgist, in the 1930s [1]. Later, a German physicist R. Hilsch made a significant contribution to the research of vortex tube [2]. The vortex tube was also

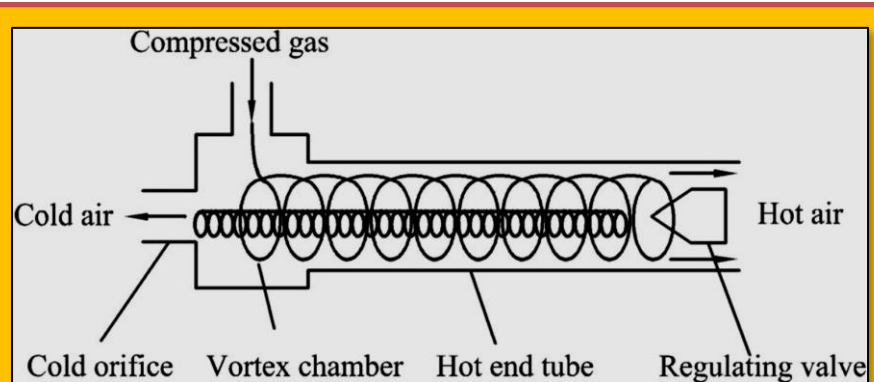


Figure 6.6.1 Airflow in a Vortex Tube

named **Ranque-Hilsch vortex tube** in honor of the two founding scientists. The structure of the vortex tube generally includes one or more nozzles, vortex chamber, cold orifice, hot end tube, and a regulating valve. The compressed gas is tangentially injected into the vortex chamber through the nozzles. Part of the gas exit from the cold orifice with a temperature lower than the inlet temperature. The rest of gas escapes from the hot end tube at a higher temperature. The mass ratio of the cold air flow to heated air flow can be adjusted by the regulating valve. The airflow in a counter-flow vortex tube is illustrated in **Figure 6.6.1**.

Research on vortex tube has been carried out for several decades, but the principle of vortex tube effect is still puzzling. Relevant theories about the pressure gradient [3], viscous friction [4], secondary flow [5] and acoustic streaming have been developed [6]. However, there is no complete explanation for energy separation. The accurate descriptions of flow field and temperature field are crucial to revealing the physical mechanism of the vortex tube. It must be admitted that the small volume and the strong swirl flow of vortex tube have made the challenge to the field measurement. Gao et al. [7] developed a Pitot tube in order to mitigate the impact of measuring the flow field. The overall view of the experimental setup is presented in **Figure 6.6.2**. [Xue et al. [8,9] studied the flow field inside tube by visual measurement and demonstrated the existence of multi-circulations. In

<sup>52</sup> Hu, Z., , Li, R., , Yang, X., Yang M., , and Zhang, Y., (2020)“ Numerical Simulation For Three-Dimensional Flow In A Vortex Tube With Different Turbulence Models”, *Numerical Heat Transfer, Part A: Applications*, Vol. 77, No. 2, 121-133

addition, the 2-D laser Doppler velocimetry was adopted by Guo et al. [10] to investigate the axial velocity distributions of the flow. And the variation of the reverse flow boundary was also discussed. Numerical simulation can overcome the difficulty of measurement and it has been proved to be applicable to study the turbulent flows[11, 12] Thakare and Parekh [13] employed different turbulence models to explore the energy separation with different working fluids. The results showed that the working fluid with large thermal diffusivity and thermal conductivity caused more significant energy separation effect except for hydrogen. However, the effect of Prandtl number on energy separation was not obvious. Thakare et al. [14] studied the influence of cold mass fraction on

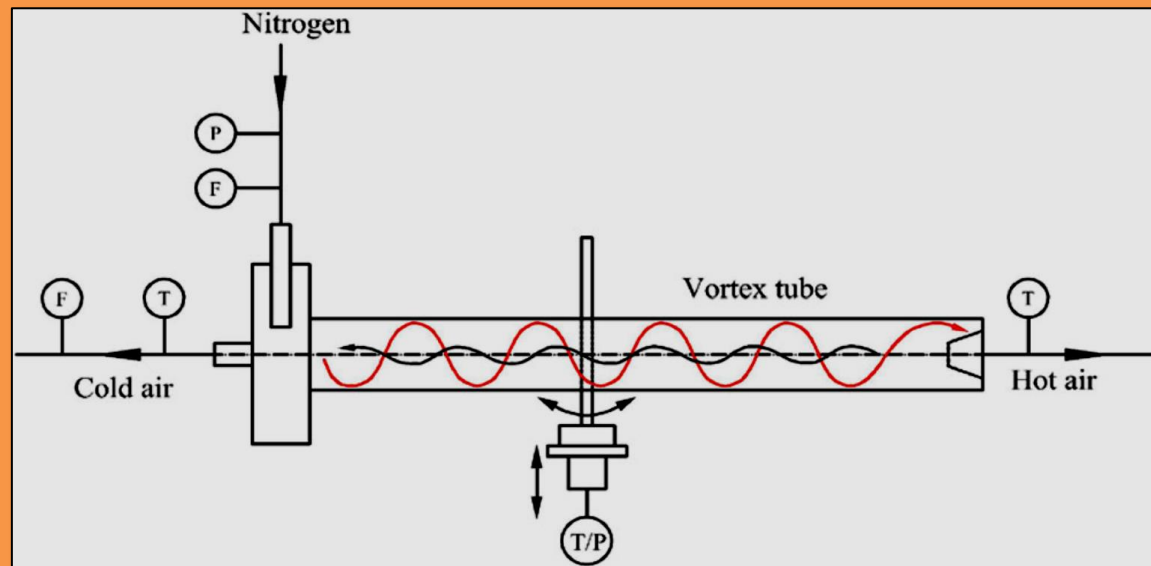


Figure 6.6.2 Schematic Diagram of Gao's Experimental Setup

energy separation efficiency and stated that when the cold mass fraction is between 0.3 to 0.35, the temperature of the cold air reached the minimum; when the cold mass fraction is 0.68, vortex tube gets the maximum cooling capacity. The numerical simulation by Kandil and Abdelghany [5] found that with the increase of cold mass fraction, the secondary flow would disappear in the tube, which was consistent with the view of Behera et al. [3].

The above researchers studied the vortex tube energy separation using two-dimensional models. More recently, Pourmahmoud et al. [15], Shamsoddini and Nezhad [16] performed numerical investigations on the three-dimensional models of a vortex tube in order to investigate the effects of the number of nozzles on the flow and cooling power of the vortex tube. Muhammad et al. [17] conducted a numerical study based on the experiment which tested the performance of vortex tube controlled by values with different shapes. CFD results were verified by the experimental work, and the maximum absolute errors of the numerical and measured values in two and three dimensions model were 4.12% and 2.3% respectively. Khait et al. [18] carried out entropy generation analysis to determine the irreversible energy conversion in the vortex tube. The standard  $k - \epsilon$  and SAS-SST turbulence models were compared and analyzed from the perspective of thermodynamics. Furthermore, optimization of vortex tube was suggested. [Guo and Zhang [19] used the RSM model to study the influence of different cold mass fraction conditions on the flow structure; the energy separation performance was explained based on the vortex breakdown theory. In numerical solutions, the accuracies of different models for the same flow phenomenon will directly affect the results and prediction. In this article, a complete three-dimensional simulation is accomplished by utilizing different turbulence models, including **Spalart-Allmaras, standard  $k - \epsilon$  model, realizable**

***k - ε model***, as well as the ***SST k - ω model*** [20], which is used in cyclone simulation, toward assessing a suitable model for the investigation of energy separation in vortex tube.

### 6.6.2 Mathematical & Geometry Models

The geometric model of vortex tube in this study is as close as possible to the experimental model reported by Gao et al. [7].

**Figure 6.6.3** depicts the structure of the vortex tube, which consists of the following components: a) a square input nozzle (2.7mm x 2.7mm, 20mm length), b) a vortex chamber (30mm diameter, 11mm thickness), c) the hot end tube (16mm diameter, 205mm length, i.e. L/D =12.8), and d) cold tube (4mm diameter, i.e. dc/D =0.25). There are four observation surfaces in the vortex tube, as given in **Figure 6.6.3**.

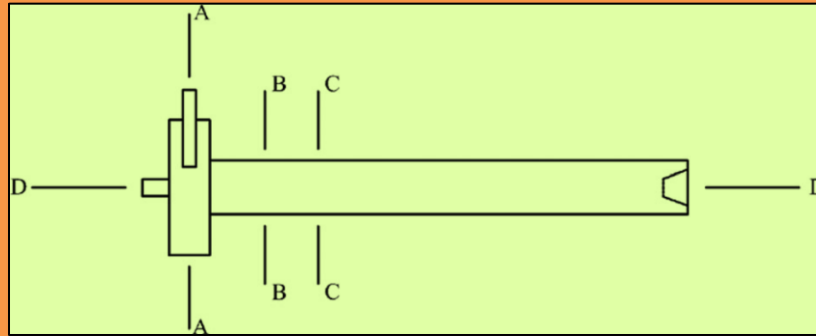


Figure 6.6.3 Side view of vortex tube. A-A: cross section at the entrance of the nozzle; B-B: the distance from the cross section of the nozzle is 23.5 mm; C-C: the distance from the cross section of the nozzle is 47.5 mm; D-D: center radial cross section of vortex tube

### 6.6.3 Governing Equations

Flow in vortex tube is assumed to be compressible and turbulent in steady state. In addition, the hypothesis has made as follows: a) Working fluid is the ideal gas. b) The physical properties of the working air are constant. The simulation of the compressible flows is governed by Navier-Stokes equations include conservations of mass, momentum and energy. In the Cartesian coordinate system, the three-dimensional N-S equation of the tensor form is as follows:

Continuity equation:

$$\frac{\partial \rho}{\partial t} + \frac{\partial(\rho u_i)}{\partial x_i} = 0$$

#### Eq. 6.6.1

Momentum equation:

$$\frac{\partial(\rho u_i)}{\partial t} + \frac{\partial(\rho u_i u_j)}{\partial x_j} = \frac{\partial p}{\partial x_i} + \frac{\partial}{\partial x_i} \left( \mu \frac{\partial^2 u_i}{\partial x_j^2} + \frac{\partial^2 u_j}{\partial x_i^2} - \frac{2}{3} \delta_{ij} \frac{\partial u_k}{\partial x_k} + \frac{\partial}{\partial x_j} \right) (-\rho \bar{u}_i \bar{u}_j)$$

#### Eq. 6.6.2

Energy equation:

$$\frac{\partial(\rho T)}{\partial t} + \frac{\partial(\rho u_j T)}{\partial x_j} = \frac{\partial}{\partial x_i} \left( \frac{\mu}{Pr} \frac{\partial T}{\partial x_j} - \rho \bar{u}_i \bar{T} \right) + S_T$$

#### Eq. 6.6.3

Equation of state for ideal gas:

$$P = \rho R T$$

#### Eq. 6.6.4

All of the turbulent transport equations are derived from the Navier-Stokes equations. Transport equation for ***Spalart-Allmaras*** model is:

$$\rho \frac{D\tilde{v}}{Dt} = G_{\tilde{v}} + \frac{1}{\sigma_{\tilde{v}}} \left[ \left\{ (\mu + \rho \tilde{v}) \frac{\partial \tilde{v}}{\partial x_j} \right\} + C_{b2} \rho \left( \frac{\partial \tilde{v}}{\partial x_j} \right) \right] - Y_v$$

**Eq. 6.6.5**

where  $G_v$  is the production of turbulent viscosity and  $Y_v$  is the destruction of turbulent viscosity that occurs in the near-wall region due to the wall blocking and viscous damping  $\tilde{v}$  is the molecular kinematic viscosity;  $\sigma_v$  and  $C_{b2}$  are constants. Transport equations for the **standard k-e model** are:

$$\begin{aligned} \frac{D\kappa}{Dt} &= \frac{\partial}{\partial x_j} \left[ \frac{1}{\rho} \left( \mu + \frac{\mu_T}{\sigma_k} \right) \frac{\partial \kappa}{\partial x_j} \right] + \frac{\mu_T}{\rho} S_{ij}^2 - \varepsilon \\ \frac{D\varepsilon}{Dt} &= \frac{\varepsilon}{\kappa} \left( C_1 \frac{\mu_T}{\rho} S_{ij}^2 - C_2 \varepsilon \right) + \frac{\partial}{\partial x_j} \left[ \frac{1}{\rho} \left( \mu + \frac{\mu_T}{\sigma_\varepsilon} \right) \frac{\partial \varepsilon}{\partial x_j} \right] \\ \text{where } \mu_T &= \rho C_\mu \frac{\kappa^2}{\varepsilon} \quad \text{and} \quad S_{ij} = \frac{1}{2} \left( \frac{\partial \bar{u}_i}{\partial x_j} + \frac{\partial \bar{u}_j}{\partial x_i} \right) \end{aligned}$$

**Eq. 6.6.6**

where  $C_1, C_2, \sigma_\varepsilon$  are constants of the  $\varepsilon$  equation (see Error! Reference source not found.). Transport equation for **SST k-ω model** is:

$$\begin{aligned} \frac{\partial(\rho\kappa)}{\partial t} + \frac{\partial}{\partial x_i} (\rho \bar{u}_i \kappa) &= \frac{\partial}{\partial x_i} \left[ \underbrace{\left( \mu + \frac{\mu_T}{\sigma_\kappa} \right) \nabla \kappa}_{\Gamma_k} \right] + G_\kappa - Y_K + S_k \\ \frac{\partial(\rho\omega)}{\partial t} + \frac{\partial}{\partial x_i} (\rho \bar{u}_i \omega) &= \frac{\partial}{\partial x_i} \left[ \underbrace{\left( \mu + \frac{\mu_\omega}{\sigma_\omega} \right) \nabla \omega}_{\Gamma_\omega} \right] + G_\omega - Y_\omega + S_\omega \end{aligned}$$

**Eq. 6.6.7**

where  $G_\omega$  represents the generation of  $\omega$ .  $\Gamma_k$  and  $\Gamma_\omega$  represent the effective diffusivity of  $k$  and  $\omega$ , respectively.  $Y_k$  and  $Y_\omega$  represent the dissipation of  $k$  and  $\omega$  due to turbulence.  $S_k$  and  $S_\omega$  are user-defined source terms. Transport equations for **realizable k-ε model** are:

$$\begin{aligned} \rho \frac{D\kappa}{Dt} &= \frac{\partial}{\partial x_j} \left[ \left( \mu + \frac{\mu_T}{\sigma_k} \right) \frac{\partial \kappa}{\partial x_j} \right] + G_k + G_b - \rho \varepsilon - Y_M \\ \rho \frac{D\varepsilon}{Dt} &= \frac{\partial}{\partial x_j} \left[ \left( \mu + \frac{\mu_T}{\sigma_\varepsilon} \right) \frac{\partial \varepsilon}{\partial x_j} \right] + \rho C_1 S_\varepsilon - \rho C_2 \frac{\varepsilon^2}{k + \sqrt{v\varepsilon}} + C_{1\varepsilon} \frac{\varepsilon}{k} C_{3\varepsilon} G_b \end{aligned}$$

**Eq. 6.6.8**

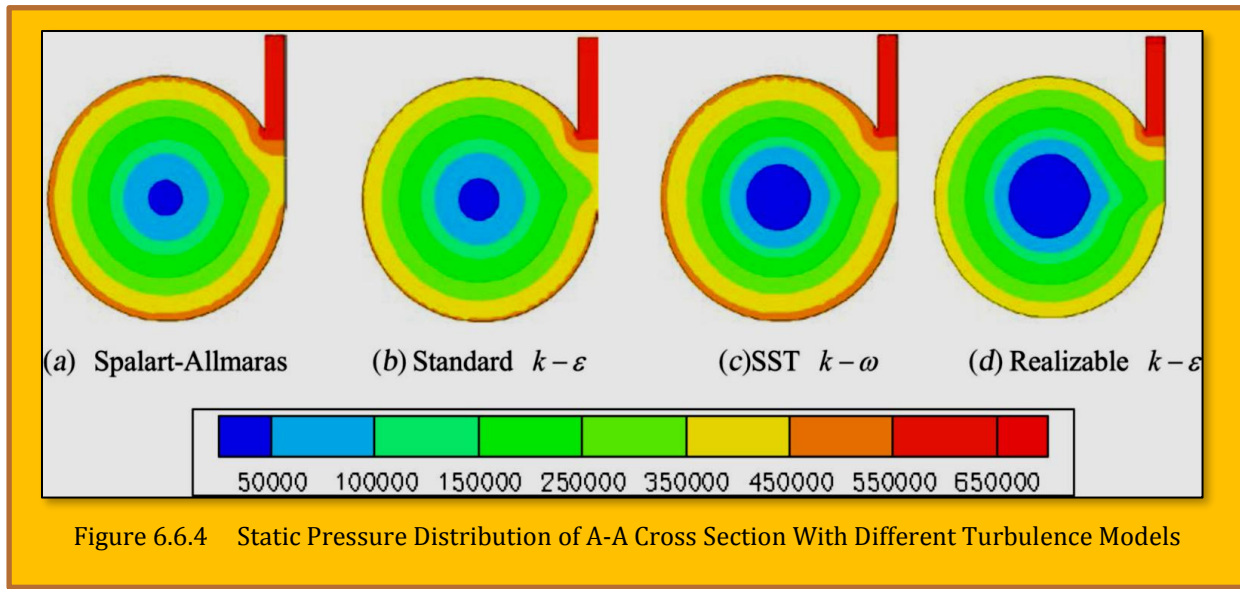
where  $C_1 = \max(0.43, \eta/\eta+5)$ ,  $\sigma_k = 1.0$ , and  $\sigma_\varepsilon = 1.2$ .

**6.6.4 Boundary Conditions and Solver**

The boundary conditions for this problem include:

- the type of inlet is pressure-inlet that the total pressure makes the static pressure reach 0.65 MPa (gauge pressure); the working fluid is nitrogen and the inlet total temperature reaches 285.6 K;

- the type of cold-exit is pressure outlet, and the magnitude of the total pressure is kept with standard atmospheric pressure; c) the type of hot-exit is also pressure-outlet, and the total pressure is adjusted to keep the cold mass fraction around 0.27 in different turbulent models. PRESSure STaggering Option (PRESTO). Scheme is used for discretization of pressure, which is reported to perform better when the steep pressure gradient is involved in the swirling flows.



## 6.6.5 Results and Discussions

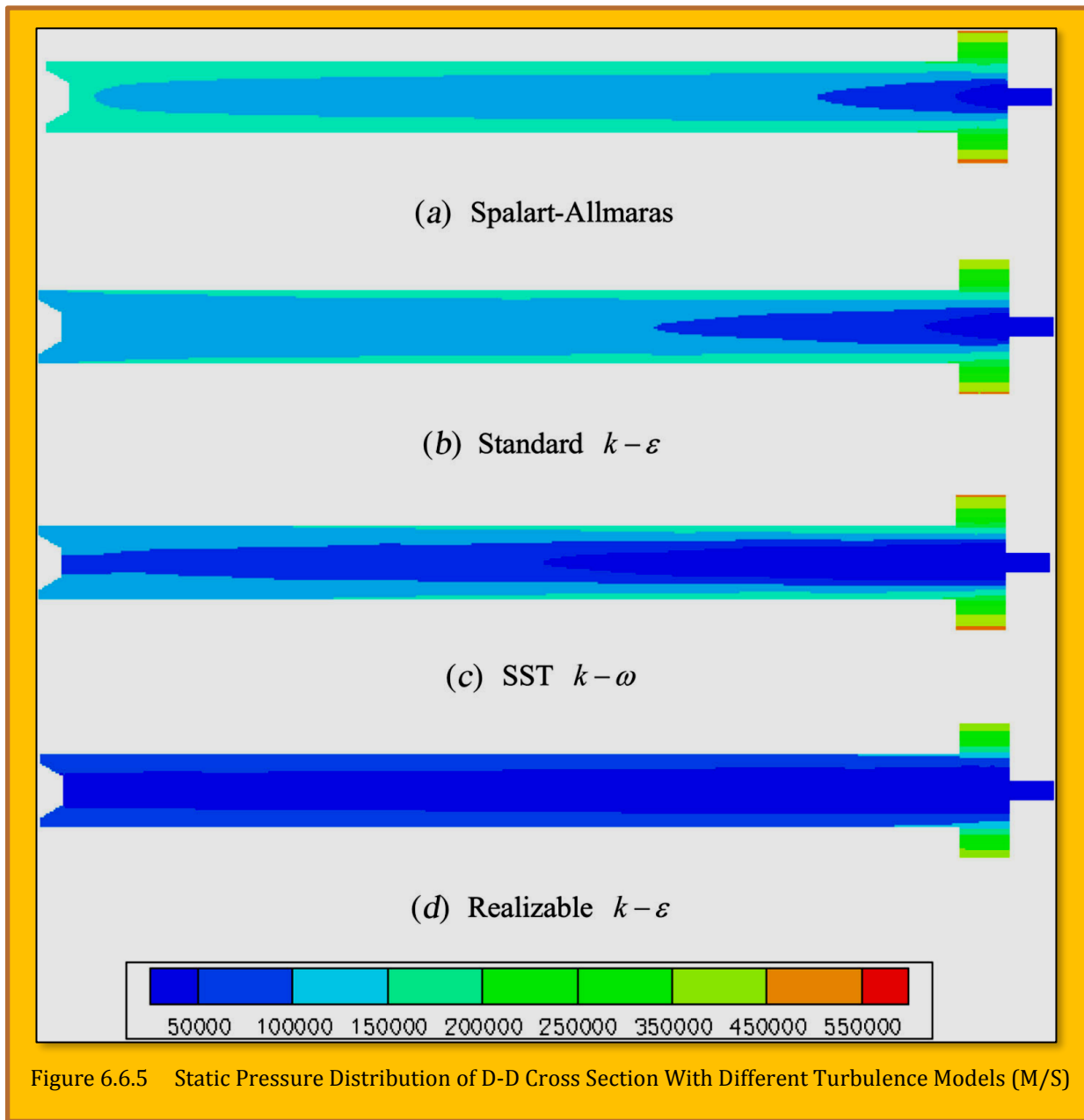
### 6.6.5.1 Pressure Distribution

When the gas injects into the vortex chamber through the nozzle at high velocity, the high pressure gas expands rapidly causing a sudden drop in pressure. The temperature drop near the injection induced by adiabatic expansion can be expressed as:

$$P_1^{\gamma-1} T_1^{-\gamma} = P_2^{\gamma-1} T_2^{-\gamma}$$

#### Eq. 6.6.9

where  $\gamma$  is the specific heat capacity ratio, which is generally 1.4 for diatomic ideal gas. The distribution of the static pressure field in the vortex tube obtained by different turbulence models is shown in **Figure 6.6.4** and **Figure 6.6.5**. As can be found in **Figure 6.6.4**, all models predict similar distribution of static pressure in the peripheral region, whereas there are evident differences in the center region. The blue region in **Figure 6.6.4 (d)** is larger than others, which means the low-pressure area calculated by realizable  $k - \epsilon$  is broader than others. On the other hand, the gas pressure increases with increasing  $r/R$ . The results support the theory of temperature drop near the injection caused by adiabatic expansion. It is also seen from **Figure 6.6.5** that the pressure in the tube is lower than the inlet pressure, which indicates that the flow in the tube is accompanied by an expansion process.



### 6.6.5.2 Tangential Velocity Distribution

Compared with the axial and radial velocities, the tangential velocity is usually the largest in value, which can reflect the flow direction of particles in the vortex tube. The fast-tangential velocity also leads to a strong centrifugal force. The distribution of the tangential velocity in the vortex tube predicted by different turbulence models is provided in **Figure 6.6.6**. It was found that the tangential velocity of gas near the nozzle can be close to the speed of sound. In the same axial section, the maximum tangential velocity appears near the wall and the velocity decreases gradually toward the center of the tube. As the distance from the inlet increases, the tangential velocity of the gas decreases. It is probable that the kinetic energy is gradually converted into thermal energy by viscous dissipation and the friction between the gas and the wall during the vortex movement. Furthermore, a proper increase of L/D value is beneficial to improve the performance of energy separation. The tangential velocity distributions obtained by different turbulence models showed difference at the near hot end. The gas swirl velocity in the hot gas region obtained by Spalart - Allnara model was significantly lower than that of other models. The hot gas region predicted by realizable  $k - \varepsilon$  model maintains a high swirl velocity. The tangential velocity distribution of C-C cross section was compared with experimental data of Gao et al. [7], Takahama [21] and Bruun [22]. All working conditions have been listed in **Table 6.6.1**. All

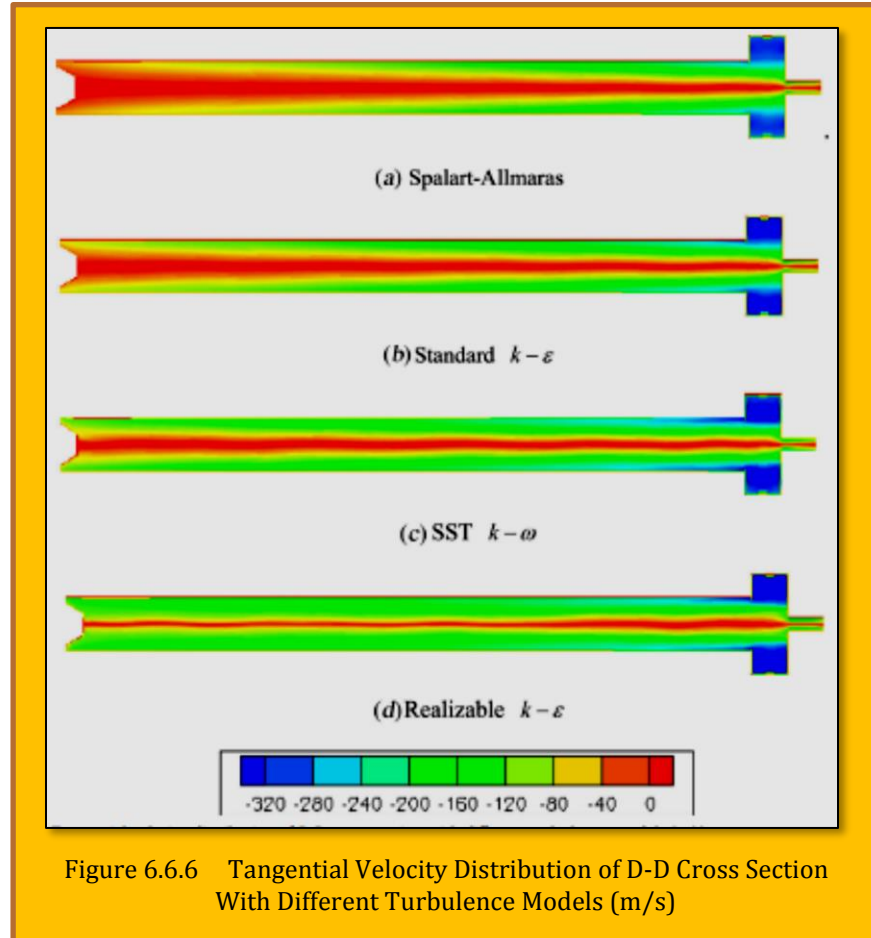


Figure 6.6.6 Tangential Velocity Distribution of D-D Cross Section With Different Turbulence Models (m/s)

data should be nondimensionalized and the non-dimension tangential velocity is defined as:

Author	D	L	Number of nozzles	dc	mc/min	Z/D
Gao et al.	16	205	1	4	0.27	2.97
Takahama	52.8	7920	4	-	0.5	0.5
Bruun	94	520	4	35	0.23	1.27

Table 6.6.1 Working Condition Used By Different Experiments (length unit: mm)

$$\hat{v}_t = \frac{v_t}{\max(v_t)}$$

**Eq. 6.6.10**

where  $V_t$  is the tangential velocity, and  $\max(V_t)$  means the maximum tangential velocity at the same section. **Figure 6.6.7** illustrates the difference between the simulation and experimental results, especially close to the center of the tube. There are many reasons for this difference. Firstly, the influence of the Pitot tube probe on the flow field in the experiments cannot be ignored. Secondly, the direction of measurement affects the velocity results. Finally, the difference in the structure and the measurement interfaces of the vortex tube bring interference to the comparison. Although there is a difference between the results, the tangential velocity in the one interface is consistent with the distribution trend. When  $r/R$  is in the range of  $0 \sim 0.7$ , the gas inside the tube remains approximately the same as the angular velocity. The tangential velocity of the gas flows reaches the highest point at  $r/R = 0.8 \sim 0.95$ . As the  $r/R$  increases further, the gas velocity drops. The simulation results of [Pourmahmoud et al. [15] and [Thakare [23] had similar conclusions. Fulton [24] suggested that the

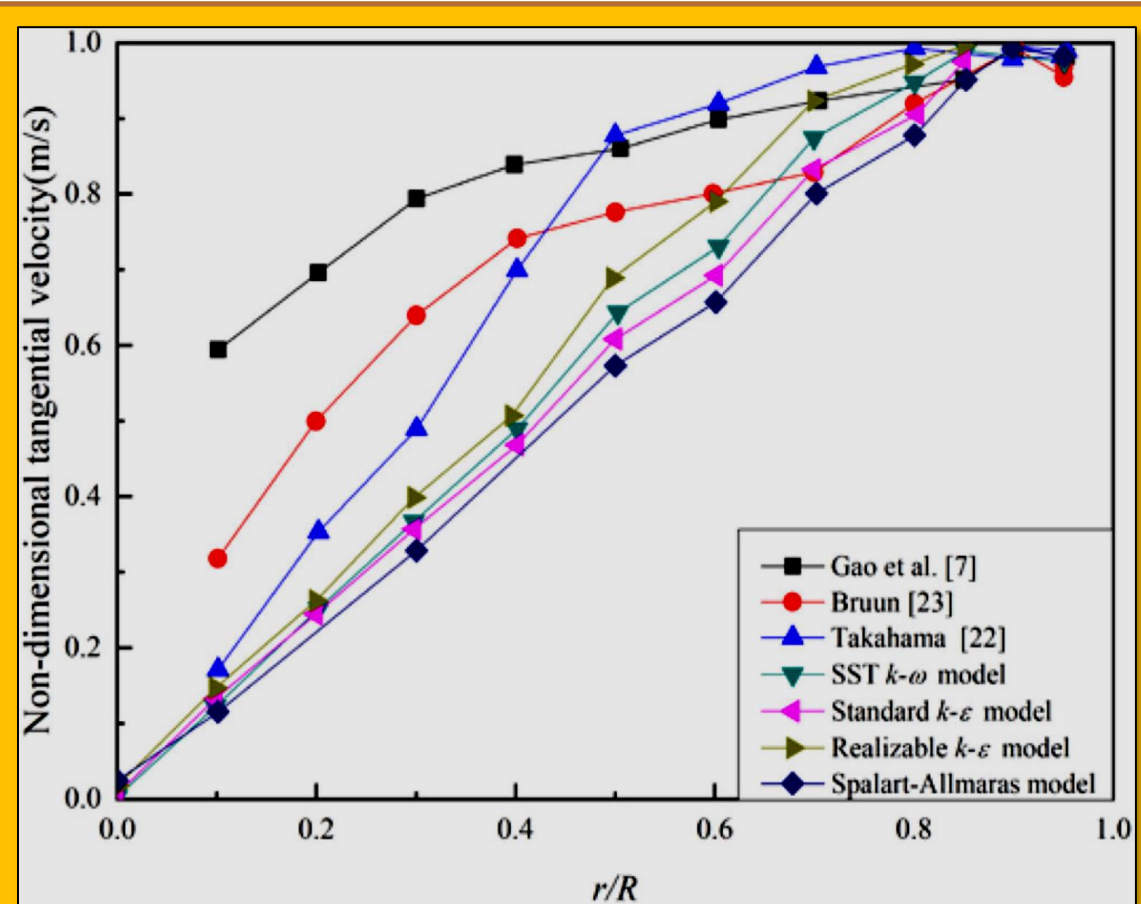


Figure 6.6.7 Comparison of The Dimensionless Tangential Velocity

angular velocity at the peripheral location was lower than that at the central location and an almost free vortex was formed near the inlet nozzle. Under the action of internal friction, the fluid in a cross section will rotate at the same angular velocity, which is similar to the rotational motion of a rigid solid. The diffusion energy transmits from the outer layer to the inner fluid, while the mechanical energy is transferred conversely. The outer gas gains more kinetic energy than the loss of internal energy and the inner gas loses kinetic energy, which leads to the temperature separation in the vortex tube. The model of this mechanism is represented in **Figure 6.6.9**.

### 6.6.5.3 Axial Velocity

**Figure 6.6.8** displays the axial velocity distribution predicted by different turbulence models. The blue area represents the gas flow to the hot end, the red and green areas represent the gas flow to the cold end. The simulation results indicate that there is a curved surface between the center and wall with zero axial velocity. The vortex tube is divided by the curved surface into two parts. The axial velocity near the center is positive and flows to the cold orifice, which is known as internal cooling vortex. The other part of the axial velocity is negative, and the flow direction is to the hot end, which is called external heat vortex. However, the result of the Spalart - Allmaras model is an exception: after the air is injected into the tube, the curved surface gradually gets closer to the center, and eventually into a point. There is a secondary circulation at the end of the hot end. The dimensionless axial velocity is defined as:

$$\hat{v}_a = \frac{v_a}{\max(v_a)}$$

**Eq. 6.6.11**

where  $V_a$  is the axial velocity, m/s. The axial velocity in the vortex tube usually does not exceed 0.4 of the maximum tangential velocity in any cross section. The maximum axial velocity of the inner vortex occurred near the center, which could be caused by the pressure gradient. The maximum axial velocity of the outer vortex is near the wall because of the energy transfer. In addition, it should be added that the simulation results of

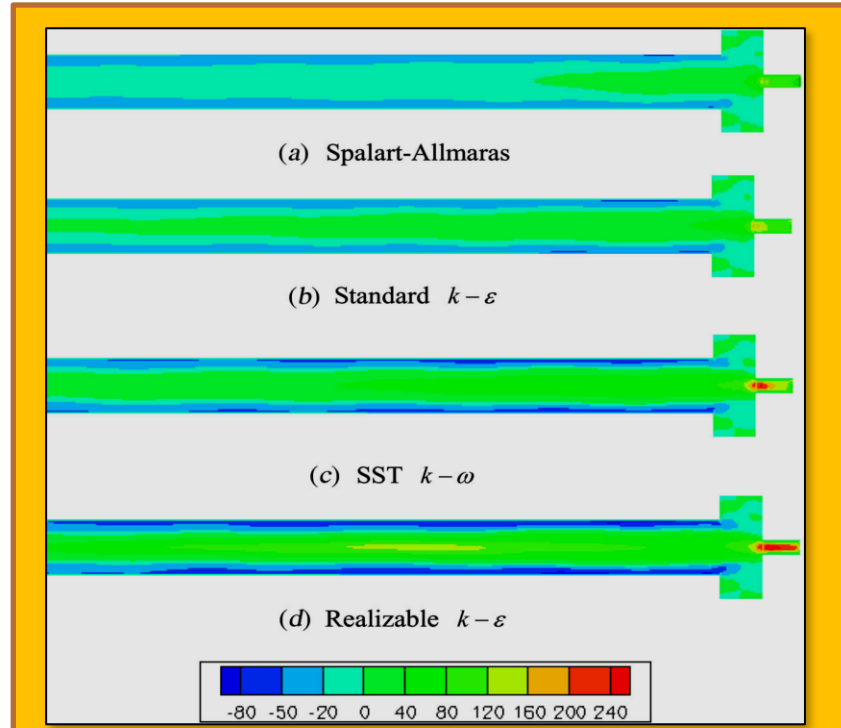


Figure 6.6.8 Axial Velocity Distribution Of D-D Cross Section With Different Turbulence Models (M/S)

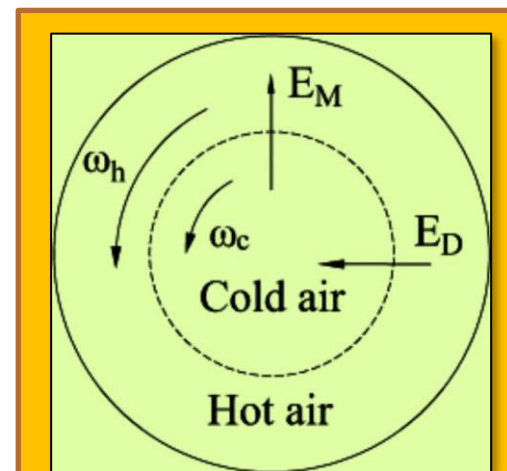


Figure 6.6.9 The Diagram of The Viscous-Shear Theory

SST  $k - \omega$  model and realizable  $k - \varepsilon$  model are closer to the experimental data than the other two models.

#### 6.6.5.4 Radial Velocity

Most of the radial velocity values are distributed in a range from -20 m/s to +20 m/s, which is less than the axial velocity and tangential velocity. Although the radial velocity can be considered as negligible compared with the other velocities, the radial velocity can still reveal some flow characteristics.

According to [Figure 6.6.7](#), the maximum radial velocity is concentrated in the tube center and the radial velocity is close to zero in the periphery zone. At the center, the average radial velocity is not zero, and the distribution of radial velocity is nearly axisymmetric, which indicates that the vortex flow pattern is likely to be a wave oscillation pattern.

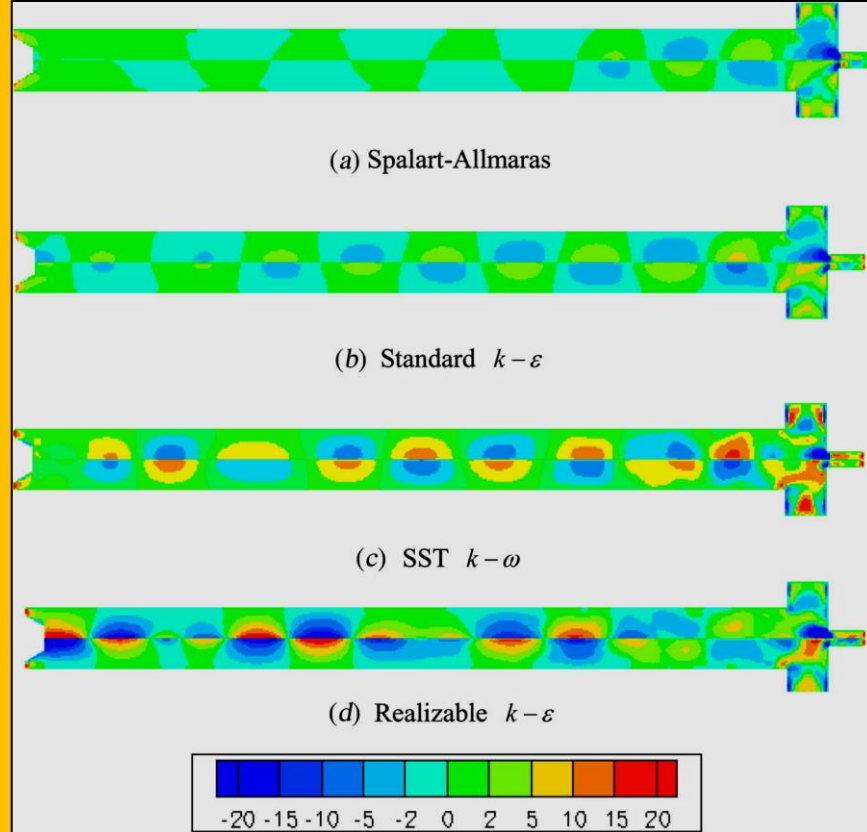


Figure 6.6.10 Radial velocity distribution of D-D cross section with different turbulence models (m/s).

#### 6.6.6 Temperature Field

The total temperature distribution of D-D cross section is indicated in [Figure 6.6.11](#). It shows that all turbulence models can reflect the energy separation phenomena. The gas expands after being injected into the vortex chamber, and the static temperature of the gas decreases rapidly. Since the

	Gao	SST $k - \omega$	Standard $k - \varepsilon$	Realizable $k - \varepsilon$	Spalart-Allmaras
In (K)	285.6	285.6	285.6	285.6	285.6
Cold (K)	270.5	253.9	257.8	271.1	258.6
Hot (K)	291.3	296.5	295.1	291.1	295.1
$\Delta T_c$ (K)	-15.1	-32.1	-27.8	-14.5	-27
$\Delta T_h$ (K)	5.7	10.9	9.5	5.5	9.5

Table 6.6.2 Outlet temperature under different models

velocity is close to the speed of sound, the total temperature in the vortex tube is still higher. In the process of gas moving to hot end in the form of a vortex flow, the internal energy is dissipated as heat as a result of the friction between the wall and gas flow, which leads to the total temperature reduction in this region. When the gas flows from the hot end to the cold end, the internal energy will be reduced again due to the kinetic energy transfer. The gas becomes colder in the center of the vortex tube. The outlet temperature of various turbulence models is listed in **Table 6.6.2**. It can be found from **Table 6.6.2** that the best energy separation effect can be obtained under the SST  $k - \omega$  model, however, the results seriously deviate from the experimental results. On the contrary, the realizable  $k - \varepsilon$  model simulation is quite close to the experimental data.

### 6.6.7 Streamline Field

**Figure 6.6.12** shows the streamlines in the D-D plane obtained from different models. The streamlines were calculated from the tangential velocity and axial velocity. It can be seen that there exists a large number of secondary circulations. The results based on the **Spalart-Allmaras** turbulence model describes that the secondary circulations are mainly concentrated in the first half of the tube (close to the cold exit). After entering the tube, the flow direction of gas changes to the cold end near the secondary circulations. The positions of the secondary circulations calculated by other models are similar. The cold end gas forced back in the middle of the vortex tube based on the standard  $k - \varepsilon$  model. Both SST  $k - \omega$  model and realizable  $k - \varepsilon$  model indicate the reversed flow occurs at the hot end.

### 6.6.8 Conclusion

A numerical study has been carried out to investigate the energy separation mechanism and flow phenomena within a vortex tube using four different turbulence models: **Spalart-Allmaras model**, **standard  $k - \varepsilon$  model**, **SST  $k - \omega$  model**, and **realizable  $k - \varepsilon$  model**. The simulation results have been compared with the available experimental data. It was demonstrated that all turbulence models can simulate temperature separation. The simulation results of different turbulence models have similar pressure field and velocity field profile. The sudden gas expansion in the vortex chamber causes the pressure drop, which is the dominated reason for the low temperature of the cold end. The pressure in other parts of the tube is lower than the inlet pressure, and the adiabatic compression is not the cause of the high temperature at the hot end. Friction between gas and wall surface and the energy transfer between different laminar flows are the main factors of the high temperature of peripheral

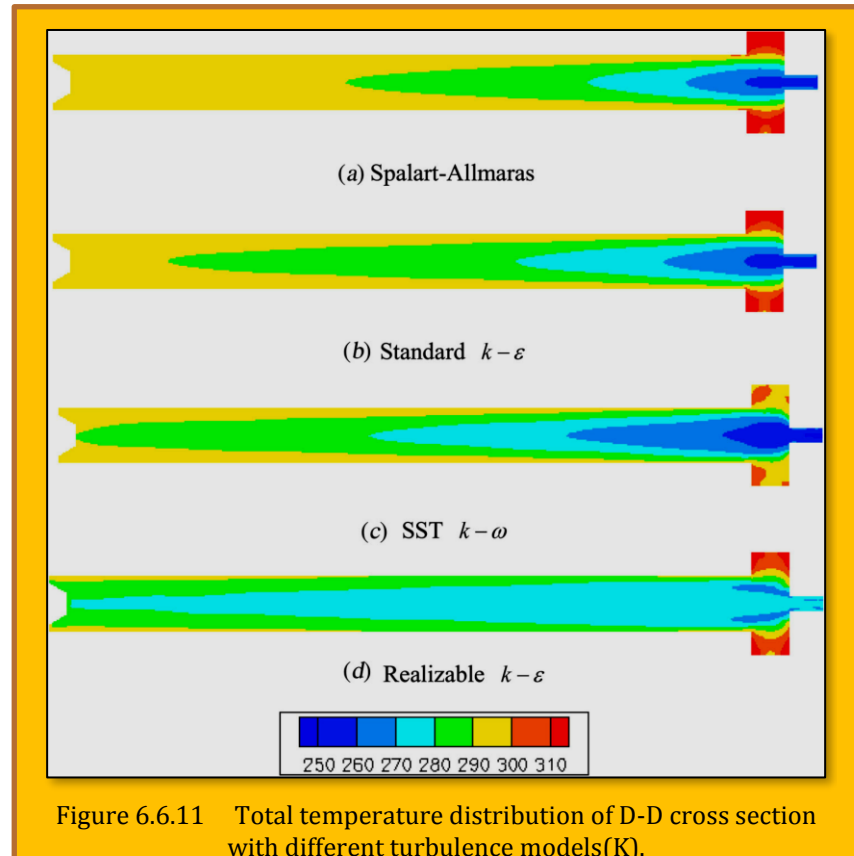


Figure 6.6.11 Total temperature distribution of D-D cross section with different turbulence models(K).

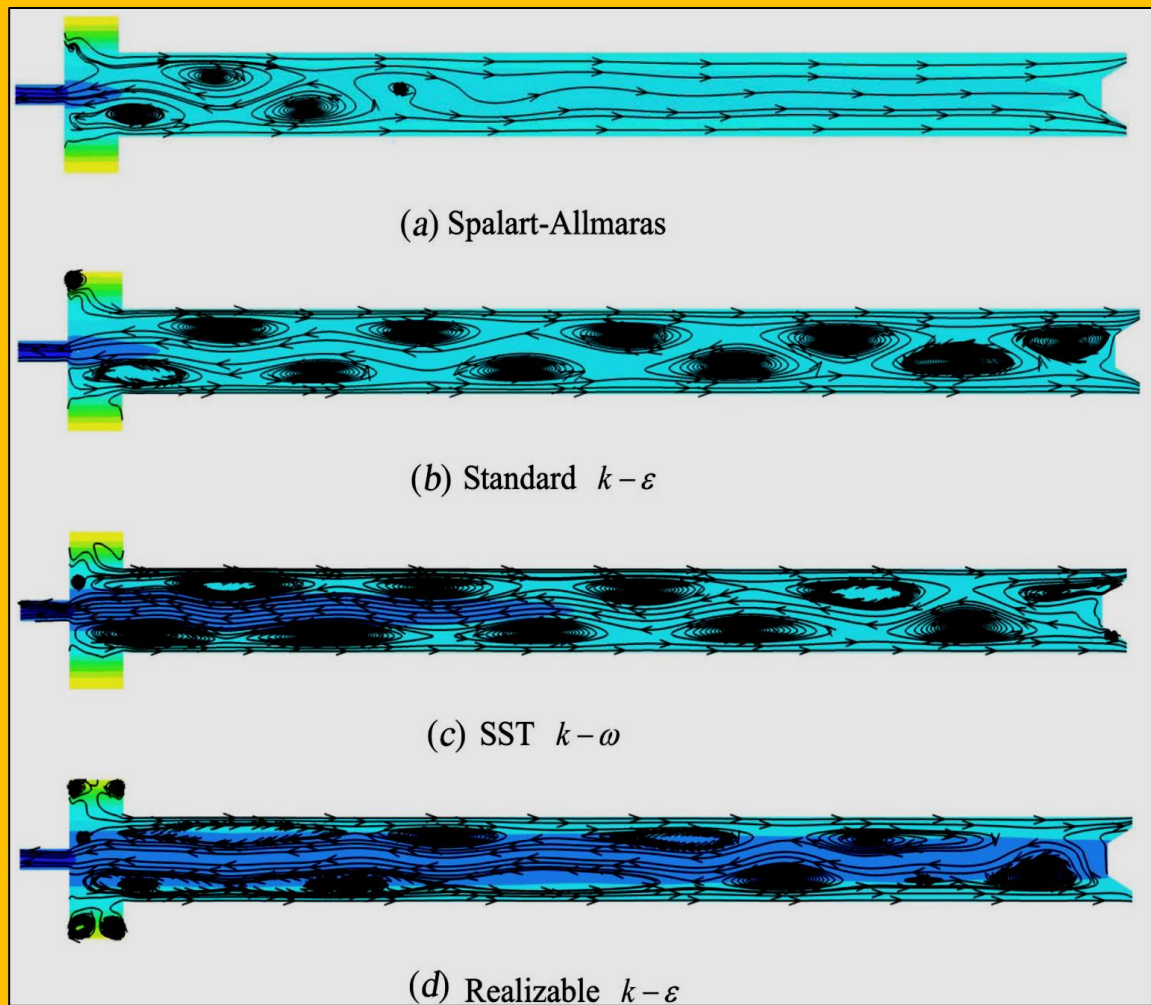


Figure 6.6.12 Instantaneous streamlines for the vortex tube in D-D plane.

gas and the low temperature of the center zone. There are significant differences in the simulation results with the various turbulence models. Based on the analysis mentioned, the **realizable  $k - \varepsilon$  model** is better than other models in terms of the structure and working conditions of the vortex tube in this study.

### 6.6.9 References

- [1] G. J. Ranque, "Experiments on expansion in a vortex with simultaneous exhaust of hot air and cold air," Phys. Radium, vol. 4, pp. 112–114, 1933.
- [2] R. Hilsch, "The use of the expansion of gases in a centrifugal field as cooling process," Rev. Sci. Instrum., vol. 18, no. 2, pp. 108–113, 1947.
- [3] U. Behera, P. J. Paul, K. Dinesh, and S. Jacob, "Numerical investigations on flow behavior and energy separation in Ranque–Hilsch vortex tube," Int. J. Heat Mass Transfer, vol. 51, no. 25–26, 2008.
- [4] Y. Xue, M. Arjomandi, and R. Kelso, "The working principle of a vortex tube," Int. J. Refrig., vol. 36, no. 6, pp. 1730–1740, 2013.
- [5] H. A. Kandil and S. T. Abdelghany, "Computational investigation of different effects on the performance of the Ranque–Hilsch vortex tube," Energy, vol. 84, pp. 207–218, 2015.
- [6] W. Wisnöe, K. M. A. Rahman, Y. Istihat, and V. D. Natarajan, "Thermo fluid-Acoustic Analysis of a Ranque-Hilsch Vortex Tube," Procedia Technol., vol. 26, pp. 544–551, 2016.

- [7] C. M. Gao, K. J. Bosschaart, J. C. H. Zeegers, and A. T. A. M. de Waele, "Experimental study on a simple Ranque–Hilsch vortex tube," *Cryogenics*, vol. 45, no. 3, pp. 173–183, 2005.
- [8] Y. Xue, M. Arjomandi, and R. Kelso, "Visualization of the flow structure in a vortex tube," *Exp. Therm. Fluid Sci.*, vol. 35, no. 8, pp. 1514–1521, 2011.
- [9] Y. Xue, M. Arjomandi, and R. Kelso, "Experimental study of the flow structure in a counter flow Ranque–Hilsch vortex tube," *Int. J. Heat Mass Transfer*, vol. 55, no. 21–22, pp. 5853–5860, 2012.
- [10] X. Guo, B. Zhang, L. Li, B. Liu, and T. Fu, "Experimental investigation of flow structure and energy separation of Ranque–Hilsch vortex tube with LDV measurement," *Int. J. Ref.*, vol. 101, 2019.
- [11] C. H. Wu, H. W. Tang, and Y. T. Yang, "Numerical simulation and optimization of turbulent flows through perforated circular pin fin heat sinks," *Num. Heat Transfer, Part A*, vol. 71, no. 2, 2017.
- [12] P. Promthaisong, W. Jedsadaratanachai, and S. Eiamsa-Ard, "3D Numerical study on the flow topology and heat transfer characteristics of turbulent forced convection in spirally corrugated tube," *Num. Heat Transfer, Part A*, vol. 69, no. 6, pp. 607–629, 2016.
- [13] H. R. Thakare and A. D. Parekh, "CFD analysis of energy separation of vortex tube employing different gases, turbulence models and discretization schemes," *Int. J. Heat Mass Transfer*, vol. 78, pp. 360–370, 2014. DOI: 10.1016/j.ijheatmasstransfer.2014.06.083.
- [14] H. R. Thakare, A. Monde, and A. D. Parekh, "Experimental, computational and optimization studies of temperature separation and flow physics of vortex tube: A review," *Renewable Sustainable Energy Rev.*, vol. 52, pp. 1043–1071, 2015.
- [15] N. Pourmahmoud, H. Zadeh, O. Moutaby, and A. Bramo, "CFD analysis of helical nozzles effects on the energy separation in a vortex tube," *Thermal Sci.*, vol. 16, no. 1, pp. 151–166, 2012.
- [16] R. Shamsoddini and A. H. Nezhad, "Numerical analysis of the effects of nozzles number on the flow and power of cooling of a vortex tube," *Int. J. Refi.*, vol. 33, no. 4, pp. 774–782, 2010.
- [17] M. A. Qyyum, A. A. Noon, F. Wei, and M. Lee, "Vortex tube shape optimization for hot control valves through computational fluid dynamics," *Int. J. Refi.*, vol. 102, pp. 151–158, 2019.
- [18] A. Khait, A. Noskov, V. Alekhin, and V. Bianco, "Analysis of the local entropy generation in a double-circuit vortex tube," *Appl. Therm. Eng.*, vol. 130, pp. 1391–1403, 2018.
- [19] X. Guo and B. Zhang, "Computational investigation of processing vortex breakdown and energy separation in a Ranque–Hilsch vortex tube," *Int. J. Refi.*, vol. 85, pp. 42–57, 2018.
- [20] M. Mori, B. Drobnić, B. Jurjević, and L. Novak, "Numerical modeling of heat transfer and flow phenomena in an axial rotating rotor cascade," *Num. Heat Transfer, Part A*, vol. 67, no. 10, 2015.
- [21] H. Takahama, "Studies on vortex tubes," *Bull. JSME.*, vol. 8, no. 31, pp. 433–470, 1965.
- [22] H. H. Bruun, "Experimental investigation of the energy separation in vortex tubes," *Proc. Institution Mech. Engineers, Part C: J. Mech. Engineering Sci.*, vol. 11, no. 6, pp. 567–582, 1969.
- [23] H. R. Thakare and A. D. Parekh, "Computational analysis of energy separation in counter-flow vortex tube," *Energy*, vol. 85, pp. 62–77, 2015.
- [24] C. D. Fulton, "Raqué's tube," *J. Am. Soc. Refrigerating Engineers*, vol. 58, pp. 473–479, 1950

## 6.7 Case Study 7 - Highly-Resolved LES of Turbulent Convective Flow Along A PWR Rod Bundle

**Author :** Djamel Lakehal

**Title :** Highly-resolved LES of turbulent convective flow along a PWR rod bundle

**Appeared in :** International Journal of Heat and Mass Transfer 122 (2018) 785–794

**Citation :** Djamel Lakehal, Highly-resolved LES of turbulent convective flow along a PWR rod bundle, International Journal of Heat and Mass Transfer, Volume 122, 2018, Pages 785-794, ISSN 0017-9310, <https://doi.org/10.1016/j.ijheatmasstransfer.2018.01.099>

(<https://www.sciencedirect.com/science/article/pii/S0017931017322007>)

A detailed numerical analysis of the turbulent convective flow along the **heated rods of an idealized Pressurized Water Reactor (PWR) sub-channel** is investigated using the CFD code *TransAT*. The flow is pretty much similar to circular pipe flow. Turbulent effects are predicted using **highly-resolved Large-Eddy Simulation (LES) with a grid resolution of up to 6 M53 cells**, resolving the viscous-affected layer. The **sub-grid scale (SGS)** viscosity produced by the model is indeed found to be of marginal effect for the grid and Reynolds number employed. Only first-order turbulence statistics are presented here. The results are discussed in detail, in particular key features specific to rod bundles, including low-Re effects in the narrow gap zone and the strong secondary flow motion, which is shown to exceed the turbulence counterpart (through the shear stress) near the wall. The secondary-flow motion induced by the mean flow is shown to be responsible for a large portion of the wall-to-flow heat transfer. The comparison of the LES results with existing DNS of pipe flow shows a very good agreement as to first-order statistics; higher-order statistics (including energy budgets) of the fluctuating fields have not been explored. A data basis has been generated for turbulence model comparison. Like in turbulent pipe flow, a physical explanation for the observed differences can be rooted in the transverse curvature effects of the bundle geometry. [Djamel Lakehal]<sup>54</sup>.

### 6.7.1 Introduction

The onset of nucleate boiling on solid wall occurs when the temperature of the wall slightly exceeds saturation [1]. The small vapor bubbles form and stay attached to the solid wall. Past the point of net vapor generation, the bubbles detach and remain trapped within a layer relatively close to the wall, beyond which – towards the core flow – they condense. Under turbulent conditions, the flow will be further affected by large and small eddies, affecting in turn the rate of wall-to-core-flow heat transfer and thus phase change, both near the wall (boiling) and far in the core flow (condensation).

The first objective of this exercise is to assess the performance of the ITM/CFD code *TransAT* [2] in predicting the turbulent convective flow upward along the heated rods of a PWR sub-channel. The key predicted quantity is the length at which the rod surface temperature reaches nucleation temperature, approximated here as the saturation temperature. For simplicity, we refer to it as the distance to the onset of nucleate boiling ( $X_{ONB}$ ). Predicting this quantity correctly requires accurate prediction of turbulent flow, since the wall temperature is strongly dependent on the flow structures, its unsteadiness and the rate of turbulent-stresses anisotropy.

The problem is inspired by the PSBT (short for PWR Subchannel and Bundle Tests) single sub-channel benchmark. The onset of nucleate boiling on the nuclear rod surface is one of many other complex mechanisms that pose challenges to the modelers [4]. Without listing all the features associated with turbulent flow in narrow gaps of sub-channels, it is perhaps useful to evoke the most important ones which the authors believe as key issues in modelling using mainstream CFD. The

<sup>53</sup> M = million

<sup>54</sup> Djamel Lakehal, "Highly-resolved LES of turbulent convective flow along a PWR rod bundle", International Journal of Heat and Mass Transfer 122 (2018) 785–794.

reader may refer to the review paper of Rehme [5] compiling early research findings on the subject, who has also noted the flow along a rod bundle is pretty much similar to circular pipe flow. Early experiments [6] revealed the existence of macroscopic pulsating flow structures (not necessarily turbulence) in the regions adjacent to the gaps, with strong implications on the mixing between adjacent subchannels.

This phenomenon was proved later on by Meyer [7]. Other important features were identified experimentally as marked characteristics of flow along rod bundles [8,9], including secondary flow motion and large-scale turbulent motions enhancing heat extraction from the heated wall. Clearly, there are incentives to resort to 3D CFD for the prediction of the detailed fluid flow and temperature distribution in rod bundles for safety issues and operational reliability of the fuel elements. Sub channel analysis ignores the fine structures of velocity and temperature distributions in the flow passages, and can thus not account for mixing effects caused by the presence of spacers or other geometrical disturbances. Large-scale turbulent motion and larger periodic pulsating structures responsible for mixing between sub-channels are out of reach of steady state approaches resorting to statistical averaged models [10]. Further, secondary flow motion could be predicted using anisotropic models (to a limited degree though) or full Reynolds stress models only. While the velocity magnitude associated with secondary flow moving within the elementary cells of the sub-channels maybe small (of the order of 10%) compared to the axial one, its implication on heat transfer is important, in particular near the wall, which appeals for the use of wall-resolved strategies. LES of turbulent flow along rod bundles are indeed rare in the literature, with the exception of the Japanese group [11-13] who produced several interesting contributions to the subject. Other contributions to the subject include the work of Merzari et al. [14] and Ninokata et al. [15].

We present the results of a LES and highly-resolved LES of turbulent convective flow upward along the heated rods of an idealized PWR sub-channel. The selected test-case is inspired by the PSBT single sub-channel benchmark [3], in terms of radial dimensions in particular, albeit the deliverables are different from the actual PSBT case. The focus here is on detailed flow profiles and temperature at the wall rather than on global parameters as required in the benchmark. The operating conditions selected here are made on purpose different from PSBT, namely the power, which has been adjusted according to the reduced length (1m instead of 3.65 m). The second objective is to provide a rich data basis to help assess the predictive performance of practical turbulence models to predict mean and RMS profiles, stresses and turbulent fluxes, wall temperature at which saturation conditions are reached.

### 6.7.2 Modelling

This work used the CFD code *TransAT*\_ developed at *ASCOMP*, which is a multi-scale, multi-physics, conservative finite-volume solver for single- and multi-fluid Navier-Stokes equations. The grid arrangement is collocated, and the solver is pressure based (Projection Type), corrected via density for compressible flows. Turbulent flows can be treated in two ways: RANS statistical models and Scale Resolving Approaches like LES and its DES and V-LES variants. LES is built within a dedicated version, with specific routines for pressure coupling, boundary conditions, diffusive fluxes and near-wall stress integration. A 2nd order implicit scheme is used for time marching. The solvers employed for pressure-velocity coupling include: GMRES, GMG & AMG, from the PETSc solver library. In LES the motion of the super-grid turbulent eddies is directly captured, whereas the effect of the smaller scale eddies is modeled or represented statistically by means of simple models, very much the same way as in Reynolds-averaged models (RANS); i.e. the usual practice is to model the sub-grid stress tensor by an eddy viscosity model. The code *TransAT* proved very efficient for LES and DNS problems [16].

### 6.7.2.1 Highly-Resolved LES

A full DNS of this flow is difficult if one takes as reference published DNS of turbulent channel flow performed in Cartesian grids. The reasons are obvious:

- 1 the high Reynolds number typical to PWR's would require grids of hundreds (up to the billion) of M cells, in particular because the near-wall resolution is key in this context,
- 2 the complex bounding geometry implies use of non-Cartesian grids, which add numerical diffusion to the discretization scheme, unless use is made of the Immersed Boundary Technique [12].

The resort to LES [17] is thus a pragmatic and defendable choice, but the meshing level or concentration may be an issue and has to be clarified first. Indeed, while a coarse mesh would not allow predicting a large portion of the structures, a very fine mesh could return results that are close to DNS in that the non-resolved eddy viscosity is marginally important; this is the essence of the so-called 'Highly-resolved LES', which applies as a simple definition to problems in which the ratio of eddy to molecular viscosity does not exceed 1.5–2, in comparison with conventional LES where this ratio should fall in the range 5–10. Other measures have been introduced, including comparing the sub grid-scale eddy viscosity to the resolved turbulence.

### 6.7.2.2 The Filtered LES Equations

In LES the motion of the super-grid turbulent eddies is directly captured whereas the effect of the smaller scale eddies is modeled or represented statistically by means of simple zero-equation models, very much the same way as in Reynolds-averaged models (RANS); i.e. the usual practice is to model the sub-grid stress tensor by an eddy viscosity model. In terms of computational cost, LES lies between RANS and DNS and is motivated by the limitations of each of these approaches. Since the large-scale unsteady motions are represented explicitly, LES is more accurate and reliable than RANS. LES involves the use of a spatial filtering operation where the fluctuation of any variable from its filtered value. Filter function is invariant in time and space, and is localized. Applying the filtering operation to the instantaneous to the instantaneous Navier-Stokes equations under incompressible flow conditions leads to the system of filtered transport equations for turbulent convective flow (the equations are well known and are not repeated here), which involve the so-called SGS stress tensor and turbulent heat flux defined as:

$$\tau = \rho(\bar{u}_i \bar{u}_j - \bar{\bar{u}}_i \bar{\bar{u}}_j) \quad , \quad q_j'' = \bar{\rho}(\bar{T} \bar{u}_j - \bar{\bar{T}} \bar{\bar{u}}_j)$$

#### Eq. 6.7.1

Only the deviatoric part of the SGS stress tensor is to be modeled using a statistical approach similar to RANS. This way, turbulent scales larger than the grid size are directly solved, whereas the effects of SGS scales are modeled.

### 6.7.2.3 SGS Modeling

LES is based on the concept of filtering the flow field by means of a convolution product. The specific super-grid part of the flow with its turbulent fluctuating content is directly predicted whereas the sub-grid scale (SGS) part is modeled, assuming that these scales are more homogeneous and universal in behavior. For turbulent flows featuring a clear inertial subrange the modeling of the SGS terms in the statistical sense could thus safely borrow ideas from the RANS context, in particular use of the zero-equation model to mimic the momentum diffusive effects on the resolved field. Use is generally made of the Eddy Viscosity Concept, linking linearly the SGS eddy viscosity and thermal diffusivity to the gradients of the filtered velocity and temperature, respectively:

$$\tau_{ij} = -2\mu_{SGS}\bar{S}_{ij} + \frac{1}{3}\delta_{ij}\tau_{ll} \quad , \quad \mu_{SGS} = (C_s\Delta)^2\bar{\rho}|\bar{S}|^2$$

$$q_j'' = -\alpha_\theta \frac{\partial \bar{T}}{\partial x_j} \quad , \quad \alpha_\theta = \frac{\mu_{SGS}}{Pr_t}$$

### Eq. 6.7.2

The closure for the eddy viscosity above follows in general the *Smagorinsky* kernel model, linking the eddy viscosity to the square of a length scale and a time scale (the inverse of the second invariant of the resolved rate of deformation tensor  $S_{ij}$ ). The model constant ( $C_s$ ) is either fixed or made dependent on the flow; this latter option is precisely the spirit of the dynamic model. A damping function is often introduced for the model constant  $C_s$  to accommodate the asymptotic behavior of near-wall turbulence.

Similarly, the same strategy could be used to close the turbulent SGS heat flux, where the thermal diffusivity could be determined either based on the resolved thermal-flow field, or alternatively based on the eddy viscosity (defined dynamically) and a fixed turbulent Prandtl number. Using the first alternative means that the turbulent Prandtl number is not imposed but is a result of the model; this is known as the *Dynamic Smagorinsky Model (DSM)*. The advantage of DSM compared the base model is that (i) the constant  $C_s$  may be negative, which does not exclude possible backscatter of energy, (ii) it returns the proper asymptotic behavior of the stresses near the wall with damping as required by the base model, and (iii) vanishes in laminar flow without ad-hoc intermittency functions.

The DSM approach is based on the application of a twice-larger filter width on top of the filtered Navier-Stokes equations. The details about the determination of the dynamic length scale for both the thermal and flow field are given by Moin et al. [18]. Many authors resorted with success to this particular SGS model, e.g. Peng and Davidson [19] and many others.

### 6.7.3 Problem Description

The problem is inspired by the PSBT sub-channel benchmark [3] in terms of radial dimensions. Though the expected deliverables are different, the focus is on detailed flow and temperature profiles in the sub-channel, together with global parameters including the heat transfer coefficient, the onset of nucleation, the pressure drop and the thermal entry length. The operating conditions of the present case are made on purpose different from PSBT, namely the power and mass flow rate, which have been adjusted according to the reduced length (1m instead of 3.65 m). The PWR fuel assembly consists of a rod bundle with water coolant flowing upward along the rods at a high Reynolds number. The rod diameter is 9.5 mm, the rod pitch is 12.6 mm and the active fuel length is typically  $\sim 3.7$  m. The hydraulic diameter for a unit cell is  $D_e = 11.8$  mm.

The coolant pressure is 15.5 MPa with temperature ranging from 290 degree C to 340 degree C. Representative values of fluid properties are density:  $\rho = 710$  kg/m<sup>3</sup>; dynamic viscosity:  $\mu = 9 \times 10^{-5}$  Pa s; thermal conductivity:  $k = 0.54$  W/m-K; heat capacity:  $C_p = 5.9$  kJ/kg-K. The mass flux is  $G \sim 3700$  kg/m<sup>2</sup> s, corresponding to a Reynolds number  $Re = GD_e/\mu \sim 4.8 \times 10^5$ , shear velocity  $u_\tau \sim 0.2$  m/s, and frictional Reynolds number  $Re_\tau \sim 10^4$ .

Several simplifications were adopted here: First, the temperature of nucleation is assumed to be equal to the saturation temperature; second, a configuration consisting of the flow along a single sub-channel with periodic conditions is assumed; third, since the shear Reynolds number for the PWR

Pressure	15.5 MPa
Saturation temperature	344.6 °C
Inlet temperature	290 °C
Mass flux	3333 kg/m <sup>2</sup> s
Heat Flux	581 kW/m <sup>2</sup>
Power	2.7 MW

Table 6.7.1 Reference operating conditions for PSBT tests [3]

channel is  $Re_\tau \sim 10^4$ , performing DNS for such flow conditions would be computationally prohibitive.

As such, the problem has been scaled down to more reasonable conditions, i.e.  $Re_\tau = 300$ . Finally, the length of the domain was reduced from the PWR case to relax the meshing requirements in the axial direction. Since the distance to the onset of nucleate boiling depends on the integrated power (heat flux times rod surface area) supplied to the fluid, the heat flux was scaled accordingly; see **Table 6.7.2**. The PSBT operating conditions are summarized in **Table 6.7.1**. The actual (reduced) operating conditions are summarized in **Table 6.7.2**.

Pressure	15.5 MPa
Saturation temperature	344.6 °C
Inlet temperature	290 °C
Mass flux	74.1 kg/m <sup>2</sup> s (or $Re_\tau = 300$ )
Heat Flux	50 kW/m <sup>2</sup>
Power	1.57 kW

Table 6.7.2 Test case 2 operating flow conditions

#### 6.7.4 Problem Setup

##### 6.7.4.1 Computational Domain, Boundary Conditions & Mesh

The dimensions of the simulation domain and boundary conditions are indicated in **Figure 6.7.1**. The geometry features cross-sectional dimensions similar to the PSBT case; rod diameter  $D = 10$  mm and pitch  $P = 13$  mm. The length is reduced from 3.6 m to 1.0 m. A novel approach was used to generate proper boundary conditions for this flow. Periodic conditions were applied in the radial and circumferential directions to mimic the effect of the neighboring rods. In the axial direction, however,

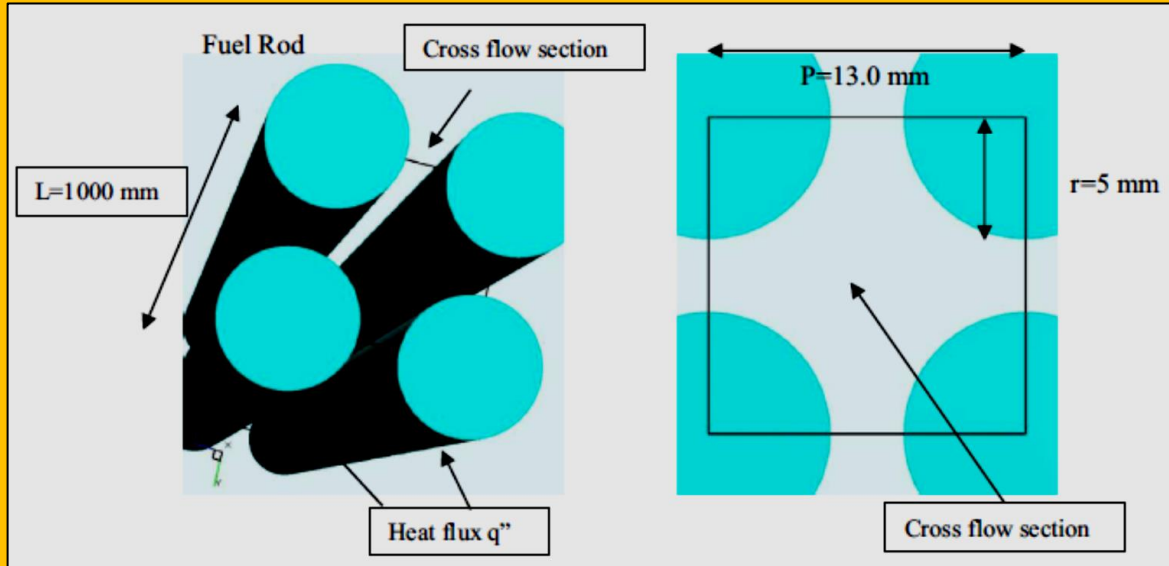


Figure 6.7.1 Computational Domain: Dimensions & B.C.s

a new technique has been developed to overcome this difficulty, known as the '*Developed & Developing Flow Hybrid Approach*'. It consists of first generating turbulence in a periodic domain of length  $2pD_e$ , then the resulting fluctuating (scaled to maintain the mass flow rate) field is imposed in the entire domain, recycled periodically: temperature is updated using inflow-outflow BCs. Two **Body-Fitted Co-ordinate (BFC) grids** were employed (**Table 6.7.3**): the medium one consists of 798 x 40 x 40 cells providing a near-wall resolution of  $y+ \sim 0.5 - 2.1$ , which allows resolving the viscous sublayer. The second grid consists of 1600 x 60 x 60 cells, providing a near-wall resolution of  $y+ \sim 0.4 - 1.5$ . (see **Figure 6.7.2**).

$Re_\tau = 300$	Number of nodes		Resolution		Grid type	Total number of cells
	$x-y$	$z$	$\Delta x^+ - \Delta y^+$	N blocks		
Grid Med	40–40	798	0.5–2.1	208	BFC	1,317,400
Grid Fine	60–60	1600	0.4–1.5	832	BFC	6,011,200

Table 6.7.3 Grid Properties Used For The LES And For The Highly-Resolved LES

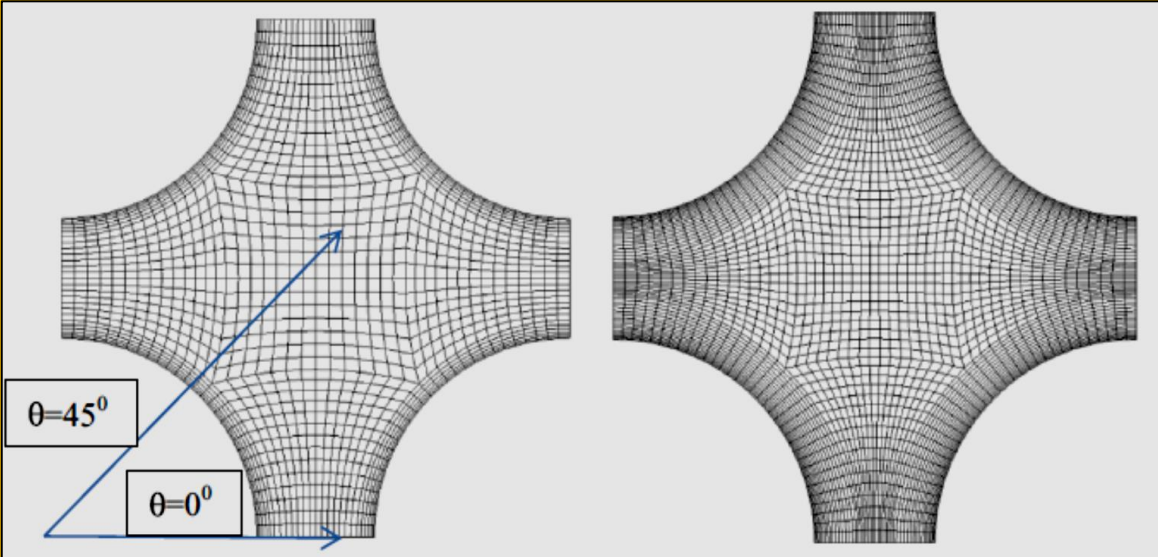


Figure 6.7.2 Medium (Left) And Fine (Right) Grids For LES (X-Y). Arrows Show 0 And 45 Degrees Segments

#### 6.7.4.2 Initial Conditions & Simulations Parameters

The initial flow conditions for the full domain were generated from an earlier flow solution obtained using cyclic inflow-outflow in a shorter  $2\pi D_e$  long domain. During this process, to speed up the turbulent flow generation, various grids of different refinements (coarse, medium and refined) were employed in a sequential way: the solution obtained on the coarse grid is mapped into the medium one, the solution of which is then passed to the fine mesh, which at the end is transferred to the final run as an initial/inflow/outflow condition. Assuming the flow to be non-homogenous with a dominant velocity fluctuation in the flow direction, component  $w_0$  (in the flow direction) fixed as the variance of  $u_s$ . The other components were defined as  $u' = 2/3w$  and  $w' = 1/3u$ . This process is innovative; it allows generating the fluctuating field to the finest mesh ( $60 \times 60$  in cross section) rather fast.

The simulations were performed on the DOE's leadership supercomputer TITAN located at ORNL, using 144 and 832 MPI cores for the medium and fine grids, respectively. The DSM model presented earlier was used in the context of LES. Statistical flow averaging was performed over 6 flow-through times for the medium grid and 4.5 flow-through times for the fine grid. The wall shear velocity  $u_s$  converged to 0.0065 m/s for the fine grid and to 0.0064 m/s for the medium one, as shown in [Figure 6.7.3](#).

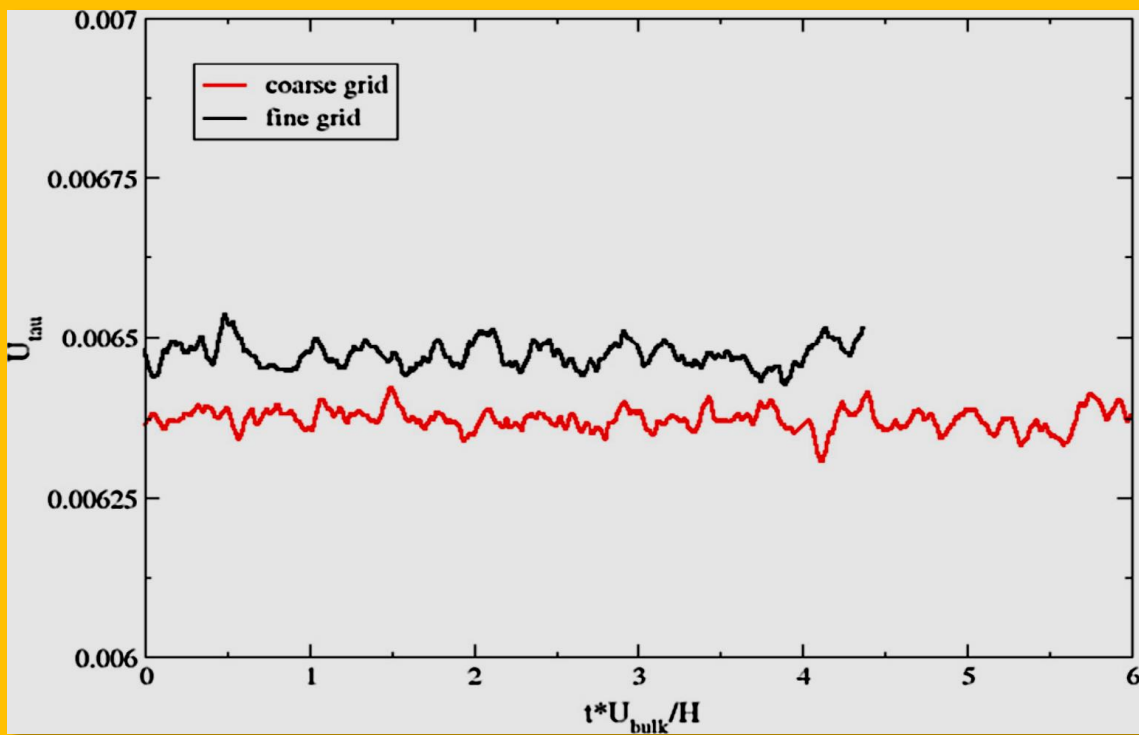


Figure 6.7.3 Frictional velocity evolution with non-dimensional time.

### 6.7.5 Flow Structures Results

The flow structure at various instances near the central area obtained for the medium and the fine grids are compared in **Figure 6.7.5**. While no major differences can be observed, the cross-sectional views show more structures developing in the fine grid simulation (left panel), as was to be expected. Temperature contours on the rod surface show intermittent patches related to turbulent eddies transporting heat from the wall to the core flow. **Figure 6.7.5** in particular (scaled view) shows the space development of the thermal field along the rod on its surface; the highest values are observed in the very upper portion of the rod. The results also confirm that the 'Developed & Developing Flow

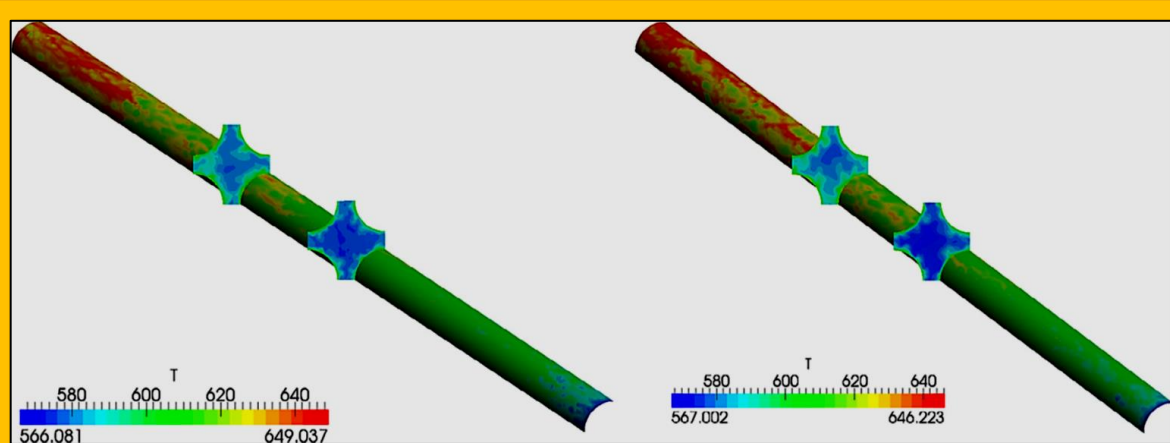


Figure 6.7.4 Fine (Left) Vs. Medium (Right) Grid: Instantaneous Cross-Sectional Velocities And Temperature Contours

'Hybrid Approach' developed for the purpose works well, in that the thermal field obtained is indeed space developing in contrast to the flow field.

The secondary-flow is discussed in the context of **Figure 6.7.5** and **Figure 6.7.6**, presenting instantaneous and time averaged cross-flow field and wall temperature fields. Important point to note is that the mean flow exhibits in both grid simulations a rather strong secondary flow motion, the effect of which can be perceived on the wall temperature contours, showing a patchy structure due to the intermittency of the mean and turbulent flow motions acting in tandem.

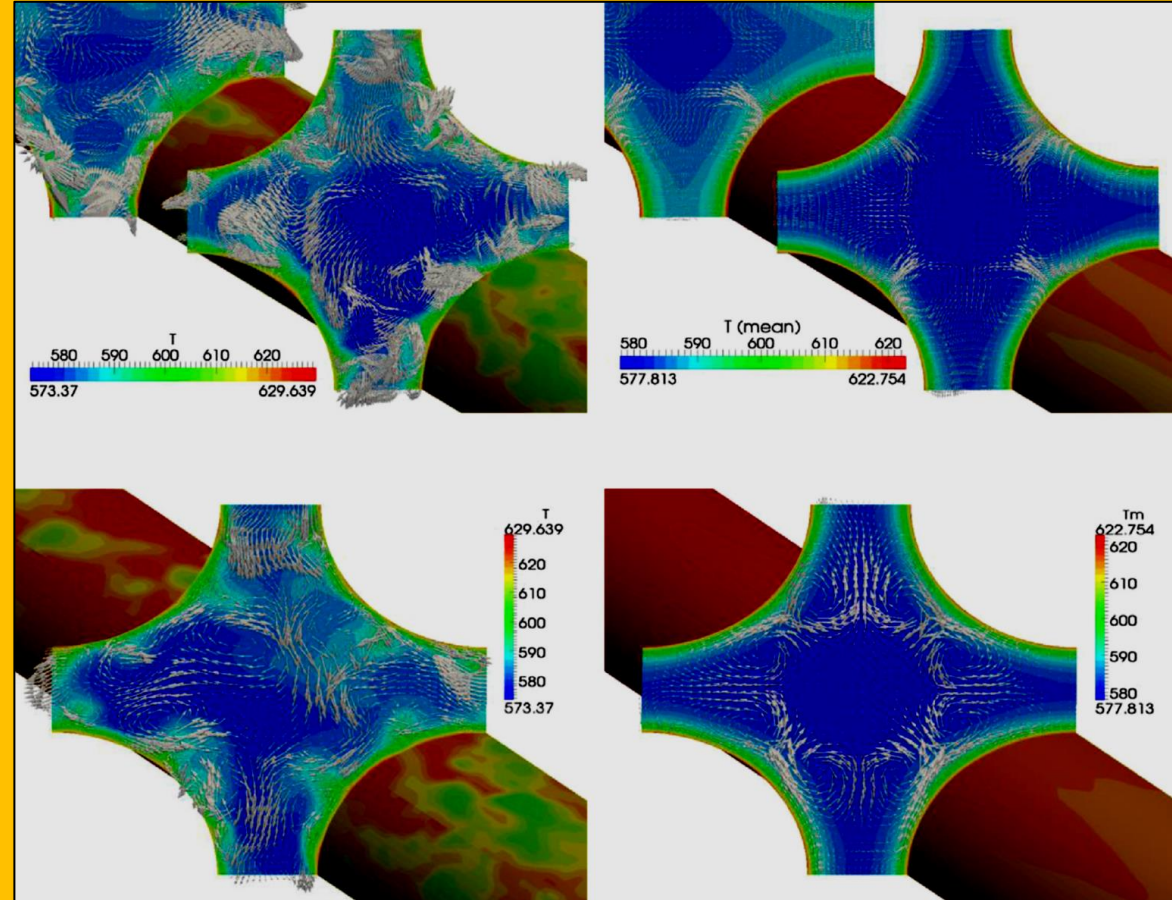


Figure 6.7.5 Fine vs. medium resolutions: Instantaneous (a and c) and time averaged (b and d) cross-sectional velocities and temperature contours

In order to quantify the strength of these cells, we introduce here a measure for the purpose in the form of the ratio of mean to turbulent cross-flow motion, referred to as the Secondary Flow Intensity (SFI), defined as:  $\text{Abs}(\langle U_V \rangle / u'v')$ . Our intention is to draw a map separating mean flow from turbulence dominated secondary-flow regions. The left panel of **Figure 6.7.7** showing contours of the shear stress ( $u_0 v_0$ ) in the cross flow reveals that this turbulent quantity is important in the near-wall region, as expected. The right panel indicates that the secondary flow intensity is dominated by the mean flow ( $\langle U_V \rangle$ ) motion near the wall ( $SFI \sim 1-2$ ), while the shear-induced counterpart prevails in the core flow region, where  $SFI \sim 0.1-0.2$ . This important result indicates that wall-to-flow heat transfer depends heavily on the secondary flow motion induced by the mean flow. The effect of these

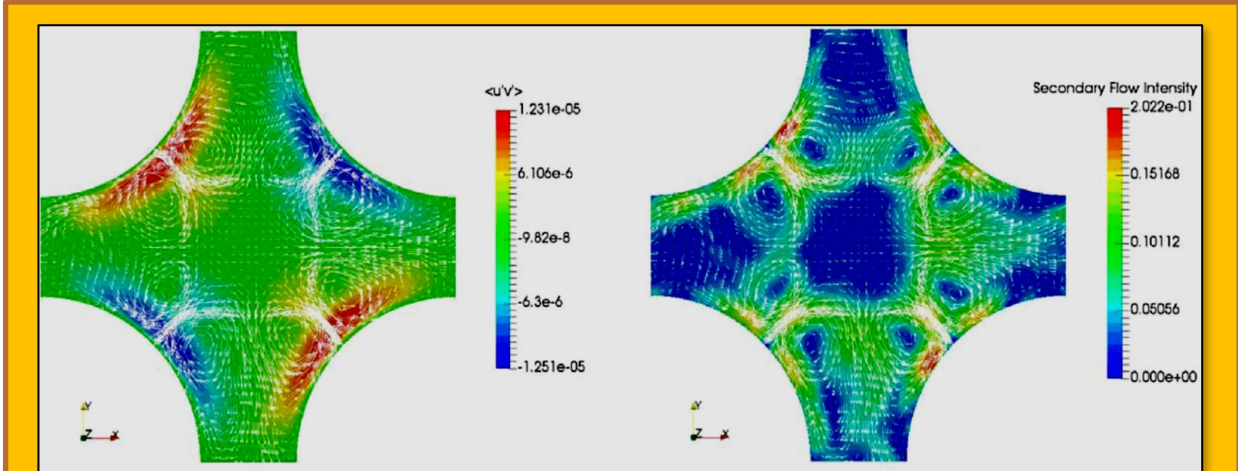


Figure 6.7.6 Time averaged cross-sectional shear-stress and secondary-flow intensity ( $|\tilde{U}\tilde{V}|=u_0 v_0$ ) contours

secondary-flow motions is clearly indicated by the instantaneous and time averaged temperature contours on the rod surface plotted in [Figure 6.7.8](#), indicating the position for saturation temperature marked by a black line. In both medium and fine-grid simulations, the line varies spatially by about 5–7% around the mean.

#### 6.7.5.1 Time Averaged Results

Time averaged results are presented in ([Figs. 9–13](#), [11–13](#) Not shown here), including flow and temperature mean and key turbulent profiles. Only fine-grid results are discussed; in most cases the medium-grid data were found globally close to the fine-grid results. Since the flow resembles turbulent flow in a pipe, use was made of available DNS data at  $Re_\tau = 360$  [20] for comparison. The DNS data are not filtered. The difference with the pipe flow is that the present one has two azimuthal segments, a short one ( $\theta = 0$  degree) with low  $Re$  effects and a full one ( $\theta = 45$  degree) extending to the core with high  $Re$  effects (see [Figure 6.7.2](#)).

The latter one should thus return the imposed shear Reynolds number at the subchannel center point, in the form of  $y+p$  center line =  $Re_\tau$ . The mean velocity profiles are plotted in [Figure 6.7.9](#). As explained earlier, the  $\theta = 0^\circ$  segment profile achieves a lower  $y+$  ( $\sim 90$ ) than the  $\theta = 45^\circ$  one. The profiles match very well the DNS data of [Eggels et al. [20], with an insignificant difference in the  $y+$  interval 40–90. This preliminary important result pleads in favor of a high quality highly-resolved LES achieved by CFD code *TransAT*.

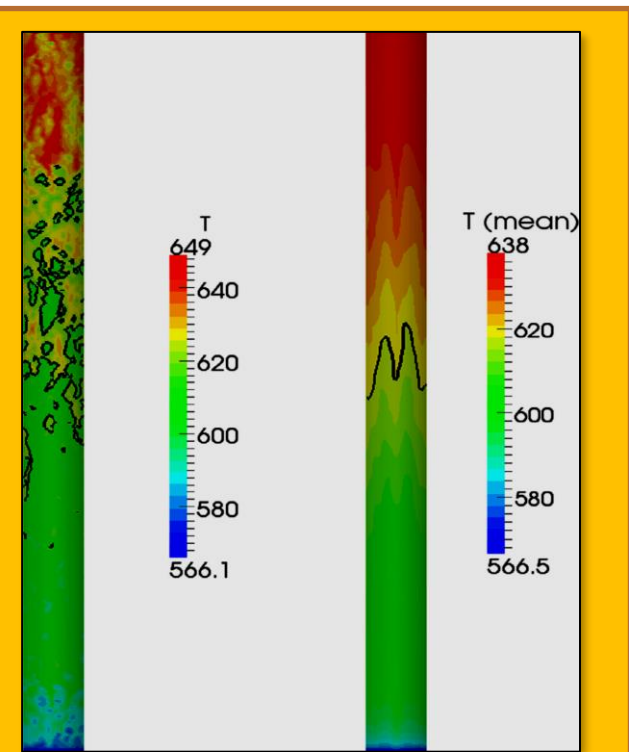


Figure 6.7.7 Fine vs. medium resolutions (scaled domain for illustration): Instantaneous and time averaged temperature contours. The black line on the right panel indicates  $X_{onb}$ , the position of  $T_{sat}$

**Figure 6.7.10** presents the mean temperature profiles normalized using  $\Delta T = (T_{\text{sat}} - T_{\text{in}})$  across the subchannel at various streamwise locations, for both segments:  $\theta = 0^\circ$  (left panel) and  $\theta = 45^\circ$  (right panel). The plots reveal deviations very close to the wall, pointing to different shapes and slopes of the thermal boundary layer, which seems to develop to about  $0.3R$  in the  $\theta = 0^\circ$  segment, against  $0.2R$  for the  $\theta = 45^\circ$  segment.

As was reported already by Ikeno and Kajishima [12] from their simulations, while the  $\theta = 45^\circ$  section exhibits a full turbulent flow profile, the  $\theta = 0^\circ$  segment results reveal strong low-Re effects, a characteristics feature specific to narrow gap zones in subchannel flows. For a complete discussion, please refer to [[Djamel Lakehal](#)]<sup>55</sup>.

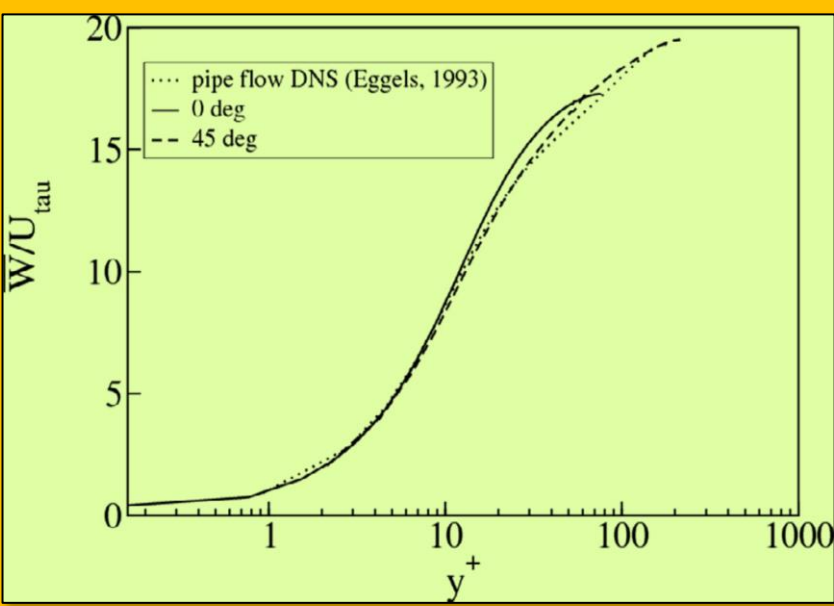


Figure 6.7.8 Mean velocity profiles across the subchannel ( $0^\circ$  &  $45^\circ$ ) compared to the DNS of Eggels et al. [20].

### 6.7.5.2 Energy Spectra Results

Results obtained with the medium grid are compared in **Figure 6.7.11**. Overall the same trend is observed as to the three velocity components, albeit some subtle differences do pertain as to the decay rate. As was to be expected from the flow statistics, energy carried out by the largest scales (f

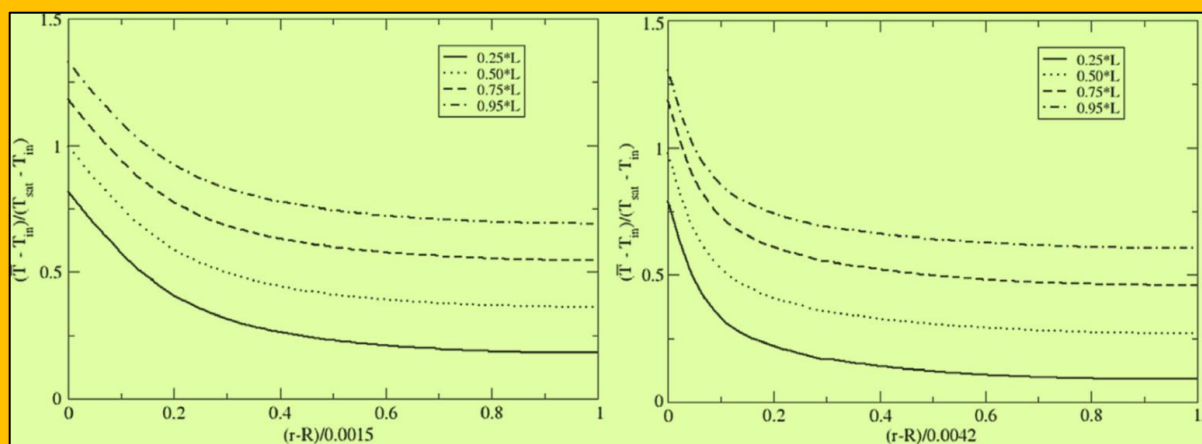


Figure 6.7.9 Mean Temperature Profiles Across The Subchannel At Various Streamwise Locations

<sup>55</sup> Djamel Lakehal, "Highly-resolved LES of turbulent convective flow along a PWR rod bundle", International Journal of Heat and Mass Transfer 122 (2018) 785–794.

$< 1 \text{ Hz}$ ) is essentially concentrated in the axial velocity component  $W$ , although the other two components carry similar amounts in the high-frequency range ( $f > 1 \text{ Hz}$ ), with a decay behavior smoother in the flow directions than the other directions. The result discussed in **Figure 6.7.12** is interesting in that it depicts other phenomena occurring at the highest-frequency range: The decay in the smallest scales range seems indeed to be rather peculiar, exhibiting a sharp drop in the range  $10 < f < 25\text{--}30 \text{ Hz}$ , before adjusting to the  $-5/3$  slope in the interval  $30 < f < 700 \text{ Hz}$ . This peculiar behavior was actually observed in the experiments conducted by Rehme [5], who pointed out to the effect of large-scale structures. The absence of a clear peak in the power spectrum translating the coherent pulsations as was found by Rehme [5] and Meyer [7] in the low frequency range ( $< 10 \text{ Hz}$ ) is due to the limitation of size of the domain and periodic conditions applied in this LES context.

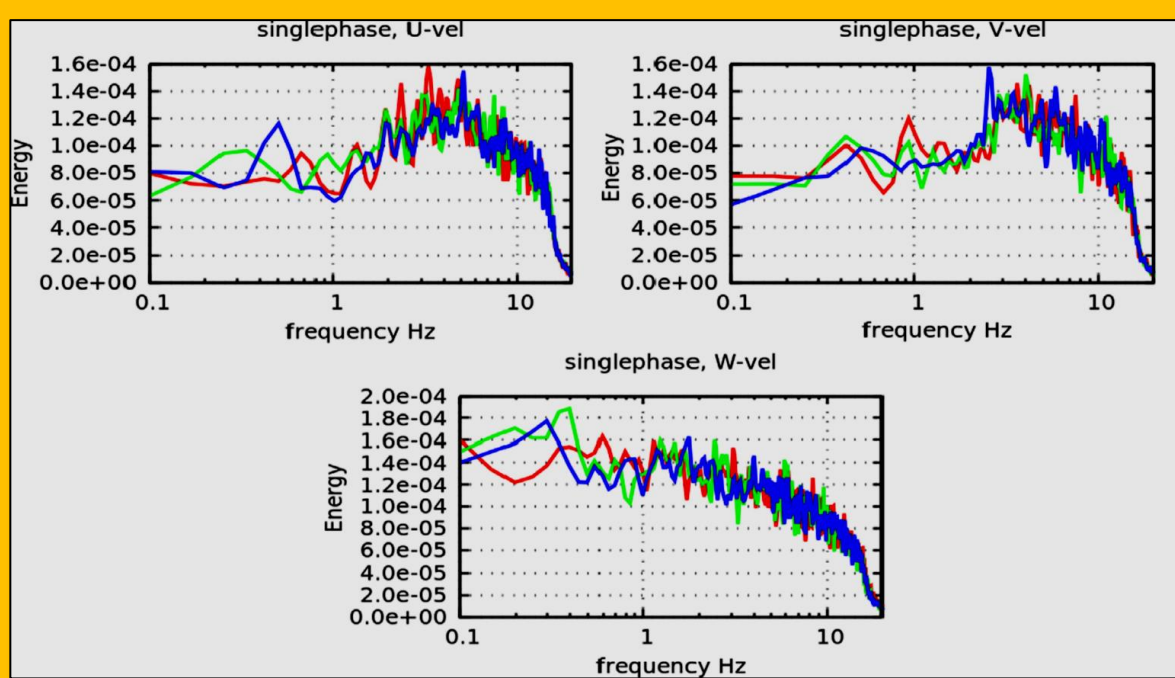


Figure 6.7.10 Low-frequency PSD of  $U$ ,  $V$  and  $W$  at various locations ( $z/L = 0.55, 80$  and  $95$ ).

### 6.7.5.3 Global Parameters Results

Global parameters results are presented in **Table 6.7.4**. The LES results are compared here to existing analytical and experimental correlations. The pressure drop between medium and fine grid is accurate to 2.2% and 5% compared to the correlation. As to the heat transfer coefficient (HTC), there are uncertainties for the case of interest, which in fact belongs to the ‘transitional cases regime’, according to Incropera and DeWitt [4], for which the correlations, in particular the Colburn one (or Dittus-Boelter), could give up to 25% error. When accounting further for the effect of neighboring rods using the Weisman correction (here  $= 1.826p/D - 1.043 = 1.33$ ), the deviations between LES and correlation is high, and is precisely 33%. If this correction is not accounted for, the LES results (fine grid in particular) are comparable to the Colburn correlation, within -5%. With more sophisticated correlations e.g. the Gnielinski and Petukov (see [4]), the analysis changes, in that the LES data are 6% than Gnielinski’s correlation and 1.9% only than Petukov’s one.

The distance to the onset of boiling is questionable in the same way, since it is directly based on the HTC correlation employed (here we took the Colburn one only). The simulation results are within a few percent’s deviations from the Colburn correlation, but 24–35% off the Colburn–Weisman variant, which is in line with the HTC deviations reported. Finally, as stated previously, there is no such a

constant line indicating  $X_{ONB}$  since the simulations have clearly shown that the effect of the secondary flow motion makes it rather undulating by 5–7% around the mean.

### 6.7.6 Conclusions

The paper reports a detailed simulation analysis of turbulent convective flow upward along the heated rods of a PWR subchannel using the CFD/CMFD code *TransAT*. Boiling effects were not considered. Turbulence was predicted using highly-resolved LES with the fine grid consisting in 6 M cells, for which the sub grid scale viscosity produced by the model was found to be of marginal effect. A novel technique known as the ‘Developed & Developing Flow Hybrid Approach’ has been developed, which consists in generating turbulence along the rod in a periodic domain, assuming developed flow conditions, while treating the temperature as a space-developing field. The comparison of the LES results with existing DNS of pipe flow shows a very good agreement as to first-order turbulence statistics. Higher-order statistics were found to require much more simulation samples to achieve ergodic flow statistics.

The results including key features specific to rod bundles were thoroughly

discussed, including low-Re effects in the narrow gap zone. The simulations revealed important information on the mechanism of secondary-flow motion and its intensity, which has been partitioned into mean and turbulent contributions. It is shown that the mean-flow contributes mostly to the secondary flow near the wall, while the turbulent part dominates the mechanism in the core flow region. The secondary-flow motion induced by the mean flow can thus be responsible for most of the heat transfer from the wall to the flow field.

The comparison with correlations as to engineering parameters show that excellent results are obtained for pressure drop, but raise important questions as to the validity of heat-transfer

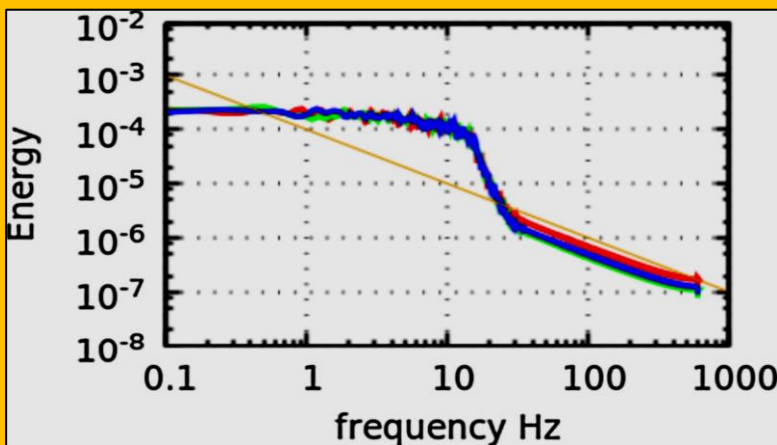


Figure 6.7.11 Low- & high-frequency PSD of W velocity at various locations ( $z/L = 0.55, 80$  and  $95$ ).

Quantity	Med. grid	Fine grid	Analytical/Exp.
Pressure drop $\Delta P$ [Pa]	10.223	10.52	10.0
Heat transfer coefficient (HTC) at $X_{ONB}$ [ $\text{kW}/\text{m}^2 \text{K}$ ]	1.495	1.535	1.62 (Colburn) 2.16 (Colburn-W*) 1.44 (Gnielinski) 1.99 (Gnielinski-W) 1.50 (Petukov) 2.0 (Petukov-W)
Distance to $X_{ONB}$ [m]	Min-max 0.49–0.57	Min-max 0.49–0.6	0.59 (Colburn) 0.79 (Colburn-W)
Thermal entry length [m]	Min-max 0.21–0.28	Min-max 0.21–0.29	0.29–0.46

\* W means with the Weisman (1959) correction factor.

Table 6.7.4 Test Case 2 Operating Flow Conditions

coefficient correlations in this transitional regime, and indirectly the location of onset of nucleate boiling. A data basis has been generated for RANS model comparison, and can be made available for use to address the predictive performance of these models. The simulation campaign has since then been extended to boiling heat transfer.

#### 6.7.6.1 Conflict of Interest

I hereby testify that there is no conflict of interest to invoke regarding the content of this paper.

#### 6.7.6.2 Acknowledgements

This work was financially supported by the US Department of Energy through the CASL project (Subcontract 4000107101). The simulations were performed on TITAN supercomputer located at ORNL Oak Ridge, TN, USA. The authors would like to acknowledge the support of the MIT team: Prof. J. Buongiorno and Dr D. Chatzikyriakou. The simulations were conducted and monitored by Daniel Caviezel.

### 6.7 References

- [1] J.G. Collier, J.R. Thome, *Convective Boiling and Condensation*, 3<sup>rd</sup> Ed., Oxford University Press, 1996.
- [2] TransAT. ASCOMP software package, 2017. <<http://www.ascomp.ch/transat>>.
- [3] A. Rubin et al., *OECD/NRC Benchmark based on NUPEC PWR subchannel and Bundle Tests (PSBT)*, NEA/NSC/DOC, 2010.
- [4] H. Incropera, J. DeWitt, *Intl. Heat Transfer*, 3<sup>rd</sup> Ed., Wiley & Sons, 1996.
- [5] K. Rehme, The structure of turbulence in rod bundles and the implications on natural mixing between the subchannels, *Int. J. Heat Mass Transfer*. 35 (2)(1992) 567–581.
- [6] D.S. Rowe, B.M. Johnson, J.G. Knudsen, Implications concerning rod bundle crossflow mixing based on measurements of turbulent flow structure, *Int. J. Heat Mass Transfer* 17 (1974) 407–419.
- [7] L. Meyer, *From discovery to recognition of periodic large scale vortices in rod bundles as source of natural mixing between subchannels: a review*, *Nuclear Eng. Des.* 240 (6) (2010) 1575–1588.
- [8] W.J. Seale, *Measurements and predictions of fully developed turbulent flow in a simulated rod bundle*, *J. Fluid Mech.* 123 (1982) 399–423.
- [9] V. Vonka, *Measurement of secondary flow cortices in a rod bundle*, *Nuclear. Eng. Des.* 106 (1988).
- [10] D. Chang, S. Tavoularis, *Simulations of turbulence, heat transfer and mixing across narrow gaps between rod-bundle subchannels*, *Nuclear Eng. Des.* 238 (1) (2008) 109–123.
- [11] T. Ikeno, T. Kajishima, *Decay of swirling turbulent flow in rod-bundle*, *J. Fluid Sci. Technol.* 1 (1) (2006) 36–47.
- [12] T. Ikeno, T. Kajishima, *LES of turbulent flow in subchannel and analysis of driving force of secondary flow*, *J. Fluid Sci. Technol.* 2 (2) (2007) 480–489.
- [13] T. Ikeno, T. Kajishima, *Analysis of dynamical flow structure in a square arrayed rod bundle*, *Nuclear Eng. Des.* 240 (2) (2010) 305–312.
- [14] E. Merzari, H. Ninokata, E. Baglietto, *Numerical simulation of flows in tight lattice fuel bundles*, *Nuclear Eng. Des.* 238 (7) (2008) 1703–1719.
- [15] H. Ninokata, E. Merzari, A. Khakim, *Analysis of low Reynolds number turbulent flow phenomena in nuclear fuel pin subassemblies of tight lattice configuration*, *Nuclear Eng. Des.* 239 (5) (2009).
- [16] D. Chatzikyriakou, J. Buongiorno, D. Caviezel, D. Lakehal, *DNS and LES of turbulent flow in a closed channel featuring a pattern of hemispherical roughness elements*, *Int. J. Heat Fluid Flow* 53 (2015).
- [17] P. Sagaut, *Large Eddy Simulation for Incompressible Flows: An Introduction*, Springer Pubs., 2005.
- [19] S.H. Peng, L. Davidson, *Large eddy simulation for turbulent buoyant flow in a confined cavity*, *Int. J. Heat Fluid Flow* 22 (3) (2001) 323–331.
- [20] J.G.M. Eggels, F. Unger, M.H. Weiss, J. Westerweel, R.J. Adrian, R. Friedrich, F.T. M. Nieuwstadt, *Fully developed turbulent pipe flow: a comparison between direct numerical simulation and experiment*, *J. Fluid Mech.* 268 (1994) 175–209.

- [21] F. Unger, R. Friedrich, *Large eddy simulation of fully-developed turbulent pipe flow*, in: Proc. 8th Sym. on Turbulent Shear Flows, Sep. 1991, Munich, Germany, 1991, 19/3/1-19/3/6.

## 6.8 Case Study 8 – 2D Evaluation of Combined Delaunay Triangulation and Remeshing for Finite Element Analysis of Conductive Heat Transfer

**Authors :** Sutthisak Phongthanapanich and Pramote Dechaumphai

**Affiliations :** Mechanical Engineering Department, Chulalongkorn University, Bangkok, Thailand

**Title of Paper :** Evaluation of Combined Delaunay Triangulation and Remeshing for Finite Element Analysis of Conductive Heat Transfer

**Citation :** Sutthisak Phongthanapanich and Pramote Dechaumphai. Evaluation Of Combined Delaunay Triangulation And Remeshing For Finite Element Analysis Of Conductive Heat Transfer. Transactions of the Canadian Society for Mechanical Engineering. 27(4): 319-339. <https://doi.org/10.1139/tcsme-2003-0018>

### 6.8.1 Abstract

A finite element method is combined with the Delaunay triangulation and an adaptive remeshing technique to solve for solutions of both steady-state and transient heat conduction problems [[Phongthanapanich & Dechaumphai](#)]<sup>56</sup>. The Delaunay triangulation and the adaptive remeshing technique are explained in detail. The solution accuracy and the effectiveness of the combined procedure are evaluated by heat transfer problems that have exact solutions. These problems include steady-state heat conduction in a square plate subjected to a highly localized surface heating, and a transient heat conduction in a long plate subjected to a moving heat source. The examples demonstrate that the adaptive remeshing technique with the Delaunay triangulation significantly reduce the number of the finite elements required for the problems and, at the same time, increase the analysis solution accuracy as compared to the results produced using uniform finite element meshes.

### 6.8.2 Nomenclature

$\alpha$  = alpha coefficient

$\beta$  = beta coefficient

$\lambda_i$  = principal quantity

$\lambda_{\max}$  = maximum second derivatives for all elements

$\varepsilon$  = surface emissivity

$\sigma$  = Stefan-Boltzmann constant

$\rho$  = density

$\xi$  = local coordinate

$A$  = element area

{B} = boundary nodal vector

[ $D_x$ ], [ $D_y$ ] = element matrices

E, F = x and y heat flux components

H = parameter

L = plate length

[M] = mass matrix

[N] = element interpolation function matrix

Q = volumetric heat

{P<sub>k</sub>} = set of voronoi

{V<sub>k</sub>} = set of voronoi boundary

{R} = element nodal vector

T = temperature

T<sub>r</sub> = medium temperature for radiation

T<sub>∞</sub> = surrounding medium temperature for convection

U = conservation variable

X, Y = principal directions

c = specific heat

dpi = nodal distribution value

h = convection coefficient or plate width

h<sub>i</sub> = proper element size

h<sub>min</sub> = minimum element size specified by users

k = thermal conductivity

l, m = direction cosines

q<sub>s</sub> = specified surface heating

q<sub>x</sub>, q<sub>y</sub> = heat flux components

t = plate thickness

v = velocity

w = width of the moving heat source

y = local coordinate

<sup>56</sup> Sutthisak Phongthanapanich and Pramote Dechaumphai, "Evaluation of Combined Delaunay Triangulation And Remeshing For Finite Element Analysis of Conductive Heat Transfer", Mechanical Engineering Department, Chulalongkorn University, Bangkok, Thailand.

### 6.8.3 Introduction

Domain discretization into a number of elements is the first step in the finite element analysis. Due to the ever increasing complexity of the domains, new improved general-purpose mesh generation algorithms have been in high demand. The Delaunay triangulation, based on the concept of the Voronoi diagram [1,2] is one of the automated mesh generation algorithms that has recently gained popularity. The algorithm can generate mesh of arbitrary geometry for both simply connected and multi-boundary domains. The procedure that is capable of generating mesh with proper nodal density and regularity of the triangulation for arbitrary two-dimensional geometry was first introduced by Weatherill and Hassan [3] and revised by Karamete *et. al.* [4]. In this paper, the Delaunay triangulation which constructs triangular meshes for both the steady-state and transient heat conduction analyses is described in details. In addition, an adaptive remeshing technique is developed and incorporated into the Delaunay triangulation in order to improve the solution accuracy of the finite element method. The technique generates an entirely new mesh based on the solution obtained from the previous mesh such that elements in regions with large changes of solution gradients become smaller and elements in areas with little changes of solution gradients grow larger.

An adaptive remeshing technique combined with the Delaunay triangulation has been developed recently to improve the efficiency and solution accuracy of the high-speed compressible flow analysis [5]. For time-dependent heat conduction problems, especially where the thermal loads (such as the heat source) have magnitudes which vary with time and move along the body of the structure, the mesh employed must adapt itself both in time and space (mesh movement) to accurately capture the transient temperature response. This paper extends the adaptive remeshing technique by using the Delaunay triangulation to deal with both steady-state and transient heat transfer problems and demonstrates its effectiveness in accurately predicting the temperature solution of a plate subjected to a highly localized surface heating and transient temperature response in the structure. The equations for heat transfer in the structure and a finite element solution algorithm are briefly described. The basic concepts of the transient adaptive remeshing technique using the Delaunay triangulation and its incorporation in the solution process are explained. The effectiveness of the adaptive remeshing technique is demonstrated by the steady-state thermal analysis of a plate subjected to a highly localized surface heating and the transient thermal analysis of a plate subjected to a moving heat source.

### 6.8.4 Finite Element Thermal Analysis

#### 6.8.4.1 Governing Differential Equations and Boundary Conditions

The thermal response of the structure in two dimensions is governed by the heat conduction equation that can be written in the conservation form as,

$$\frac{\partial U}{\partial t} + \frac{\partial E}{\partial x} + \frac{\partial F}{\partial y} = Q$$

**Eq. 6.8.1**

where the conservation variable  $U$  and the heat flux components  $E$  and  $F$  are,

$$U = \rho c T , \quad E = q_x = -k \frac{\partial T}{\partial x} , \quad F = q_y = -k \frac{\partial T}{\partial y}$$

**Eq. 6.8.2**

and  $Q$  is the volumetric heat. The heat flux components  $q_x$  and  $q_y$  are related to the temperature gradients by **Fourier's law**. The heat conduction equation shown in **Eq. 6.8.1** is to be solved together with an appropriate **initial condition** of,

$$T(x, y, o) = T_0(x, y)$$

**Eq. 6.8.3**

and ***boundary conditions*** that may consist of,

$$\begin{aligned} T(x, y, t) &= T_1(x, y, t) && \text{specified temperature} \\ q &= q_s && \text{specified surface heating} \\ q &= h(T_s - T_\infty) && \text{surface convection} \\ q &= \varepsilon\sigma(T_s^4 - T_r^4) && \text{surferadiation} \end{aligned}$$

**Eq. 6.8.4**

where  $q$  is the conduction heat flux normal to the surface boundary,  $h$  is the convection coefficient,  $T_\infty$  is the medium temperature for convection,  $\varepsilon$  is the surface emissivity,  $\sigma$  is the Stefan-Boltzmann constant, and  $T_r$  is the medium temperature for radiation.

#### 6.8.4.2 Finite Element Equations

The finite element equations are derived from [Eq. 6.8.1](#) by using the Taylor-Galerkin algorithm described in [6]. The basic concept of the Taylor-Galerkin algorithm is to use Taylor-series expansion in time to establish recurrence relations for time marching, and the method of weighted residuals with Galerkin's criterion for spatial discretization. The key feature of the algorithm is to assume the distribution of the element heat fluxes  $E$  and  $F$  in the same form as the element temperature distribution  $T$ , that is,

$$\begin{aligned} T(x, y, t) &= N(x, y)T(t) \\ E(x, y, t) &= N(x, y)E(t) \\ F(x, y, t) &= N(x, y)F(t) \end{aligned}$$

**Eq. 6.8.5**

where  $N(x, y)$  is the element interpolation function [7], and  $T(t)$ ,  $E(t)$  and  $F(t)$  are the vectors of the element nodal quantities. The finite element equations obtained are in the form,

$$[M](\Delta U)^{n+1} = \Delta t([D_x]\{E\}^n + [D_y]\{F\}^n + \{R\}^n + \{B\}^n)$$

**Eq. 6.8.6**

where  $\{\Delta U\}^{n+1}$  is the nodal conservation variable increment at the time step  $n+1$ , and  $[M]$  is the mass matrix defined by,

$$\{\Delta U\}^{n+1} = \{U\}^{n+1} - \{U\}^n$$

**Eq. 6.8.7**

$$[M] = \int_A \{N\}[N]dA$$

**Eq. 6.8.8**

where  $A$  is the element area. On the right side of [Eq. 6.8.6](#),  $\Delta t$  denotes the time step, and the matrices  $[D_x]$  and  $[D_y]$  are,

$$[D_x] = \int_A \left\{ \frac{\partial N}{\partial x} \right\} [N]dA , \quad [D_y] = \int_A \left\{ \frac{\partial N}{\partial y} \right\} [N]dA$$

**Eq. 6.8.9**

The element nodal vector  $\{R\}$  associated with the heat source  $Q$  is defined as,

$$\{R\} = \int_A \{N\} Q dA$$

**Eq. 6.8.10**

The vector  $\{B\}$  representing the boundary nodal vector is defined as,

$$\{B\} = \int_S \{N\} [N] dA (l\{E\} + m\{F\}) = \int_S \{N\} [N] dA \{q\}$$

**Eq. 6.8.11**

where  $l$  and  $m$  are the components of a unit vector normal to the element boundary. The vector  $\{q\}$  appearing in the equation may be replaced by different types of boundary conditions as shown in [Eq. 6.8.4](#). In addition, if the mass matrix in [Eq. 6.8.8](#) is lumped, the finite element equations ([Eq. 6.8.6](#)) can be solved explicitly, thus avoiding the solution of a set of simultaneous equations. For steady-state case, the left-hand-side of [Eq. 6.8.6](#) becomes zero. Nodal temperatures are solved by using [Eq. 6.8.5](#) and [Eq. 6.8.2](#).

## 6.8.5 Delaunay Triangulation For Thermal Analysis

### 6.8.5.1 Concept and Algorithms Survey

**Bowyer [1]** and **Watson [2]** proposed the method of Dirichlet tessellation or Voronoi diagram, by which a domain is decomposed into a set of packed convex polygons. For a given set of points in space,  $\{P_k\}, k=1, \dots, n$ , the regions  $\{V_k\}, k=1, \dots, n$ , are boundaries assigned to each point  $P_k$  and represent the space closer to  $P_k$  than to any other points in the set. Therefore, these regions satisfy,

$$V_k = \{P_i : |p - P_i| < |p - P_j|, \forall j \neq i\}$$

**Eq. 6.8.12**

[Eq. 6.8.12](#) says that the area in the domain identified by any points  $p$  is the Voronoi of the point  $P_i$  if and only if the distance from points  $p$  to  $P_i$  is less than distance from points  $p$  to other points  $P_j$ . If all the points which have some segments of a Voronoi boundary in common [ $D_y$ ] are joined, the resulting shape is a Delaunay triangulation as shown in [Figure 6.8.1](#). In graph theory, the characteristic of Delaunay triangulation can be defined such that the graph which any circle in the plane is said to be empty if it contains no vertex in its interior. This defining characteristic of the Delaunay triangles is called the empty circumcircle property.

Among the methods for Delaunay triangle construction, the Bowyer-Watson

algorithm [1,2] is not highly complicate. The main procedure uses the empty circle property, or the Delaunay criterion, to control the modification of the existing Delaunay triangulation through node insertion. For simplicity of the domain triangulation, the incremental insertion algorithm of Lawson [8], which is based on edge flips, is a method of choice. By inserting a node into the domain, the triangle that contains the node is refined. A local non-Delaunay edge is flipped and the triangulation

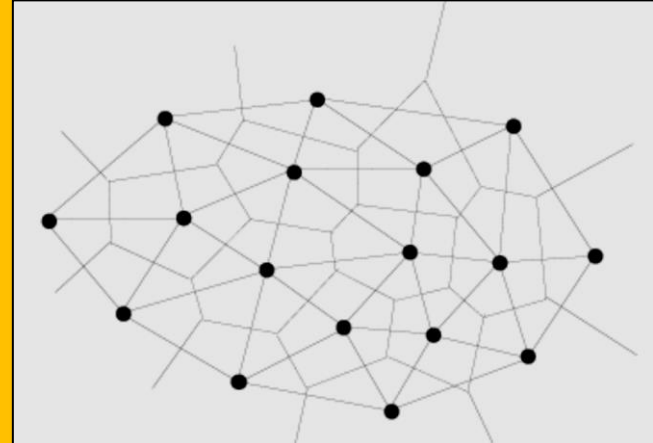


Figure 6.8.1 Delaunay triangulation dual of Voronoi diagram for a given set of points

is globally Delaunay. The Divide-and-Conquer algorithm [9] was also proposed for Delaunay triangulation. The algorithm starts by sorting the nodes in  $x$ -direction, then the domain is perpendicularly split. The Delaunay triangulation of each part is computed recursively and the resulting mesh are merged together. An optimization of the Divide-and-Conquer algorithm, proposed by Dwyer [10], splits the set of nodes into vertical strips. The final mesh is constructed by merging the resulting triangulation of each strip along the horizontal and the vertical lines. The Sweep line algorithm of Fortune [11] is another algorithm that starts by sweeping a line up in a  $y$ -direction and successively considers encountered nodes for triangular construction. The  $x$ -coordinate of a point to be located is bucketed to get close to the correct frontier edge, and then the algorithm walks to the left or right until it reaches the correct edge. As each node is encountered by the sweep line, new bisectors of the lines joining two nodes are introduced. The triangle, formed by three nodes, has the point of intersection of three bisectors as the circumcenter.

#### 6.8.5.2 Mesh Generation Procedure

The **Bowyer-Watson algorithm** is implemented in this paper because of its simplicity for mesh generation. In this algorithm, when a new vertex is inserted, each triangle whose circumcircle contains the new vertex is no longer Delaunay and is thus deleted all other triangles remain Delaunay are left undisturbed. Each vertex of the insertion polyhedron is then connected to the new vertices creating a new edge. The algorithm was then extended and applied to an unsteady high-speed compressible flow analysis [5]. In this paper, the algorithm is extended to both steady-state and transient thermal analyses. The key idea of the algorithm is summarized in the algorithm I below;

##### **Algorithm I; Delaunay Triangulation**

1. Let  $P$ ,  $k = 1, \dots, n$ , be the set of nodes on the boundaries of domain that stored in sequence of counter-clockwise direction for all outside boundaries and clockwise direction for all inside boundaries. Let  $T$  be the empty set of Delaunay triangles.
2. Let  $p_i$  be a node number  $i$  in the set  $P$  and  $t_i$  be a triangle number  $i$  in the set  $T$ .
3. Create an initial convex hull triangle that contains all boundary nodes inside. Add the triangle to  $T$ .
4. Read next boundary node  $p_i$  from  $P$ .
5. Search triangle  $t_i$  in  $T$  which contains the node  $p_i$  inside. The search starts from the triangle which was formed last and uses Lawson's algorithm [8,12] to march from one triangle to the next in the direction of  $p_i$ . This algorithm performs the shortest path searching strategy and removes the need to search through the entire domain.
6. Destroy surrounding triangles of  $t_i$  which lie within a circle centered at a vertex of the Voronoi diagram. Delete these triangles from  $T$ . Then form the new triangles that are connected to the node  $p_i$ . These triangles must pass the in-circle criterion. Add new forming triangles into  $T$  and determine the neighboring triangles of the triangles.
7. Repeat steps 4 to 6 until all nodes in  $P$  are considered.
8. Search for all triangles that have one or more vertices connected to any vertices of initial convex hull triangles outside the domain or lie inside holes in the domain and delete these triangles from  $T$ .

#### 6.8.5.3 Automatic Node Creation Procedure

The Delaunay triangulation algorithm described above does not explain the method for creating new nodes inside the domain. So far, researchers have introduced several approaches for creating new nodes inside the domain by refining boundary triangles such that the set of boundary points guide new node placements [13,14,15]. With the Rebay's algorithm [15], the new node is placed on the Voronoi segment associated with a triangulation edge which chosen in an attempt to generate a new triangle with prescribed size at its position. The automatic point creation procedure in this paper was derived from the algorithm suggested by Weatherill and Hassan [3] and Karamete *et. al.* [4]. The shape and size of triangles or density of nodes inside the domain are controlled by two coefficients, the Alpha and the Beta coefficients. The Alpha coefficient controls node density by changing the

allowable shape of the formed triangles. The Beta coefficient controls the regularity of triangulation by disallowing node within a specified distance of each other to be inserted in the same sweep of the triangles within the field. The suggested values of both the Alpha and the Beta coefficients for coarse and fine triangular mesh are 0.8 and 0.9, and 0.5 and 0.6 respectively.

The main idea of the automatic node creation procedure is the search for the triangle that conforms with both Alpha and Beta testing criteria and a new node placement at the centroid of that triangle. New triangles can then be created by Delaunay triangulation algorithm as described in algorithm I. The detailed implementation of the automatic node creation procedure is described in algorithm II as follows.

### **Algorithm II; Mesh Refinement**

1. Let  $P, k = 1, \dots, n$ , be the set of nodes on the boundaries of domain that are stored in sequence of counter-clockwise direction for all outside boundaries and clockwise direction for all inside boundaries.
2. Let  $V$  be the empty set of new inserted nodes and let  $T$  be the set of Delaunay triangles determined with algorithm I.
3. Compute the nodal distribution value  $dp_i$  for each boundary node  $p_i$  by,

$$dp_i = \frac{1}{M} \sum_{j=1}^M |p_j - p_i|$$

**Eq. 6.8.13**

Where  $| |$  is the Euclidean distance assuming that node  $i$  is surrounded by  $M$  nodes (see **Figure 6.8.2**).

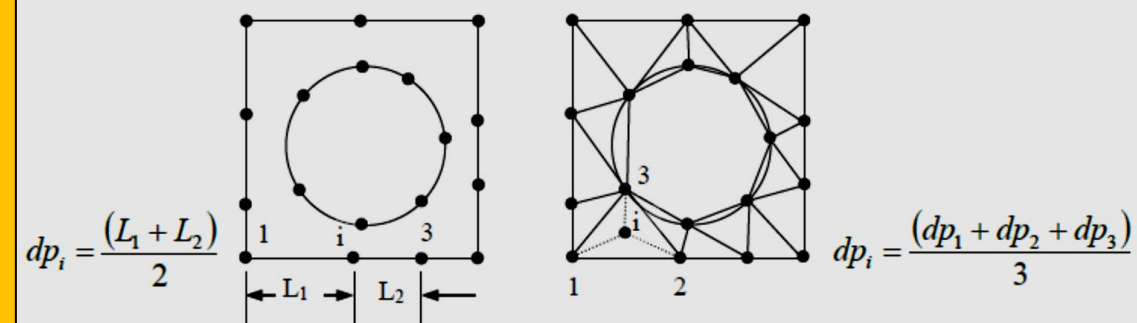


Figure 6.8.2 Calculation of the nodal distribution values

4. Read triangle  $t_i$  from  $T$ .
5. Calculate centroid of the triangle  $t_i$  and define as node  $Q$ , then compute the nodal distribution value of node  $Q$  by using **Eq. 6.8.13**. Compute the distance  $d_m$ ,  $m=1, 2, 3$ , from node  $Q$  to each of the three vertices of the triangle  $t_i$ .
6. Perform the Alpha test for node  $Q$ .  
If  $d_m < (\alpha dp_q)$  for any  $m = 1, 2, 3$ , then reject the node  $Q$  and go to step 4.
7. Compute the distance  $s_j$  for any  $j=1, \dots, N$  from node  $Q$  to be inserted to the other nodes.
8. Perform the Beta test for node  $Q$ .  
If  $s_j < (\beta dp_q)$  for any  $j = 1, \dots, N$ , then reject the node  $Q$  and go to step 4.

9. Accept the node Q for insertion by the Delaunay triangulation algorithm (Algorithm I) and add node Q into V.

10. Repeat steps 4 to 9 until all triangles in T are considered.

11. Perform the Delaunay triangulation of the derived nodes in V by Algorithm I.

A demonstration of a domain refinement by creating a new node inside the domain by Algorithm I and II is shown in **Figure 6.8.3**. *The new node that conforms with both the Alpha and Beta testing criteria is inserted at the centroid of the triangle and applied the in-circle testing criterion to all neighborhood triangles.* With this process, a new mesh with refined triangles is formed.

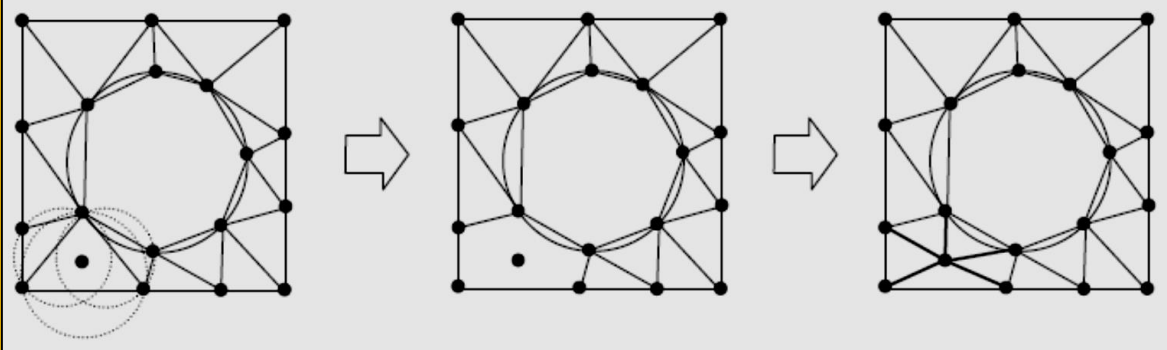


Figure 6.8.3 Mesh refinement with automatic node creation scheme (Algorithm II) and Delaunay triangulation (Algorithm I)

#### 6.8.5.4 Mesh Smoothing

Shapes and sizes of triangles formed from the previous step can be improved by applying a mesh smoothing technique. This paper uses the Laplacian smoothing technique because of less computational time requirement comparing to other techniques, such as the centroid technique [13]. The point repositioning formula is derived from the finite difference approximation of the Laplace's equation. Each interior node is moved successively to the centroid of the area which is formed by connecting neighboring nodes. Several passes are made through the entire set of all interior nodes to produce optimized shape and size of the triangles. The new node locations using the Laplacian smoothing are computed with,

$$x_{ic} = \frac{\sum_{i=1}^M x_i}{M} \quad , \quad y_{ic} = \frac{\sum_{i=1}^M y_i}{M} \quad i = 1, 2, \dots, M$$

**Eq. 6.8.14**

where  $x_i$  and  $y_i$  are the coordinates of the surrounding  $M$  nodes. To demonstrate the efficiency of the Delaunay triangulation algorithm and the Laplacian smoothing technique, **Figure 6.8.4** shows the progress of the domain discretization refinement for a lug with holes geometry.

#### 6.8.6 Adaptive Remeshing Technique

The remeshing technique generates an entirely new mesh based on the solution obtained from a previous mesh. The technique was first introduced and applied for high-speed compressible flow analysis [16]. In this paper, the technique is modified and incorporated into the Delaunay triangulation and the finite element method to analyze both the steady-state and transient heat conduction problems. There are two main steps in the implementation of the adaptive remeshing technique; the first step is the determination of proper element sizes and the second step is the

generation of the new mesh.

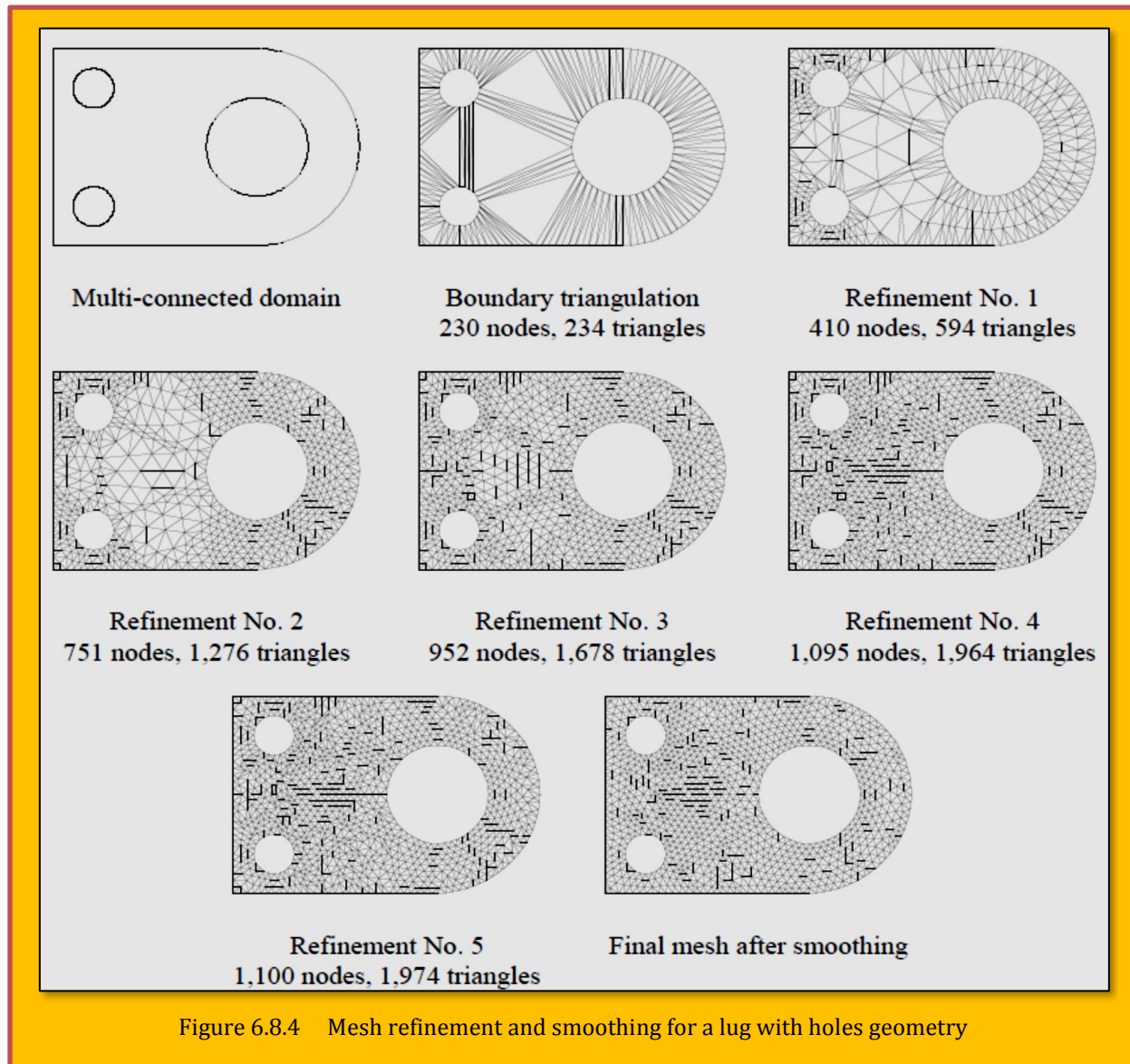


Figure 6.8.4 Mesh refinement and smoothing for a lug with holes geometry

### 6.8.6.1 Element Size Determination

The second derivative type error indicator is used to determine the proper element sizes because the assumed element temperature distribution is linear [17]. The temperature  $T$  is used as the indicator to compute the proper element sizes at different locations in the domain. Grid adaptation is generally accomplished by enforcing the requirement of equal distribution of the indicated error [16,17], then a new mesh should be generated with the proper element size  $h_i$  determined according to the principal quantity  $\lambda_i$ ,

$$h_i^2 \lambda_i = h_{min}^2 \lambda_{max} = \text{constant}$$

**Eq. 6.8.15**

where  $\lambda_i$  is the corresponding second derivatives of the element considered,

$$\lambda = \max \left( \left| \frac{\partial T}{\partial x} \right|, \left| \frac{\partial T}{\partial y} \right| \right)$$

#### **Eq. 6.8.16**

In **Eq. 6.8.15**,  $\lambda_{max}$  is the maximum second derivatives for all elements and  $h_{min}$  is the minimum element size specified by users.

#### **6.8.6.2 Adaptive Mesh Regeneration**

The new proposed adaptive mesh regeneration is based on the concepts of the Delaunay triangulation and the mesh refinement as described by Algorithm I and II. The new mesh is constructed using the information from the previous mesh (background mesh), such that it consists of small elements in the regions with large changes in solution gradients, and large elements in the other regions where the changes in solution gradients are small. The advantage of the proposed algorithm is no new parameter introduced, then it is easy to implement the adaptive remeshing process without difficulty choices of a combination of mesh regeneration parameters. Detailed process of adaptive remeshing technique is described in algorithm III as follows.

#### **Algorithm III; Adaptive Remeshing**

1. Let  $P, k = 1, \dots, n$  be the set of nodes of the background mesh. Let  $T, l = 1, \dots, m$  be the set of triangles of the background mesh.
2. Let  $NP$  be the empty set of nodes and  $NT$  be the empty set of triangles.
3. Calculate the new proper element size  $h_i$  of all the nodes of the background mesh by **Eq. 6.8.15** and **Eq. 6.8.16**. Then re-discretize all boundaries of the domain based on the new proper elements size  $h_i$  and recompute the nodal distribution values  $d_{pi}$  for all the boundary nodes before adding all nodes to  $NP$ .
4. Obtain nodal values of the new mesh by interpolating the nodal values of the background mesh. Construct boundary triangles from the new boundary nodes in  $NP$  by Algorithm I and store all the new triangles in  $NT$ .
5. Refine the boundary triangles based on the given values of the Alpha and Beta coefficients by Algorithm II and store all new inserted nodes in  $NP$ .
6. Read next interior node  $p_i$  of the background mesh from  $P$ .
7. If  $h_i > h_{max}$  then go to step 6.
8. Search triangle  $t_i$  in  $NT$  which contains the node  $p_i$  using the method described in step 5 of Algorithm I. Then calculate the centroid of the triangle  $t_i$  and define as node  $Q$ , and compute the nodal distribution value of node  $Q$  by **Eq. 6.8.14**.
9. Compute the distance  $d_m, m=1, 2, 3$ , from node  $Q$  to each of the three vertices of the triangle  $t_i$ .
10. If  $h_i > \text{average of } d_m$  or  $h_{min} > d_m, m=1, 2, 3$  then go to step 6.
11. Otherwise accept the node  $Q$  for insertion by the Delaunay triangulation algorithm (Algorithm I) and add node  $Q$  into  $NP$ .
12. Repeat steps 6 to 11 until all nodes in  $P$  are considered.
13. Perform the Delaunay triangulation of the inserted nodes in  $NP$  by Algorithm I and smooth the mesh.

#### **6.8.7 Algorithm Evaluation**

To demonstrate the capability of the adaptive remeshing technique with the Delaunay triangulation in reducing the numbers of finite elements, two examples of thermal analyses with exact solutions are used for the evaluation. These two problems are:

- (1) steady-state heat conduction in a square plate subjected to a highly localized surface heating,
- (2) transient heat conduction of a long plate subjected to a moving heat source.

### 6.8.7.1 Steady-State Heat Conduction In A Square Plate Subjected To A Highly Localized Surface Heating

This example is first used to evaluate the efficiency of the Delaunay triangulation and the adaptive remeshing technique as described because the temperature distribution can be expressed in symbolic form. The plate temperature distribution, which is a solution to the Poisson's equation with boundary conditions of zero temperature along the four edges, is shown in [Figure 6.8.5](#). The applied surface heating distribution is given by,

$$\frac{q}{kt} = 2y(1-y) \left[ \tan^{-1} \beta - \frac{\alpha(1-2x)}{\sqrt{2}(1-\beta^2)} + \frac{\alpha^2 \beta x(1-2x)}{2(1-\beta^2)^2} \right] \\ + 2x(1-x) \left[ \tan^{-1} \beta - \frac{\alpha(1-2y)}{\sqrt{2}(1-\beta^2)} + \frac{\alpha^2 \beta y(1-2y)}{2(1-\beta^2)^2} \right]$$

[Eq. 6.8.17](#)

where  $q$  is the applied surface heating,  $k$  is the plate thermal conductivity,  $t$  is the plate thickness, and

$$\beta = \alpha \left( \frac{x+y}{\sqrt{2}} - 0.8 \right)$$

[Eq. 6.8.18](#)

The exact solution for the temperature distribution is,

$$T(x, y) = x(1-x)y(1-y)\tan^{-1}\beta$$

[Eq. 6.8.19](#)

The temperature contours for the exact solution are shown in [Figure 6.8.5](#). The figure shows a steep temperature gradient along the  $s$ -direction at  $s$  equal to 0.8. The magnitude of the temperature gradient is caused by the large value of the parameter  $\alpha$ . Both the temperature and the applied surface heating distributions along the plate diagonal in the  $s$ -direction are shown in [Figure 6.8.6](#).

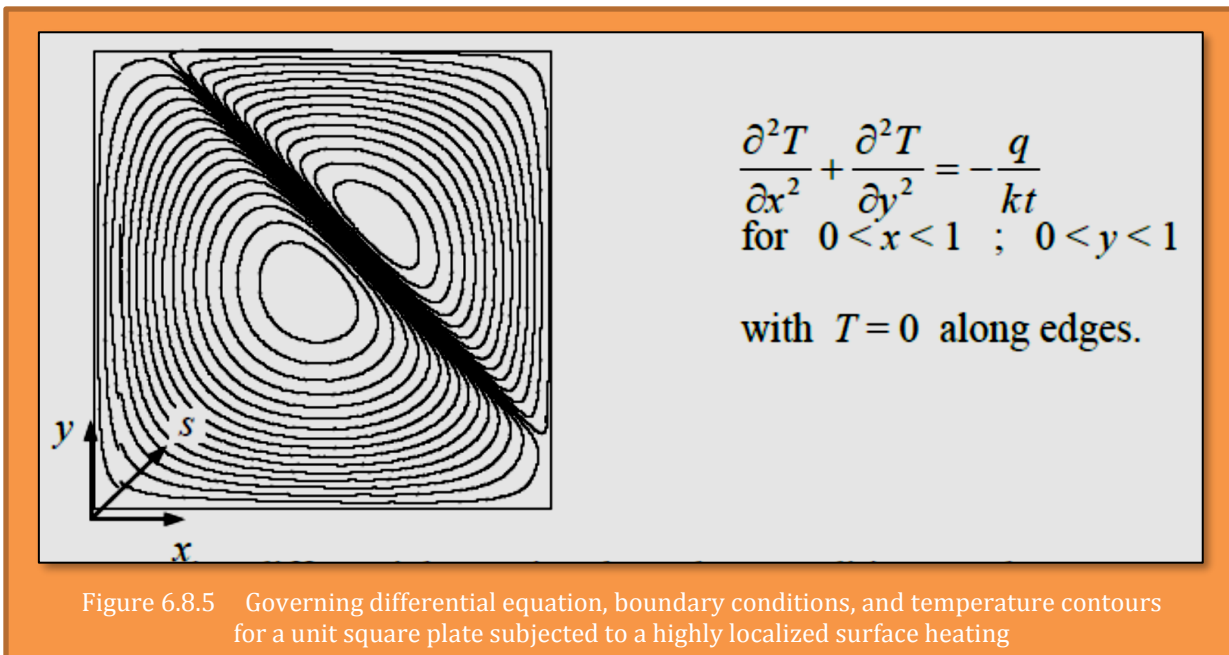


Figure 6.8.5 Governing differential equation, boundary conditions, and temperature contours for a unit square plate subjected to a highly localized surface heating

The figure shows the steep gradients and the rapid change in surface heating distribution in a narrow domain around  $s = 0.8$ .

Both uniformly refined meshes and adaptive meshes are used in the analysis to illustrate the advantages of the adaptive remeshing technique. For uniformly refined meshes, the first, second and third model and their corresponding temperature solution contours are shown in **Figure 6.8.6**. The three adaptive meshes and their corresponding temperature solution contours are shown

in **Figure 6.8.8**. The figure shows improved solution accuracy as compared to those obtained from the uniform meshes using approximately the same numbers of unknowns. **Figure 6.8.9** shows the comparison of the exact temperature solution and the predicted temperature from the third nonadaptive and adaptive meshes.

### 6.8.7.2 The Transient Heat Conduction In A Long Plate Subjected To A Moving Heat Source

A flow chart describing the generating adaptive mesh movement to capture transient temperature response in a structure [see **Figure 6.8.10**].

To demonstrate the capability of the Delaunay triangulation combined with the adaptive remeshing technique for such transient heat conduction analysis, a long plate subjected to a moving heat source along an edge is considered. A steel plate with dimension of  $1.00 \times 0.02$  m., in **Figure 6.8.11**, is subjected to an intense moving heat source along the top edge. The heat source with a uniform power density of  $56,700$  W/cm<sup>2</sup> and a width of 0.25 mm moves at a speed of 0.1 m/s. With the boundary condition of 0°C along the other three edges as indicated in the figure, the exact plate temperature response can be derived [18] in form of infinite series as,

$$T(\xi, y) = \frac{qe^{-H\xi}}{Lk} \times$$

$$\left\{ \sum_{n=2,4}^{\infty} \frac{1}{\lambda_n \left( H^2 + \frac{n^2 \pi^2}{4L^2} \right)} \left[ H(2\sin(\alpha)\cosh(HW)) \frac{n\pi}{2L} (2\cos(\alpha)\sinh(HW)) \right] [A_n] \right. \\ \left. + \sum_{n=1,3}^{\infty} \frac{1}{\lambda_n \left( H^2 + \frac{n^2 \pi^2}{4L^2} \right)} \left[ H(2\cos(\alpha)\sinh(HW)) \frac{n\pi}{2L} (2\sin(\alpha)\cosh(HW)) \right] [B_n] \right\}$$

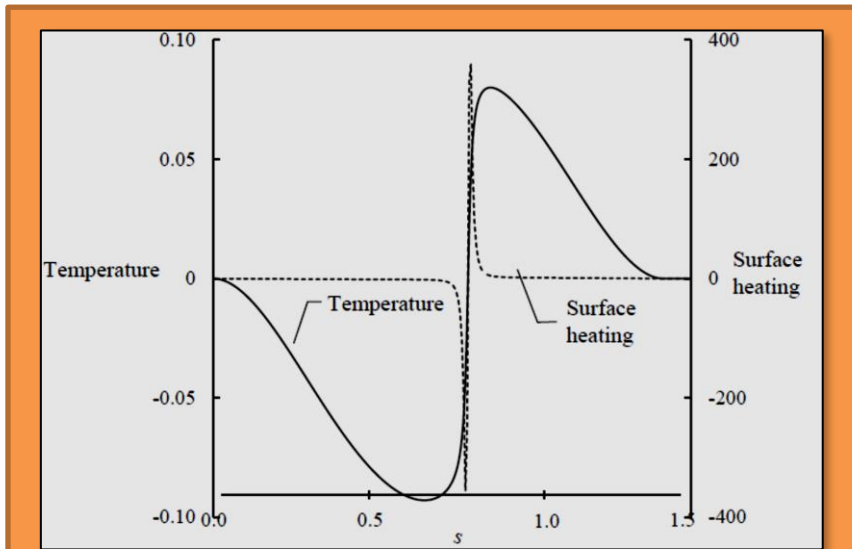


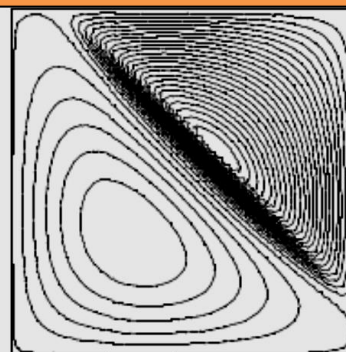
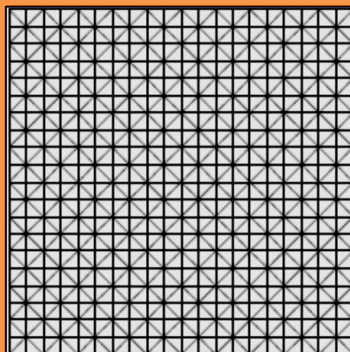
Figure 6.8.6 Plate temperature and surface heating distributions along a diagonal direction of the plate

$$\text{where } A_n = \sum_{n=2,4}^{\infty} \left[ \sin\left(\frac{n\pi\xi}{2L}\right) \left( \frac{\sinh\lambda_n y}{\cosh\lambda_n h} \right) \right]$$

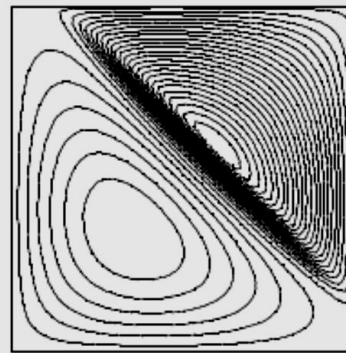
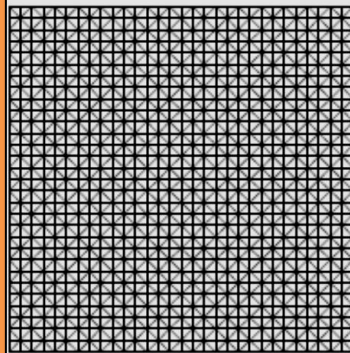
$$\text{and } B_n = \sum_{n=1,3}^{\infty} \left[ \cos\left(\frac{n\pi\xi}{2L}\right) \left( \frac{\sinh\lambda_n y}{\cosh\lambda_n h} \right) \right]$$

**Eq. 6.8.20**

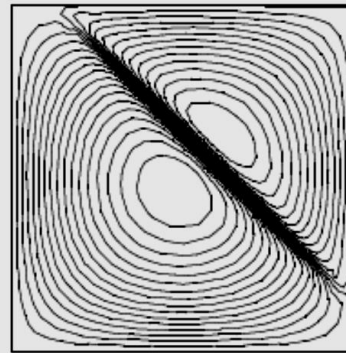
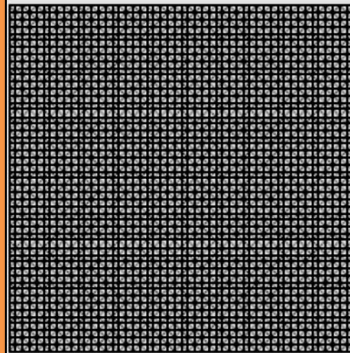
where the origin and the direction of the  $\xi - y$  coordinate system are shown in [Figure 6.8.11](#),  $q$  is the density of the moving heat source,  $h$  is plate width, and  $H$  is the parameter defined by,



**1<sup>st</sup> Mesh:**  
800 Triangles  
441 Nodes



**2<sup>nd</sup> Mesh:**  
1,800 Triangles  
961 Nodes



**3<sup>rd</sup> Mesh:**  
5,000 Triangles  
2,601 Nodes

Figure 6.8.7 Uniform refined meshes and their temperature solution contours for a plate subjected to a highly localized surface heating

$$H = \frac{\rho c_v}{2k}$$

**Eq. 6.8.21**

where  $\rho$  is the plate density,  $c$  is the specific heat,  $v$  is the velocity of the moving heat source, and  $k$  is the plate thermal conductivity. The parameter  $\alpha$  and  $\lambda_n$  in **Eq. 6.8.20** are defined by

$$\alpha = \frac{n\pi w}{2L} , \quad \lambda_n = \sqrt{\frac{n^2\pi^2}{4L^2} + H^2}$$

**Eq. 6.8.22**

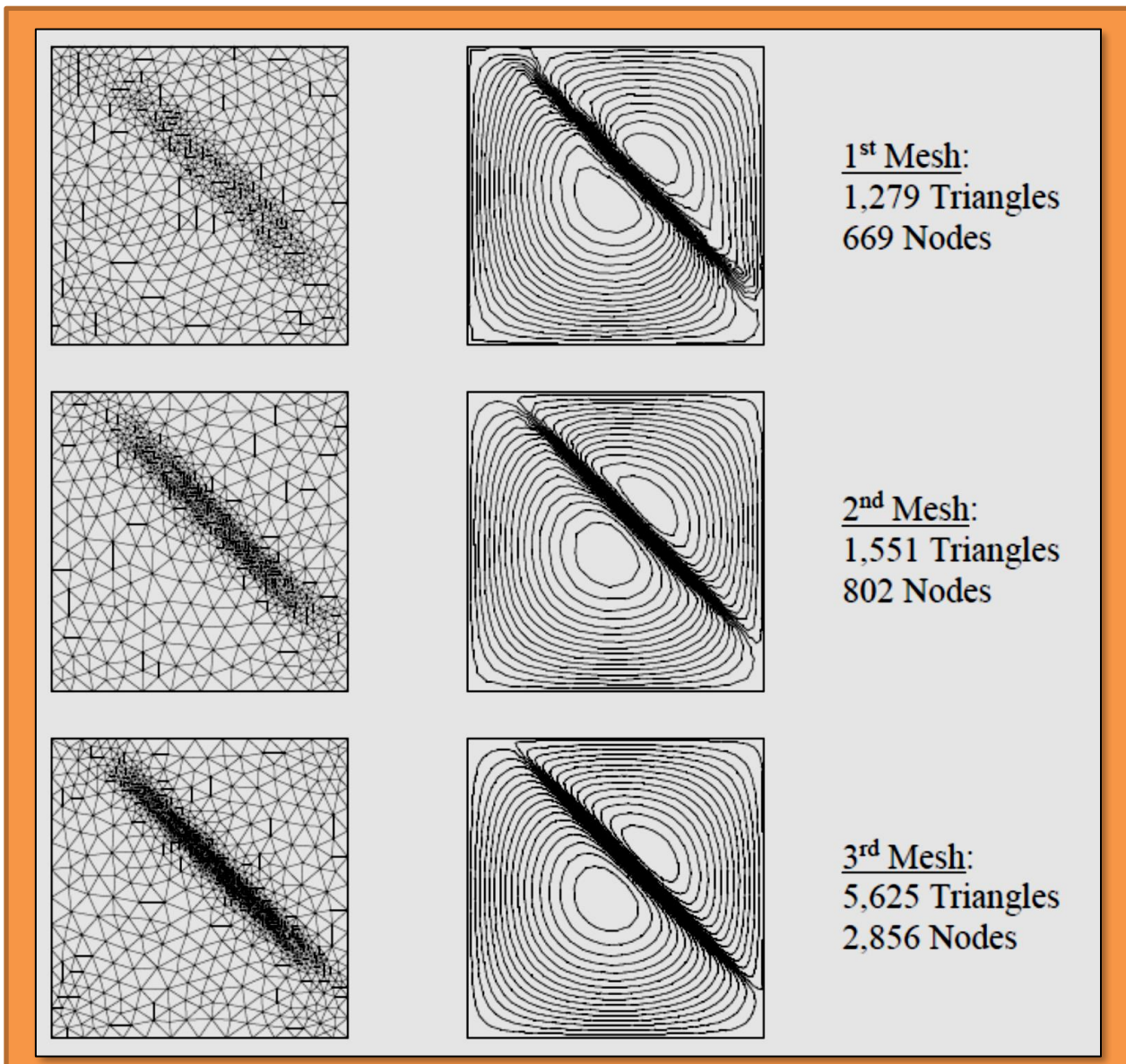


Figure 6.8.8 Adaptive meshes and their temperature solution contours for a plate subjected to a highly localized surface heating

respectively, where  $L$  is the plate length, and  $w$  is the width of the moving heat source that is simulated by a square pulse.

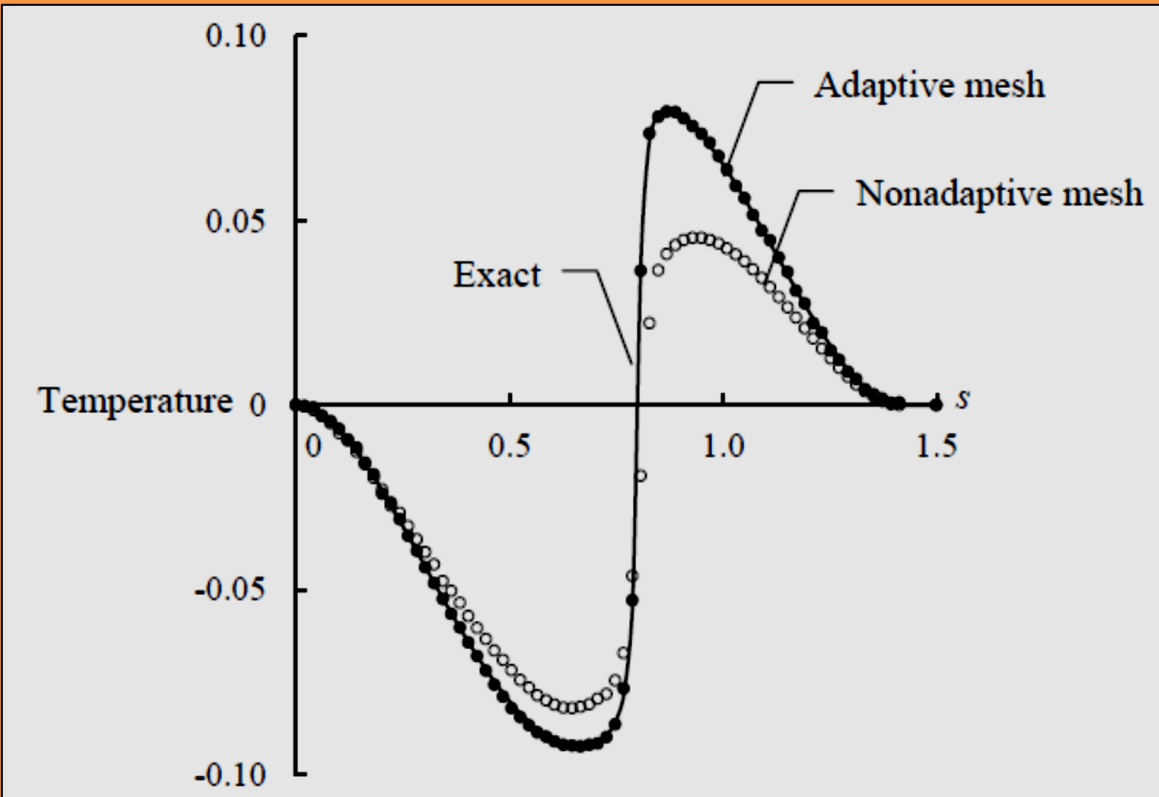


Figure 6.8.9 Comparison of the exact temperature solution and the predicted temperatures from the third nonadaptive and adaptive meshes

[Figure 12 of [Phongthanapanich & Dechaumphai](#)<sup>57</sup>] shows the predicted transient temperature response and temperature contours at four different times as the heat source moves across the plate using a nonadaptive finite element mesh. The nonadaptive mesh consisting of 2,400 triangles and 1,407 nodes was generated from the specified 0.005 uniform element size in the  $\xi$ -direction and graded element sizes in the  $y$ -direction. The temperature distribution given by Eq. 6.8.20 suggests the graded element sizes in the  $y$ -direction with smaller elements on the upper surface and larger elements along the bottom surface. The figure shows high temperatures and temperature gradients at the heat source impingement location with a predicted peak temperature of 272°C. [Figure 13 of [Phongthanapanich & Dechaumphai](#)<sup>58</sup>] illustrates the predicted temperature response and temperature contours at the same four times of the transient adaptive finite element meshes as the heat source moves across the plate. A typical transient adaptive mesh consists of approximately 300 triangles and 200 nodes with the prescribed smallest element size of 0.001. The figure shows high

<sup>57</sup> Sutthisak Phongthanapanich and Pramote Dechaumphai, "Evaluation of Combined Delaunay Triangulation And Remeshing For Finite Element Analysis of Conductive Heat Transfer", Mechanical Engineering Department, Chulalongkorn University, Bangkok, Thailand.

<sup>58</sup> Sutthisak Phongthanapanich and Pramote Dechaumphai, "Evaluation of Combined Delaunay Triangulation And Remeshing For Finite Element Analysis of Conductive Heat Transfer", Mechanical Engineering Department, Chulalongkorn University, Bangkok, Thailand.

temperature and temperature gradients at the heat source impingement location with the predicted peak temperature of  $300^{\circ}\text{C}$  comparing to  $302^{\circ}\text{C}$  from the exact solution of [Eq. 6.8.20](#).

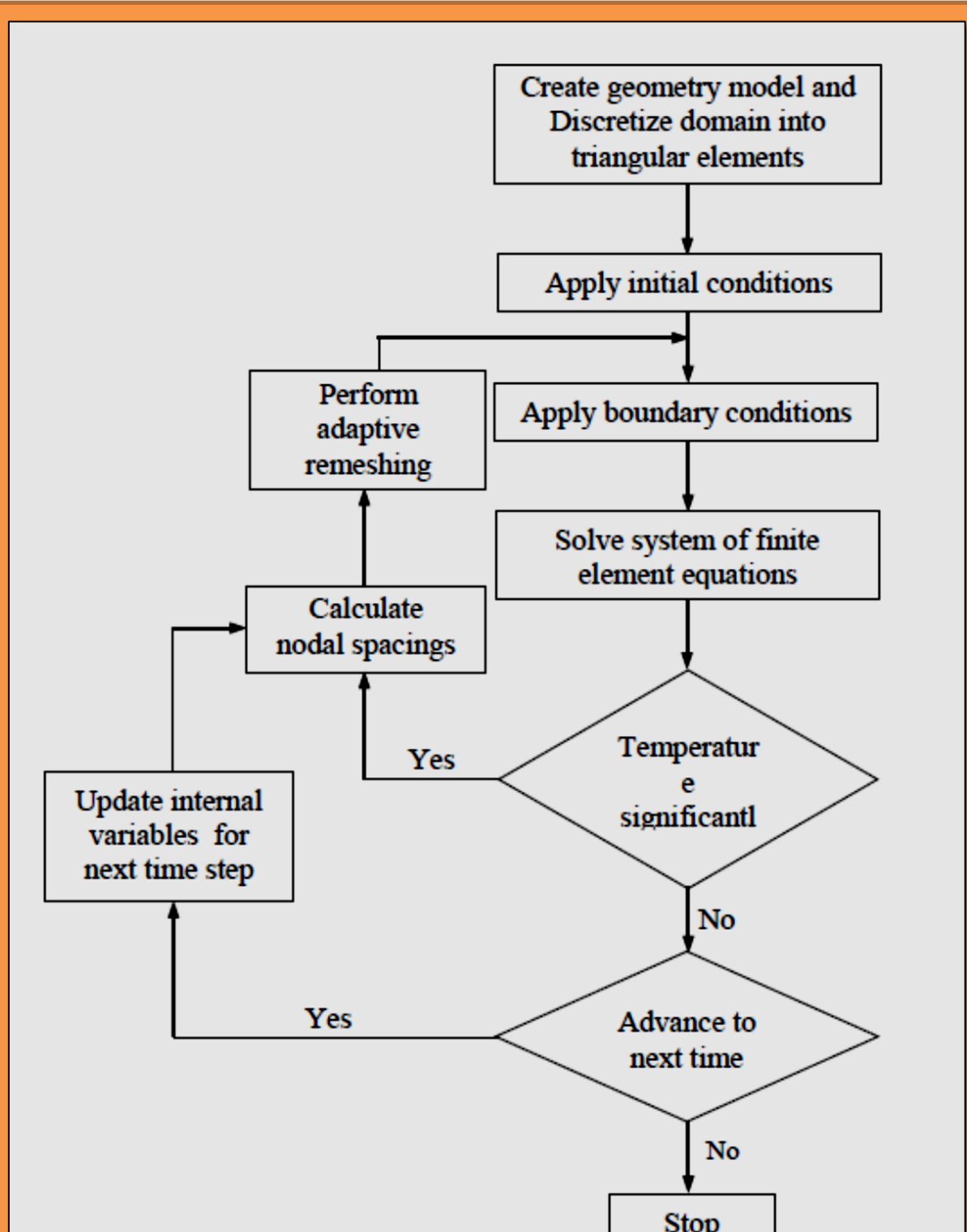


Figure 6.8.10 Flow-chart for generating adaptive mesh movement to capture transient temperature response in a structure

The exact and the predicted temperature distributions along the top surface are shown in [Figure 14 of Phongthanapanich & Dechaumphai]<sup>59</sup>. A scale enlargement that provides a better comparison of these temperature distributions at the heat source impingement location is shown in Fig. 15 of the same source. This latter figure demonstrates that the adaptive mesh provides improved temperature solution accuracy for both the magnitude and the distribution compared to the standard nonadaptive mesh. The errors in the peak temperatures predicted by using the nonadaptive mesh and the adaptive mesh are 9.9% and 0.7%, respectively.

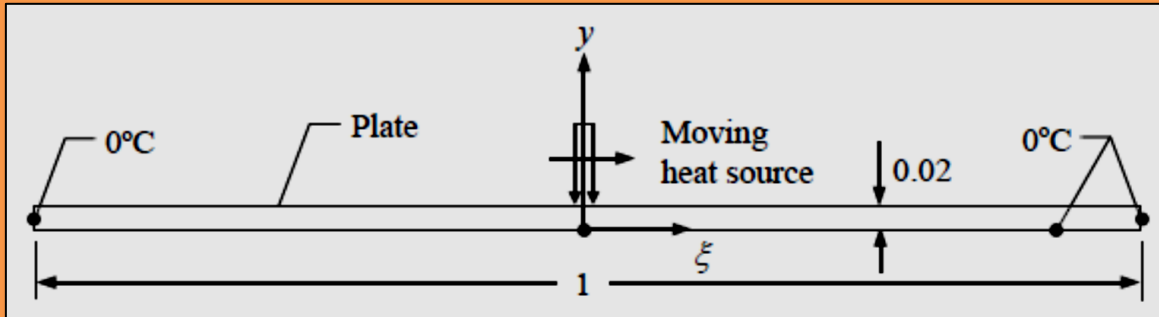


Figure 6.8.11 Problem statement for transient thermal analysis of a plate subjected to a moving heat source

### 6.8.8 Conclusions

The adaptive finite element method using Delaunay triangulation for heat transfer analysis was presented. The concept of the Delaunay triangulation for 2D mesh construction was explained. The mesh generation procedure with automatic node creation and mesh smoothing were described in detail. The solution accuracy was further improved by implementing an adaptive remeshing technique to the Delaunay triangulation algorithm. The adaptive remeshing technique places small elements in the regions with large changes of temperature gradients. At the same time, larger elements are generated in other regions to reduce the total number of unknowns and the computation time.

A steady-state heat conduction in a plate subjected to highly localized surface heating with a known exact solution was used to demonstrate that the adaptive remeshing technique reduces the analysis solution error and increases the computational efficiency relative to uniformly regular meshes. For the time-dependent problem, a transient analysis of conduction heat transfer in a plate subjected to a moving heat source was presented. The example demonstrates that the transient adaptive meshes can increase the analysis solution accuracy, and at the same time, significantly reduce the total number of unknowns as compared to the standard nonadaptive mesh.

### 6.8.9 Acknowledgements

*The authors are pleased to acknowledge the Thailand Research Fund (TRF) for supporting this research work.*

### 6.8.10 References

1. Bowyer, A., Computing Dirichlet Tessellations, *Comp. J.*, 24, 1981, pp. 162-166.
2. Watson, D.F., Computing the n-Dimensional Delaunay Tessellation with Application to Voronoi Polytopes, *Comp. J.*, 24, 1981, pp. 167-172.

<sup>59</sup> Sutthisak Phongthanapanich and Pramote Dechaumphai, "Evaluation of Combined Delaunay Triangulation And Remeshing For Finite Element Analysis of Conductive Heat Transfer", Mechanical Engineering Department, Chulalongkorn University, Bangkok, Thailand.

3. Weatherill, N.P. and Hassan, O., Efficient Three-Dimension Delaunay Triangulation with Automatic Point Creation and Imposed Boundary Constraints, *Int. J. Numer. Methods Eng.*, 37, 1994, pp. 2005-2039.
4. Karamete, B.K., Tokdemir, T. and Ger, M., Unstructured Grid Generation and a Simple Triangulation Algorithm for Arbitrary 2-D Geometries Using Object Oriented Programming, *Int. J. Numer. Methods Eng.*, 40, 1997, pp. 251-268.
5. Phongthanapanich, S. and Dechaumphai, P., Underwater Explosion Simulation by Transient Adaptive Delaunay Triangulation Meshing Technique. Technical Report submitted to the Royal Thai Navy, TR-3894. Bangkok, Thailand, 2002.
6. Dechaumphai, P., Thornton, E.A. and Wieting, A.R., Flow-Thermal-structure study of aerodynamically heated leading edges, *J. Spacecr. Rockets*, 26, 1989, pp. 201-209.
7. Zienkiewicz, O.C and Taylor, R.L., Finite Element Method. Vol.1 Fifth Ed., Butterworth-Heinemann, Woburn, MA, 2000.
8. Lawson, C.L., Software for C1 Surface Interpolation. Mathematical Software III, Edited by J. R. Rice., Academic Press, New York, 1977.
9. Guibas, L. and Stolfi, J., Primitives for the Manipulation of General Subdivisions and the Computation of Voronoi Diagrams, *ACM Trans. on Graphics*, 4, 1985, pp. 74-123.
10. Dwyer, R.A., A Faster Divide-and-Conquer Algorithm for Constructing Delaunay Triangulations, *Algorithmica*, 2, 1987, pp. 137-151.
11. Fortune, S., A Sweepline Algorithm for Voronoi Diagrams, *Algorithmica*, 2, 1987, pp. 153-174.
12. Sloan, S.W., A Fast Algorithm for Generating Constrained Delaunay Triangulations, *Comp. Struct.*, 47, 1993, pp. 441-450.
13. Frey, W.H., Selective Refinement: A New Strategy for Automatic Node Placement in Graded Triangular Meshes, *Int. J. Numer. Methods Eng.*, 24, 1987, pp. 2183-2200.
14. Borouchaki, H. and George, P.L., Aspects of 2-D Delaunay Mesh Generation, *Int. J. Numer. Methods Eng.*, 40, 1997, pp. 1957-1975.
15. Rebay, S., Efficient Unstructured Mesh Generation by Means of Delaunay Triangulation and Bowyer-Watson Algorithm, *J. Comput. Phys.*, 106, 1993, pp. 125-138.
16. Peraire, J., Vahdati, M., Morgan, K. and Zienkiewicz, O.C., Adaptive Remeshing for Compressible Flow Computations, *J. Comput. Phys.*, 72, 1987, pp. 449-466.
17. Dechaumphai, P. and Morgan, K., Transient Thermal-Structural Analysis using Adaptive Unstructured Remeshing and Mesh Movement. *Thermal Structures and Materials for High-Speed Flight*, American Institute of Aeronautics and Astronautics, Washington, D. C., 1992, pp. 205-228.
18. McGowan, D.M., Camarda, C.J. and Scotti, S.J., A Simplified Method of Thermal Analysis of a Cowl Leading Edge Subjected to Intense Localized Heating, NASA TP-16505, 1990.

## 6.9 Case Study 9 - 3D Heat Transfer for Hypersonic Flow Using Shock Wave/Boundary-Layer Interactions with Wall-Modeled LES (WMLES)

**Authors :** Lin Fu, Sanjeeb Bose, Parviz Moin

**Affiliation :** Stanford University, Stanford CA 94305-3024, USA

**Title :** Heat transfer in three-dimensional intersecting shock-wave/turbulent boundary-layer interactions with wall-modeled large-eddy simulations

**Original Appearance :** arXiv:submit/3355078 [physics.flu-dyn] 4 Sep 2020

**Source :** <https://www.researchgate.net/publication/344119729>

The accurate prediction of aerothermal surface loading is of paramount importance for the design of high speed flight vehicles. In this work, we consider the numerical solution of hypersonic flow over a double-finned geometry, representative of the inlet of an air-breathing flight vehicle, characterized by 3D intersecting shock-wave/turbulent boundary-layer interaction at Mach 8.3 [Fu et al.]<sup>60</sup>. High Reynolds numbers ( $Re_L \approx 11.6 \times 10^6$  based on free-stream conditions) and the presence of cold walls ( $T_w/T_0 \approx 0.27$ ) leading to large near-wall temperature gradients necessitate the use of wall-modeled large-eddy simulation (WMLES) in order to make calculations computationally tractable. The comparison of the WMLES results with experimental measurements shows good agreement in the time-averaged surface heat flux and wall pressure distributions, and the WMLES predictions show reduced errors with respect to the experimental measurements than prior RANS calculations. The favorable comparisons are obtained using an LES wall model based on equilibrium boundary layer approximations despite the presence of numerous non-equilibrium conditions including three dimensionality, shock-boundary layer interactions, and flow separation. Lastly, it is also demonstrated that the use of semi-local eddy viscosity scaling (in lieu of the commonly used van Driest scaling) in the LES wall model is necessary to accurately predict the surface pressure loading and heat fluxes.

### Nomenclature

x,y,z = coordinate in the inertial coordinate system, m  
 L<sub>r</sub> = reference length for normalization, m  
 t = physical time, s  
 $\rho$  = density, kg=m<sup>3</sup>  
 P = pressure, Pa  
 P<sub>0</sub> = total pressure, Pa  
 T = temperature, K  
 T<sub>0</sub> = total temperature, K  
 S = constant parameter in the Sutherland's Law, K  
 u = velocity vector, m=s  
 S<sub>ij</sub> = strain rate tensor, 1=s  
 E = total energy, Pa  
 $\mu$  = dynamic viscosity, Pa . s  
 $\mu_{t,wm}$  = turbulent eddy viscosity (in wall model), Pa . s  
 k = fluid thermal conductivity, W. m<sup>-1</sup> . K<sup>-1</sup>  
 c = sound speed, m/s

$\gamma$  = ratio of specific heats  
 $Re_\infty$  = free-stream unit Reynolds number  
 $Re_{50}$  = Reynolds number based on the boundary layer thickness  
 Q<sub>w</sub> = wall heat flux, W. m<sup>-2</sup>  
 h<sub>wm</sub> = wall model matching location, m  
 $\tau_w$  = wall shear stress, Pa  
 $u_t$  = friction velocity at the wall, m/s  
 $\nu_w$  = wall kinematic viscosity, m<sup>2</sup>/s  
 $c_p$  = specific heat capacity at constant pressure, J/K  
 $c_v$  = specific heat capacity at constant volume, J/K  
 $\tau_{ij}^{SGS}$  = sub grid stress, Pa  
 $\tau_{ij}^{SGS}$  = sub grid heat flux , w.m<sup>-2</sup>  
 $\alpha$  = wedge angle  
 $\kappa$  = von Karman constant  
 Pr = molecular Prandtl number  
 Pr<sub>t</sub> = turbulent Prandtl number  
 Ma = Mach number

---

<sup>60</sup> Lin Fu, Sanjeeb Bose, Parviz Moin, "Heat transfer in three-dimensional intersecting shock-wave/turbulent boundary-layer interactions with wall-modeled large-eddy simulations", arXiv:submit/3355078 [physics.flu-dyn], Sep 2020.

D = near-wall damping function in the eddy viscosity model

$y^+$  = dimensionless wall-normal coordinate based on the wall viscous length scale

$u^+$  = streamwise velocity normalized by the wall friction velocity

B = intercept constant in the log law

### 6.9.1 Introduction

Hypersonic wall-bounded flows for realistic flight vehicles can be characterized by high Reynolds numbers and cold surface temperatures compared to the free-stream stagnation temperature. The prohibitive computational cost associated with high Reynolds numbers are well known [1], while the cold wall conditions exacerbate near-wall resolution requirements associated with the large temperature gradients in the vicinity of peak viscous dissipation. As a result, direct numerical simulations of these flows have been largely limited to simple geometries with low Reynolds numbers, e.g. the high-speed compressible boundary layer flows [2], the hypersonic boundary-layer transitional flow for a flared cone [3], the turbulent boundary layer along a compression ramp [4], the transitional shock/boundary-layer interaction [5].

When more realistic geometries and conditions are considered, the RANS approach is commonly used in industrial settings due to reduced computational costs compared to DNS strategies. However, RANS based approaches have been demonstrated to have limited accuracy in hypersonic flow regimes; significant errors in peak aerodynamic heating ( $\sim 25\%$ ) [6] are observed and macroscopic flow characteristics are misrepresented, in particular when laminar/turbulent transition or boundary layer separation are present [7][8]. Cold wall conditions in hypersonic flow regimes also challenge traditional RANS models (e.g., *Spalart-Allmaras*,  $k-\omega$ ) to predict near-wall turbulent fluctuations or transverse heat fluxes [9] even in zero-pressure gradient boundary layers. Algebraic RANS closures, such as the Baldwin-Lomax model [10], have been shown to offer reasonable predictions in high Mach number boundary layer flows [11]. However, the application of these models to the double-finned inlet flow presently considered show substantial errors in the surface heat fluxes and in the extent of flow separation [12].

Large-eddy simulations have been shown to offer superior accuracy in the prediction of many of these flow regimes, however, near-wall resolution requirements are prohibitive in high Reynolds number conditions. Alternatively, the WMLES approach, where flow structures that scale with the boundary layer thickness while effects of unresolved near-wall eddies (at viscous length scales,  $l_v = v/u_\tau$ ) are modeled, has been shown to be computationally tractable for high Reynolds number flows and predictive of complex flow phenomena [13]. In the context of high-speed flows, these approaches have been successfully applied to the prediction of shock-induced separation [14][15], oblique shock wave interaction with lateral confinement and boundary layer separation [16][17], transitional flows [18][19][20], and aerodynamic heating [21][22]. However, most of the high speed applications of WMLES have been conducted in relatively simple geometries or without the presence of relevant cold wall conditions. To this end, the present work considers a canonical model of a realistic inlet of an air-breathing hypersonic vehicle [23].

The configuration consists of two sharp fins mounted on a flat plate. An incident hypersonic turbulent boundary layer approaches the two vertical fins generating a crossing shock pattern resulting in high local aerothermal loading and flow separation. The objective of this investigation is to assess the suitability of wall modeled LES in this complex geometry and flow regime with emphasis on the ability to predict surface heat fluxes, mechanical loading, and separation that arises from the impinging shock structure.

### 6.9.2 LES Governing Conservation Equations

The **Favre-averaged** compressible Navier-Stokes equations in the conservative form are

$$\frac{\partial \bar{\rho}}{\partial t} + \frac{\partial \bar{\rho} \tilde{u}_j}{\partial x_j} = 0$$

$$\frac{\partial \bar{\rho} \tilde{u}_i}{\partial t} + \frac{\partial \bar{\rho} \tilde{u}_i \tilde{u}_j}{\partial x_j} + \frac{\partial \bar{P}}{\partial x_i} = \frac{\partial \tilde{\sigma}_{ij}}{\partial x_j} - \frac{\partial \tau_{ij}^{sgs}}{\partial x_j}$$

$$\frac{\partial \bar{E}}{\partial t} + \frac{\partial (\bar{E} + \bar{P}) \tilde{u}_j}{\partial x_j} = \frac{\partial}{\partial x_j} \left( k \frac{\partial \bar{T}}{\partial x_j} \right) + \frac{\partial \tilde{u}_i \tilde{\sigma}_{ij}}{\partial x_j} - \frac{\partial Q_j^{sgs}}{\partial x_j} - \frac{\partial (\tilde{u}_i \tau_{ij}^{sgs})}{\partial x_j}$$

**Eq. 6.9.1**

where  $\rho$ ,  $P$ , and  $T$  denote the fluid density, pressure, and temperature, respectively.  $u_i$  denotes the velocity component in the  $x_i$  coordinate direction.

$$\bar{E} = \bar{\rho} \tilde{e} + \bar{\rho} \tilde{u}_k \tilde{u}_k / 2$$

**Eq. 6.9.2**

denotes the total energy, and

$$\tilde{\sigma}_{ij} = \mu \bar{T} (\tilde{S}_{ij} - 1/3 \tilde{S}_{kk} \delta_{ij})$$

**Eq. 6.9.3**

is the resolved deviatoric stress tensor, and

$$\tilde{S}_{ij} = \frac{1}{2} \left( \frac{\partial \tilde{u}_i}{\partial x_j} + \frac{\partial \tilde{u}_j}{\partial x_i} \right)$$

**Eq. 6.9.4**

is the resolved strain rate tensor. The sub grid stress  $\tau_{ij}^{sgs}$  and heat flux  $Q_{ij}^{sgs}$  arising from the effect of unresolved eddies are defined as

$$\tau_{ij}^{sgs} = \bar{\rho} (\tilde{u}_i \tilde{u}_j - \tilde{u}_i \tilde{u}_j) , \quad Q_{ij}^{sgs} = \bar{\rho} (\tilde{e} \tilde{u}_i - \tilde{e} \tilde{u}_j)$$

**Eq. 6.9.5**

The sub grid stresses and heat fluxes are presently closed with a Vreman eddy viscosity model [24] supplemented with a constant turbulent Prandtl number ( $Pr_t = 0.9$ ). The equation of state for the fluid is a calorically perfect gas,

$$\bar{P} = \bar{\rho} R \bar{T}$$

**Eq. 6.9.6**

where  $R$  denotes the specific gas constant. The relation between the dynamic viscosity and the temperature is characterized by the Sutherland's law with a model constant  $S/T_r = 1.38$ ;  $T_r = 80$  K, and the Prandtl number is 0.72. The calorically perfect gas assumption is adopted based on the low free-stream temperature for the configuration under consideration,  $T_\infty = 80$  K. For brevity, the operator symbol  $\bar{\cdot}$  (Reynolds average) and  $\tilde{\cdot}$  (Favre average) are omitted hereafter.

**6.9.2.1 LES Wall Model Based on Equilibrium Boundary Layer Approximations**

As the near-wall eddies whose size are characterized by viscous length scales are not resolved in the present formulation, their aggregate effect on the wall stress and heat flux must be modeled. (For a detailed description of the wall model formulation, see [13] [25].) The present LES wall model assumes that the pressure gradient and convection effects can be neglected for unresolved eddies

between the wall and the local LES resolution (of grid size,  $\Delta$ ), and that these eddies reach a statistically stationary state over the duration of the simulation time step ( $\Delta t$ ). With these approximations, the simplified momentum and total energy equations can be written as

$$\frac{d}{dy} \left[ (\mu + \mu_{t,wm}) \frac{du||}{dy} \right] = 0$$

**Eq. 6.9.7**

$$\frac{d}{dy} \left[ (\mu + \mu_{t,wm}) u_{||} \frac{du||}{dy} + c_p \frac{\mu}{Pr} \frac{\mu_{t,wm}}{Pr_{t,wm}} \frac{dT}{dy} \right] = 0$$

**Eq. 6.9.8**

where  $y$  and  $u_k$  denote the wall-normal coordinate and the velocity component parallel to the wall, respectively.  $c_p$ , and  $Pr$  denote the specific heat capacity at constant pressure, and the molecular Prandtl number, respectively. Turbulent stresses and heat fluxes are modeled with an eddy viscosity,  $\mu_{t,wm}$ , given by the following mixing length model:

$$\mu_{t,wm} = \kappa \rho y \sqrt{\frac{\tau_w}{\rho}} D$$

**Eq. 6.9.9**

where  $\kappa = 0.41$  is the von Karman constant. In order to recover the linear behavior in the viscous sublayer and the buffer layer in a zero-pressure gradient limit, the damping function  $D$  is defined as

$$D = \left[ 1 - \exp \left( -\frac{y_{vD}^+}{A^+} \right) \right]^2$$

**Eq. 6.9.10**

where the dimensionless constant  $A^+ = 17$  indicates the characteristic length scale of the exponential damping.

$$y_{vD}^+ = \frac{y}{\left( \frac{\nu_w}{u_\tau} \right)}$$

**Eq. 6.9.11**

where  $\nu_w$  and  $u_\tau$  denote the kinematic viscosity and friction velocity at the wall. However, it is shown in [26][27] that the van Driest transformation performs poorly in collapsing the compressible velocity profile onto the incompressible counterpart for wall-bounded flows with cold wall condition. Due to this, we additionally consider in this work a semi-local scaling

$$y_{SL}^+ = \frac{\rho(y) \sqrt{(\tau_w / \rho)} y}{\mu(Y(y))}$$

**Eq. 6.9.12**

where the dynamic viscosity is computed based on the local conditions at an off-wall distance,  $y$ , and  $y_{SL}^+$  is used in place of  $y_{vD}^+$  in **Eq. 6.9.10**. The boundary conditions for **Eq. 6.9.7** and **Eq. 6.9.8** for

the velocity and temperature are no-slip, isothermal conditions at the wall ( $u_{||}(y = 0) = 0$ ;  $T(y = 0) = T_w$ ) and the interior LES conditions ( $u_{||}(h_{wm}) = u_{LES}$ ;  $T(h_{wm}) = T_{LES}$ ) at a distance,  $h_{wm}$ , from the wall. In this work, the matching location is chosen as the first off-wall cell center in the local wall-normal direction. Although Kawai and Larsson [28] propose that the matching location should be several cells away from the wall to provide better resolved solution for the wall model as the boundary condition, recent investigations have shown that the first-cell coupling is sufficient for the prediction of relevant quantities of interest such as the skin friction or wall heat fluxes (see [18]). This choice is further validated by this study through the comparisons with the available experimental data in later sections. It is worthwhile to note that while the wall model does not explicitly contain the non-equilibrium pressure gradient or convection effects, the influence of these phenomena are implicitly present in the time dependent far field boundary conditions that the interior LES provides.

### 6.9.3 Numerical Methods

The compressible, finite-volume code *charLES* [29], is used to conduct the numerical simulations herein. The numerical method consists of a low dissipation, approximate entropy-preserving scheme and utilizes artificial properties to capture solution discontinuities. The LES governing equations are temporally integrated by the explicit third-order strong-stability-preserving (SSP) Runge-Kutta method [30]. The spatial and temporal schemes converge to second and 3<sup>rd</sup> order with respect to the nominal mesh spacing and time step, respectively. Computational meshes based on arbitrary

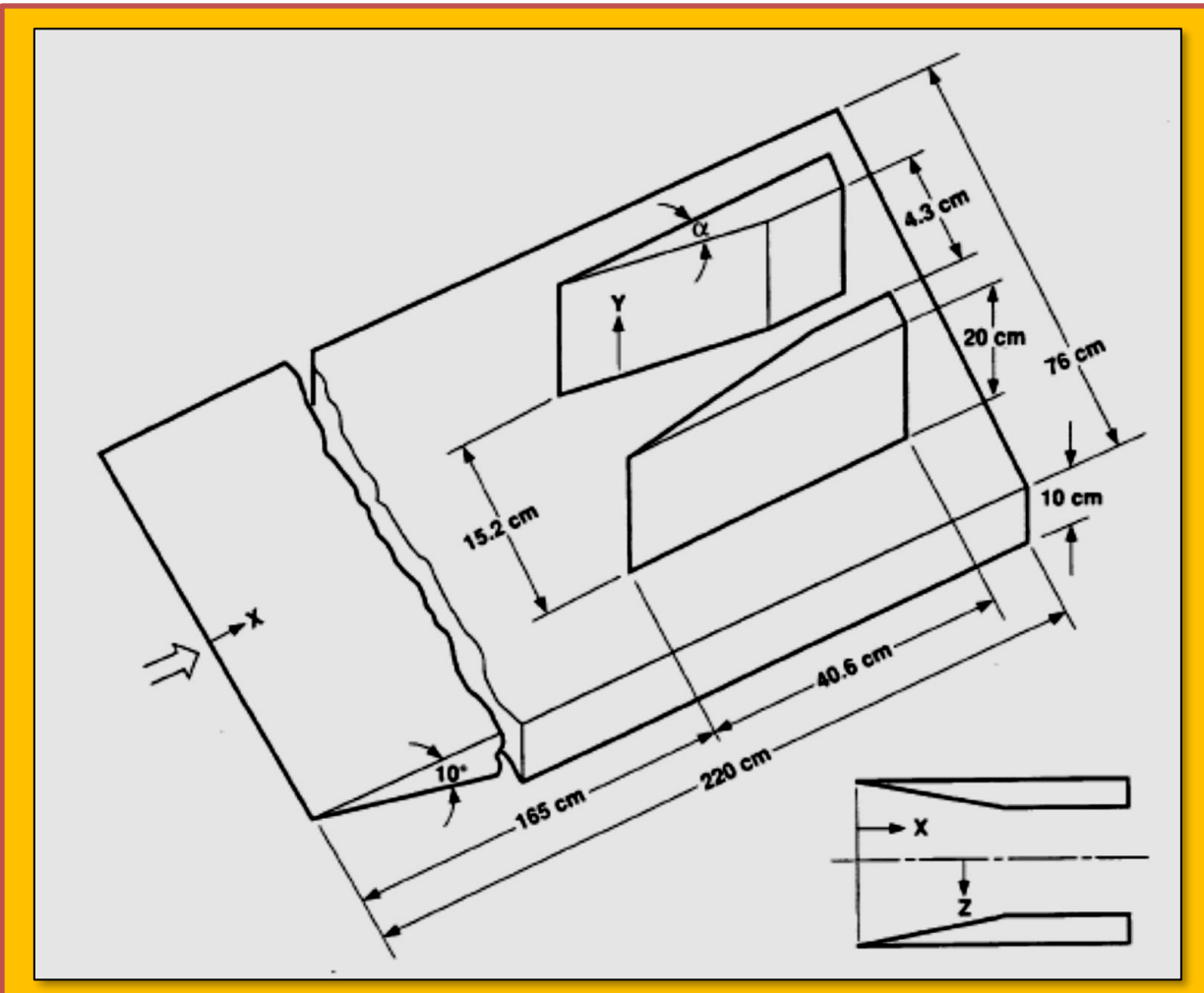


Figure 6.9.1 The Geometry Parameters and the Computational Coordinate System

polyhedral are constructed from the computation of Voronoi diagrams associated with the specification of the location of the degrees of freedom clipped against the domain boundaries [31]. Additional details of the numerical method and relevant solver validation can be found in [32], [33], [34], [29], and [35].

#### 6.9.4 Double-Finned Problem Definition and Computational Setup

The present geometry and computational setup follow those described in the experiment of a  $15^\circ$  double-finned configuration [23]. The geometry is composed of two sharp fins with wedge angle =  $15^\circ$  fastened to a flat plate, as shown in **Figure 6.9.1**. Specifically, each fin is 20 cm high and 40.6 cm long, and the flat plate is 220 cm long and 10 cm high. The double fins are placed 165 cm downstream of the leading edge of the flat plate such that there is sufficient length for a turbulent boundary layer to develop. The free-stream flow measured 3 cm ahead of the double fins (i.e. at  $x_0 = 162$  cm) has a Mach number  $Ma_\infty = 8.23$  and Reynolds number  $Re_{80} = 1.7 \times 10^5$  based on the local boundary layer thickness  $\delta_0 = 3.25$  cm. The wall is isothermal at  $T_w = 300$  K which is substantially colder than the stagnation temperature  $T_0 = 1177$  K. In the following discussion, velocity, temperature, density and length are normalized by the sound speed  $c_r = 179$  m/s, the reference temperature  $T_r = 80$  K, the reference density  $\rho_r = 0.0186$  kg/m<sup>3</sup> and the reference length  $L_r = 1$  cm.

The arrow indicates that the fluid flows from the leading edge of the flat plate towards the double fins. The leading edges of both the flat plate and the double fins are sharp and the model is symmetric

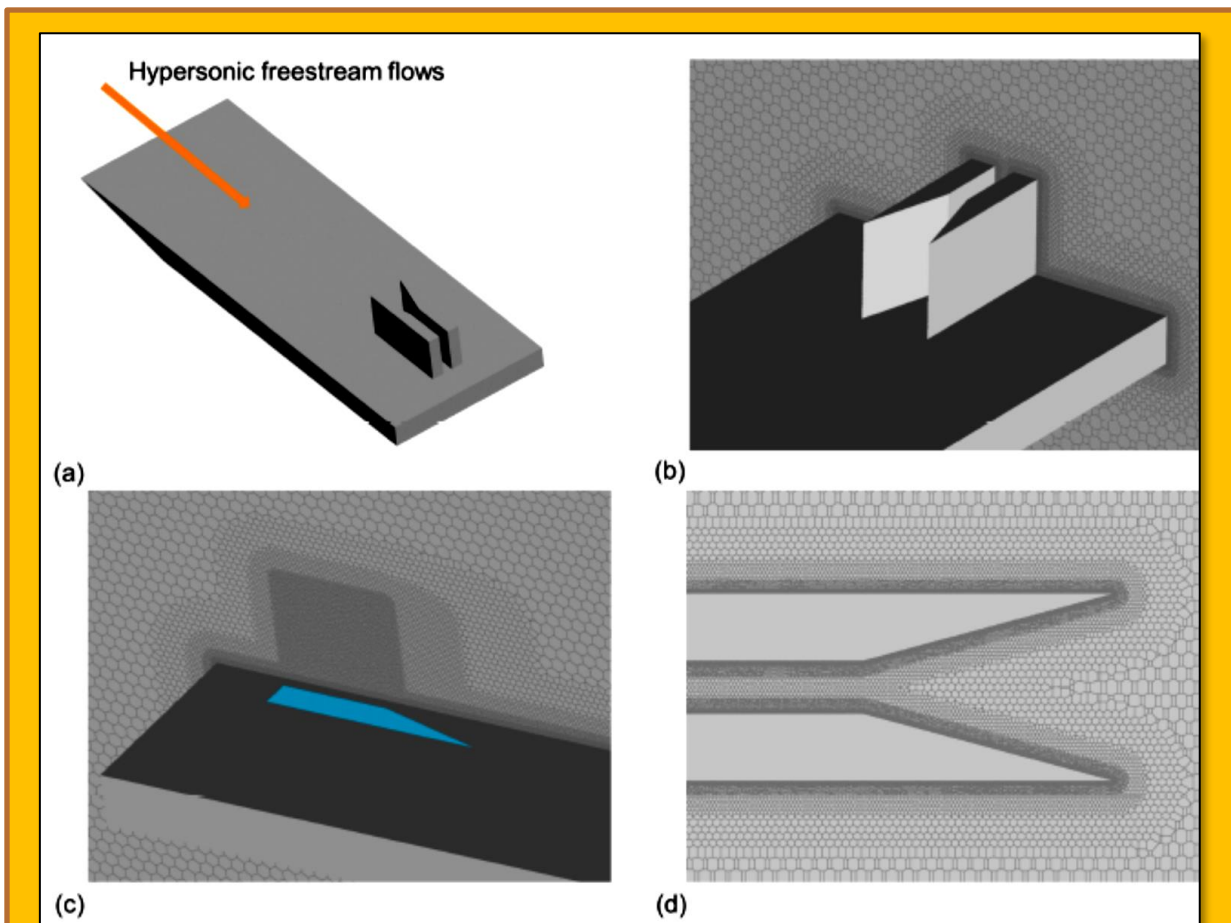


Figure 6.9.2 Computational geometry and mesh sketch for the double-fin simulations: (a) the overview of the computational geometry; (b,c,d) the zoom-in views of the Voronoi mesh distributions (70M total mesh elements)

with respect to the plane  $z = 0$  cm. The free-stream condition is defined 3 cm ahead of the double fins at  $x_0 = 162$  cm. The figure is adapted from [Figure 6.9.2](#) of [23].

The computational geometry is given in [Figure 6.9.2 \(a\)](#). The computational domain is sufficiently large such that there are no artificial reflections from the far-field outflow boundaries. The inlet flow condition is imposed by combining a uniform flow with the turbulence fluctuation generated by the synthetic turbulence generation method. Freestream conditions upstream of the sharp leading edges are adjusted such that the Mach number (behind the leading edge shock) matches the experimental measurements upstream of the double fin entrance. The computational domain is discretized with the  $7 \times 10^7$  Voronoi mesh elements adaptively clustering near the wall, as shown in [Figure 6.9.2 \(b, c, d\)](#).

Based on the resolution of the finest Voronoi mesh element near the wall, the turbulent boundary layer at  $x_0 = 162$  cm is resolved by approximately 40 cells. (The present resolution is much coarser than that previously employed for studying the confinement effects in shock wave/turbulent

$(\Delta x, \Delta y, \Delta z)/\delta_o  _{min}$	$(\Delta x, \Delta y, \Delta z)/\delta_o  _{max}$
$2.5 \times 10^{-2}$	$1.0 \times 10^{-1}$

Table 6.9.1 Grid parameters inside the turbulent boundary layer upstream of the double fins

boundary layer interactions, see Table 1 of [16]). The resolution is coarsened further away from the wall to a maximum of  $\approx 0.1\delta_o$  (see [Figure 6.9.2 \(d\)](#)). It is infeasible to further coarsen the deployed grid for the following two reasons. First, further coarsening the grid will lead to insufficient resolution to properly capture the boundary layer growth from the sharp leading edge. Second, the side wall separation is small, and this resolution is sufficient to capture the side wall separation bubble. Capturing the side wall separation is necessary in order to properly predict the surface heat flux distribution. Nonetheless, the present first off-wall mesh resolution is roughly 400-time coarser when compared to that required by the RANS simulations (see [Table 6.9.1](#)).

## 6.9.5 Results and Discussion

In this section, the numerical results from WMLES with the semi-local scaling based damping function ([Eq. 6.9.12](#)) are analyzed and compared against the experimental measurements. The predictions of the WMLES using the van Driest scaling ([Eq. 6.9.11](#)) will also be assessed. Unless otherwise indicated, the bracket  $\langle \rangle$  denotes time-average operator,  $f = f - \langle f \rangle$  denotes the fluctuation defined based on the Reynolds average, and  $f'' = f - \langle \rho f \rangle / \langle \rho \rangle$  denotes the fluctuation defined based on the Favre average.

### 6.9.5.1 WMLES with Semi-Local Scaling Based Damping Function

#### 6.9.5.1.1 Overall Statistics

[Figure 6.9.3](#) shows the time- and spanwise-averaged Mach number contour on a wall-normal plane and the instantaneous streamwise velocity distribution on a wall-parallel plane at  $y/L_r = 0.3616$  between the leading edge of the flat plate and that of the double fins. A weak shockwave is generated at the leading edge of the flat plate, and slightly decreases the Mach number downstream as shown in [Figure 6.9.3 \(a\)](#). The instantaneous streamwise velocity field in [Figure 6.9.3 \(b\)](#) reveals that the boundary layer transitions, and eventually becomes fully turbulent ahead of the double fins. The turbulent boundary layer appears sustained for approximately  $25\delta_o$  upstream of the double fin entrance. More quantitative comparisons of the flow statistics between the experimental data and the WMLES results at  $x/L_r = 162$ , just upstream of the fins, are given in [Figure 6.9.4](#). While all the statistics close to the boundary layer edge are in good agreement, there are notable discrepancies inside the boundary layer. The discrepancies are in part due to the lingering effect of artificial inflow conditions and relatively short developing length of the incoming boundary layer from the sharp leading edge of the plate.

The results of a grid convergence study at  $x/L_r = 162$  is shown in **Figure 6.9.5**. The fine grid denotes the mesh with parameters given in **Table 6.9.1**. The resolutions of the medium and coarse grids are 50% and 70% coarser than that of the fine grid in each coordinate direction, respectively. While the density profile is not sensitive to mesh refinement, the mean streamwise velocity just upstream of the fins exhibits considerable sensitivity to the grid resolution. In particular, the boundary layer thickness predicted from the medium and coarse grids is 38% smaller than that given by the experiment, and consequently the local effective Reynolds number differs from the experimental setup as well.

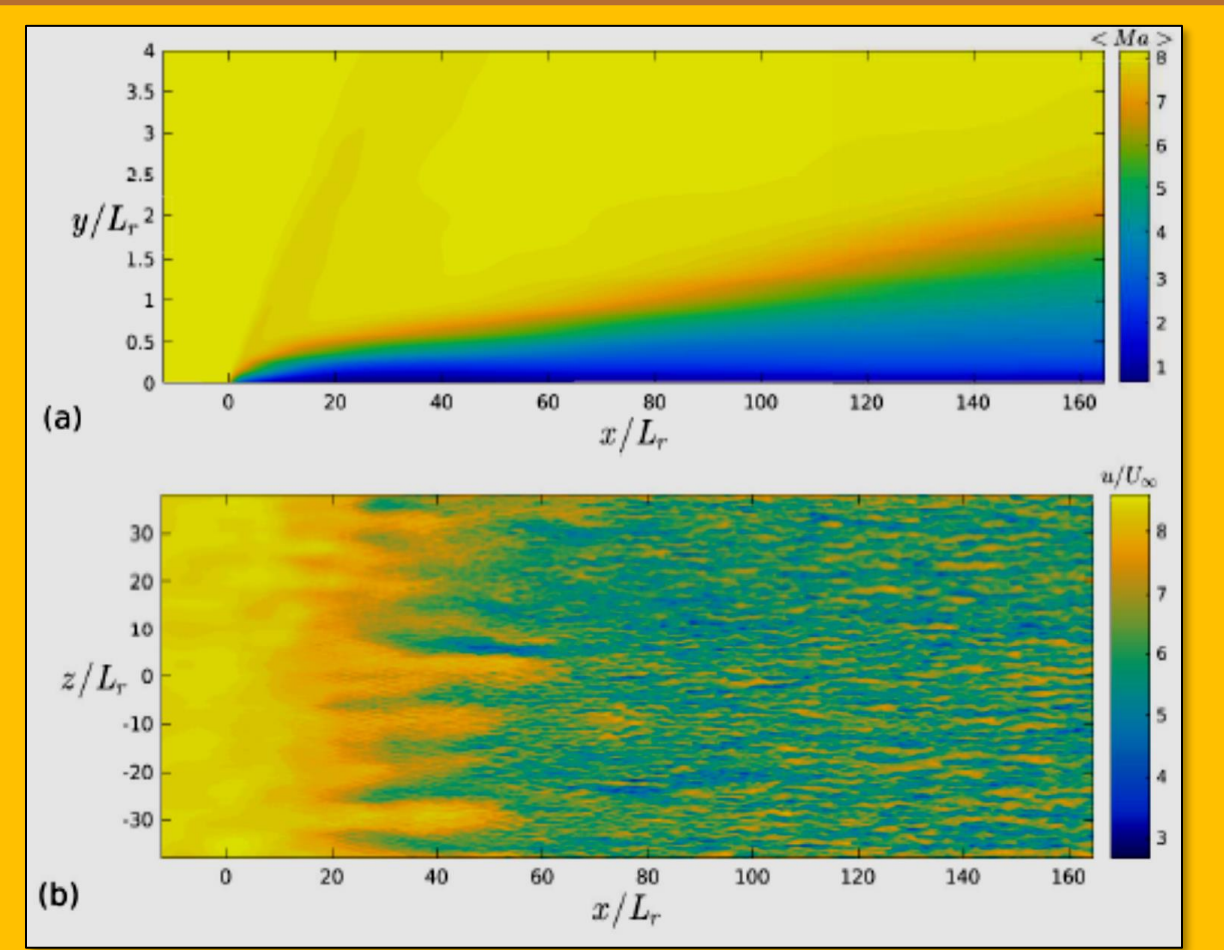


Figure 6.9.3 (a) Time- and spanwise-averaged Mach number contour on the wall-normal x-y plane and (b) the instantaneous streamwise velocity distribution on the wall-parallel x-z plane of  $y/L_r = 0.3616$ . In panel (b), the high-speed region is associated with the oblique shock wave originating from the leading edge of the flat plate at  $x/L_r = 0$ .

Hereafter, only the simulation results from the fine grid will be discussed and the rationality for this resolution choice will be addressed by comparing the WMLES results with the experimental data at downstream locations.

**Figure 6.9.6** shows the time-averaged  $y_+$  at the first off-wall cell centers, i.e. the matching locations for the wall model. The largest  $y_+$  appears around the leading edges of the double fins and the regions where the shock waves impinge on the surfaces. It is clear that the near-wall flow is not directly resolved in the simulations and the wall model plays a pivotal role in the predicted flow states. The  $y_+$  values near the shock impingement location below  $y_+ \approx 20$  suggesting that the details of the LES wall model damping function,  $D(y_+)$ , may significantly impact the flow solutions. The instantaneous

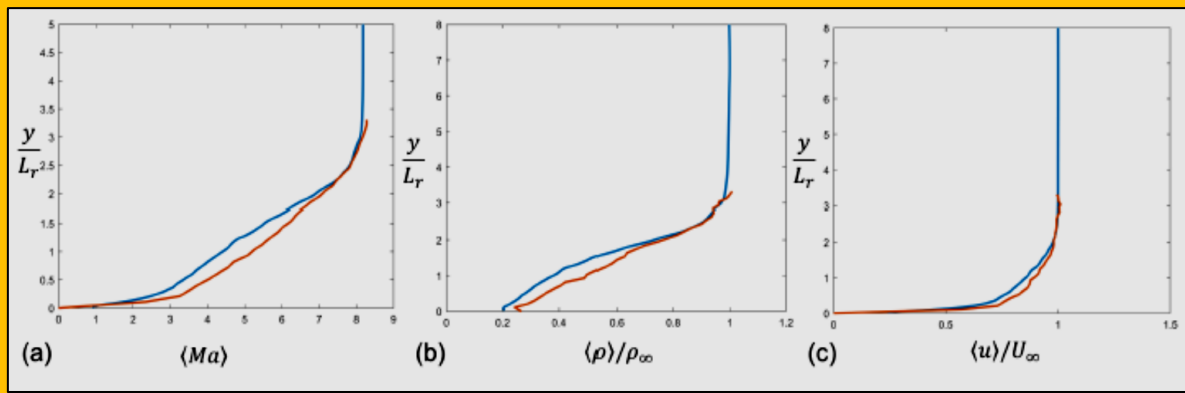


Figure 6.9.4 Time and Spanwise Averaged Distributions of (a) Mach number, (b) Density, and (c) Streamwise Velocity at  $x/L_r = 162$ . The blue and red lines denote the results from WMLES and experiment [23], respectively

surface heat flux distribution, the time-averaged surface heat flux, surface pressure, and surface shear stress distributions are shown in **Figure 6.9.7**. The instantaneous surface heat flux distribution in **Figure 6.9.7 (a)** demonstrates that the flow is highly unstable after the double shockwaves induced by the fin leading edges intersect around the shoulders. As shown in **Figure 6.9.7 (b)(c)(d)**, right downstream of the shock waves intersection, the distributions of the time-averaged surface heat flux, surface pressure and surface stress attain local maxima around the centerline on the plate. Furthermore, the excessive aerodynamic heating and friction are generated around the shock impingement locations on the fin surfaces.

The fine grid denotes the mesh with parameters given in **Table 6.9.1**. The resolutions of the medium and coarse grids are 50% and 70% coarser than that of the fine grid in each coordinate direction, respectively. EXP denotes the experimental data [23].

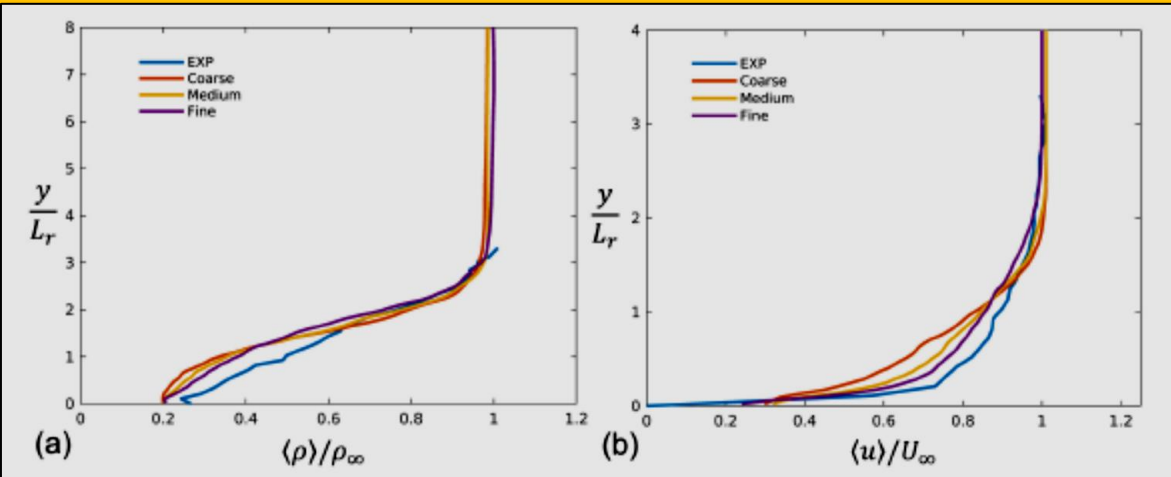


Figure 6.9.5 Time- and spanwise-averaged distributions of (a) density and (b) streamwise velocity at  $x/L_r = 162$ . The fine grid denotes the mesh with parameters given in **Error! Reference source not found..**

The resolutions of the medium and coarse grids are 50% and 70% coarser than that of the fine grid in each coordinate direction, respectively. EXP denotes the experimental data [23].

### 6.9.5.1.2 Data Analyses in x-z and x-y Planes

The time-averaged surface pressure and heat flux distributions along the centerline of the plate

between the two fins as well as the double-shock intersection location based on the inviscid theory are given in **Figure 6.9.9**. The predicted time-averaged pressure distribution from WMLES is in good agreement with the experiment including in the region downstream of the shock intersection. The static pressure first increases significantly due to the shockwave intersection and subsequently exhibits a rapid drop due to the expansions emanating from the fin shoulders, as depicted by **Figure 6.9.8 (a)**.

It is also observed that the peak surface pressure  $\langle P_w \rangle / P_{w,\infty} \approx 22$  is considerably lower than the prediction from the inviscid theory,  $\langle P_w \rangle / P_{w,\infty} \approx 45$  [37]. Further downstream at  $x/L_r \approx 198$ , a smaller pressure peak appears due to the second crossing of the reflected shock waves. In terms of the heat flux distribution, the agreement with the experimental data is also favorable across the entire channel between the double fins. The streamwise variation of the surface heat flux follows that of the surface pressure qualitatively. In detail, both the experiment and the WMLES results exhibit an initial decline at  $x/L_r \approx 170$ , and the predicted heat flux is 20% smaller than that from the experiment in the pre-shock region of  $x/L_r \approx 180$ , which is the location of a secondary small flow separation. Downstream of the shock wave intersection, the peak heat flux shows 4% discrepancy between the WMLES results and the experimental data. Similar differences are also observed further downstream at  $x/L_r = 194$  in the low pressure region and heat flux valley (see also **Figure 6.9.8**). Nevertheless, the present prediction of both quantities shows a much better agreement with the experiment than those from the RANS simulations [37][36].

In the RANS solutions, the heat flux plateau around  $x/L_r = 180$  before the shock wave intersection is completely missed and great sensitivity is noticed with regard to the choice of length scale definition in the Baldwin-Lomax model (see **Figure 6.9.4** and **Figure 6.9.5** in [37]). Both the zero-equation BL model and the two-equation  $\kappa - \epsilon$  overpredict the peak pressure and the peak heat flux by about 20% (see [Error! Reference source not found.](#) and **Figure 6.9.8** in [36]). As shown in **Figure 6.9.8**, the predicted nominal shock impingement location on the side fins is around  $x/L_r = 192$  and is similar to the RANS method prediction (see [Error! Reference source not found.](#) of [37]).

To characterize the boundary-layer flow separation, it was observed that the flow separates around the region where the shock wave impinges on the fin surface. While the overall agreement is good, the predicted streamwise separation close to the fin surface starts at  $x/L_r = 190$ , which is delayed compared to the sketch from the experiment at  $x/L_r = 187$ . As summarized in [36], the two-equation  $\kappa - \epsilon$  model does not capture this streamwise separation.

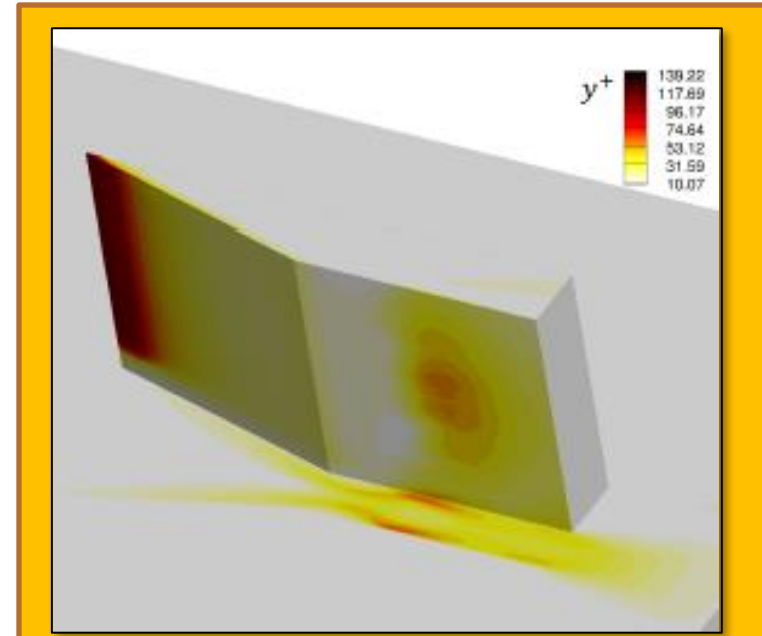


**Figure 6.9.6** Distribution of the time-averaged  $y^+$  at the first off-wall cell centers. For facilitating the presentation, only the data over the flat plate and one vertical fin are shown

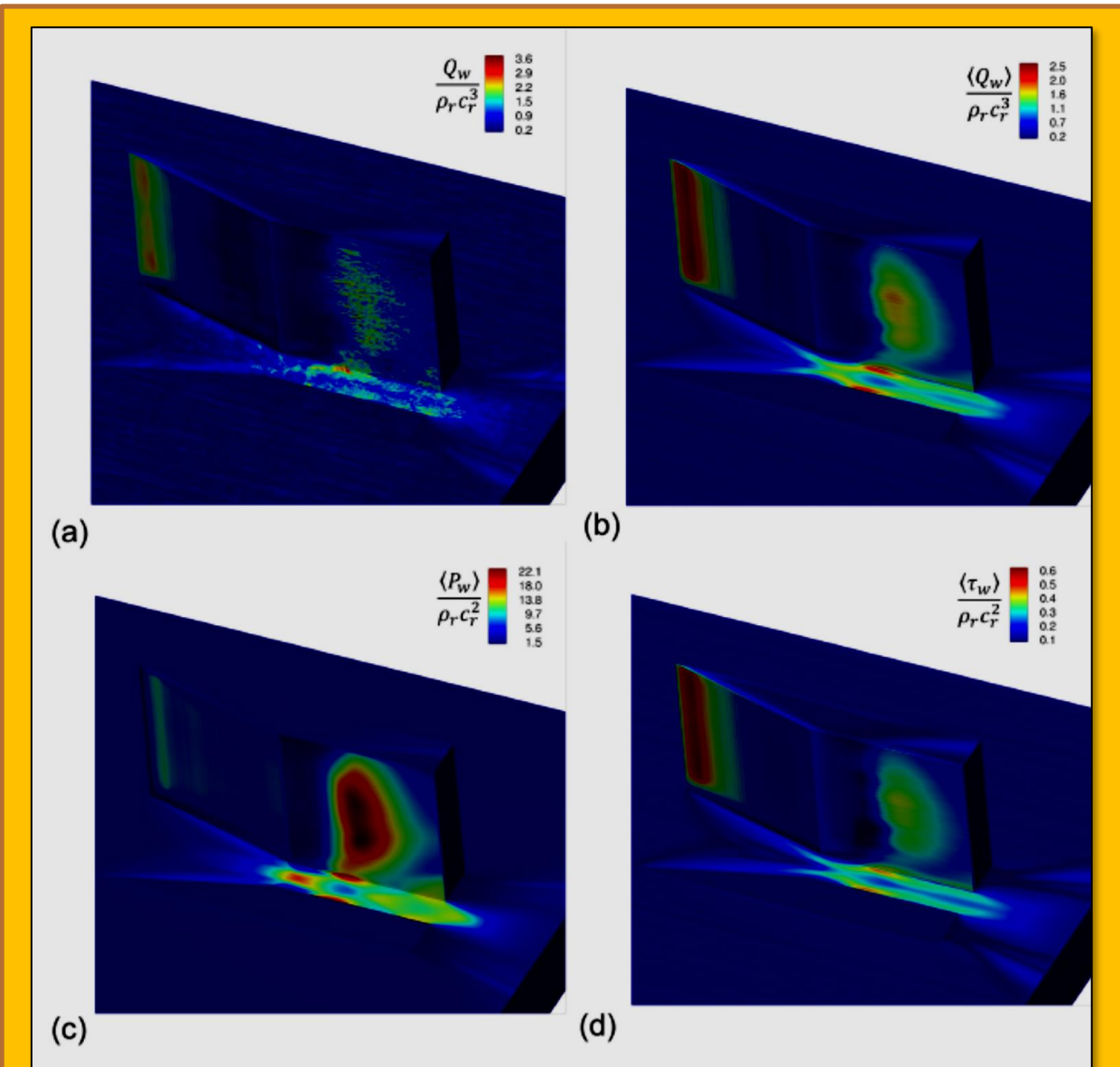


Figure 6.9.7 (a) Instantaneous Surface Heat Flux Distribution, (b) Time-Averaged Surface Heat Flux Distribution, (c) Time-Averaged Pressure Distribution, and (d) Time-Averaged Surface Shear Stress Distribution. The location of the double-shock intersection based on the inviscid theory is around the midpoint of the two fin shoulders. For facilitating the presentation, only the data over the flat plate and one vertical fin are shown

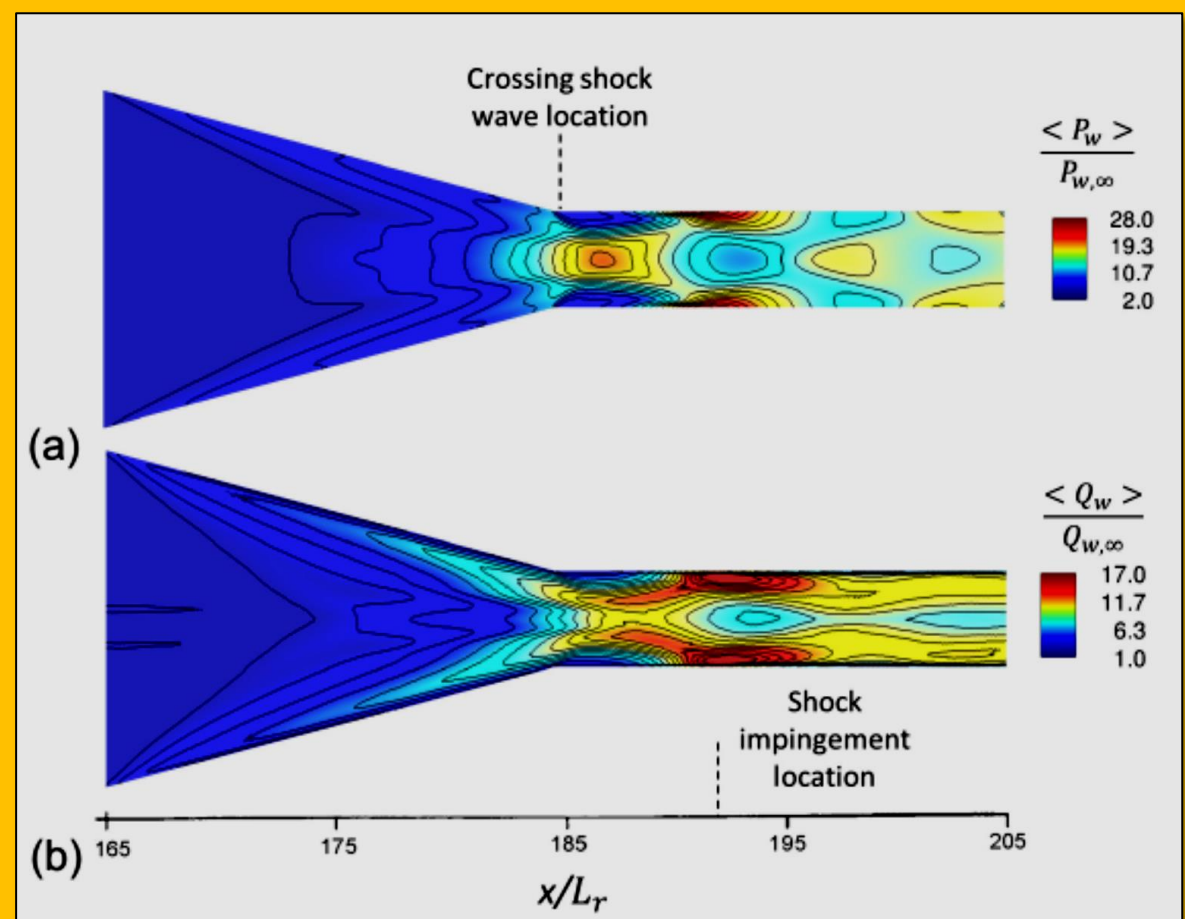


Figure 6.9.9 Distributions of the Time-Averaged (a) Surface Pressure and (b) Surface Heat Flux on the Flat Plate at  $y/L_r = 0$ . The location of the double-shock intersection based on the inviscid theory is also shown in the plots. Also shown is the shock impingement location around  $x/L_r = 192$

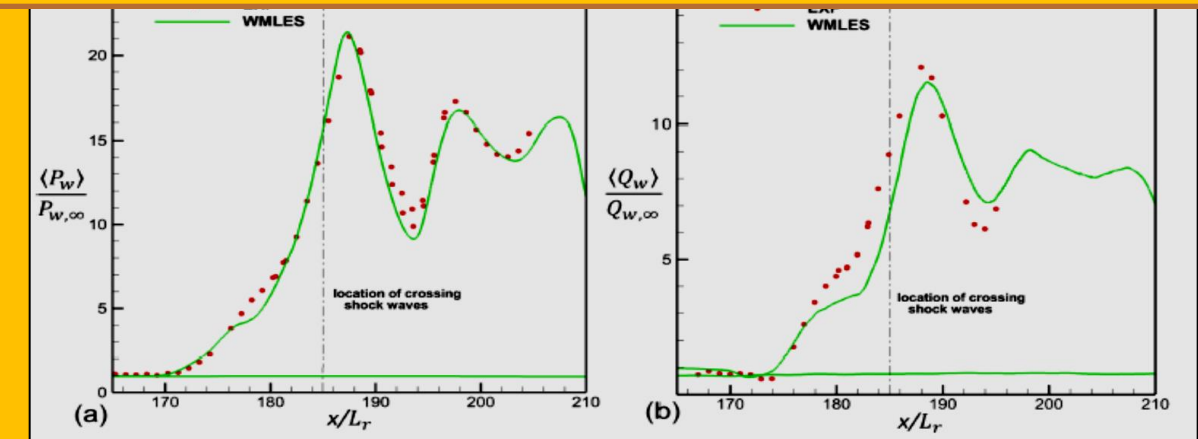


Figure 6.9.8 Streamwise Distributions of The Time-Averaged (a) Surface Pressure and (b) Surface Heat Flux On The Flat Plate at  $y/L_r = 0$  and  $z/L_r = 0$ . The green lines and the red dots denote the results from the WMLES simulation and the experiment, respectively. The location of the double-shock intersection based on the inviscid theory is also shown in the plots

The near-wall root-mean-square (R.M.S) statistics of the pressure, temperature and streamwise velocity are given in Error! Reference source not found.. The near-wall peak temperature and streamwise velocity fluctuations mainly occur around the secondary lines of separation, in particular at the location where the shockwaves intersect. On the other hand, the peak pressure fluctuations occur on the fin surfaces. The distributions of the time-averaged wall-normal turbulent heat flux and Reynolds shear stress in the central wall-normal plane. The magnitudes of both quantities grow rapidly due to the presence of flow separation at  $x/L_r = 175$ , and are further amplified by the shock intersection around  $x/L_r = 185$ . In addition, the primary vortex and the centerline counter-rotating vortex also flip the sign of the wall-normal turbulent heat flux and the Reynolds stress at a certain wall-normal distance, resulting in a layered distribution. The impact of this layered distribution on the time-averaged temperature distribution will be discussed in the next section.

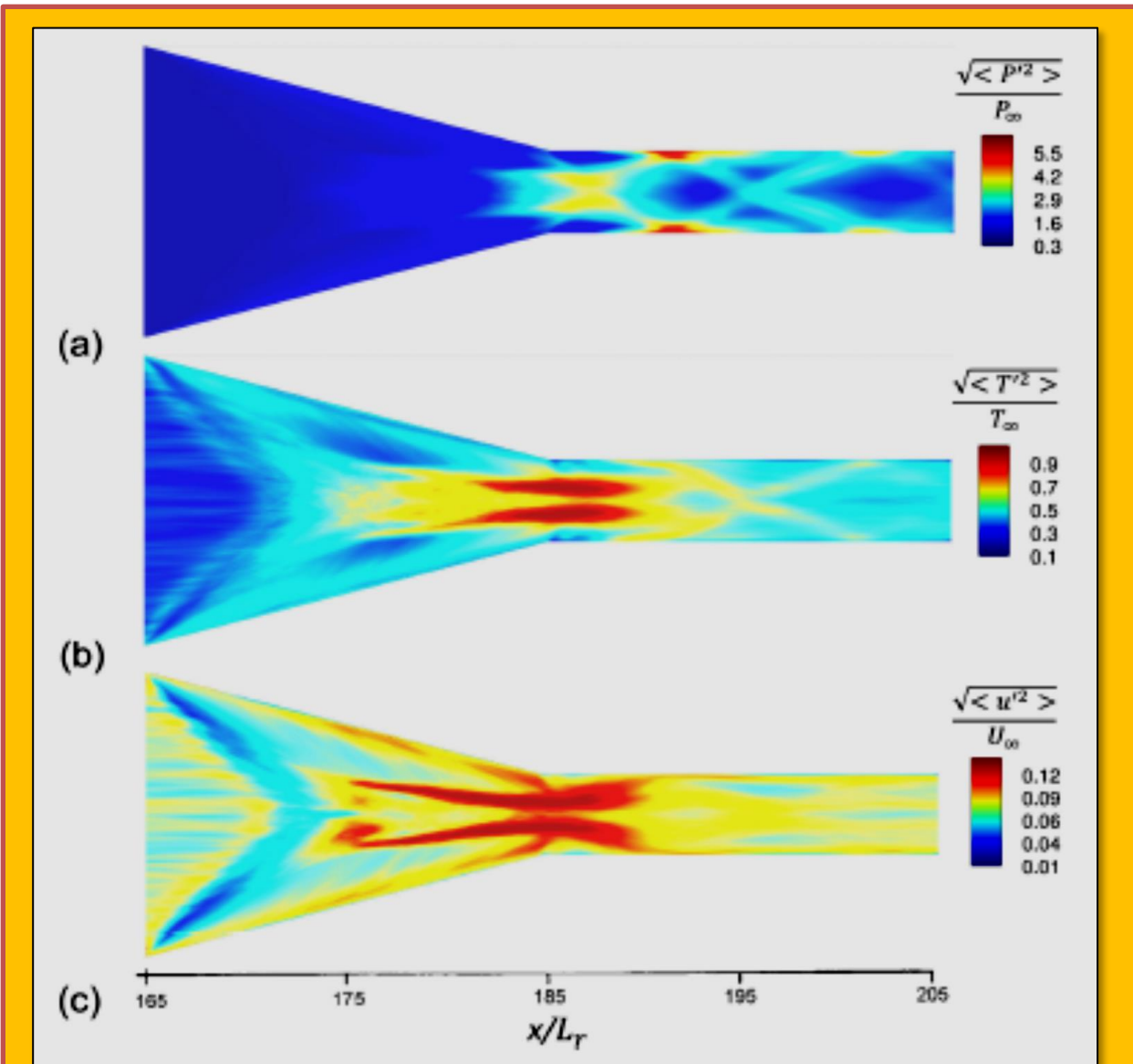


Figure 6.9.10 Included in this figure are the R.M.S statistics of the (a) Pressure, (b) Temperature and (c) Streamwise Velocity Fluctuations. These statistics are projected to the plate surface from the first off-wall cell centers.

**Note** – For Data analyses in y-z planes, readers are encouraged to consult the source [[Fu et al.](#)]<sup>61</sup>.

#### 6.9.5.2 WMLES with Van Driest Scaling Based Damping Function

The sensitivity of the results to the coordinate scaling the wall model eddy viscosity is further evaluated. Wall modeled LES calculations on the “fine” grid using identical freestream boundary conditions described above were additionally performed using the van Driest damping function [28].

---

<sup>61</sup> Lin Fu, Sanjeeb Bose, Parviz Moin, “*Heat transfer in three-dimensional intersecting shock-wave/turbulent boundary-layer interactions with wall-modeled large-eddy simulations*”, arXiv:submit/3355078 [physics.flu-dyn], Sep 2020.

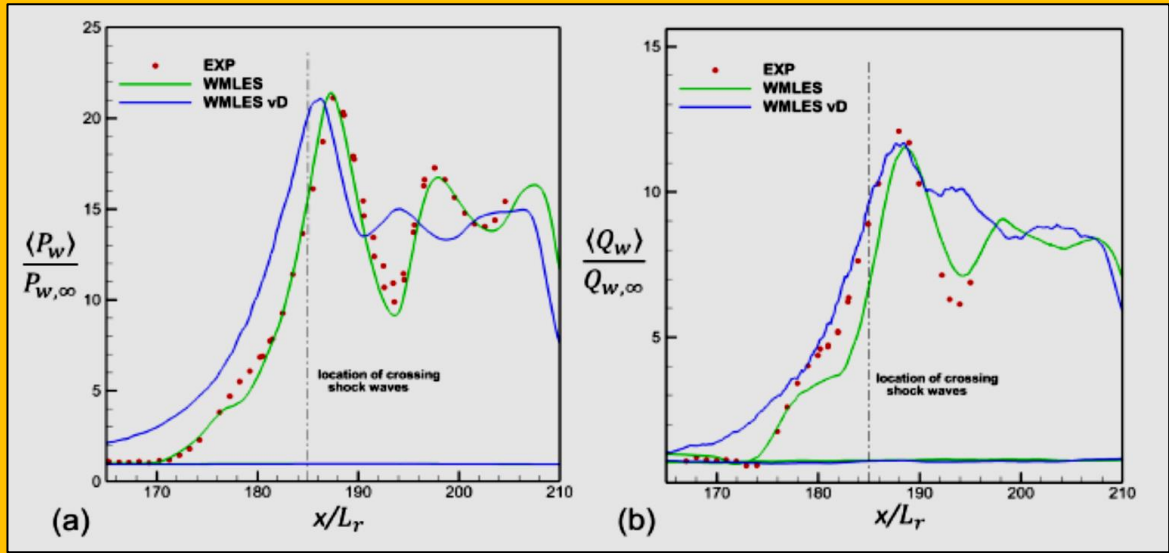


Figure 6.9.11 Streamwise distributions of the time-averaged (a) surface pressure and (b) surface heat flux on the flat plate at  $y/L_r = 0$  and  $z/L_r = 0$ . The green lines, the blue lines and the red symbols denote the data from the WMLES with the semi-local scaling, the WMLES with van Driest scaling, and the experiment, respectively

The comparison of the time-averaged pressure and heat flux distributions between the WMLES with the van Driest scaling and that with the semi-local scaling is provided by [Figure 6.9.11](#) and [Figure 6.9.12](#). For all the concerned quantities, the accuracy of the WMLES deteriorates substantially when the van Driest scaling is deployed for the damping function in the near-wall eddy viscosity model. In terms of the streamwise distributions, both the mean pressure and heat flux are notably overpredicted around the entrance of the double fins. Moreover, the variation trends of both quantities are also poorly captured after the shock intersection. For the spanwise distributions, the maximum

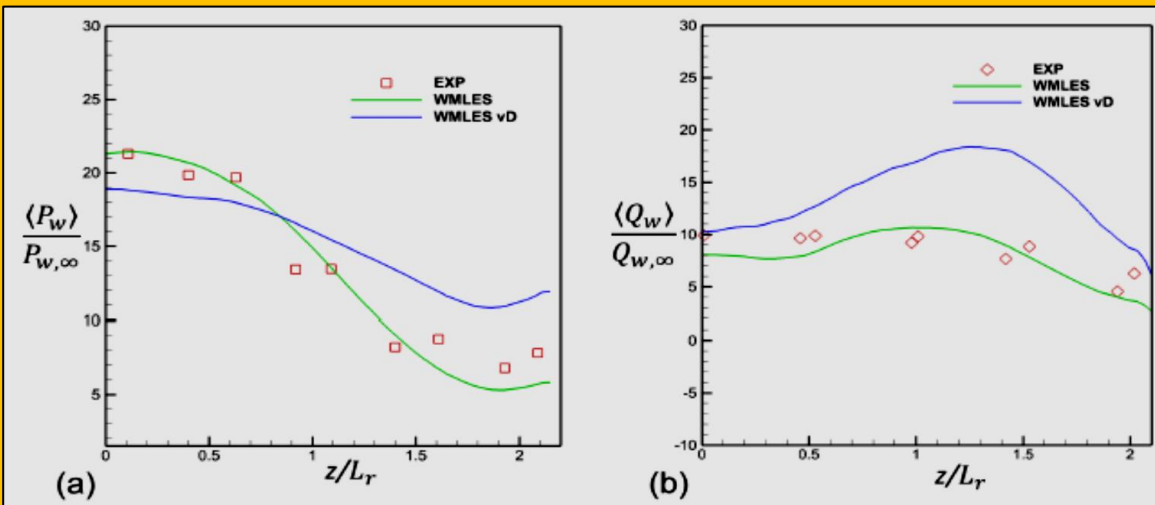


Figure 6.9.12 Spanwise distributions of (a) the time-averaged surface pressure at the streamwise station  $x/L_r = 187.5$  and (b) the time averaged surface heat flux at the streamwise station  $x/L_r = 185.8$ . The green lines, the blue lines and the red symbols denote the data from the WMLES with the semi-local scaling, the WMLES with the van Driest scaling, and the experiment, respectively

discrepancy rises up to 50% when compared to the experimental data and the WMLES result with the semi-local scaling.

Further evidenced by **Figure 6.9.13**, the predicted wall pressure distribution is significantly different from the result with semi-local scaling, and the peak pressure drops by 25% when compared to (see **Figure 6.9.8 (a)**). This result is consistent with the observations that semi-local scaling functions better collapse compressible velocity profiles to their incompressible counterparts compared to the van Driest transformation, particularly in the viscous sublayer with isothermal wall conditions [40][26][27].

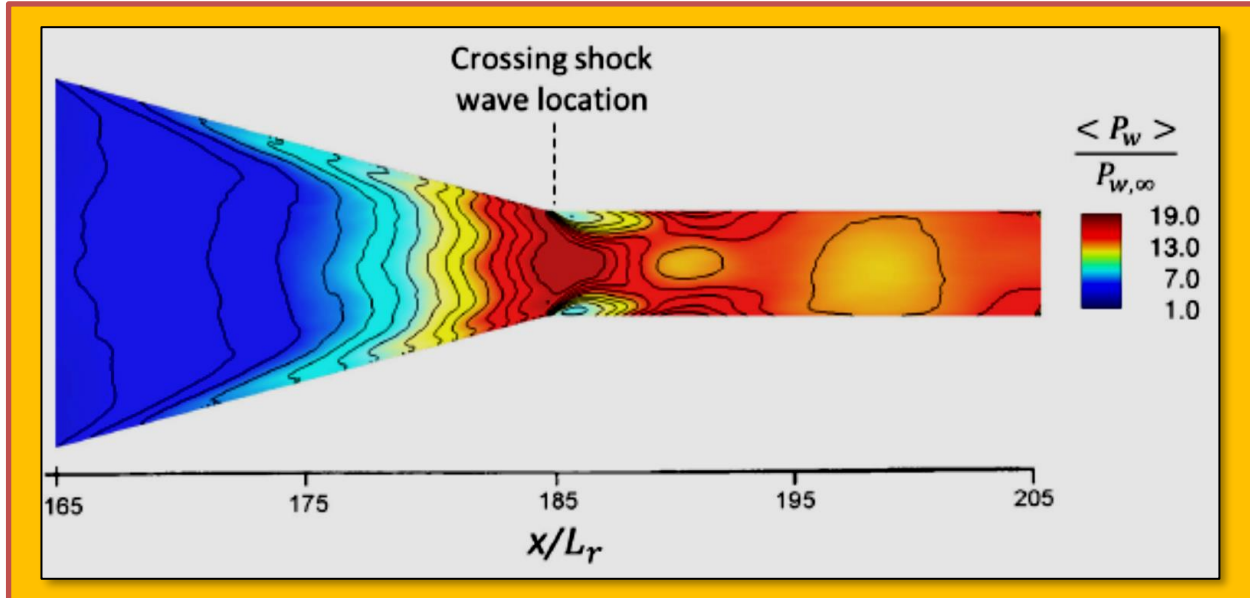


Figure 6.9.13 Distribution of the time-averaged pressure on the flat-plate surface at  $y/L_r = 0$ . The location of the double-shock intersection based on the inviscid theory is also shown in the plot. The result reported in this plot is from WMLES with van Driest scaling based damping function

## 6.9.6 Conclusions

In this study, the three-dimensional intersecting shock-wave/turbulent boundary-layer interaction flow over double fin geometry is investigated using wall modeled large eddy simulation. Despite the complexity of the shock/boundary layer interaction and presence of small separation bubbles, the WMLES agrees favorably with experimental data for mechanical loading, surface heat fluxes, and for the prediction of the secondary separation in both the shock impingement and post-shock regimes. The wall modeled LES calculations include the semi-local scaling of the eddy viscosity, which was necessary to predict accurately the heat fluxes and wall pressure distributions. The resultant errors in the WMLES are shown to be significantly smaller than prior RANS simulations of this configuration using either Baldwin-Lomax or  $\kappa - \epsilon$  models. The coarseness of the WMLES calculations (relative to the boundary layer thickness or size of the separation bubble) suggest that this approach may be tractable for more complex configurations.

## 6.9.7 Acknowledgments

*This work was funded by the US Air Force Office of Scientific Research (AFOSR), Grant #1194592-1-TAAHO. Supercomputing resources were provided through the INCITE Program of the Department of Energy (DOE). Mori Mani and Matthew Lakebrink from Boeing Research & Technology are greatly acknowledged for suggesting this case to the authors. The first author appreciates the useful discussions with Kevin Griffin at CTR, Stanford University.*

## 6.10 Case Study 10 - Comparison of Steady and Unsteady RANS Heat Transfer Simulations of Hub and End all of a Turbine Blade Passage

**Authors :** Lamyaa A. El-Gabry , Ali A. Ameri

**Citation :** El-Gabry, L. A., and Ameri, A. A. (November 15, 2010). "Comparison of Steady and Unsteady RANS Heat Transfer Simulations of Hub and Endwall of a Turbine Blade Passage." *ASME J. Turbomachinery* July 2011; 133(3): 031010. <https://doi.org/10.1115/1.4002412>

The necessity of performing an unsteady simulation for the purpose of predicting the heat transfer on the end wall surfaces of a turbine passage is addressed by [El-Gabry and Ameri]<sup>62</sup>. This is measured by the difference between the two solutions obtained from a steady simulation and the time average of an unsteady simulation. The heat transfer coefficient (Nusselt number) based on the adiabatic wall temperature is used as the basis of the comparison. As there is no film cooling in the proposed case, a computed heat transfer coefficient should be a better measure of such difference than, say, a wall heat flux. Results show that the effect of unsteadiness due to wake passage on the pressures and recovery temperatures on both hub and casing is negligible. Heat transfer on the end walls, however, is affected by the unsteady wake; the time-averaged results yield higher heat transfer; in some regions, up to 15% higher. The results for the end wall heat transfer were compared with results in open literature and were found to be comparable.

### 6.10.1 Introduction

Gas turbine heat transfer remains an important topic of concern as turbine inlet temperatures continue to rise and combustor exit profiles continue to flatten with the goal of maximizing power output and efficiency. This in turn means higher gas-side heat transfer to the hot gas path components, including the vane and blade and, in particular, the end walls, which are now experiencing temperatures nearly as high as the peak temperatures near the midspan.

Of importance to understanding the end wall heat transfer is describing and characterizing end wall flows. As early as 1976, [Langston et al.]<sup>63</sup> wrote that "the literature is certainly not lacking in experimental studies of end wall flows in turbine cascades" but is lacking a "complete analytical solution" of the end wall flows. In this 1976 paper, [Langston et al.] cited the potential of numerical models to fill in that gap, which, one can argue, has yet to be entirely filled, which, that is, where the present research and other papers on computational fluid dynamics (CFD) modeling of end wall flow and heat transfer continue to play an important role in our understanding of this critical region of the turbine passage. [Langston et al.] used ink to visualize flow near the end walls of a cascade and measured pressures and velocities at axial locations within the passage. [Gregory-Smith et al.]<sup>64</sup> presented the flow visualization of the end wall and made measurements in a cascade with the goal of calculating the vorticity in the passage.

There have also been several review papers that survey literature on secondary flows in turbine passages and that highlight results of turbine end wall aerodynamics and heat transfer studies. The dominant secondary flow structures highlighted include the cross-passage flow that crosses from the pressure side to the suction side and what is commonly referred to as the horseshoe vortex that forms at the stagnation point on the leading edge, where the flow separates into a pressure side and a suction side leg. There are additional forms of secondary flow, including corner vortices. There are

<sup>62</sup> Lamyaa A. El-Gabry, Ali A. Ameri, "Comparison of Steady and Unsteady RANS Heat Transfer Simulations of Hub and End wall of a Turbine Blade Passage", Journal of Turbomachinery, JULY 2011.

<sup>63</sup> Langston, L. S., Nice, L. M., and Hooper, R. M., 1976, "Three Dimensional Flow Within a Turbine Cascade Passage," ASME Paper No. 76-GT-50.

<sup>64</sup> Gregory-Smith, D. G., Graves, C. P., and Walsh, J. A., 1988, "Growth of Secondary Losses and Vorticity in an Axial Turbine Cascade," ASME J. Turbomachine, 110, pp. 1-8.

three “corners”: the first is between the pressure side surface and the hub, the second is between the suction side surface and the hub, and the third is between the leading edge surface and the hub.

Near the blade tip, the dominant secondary flow feature is the tip leakage vortex that manifests itself along the suction side of the airfoil. The losses due to tip leakage flow can account for up to 1/3 of the total stage losses, as suggested by [Boyle et al.]<sup>65</sup>, making them important from an aerodynamics perspective as well as their impact on heat transfer. Research in the topic of near-tip flows and heat transfer started with basic research using very basic geometry to represent flat and grooved rectangular tip models. These studies, among other things, established that the effect of relative motion between the blade and casing on heat transfer is negligible, which was consequently followed by a series of linear cascade tests using three-blade, four-blade, and five-blade cascades to measure static pressure and local heat transfer distribution on the airfoil, tip, and casing surfaces for a variety of tip geometries.

Experimental data obtained in stationary cascades offer detailed measurements; however, results may not scale to the actual engine conditions or be truly representative of a true rotating blade in an engine. Therefore, experimental data have also been obtained at engine conditions in rotating rigs. [Haldeman and Dunn]<sup>66</sup> at the Ohio State University Gas Turbine Laboratory measured the heat transfer for the vane and blade of a rotating high pressure turbine stage operating at design corrected conditions using a large shock-tunnel facility.

For the blade, Stanton number is reported at 20% and 96% spans at the blade tip and on the shroud. [Polanka et al.]<sup>67</sup> also made pressure and heat flux measurements on the tip and shroud under rotating conditions at the U.S. Air Force Turbine Research Facility, which is a full scale rotating rig. These test setups are far more representative of engine conditions, however, the test data are sparse and a limited number of discrete measurements are available as compared with the cascade tests.

In addition to the experimental research on end wall aerodynamics and heat transfer, there have been a number of computational studies on the subject, several of which complement the experimental work. The 9H tip heat transfer experiments of [Bunker et al.]<sup>68</sup> were modeled using in-house Reynolds-averaged Navier-Stokes \_RANS\_ codes and the OSU tests were modeled using the commercial CFD code STARCD \_17\_ and an in-house GE-developed code *Tacoma* . [Polanka et al.]<sup>69</sup> presented a comparison between numerical predictions and experimental results of [Polanka et al.]. The conclusions were that the agreement between the test and the CFD is “very good” on the airfoil and “moderately good” on the end walls and tip; the tip heat transfer was overpredicted by the CFD and although the shroud pressure distribution was accurately predicted with the 3D RANS solver, the heat transfer there was overpredicted by a factor of 2.

Wake effects and unsteadiness were investigated by [Pullman]<sup>70</sup>, who used test measurements to show the vortex formation at the stator exit and their development within the rotor passage to the rotor exit. Using the experimental measurements at the stator exit as boundary conditions to a rotor

<sup>65</sup> Boyle, R. J., Haas, J. E., and Katsanis, T., 1985, “Predicted Turbine Stage Performance Using Quasi-Three-Dimensional and Boundary Layer Analyses,” *J. Propulsion Power*, 1, pp. 242–251.

<sup>66</sup> Haldeman, C. W., and Dunn, M. G., 2004, “Heat-Transfer Measurements and Predictions for the Vane and Blade of a Rotating High-Pressure Turbine Stage,” *ASME J. Turb.*, 126, pp. 101–109.

<sup>67</sup> Polanka, M. D., Hoying, D. A., Meininger, M., and MacArthur, C. D., 2003, “Turbine Tip and Shroud Heat Transfer and Loading—Part A: Parameter Effects Including Reynolds Number, Pressure Ratio, and Gas-to-Metal Temperature Ratio,” *ASME J. Turb.*, 125, pp. 97.

<sup>68</sup> Bunker, R. S., Bailey, J. C., and Ameri, A., 2000, “Heat Transfer and Flow on the First-Stage Blade Tip of a Power Generation Gas Turbine: Part 1—Experimental Results,” *ASME J. Turb.*, 122, pp. 263–271.

<sup>69</sup> Polanka, M. D., Clark, J. P., White, A. L., Meininger, M., and Praisner, T. J., 2003, “Turbine Tip and Shroud Heat Transfer and Loading Part B: Comparison Between Prediction and Experiment Including Unsteady Effects,” *ASME Paper No. GT2003-38916*.

<sup>70</sup> Pullman, G., 2004, “Secondary Flows and Loss Caused by Blade Row Interaction in a Turbine Stage,” *ASME Paper No. GT2004-53743*.

CFD model, the predictions of the aerodynamic losses \_using steady and unsteady analyses are calculated and the flow field at the rotor exit is predicted and compared with test data. The steady simulation predicted 10% less loss in the rotor row than the unsteady simulation.

The present work focuses on the effect of unsteadiness due to wake passage on the end wall heat transfer as well as pressures and temperatures as predicted using an unsteady 3D RANS solver. The vehicle for this computational study is the E3 high pressure turbine blade, which has been reported extensively in literature. Time-resolved test measurements are not available for the E3 HPT blade; therefore, qualitative comparisons of the CFD results will be made with HPT data in open literature, to serve as a check on the CFD results. The primary question this research seeks to answer is whether an unsteady analysis gives the same answer as a steady analysis. For this size model  $\sim 2 \times 10^6$  nodes, it takes 500 clock hours to reach a converged steady state solution. Also, it takes the same model 25,000 clock hours to converge the unsteady

simulation. The question is: Is the added time and complexity of running unsteady worth it?

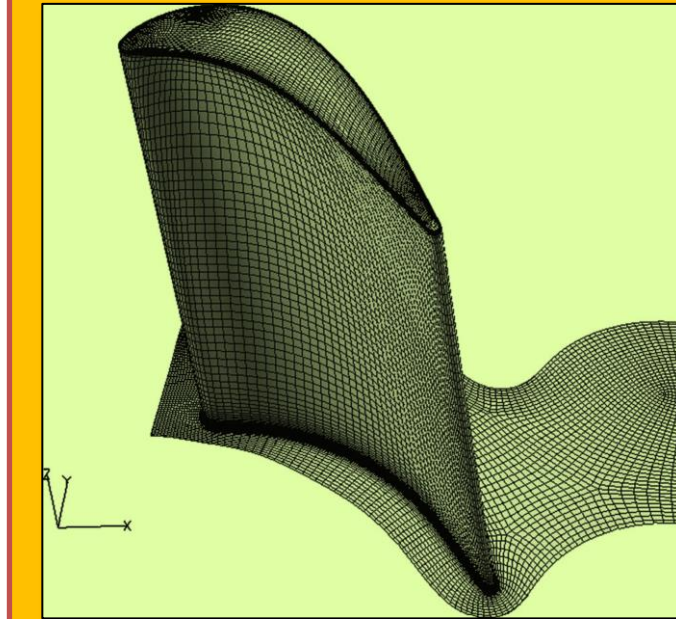


Figure 6.10.1 Grid on the Solid Surfaces of the Geometry

### 6.10.2 Computational Method

A 3D RANS code developed at the *NASA Glenn Research Center* has been used to predict pressures, temperatures, and heat transfer in a single blade passage of the *GE-E3* gas turbine. The code was Glenn-HT and was described in detail by [Ameri et al.]<sup>71</sup>. It uses a finite volume discretization scheme and is second order accurate in time and space. The turbulence model used in the calculations was the low Reynolds number  $k-\omega$  model by [Wilcox], which is integrated to the wall; a nondimensional grid spacing  $y+$  of near 1 is maintained on all wall surfaces, including the blade and end walls. The code was run on 48 processors of a *Xeon Linux Cluster* using message passing interface for parallel processing.

The E3 gas turbine has 46 vanes and 76 blades and the blade rotates at 8400 rpm. The blade tip clearance is 2% of the blade span. The present research focuses on the effect of the upstream vane wake on the blade. The domain of this computation is restricted to a single blade passage; this simplification of using a vane/blade ratio of 1 is based on a separate preliminary study, which showed that for purposes of computing average heat transfer, the wake frequency for a 1:1 ratio produces a very similar result as compared with a 2:3 ratio. The 2:3 ratio is an approximation to the actual vane/blade count, which was 46:76.

The inlet of the domain is located at 15% axial chord upstream of the blade leading edge \_midway between the vane trailing edge and the blade leading edge\_ and the exit of the domain is at 50% axial chord downstream of the blade trailing edge. To create the multiblock structured grid needed for the solver *GRIDPRO™*, commercially available software for generating structured meshes was used.

<sup>71</sup> Ameri, A. A., Steinhorsson, E., and Rigby, D., 1998, "Effect of Squealer Tips on Rotor Heat Transfer and Efficiency," ASME J. Turbomachine., pp. 753–759.

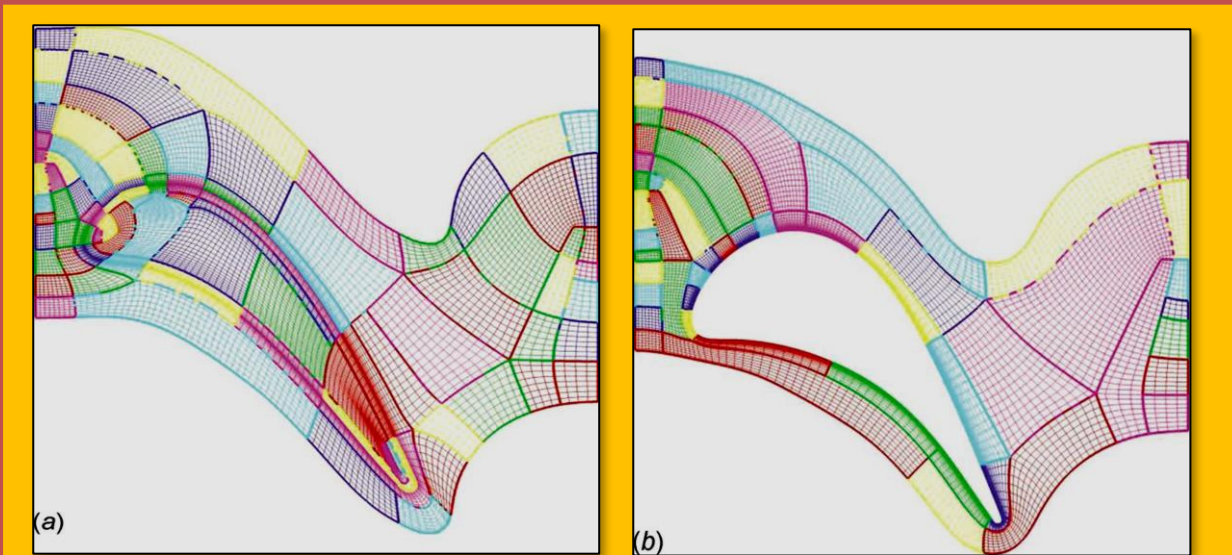


Figure 6.10.2 (a) Casing surface mesh showing multiblock structure and (b) hub surface mesh showing multiblock structure

shows the surface mesh on the solid airfoil and hub. **Figure 6.10.2a** shows the grid on the casing surface highlighting the multiblock structure of the grid blocks. **Figure 6.10.2b** shows the grid structure on the hub surface. The grid consists of 164 blocks and a total of  $1.8 \times 10^6$  nodes. There are 65 nodes across the tip clearance gap in the radial direction and 101 nodes from the hub to tip of the blade. The grid independence of the solution was established.

A dimensionless time step of 0.005 was used based on earlier investigations in which the time step was varied from 0.001 to 0.01. For the selected time step of 0.005, 320 steps were required to complete one period; (i.e., the passing of a wake across a single blade passage), which is sufficiently fine, a resolution for purposes of this study. Based on the selected time step, blade count, and RPM, there were 320 time steps over the period of one wake passage.

### 6.10.3 Boundary Conditions

A separate computation of the vane flow was used to establish the inlet boundary conditions used in the present blade analysis. The total pressure and temperature at the vane exit were calculated using

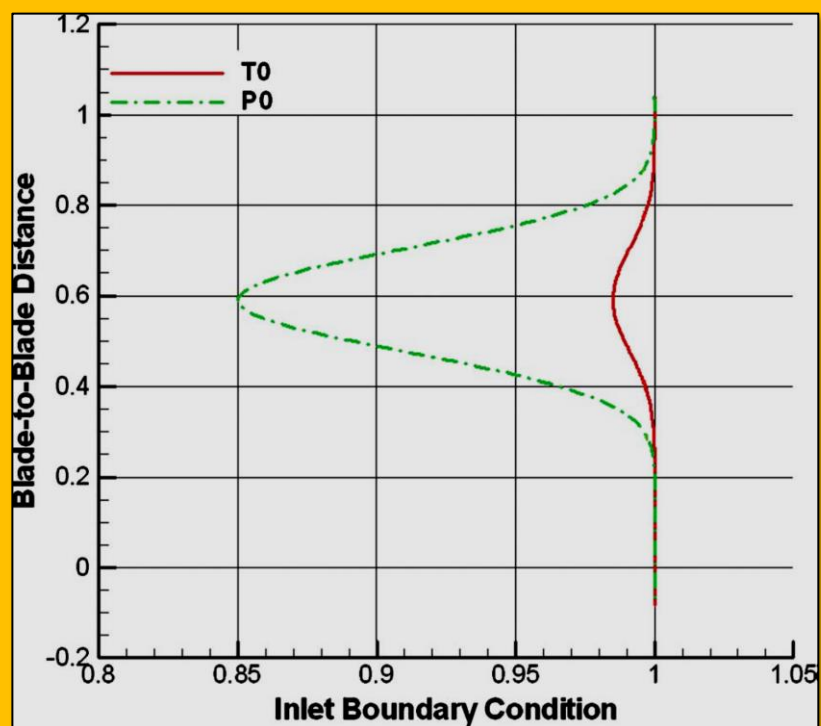


Figure 6.10.3 Total temperature ( $T_0$ ) and total pressure ( $P_0$ ) at the blade inlet

the same code and methodology and the wake profile is taken from the midspan of the vane computation and used for the entire span of the inlet section to the blade. The total pressure in the vane wake was approximated with a trigonometric function

$$p_{t,\theta}(0, \theta) = p_{0,bg} \{1 - 0.15\sin[n\theta/2 + \pi t/\tau]^{10}\}$$

#### **Eq. 6.10.1**

Likewise, the total temperature wake behind the vane was approximated using a second trigonometric function

$$T_{t,\theta}(0, \theta) = T_{0,bg} \{1 - 0.05\sin[n\theta/2 + \pi t/\tau]^{10}\}$$

#### **Eq. 6.10.2**

**Figure 6.10.3** shows the normalized inlet total temperature and total pressure wakes as applied to the blade inlet. The wake turbulence and length scale were similarly obtained and approximated with trigonometric functions and specified at the blade inlet. The background level for turbulence intensity was 2% and the amplitude was 5% for a peak value of 7%, i.e.,

$$Tu(t, \theta) = Tu_{b,g} + Tu_{amp} \{\sin[n\theta/2 + \pi t/\tau]^6\}$$

#### **Eq. 6.10.3**

The wake turbulence length scale was also fitted with the same function, where the background length scale was set to 10% axial chord and the peak length scale was set to 25% axial chord. To simulate the near wall boundary layer effects, a boundary layer profile for the inlet total pressure and temperatures is applied at the inlet section that extends to 1% span from the hub and casing. At the exit of the domain, a constant static pressure boundary condition is applied at the hub and a radial equilibrium is enforced. No-slip boundary conditions are applied to all solid surfaces in the domain, including airfoil, hub, and casing. The heat transfer coefficient is defined as

$$h = \frac{Q_w}{T_{aw} - T_w}$$

#### **Eq. 6.10.4**

where  $Q_w$  is the wall heat flux,  $T_w$  is the wall temperature, and  $T_{aw}$  is the adiabatic wall temperature. Therefore, in order to calculate heat transfer coefficient defined as such, it is necessary to run two separate analyses; one in which the walls have zero heat flux in order to determine the adiabatic wall temperatures and a second with a prescribed wall temperature in order to calculate the heat flux. For the runs with a prescribed wall temperature, a constant temperature of 0.7 (normalized using inlet total temperature) is applied to all walls. The steady state boundary conditions are based on the average of the unsteady computations.

#### **6.10.4 Results and Discussion**

**Figure 6.10.4** shows the instantaneous pressure distribution on the hub surface at equal times over the period of one wake passage. The image outlined with the dashed line shows the time-averaged pressure distribution. These time-averaged results are compared with a steady simulation in which there is no wake at the inlet. The inlet boundary condition for the steady simulation is the area average of the unsteady boundary condition in **Figure 6.10.3**.

The instantaneous pressure distributions in **Figure 6.10.4**, particularly the position and extent of the low pressure region on the suction side, illustrate the effects of the wake passage. This region of minimum pressure is indicative of a vortex that is traveling along the suction side (perhaps the suction side (SS) leg of the horseshoe vortex). As time passes from  $t=0$  to  $t=T/4$ , this low pressure region moves along the SS edge and extends in the blade to blade direction. As it approaches the

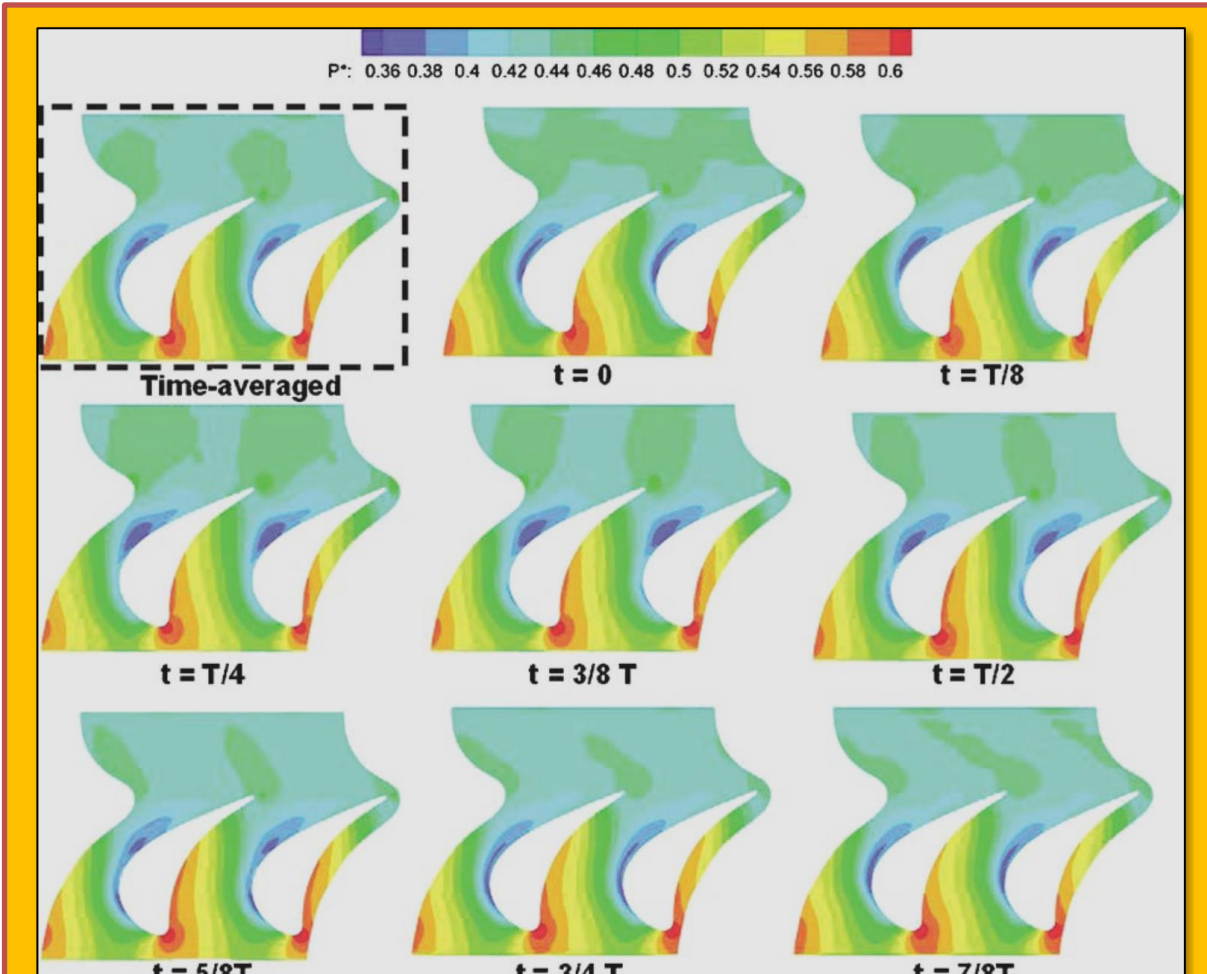


Figure 6.10.4 Instantaneous and time-averaged „dashed... hub surface pressure for a wake passing

trailing edge (TE), it appears to move away from the SS edge toward the pressure side (PS) trailing edge and begins to diffuse. At some time between  $T/4$  and  $3/8T$ , a second low pressure region emerges near the leading edge before the high point of curvature (high-C) that also moves along the SS edge extends and diffuses as before. The periodic growth, diffusion, and movement of this low pressure region indicate an interaction between the end wall secondary flows and the upstream wake.

Likewise, the instantaneous heat flux images in **Figure 6.10.5** suggest an interaction between the wake passage and the end wall heat transfer on the hub. In discussing the pressure, we focused on the low pressure region along the suction side and noted the presence of two low pressure regions at the same time during part of the period: one region is diffusing into the passage near the trailing edge and one is beginning to grow as it moves along the SS edge near the leading edge. In **Figure 6.10.5**, let us focus our attention on the high heat transfer regions shown in red. At the leading edge, there is high heat transfer due to stagnation that extends along the PS edge and grows. There is a low heat transfer region between the passages that moves along the SS edge and grows then diffuses across the passage to PS edge. In doing so, it mixes with the high heat transfer fluid and reduces the heat transfer, resulting in what appears to be a break in the high heat flux zone along the PS edge. The latter piece of the high heat transfer region along the PS edge shrinks in extent and decreases in magnitude as it diffuses and appears to “shed” at the trailing edge.

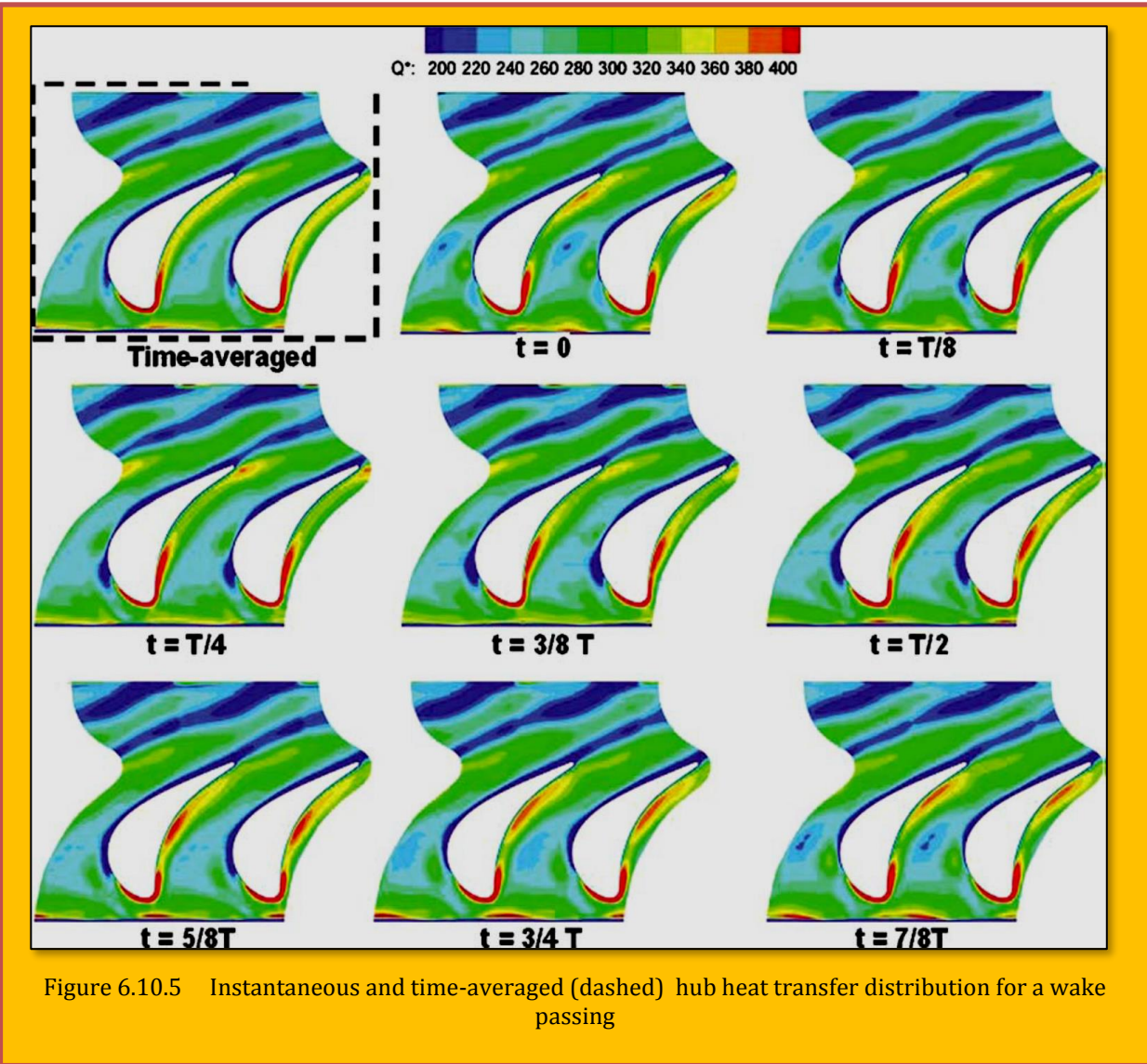


Figure 6.10.5 Instantaneous and time-averaged (dashed) hub heat transfer distribution for a wake passing

The pressure distribution on the casing and hub surfaces is plotted in [Figure 6.10.6](#) and [Figure 6.10.7](#), respectively, nondimensionalized by the inlet total pressure. [Figure 6.10.7](#) is actually a repeat of the time-averaged contour plot in [Figure 6.10.5](#) outlined with a dashed line. The airfoil outline shown in [Figure 6.10.6](#) and [Figure 6.10.9](#) and other casing images to follow is the projection of the tip surface on the casing.

On the casing surface, there is a region of high pressure in the forward part of the passage above the pressure side surface of the airfoil whose outline is shown in [Figure 6.10.6](#). This high pressure corresponds to the stagnation region of the airfoil near the tip. There is a low pressure region near the trailing edge of the airfoil, which likely corresponds to higher tip flow speeds.

On the hub surface [Figure 6.10.7](#), the stagnation region at the leading of the airfoil results in a high pressure zone that extends into the passage along the pressure side. On the suction side is a low pressure region just past the high-C \_curvature\_ of the airfoil that increases along the passage likely to correspond with the suction side leg of horseshoe vortex forming at the leading edge and growing as it moves through the passage and interacts with the cross-passage flow.

Contour plots of pressure on the casing and hub surfaces were also obtained from a steady state CFD model and compared with the time-averaged distributions. There was no discernable difference between the time-averaged and steady state contours that could be identified from the contour plots. Therefore, the difference between the time-averaged and steady state local pressures is plotted instead in **Figure 6.10.9** and **Figure 6.10.8**.

**Figure 6.10.9** shows the difference between the time-averaged and steady state pressure results on the casing surface as a percentage of the time-averaged results. Clearly, there is negligible difference between the two solutions; the largest difference is on the order of 2% and is located slightly forward of the high-C point on the casing surface and further aft at the high-C point on the hub surface. However, a 2% difference is not significant enough to justify/warrant a transient CFD analysis.

**Figure 6.10.10** and **Figure 6.10.11** show the adiabatic wall temperature distribution on the casing and hub surfaces, respectively, nondimensionalized by the inlet total temperature. Note that the two figures are not plotted at the same scale to illustrate trends and enable discussion. In **Figure 6.10.10**, the adiabatic wall temperature on the casing surface exceeds the inlet

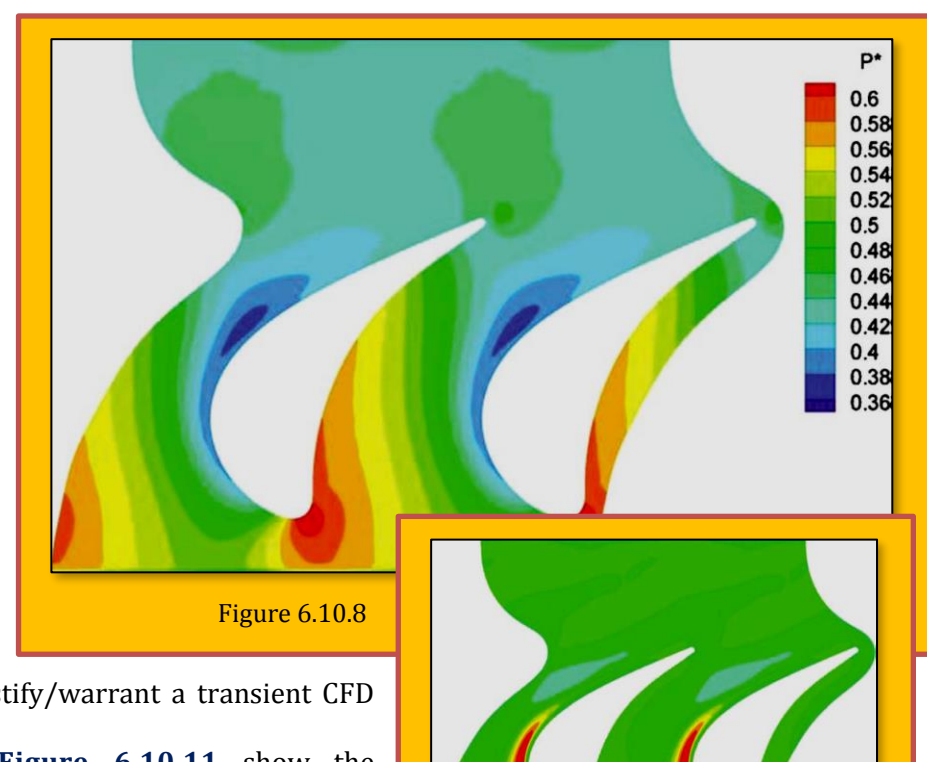
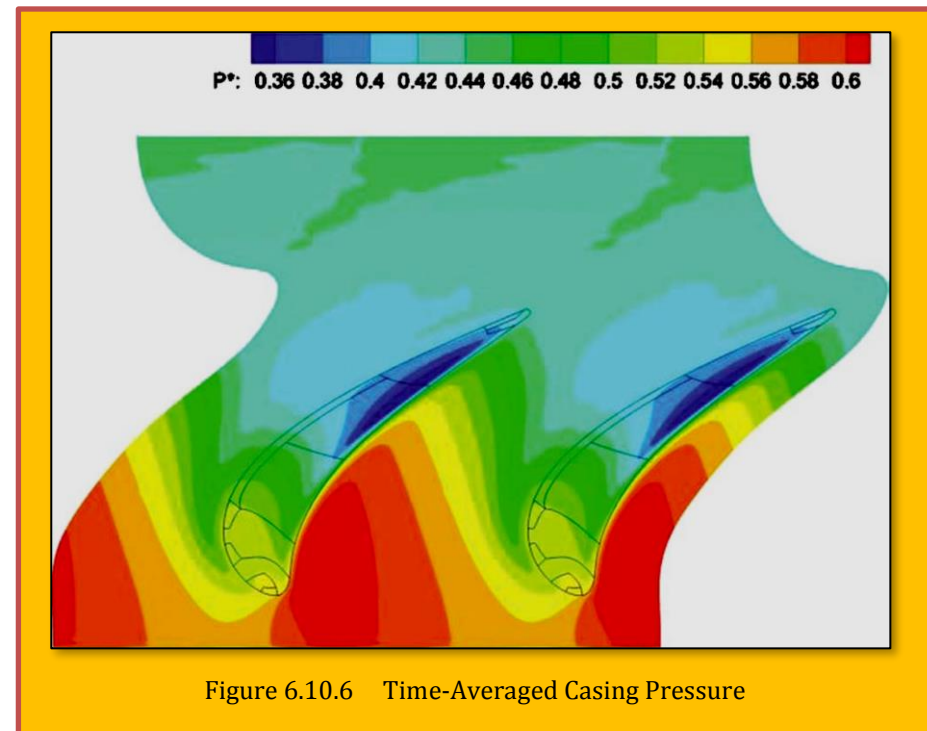


Figure 6.10.7 Difference in hub pressure distribution between the time-averaged and steady results

total temperature (i.e., the dimensionless  $T_{aw}$  exceeds 1); this occurs at the stagnation region and along the pressure side edge of the airfoil tip. The rise in adiabatic wall temperature can be attributed to work processes in the near-tip region, where energy is imparted from the rotating fluid in the tip gap to the stationary casing, thereby increasing the total temperature at the casing surface.

The rise in adiabatic wall temperature on the casing surface was noted by [Thorpe et al.] experimentally and

numerically: "In the tip gap, the stagnation temperature is shown to rise above that found at stage inlet by as much as 35% of stage total temperature drop." A similar finding is ascertained from **Figure 6.10.10**, which shows the maximum adiabatic wall temperature to be 1.06 and the exit adiabatic wall temperature to be 0.84; therefore, the rise in adiabatic wall temperature 0.06 is about 1/3 of the total temperature drop for the rotor passage.

On the hub surface **Figure 6.10.11**, there are no regions where the dimensionless adiabatic wall temperature exceeds unity since there are no rotating/stationary frames of references in the hub wall unlike the casing. The adiabatic wall temperature decreases along the flow passage because work is extracted from the stage.

The low pressure region of **Figure 6.10.7** discussed earlier as being attributable to recirculation in the horse shoe vortex results in a region of minimum adiabatic wall temperatures at the high-C point and aft. The adiabatic wall temperature results in **Figure 6.10.10** and **Figure 6.10.11** are obtained through the time-averaging of the transient CFD solutions and are compared with steady state results. **Figure 6.10.12** and **Figure 6.10.13** use the same scale and show the difference

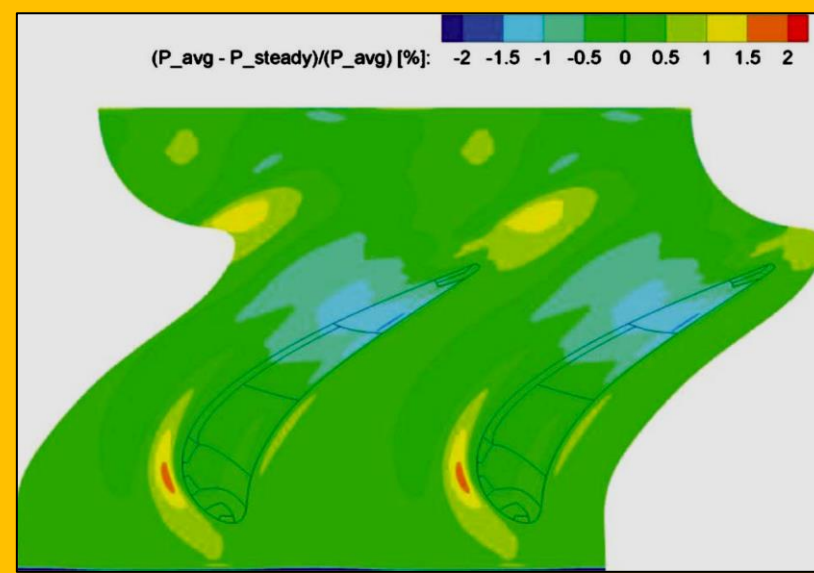


Figure 6.10.9 Difference in casing pressure distribution between the time-averaged and steady results

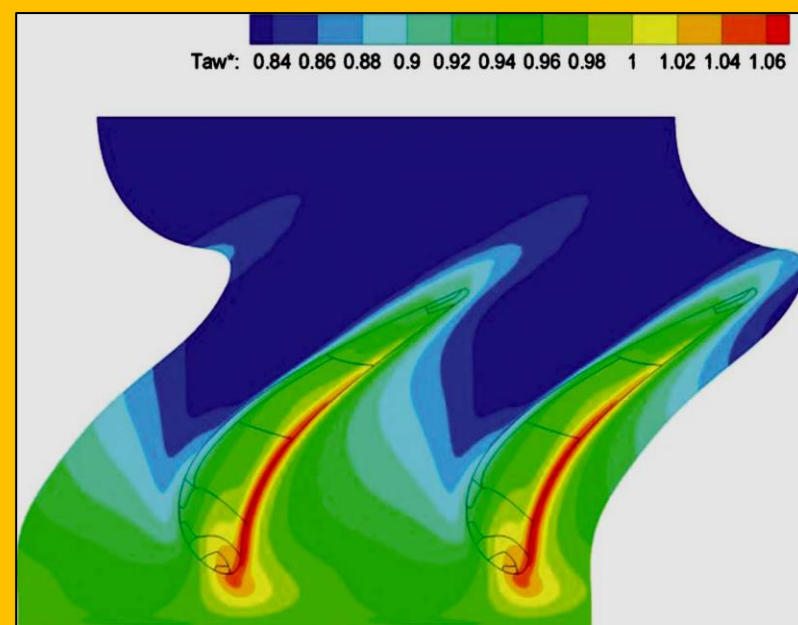


Figure 6.10.10 Time-averaged casing adiabatic wall temperature

between the time-averaged and steady state adiabatic wall temperatures as a percentage of the temperature difference between the adiabatic wall and the isothermal wall, i.e.,

$$\frac{\bar{T}_{aw} - T_{aw}}{\bar{T}_{aw} - T_w}$$

**Eq. 6.10.5**

This is a more physical representation of the difference as the denominator is indicative of the driving temperature for heat transfer. **Figure 6.10.12** shows that the time-averaged casing surface adiabatic wall temperatures are about 4-6% lower than the steady results. For the hub surface, **Figure 6.10.12** shows that the time-averaged hub surface adiabatic wall temperatures are up to 8% lower than those predicted by a steady state simulation. The region of largest difference is in the forward region of the hub surface.

The dimensionless wall heat flux, as defined in the nomenclature, is plotted in **Figure 6.10.14** and **Figure 6.10.15**. **Figure 6.10.14** shows the time averaged wall heat flux distribution on the casing surface. The area of highest heat transfer is the region of the casing above the pressure side edge of the airfoil tip due to the entry of tip leakage flow into the clearance gap, consistent with **Figure 6.10.10**.

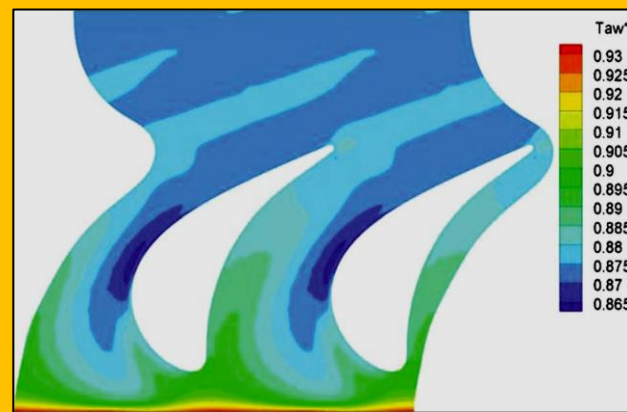


Figure 6.10.11 Time-averaged hub adiabatic wall temperature

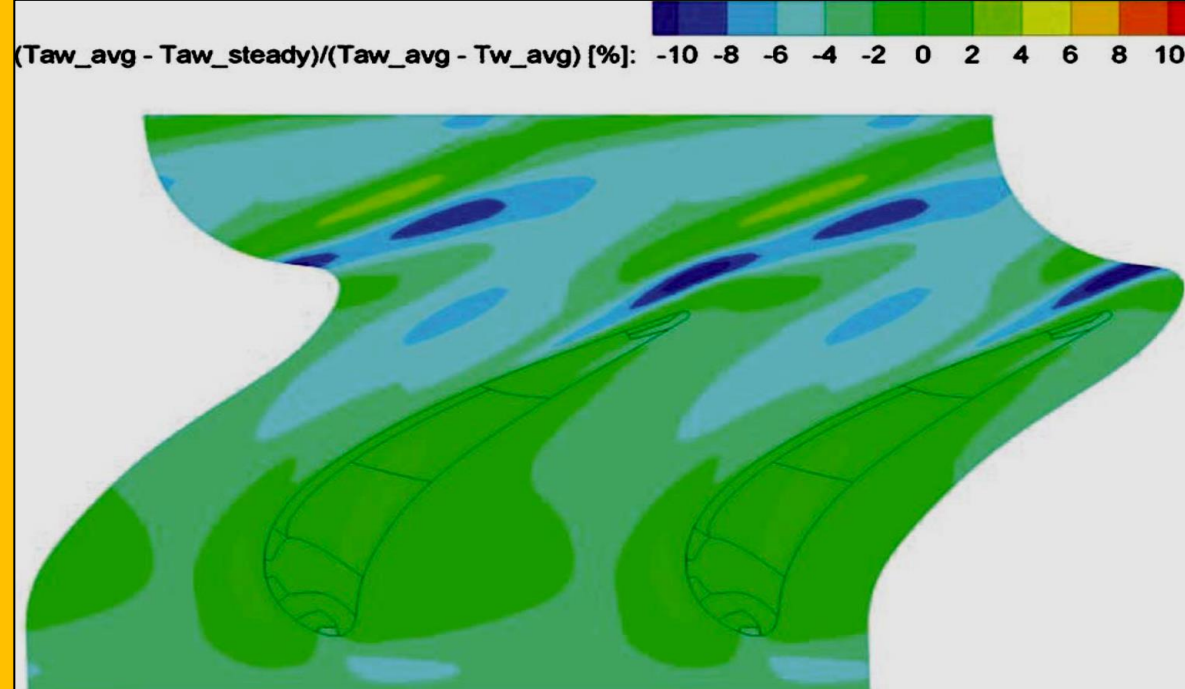


Figure 6.10.12 Difference in casing adiabatic wall temperature distribution between the time-averaged and steady results

The heat transfer rates at the hub surface shown in **Figure 6.10.15** repeat of the dash-outlined image in Error! Reference source not found. are lower than those found on the casing surface **Figure 6.10.14**. The area of highest heat transfer is on the hub surface near the leading edge in the stagnation region and penetrates at a lower magnitude along the pressure side surface aft toward the trailing edge. The heat transfer rate on the end walls obtained through time averaging is compared with the steady state-predicted heat fluxes and the difference between the time-averaged and steady results for the casing and hub are shown in **Figure 6.10.16** and **Figure 6.10.17**, respectively.

On the casing surface **Figure 6.10.16**, the time-averaged solution predicts up to 10% higher heat transfer in some regions, specifically in the region above the SS edge of the tip. The streaks of large positive and large negative differences past the trailing edge in the wake of the blade can be neglected; they likely indicate a slight offset in the distribution rather than a fundamental difference in the prediction.

On the hub surface **Figure 6.10.17**, the unsteadiness increases the heat transfer by up to 10%; the largest difference is at the leading edge and along the pressure side edge into the passage. Generally, there are larger differences in the local heat transfer prediction on the hub surface than on the casing surface with the effect on the casing being highly localized to the region past the suction side and nearly zero difference everywhere else.

Figures 18 and 19 of [El-Gabry and Ameri]<sup>72</sup>, shows the Nusselt number distribution on the casing and hub surfaces, respectively, while **Figure 6.10.18** show the difference between the time-averaged and steady state Nusselt numbers.

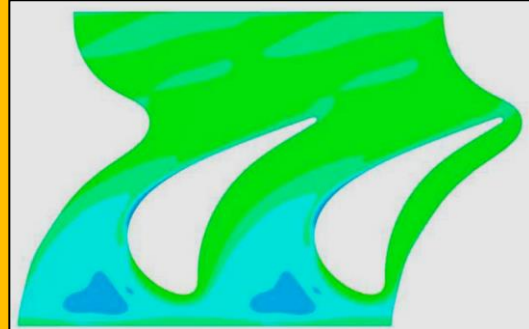


Figure 6.10.13 Difference in hub adiabatic wall temperature distribution between the time-averaged and steady results

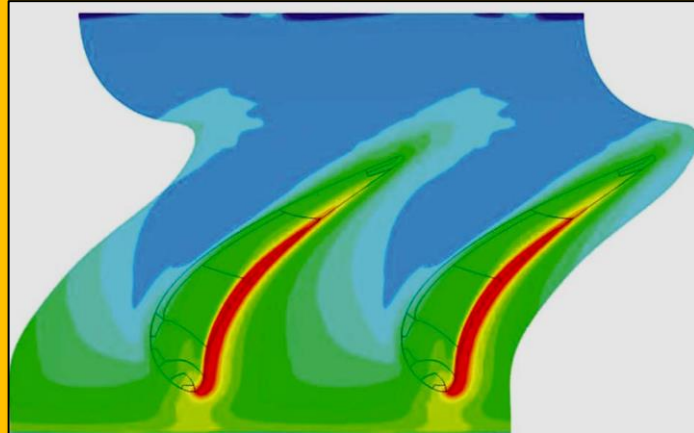


Figure 6.10.14 Time-averaged casing heat transfer rate

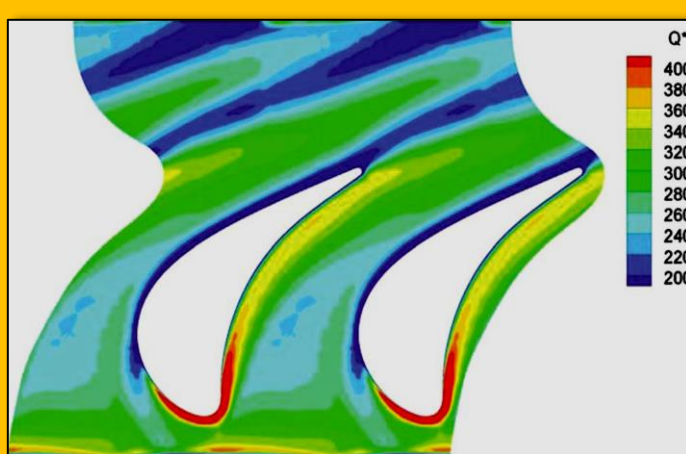


Figure 6.10.15 Time-averaged hub heat transfer rate

<sup>72</sup> Lamyaa A. El-Gabry, Ali A. Ameri, "Comparison of Steady and Unsteady RANS Heat Transfer Simulations of Hub and End wall of a Turbine Blade Passage", Journal of Turbomachinery, JULY 2011.

The region of highest Nusselt number on the casing surface is also the region of highest heat transfer **Figure 6.10.14** and highest adiabatic wall temperature **Figure 6.10.10**, which is above the pressure side edge of the blade tip. Not surprisingly, the region showing significant difference in the effect of time-averaging is at the same location, where there were significant differences in the heat flux predictions **Figure 6.10.16**; the effect of the wake on adiabatic wall temperature for the casing surface was shown to be negligible **Figure 6.10.12**.

On the hub surface, the region of highest Nusselt number is at the stagnation region along the airfoil leading edge, as shown in figure 19 of [El-Gabry and Ameri]<sup>73</sup>, this was also the region of highest heat flux per **Figure 6.10.15**. Whereas the casing surface adiabatic wall temperatures were unaffected by the wake; the hub surface temperatures were lower when the unsteadiness due to wake passage was considered. The heat flux distribution on the hub was also influenced by the wake passage. Therefore, one finds that the Nusselt number, which is driven by heat flux and temperature difference, is influenced by wake passage, as shown.

The largest effect unsteadiness due to wake passage has on Nusselt number is along the leading edge of the airfoil but also along the pressure side surface. The unsteadiness increases the local Nusselt numbers by up to and above 10%.

#### 6.10.5 Heat Transfer Comparison With Open Literature

As previously mentioned, there are no experimental results for end wall pressures, temperatures, or heat flux for the GE-E3 HPT blade. However, there are other results for other engine blades in open literature that can serve as a qualitative comparison to ensure that the trends predicted by the CFD are sensible.

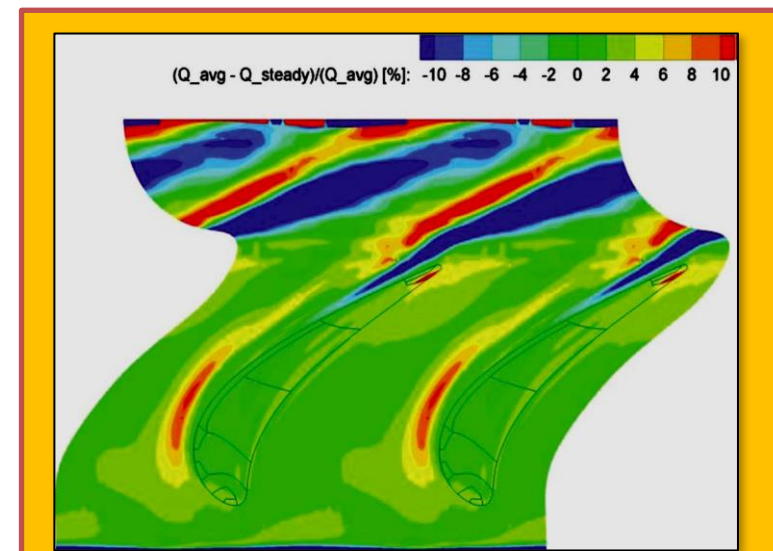


Figure 6.10.16 Difference in casing heat transfer rate between the time-averaged and steady results

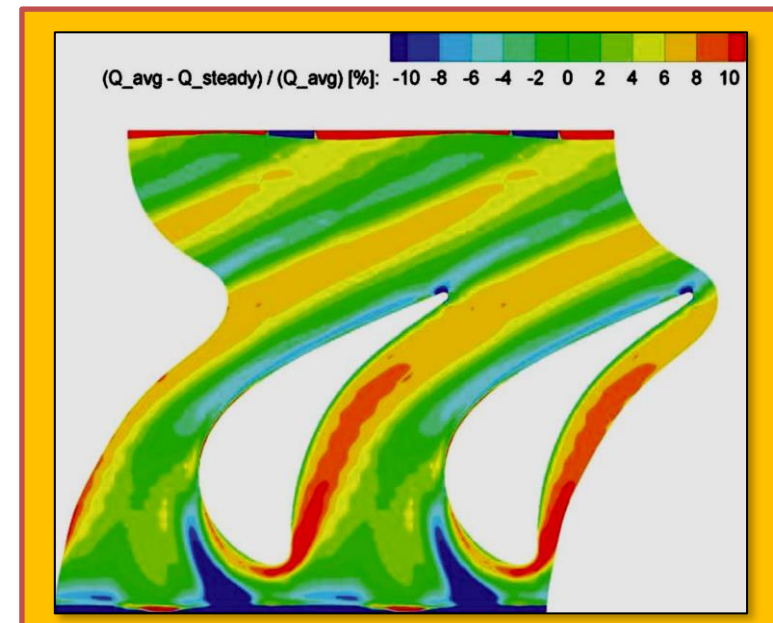


Figure 6.10.17 Difference in hub heat transfer rate between the time averaged and steady results

<sup>73</sup> Lamyaa A. El-Gabry, Ali A. Ameri, "Comparison of Steady and Unsteady RANS Heat Transfer Simulations of Hub and End wall of a Turbine Blade Passage", Journal of Turbomachinery, JULY 2011.

### 6.10.6 Comparison of Casing Heat Flux With [Epstein et al.]

[Epstein et al.]<sup>74</sup> measured the time-resolved static pressure and heat flux to the casing wall in a blow down turbine test rig. The turbine tested was a transonic high pressure turbine scaled from a Rolls Royce engine. A detailed quantitative comparison with the casing measurements of Epstein et al. can be found in Ref.<sup>75</sup>. A key finding of that research is that a large percentage of the total casing heat flux, nearly 45% of the total heat load, comes from the flow over the rotor blade tip; the tip area represents about 30% of the total casing area and contributes 45% of the total heat flux. Similarly, the present results for the E3 show that the above rotor tip region constitutes about 12% of the total casing surface area and contributes about 22% of the total heat casing heat load.

A comparison of *Fig. 22* (Not shown) viewing the experimental results for the casing heat flux on data from Ref.<sup>76</sup> and **Figure 6.10.14** showing the CFD-predicted nondimensional heat flux for the E3 show similar trends; the region of high heat transfer is in the over tip region above the pressure side edge and decreases toward the trailing edge. A region of slightly higher heat flux extends from the leading edge toward the inlet. The heat flux decreases along the passage and reaches a minimum at the rotor wake region.

### 6.10.7 Comparison of Hub Heat Transfer With Tallman et al.

[Tallman et al.]<sup>77</sup> presented contour plots of the hub Stanton number using a RANS solver. Figure 23 of [El-Gabry and Ameri]<sup>78</sup>, shows the CFD-predicted Stanton number. The test data are shown in Ref<sup>79</sup>; however, the measurements are sparse on the hub surface and insufficient to generate a contour plot. Therefore, the CFD results will be used for comparison.

Notable features in the Stanton number distribution include the high heat transfer region at the leading edge and the moderate to high heat transfer along the pressure side edge of the passage. [Figure 24 (Not shown here)]<sup>80</sup> presents the time-averaged Nusselt number

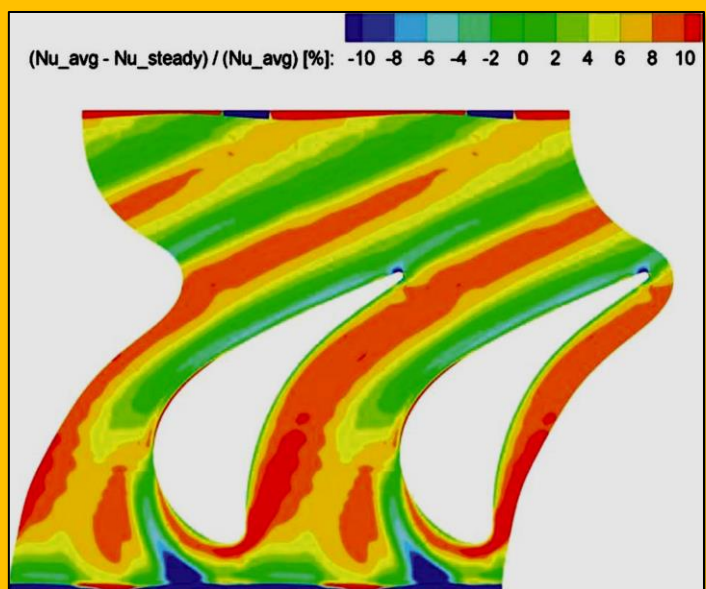


Figure 6.10.18 Difference in hub Nusselt number between the time averaged and steady results

<sup>74</sup> Epstein, A. H., Guenette, G. R., Norton, R. J. G., and Yuzhang, C., 1985, "Time Resolved Measurements of a Turbine Rotor Stationary Tip Casing Pressure and Heat Transfer Field," AIAA Paper No. 85-1220.

<sup>75</sup> Ameri, A. A., Rigby, D. L., Steinhorsson, E., Heidmann, J., and Fabian, J. C., 2008, "Unsteady Analysis of Blade and Tip Heat Transfer as Influenced by Upstream Momentum and Thermal Wakes," ASME Paper No. GT2008-51242.

<sup>76</sup> See 165.

<sup>77</sup> Tallman, J. A., Haldeman, C. W., Dunn, M. G., Tolpadi, A. K., and Bergholz, R. F., 2006, "Heat Transfer Measurements and Predictions for a Modern High Pressure, Transonic Turbine, Including End walls," ASME Paper No. GT2006-90927.

<sup>78</sup> Lamyaa A. El-Gabry, Ali A. Ameri, "Comparison of Steady and Unsteady RANS Heat Transfer Simulations of Hub and End wall of a Turbine Blade Passage", Journal of Turbomachinery, JULY 2011.

<sup>79</sup> R. F., 2006, "Heat Transfer Measurements and Predictions for a Modern High Pressure, Transonic Turbine, Including End walls," ASME Paper No. GT2006-90927.

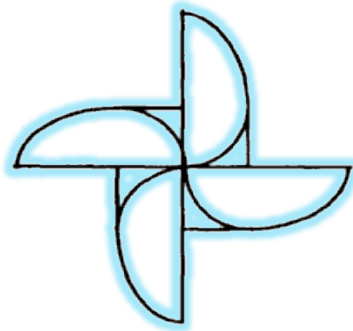
<sup>80</sup> See Previous.

distribution for the hub surface of the E3 blade; the data is identical to [Fig. 19 (same source)] presented earlier; however, the range has been modified to better highlight features and draw comparisons to the Stanton number distribution for the hub in [Fig. 23]. The contours in [Figs. 23 and 24]<sup>81</sup> are similar: The heat transfer peaks at the leading edge due to stagnation and decreases with a relatively high heat transfer region along the PS edge. There is a much narrower low heat transfer region along the suction side, similar to the blade analyzed.

#### 6.10.8 Conclusions

The end wall pressures, temperatures, and heat transfer have been computed using an unsteady RANS calculation, time averaged, and compared with steady state predictions to evaluate the effect of unsteadiness due to wake passage. Results obtained using the *k*-omega turbulence model show that the effect of unsteadiness on the average end wall pressures on both hub and casing is negligible; the unsteadiness increases the pressure prediction in some areas by up to 2%. The area, where the pressure is most affected by unsteadiness, is on the suction side part of the passage for both hub and casing and the effect of unsteadiness seems to extend over a slightly larger area on the hub than the casing. The contribution of unsteadiness due to wake passage on the recovery temperature on the casing is negligible over most of the surface. On the hub surface, the time-averaged results yield lower recovery temperature predictions in the forward region of the passage.

Heat transfer on the end walls is affected by the unsteady wake more than the pressures and temperatures. The time-averaged results yield higher heat transfer; in some regions, the increase is up to 15%. On the casing surface, the increase in heat transfer is more localized and appears on the suction side region of the passage, where the peak pressure difference between the time averaged and steady results occurred. The effect on the hub surface is less localized and the increase in heat transfer predictions can be seen all along the pressure side edge and penetrate well into the passage. As there are no experimental data available to validate the CFD results for the E3, the results for the end wall heat transfer were compared with results in open literature. For the casing, the results were comparable to experimental measurements of [Epstein et al.] quantitatively in terms of the influence of the above-rotor tip area to the overall shroud heat flux and qualitatively in terms of the pattern of heat transfer on the surface. For the hub surface, the results were compared with results from [Tallman et al.] and were also found to be similar, thereby verifying the unsteady Reynolds-averaged Navier-Stokes (URANS) calculations of the present work.




---

<sup>81</sup> See Previous.

## 7 Heat Transfer Applications in Automotive Engineering

### 7.1 Background

In automotive applications, CFD analysis can be used for all components and systems that interact with fluids. There are literally hundreds of such components and systems namely, air, water, fuel, exhaust gases, coolants, hydraulic fluids, lubricants, etc. The automotive CFD applications are generally classified as Powertrain and Non-Powertrain applications. The term Powertrain is the intervening mechanism by which power is transmitted from engine to an axle that it drives. Therefore power train applications is associated with the power (engine) such as In-cylinder flow,

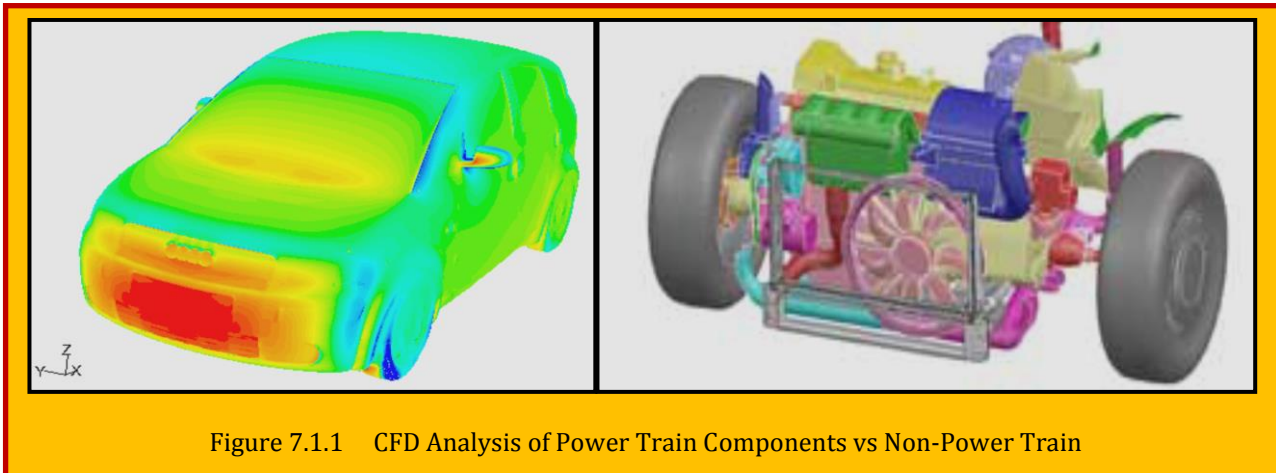


Figure 7.1.1 CFD Analysis of Power Train Components vs Non-Power Train

valve flow, pumps, cooling jackets, air intake system, filters, mufflers, exhaust manifold, clutches, transmissions, and many more as depicted in

**Figure 7.1.1<sup>82</sup>**. The Non-Powertrain components are external aerodynamics, cabin comforts, heat exchangers, hydraulics, acoustics and more. The CFD analysis of the above mentioned systems can be routinely carry out using a combination of steady-state and transient solver. For an overview of basic automobile component, readers encourage to consult with<sup>83</sup>. In order to reduce the fuel consumption, reduction of drag force is an essential process in vehicle aerodynamics. To delay the flow separation at the rear, bump-shaped vortex generators (VG) at the roof end of a car are designed<sup>84</sup>.

#### 7.1.1 Case Study 1 – Simulation of Windshield De-Icing

As a Non-Powertrain CFD application consider windshield deicing simulations. It involves interaction between the airflow and two modes of heat transfer, basically conduction and convection. A variety of factors play a very important role in accurately predicting the deicing process and deicing pattern. These

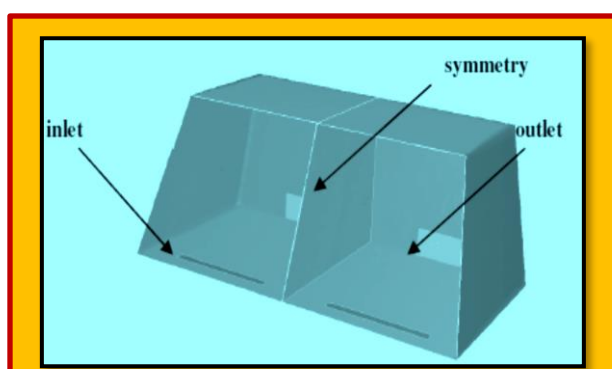


Figure 7.1.2 Geometry Specification

<sup>82</sup> Sovani, Sandeep: "CFD Applications in the Automotive Industry", Fluent Inc. 2006.

<sup>83</sup> "Automotive Fundamentals", Elsevier Science, 2003.

<sup>84</sup> Mohan Jagadeesh Kumar M, "Effect of Vortex generators on Aerodynamics of a Car: CFD Analysis", VIT University, Vellore, Tamil Nadu, India.

factors include defroster angle with the windshield, mesh size and mesh type close the windshield and defroster outlet, thermal conductivity and specific heat considerations due to composite laminate windshield, effect of the melting of ice due to deicing, turbulence modeling, etc.

### 7.1.2 Meshing

Simplified cabin geometry is considered for the as shown in. The ice layer and the windshield are meshed with prism cells. A few layers of prism shaped cells are grown inside the cabin, attached to the windshield to allow better flow development as the air comes out of the defroster outlet (inlet of the domain). The remaining region is meshed with uniform **Figure 7.1.2** size tetrahedral cells. The mesh in the geometry is shown in **Figure 7.1.3**. On actual models, hex core type mesh can be generated to reduce computational cost. The effect of mesh type near the windshield is considered here. A default mesh with only tetrahedral cells in the cabin is created. The second mesh has about 10 boundary layered cells grown from the windshield surface to allow better flow development.

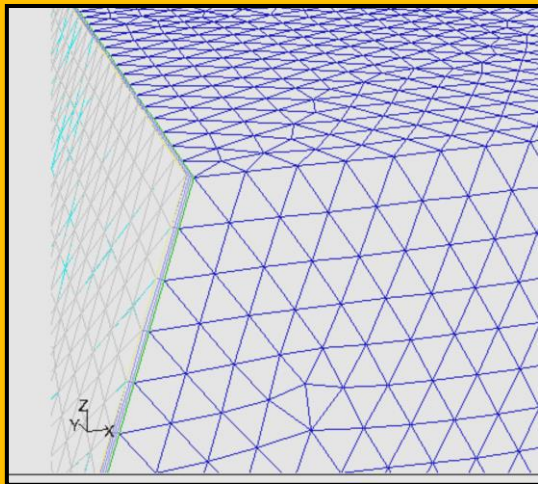
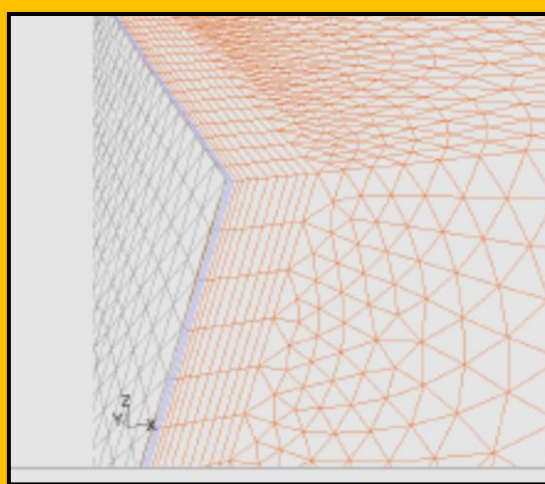


Figure 7.1.3 Effects of mesh a) Full Tetra



b) Boundary Layer

### 7.1.3 Velocity Contours and Convection De-Icing

**Figure 7.1.4** shows the comparison of velocity contours on a center-plane whereas **Figure 7.1.5** shows the comparison of deicing rate. The velocity field on the full-tetrahedral mesh is quite diffusive and is not very well attached with the windshield whereas on the boundary layered mesh very well

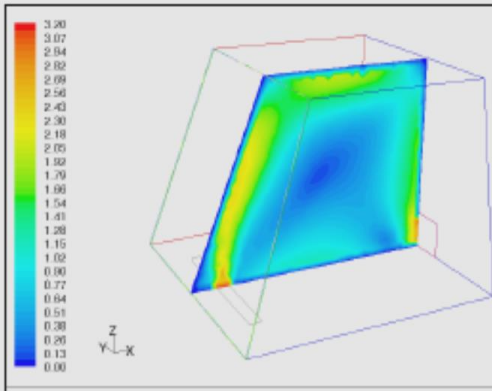
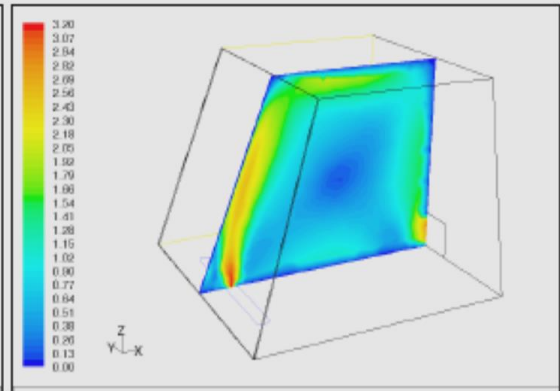


Figure 7.1.4 Comparison of Velocity field- a) Full Tetra



b) Boundary Layer

aligned with the windshield and is also attached with it. This change is the flow-field translates into a big difference when the deicing patterns are compared. Clearly, the rate of deicing is underpredicted by the full-tetrahedral mesh. Therefore, resolving the near wall mesh properly is very important to correctly predict the deicing patterns.

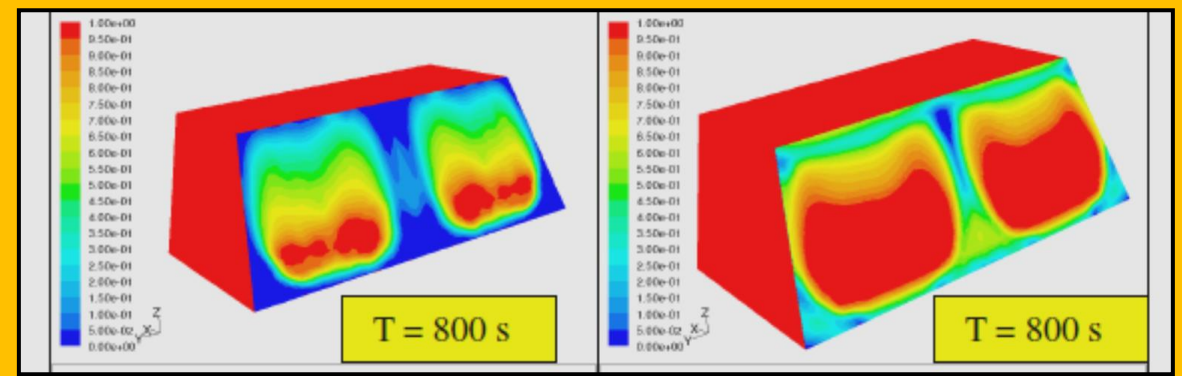


Figure 7.1.5 Contours of Liquid Fraction (De-Icing)

#### 7.1.4 Effect of Turbulence Modeling

The effect of various turbulence modeling is studied as well. The case (with prism layered mesh inside the cabin grown from the windshield) was run with standard k- $\omega$  model and standard k- $\epsilon$  model. The k- $\omega$  turbulence model is based on the Wilcox k- $\omega$  model and is found to be good for all-bounded flows and free shear flows. The standard k- $\omega$  model predicts a flow-field that is very well attached to the windshield. This results in faster de-icing of the windshield which is shown in **Figure 7.1.6** below.

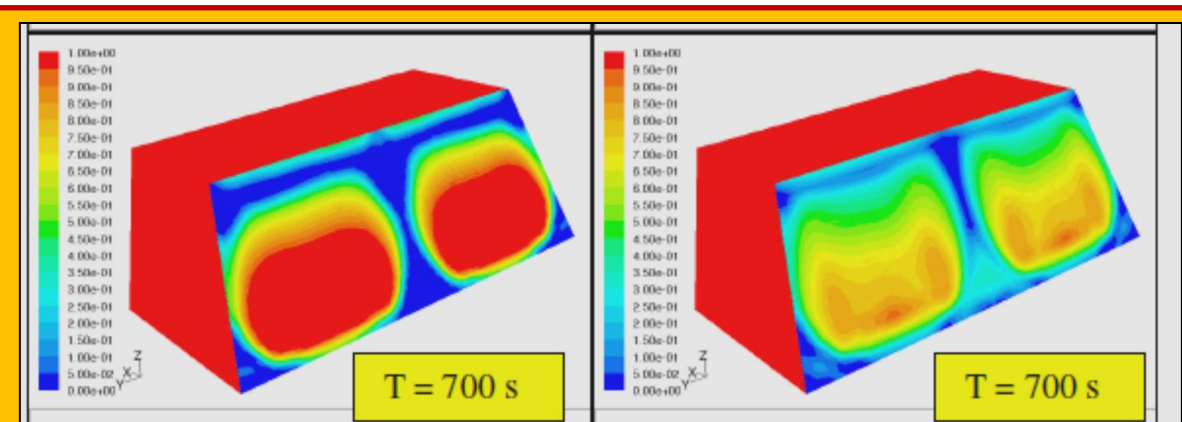


Figure 7.1.6 Comparison of turbulent model    a) standard k-omega    b) standard k-epsilon

## 7.2 Powertrain

Finite Element Analysis (FEA) and Computational Fluid Dynamics (CFD) are essentials in automotive powertrain and its associated components. It provides an specific CAE solutions for powertrain to improve fuel efficiency, design & weight optimization and performance enhancement, as shown in **Figure 7.2.1** [IAV Automobile Engineering]. The Powertrain & sub-systems includes [as depicted in hiteach]:

- Internal Combustion (IC) engine
  - Cold Flow Analysis
  - Multiphase Flow Analysis
  - Combustion Analysis

- Spray and Droplet Analysis
- Flame Analysis
- Heat Transfer Analysis
- Transmission
  - Fatigue Analysis (High Cycle)
  - Static Structural Analysis
  - Vibration (Modal) Analysis
- Driveshaft
- Static Structural Analysis
- Vibration (Modal) Analysis
- Fatigue Analysis
- Analysis of Composites
- Differentials
  - Structural Analysis
  - Modal Analysis
  - Fatigue Analysis

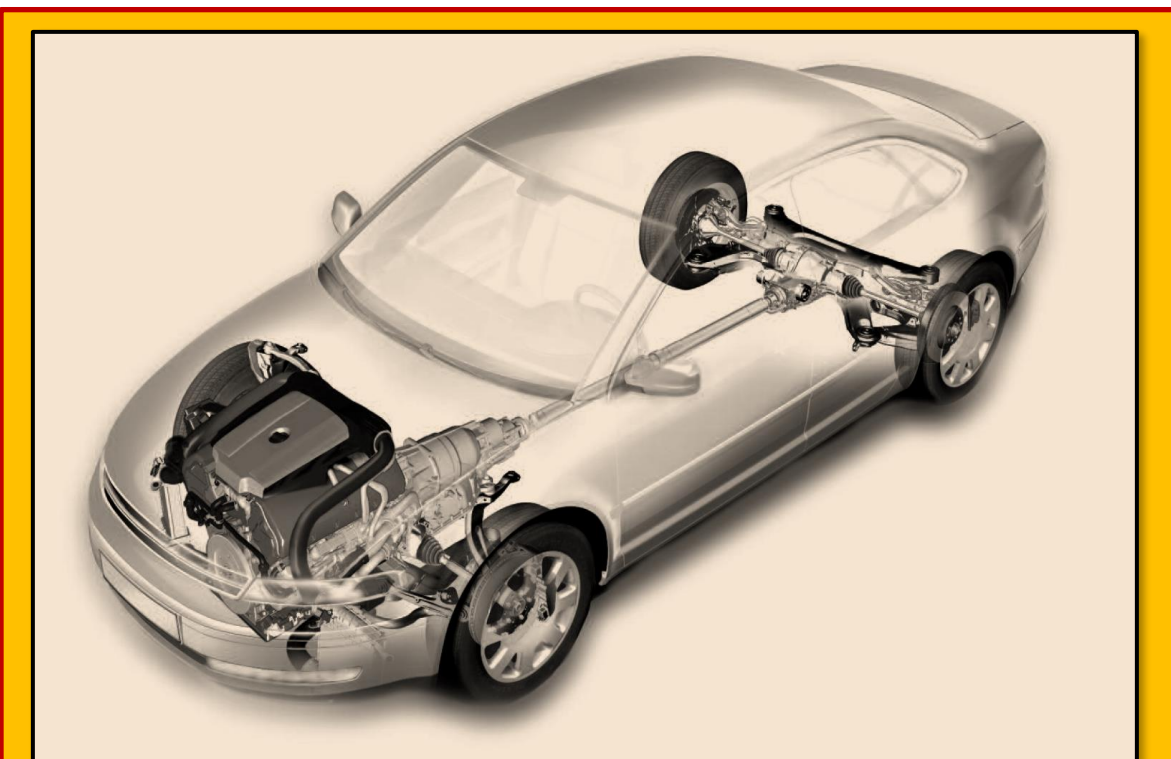


Figure 7.2.1 Elements of Powertrain (Courtesy of IAV automobile engineering)

### 7.3 Powertrain Cooling

#### 7.3.1 Engine Cooling Block

As essential components of the basic system, is the engine block cooling system, are shown in **Figure 7.2.2**. The coolant is driven round the system by a centrifugal pump which is traditionally belt driven from the engine. The coolant passes through the engine where it picks up the rejected heat and is passed to a heat exchanger, the radiator where the heat is in turn transferred to the cooling air which passes over the outside of the radiator surface. The flow of cooling air through the radiator matrix is generated by a combination of fan and rams air that comes from the

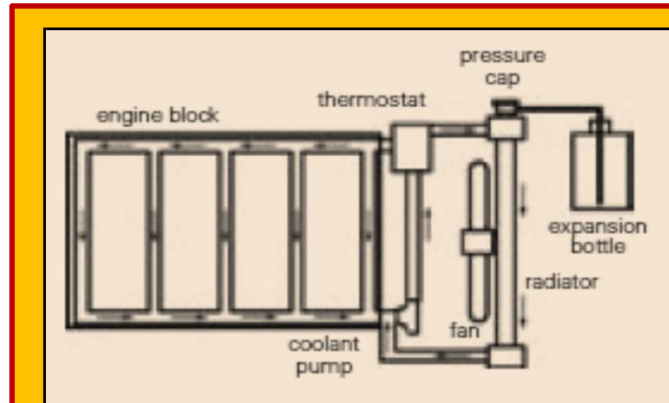


Figure 7.2.2 Basic layout of engine cooling system

movement of the vehicle over the ground. The fan can be either engine or electric motor driven. When the engine starts from cold, the thermostat outlet to the radiator is closed and the coolant flow generated by the pump passes only through the cylinder head and engine block. The engine and coolant gradually warm up until the stage is reached at which the wax thermostat responds to the increasing coolant temperature and the outlet to the radiator opens. The process of radiator heat rejection to the atmosphere is initiated and at this stage the thermostat takes over control of the system – as the temperature of the coolant at outlet from the engine reaches its control point, so the thermostat opens to increase flow to the radiator and inversely, as the temperature drops below the control point, the thermostat closes down to reduce the coolant flow to the radiator.

In the early days of the automobile water was the standard cooling fluid because of its very attractive thermo-physical properties as well as its wide availability and low cost. However, water has two basic weaknesses. The first is the relatively high freezing point of 0°C, which resulted in the risk of ice formation within the system in cold ambient. The freezing of water accompanied by a significant increase in its specific volume and the accompanying expansion frequently resulted in the destruction of engine block and/or radiator. The second weakness is the relatively low boiling point of the fluid. The solution to the first problem was to mix a percentage of ethylene glycol with the water that has the effect of reducing the freezing point, the more ethylene glycol, the greater is the reduction. The relatively low boiling temperature of pure water carries the risk that should coolant temperatures become high enough, boiling occurs with the resultant loss of coolant as pressure relief systems operate. In the early days, this problem was compounded by the unreliability of pump shaft seals, which could also result in significant coolant loss. The Swiss solution to these problems was to locate water taps and pouring vessels at the top of each of the Alpine mountain passes! The use of ethylene glycol in the coolant is part of the more modern solution to this problem as the boiling point of the 50/50 mixture increased to 108°C, at atmospheric pressure. This also has the advantage that it increases the available temperature difference for heat transfer in the radiator.

### 7.3.1.1 System Component: Radiator

The most important keys to a successful engine cooling system are the heat exchangers and the two generators of fluid flow – the coolant pump and the fan. Two basic heat exchanger core configurations are used in automotive radiators, both in aluminum – the mechanically expanded round tube and plate fin surface and the brazed core with flat sided tubes and corrugated louvered fin. The tube-and-fin surfaces ([Figure 7.3.2](#)) are restricted to the lower cooling duties as the surfaces cannot compete with the high specific performance and low air side pressure drop characteristics of the tube and center configuration. This remains true even with advanced versions of the former using oval tubes and louvered fin. The advantages of the tube-and-center configuration come from the flattened tube which contributes to the low air side pressure drop and the louvers in the fin that greatly enhance heat transfer coefficients. The enhancement comes from the fact that the inclined louvers serve to realign the air flow with their plane and as such provide multiple leading edges which result in thin boundary layers and high heat transfer. It is possible to cut louvers into the tube-and-fin surfaces but they are less effective because they cannot be cut close to the tube wall for fear of weakening the mechanical joint between fin and tube and enhancement is proportional to the cut length of louver.

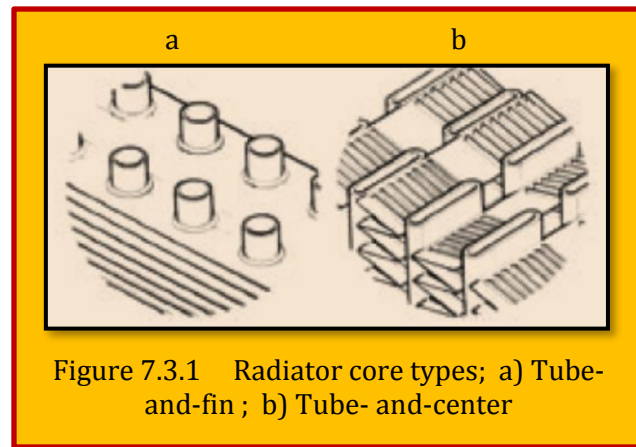


Figure 7.3.1 Radiator core types; a) Tube-and-fin ; b) Tube- and-center

Whilst the tube-and-fin surfaces cannot compete with the tube-and-center versions on pure performance, the reasons they are sometimes used for the lesser cooling duties is a question of cost. With no need for the use of brazing neither sheet nor the brazing process itself, under some conditions they can be cheaper to produce. The 2D image of laminar flow that becomes parallel to the louvers shown in **Figure 7.3.2** is not the whole picture. At low velocities the boundary layers on the louvers become sufficiently thick to effectively block off the gap between louvers with the result that the air switches back to flowing between the fins and thus straight through the radiator without being deflected by the louvers. At the high velocity end of the operating range the simple laminar flow can begin to be disturbed by the shedding of vortices from some of the louvers (see **Figure 7.3.2**). This enhances heat transfer further but at an increasing flow resistance penalty.

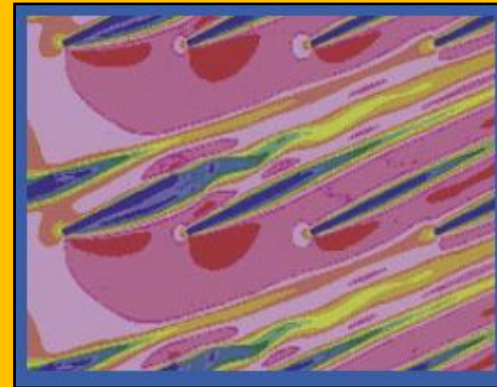


Figure 7.3.2 CFD Analysis showing Flow Instability from Louvers at High velocity

### 7.3.1.2 System Component: Fans

A fan is required to generate the necessary air flow with the vehicle stationary and to supplement the ram air generated flow with the vehicle moving. In the early days of the automobile the fans were driven by the engine. This option still exists with the highest powered engines but in most cases the duty is taken over by electrically driven fans. The disadvantage of the engine driven fan is the fact that it has to be capable of delivering the required air flow at low engine and vehicle speeds which means that it is over designed for higher engine speed with resultant absorption of more power than necessary. The reason for the use of an engine driven fan is that for high powered vehicles the demand for cooling air can be so great that insufficient electrical power is available to meet the need electrically. In some cases viscous fan drives are used with engine driven fans in order to reduce the power consumed at higher engine speeds. Electrical fans can be located before or behind the front end heat exchanger module (see **Figure 7.3.3**). One, two or even three fans distributed between fronts and back can be used. The fans can be shrouded or open. The shroud is used to reduce the risk of air recirculation from downstream back into the front of the heat exchanger. The open fan configuration makes better use of the ram generated air flow. A high level of expertise combined with extensive practical experience



Figure 7.3.3 Electrically Driven Fan

goes into the development of a new fan design. To ensure optimum performance the design must be specific to the eventual system and its operating environment. The first design step uses 1-D design tools to establish the important fan load points based on a systems level analysis. Axis-symmetric 2D tools are then used to determine the flow profile at inlet to the fan. The process continues with the development of the NACA (National Advisory Committee for Aeronautics) based blade profiles, a

process that again requires significant experience in the manipulation of the input. A final CFD (Computational Fluid Dynamic) based fine-tuning process considers flow uniformity, blade loading and the elimination of flow separation at blade leading and trailing edges.

## 7.4 Case-Study 2 - Cooling Jacket Design

The complex shape of the cooling jacket is influenced by multiple factors including the shape of the engine block and optimal temperature at which the engine runs<sup>85</sup>. A very large cooling jacket would be effective in transporting heat away from the cylinders, however, too large of a geometry results in extra weight to be transported. Also, engineers would like the engine to reach its optimal operating temperature quickly. In the following, we describe the major components of the geometry and the design goals of the mechanical engineers responsible for the analysis.

### 7.4.1 Cooling Jacket Geometry

The cooling jacket geometry consists mainly of three components: the cylinder head which is the top, the bottom called the cylinder block, and a thin component connecting the cylinder head and block called the gasket. These three main components are shown pulled apart in **Figure 7.4.1** for illustration. The cylinder head (top) is responsible for transferring heat away from the intake and exhaust ports at the top of the engine block. The cylinder block is responsible for heat transfer from the engine cylinders and for even distribution of flow to the head. This cooling jacket is used with a four cylinder engine block. Between the cylinder head and block lies the cooling jacket gasket, depicted in **Figure 7.4.1** as small red ellipses, the actual location of which is revealed by red holes at the top of the cylinder block. The gasket consists of a series of small holes that act as conduits between the block and head. These ducts can be quite small relative to the overall geometry but nonetheless are very important because they are used to govern the motion of fluid flow through the cooling jacket as described in the next section.

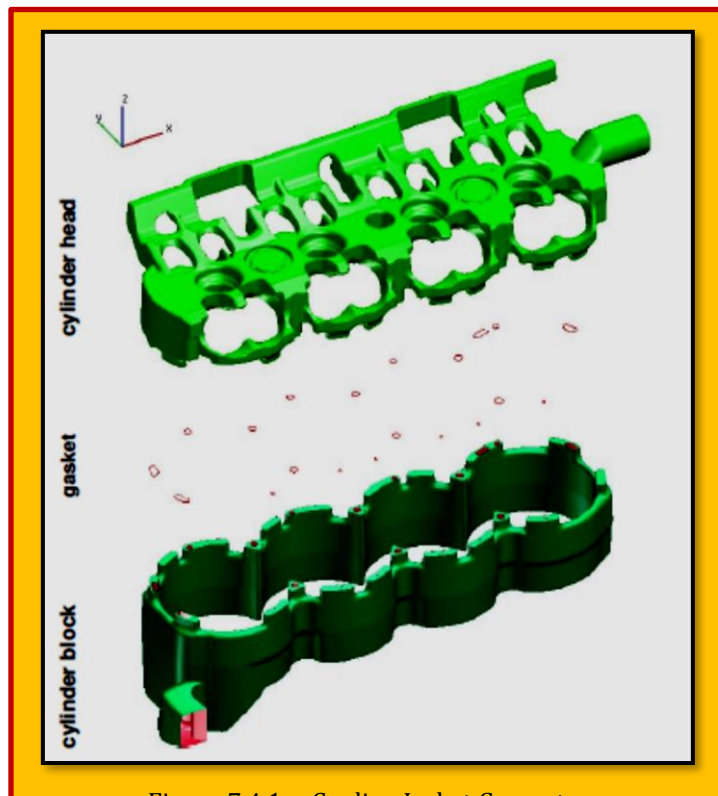


Figure 7.4.1 Cooling Jacket Geometry

### 7.4.2 Design Objectives

There are two main components to the flow through a cooling jacket: a *longitudinal* motion lengthwise along the geometry and a *transversal* motion from cylinder block to head and from the intake to the exhaust side. These two components are sketched in **Figure 7.4.2**. The location of the inlet and outlet are also indicated. Four main design goals are essential for the mechanical engineers:

1. to obtain an even distribution of flow to each engine cylinder

<sup>85</sup> Robert S. L., Christoph G. Helmut, Schneider, Helwig Hauser, H., Hagen, H., "Visual Analysis and Exploration of Fluid Flow in a Cooling Jacket".

2. to avoid regions of stagnant flow
3. to avoid very high velocity flow
4. Minimize the fluid pressure loss between the inlet and the outlet.

The first design goal, an even distribution of fluid to each cylinder, is intuitive. An even distribution flow should result in an even rate of heat transfer away from each cylinder, intake port, and exhaust port. The second goal, avoiding regions of stagnant flow is very important. Stagnant flow does not transport heat away and can lead to boiling conditions. Boiling fluid can indicate potential problem areas in the cooling jacket geometry that lead ultimately to overheating. We note that the optimal cooling jacket temperature is about 90°C or 363°K. The third goal, to avoid regions of velocity too high in magnitude is less obvious. High velocity flow can lead to *cavitation*, the formation of low-pressure bubbles, such as those resulting from the rotation of a marine propeller. Firstly, cavitation waste energy in the form of noise. Secondly, cavitation can also lead to damage to the walls of the cooling jacket itself over the long term. Cavitation is associated with explosions and unnecessary vibration. Erosion of the boundary surfaces can result in a shorter product lifetime. The fourth design goal is to minimize pressure loss across the cooling jacket geometry. The water pump (not shown) located at the cooling jacket's inlet is responsible for maintaining a specified pressure at the inlet. The greater the pressure drop between the cooling jacket's inlet and outlet, the more energy the water pump requires in order to maintain the desired pressure. An ideally straight pipe with an inlet and outlet of equal size would exhibit no pressure loss across its geometry, thus a water pump would require much less energy in this case. Generally, the smaller the cooling jacket gasket, the larger the pressure loss. Curves in the geometry can also cause pressure losses<sup>86</sup>. The main variable in cooling jacket design lies in the gasket. Engineers adjust the number, location, and size of the conduits in their pursuit of the ideal fluid motion.

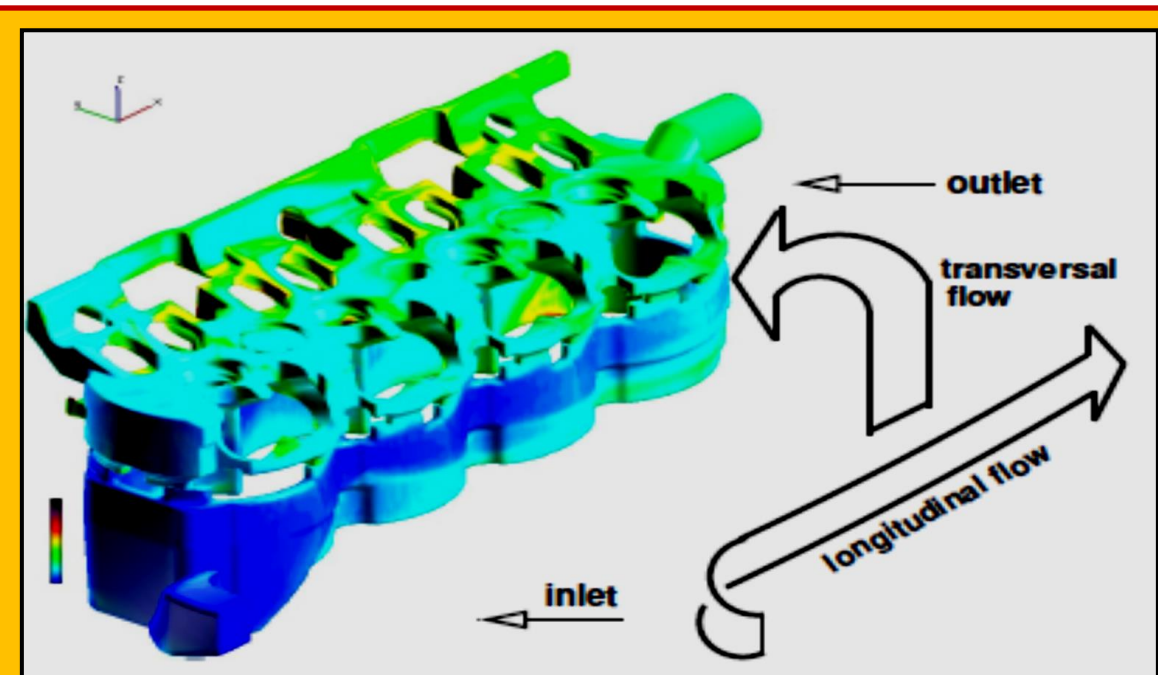


Figure 7.4.2 Temperature Contours

<sup>86</sup> Robert S. L. Christoph G. Helmut, Schneider, Helwig Hauser, H., Hagen, H., "Visual Analysis and Exploration of Fluid Flow in a Cooling Jacket".

### 7.4.3 Meshing

The grid geometry consists of over 1.5 M unstructured, adaptive resolution tetrahedral, hexahedra, pyramids, and prism cells. We also focus on steady flow data for this case because for the cooling jacket, engineers are most interested in investigating the behavior of fluid flow after the simulation has reached a stable state. The fluid in the cooling jacket should reach its optimal temperature rapidly and then ideally remain in this state.

## 7.5 Electric Powertrains

An electric vehicle (EV) is a vehicle that is powered, at least in part, by electricity. EV configurations include battery electric vehicles (BEVs) which are powered by 100% electric energy, various hybrid-electric vehicles (HEVs), and plug-in hybrid electric vehicles (PHEVs). This summary presents the differences between these basic EV configurations.

### 7.5.1 Battery Electric Vehicles

A battery electric vehicle (BEV) is a vehicle that is powered entirely on electric energy, typically a large electric motor and a large battery pack. Based on the type of transmission; the use of a clutch, gearbox, differential, and fixed gearing; and the number of battery packs and motors there are many variations on the BEV design. However, a basic BEV system is shown in [Figure 7.5.1](#).

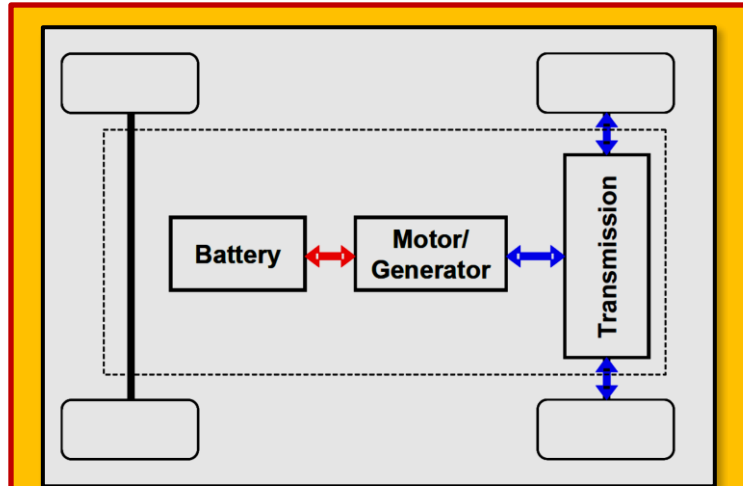


Figure 7.5.1 Schematic of a Battery Electric Vehicle (BEV) Powertrain

### 7.5.2 Mild Hybrid Electric Vehicles

Unlike a BEV, a hybrid electric vehicle (HEV) relies on two energy sources, usually an internal combustion engine and an electric battery and motor/generator. A Mild Hybrid is the least electrified type of HEV. A Mild Hybrid is a conventional internal combustion engine (ICE) vehicle with an oversized starter motor that can also be used as a generator, usually called an integrated starter-generator (ISG) or a belted alternator starter (BAS), and an oversized battery that powers and is recharged by the motor. A simple Mild Hybrid system is shown in [Figure 7.5.2](#). In a Mild Hybrid, the engine must always be on while the vehicle is moving. However, the motor/generator can be used to enable idle stop in which the engine is turned off while the vehicle is at idle. The motor/generator can be used at high loads to assist the

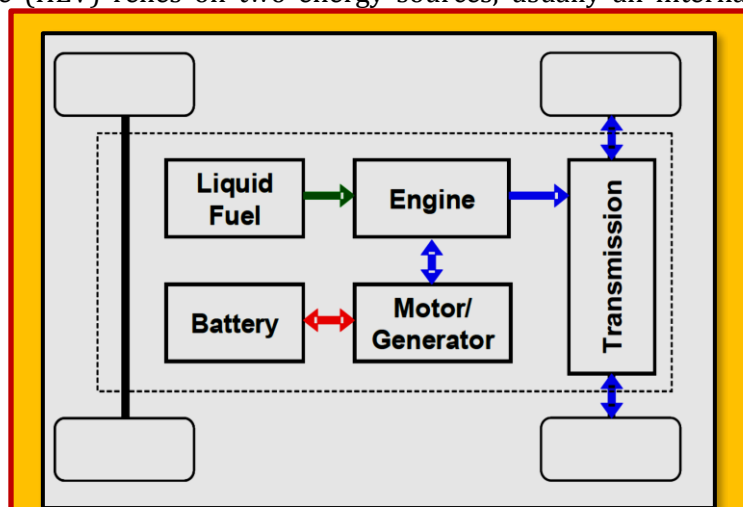


Figure 7.5.2 Schematic of a Mild Hybrid Powertrain

engine and increase vehicle performance. At low loads, it increases load on the engine and recharges the electric battery. There is a series and parallel version of (BEV) which details can be found in<sup>87</sup>. The design of a full electric vehicle requires the development and optimization of a complete electric powertrain, including battery, power electronics, electric machine, sensors and control system. When designing an electrical platform, from the very beginning of the V-cycle, it is mandatory to rely on modeling and simulation tools in order to drive the main choices and then to optimize the system. The paper presents an electric powertrain simulation platform developed under Matlab-Simulink, with the intention of optimizing performances and powertrain efficiency (highly linked with vehicle range). This is used in order to choose battery technology (Lithium-Ion, Nickel-Cadmium...) and dimensioning according to criteria and driving cycles<sup>88</sup>.

## 7.6 Internal Combustion Engine (ICE)

The ***internal combustion engine (ICE)*** is today the most widely used energy source in the automotive and naval industry. It has therefore become increasingly important to improve the efficiency of the engines to reduce fuel consumption, emission levels and noise pollution. Since the introduction of the IC engine in the late 19<sup>th</sup> century its development has resulted in a constant reduction of fuel consumption and emission levels, while the power output per cylinder volume has continued to increase. (See **Figure 7.6.1**).

The IC engine comes in many different types and sizes but can be divided in the category of the two stroke cycle or the four stroke cycle which can either be run by the Otto or the Diesel principle. For Otto engines the pre-mixed air-fuel mixture is ignited by a spark from a sparkplug while for the Diesel principle the air is compressed beforehand in the cylinder and the incoming fuel spray is ignited by the high pressure and temperature<sup>89</sup>.

The four stroke cycle starts with the piston positioned in TDC (Top Dead Center) and as the piston travels down towards BDC (Bottom Dead Center) the intake valve opens, letting the fresh charge of air-fuel mixture to enter the cylinder during the intake stroke, see **Figure 7.6.2 (a)**. With the piston at BDC the intake valve closes and as the piston travels towards TDC again the fresh charge is compressed during the compression stroke, see **Figure 7.6.2 (b)**.

As the piston reaches TDC the compressed air-fuel mixture is ignited by the spark plug and the chemical energy of the fuel is converted to heat during combustion. This increases the cylinder gas temperature and pressure therefore adding work to the crankshaft during the power stroke or expansion stroke, see **Figure 7.6.2 (c)**. When the piston reaches BDC again the exhaust valve opens and as the piston travels towards TDC the exhaust gas is pushed out from the cylinder during the exhaust stroke, see **Figure 7.6.2 (d)**. When the piston has reached TDC the cycle is restarted again. In one power cycle the



Figure 7.6.1 Typical in-Cylinder Process of an IC Engine

<sup>87</sup> "Electric Powertrains", MIT Electric Vehicle Team, April 2008.

<sup>88</sup> N. Janiaud, F. Vallet, M. Petit, and G. Sandou. "Electric vehicle powertrain simulation to optimize battery and vehicle performances", IEEE Explore.

<sup>89</sup> Stefan Gundmalm, "CFD modeling of a four stroke S.I. engine for motorcycle application", Master of Science Thesis Stockholm, Sweden 2009.

crankshaft has done two full revolutions (720 crank angle degrees or CAD) and the piston has traveled up and down the cylinder four times, therefore the name four stroke cycle. For in-depth analysis, please refer to [Karash & shaban]<sup>90</sup>.

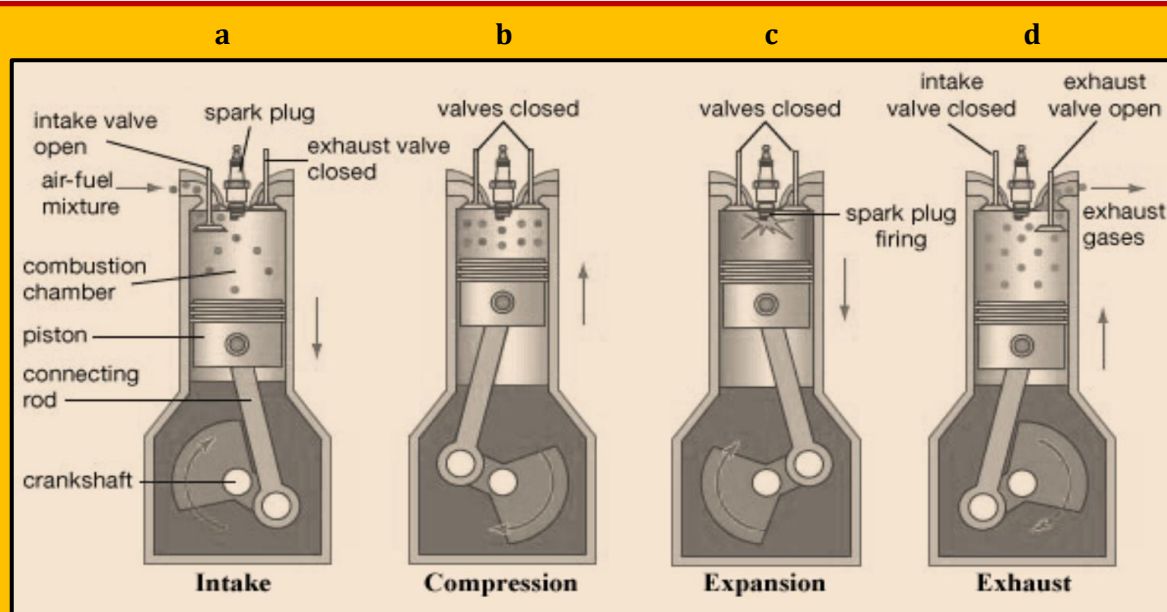


Figure 7.6.2 The four phases of the four stroke IC engine: intake, compression, expansion or power and Exhaust

### 7.6.1 Abnormal Combustion Phenomena

As the flame propagates across the combustion chamber the unburned mixture ahead of the flame (called the *end-gas*) is compressed, causing its pressure, temperature and density to increase. Some of the end-gas air-fuel mixture may then undergo chemical reactions prior to the normal combustion when the flame front reaches the end-gas. These chemical reactions may cause the end-gas to auto ignite, releasing a large part or all of their chemical energy. This causes the end-gas to burn very rapidly with flame velocities of up to 1000 m/s and it creates high frequency pressure oscillations inside the cylinder that produce the sharp metallic noise called **knock**. Knock is mainly caused by high pressure and temperature in the end-gas but depends also on the octane number of the fuel. Knock is common in engines with a high compression ratio  $\epsilon$ , which leads to a high cylinder pressure and an increased risk of knock when the end-gas is compressed further by the propagating flame. The pressure waves that knock creates, lead to high mechanical load on the engine, causing damage to the material. Knock can be detected by knock sensors, for example with an accelerometer in the cylinder walls that detects high frequency pressure oscillations. Knock can then be avoided by adjusting the spark timing automatically when knock is detected in the engine. By retarding the time of spark discharge the maximum cylinder pressure is lowered with a decreased risk of knock as result.

The other abnormal combustion phenomenon is **surface ignition**. This phenomenon is caused when the air-fuel mixture is ignited by an overheated surface in the engine, like the valves or the sparkplug. It is defined as ignition by any other source than the spark of the sparkplug. It can occur before the spark ignition (pre-ignition) or after (post-ignition). Either way it means that the combustion process is no longer controlled by the ignition of the spark. When surface ignition results in knock in the end-gas it is called **knocking surface ignition**. Knock can be considered a bigger problem than surface

<sup>90</sup> Emad Toma Bane Karash & Tараq Shaban, "Internal Combustion Engine", June 2019.

ignition, since surface ignition can be avoided with proper engine design. Knock on the other hand is an inherent constraint on engine performance and efficiency since it limits the maximum compression ratio that can be used with any given fuel.

### 7.6.2 Methods for Dynamic Mesh Motion

When simulating internal combustion engines the mesh will never be static since there is always deformation of the mesh by either the piston or the valve motion. Using a static mesh can only give very little information of the actual flow in an engine. Therefore it is very important to be able to perform the simulation on a mesh that can be deformed by the motion of the boundary, in this case the piston and the valves. In this chapter some methods for handling dynamic mesh motion is described.

#### 7.6.2.1 Automatic Mesh Motion

The motion of the boundaries is decided by the valve lift curves and the piston motion but for the internal mesh points an iterative motion solver was developed by [Jasak and Tuković]. The automatic mesh motion solver is based on a motion equation that calculates the velocity of the mesh point. The solver is described shortly in this chapter but the reader is referred to<sup>91</sup> for more detailed information. The automatic mesh motion solver is based on the Laplace equation which governs the mesh motion and is solved for the point velocity field  $\mathbf{u}$ , with constant or variable diffusivity  $\gamma$ ,

$$\nabla \cdot (\gamma \nabla \mathbf{u}) = 0 \quad \text{Eq. 7.6.1}$$

The solution provided by the Laplace operator is always bounded also when the diffusivity is not uniform within the computational domain<sup>92</sup>. The position of the mesh points are then calculated with:

$$\mathbf{x}_{\text{new}} = \mathbf{x}_{\text{old}} + \mathbf{u} \Delta t \quad \text{Eq. 7.6.2}$$

Where  $\mathbf{x}_{\text{old}}$  and  $\mathbf{x}_{\text{new}}$  are the point positions before and after mesh motion, and  $\Delta t$  is the time step. Solving the **Laplace equation** for the motion velocity instead of the point positions is preferred since the velocity changes slower and a better initial guess is available and it reduces round-off errors<sup>93</sup>. To preserve the mesh validity during mesh motion and to avoid degenerate cells, the motion is discretized by a second order tetrahedral finite element method. This discretization produces a sparse and symmetric positive definite matrix, which allows the use of an iterative solver called **Algebraic Multigrid (AMG)**. This discretization requires the polyhedral cells to be consistently decomposed into tetrahedral cells. This is done on the fly by the solver by introducing a point in the cell center and split the faces into triangles, as can be seen in **Figure 7.6.3**. Consistency in tetrahedral connectivity is obtained by using identical face decomposition for cells that share an internal face. The automatic mesh motion strategy will preserve mesh quality and validity for an arbitrary interval, but eventually

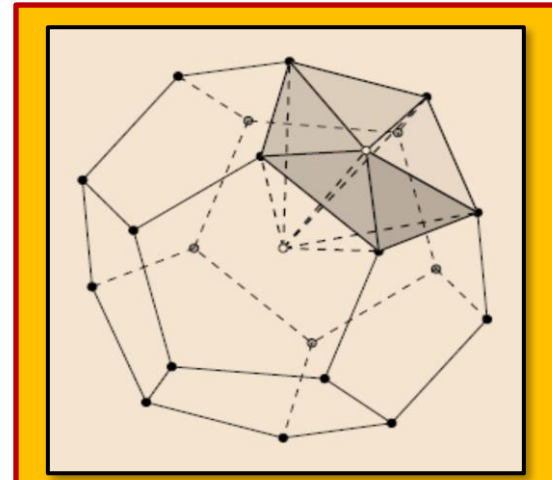


Figure 7.6.3 Decomposition of Poly cells into Tetra

<sup>91</sup> H. Jasak, Z. Tukovic, "Automatic Mesh Motion for the Unstructured Finite Volume Method", Journal of Computational Physics, 2004.

<sup>92</sup> T. Lucchini, G. D'Errico, F. Brusiani and G.M. Bianchi, "A Finite-Element Based Mesh Motion Technique for Internal Combustion Engine Simulations", SAE Paper, 2007.

<sup>93</sup> H. Jasak, Z. Tukovic, "Automatic Mesh Motion for the Unstructured Finite Volume Method", Journal of Computational Physics, 2004.

the mesh will become too compressed or stretched which will impact the quality of the solution. A way to check this is described in the following chapter.

### 7.6.3 Valve Closure Problem

One problem with the moving mesh strategy is the valve closure. As the valve moves closer and closer to the cylinder head it will cause the cells between the top of the valve and the cylinder head to become more and more compressed. Eventually they will have very low quality or even be inverted or have zero volume which results in numerical errors and abortion of the calculation. An approach to simulate the contact between the valve and the cylinder head was developed in<sup>94</sup> and is called attach-detach boundary. When the valve lift is lower than a pre-set arbitrary value (usually  $\sim 0.1$  mm) the valve is considered closed. These two new set of boundary faces will separate the cylinder volume from the duct volume by acting as a wall boundary (one set of faces for the cylinder volume and one set for the duct volume). In this way the valve is simulated as closed without changing the geometry of the valve or the cylinder head, and there is no need to modify the solver or the mesh. There will be a small change in the valve opening and closure time but if the value of minimum valve lift is small the difference will be negligible.

### 7.6.4 Physics

Up to now we were concern with meshing issues (pre-processing) of the problem. Now we take the physics involved in process. The processes in IC Engines are extremely complex and include **turbulence, heat transfer, 2-phase flow, evaporation and mixing, spray-wall impingement dynamics and films, chemistry and turbulence-chemistry interactions, real-gas effects, high-speed flow, radiation etc.**<sup>95</sup> Three of the most important issues are **Turbulence Modeling, Spray Modeling and Combustion with Real Fuel Modeling's**, which are challenging in their own right.

### 7.6.5 Case Study 3 - An Original Approach To Address 3D Automatic Meshing For Internal Combustion Engine (ICE) Simulation Using Hybrid Body Fitted Grid and Embedded Remeshing Process<sup>96</sup>

#### 7.6.5.1 Introduction and Background

The undesired environmental consequences of transport activity will require further action in particular on air pollutant emissions and greenhouse gas emissions. Combustion system technology and increased combustion process understanding and control are three of the solutions towards cleaner engines operating under complex conditions often at the limits of stability. **3D CFD** solvers must keep in pace with such evolutions to effectively model systems with increased complexity so as to actively contribute to the design and optimization of powertrains. As the perception of 3D CFD's added value in the powertrain development increases, its remaining weaknesses are also brought under the spotlight. Three of the traditionally most noteworthy are: mesh generation, chain of models for multi-physics calculations, solver parallel efficiency and accuracy.

The mesh generation process remains a long expertise laden process with more or less manual user intervention which limits the deployment of 3D CFD to specialized/trained users. These issues are often dealt with in an integrated fashion in modern meshing methodologies. In recent years, tremendous advances have been made in automatic unstructured mesh generations in particular, the triangular and tetrahedral mesh generations using Octree, Delaunay and advancing front methods<sup>97</sup>.

---

<sup>94</sup> T. Lucchini, G. D'Errico, H. Jasak and Z. Tukovic, "Automatic Mesh Motion with Topological Changes for Engine Simulation", SAE Paper, 2007-01-0170, 2007.

<sup>95</sup> Internal Combustion Engines Magazine, CD-Adapco®.

<sup>96</sup> B.Réveillé, N.Gillet, J.Bohbot, O.Laget, "An original approach to address 3D automatic meshing for internal combustion engine simulation using hybrid body fitted grid and embedded remeshing process", IFP Energies Nouvelles, Fr.

<sup>97</sup> P.L. George, H. Borouchaki, P.J. Frey, P. Laug and E. Saltel, *Mesh generation and mesh adaptivity: theory, techniques, chapter in Encyclopedia of computational mechanics*, Hughes ed., John Wiley & Sons Ltd., 2004.

After an overview of the wide variety of solutions which have been proposed, we presents **how to tackle the weaknesses through mesh process automation, the solver physical accuracy near the wall region and solver parallel efficiency**. It has been the main driver behind the development of **IFP-C3D**'s new unstructured hybrid core and to its coupling with **CENTAUR<sup>98</sup> - CentaurSofts unstructured hybrid meshes**. **OMEGA (Optimized MESH Generation Automation)** uses a direct coupling procedure between the *IFP-C3D* solver and *Centaur*.

Thanks to this automatic procedure, the engineering time needed for body fitted 3D CFD simulation in ICE, is drastically reduced from a few weeks to a few hours. Valve and piston motion laws are just given as input files and geometries and meshes are automatically moved and generated. Unlike other procedures, this automatic mesh generation does not use an intermediate geometry discretization (STL file, tetrahedral surface mesh) but directly the original CAD that has been modified thanks to the geometry motion functionalities integrated into the masher. All the meshes generated by the tool discretize precisely the surface geometry (nodes are projected on the correct CAD surfaces) to guarantee a correct flow prediction in particular around intake valves and piston singularities.

### 7.6.5.2 Hybrid IFP-C3D Combustion Solver

As the supercomputing world evolves towards super-scalar machines, **IFPEN** has developed a new parallel unstructured CFD solver, **IFP-C3D<sup>®</sup>**, that is adapted to such computing platforms/architectures. It is entirely dedicated to the simulation of compressible reactive flows with combustion and sprays. Moving-mesh strategies are integrated with all physical models needed to simulate internal combustion engines. Original moving-mesh functionalities make it simple to use the code for complex moving geometries with pistons and intake/exhaust valves. Dynamic mesh management has been implemented to re-mesh and adapt the grid with the geometric moving part motion. The code is fully parallelized for shared and distributed memory computers and uses optimized parallel mathematical libraries for linear algebraic system calculations. IFP-C3D solves the conservation equations of mass, mass species, momentum energy and the k-ε turbulence equations for chemical reactive flows with sprays. Many fictive species are also used in the code to model tracers of real species or to add tracers for physical modeling. Fictive species satisfy the conservation equation of mass and momentum but are not taken into account for conservation of energy. The conservation equations are solved using the **Arbitrary Lagrangian Eulerian Formalism** to take into account the effect of the moving geometric parts and of the large volume variations. The time splitting method is used to decompose the physical time-step into three stages. The time-splitting begins with the source terms (stage A), then follows a full implicit Lagrangian stage (stage B), and finally a sub-cycled explicit Eulerian phase (stage C).

#### 7.6.5.2.1 Mesh Generation

Initially written for hexahedral unstructured meshes, Stage B and Stage C have been modified to work with unstructured hybrid grids. Stage B "Lagrangian stage", uses the original Semi-Implicit method introduced by [Patankar] in its fully implicit version. The coupled implicit equations (momentum, temperature and pressure) are solved with the SIMPLE algorithm. The use of the ILU preconditioning and of the BiCGSTAB method for the pressure solver gives a better rate of convergence of the SIMPLE algorithm to avoid small pressure oscillations in particular for tetrahedral cells. The fluxes of scalars such as mass, internal energy and turbulence quantities are computed between cells using the *VOFIRE* scheme<sup>99</sup> based on the construction of anti-dissipative flux to reduce numerical dissipation. This scheme is particularly adapted to hybrid grids.

For body fitted solvers, the internal combustion engine simulation needs to be able to re-mesh regions where the volume variation or displacement leads to distorted cells or to small volume cells.

---

<sup>98</sup> CENTAUR Hybrid Grid Generation Software, CentaurSoft, <https://www.centaursoft.com/>

<sup>99</sup> B. Despres, F. Lagoutière, E. Labourasse, I. Marmajou "An Anti-dissipative Transport Scheme on Unstructured Meshes for Multicomponent Flows", The International Journal on Finite Volumes, IJFV , 7, pp 30-65, (2010).

This remeshing task can be local or global but has to be implemented in parallel to maintain the parallel efficiency of the solver. Previous IFPEN work has shown that local remeshing using swapping, refinement and coarsening operations is an interesting solution but requires too much processing during the engine cycle to be acceptable. These tests have shown that a global remeshing of the geometry allows to reduce the number of remeshing stages needed and provides better parallel performance thanks to an improved load balancing. Moreover, global remeshing is compatible with one step external mesh generation whereas local remeshing requires remeshing be undertaken during the simulation (as with AMR solvers). The global remeshing process developed in IFP-C3D uses a conservative interpolation to transfer numerical results from the original mesh to the new mesh<sup>100</sup>.

#### 7.6.5.2.2 Parallelism

Parallelism is the key for performance on any system manufactured today. All domestic high performance systems in quantity production use commodity microprocessors at the core of their design. It has been repeatedly shown that such CPUs routinely achieve only 20% of their peak performance on real scientific codes. Clearly, an application must scale to hundreds of CPUs on such systems, if it is to achieve the sustained performance to stay competitive in high-end computing and to give simulation return times compatible with industrial requirements. For large calculations and to use IFP-C3D on super-scalar machines, the MPI parallelism has been implemented. The MPI partitioning routine was developed to manage the moving grid algorithm with remapping and the decomposition of the 3D domain into sub-domains, each consisting of a number of cells. Each MPI process within the group computes one sub-domain. IFP-C3D uses the METIS generic graph partitioning library to decompose and distribute the 3D domains. This decomposition is done when IFP-C3D loads a new mesh, at the beginning of the calculation and also at each remapping stage. MPI exchange routines were developed to manage the data exchange at cells, vertex, face centers (both fluid and wall).

#### 7.6.5.3 Automatic Mesh Generation Procedure

The automatic mesh generation procedure which identifies and meshes all the phases required to simulate an engine cycle is based on 3 key components :

- A hybrid meshes with the following capabilities:
  - Advanced geometrical entity movement with activation/deactivation (useful for piston and valve motion, effective valve closing with or without attached port deactivation)
  - Advanced meshing CAD and geometrical sources that can be activated or deactivated
  - Fast & parallel meshing capabilities including user configurable quality metrics
  - Script ability of all the above functionalities so as to execute the meshes in batch mode
  - These criteria lead *IFPEN* to select the Centaur meshes from *Centaursoft* for which specific developments were performed in collaboration with the editor so as to add the few missing functionalities.
- A scriptable fast and parallel mesh deformation software with quality metrics to assess when a deformed mesh falls outside the required criteria.
- A new wrapper software tool that automates the previously manual mesh generation process by:
  - automatically predetermining each iso-topological computation phase using user knowhow (previous manual work) and valve & piston motion based heuristics. Each

---

<sup>100</sup> J.Bohbot, N.Gillet "Impact of different mesh remapping techniques on 3d simulations in internal combustion engines". Proceedings of the European Conference on Computational Fluid Dynamics, Egmond aan Zee, The Netherlands, September 5-8, 2006.

predetermined phase is characterized by a meshing crank angle and initial & final crank angles allowing maximal phase length while theoretically respecting deformation and quality criteria.

- coupling the 2 previous tools to generate - from a single reference mesh project - the initial mesh of each phase and verify that the user specified mesh quality criteria are respected throughout the phase and if necessary readjust phase length based on effective mesh deformation. The motion capabilities of IFP-C3D do not constrain the meshing crank angle as mesh movement may go forwards or backwards in time.
- if necessary iterating on the previous two items, with feedback from IFP-C3D effective deformations as extra constraints for the heuristics, until a feasible phase is found (for details please refer to <sup>101</sup>).

The use of a unique reference project was a major focus of the procedure implementation as it is key in reducing the engineering time spent on generating the meshes. this reference project therefore contains:

- All valves which are all opened and all attached ports
- All CAD and geometrical sources required throughout the entire engine cycle. Their activation or deactivation per phase is based on user supplied procedure inputs (injection event, ignition event, ...) or geometrical status (valve is open or closed)

The tool called OMEGA (Optimized MEsh Generation Automation) was also thought so that:

- once the reference project exists it is simple to:
  - change piston motion (through new motion file or new cinematic characteristics)
  - change valve motion (through new motion file or phase offset specification)
  - change a part of the CAD (piston/valve/port/...)
  - change meshing parameters to apply on the entire family of meshes
- piston position offset can be specified so as to adapt effective mesh compression ratio to user input
- it is multi-cylinder compatible (tool is ready IFP-C3D code work will come) without any limits on number of valves, pistons and cylinders

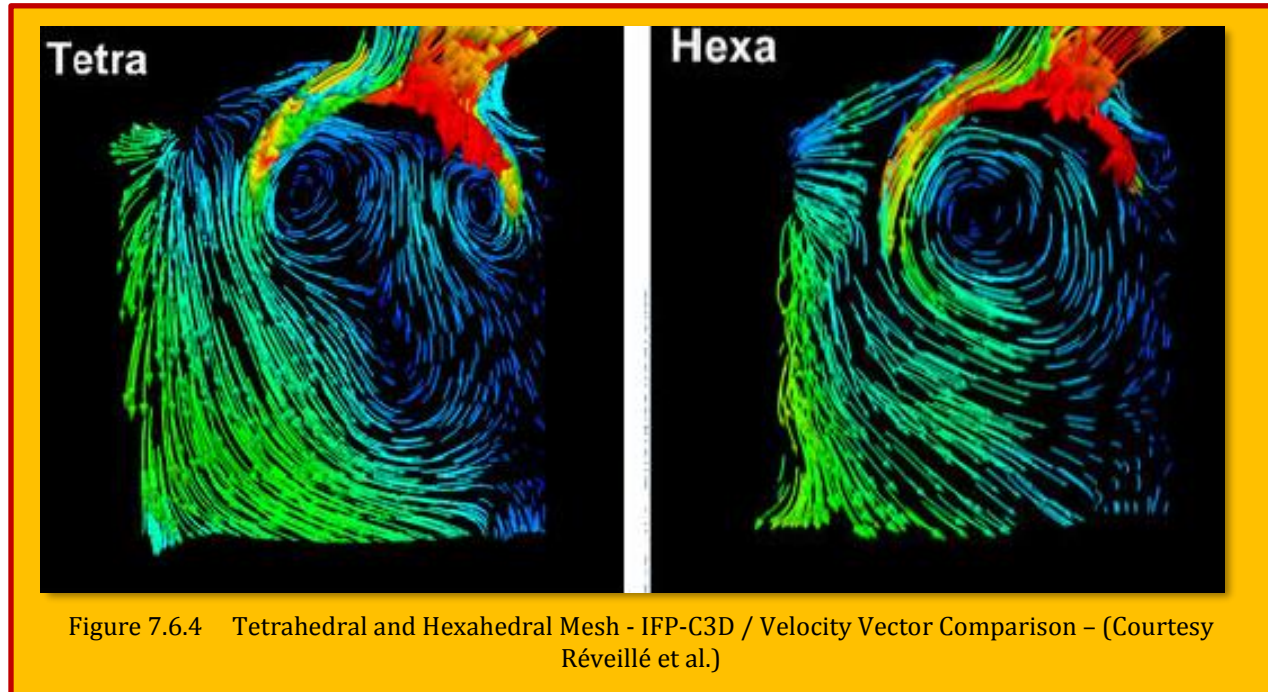
As discussed earlier, OMEGA was designed as a preprocessing tool rather than integrated in IFP-C3D because mesh generation parallelism is not as good as CFD solver parallelism and global remeshing is better for load balancing than local in-solver remeshing. Since generally a mesh family is not used for only one operating point computation, time is saved each time the mesh family is reused (injection strategy or spark advance variation). The development of the automatic mesh generator OMEGA was carried out so as to further the reduction of the ICE simulation return time from CAD import to numerical results. Due to the MPI parallelism, the calculation return time has been massively reduced from more than one week with the serial code KMB with a coarse grid (~80.000 cells) to 24 hours using refined grids (~2M cells) on 256 cores. Using the new calculation core for hybrid grids, the mesh generation task has been reduced to six days when using tetrahedral grids generated with an external meshed based on the advancing front method. The CAD cleaning task is also reduced. Tetrahedral grids are fully adapted to take into account all geometric features that we can be found in an ICE. Finally, to massively reduce the time spent on the mesh generation, the automation tool

---

<sup>101</sup> B.Réveillé, N.Gillet, J.Bohbot, O.Laget, "An original approach to address 3D automatic meshing for internal combustion engine simulation using hybrid body fitted grid and embedded remeshing process", IFP Energies Nouvelles, Fr.

OMEGA is very efficient and less than a half/day is needed to prepare the Centaur project before the mesh generation. Thanks to OMEGA and the new hybrid IFP-C3D core, the simulation return time is reduced to 2 days which is close to Cartesian non body fitted approaches.

Moreover, when using refined tetrahedral grids, the aerodynamic patterns are better predicted than with a hexahedral grid - due to the mesh's more isotropic nature and easier local refinements near the valve curtains (see [Figure 7.6.4](#)) and all the surface geometric features can be taken into account with ease such as the spark plug, the cylinder head.



#### 7.6.5.4 Cylinder Multi-Cycle Engine Simulation

In order to validate the methodology and tools, a rather coarse 4-cylinder multi-cycle simulation was set up and carried out on a virtual engine geometry based on a single cylinder optical engine. This multi-cylinder configuration, served as a validation of all events that must be managed during the simulation of new engine concepts (such as cylinder deactivation, variable valve actuator...). The OMEGA tool was used to generate the meshes of the entire engine cycle. Given the quality constraint imposed and the mesh sizes requested for this validation case, OMEGA generated 52 meshes so as to ensure tetrahedra quality throughout the cycle. The mean tetrahedra sliver value is in the range [1,2-1,36] which guarantees a correct behavior of the spatial numerical scheme ([Figure 7.6.5](#)). 4 engine cycles were computed using 256 cores resulting in a simulation return time equal to 24h per cycle. The multi-cylinder simulation allows a improved load balancing compared to a single cylinder configuration as to the average number of cell remains constant (in this rather coarse case around 1.3M cells).

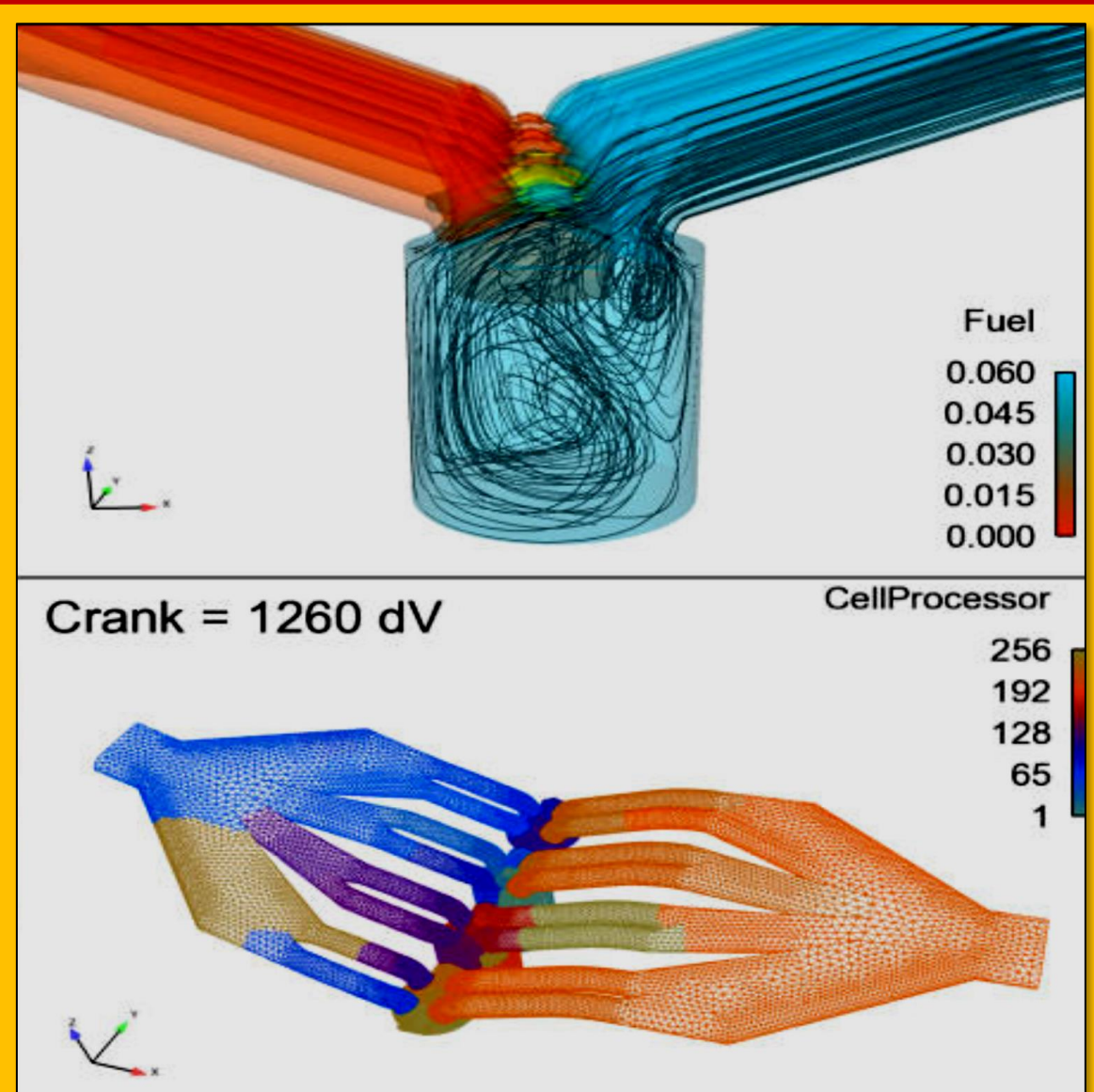


Figure 7.6.5 Engine Simulation (Flame Surface Density and Velocity Streamlines) and MPI Partitioning – (Courtesy Réveillé et al.)

#### 7.6.5.5 Conclusion

After an overview of existing solutions, IFPEN decided to implement that which it deemed the best compromise in terms of mesh setup simplicity, simulation result accuracy and parallel efficiency. After implementing hybrid grid functionalities – so as to benefit from simple automatic tetrahedral dominant mesh generations - to the pre-existing hexahedral unstructured solver IFP-C3D, the OMEGA (Optimized MEsh Generation Automation) tool was created to couple IFP-C3D's mesh deformation abilities to CENTAUR's hybrid grid generation power to automatically generate all the body fitted hybrid meshes needed to simulate an entire engine cycle. Using OMEGA, meshes for a 4 cylinder 16 valves virtual engine were generated in less than 24 hours (starting from good CAD import) using 16 cores. This new approach, drastically improves internal combustion engine 3D simulation setup but also run time. As a consequence 3D CFD's contribution to powertrain

development is enhanced by maximizing its prefiltering ability which helps focus experimental tests on the most promising geometries identified. For additional info, please consult the [Réveillé et al.]<sup>102</sup>.

## 7.7 Case Study 4 - Predicting Surface Temperature of the Exhaust System

The thermal model and simulation of vehicles components is necessary within the development phase of the vehicle production process, as investigated by [Moya]<sup>103</sup>. It is important to understand the thermal processes of high temperature components in the vehicle, such as the exhaust system. The exhaust system presents a high thermal activity that increases the temperature of the exhaust system itself and the nearby surrounding engine components, due to the large amount of heat transferred by radiation. The aim of this thesis is to develop a method that predicts the surface temperature of the exhaust system to ensure that no component overheats. This method includes coupling of CFD with heat transfer software. The thermal model and simulation of the vehicle components is very important in the design, optimization and management of vehicle power systems. It is necessary to determine the vehicle parts that present the highest temperature and the heat transferred between these parts, such as exhaust system. It contains much thermal activity due to the high temperature of the exhaust gas flowing through the system and chemical reaction in the catalytic converter. Therefore, a method development of the exhaust system temperatures is necessary to ensure that no component overheats. One of the aims of developing this method is to increase the efficiency of the verification process. The method is based on CAE tools currently used at Volvo Cars Corporation for under-hood thermal management. The method includes coupling a CFD (convection heat transfer) software with a heat transfer software (radiation and conduction heat transfer) that models the 1D flow inside the exhaust system

### 7.7.1 Heat Transfer Methodology

It is important to understand the heat transfer modes and the equations used in this model.

#### 7.7.1.1 Conduction

The heat transfer by conduction happens due to a temperature gradient across a medium. Fourier's Law governs the conduction heat transfer and the heat transfer occurs in the direction of decreasing temperature. Considering the exhaust system wall shown in **Figure 7.7.1** with  $T_{s1} > T_{s2}$ , the temperature difference causes conduction heat transfer in the positive x-direction. The heat transfer rate ( $\dot{Q}_{cond}$ ) depends on the temperature difference  $\Delta T$ ; the wall thickness (x); the cross-sectional area (A); and the material conductivity ( $\kappa$ ).

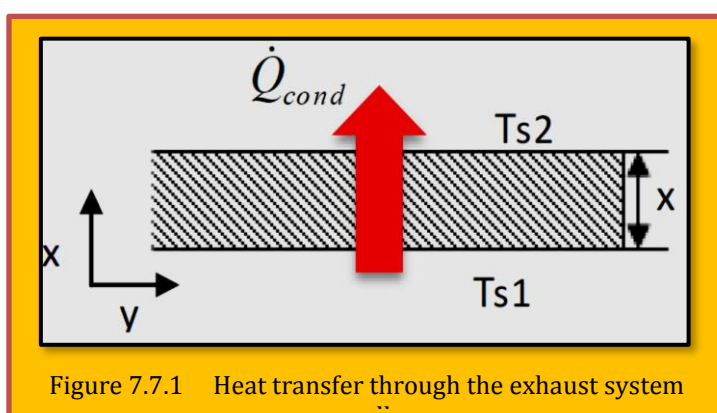


Figure 7.7.1 Heat transfer through the exhaust system

<sup>102</sup> B.Réveillé, N.Gillet, J.Bohbot, O.Laget, "An original approach to address 3D automatic meshing for internal combustion engine simulation using hybrid body fitted grid and embedded remeshing process", IFP Energies Nouvelles, Fr.

<sup>103</sup> Begoña León Moya, "Fluid and Thermodynamic Under-hood Simulations", Thesis for the Degree of Master of Science, Lund University.

### 7.7.1.2 Convection

Heat transfer by convection occurs due to energy transfer between a surface and a fluid moving over the surface. A region in the fluid, called the *hydrodynamic boundary layer*, is developed due to the interaction between the fluid and the surface (see [Figure 2.7.3](#)). The velocity inside this region varies from zero at the surface to a finite value  $u_\infty$ . Furthermore, a *thermal boundary layer* is developed due to the temperature difference between the fluid and the surface. The size of this layer may not be the same as that of the hydrodynamic layer. The convection heat transfer occurs due to the random molecular movement and the bulk motion of the fluid within the boundary layer. Near the surface, where the velocity of the fluid is low, the molecular diffusion dominates. The layer grows as the flow progresses in the  $x$ -direction, which leads to a contribution of the bulk fluid motion. During the boundary layer development, the flow can be laminar and turbulent in many cases where the laminar section precedes the turbulent section. The laminar flow is greatly ordered and streamlines can be seen along this section. The ordered flow continues until it reaches the transition zone where the flow passes from a laminar to a turbulent flow. The turbulent flow is mainly random and highly irregular, which contributes to a mixing within the boundary layers. The mixing is mainly caused by the stream-wise vortices close to the flat plate.

The transition from laminar to turbulent flow depends on the triggering mechanisms. The turbulent flow is reached depending on if the triggering mechanism is amplified or diminished in the direction of the fluid flow. The fluid flow is divided into internal and external flow. The internal flow is defined as one where the growth of the boundary layer is confined and the external flow is defined as one where the boundary layer can grow without bounds. The heat transfer in the exhaust system can be divided into:

- Forced convection heat transfer between the exhaust system and the surrounding air.
- Radiation to surrounding parts.
- Conduction with all the connecting parts.
- Forced convection heat transfer between the exhaust system and the exhaust gas.

Assuming a simple one-dimensional heat transfer shown in [Figure 7.7.2](#). The external heat transfer, the conduction and the internal heat transfer in the exhaust system can be defined as follows,

$$\begin{aligned} Q_{\text{ext}} &= Q_{\text{conv}} + Q_{\text{rad}} = h_s A_s (T_{s2} - T_a) + \sigma A_s (T_{s2}^4 - T_a^4) \\ Q_{\text{cond}} &= \frac{K \cdot A}{t} (T_{s1} - T_{s2}) \quad \text{and} \quad Q_{\text{int}} = h_{\text{int}} \cdot A \cdot (T_f - T_{s1}) \end{aligned} \quad \text{Eq. 7.7.1}$$

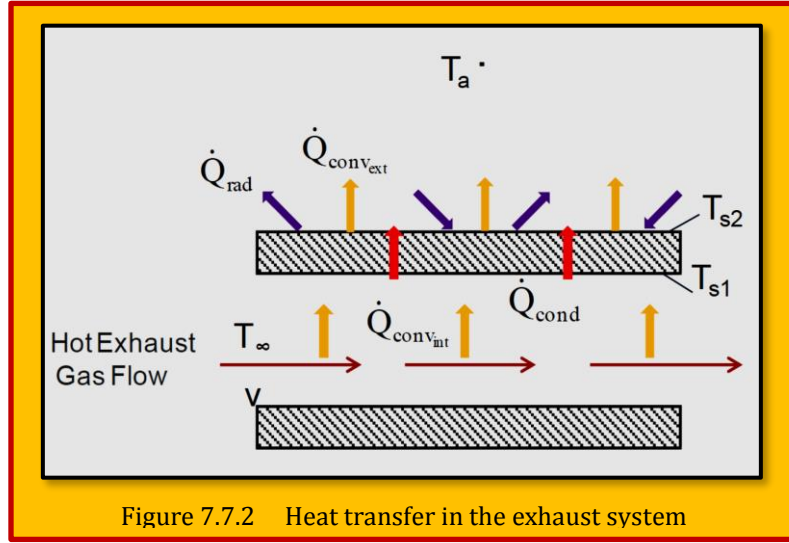


Figure 7.7.2 Heat transfer in the exhaust system

It is important to notice that the fluid in the developed exhaust model corresponds to exhaust gas with a pulsating nature. Several experiments show that the heat transfer rates in exhaust gases are higher than expected due to the pulsating nature of the flow in the exhaust manifold. Therefore, it is necessary to introduce the Convective Augmentation Factor (CAF), as defined below:

$$\text{CAF} = \frac{\text{Nu}_{\text{effective}}}{\text{Nu}_{\text{theoretical}}} \quad \text{Eq. 7.7.2}$$

This parameter should be applied to take into account the gas pulsations and sharp changes in the geometry. Based on previous research, the proper CAF value for exhaust gases is 2.5.

### 7.7.2 Exhaust System

The exhaust system collects the gas coming from the engine and treats it before the gas is released to the atmosphere. The exhaust system described in this thesis is composed of the manifold, turbocharger, catalytic converter and flexible pipe as illustrated in **Figure 7.7.3**. It is important to notice that the exhaust system also incorporates a muffler and an exhaust gas recirculation system (EGR system). However, these parts are not further investigated here. The exhaust gases leave the engine cylinder and are collected in the manifold. The gas streams flow inside the manifold and converge at the turbocharger. The turbocharger is divided into the turbine, center housing and compressor. The exhaust gas flows through the turbine spinning blades leading to a pressure decrease in the exhaust gas. The combustion gases present enough pressure and temperature to produce a torque to drive the turbine to a very high speed. This rotation makes the compressor rotate as well since both contain the same shaft. The compressor takes air from outside and forces it to pass through the volute where it is compressed. The compressor is made up of an impeller, a diffuser and volute housing. The compressor increases the density of intake air entering the combustion chamber. The turbocharger geometry determines how the exhaust gas passes through the turbine and the compressor, influencing the overall turbocharger performance.

The two-way catalytic converter is applied to reduce the emission of combustion engines. The gas coming from the turbocharger consists of products of combustion and unburned hydrocarbons, which are hazardous for the environment. The **catalytic converter** presents two components: the **Diesel Oxidation Catalyst (DOC)** and the **Diesel Particulate Filter (DPF)**. The majority of the automotive catalytic converters contain a substrate made of metal or ceramic that supports the noble

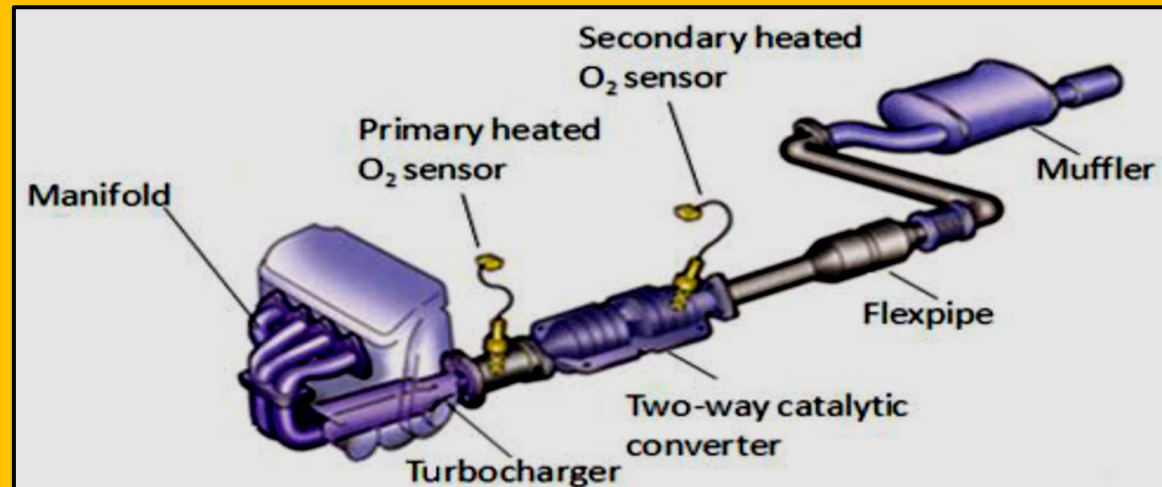


Figure 7.7.3 Exhaust System

metal. The most common metals used as catalysts are platinum, palladium and rhodium. The substrate consists of numerous channels with different geometries and an equivalent diameter of approximately 1mm. The exhaust gas passes through the substrate cells where oxidation reactions take place. The harmful compounds of the exhaust gases are converted into harmless compounds according to the following reactions.

### 7.7.3 Method Development and Setup

A method to predict the exhaust system temperature is described here. The inlet boundary condition is specified as one with a constant mass flow rate and with a representative temperature. The method approximates the transient driving conditions with an equivalent steady-state condition. The method is validated against the results from the wind tunnel test. The method is developed by coupling CFD software with heat transfer analysis software (*RadTherm*)®. The external boundary conditions are obtained from 3D CFD simulations carried out in Fluent® and the internal boundary conditions are derived from coupling with *RadTherm*. *This coupling is necessary in order to model the advection of air temperature from the front to the rear of the vehicle which cannot be performed by only one-step import of convection coefficients from CFD*. One-dimensional models of internal flow in piping systems provide significant advantages over 3D CFD by reducing both the model complexity and the computational time required to perform a simulation in some applications. On one hand, Fluent solves the governing differential equations (Non-linear Navier-Stokes) and calculates heat transfer coefficients ( $h_{ext}$ ) and film temperatures ( $T_{surf}$ ) that are used as external boundary conditions in *RadTherm*. On the other hand, *RadTherm* performs an energy balance based on calculations of convection, conduction and radiation. The initial simulation uses estimated external boundary conditions (heat transfer coefficients and film temperatures) in order to provide an initial temperature profile of the exhaust system. This temperature profile is imported into the CFD software and used as a boundary condition. Multiply surface elements are grouped to form "patches" for radiative purposes to save computational effort. These *RadTherm* simulations are running on 8cpu cluster. Before running the thermal model, it is necessary to define the environmental conditions. In this model the environment surrounding is modeled by the box environment. The bounding box environment is used for radiation exchange purposes. The temperature of the environment and the offset distance from the geometry to the walls of the box may be specified. A constant temperature of 70C and an offset distance of 1mm are used in this model.

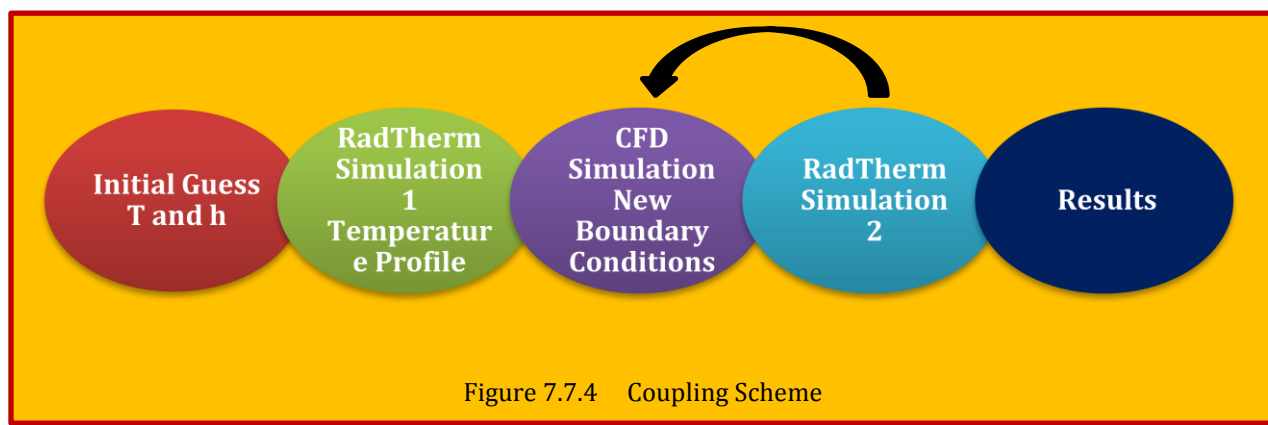


Figure 7.7.4 Coupling Scheme

### 7.7.4 CFD Coupling

The CFD coupling process is automated using a script developed by VCC. First, the thermal model is run using estimated boundary conditions to provide a temperature profile that is imported into the CFD code. The CFD model is run to convergence and new convection boundary conditions are exported to the thermal model. Finally, the thermal model is re-run providing a new temperature

profile. This coupling loop continues five times more. An overview of the modeling process is shown in **Figure 7.7.4**.

### 7.7.5 Thermal Model Development

#### 7.7.5.1 Characterization of the Manifold

There are five streams coming into the manifold one in each inlet and all of these streams converge into the turbocharger inlet. The first step to simulate the manifold is to define the value of the total mass flow rate and the inlet temperature of the exhaust gas in each manifold inlet. It is assumed that the mass flow is equal distributed in each pipe, which means that amount of exhaust gas coming into each manifold inlet is the same and it can be obtained dividing the total mass flow rate by the number of inlets. The inlet gas temperature was estimated based on the temperature measured at the turbocharger inlet. As a first approximation, the inlet temperature of the exhaust gas was assumed the same in all the streams; however the results show that the temperature distribution at the inlet is not uniform, which means that each stream coming into the manifold presents a different temperature. The inlet temperature of the streams differs only by 10-20 °C and the left stream presents the highest temperature while the right stream has the lowest temperature.

Typical flow conditions in driving cases produce Re numbers higher than 2300 which means that the flow inside the manifold is turbulent. Even in cases where the Re is lower than 2300, the flow would remain turbulent because the exhaust valves and the pulsation effects do not favor the transition to the laminar region. *RadTherm* is able to calculate the heat transfer rates between the exhaust gas inside the manifold and the manifold inner wall by setting fluid streams inside the manifold geometry. Fluid streams are used in *RadTherm* to model a fluid inside pipes. When fluid streams are used in *RadTherm*, the heat transfer coefficients are automatically calculated by correlations based on flow rate and geometry. The mass flow rate and inlet temperature of each stream should be set as input and also the inlet, outlet and direction of the streams. In order to setup the streams in *RadTherm* it is necessary to split the geometry in several parts as it is shown in the **Figure 7.7.5**. Advection links are used in *RadTherm* to connect streams allowing transmitting the stream properties from one stream to another. When two streams are connected, the outlet properties of one stream are the same as the inlet properties of the other stream. In this model advection links are required to connect upper streams with the stream coming into the turbocharger. Convective effects of the stream are modeled by setting a convection boundary condition on each part bounding the fluid represented by

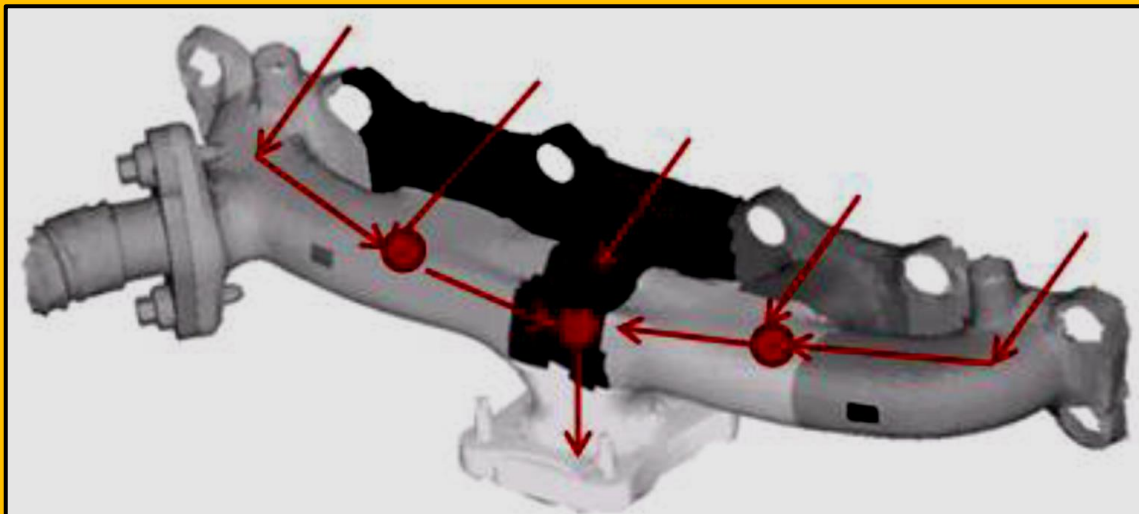


Figure 7.7.5 Manifold with Five Streams Connected by Advection Links

different colors in **Figure 7.7.5**. The convection coefficient can be calculated using the correlations shown in Appendix A of [B. León Moya]<sup>104</sup>.

It is noteworthy that there is not any stream in the EGR. In this model the exhaust gas does not flow through the EGR since it was closed during the wind tunnel tests. In case that the EGR is open, another stream should be setup inside this part and a certain percent of the exhaust gas will be released through this pipe. The Convective Augmentation Factor (CAF) equal to 2.5 is applied in the streams to take into account the gas pulsations and sharp changes in the geometry. **Table 7.7.1** shows the temperatures predicted by RadTherm using two different CAF values. The first column correspond to the data obtained in the tunnel test, the second column contains the temperatures predicted when a CAF equal one is applied and the last column corresponds to the temperature predicted when a CAF equal to 2.5 is used.

As can be seen in **Table 7.7.1**, the Convective Augmentation Factor presents a high influence in the surface temperatures. The simulation carried out

with a CAF equal to 2.5 leads to a better prediction of surface temperature than using a CAF equal to 1 showing a maximum temperature deviation of three degrees. It is worth mentioning that these simulations were carried out by *RadTherm* without CDP coupling in order to reduce the computational time. The external convective coefficients and temperatures were imported from the same CFD data in all the simulations shown.

Temperature C	Tunnel test	CAF = 1	CAF=2.5
Exhaust manifold, right	537	479	528
Exhaust manifold, center	590	566	594
Exhaust manifold, left	567	526	570
Exhaust manifold, left, at EGR pipe	441	367	445

Table 7.7.1 CAF influence in the surface temperature prediction

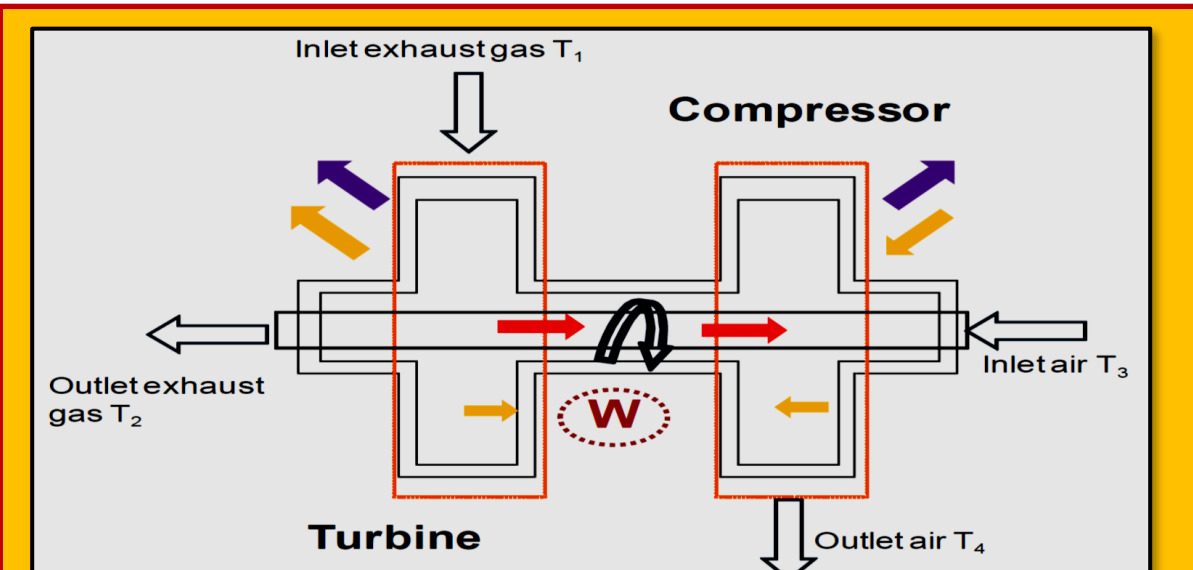


Figure 7.7.6 Heat Transfer Model of the Turbocharger for all Modes on HT

<sup>104</sup> Begoña León Moya, "Fluid and Thermodynamic Under-hood Simulations", Thesis for the Degree of Master of Science, Lund University.

### 7.7.5.2 Case Study 4.1 – Exhaust Manifold with Transient BC Velocity and Temperature<sup>105</sup>

Not to deviate from current discussion, **TCFD is an automated workflow** with successfully merged benefits of an **open-source** (perpetual, unlimited users, jobs, and cores, customizable, etc.) with benefits of commercial codes (professional support, well tested, ready for the industry, robust, accurate, automated, GUI, ...). TCFD is fully automated, it can run the whole workflow by a single command: data input, new case is written down, mesh is created, case is set-up, case is simulated, results are evaluated and the results report is written down. Both GUI and batch mode. Data in - data out. TCFD is mainly focused on supporting the engineers in their real value added work. TCFD is fully automated and the beauty of TCFD is that it is the user who decides how deep to dive into a CFD or not at all. And all the options remain open at the same time.

#### 7.7.5.2.1 Input data

The surface model data in [.stl](#) file format together with physical inputs are loaded in [TCFD](#). Other option would be loading an external mesh in *OpenFOAM®* mesh format, or loading an MSH mesh format (Fluent mesh format). This CFD methodology employs a multi component approach, which means the model is split into a certain number of regions. In [TCFD](#) each region can have its own mesh and individual meshes communicate via interfaces.

#### 7.7.5.2.2 CFD Simulation Set-up

- Compressible flow model
- Transient flow model
- Medium: Hot air
- Temperature at inlet:  $T = 543$  [K]
- Viscosity:  $\mu = 1.831e-5$  [Pa.s]
- Mass Flow Rate: 0.00468 [kg/s]
- Interface: None
- Turbulence Model: k- $\omega$  SST
- Mesh: snappyHexMesh, hexadominant
- Mesh Cells: 345250
- Number of components: 1
- CPU time: 3 [core.hours]

For more details of CFD Simulation Set-up see [TCFD Manual](#).

#### 7.7.5.2.3 Running CFD Simulation

The simulation can be run on any number of parallel processors (see link below). Immediately after the simulation is started, the user can follow the progress of all the important quantities in a [HTML report](#): flow rates, residuals, efficiency, torque, pressure difference and many others. These run-time functions give the user valuable information of the simulation convergence and also the availability to stop the simulation before its expected end. <https://youtu.be/EIn2oUIX6VM>

### 7.7.6 Characterization of the Turbocharger

One-dimensional (1D) models are commonly employed to study the performance of turbocharger engine. Much research shows that heat flows inside the turbocharger are non-negligible and they should be included in the turbocharger model. The turbocharger is divided into compressor and turbine and these parts are connected through a bearing housing. Several researchers have shown that heat transfer is not small during the compression and the expansion; therefore, a 1D heat transfer model is developed and validated against the experimental measurements. A simply scheme of energy changes can be seen in the [Figure 7.7.6](#).

---

<sup>105</sup> CFD Support

### 7.7.7 Characterization of the Catalytic Converter

A catalytic converter is an exhaust emission control device that converts toxic gases and pollutants in exhaust gas from an internal combustion engine to less toxic pollutants by catalyzing a redox reaction (an oxidation and a reduction reaction). Catalytic converters are usually used with internal combustion engines fueled by either gasoline or diesel including lean-burn engines as well as kerosene heaters and stoves. The catalytic converter can be divided into two components: the diesel oxidation catalyst (DOC) and the diesel particulate filter (DPF). The catalytic used in diesel engines is usually a two ways catalytic illustrated in **Figure 7.7.7**. For details in other characterization such as the catalytic inlet, DOC, the catalytic part between the DOC and the DPF, the DPF, and the catalytic outlet cone, readers encouraged to consult with [B. León Moya]<sup>106</sup>.

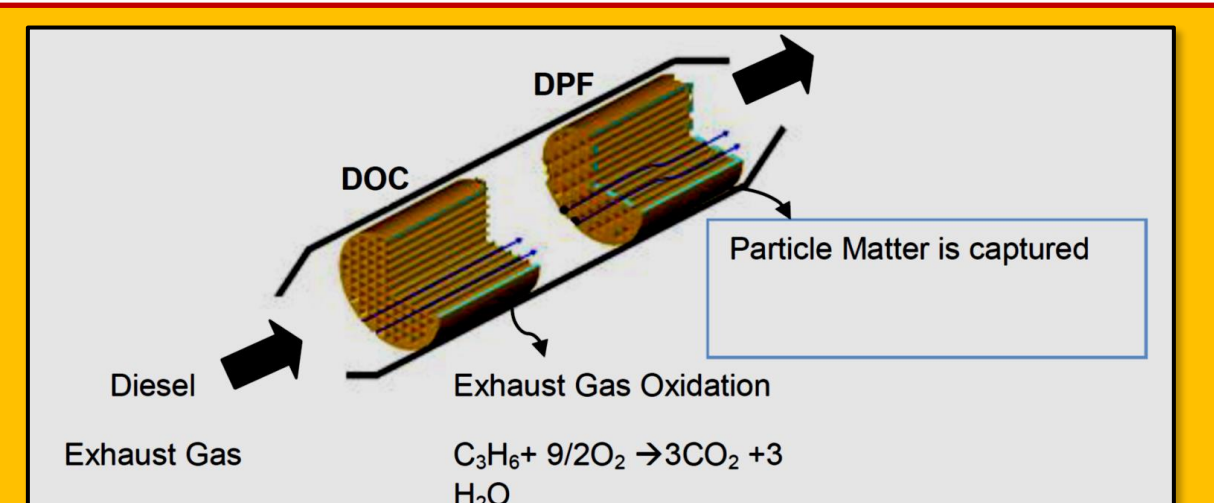


Figure 7.7.7 Catalytic Converter

### 7.7.8 Characterization of the Exhaust Pipe and Flex-Pipe

After the treatment of the exhaust gas inside the catalytic converter, the concentration of soot and dangerous compounds is low enough to fulfill the restrictions of the environmental law EURO 5 99/96/EC. This clean stream passes through the flex-pipe and the exhaust pipe, which leads to a forced convection heat transfer between the exhaust gas and the inner wall of the pipe. The flex-pipe presents a ringed surfaced surrounded by a mesh made of stainless steel that is modeled in RadTherm by a three layers straight pipe. The gas inside the exhaust pipe is modeled in RadTherm as a stream by defining the inlet, the outlet and the direction of the flow. An advection link is required to connect this stream with the upstream fluid node.

### 7.7.9 Results and Discussion

Through this section the most relevant results are presented and discussed. A driving case (HCTR70) was tested in the wind tunnel in order to validate the model described in this thesis. The HCTR70 is defined as a hill climb test with a 1600 kg trailer. The test is performed under a constant velocity of 70km/h and finishes when stable conditions are reached. The duration of the hill climb tests is usually

Ambient Temperature C	27
Vehicle Speed (Km/h)	70
Engine Speed (rpm)	2864
Engine Load (Nm)	244

Table 7.7.2 Wind Tunnel Test

<sup>106</sup> Begoña León Moya, “Fluid and Thermodynamic Under-hood Simulations”, Thesis for the Degree of Master of Science, Lund University.

set according to a specific distance; this means that the test is finished when the car has traveled a specific number of kilometers. However, the tunnel test used in this model was carried out until stable conditions were reached, ensuring that constant temperatures were achieved. The characteristic parameters of the tunnel test and the vehicle are shown **Table 7.7.2**.

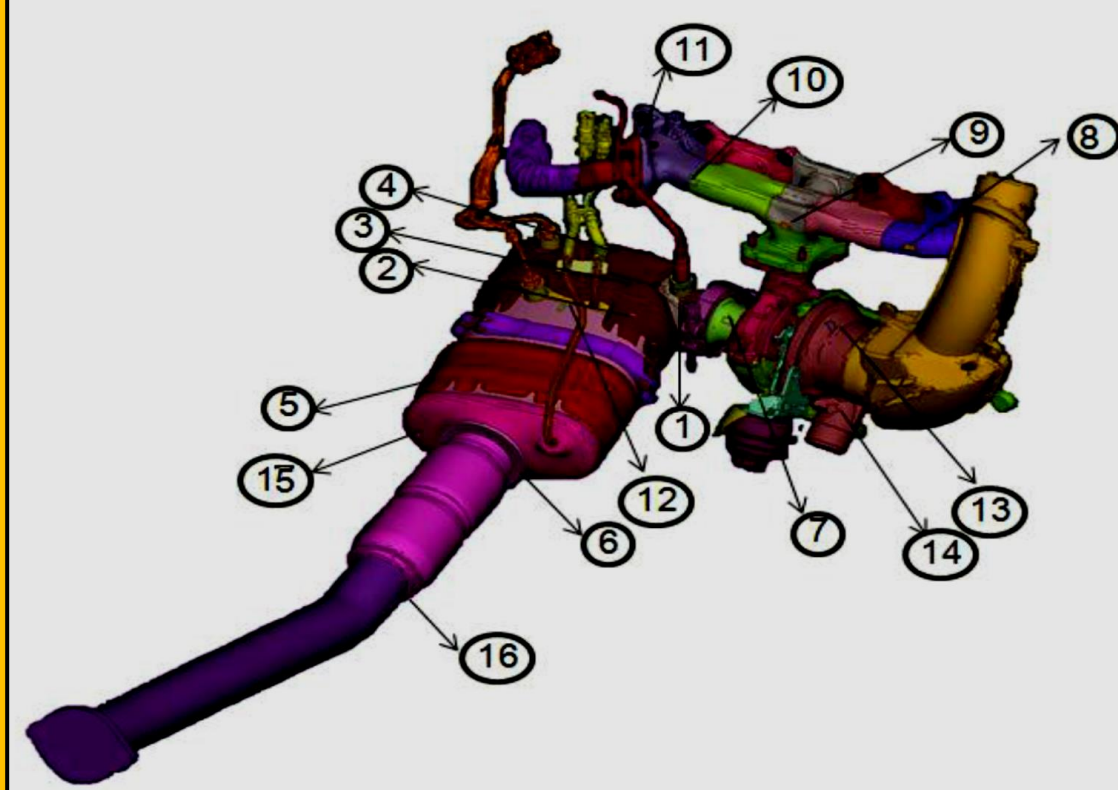


Figure 7.7.8 Instrumentation of the Exhaust System

### 7.7.10 Validation

This section shows and discusses the results obtained by coupling *RadTherm* and *Fluent* until convergence is reached. The model developed is able to predict surface temperature all around the engine. However, this section only focuses on the analysis of the exhaust surface temperature based on the elements labeled. The temperature values from the tunnel test are compared with the simulation results based on the temperature of the mesh elements located in approximately the same positions as the thermocouples. The comparison of both temperature profiles is shown in **Figure 7.7.9**. A  $\pm 5\%$  of error is illustrated showing that only some points present a deviation higher than 5%. Accordingly, the highest deviation corresponds to element number 6 located in the catalytic cone out. Two thermocouples were placed in this part of the catalytic, as shown in **Figure 7.7.9**. The tunnel test shows that the gradient temperature between the thermocouple 6 and 15 is 50C, whereas the model provides a gradient temperature of approximately 180C. This deviation is likely be due to the reduction of the cross-sectional area where the gas flows from the catalytic cone out to the flexible pipe, which presents an area around five times lower than the catalytic converter. As explained in section 4, the gas inside the catalytic cone out is simulated as a fluid node which cannot simulate the flow acceleration because of the sharp change of the cross-sectional area. The figure also shows a high deviation between the model and the tunnel test data in thermocouple 16, located right after the flexible pipe. A possible reason for this deviation is that the geometry of the flexible pipe is not

properly defined in RadTherm. The flexible pipe presents a ringed surface surrounded by a mesh made of stainless steel, although this geometry is not modeled in RadTherm. It is important to note that the temperatures shown in **Figure 7.7.9** correspond to temperatures of mesh elements located close to the thermocouples, inducing some error, especially in areas with large temperature gradients. Both point 16 and point 6 are located on surfaces that present high temperature gradients.

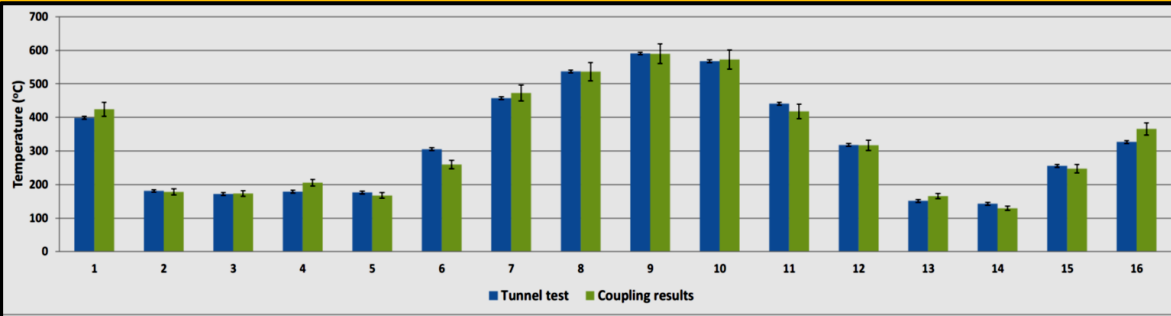
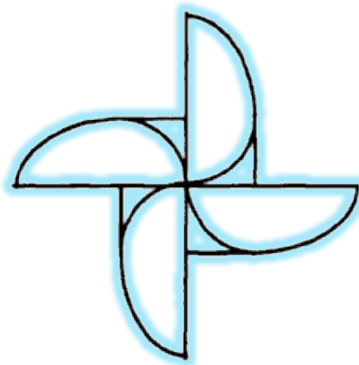


Figure 7.7.9 Comparison between the model results and the tunnel test data



## 8 Heat Exchangers

A heat exchanger is a device built for efficient heat transfer from one medium to another. In order to predict and control food quality during heating process, CFD has been used to simulate and study the flow distribution and temperature distribution of fluid. The trend towards aseptic processing, combine with the aim of minimizing cooked flavors in heat processed products is leading heat exchangers to be constantly redesigned and improved. In this case, CFD can be used to optimize such redesign of heat exchangers. Traditionally, CFD analysis has been applied to simulate the flow of a fluid around obstacles and through hollow areas in order to control temperatures, reduce resistance to flow and/or optimize phenomena such as lift. [Khudheyer and Mahmoud] conducted three-dimensional CFD simulations to investigate heat transfer and fluid flow characteristics of a two-row plain fin-and-tube heat exchanger using Open FOAM, an open-source CFD code. Heat transfer and pressure drop characteristics of the heat exchanger were investigated for Reynolds numbers ranging from 330 to 7000. The most accurate simulations for heat transfer in laminar flow are found using the laminar flow model, while heat transfer in transitional flow is best represented with the SST k-omega turbulence model, and heat transfer in turbulent flow is more accurately simulated with the k-epsilon turbulence model. Reasonable agreement was found between the simulations and experimental data, and the open-source software has been sufficient for simulating the flow fields in tube-fin heat exchangers.

### 8.1 Case Study – Steady Heat Transfer in Fin and Tube Heat Exchanger

Vestas produces compact tube-and-fin heat exchangers for ship motors, as well as other types of heat exchangers and cooling towers (**Figure 8.1.1**). The heat exchanger cools heated, compressed air from the motor with cooling water. Fins are used to increase heat transfer area on the air side, since the air has the largest influence on the overall heat transfer resistance<sup>107</sup>.



Figure 8.1.1 Vestas Air Coil Heat Exchanger

#### 8.1.1 Problem Formulation

[Hansen]<sup>108</sup> investigated the 3D heat transfer and fluid flow characteristics of a two row plain fin-and-tube heat exchanger using OpenFOAM®. Heat transfer and pressure drop characteristics of the heat exchanger are investigated for Reynolds numbers ranging from 330 to 7000. Fluid flow and heat transfer are simulated and results compared using both laminar and turbulent flow models (***k-ε, and Menter SST k-ω***), with steady-state solvers to calculate pressure drop, flow, and temperature fields. Model validation is carried out by comparing the simulated case ***Friction factor f*** and ***Colburn factor j*** to experimental results from the literature. Here, the geometrical parameters for a two-row heat

<sup>107</sup> A., M., Hansen, "CFD simulation of a fin-and-tube heat exchanger", Master of Science Thesis Computational Chemical Engineering, Group for Chemical Fluid Flow Processes Aalborg University Esbjerg, Neils Bohrs Vej 8, DK-6700 Esbjerg, Nov. 2008.

<sup>108</sup> See Previous.

exchanger based on experimental research<sup>109</sup>. The parameters of interest: friction factor  $f$  and Colburn  $j$ -factor are widely used in industry to characterize pressure drop and heat transfer, respectively, and thereby determine heat exchanger performance and suitability for specific duties. Determining and using these parameters for performance prediction is part of the heat exchanger design process.

### 8.1.2 Performance Parameters

The two-row fin-and-tube heat exchanger studied has a staggered tube arrangement, as illustrated in **Figure 8.1.2** [Songs and Nishino, 2008].

Analyzing flow and heat transfer using CFD can make calculations to predict heat exchanger performance. However, it is not possible to perform CFD simulation on the entire heat exchanger, due to the large number of volumes and calculations required. Therefore, a small section of a heat exchanger consisting of one channel of air between two fins, with the air flowing by two tubes is modelled for this project (see Figure 8.1.2 & **Figure 8.1.3**). Simulations of the air flow through this passage are carried out,

while relevant characteristics of the air flow are sampled and averaged at the inflow, minimum free-flow area(s), and outflow. The characteristics sampled are: flow velocity (in all three directions:  $x$ ,  $y$ , and  $z$ ), temperature, pressure, and turbulence model parameters  $\kappa$ ,  $\varepsilon$ , and  $\omega$ . These measurements are then used for calculating relevant performance parameters such as **Pressure**

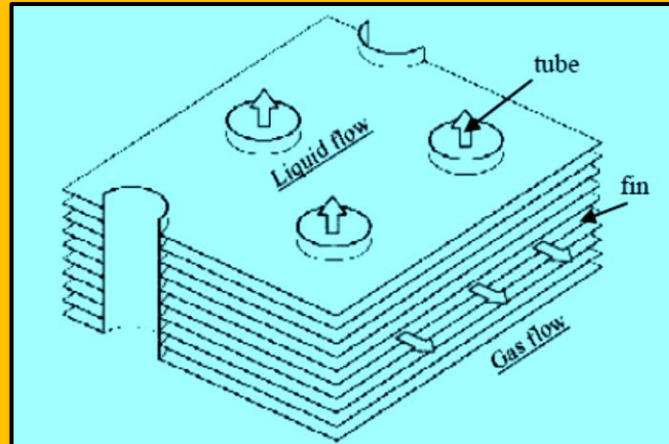


Figure 8.1.2 Typical Fin and Tube Heat Exchanger section with staggered tube arrangement

Geometric Parameter	Symbol	Dimension
Fin Thickness	$t$	0.13 mm
Fin Pitch	$P_f$	2.240mm
Fin collar outside diameter	$D_c$	10.23mm
Transverse pitch	$P_t$	24.40mm
Longitudinal Pitch	$P_l$	21.00mm
Tube wall thickness	$\delta$	0.336mm
Number of Tube row		2

Table 8.1.1 Geometric Parameter of Heat Exchanger

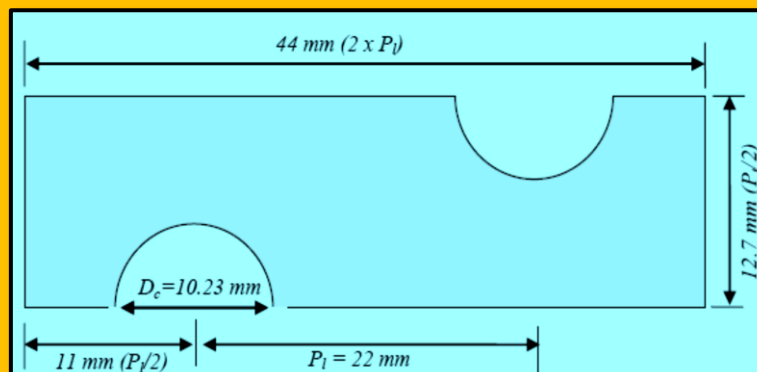


Figure 8.1.3 Computational Domain and Geometric Parameters

<sup>109</sup> Wang, Chi-Chuan; Chang, Yu-Juei; Hsieh, Yi-Chung; Lin, Yur-Tsai. "Sensible heat and friction characteristics of plate fin-and-tube heat exchangers having plane fins", International Journal of Refrigeration, Vol. 19, No. 4 (1996) pp. 223-230.

*Drop, Friction and Colburn factors, Heat Transfer rate, Reynold's Number, etc.).*

### 8.1.2.1 Reynolds Number

The Reynold's number represents the ratio of flow inertial forces to viscous forces. The Reynold's number characteristic dimension for this study is the tube collar diameter  $D_c$  where  $V$  is the minimum free-flow air velocity (in the minimum flow cross-section of the tube row), and is calculated:

$$Re = \frac{\rho V D_c}{\mu} \quad \text{where } V = V \cdot \left[ \frac{P_t \cdot F_p}{P_t \cdot F_p - D_c \cdot F_p - t(P_t - D_c)} \right] \quad \text{Eq. 8.1.1}$$

### 8.1.2.2 Fanning friction factor-f

The Fanning friction factor is the ratio of wall shear stress to the flow kinetic energy. It is related to pressure drop in tube-and-fin heat exchangers as:

$$f = \frac{A_c}{A_o} \frac{\rho_m}{\rho_{in}} \left[ \frac{2\rho_{in} \Delta p}{G^2} - (K_c + 1 - \sigma^2) - 2 \left( \frac{\rho_{in}}{\rho_{out}} - 1 \right) + (1 - \sigma^2 - K_c) \frac{\rho_{in}}{\rho_{out}} \right]$$

**Eq. 8.1.2**

### 8.1.2.3 Colburn j-factor

The Colburn j-factor is the ratio of convection heat transfer (per unit duct surface area) to the mount virtually transferable (per unit of cross-sectional flow area):

$$j = \frac{Nu}{Re_{D_c} \cdot Pr^{1/3}} \quad \text{where } Nu = \frac{h}{k/D_h} \quad \text{and } D_h = \frac{4(F_p - t)(P_t - D_c)P_l}{2 \left( P_l P_t - \frac{\pi D_c^2}{4} \right) + \pi D_c (F_p - t)} \quad \text{Eq. 8.1.3}$$

The Nusselt number is based on the hydraulic diameter  $D_h$ . There are different calculations for this available in the literature<sup>110</sup>. The hydraulic diameter in this study is the ratio of the 4 times the minimum free flow air-side area to the wetted perimeter (ratio of air-side surface area to heat exchanger length).

### 8.1.2.4 Pressure Drop

The pressure drop determines the amount of pumping power needed to run a heat exchanger. It is therefore important to characterize the pressure drop for design. This section describes how the pressure drop relates to the pumping power, followed by a description of what causes the pressure drop and finally the pressure drop equations for tube-and-fin heat exchangers are presented. Pumping power  $P$  is often seen as an important design constraint because the pressure drop in a heat exchanger (along with associated pressure drops in the inlet/outlet headers, nozzles, ducts, etc.) is proportional to the amount of fluid pumping power needed for the heat exchanger to function, as given by the following expression

$$P = \frac{\dot{m} \Delta P}{\rho}$$

**Eq. 8.1.4**

The overall pressure drop consists of two parts:

---

<sup>110</sup> Fornasieri, E., Mattarolo, L. "Air-side heat transfer and pressure loss in finned tube heat exchangers: state of art", Proceedings of the European Conference on Finned Tube Heat Exchangers, Lyon, France, (April 1991).

- Pressure drop in the heat exchanger core, and
- Pressure drop from associated devices the fluid flows through before and after the heat exchanger core (i.e. inlet/outlet manifolds, nozzles, valves, fittings, ducts, etc.).

The core pressure drop is due to the following:

- Friction from the fluid flowing across the heat transfer surface (i.e. skin friction, form drag, internal contractions and expansions).
- Momentum effect (fluid density changes causing a pressure drop).
- Sudden contraction or expansion at inlet and/or outlet.
- Gravity effects (if there is a change in elevation between the inlet and outlet of the exchanger – normally negligible with gases) causing a pressure drop (static head) from the change in elevation. This pressure drop is given by the following expression:  $\Delta p = \pm (\rho mgL/g_c)$ , with the “+” used in the case of vertical up-flow, while the “-” is used for vertical down-flow.

The actual calculation for pressure drop depends on the specific type of heat exchanger being studied. For fin-and-tube heat exchangers, the pressure drop equation is given by<sup>111</sup>:

$$\frac{\Delta p}{P_{in}} = \frac{G^2}{2g_c} \cdot \frac{v_1}{P_{in}} \left\{ \left[ (K_c + 1 - \sigma^2) + 2 \left( \frac{v_2}{v_1} - 1 \right) \right] + f \frac{A}{A_c} \frac{v_m}{v_1} - (1 - \sigma^2 - K_e) \frac{v_2}{v_1} \right\} \quad \text{Eq. 8.1.5}$$

However, the entrance and exit loss effects  $K_c$  and  $K_e$  become zero when flow is normal to the tube banks or through wire matrix surfaces, resulting in the following equation:

$$\frac{\Delta P}{P_{in}} = \frac{G^2}{2g_c} \cdot \frac{v_1}{P_{in}} \left[ (1 + \sigma^2) \left( \frac{v_2}{v_1} - 1 \right) + f \frac{A}{A_c} \frac{v_m}{v_1} \right] \quad \text{Eq. 8.1.6}$$

Where  $G = u * \rho$ .  $G$  is the mass velocity entering the core based on minimum free-flow area.  $g_c = A$  gravitational constant (equals 1 when working with SI units).

$v_1$  - Specific volume ( $1/\rho$ ) at inlet temperature.

$v_2$  - Specific volume ( $1/\rho$ ) at outlet temperature.

$v_m$  - Average Specific volume ( $v_1 + v_2 / 2$ ).

$\sigma$  - Sigma represents the ratio of minimum free-flow area to frontal area.

$A_c$  - Flow cross-sectional area.

Here, we used [Error! Reference source not found.](#) to calculate the friction factor for the CFD simulations, since the pressure measurements are taken at the inflow and outflow of the computational domain, and the entrance and exit loss effects would occur prior to and after the inflow and outflow, respectively.

### 8.1.3 Classification of Heat Exchangers

Heat exchangers can be classified according to **construction type**, **flow arrangement**, or **surface compactness**, among other types possible. If the classification is by construction, the types of heat

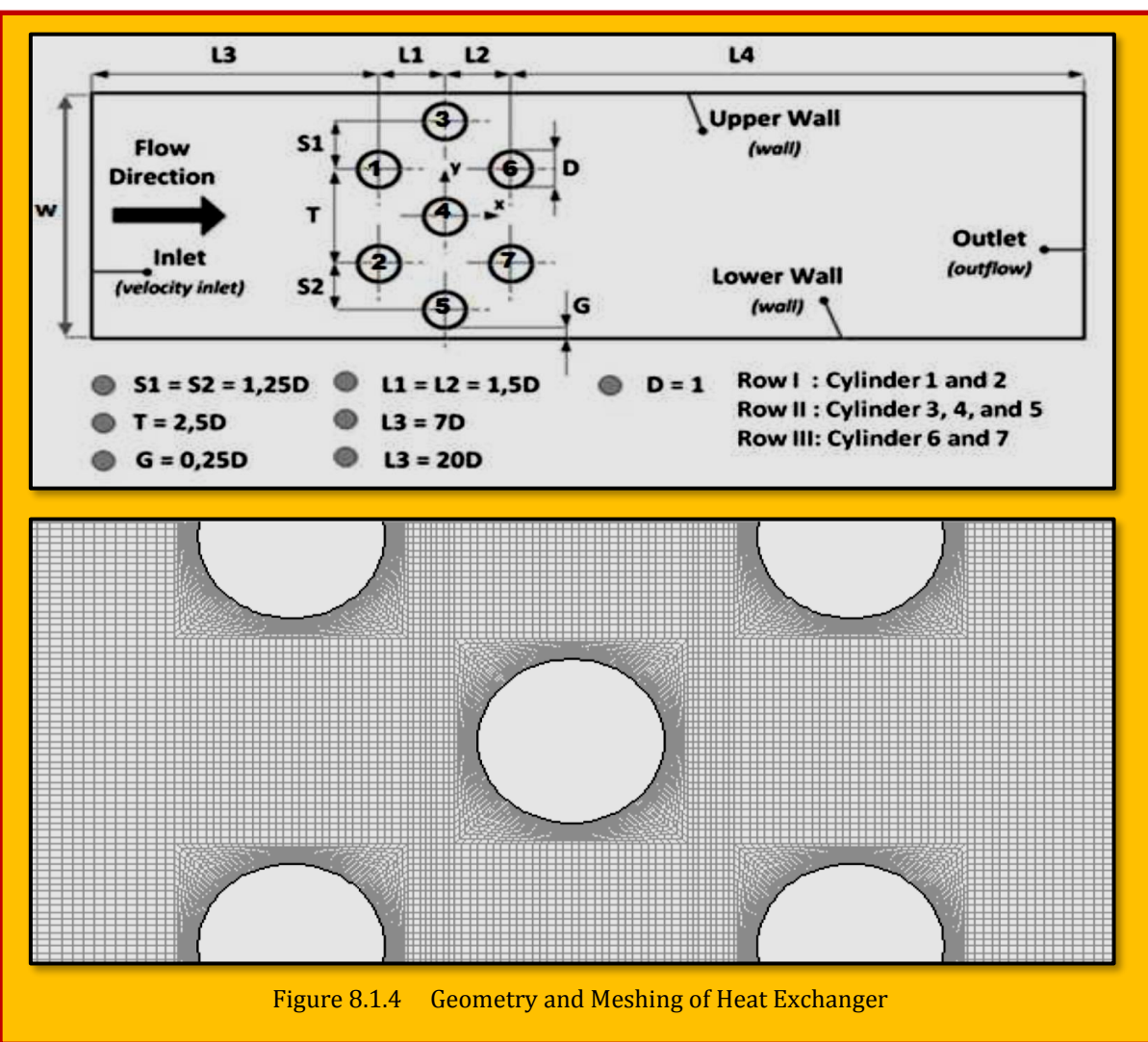
---

<sup>111</sup> Wang, Chi-Chuan; Chang, Yu-Juei; Hsieh, Yi-Chung; Lin, Yur-Tsai. "Sensible heat and friction characteristics of plate fin-and-tube heat exchangers having plane fins", *International Journal of Refrigeration*, 1996.

exchangers are: plate, tubular, extended surface, or regenerative. If classification is by flow arrangement, the types can include single-pass or multi-pass of counter-flow, parallel-flow, cross-flow, or combinations of flow.

### 8.1.3.1 Fin & Tube Heat Exchangers

The fin-and-tube heat exchanger studied is classified as extended surface, single-pass with cross-flow (simplifying the header design at the entrance and exit). This type of heat exchanger is widely used in various thermal engineering applications, including chemical plants, food industries, HVAC, automotive, aircraft, and more. They consist of a block of parallel continuous fins with round tubes mechanically or hydraulically expanded into the fins, a popular heat exchanger designed for fluid to flow in the tubes and gas between the fins. The advantages to using more compact heat exchangers such as the fin-and-tube are many. The extended surfaces (fins) are designed to increase the heat transfer area per unit volume, resulting in compact units of reduced space and weight (up to 10 times greater surface area per unit volume when compared to shell-and-tube exchangers), with higher heat transfer coefficients than other less compact heat exchanger types. There is also flexibility when designing the surface area distribution between the hot and cold sides. Substantial cost savings are expected. For sensitive materials, tighter temperature control is an advantage, improving product quality. Multiple fluid streams can be accommodated. There are also limitations to using fin-and-tube



heat exchangers. Normally one side must be a gas or liquid with a low coefficient of convection,  $h$ . They are difficult to mechanically clean, requiring non-corrosive clean fluids. Temperature and pressure limits are lower than some other types due to brazing or mechanical expansion when joining the fins to the tubes (though pressure can be high on the tube side). **Figure 8.1.4** shows geometry and meshing for fin/tube heat exchangers.

### 8.1.3.2 Oval Tube

A certain reserve for increasing efficiency of transversely finned tubes resides in converting to a noncircular shape of the cross section of the fin-carrying tube. Under definite conditions, specifically, with stringent limitations on the aerodynamic drag of a heat exchanger, it is reasonable to use shaped (generally plane-oval or elliptical) tubes in lieu of circular carrying tubes<sup>112</sup>. Geometric characteristics of such tube bundles include additional parameters among which are the relation of longitudinal and lateral dimensions of the cylinder cross section and the attack angle of the profile with respect to the direction of the incident flow (see **Figure 8.1.5**). As works on heat transfer and aerodynamics of smooth and finned shaped cylinders demonstrated, the search for optimal values of these parameters can be tied with the prospects for improving the developed surfaces. **Figure 8.1.6** shows effects of different  $d_2/d_1$  tube on transverse flow.

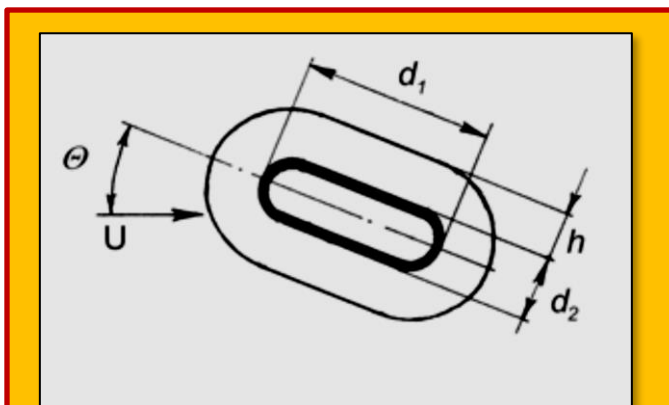


Figure 8.1.5 Geometric Characteristics of a Plane-Oval Finned Tube

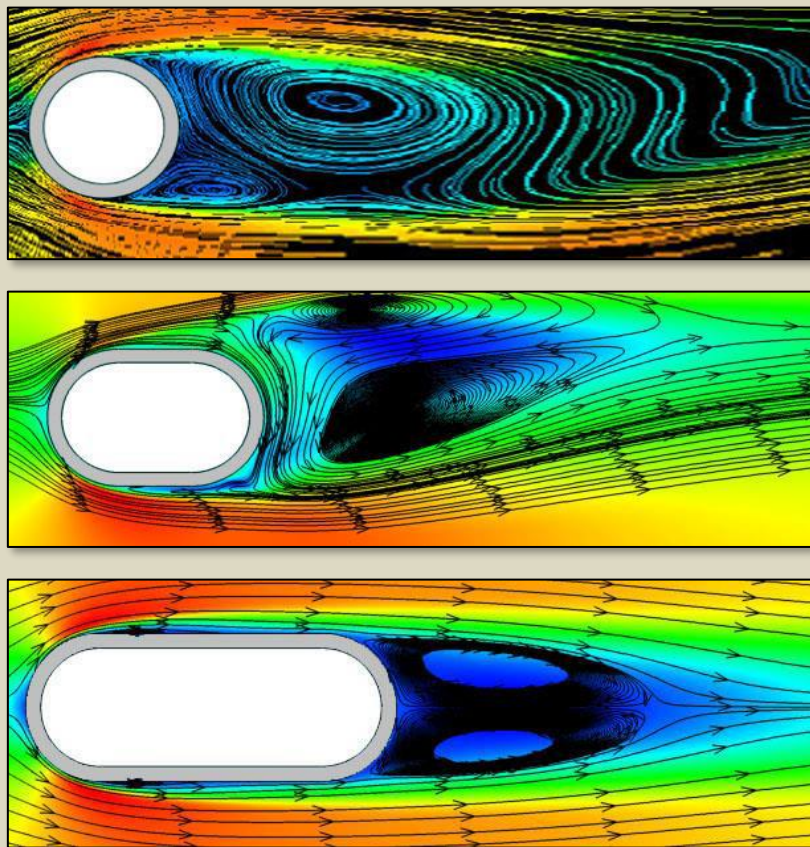


Figure 8.1.6 Effects of Different  $d_2/d_1$  Tube Ratio on Transverse Flow

<sup>112</sup> Pis'mennyi, E.N., Terekh, A.M. and Razumovskiy, V.G., "Enhancement of Heat Transfer in the Bundles of Transversely-Finned Tubes", National Technical University of Ukraine "Kyiv Polytechnic Institute" Ukraine.

### 8.1.4 Governing Equations and Numerical Schemes

The governing equations for this project are the three-dimensional continuity, Naiver-Stokes for momentum, energy, and scalar transport equations for steady-state flow can be written as follows:

Continuity	$\frac{\partial(\rho u_i)}{\partial x_i} = 0$	Eq. 8.1.7
Momentum	$\frac{\partial}{\partial x_i}(\rho u_i u_j) = \frac{\partial}{\partial x_i} \left( \mu \frac{\partial u_j}{\partial x_i} \right) - \frac{\partial p}{\partial x_j}$	
Energy	$\frac{\partial}{\partial x_i}(\rho u_i T) = \frac{\partial}{\partial x_i} \left( \frac{\kappa}{C_p} \frac{\partial u_j}{\partial x_i} \right)$	
Transport (for Scalars)	$\frac{\partial(\rho u_i \varphi)}{\partial x_i} = \frac{\partial}{\partial x_i} \left( \Gamma_\varphi \frac{\partial \varphi}{\partial x_i} \right) + S_\varphi$	

The first three equations are used in the CFD computations to calculate the flow field for both thermal and fluid (air) dynamics, solving for heat transfer and pressure drop. They are discretized and solved by the finite volume method using OpenFOAM, an open-source CFD code. It is solved on a staggered grid using solvers for laminar and turbulent flow, with the latter solution solved using the Reynolds Averaged Navier-Stokes equations (RANS) with both  $\kappa-\varepsilon$  and SST  $\kappa-\omega$  turbulence models. To ensure coupling between velocity and pressure, the SIMPLE algorithm is used.

### 8.1.5 Boundary Conditions

The computational domain has contains boundary conditions as shown in **Figure 8.1.7** with the following conditions:

- Tube surfaces: Dirichlet BC:  $T = T_w$ , Air velocity:  $u = v = w = 0$ .
- Fins - Dirichlet BC:  $T = T_{fw}$  Air velocity:  $u = v = w = 0$
- Inlet - Dirichlet BC: Uniform velocity  $u = u_{in}$ ,  $v = w = 0$   $T = 5^\circ C$ .
- Outlet - Neumann BC: Zero gradients,  $u$ ,  $v$ ,  $w$ , pressure, and temperature. (One-way),

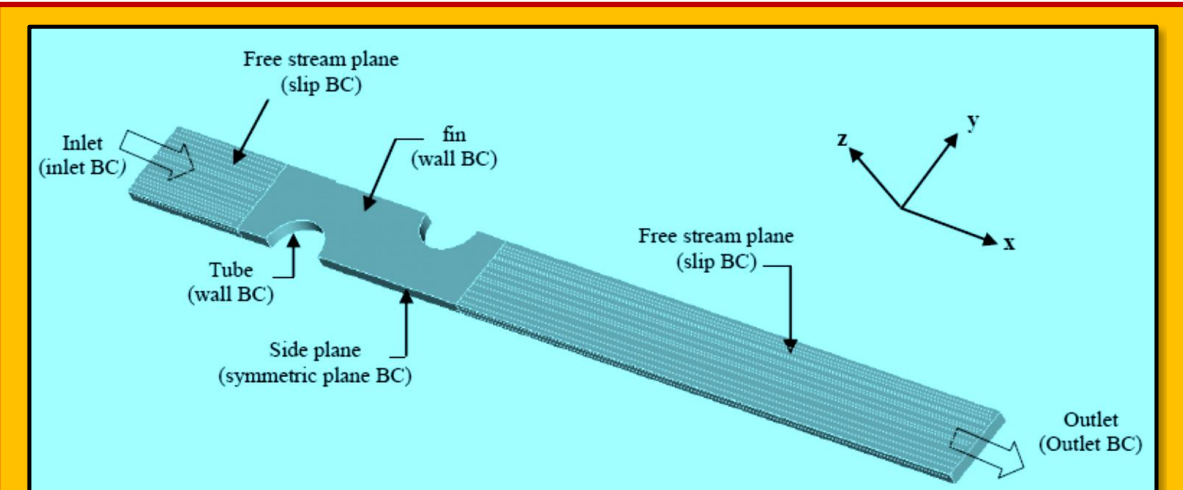


Figure 8.1.7 Boundary Conditions

- Free stream planes: (top and bottom planes of the extended surface areas): slip conditions:  $(\partial u / \partial z) = 0, (\partial v / \partial z) = 0, w = 0, (\partial T / \partial z) = 0$ .
- Side Planes: symmetry planes  $(\partial u / \partial y) = 0, v = 0, (\partial w / \partial y) = 0, (\partial T / \partial y) = 0$

The entire computational domain was made up of 50,375 finite volumes, with a structured grid throughout most of the domain, while the areas around the tubes are more unstructured. The cell number was chosen based on the results of a grid independence test (next).

### 8.1.6 Grid Independence Study

In all, there were 11 different grid systems investigated to determine how fine the grid must be and to validate the solution independency of the grid. The tetrahedral meshes contained the following number of fluid elements (approximately): 8,000, 25,000, 50,000, 75,000, 100,000, and 150,000, while the hexagonal meshes contained approximately 3,000, 30,000, 50,000, 67,000, and 117,000 cells. The pressure drop between inlet and outlet was found for each simulation, and the results compared to determine when the grid is considered independent (see **Figure 8.1.8**).

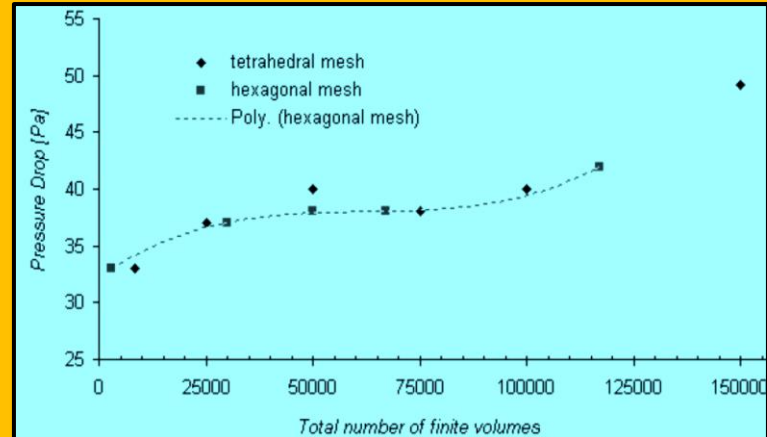


Figure 8.1.8 Grid Independence Study

### 8.1.7 Flow Characteristic

#### 8.1.7.1 Velocity Observations

In both cases, as the air flows around the first tube, it begins to speed up and then the air velocity increases again as it goes around the second tube. This is verified by the samples taken in the case files for average velocities at the minimum free-flow areas, which showed that the velocity going around the second tube is faster than that going around the first tube. The minimum free-flow area is the area of the heat exchanger between two transverse tubes, so the area just above tube one or just below the second tube are the minimum free-flow areas. The flow is forced to speed up, as the tubes act as a type of pipe contraction in the air flow channel. The highest velocity areas are just off the streamlines flowing directly around the tubes, and located at the area of minimum free-flow. It is observed that the size of the tubes impact the Reynolds number of the air flowing around them, since with larger tubes (at the same distance from each other), there would be an even smaller minimum free-flow area if the transverse pitch remained the same. In this study, the characteristic length for the Reynolds number is the tube collar diameter, and it can be seen here, that increases in this parameter (while keeping transverse pitch the same) can induce higher velocities and with it a higher turbulence and Reynolds number. In the case of higher air flow, the recirculation zones behind each tube contain small backflow areas, while the second recirculation zone appears larger.

#### 8.1.7.2 Kinetic Energy k distribution

The kinetic energy contour plots can be seen to verify previous observations made regarding flow. **Figure 8.1.9** illustrates the kinetic energy  $k$  distribution for the low Reynolds number case where using a SST  $\kappa-\omega$  model for inlet velocity 0.3 (top) and 6.2 (bottom). There is no kinetic energy increase in the areas behind the tubes for this case. The kinetic energy increases (slightly) in a different area

corresponding to the increase in velocity as the air flows around the second tube. In related matter, the lower Reynolds number, which is exhibiting higher kinetic energy is in the area of higher temperatures, however, this illustrates that even at very low flow rates, and some turbulent kinetic energy could still be present. For kinetic energy in the higher-Reynolds number case, an increase in kinetic energy is found clearly after the first tube, in the same area as the recirculation zones observed in the higher Reynolds values. According to this plot, then, the second recirculation zone is not as turbulent as the first recirculation zone. This makes sense because the direction of flow has changed as the air moves between the two tubes, and is directed more *downward* at an angle. The flow rounds the tube at an angle making less of an impact with the tube and *missing* the recirculation zone.

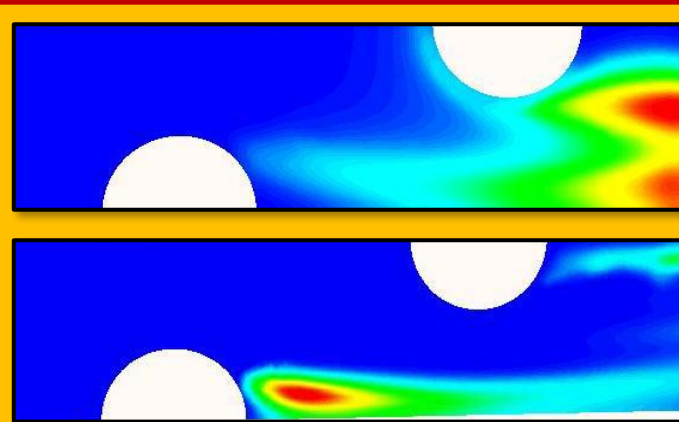


Figure 8.1.9 Contours of Turbulent Kinetic Energy  $\kappa$  Using SST  $\kappa-\omega$  Model in Different Inlet Velocities

### 8.1.8 Characteristics of Heat Transfer

The contours illustrating the local temperature distributions for the same cases as in the previous section are illustrated in **Figure 8.1.10**. Where the collaboration between flow direction and temperature streamlines is made (Flow velocity streamlines shown in top picture, and isothermal pattern shown in the lower picture). The first most noticeable difference between the two Reynolds number heat transfer characteristics is that once steady-state is reached, the slower-moving air (0.3 m/s) is heated up much more in the first two rows than in the case of higher Reynolds number flows. This must be due to the fact that the air flows so slowly, that there is much more time to absorb the heat (longer "residence time"). Had the initial inlet conditions been made cyclical, then comparisons could be made deeper into the heat exchanger (for example after 10 or 12 rows) and see how the heat transfer compares.

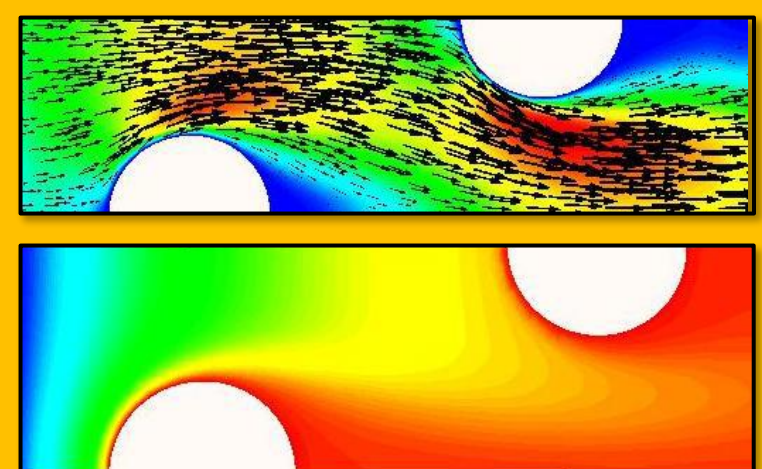


Figure 8.1.10 Collaboration Between Flow Direction and Temperature Streamlines

Although streamlines are not physically drawn onto temperature profile, they can be seen fairly clearly with the color contrast lines. It is seen that the temperature streamlines run practically perpendicular to the velocity streamlines in the beginning of the airflow channel, with the isothermal stream lines running vertical and the velocity of the flow horizontal. This acts as a cross-flow heat exchange, with the flow directly bringing the heat with it. It can then be seen that after the air has flowed through the initial section of the heat exchanger, this "synergy" between flow and heat

transfer is no longer as effective. This means that the heat transfer coefficient is changing according to the streamline the flow is in at the time. It can be seen that the higher Reynolds number flow has not only a lower temperature change than the previous example, but also a different pattern (different kinds of isothermal stream lines). The largest temperature changes for this case are occurring in the recirculation and “slow velocity” zones (shown previously in the vector and velocity contour plot) just after each of the tubes. As in the slow-moving flow in the case with 0.3 m/s velocity, the slow-moving areas of the heat exchanger are also better able to absorb heat. The staggered tube arrangement is designed to have these slower-moving and recirculation areas to keep the heat flowing to the air, but at the same time, not allowing recirculation zones to “stagnate” as can occur in inline arrangements where these zones do not keep flowing [Jang et al., 1995].

### 8.1.9 Choice of different Turbulence Modelling as available in OpenFOAM®

It was decided that it is good exercise to go through some different Turbulence models commonly available and decide which one is best suited for project in hand. The first parameter considered is the Reynolds numbers, then the compressibility factor. The Reynolds number studied for the heat exchanger flow in this project range from approximately 330 to 7000, which means that the flows can be laminar, transitional, or turbulent. Because these flow regimes behave differently, it can be necessary to model the flow in different ways. In this project, two turbulence models ( **$\kappa-\varepsilon$  and Menter SST  $\kappa-\omega$** ) are utilized in order to investigate which is best to use for the different types of flow. A laminar flow model is also used for comparison with the turbulence models. Several variations of the  $\kappa-\varepsilon$  model have been made, as well as low-Reynolds numbers modifications of it. The high Reynold's number models listed use log-law type wall functions (i.e. *Menter SST  $\kappa-\omega$* ). The low Reynolds number models calculate flow to the wall, and with these models, it is important for the  $y^+$  value to be approximately 1, whereas with high-Reynolds models,  $y^+$  should range from approximately 30-60 to 300-400 in the log layer. In this project, the  $\kappa-\varepsilon$  and Menter  $\kappa-\omega$  SST models, both of which utilize RANS equations, are used as turbulence models. To achieve that, the relevance of particular type of flow involved, complexity of the physics and time, whether the model is for compressible or incompressible flow, and how well-known is the model (for accuracy), all considered. Keeping these thoughts in mind, the 8 turbulence models available for compressible flow (compressible flow modelling is necessary, since air is flowing through the heat exchanger) in OpenFOAM® were considered:

- Spallart-Allmaras,
- Standard  $\kappa-\varepsilon$ ,
- RNG  $\kappa-\varepsilon$ ,
- Menter SST  $\kappa-\omega$ ,
- Realizable  $\kappa-\varepsilon$ ,
- LRR  $R-\varepsilon$ ,
- Launder-Gibson  $R-\varepsilon$ , and
- Launder-Sharma  $\kappa-\varepsilon$ .

### 8.1.10 Turbulence Modeling

After careful consideration, it was decided on using the  **$\kappa-\varepsilon$**  as well as **Menter SST  $\kappa-\omega$**  turbulence models. These include two equations for expressing turbulence in these models:

- For the turbulent kinetic energy  $\kappa$  (to express the turbulence velocity),
- For the rate of dissipation of the turbulent kinetic energy  $e$  (to express the turbulence length scale) in the  $k-\varepsilon$  model or of the specific dissipation rate  $\omega$  in the  $\kappa-\omega$  model.

The  $k-\varepsilon$  model is the simplest and most widely validated turbulence model, with only initial or boundary conditions required to be supplied, and has had good performance in the past with certain types of flows, although performance has not been the best for flows with curved boundary layers,

swirling or anisotropic flows. The *Menter SST k- $\omega$*  model improves the  $k-\varepsilon$  model at the near-wall by using a  $k-\omega$  model at the near-wall region while retaining the  $k-\varepsilon$  model for the free-stream turbulent region far away from the wall. It is also well-known and used in industry. For this project, these two models: results from using the  $k-\varepsilon$  and  $k-\omega$  models are compared, along with the laminar model. For future work with this type of flow, the *realizable k- $\varepsilon$*  and *RSM* models would be of interest to test in order to study the effect of anisotropic Reynold's stresses on the flow and simulation results.

### 8.1.11 Comparison of Friction Factor

For these simulations, only the friction factor was calculated and compared with experimental data. However, it was found that the patterns in the graph were somewhat similar for the experimental and simulated values, and that the flow models followed the same pattern, with a gradually decreasing friction factor as Reynolds number increases. Also, the different flow models achieved nearly the same results. The simulations with temperature included in the calculations were then run to see how the simulations actually compared with the experiments. It can be seen that in all cases the friction factor was decreasing with increasing Reynolds number. All of the models underestimated the friction factor, including the transient case. At the lower laminar flows (the first four points at the lower Reynolds number), of Reynolds number from 330 to 1300, all the models found nearly identical results. As the flow moved into transition, it appears the laminar flow model came much closer to the experimental values. At the transition point from transition to turbulent, which appears to have a critical Reynold's value of between 1700 and 2900 (the exact value is not known, since there weren't enough data points given to be sure), once again, none of the models were better than another. After moving into turbulent flow, however, the  $k-\omega$  SST had the best accuracy, and the laminar flow model able to model the friction factor compared to the  $k-\varepsilon$  model. The results fit reasonably with what how the different models calculate the flow. Both the  $k-\omega$  and  $k-\varepsilon$  are two-equation models created for calculate turbulence, turbulent kinetic energy, etc., and therefore in laminar flow the additional turbulence terms do not increase the accuracy since there is no turbulence to model in laminar flow anyway. The  $k-\varepsilon$  model was the least accurate flow model of them all, and this is probably due to that the equations only model kinetic energy and dissipation and are accurate for free-flowing fluids, and therefore the friction factor against the wall is not capable of being accurately calculated.

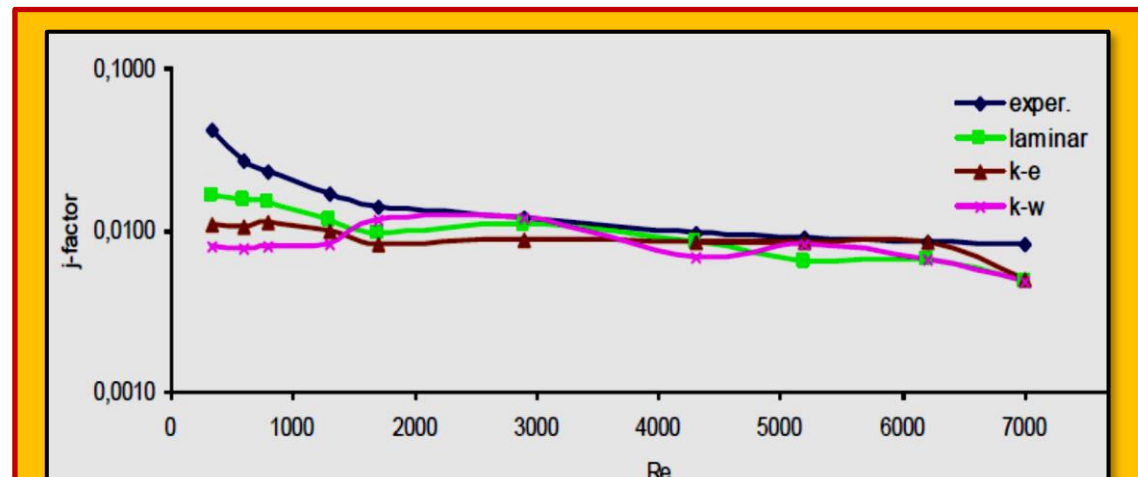


Figure 8.1.11 Colburn  $j$ -factor against Reynolds number for different Inlet Airflow Velocities and Flow Models

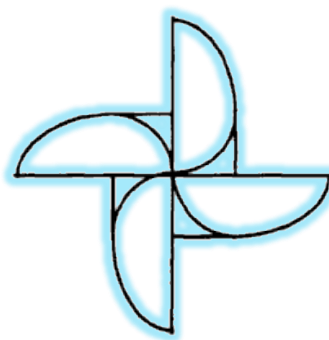
### 8.1.12 Comparison of Colburn $j$ -Factor

The heat transfer characterization parameter Colburn  $j$ -factor has been calculated from the

simulation results for the different flow models. The flow models showed very clear differences in abilities to simulate heat transfer at the different Reynolds numbers. The laminar flow model was the best for predicting the  $j$ -factor, as would be expected. The transition heat flow was best characterized with the  $\kappa-\omega$  turbulence model, while turbulent heat flow was best calculated using the  $\kappa-\varepsilon$  model. Although at the very highest Reynolds number, 7000, none of the models were accurate. **Figure 8.1.11** displays Colburn  $j$ -factor against Reynolds number for different inlet airflow velocities and flow models (laminar, and turbulence models  $k-\varepsilon$  and  $k-\omega$ ).

### 8.1.13 Conclusion

The aim of this study was to make CFD simulations to validate the results against experimental data. The system to study was a fin-and-tube heat exchanger. The purpose of the work was to investigate the possibilities of eventually using CFD calculations for design of heat exchangers instead of expensive experimental testing and prototype production. Ten different inlet flow velocities ranging from 0.3 m/s to 6.2 m/s and corresponding to Reynolds numbers ranging from 330 to 7000 were simulated in the three different flow models (laminar,  $\kappa-\varepsilon$ , and SST  $\kappa-\omega$  turbulence models). A sampling dictionary was written into the CFD model to record pressure and temperature measurements at the inlet and outlet of the heat exchanger model. Using the simulation results and some specific non-dimensional numbers, calculations related to heat flow and pressure loss can be carried out to determine the Fanning friction factor and Colburn  $j$ -factor for comparison with the literature values used for the validation. It was found that the flow model accuracy depended on the flow regime and whether the friction factor  $f$  or  $j$ -factor was being determined. From the experimental values given in the literature, the laminar flow region for this particular geometry of heat exchanger switched to transitional at around Reynolds number 1300, and moving to transitional around Reynolds number 2900. For friction factor determination, little difference is found between the flow models simulating laminar flow, while in transitional flow, the laminar flow model produced the most accurate results (for friction factor) and the SST  $\kappa-\omega$  turbulence model was more accurate in turbulent flow regimes. For heat transfer, the laminar flow model calculated the most accurate  $j$ -factor, while for transitional flow the SST  $\kappa-\omega$  turbulence model was more accurate than  $\kappa-\varepsilon$ . The flow model can be chosen based on what is being studied (heat flow or pressure drop) and the flow regime. In conclusion, it is found that the pressure drop and heat transfer characteristics of a fin-and-tube heat exchanger can be determined to within a reasonable accuracy with CFD computations<sup>113</sup>.




---

<sup>113</sup> A., M., Hansen, "CFD simulation of a fin-and-tube heat exchanger", Master of Science Thesis Computational Chemical Engineering, Group for Chemical Fluid Flow Processes Aalborg University Esbjerg, Neils Bohrs Vej 8, DK-6700 Esbjerg, Nov. 2008.

## 9 HVAC in Building and Related Issues

In early age of construction, the most of building related issues such as ventilation analysis, wind loading, wind environment etc. were conducted by the wind tunnel tests, but today all these test can be done effectively with CFD technique. CFD technique can resolve all above mentioned issues in very short time period and it is very economical as well as strong approach than the older one (experimental).<sup>[3]</sup> Recently Computational fluid dynamics is used as a sophisticated airflow modelling method and can be used to predict airflow, heat transfer and contaminant transportation in and around buildings. CFD plays an important role in building design, designing a thermally-conformable, healthy and energy-efficient building. CFD can examine the effectiveness and efficiency of various Heating ventilation and air conditioning (HVAC) systems by easily changing the different types and location of different components of diffuser types and locations, supply air conditions and system control schedules. Furthermore, CFD helps in developing passive heating/cooling/ventilation strategies (e.g. natural ventilation<sup>114)</sup> by modelling and optimizing building site-plans and indoor layouts. Globally building sector shares approximately 40% of total energy consumption<sup>115</sup>. In present era, there is a huge gap in energy consumption and energy production. As building sector share a huge amount of the total consumption, hence it becomes essential to investigate the optimum configuration for building to reduce the building's share of energy. In order to achieve this, CFD can play an important role. Energy simulation and CFD programs are important building design tools which are used for evaluation of building performance, including thermal comfort, indoor air quality mechanical system efficiency and energy consumption<sup>116</sup>. CFD in buildings mainly used for one or more followings purposes:

- Thermal analysis: through walls, roof and floor of buildings
- Ventilation analysis
- Orientation, site and location selection of buildings based on local geographical and environmental conditions.

### 9.1 Thermal Analysis in Buildings

In buildings, heat transfer takes place in its all modes i.e. conduction, convection and radiation. In order to reduce heat losses from buildings, CFD analysis can be done for the optimum configuration of composite walls, roof and floor. The differential form of the general transport equation is as follows:

$$\underbrace{\frac{\partial(\rho\phi)}{\partial t}}_{\text{transient}} + \underbrace{\nabla(\rho\mathbf{u}\phi)}_{\text{Convection}} = \underbrace{\nabla(k\Delta\phi)}_{\text{Diffusion}} + \underbrace{S_\phi}_{\text{Source}}$$

**Eq. 9.1.1**

The numerical solution of above equation can be obtained by finite difference method (FDM), finite volume method (FVM) and finite element method (FEM). In buildings, for heat transfer analysis, the scalar function  $\phi$  in Eq. 9.1.1 is replaced by Temperature (T), diffusion coefficient  $\Gamma$  is replaced by thermal conductivity k and the source term  $S_\phi Q_i$  is replaced by heat generation term S or by any heat radiation source  $Q_i$  or by both (depending upon the nature of source available) and we have different forms of equation for different cases. For simplicity and easy understanding, only 1-

---

<sup>114</sup> Natural ventilation is the use of wind and thermal buoyancy to create air movement in and out of your home without the use of mechanical systems, with the goal of bringing fresh air into your home. During nighttime in the summer months natural ventilation can provide free cooling and reduce your home energy use.

<sup>115</sup> Wikipedia.

<sup>116</sup> Zhai, Zhiqiang John; Chen, Qingyan Yan (2005), "Performance of coupled building energy and CFD simulations", Energy and Buildings, 37 (4): 333,

Dimensional cases have been discussed. In buildings the heat transfer analysis can be done for all parts of buildings (walls, roof and floor) in following two ways

1. Steady State Thermal Analysis
2. Transient Thermal Analysis

## 9.2 Ventilation Analysis

The ventilation study in buildings is done to find the thermally comfortable environment with acceptable indoor air quality by regulating indoor air parameters (air temperature, relative humidity, air speed, and chemical species concentrations in the air). CFD finds an important role in regulating the indoor air parameters to predict the ventilation performance in buildings. The ventilation performance prediction provides the information regarding indoor air parameters in a room or a building even before the construction of buildings. These air parameters are crucial for designing a comfortable indoor as well as outdoor environment. This is because the design of appropriate ventilation systems and the development of control strategies need detailed information regarding the following parameters;

- Airflow
- Contaminant dispersion
- Temperature distribution

The aforesaid information's are also useful for an architect to design the building configuration. From the last three decade, the CFD technique is widely used with considerable success in building. Recently ventilation and its related fields has becomes a great part of wind engineering. A ventilation study can be done using wind tunnel investigation (experimentally) or by CFD modeling (theoretically). Natural ventilation system is always preferred over the forced ventilation system, as it causes to save the burning of fuel, which is economical as well as nature friendly. In present era, due to development of a lot of CFD software and other building's energy simulation software, it becomes quite easy to assess the possibility of natural/forced ventilation system in a building. CFD analysis is quite useful than the experimental approach because here we can find other related relations among the variables in post-processing. The data obtained either experimental or numerically is useful in two ways:

1. better comfort of user.
2. It provides the data which is used as input to the heat balance calculation of the buildings.

### 9.2.1 Numerical Simulations of the Effect of Outdoor Pollutants on Indoor Air Quality of Buildings next to a street canyon

To explore the effect of traffic pollution on indoor air quality of naturally ventilated buildings in the vicinity of a street canyon, the wind flow and pollutant distributions in and around buildings with different Window Opening Percentages (i.e. WOP, the percentage of the total window opening area to the total facade area) were investigated by three-dimensional numerical simulations [Yang et al.]<sup>117</sup>. The numerical results show that the WOP changes the pressure distribution around the downstream building, which is due to the infiltration of air into the street canyon through the opening windows of both the upstream and downstream buildings. When the indoor air of the downstream building is supplied by the outdoor air from the street canyon, the ventilation flux will be increased with increasing WOP. If the indoor air is taken in from the protected side of the downstream building, however, the trend of the ventilation flux is found reverse. The results also indicate that the effective source intensity, which is introduced to quantify the amount of traffic pollutant entering into buildings through unit ventilation area, decreases as the WOP increases. When the WOP reaches

---

<sup>117</sup> Fang Yang, Yanming Kang, Yongwei Gao, Ke Zhong, "Numerical simulations of the effect of outdoor pollutants on indoor air quality of buildings next to a street canyon", Building and Environment, Volume 87, May 2015.

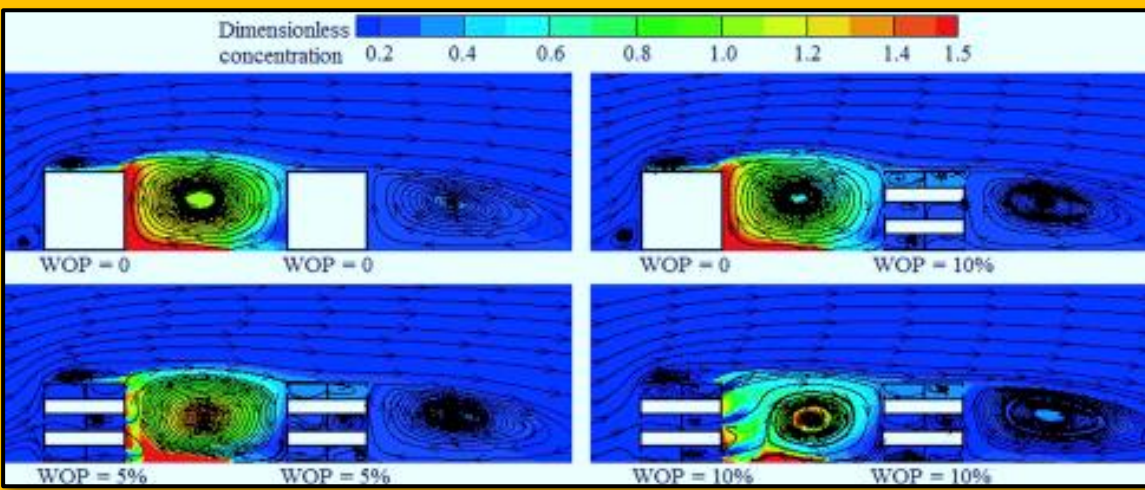


Figure 9.2.3 Impact of Window Opening Percentage (WOP) on indoor air quality

10%, the averaged effective intensity is reduced by 30% compared to the reference case when all windows are closed. It means that if a naturally ventilated room in the downstream building has a fixed ventilated area over different seasons, the room will take in more pollutants from outdoors in winter than in other seasons. **Figure 9.2.3** illustrates the effect of widow opening percentage (WOP) on indoor air quality. Another study using *FlowVent®* shows effect of window loading inventing the outdoor pollutant as shown in **Figure 9.2.1**, while **Figure 9.2.2** displays air pollution effects between buildings separated by a street.

### 9.3 HVAC & Environmental Issues

Heating, Ventilating and Air Conditioning, HVAC, is a huge field. HVAC systems include a range from the simplest hand-stoked stove, used for comfort heating, to the extremely reliable total air-conditioning systems found in submarines and space

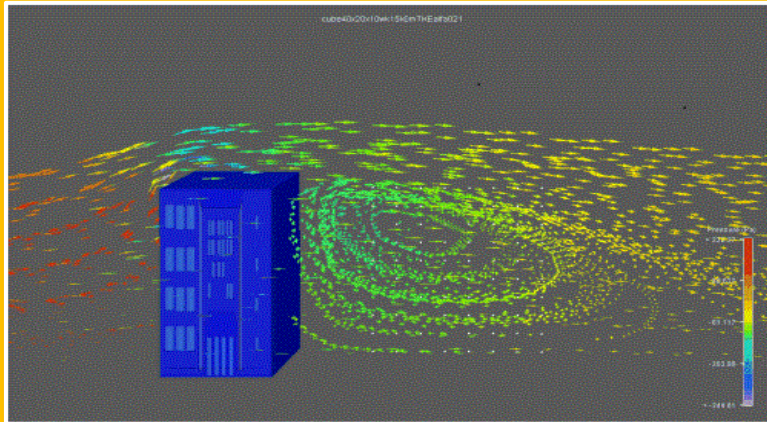


Figure 9.2.1 Effect of window loading in outdoor pollutants

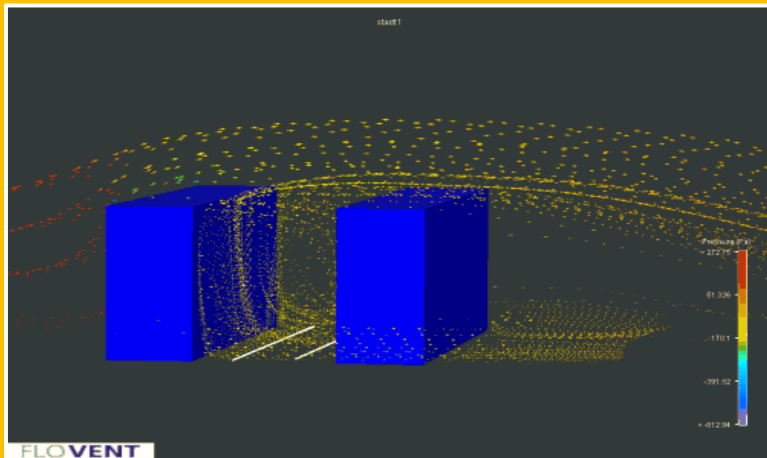


Figure 9.2.2 Pollution between two buildings separated by a street

shuttles<sup>118</sup>. Cooling equipment varies from the small domestic unit to refrigeration machines that are 10,000 times the size, which are used in industrial processes. Depending on the complexity of the requirements, the HVAC designer must consider many more issues than simply keeping temperatures comfortable. This chapter will introduce you to the fundamental concepts that are used by designers to make decisions about system design, operation, and maintenance. The title, "HVAC," thus captures the development of our industry. The term "air conditioning" has gradually changed, from meaning just cooling, to the total control of:

- Temperature
- Moisture in the air (humidity)
- Supply of outside air for ventilation
- Filtration of airborne particles
- Air movement in the occupied space

We will use the term "air conditioning" to include all of these issues and continue to use "HVAC" where only some of the elements of full air conditioning are being controlled. The textbook *Principles of Heating, Ventilating, and Air Conditioning*<sup>119</sup>, starts with a concise and comprehensive history of the HVAC industry. HVAC evolved based on:

- Technological discoveries, such as refrigeration, that were quickly adopted for food storage.
- Economic pressures, such as the reduction in ventilation rates after the 1973 energy crisis.
- Computerization and networking, used for sophisticated control of large complex systems serving numerous buildings.
- Medical discoveries, such as the effects of second hand smoke on people which influenced ventilation methods.

### 9.3.1 Introduction to Air-Conditioning Processes

As mentioned earlier, the term "air conditioning," when properly used, now means the total control of temperature, moisture in the air (humidity), supply of outside air for ventilation, filtration of airborne particles, and air movement in the occupied space. There are seven main processes required to achieve full air conditioning and they are listed and explained below. The processes are:

#### 9.3.1.1 Heating

The process of adding thermal energy (heat) to the conditioned space for the purposes of raising or maintaining the temperature of the space.

#### 9.3.1.2 Cooling

Process of removing thermal energy (heat) from the conditioned space for the purposes of lowering or maintaining the temperature of the space.

#### 9.3.1.3 Humidifying

Procedure of adding water vapor (moisture) to the air in the conditioned space for the purposes of raising or maintaining the moisture content of the air.

#### 9.3.1.4 De-Humidifying

Practice of removing water vapor (moisture) from the air in the conditioned space for the purposes of lowering or maintaining the moisture content of the air.

#### 9.3.1.5 Cleaning

Process of removing particulates, (dust etc.,) and biological contaminants, (insects, pollen etc.,) from

---

<sup>118</sup> Robert McDowell, P. Eng. "Fundamentals of HVAC Systems", Butterworth-Heinemann publications, ISBN-10: 0-12-372497-X, 2006.

<sup>119</sup> Sauer, Harry J. Jr., Ronald H. Howell, William J. Coad. 2001. "Principles of Heating, Ventilating, and Air Conditioning", Atlanta: ASHRAE.

the air delivered to the conditioned space for the purposes of improving or maintaining the air quality.

### 9.3.1.6 Ventilating

The process of exchanging air between the outdoors and the conditioned space for the purposes of diluting the gaseous contaminants in the air and improving or maintaining air quality, composition and freshness. Ventilation can be achieved either through **natural ventilation** or **mechanical ventilation**. Natural ventilation is driven by natural draft, like when you open a window. Mechanical ventilation can be achieved by using fans to draw air in from outside or by fans that exhaust air from the space to outside.

### 9.3.1.7 Air Movement

Process of circulating and mixing air through conditioned spaces in the building for the purposes of achieving the proper ventilation and facilitating the thermal energy transfer.

## 9.3.2 The Role of CFD In HVAC System Optimization

Computational fluid dynamics (CFD), allows engineers to visualize flow velocity, density, thermal impact and chemical concentrations for any region where the flow occurs, enabling engineers to analyze the problem areas and suggest the best solutions. While CFD is used across the construction industry for analysis and design optimization of an HVAC system, some organizations and individuals have been slow to fully utilize it within their practices, citing restrictions such as cost, unreliability, and inaccessibility. CFD is used extensively when designing HVAC systems for non-standard systems, e.g., stadiums, large atriums, concert halls, natural ventilation systems, smoke ventilation etc. and most of these systems could not be accurately designed without using CFD<sup>120</sup>.

### 9.3.2.1 Why Use CFD Analysis in HVAC Design

Engineers designing HVAC systems face the challenge of meeting aggressive sustainability and energy-efficiency targets while delivering comfortable environments at a reasonable cost<sup>121</sup>. Traditional design methods involve the use of hand calculations requiring many simplifying assumptions, which limit the accuracy of calculations. Incorporating CFD simulation into the design process offers a level of reassurance, allowing a complex design to be tested as a computer model before any construction cost is incurred. Design certainty can be established as scenarios can be accurately simulated with the calculated results graphical displayed providing an "easy to relate to" representation. More and more, engineers are moving to CFD to compute airflow patterns and space temperatures based on complete 3D geometries with fewer assumptions, resulting in a greater level of accuracy.

#### 9.3.2.1.1 Performance Prediction

One of the most notable advantages of using CFD in HVAC design, is the ability to simulate fluid flows and analyze HVAC performance without actually installing the HVAC system or even building a prototype. This allows for significant problems, and ultimately solutions, to be identified and devised to enhance a building's overall HVAC performance.

#### 1.1.1.1 Provides Key HVAC Design Parameter Information

Due to key advances in HVAC/IAQ technology, broader and more detailed information about the flow within an occupied zone is required, and the CFD technique satisfies this requirement better than any other method (e.g. experimental or theoretical methods).

#### 1.1.1.2 Using CFD For Validation/Optimization of HVAC Design Parameters

An HVAC system and the finer details such as location and number of diffusers and exhausts, temperature and flow rate of the supplied air etc. can be optimized and validated for an occupant

---

<sup>120</sup> Envenio Blog, 2016.

<sup>121</sup> see previous.

structure and for increased occupant comfort.

#### 1.1.1.3 Modification Of Malfunctioning HVAC Systems

Design modification can be suggested, these modification can further be simulated and any kind of malfunctioning of HVAC system can be mitigated for improved performance and better HVAC within a building. Examples of HVAC CFD Analysis In Practice

- Industrial ventilation design
- Swimming pool ventilation
- General office/room simulations
- Fume hood design
- Effective smoke evacuation in smoking lounges
- Fire simulations for ware houses
- Thermal assessment of data centers and server rooms
- Smoke and fire propagation simulations and implementation of fire safety in occupant structures

CFD is used extensively when designing HVAC systems for non-standard systems, e.g., stadiums, large atriums, concert halls, natural ventilation systems, smoke ventilation etc. and most of these systems could not be accurately designed without using CFD.

#### 9.3.3 Case Study 1 - Aircraft Hangar Fire & Smoke Model

Aircraft hangars, by their very nature, pose a unique challenge for fire safety engineers. Large, open floored areas with high roof decks house aircraft contents worth millions of dollars. In addition to the large amounts of jet fuel, a number of the maintenance activities that take place within hangars provide a host of ignition sources. Large aircraft wings, fuselages and scaffolding also have the potential to restrict fire detection, suppression and the flow of smoke, presenting a potentially lethal cocktail. For fire safety design to be effective, a number of issues must first be considered. These include fire source, heat transfer, fire detection and alarm, human behavior, smoke movement, toxicity and pollution. CFD modelling is proving highly effective in this area to solve fundamental equations about fluid flow and heat transfer, both commonly associated with fire. The result is that predictions can be made as to how smoke and heat will move throughout the hangar. Being able to predict how fire, smoke and heat will spread inside an individual hangar, has life-saving consequences, enabling the most effective fire-safety procedures to be implemented, and risk assessment to be more accurate. Ventilation design depends on several factors such as placement of the diffusers, diffuser geometry or placement of the exit vent. Along with this, fluid flow conditions such as velocity or temperature of inlet flow determine the air flow pattern inside the aircraft.

We performed a case study for HVAC design of an aircraft hangar. The aircraft hangar has twelve inlets, shown in red and three outlet ducts, shown in blue on the roof, see below in

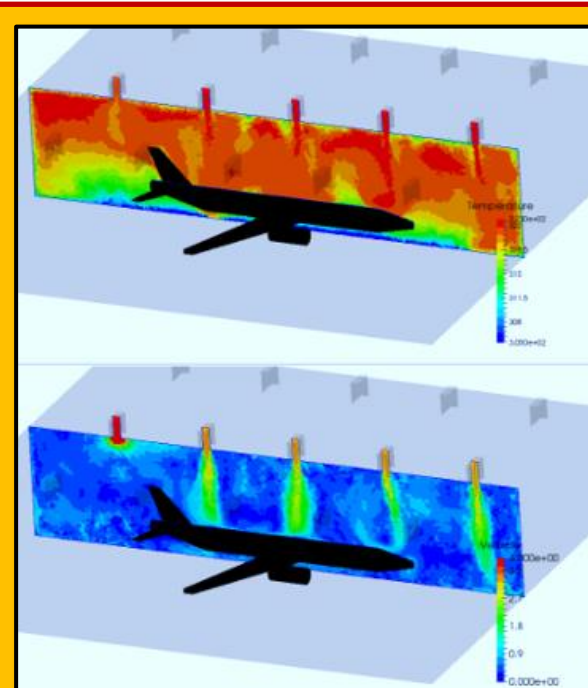


Figure 9.3.1 Study for HVAC Design of an Aircraft Hangar

'reference images'. All other boundaries are no-slip walls. Molded fluid is air, treated as an ideal gas with temperature-dependent variable density. Air enters at 6 m/s with a fixed temperature of 50 C. The aircraft surfaces have a heat transfer coefficient equal to 15 W/m<sup>2</sup>-K and a reference temperature of 30 C. Hangar walls have a heat transfer coefficient of 10 W/m<sup>2</sup>-K and a reference temperature of -3 C. A subdomain located aft of the starboard elevator is the location of a simulated fire, shown as a small square in the figure above. In this subdomain smoke source is active. Smoke is supplied at a rate of 1 kg/sec. These sources create a three-dimensional smoke plume that billows upward under buoyant forces, and advects outward with flow created by the ventilation system.

### 9.3.3.1 Results

**Figure 9.3.1** show the temperature distribution on a vertical slice that transects the aircraft fuselage. Velocity magnitude distributions show speed of air flow on a horizontal slice halfway up the aircraft fuselage and on a vertical slice that transects the fuselage. Scalar (smoke) concentration is shown on a horizontal slice halfway up the aircraft fuselage, and two images show the vertical structure and internal concentration distribution of the smoke plume at the end of the simulation.

### 9.3.4 Case Study 2 - CFD Modeling Approach for HVAC Systems Analysis

An (HVAC) system consisting of a simplified building with one room was modelled and simulated considering both the internal and the external conditions, was investigated by [Mahu, et al.]<sup>122</sup>. The numerical model was designed to concurrently take into account:

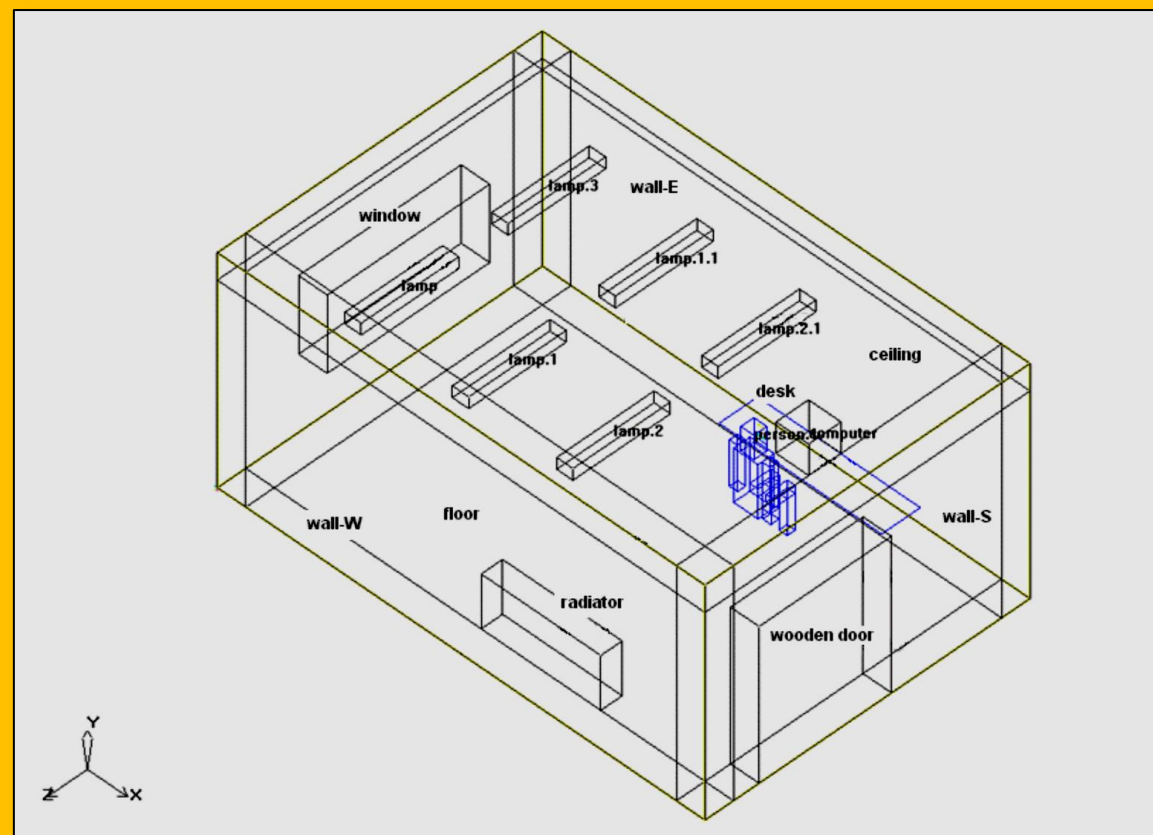


Figure 9.3.2 Building Schematic with Internal Configuration

<sup>122</sup> R. Mahu, F. Popescu and I.V. Ion, "CFD Modeling Approach for HVAC Systems Analysis", Chem. Bull. "POLITEHNICA" Univ. (Timisoara), Volume 57(71), 2, 2012.

- (1) the internal buoyancy-driven convective heat transport,
- (2) the conductive heat flow through the solid walls,
- (3) the external convective cooling induced by the lower temperature wind, and
- (4) the internal and external radiative heat transfer.

In order to avoid making approximations by specifying an average value for the external heat transfer coefficient (HTC), the external boundary of the numerical model was modified to include a significant external volume around the building. Thus, the flow around the building was directly simulated and the external and internal HTCs were computed on-the-fly. The coupled fluid flow thermal transfer simulation was performed to evaluate the internal environment comfort level. (see [Figure 9.3.2](#)).

#### 9.3.4.1 Modeling and Simulation Approach

In order to increase the level of solution accuracy, a coupled fluid flow, thermal transfer solution was preferred. This implies that the numerical model must be able to simulate not only the internal and external heat transfer, but also the internal and external flow, at one time. A combined approach of using *ANSYS Airpak 3.0* for numerical model preparation and final post-processing and *ANSYS Fluent 12.0* for solution calculation and initial post-processing, proved to be optimal. The predefined geometry construction and meshing features of *Airpak* software greatly facilitated the preprocessing step, while the parallel processing capabilities of *Fluent* software offered a very short solution turnaround time. A fully structured, multi-block discretization was created using the semi-automated tools in *Airpak*. The unsteady-state Reynolds-Averaged Navier-Stokes (RANS) model was selected, with RNG k- $\epsilon$  turbulence modeling. No solar heat input was considered. All material data was taken from the available standard *Airpak* material libraries. The RNG  $k$ - $\epsilon$  turbulence model is similar to the

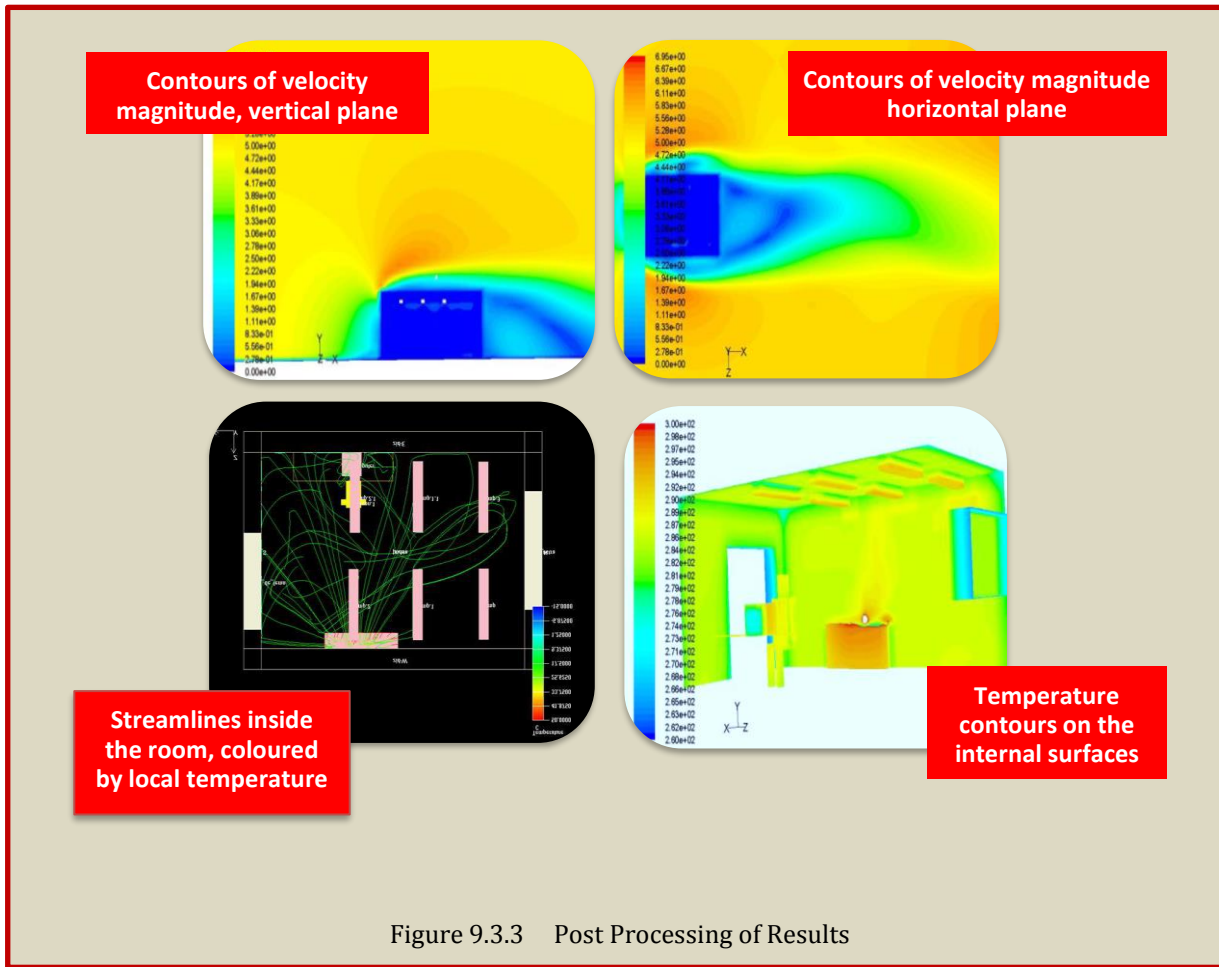


Figure 9.3.3 Post Processing of Results

standard  $k-\varepsilon$  model, but uses an improved derivation based on a statistical technique, called "renormalization group theory". Several terms in the  $k$  and  $\varepsilon$  transport equations have been modified, while the model constants, empirical for the standard  $k-\varepsilon$  model, have been analytically derived.

### 9.3.4.2 Results and Discussion

The results indicate that the flow field is highly non-uniform both on the inside and on the outside of the building. A complex pattern of airflow is present on the inside, mainly driven by the 3000W heat source on the western wall. The contribution of the other heat sources (computer and lamps) is, nevertheless, significant. On the outside, large recirculation regions form on all sides except for the northern face, which is a typical behavior for a bluff body flow, including the unstable, vortex-shedding wake. This suggests a highly variable (space and time) HTC distribution on the external surfaces. Although not verified with the current model, it is most probable that this HTC distribution greatly depends on the wind direction, and a full wind spectrum should be simulated and results recorded in the case of a real building design process.

The wind-chill factor is significantly felt including on the internal surfaces of the building, more visibly on the lower insulating parts, for instance the door and window surfaces, which suggests that the heat loss contribution of these areas is very important and should be carefully taken into consideration during the design stage. The temperature field distribution and values recorded around the human model can be considered acceptable, therefore under the simulated conditions, the thermal regulating inside heat source seems to be adequate. **Figure 9.3.3** demonstrate some of the available post-processing capabilities: data contours on planes or slices with various orientations, external or internal path lines, colored by any given variable, data contours on domain boundaries.

## 9.3.5 Case Study 3 - Investigation of the Natural Ventilation of Wind Catchers with Different Geometries in Arid Region Houses

**Authors :** N. Sakhri<sup>1</sup>, Y. Menni<sup>2</sup>, H. Ameur<sup>3</sup>, A. J. Chamkha<sup>4</sup>, N. Kaid<sup>3</sup>, M. Bensafi<sup>1</sup>, G. Lorenzini<sup>5</sup> and O. D. Makinde<sup>6</sup>

**Affiliations :** <sup>1</sup>Laboratory of Energy in Arid Areas (ENERGARID) University of Bechar, P.O. Box 417, 08000, Bechar, Algeria

<sup>2</sup>Unit of Research on Materials and Renewable Energies, Department of Physics, Faculty of Sciences, Abou Bekr Belkaid University, P.O. Box 119, 13000, Tlemcen, Algeria

<sup>3</sup>Department of Technology, University Centre of Naama - Salhi Ahmed, Algeria

<sup>4</sup>Faculty of Engineering, Kuwait College of Science and Technology, Doha, Kuwait

<sup>5</sup>Department of Engineering and Architecture, University of Parma, Italy

<sup>6</sup>Faculty of Military Science, Stellenbosch University, Saldanha 7395, South Africa

**Title of Paper :** Investigation of the natural ventilation of wind catchers with different geometries in arid region houses

**License :** Creative Commons Attribution-Non Commercial 4.0 International License.

**Source :** <https://doi.org/10.15282/jmes.14.3.2020.12.0557>

**Reprint Status :** Slight Adaptation due to Formatting

**Adapted From :** Journal of Mechanical Engineering and Sciences (JMES) ISSN: 2289-4659 e-ISSN: 2231-8380 Vol. 14, ISSUE 3, 7109 – 7124

### 9.3.5.1 Abstract

The wind catcher or wind tower is a natural ventilation technique that has been employed in the Middle East region and still until nowadays. The present paper aims to study the effect of the one-sided position of a wind catcher device against the ventilated space or building geometry and its natural ventilation performance. Four models based on the traditional design of a one-sided wind catcher are studied and compared. The study is achieved under the climatic conditions of the Southwest of Algeria (arid region). The obtained results showed that the front and Takhtabush's models were able to create the maximum pressure difference ( $\Delta P$ ) between the windward and leeward of

the tower-house system. Internal airflow velocities increased with the increase of wind speed in all studied models. For example, at  $V_{wind} = 2$  m/s, the internal flow velocities were 1.7, 1.8, 1.3, and 2.5 m/s for model 1, 2, 3, and 4, respectively. However, at  $V_{wind} = 6$  m/s, the internal flow velocities were 5.6, 5.5, 2.5, and 7 m/s for model 1, 2, 3, and 4, respectively. The higher internal airflow velocities are given by *Takhtabush*, traditional, front and middle tower models, respectively, with a reduction rate between the tower outlet and occupied space by 72, 42, 36, and 33% for the middle tower, *Takhtabush*, traditional tower, and the front model tower, respectively. This reduction is due to the due to internal flow resistance. The third part of the study investigates the effect of window (exist opening) position on the opposite wall. The upper, middle and lower window positions are studied and compared. The air stagnation or recirculation zone inside the ventilated space reduced from 55% with the lower window to 46% for the middle window and reached 35% for the upper window position. The Front and *Takhtabush* models for the one-sided wind catcher with an upper window position are highly recommended for the wind-driven natural ventilation in residential houses that are located in arid regions.

### 9.3.5.2 Introduction

#### 9.3.5.2.1 Thermal Comfort

Thermal comfort was and still a significant concern, especially after the petrol crisis and fuel price rises. Occupied spaces must be conditioned and controlled. Forty percent of the total world energy consumption is used by the building sector, especially in office buildings that produce more carbon and greenhouse gas. In the USA and UK office buildings, more than 70% of energy is used only by lighting and ventilation [1]. HVAC (Heating, Ventilating and Air Conditioning) systems can be responsible for almost 68% of energy consumption in residential buildings [2]. The building ventilation can be provided naturally, mechanically, or by both sources called hybrid ventilation. The natural ventilation is defined as the natural air movement inside a structure without any contribution of fans or mechanical equipment. The two main types of the natural ventilation types the wind-driven and buoyancy-driven natural ventilation [3].

By experiments and numerical simulation, Mansor et al. [4] studied the effect of natural and artificial ventilation inside a car on the thermal comfort of passengers. They developed a numerical model to predict the reduction of internal car temperature by increasing the mass flow rate of ventilation. Other researchers studied the heat transfer efficiency [5-7]. In addition, Phase Change Materials (PCMs) technology is widely used in arid regions to enhance the occupant's thermal comfort [8-11]. For cooling applications, Dulaimi et al. [12] investigated the thermal performance of a natural draft wet cooling tower, natural draft condition, and a forced draft condition created by an axial fan. Their results showed a 22% increase in the cooling effectiveness in comparison with the traditional techniques. Zafirah and Mardiana [13] evaluated the performance of an air-to-air energy recovery system in terms of latent efficiency. They recovered energy to enhance the thermal comfort inside buildings under a hot and humid climate.

#### 9.3.5.2.2 Natural Ventilation

Wind-driven ventilation occurs via pressure difference between the windward and leeward or between inlet and outlet openings in a ventilated space [14]. Buoyancy-driven ventilation occurs via the density difference between the warm and cold air existing in the same structure [15-25]. Warm air (less dense) leaves the ventilated space through upper openings, and it is replaced by the cold outside air (denser) via openings such as doors and windows. The solar chimney is an example of buoyancy-driven natural ventilation. Natural ventilation appears as a sustainable solution for thermal comfort, health, and air quality improvement. A study on 12 public office buildings in Northern California touched 880 workers showed that the natural ventilation is more satisfactory with less sick building symptoms in comparison with the mechanical and HVAC ventilation [26].

### 9.3.5.2.3 Wind-Driven Natural Ventilation

The wind vertical profile in atmospheric boundary layer (ABL) follows a logarithmic power law:

$$\frac{u}{u_r} = \left( \frac{z}{z_r} \right)^\alpha$$

**Eq. 9.3.1**

where  $u$  is the wind speed at  $z$  height,  $u_r$  is the reference of wind speed at a reference height  $z_r$ ,  $\alpha$  is an empirical parameter, the exponent ( $\alpha$ ) is an empirically derived coefficient that varies dependent upon the stability of the atmosphere (Figure 9.3.4). For neutral stability conditions, ( $\alpha$ ) is approximately 0.143 [27].

### 9.3.5.3 Mathematical Modelling of the Problem

#### 9.3.5.3.1 Governing Equations

Liquids and gases circulating at low speeds behave like incompressible fluids [28, 29]. The governing equations for an incompressible fluid like atmospheric air in the rigorous sub-layer are written in initial notation as follow:

$$\text{Continuity: } \nabla \cdot u_i = 0$$

$$\text{Momentum: } \rho \frac{Du_i}{Dt} = \nabla p + \mu \frac{\partial^2 u_i}{\partial x_j}$$

$$\text{Energy: } \rho c_v \frac{DT}{Dt} = k \nabla^2 T + \tau_{ij} \frac{\partial u_i}{\partial x_j} \quad \tau_{ij} = \mu \left( \frac{\partial u_i}{\partial x_j} + \frac{\partial u_j}{\partial x_i} \right)$$

**Eq. 9.3.2**

Where  $D/Dt$  is the total (substantial) derivative and  $\nabla$  is the divergence vector. The study of building natural ventilation is composed of two parts: envelope flows and internal air motion [30]. The envelope flows study the effect of wind on the ventilated space envelope that is also called the wind-

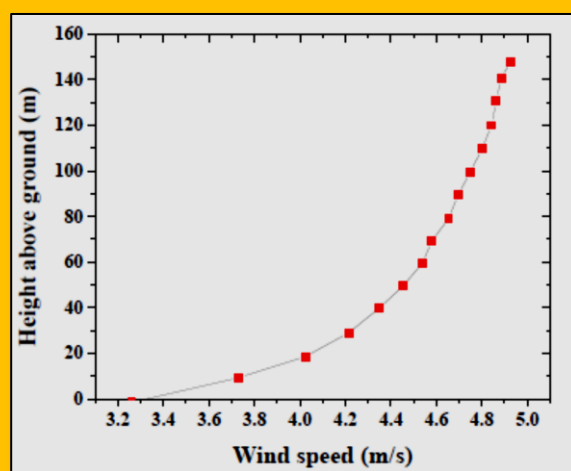


Figure 9.3.4 Vertical wind profile speed (for an open space, roughness class = 0.5, roughness length = 0.0024 m,  $u_r = 3$  m/s,  $z_r = 10$  m)

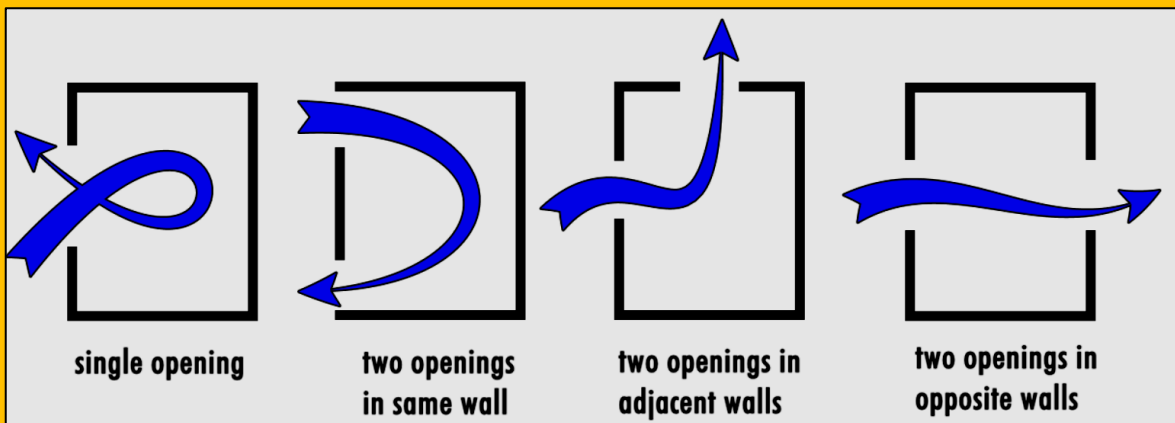


Figure 9.3.5 Types of the wind-driven natural ventilation

structure interaction. Internal airflow studies the interior airflow characteristics (pressure, velocity, streamline, etc.). For the wind-driven natural ventilation, the external and internal pressure fields, as well as the internal airflow, must be identified. The internal airflow velocity is one of the six basic parameters of thermal comfort. It plays a vital role in heat losses through the convection and evaporation for inhabitants inside a structure (a residential or an office building), enhancing thus the IAQ and providing suitable living conditions. As illustrated in [Figure 9.3.5](#), the natural ventilation device must be well-chosen and placed in a proper distribution of internal air to meet the standards of thermal comfort requirements.

### 9.3.5.3.2 Wind Catchers Between Past, Present and Future

Wind catchers or BADGERS were used in the Middle-East region since old times. They have been known as an Iranian ventilation technique used in houses and mosques or related to the Qanat (an underground water system) [31], or to cool down the water in a reservoir and Yakhchal (an ice storage space) [32]. However, the wind catcher technique back to 1300 B.C in the Pharaonic times [33-36], as shown in [Figure 9.3.6](#). The traditional wind towers or catchers work in the presence and absence of wind by both pressure and buoyancy forces. In the presence of the wind, the device catches the prevailing winds. It redirects the airflow inside the building by using the pressure difference between the windward and leeward of (tower-structure) the system, and between the tower inlet and outlet, which is in the same time the air discharge opening. In the absence of the wind, the buoyancy forces are dominants, and the wind catcher works like a chimney. The night cooling is another advantage of wind catchers.

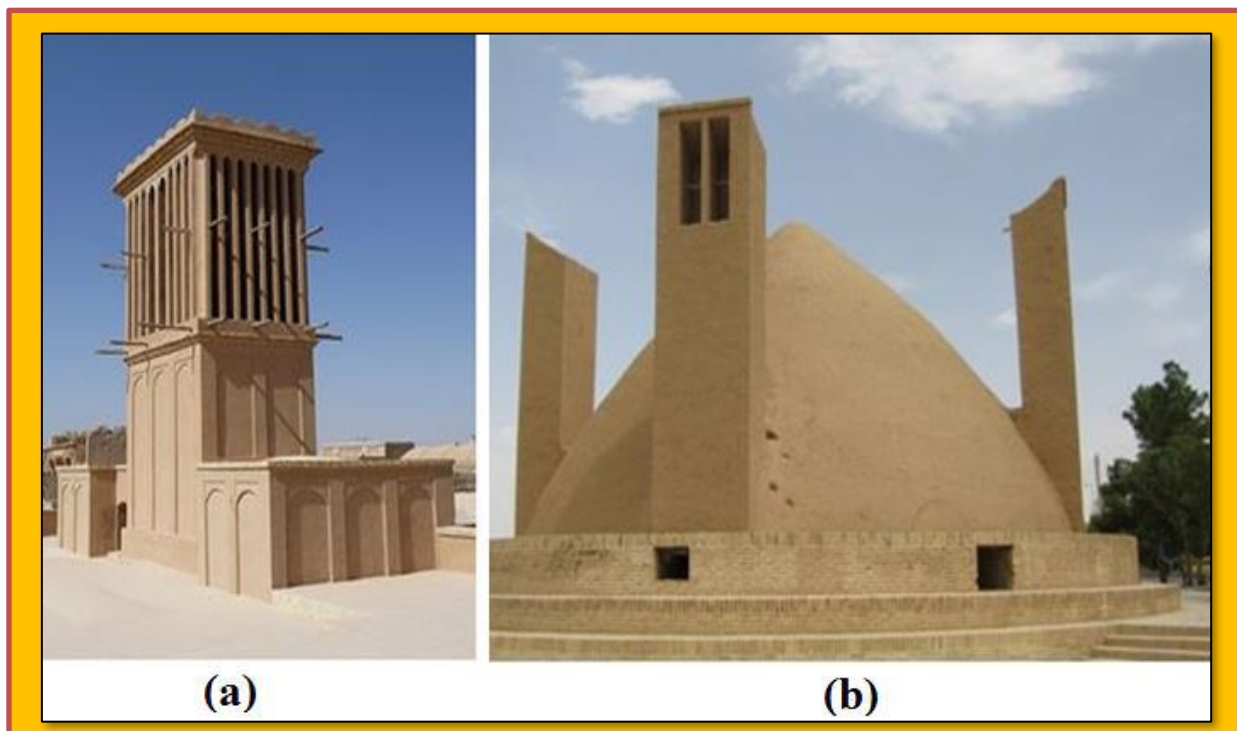


Figure 9.3.6 Yazd traditional wind-catcher for: (a) house ventilation and (b) water cooling

The modern wind catchers or mono-draught catch the wind near the building roof. They present the advantage of two to four-sided wind catchers able to work 360° with various wind directions and angles. Nevertheless, the turbulence in the building roof level can decrease the ventilation performance by reducing the airflow rate entering the device ([Figure 9.3.7](#)).

The newly proposed models are based on a traditional design. The first model is a traditional Iranian wind catcher with an air-channel between the device and the ventilated space. This model is similar

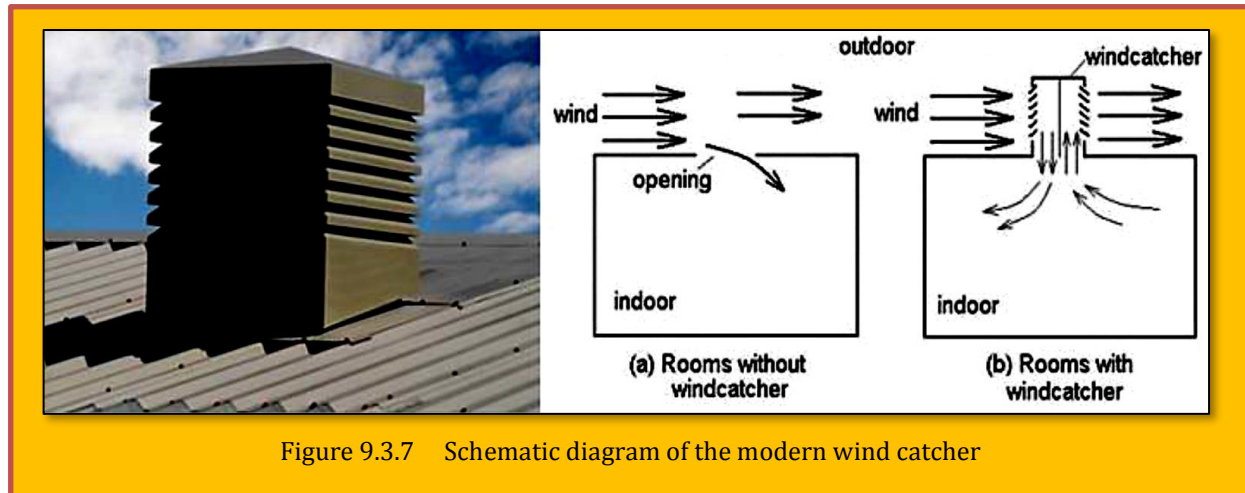


Figure 9.3.7 Schematic diagram of the modern wind catcher

to the wind catchers that are used with water reservoirs. The second model is the *Malqaf* in Egyptian houses, as shown in **Figure 9.3.8**. *Malqaf* is the Arabian name of wind catcher. A very good example of *Malqaf* use appears in Muhib Al-Din house (1350) in Cairo [37]. A natural ventilation system combines *malqaf*, *dorq'ah* (the central part of the structure) and the lantern in one structure to ensure a good circulation of fresh air in the *qa'a* (reception hall). *Malqaf* is placed in the windward side, facing the prevailing winds (**Figure 9.3.9**). It is generally made of wood or local materials with a 30° to 45° inclined roof in the opposite wall that is facing the prevailing winds [38].

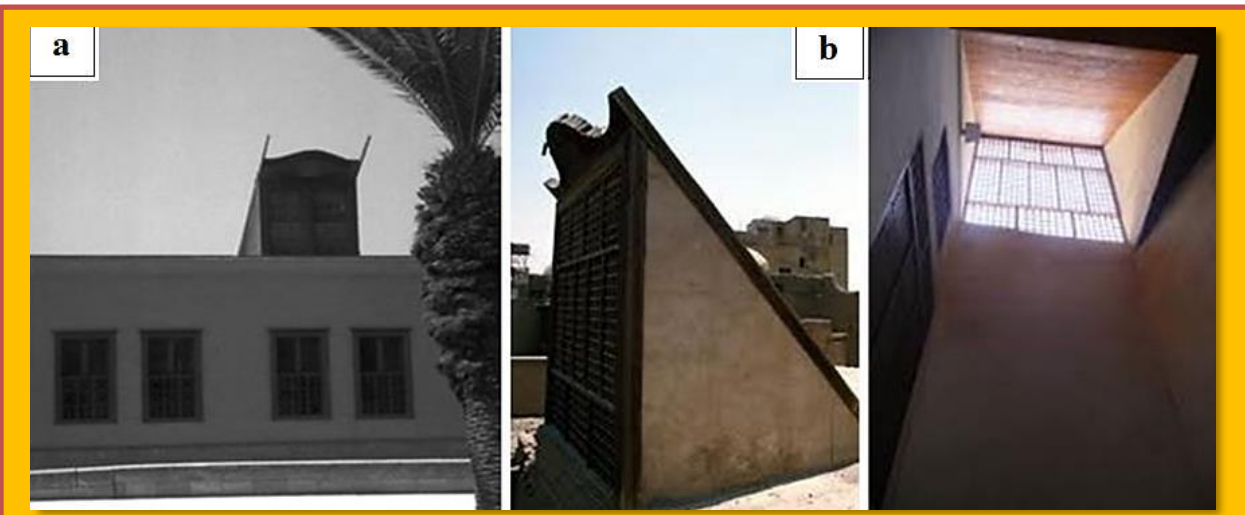


Figure 9.3.8 Malqaf at Al-Jawhara house in Cairo, Egypt with outside and inside view of the device

The third model is a one-sided wind catcher placed in the middle of the ventilated space roof to simulate the modern wind catcher. The fourth model is an old technique named *Takhtabush* (**Figure 9.3.10a**). *Takhtabush* is a covered outdoor sitting area located off the courtyard and in the nearest area to the entrance covered by a wooden grid called *Musharabia* [39, 40]. The new model is based on the geometry and position of *Takhtabush* (**Figure 9.3.10b**). It is placed in the windward side of the ventilated space, and the tower outlet is in the upper corner of the windward wall with an inclined base.

#### 9.3.5.4 Numerical Simulation of External Airflows Around A Tower-House System

Computational Wind Engineering (CWE) is a computational tool for wind-structure and natural ventilation studies. The outside domain or macroclimate is the atmospheric air considered as

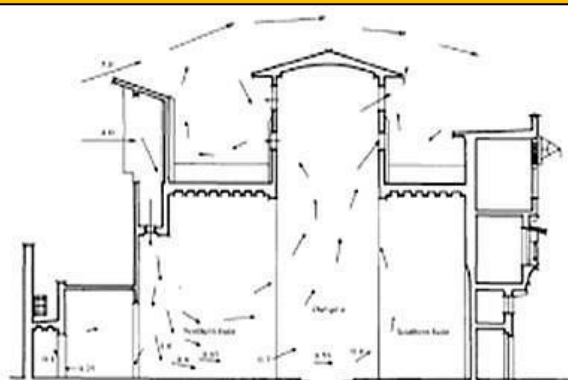


Figure 9.3.9 House of Muhib Ad-Din equipped with Malqaf, Cairo [33]

incompressible [41]. The macro domain dimensions (Figures 8 and 9; not shown here – please refer to [Sakhri et al.])<sup>123</sup> were chosen under the recommendation of [42, 43] to take into account the blockage ratio effect (equal to 16% in our case). The wind catcher height ( $H$ ) is equal to 9 m.

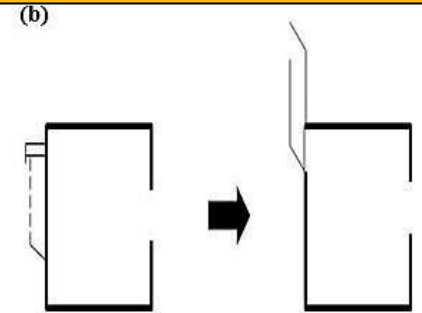


Figure 9.3.10 (a) Takhtabush in an old Egyptian house and (b) New model is based on the geometry and position of Takhtabush

#### 9.3.5.4.1 Geometry and Dimension

For all studied models, the maximum value of  $H$  is equal to 9m. The top and side views of the four models are presented. The cross-section of the wind catcher device and the air channel is  $1 \text{ m}^2$  square shape. The inlet and outlet sections of the tower are equal to one  $\text{m}^2$ . Dimensions of the envelope of the ventilated space are chosen to simulate real room conditions, with  $L \times H = 5 \times 5 \text{ m}^2$  for the envelope. The surface of the window or air exit opening is equal to  $1 \text{ m}^2$ . An inclination by  $45^\circ$  in the roof catcher is chosen due to its aerodynamic efficiency and high airflow velocity, in comparison with the flat roof [44, 45] (Figure 10; not shown here – please refer to [Sakhri et al.])<sup>124</sup>.

Model	Cells	Faces	Nodes
1	217 008	327 181	110 167
2	171 364	258 373	87 005
3	237 348	357 644	120 290
4	177 346	267 442	90 090

Table 9.3.1 Grid information of the simulation cases

<sup>123</sup> N. Sakhri, Y. Menni, H. Ameur, A. J. Chamkha, N. Kaid, M. Bensafi, G. Lorenzini and O. D. Makinde, "Investigation of the natural ventilation of wind catchers with different geometries in arid region houses", DOI: <https://doi.org/10.15282/jmes.14.3.2020.12.0557>

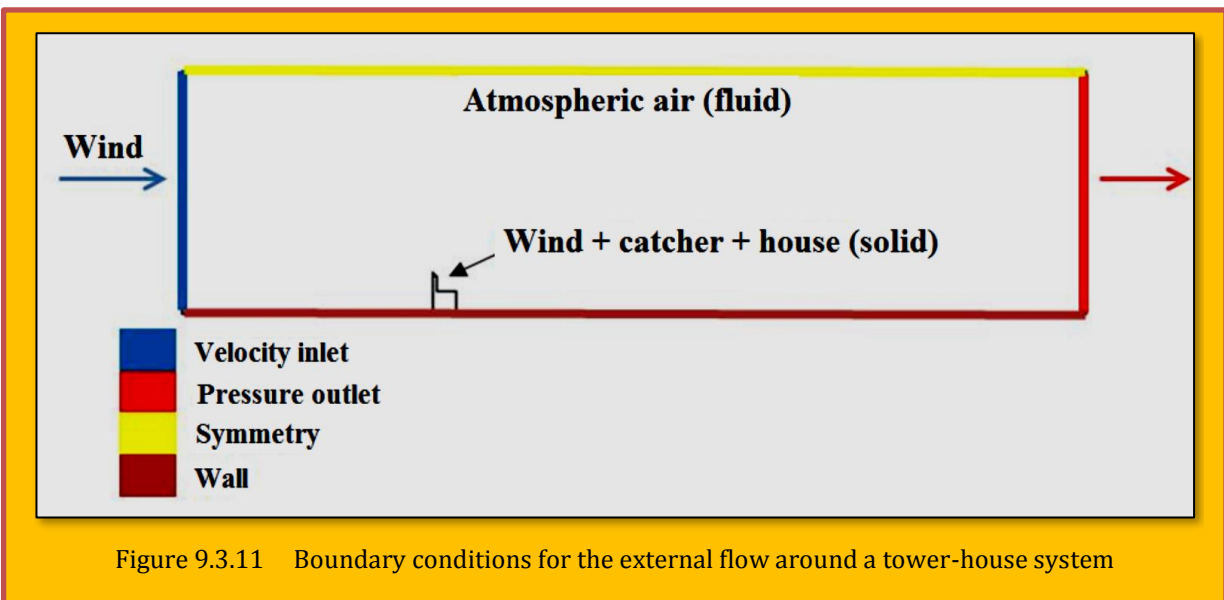
<sup>124</sup> See Previous

### 9.3.5.4.2 Meshing

To capture the details of the wind-structure interaction, a refined tetrahedral mesh is used starting from  $10^{-3}$  m near the boundary layer of the tower-house system to  $10^{-2}$  m near the outside domain borders (Figure 11; not shown here – please refer to [Sakhri et al.])<sup>125</sup>). **Table 9.3.1** provides the grid details for each model.

### 9.3.5.4.3 Boundary Conditions

The domain contains fully turbulent atmospheric air with a steady-state, and the house tower is considered as solid. Values of the velocity and pressure are set at the inlet and outlet sections, respectively. Symmetry and wall conditions are set for the upper border and domain base, respectively (**Figure 9.3.11**). The walls of the wind catcher and house are smooth. The k- $\epsilon$  model with pressure-based and standard wall function is used for the turbulence modeling. The **SIMPLE** method with the second-order upwind discretization scheme is used in this study due to its performance in CWE studies [46-51].



The south-west of Algeria was taken as a case study (Figure 13; not shown here – please refer to [Sakhri et al.])<sup>126</sup>. It concerns an arid region characterized by the thermal discomfort, especially in the summer season. The mean wind speeds in this region are as follows: Béchar with 3.7 m/s, Adrar with 6.1 m/s, and Tindouf with 5.7 m/s [52]. The wind speed at domain inlet is 3 m/s (reference: Bechar region wind speed).

### 9.3.5.5 Results and Discussion

The total pressure analysis of external envelope flows of a house equipped with a wind catcher device present a positive pressure on the windward side and a negative pressure on the leeward side for all models. The value 20.8 Pa of external pressure difference on the wind catcher was created in model 4 (*Takhtabush*), followed by 20.6 Pa for the traditional tower, 18.1 Pa for the front model tower, and 16 Pa for the middle tower (**Table 9.3.2**).

<sup>125</sup> N. Sakhri, Y. Menni, H. Ameur, A. J. Chamkha, N. Kaid, M. Bensafi, G. Lorenzini and O. D. Makinde, "Investigation of the natural ventilation of wind catchers with different geometries in arid region houses", DOI: <https://doi.org/10.15282/jmes.14.3.2020.12.0557>

<sup>126</sup> N. Sakhri, Y. Menni, H. Ameur, A. J. Chamkha, N. Kaid, M. Bensafi, G. Lorenzini and O. D. Makinde, "Investigation of the natural ventilation of wind catchers with different geometries in arid region houses", DOI: <https://doi.org/10.15282/jmes.14.3.2020.12.0557>

Model	Wind-catcher				Room			
	Total pressure (Pa)		Pressure Coefficient		Total pressure (Pa)		Pressure Coefficient	
	Windward	Leeward	Windward	Leeward	Windward	Leeward	Windward	Leeward
Model 1 Traditional	13.1	-7.5	21	-12.5	-6	-8	-12.5	-12.5
Model 2 Front	11.4	-6.7	12.1	-12.4	13.3	-7.3	20.8	-12.4
Model 3 Middle	9	-7	11.2	-12.4	12.4	-7.4	19.6	-12.4
Model 4 Takhtabush	13.6	-7.2	14.4	-12.1	12.1	-7.2	21.5	-12.1

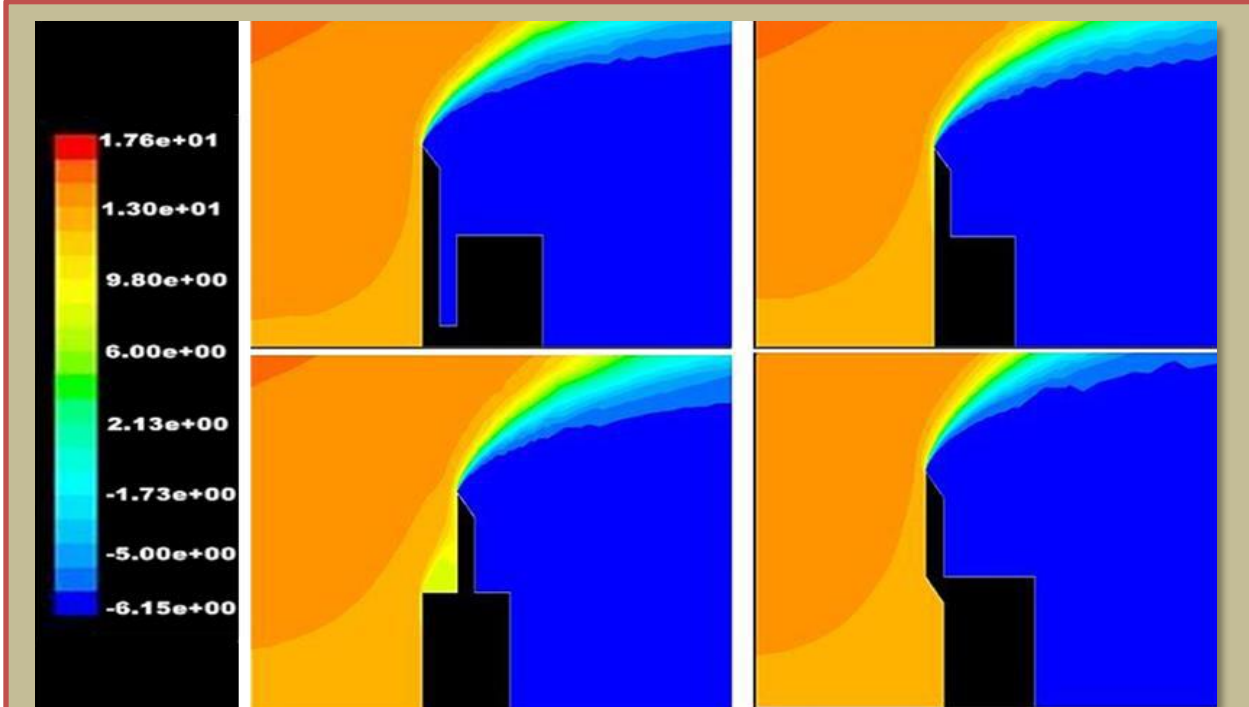
Table 9.3.2 External total pressure (Pa) and pressure coefficients of the models under investigation

For the external pressure of the envelope, the maximum values of the created pressure difference were 20.6, 19.8, 19.3 Pas for models 2, 3, and 4, respectively. For the first model, (-2) Pa was the  $\Delta P$  across the envelope equipped with a traditional wind catcher (Figure 9.3.12). This value was the result of the place of a traditional wind catcher, which acts as a protection or a shield. A negative pressure is created in both wind and leeward sides of the ventilated space and prevents the interaction between the wind and envelope windward side. Pressure coefficient is defined as:

$$C_p = \frac{P - P_{ref}}{0.5\rho V_{ref}^2}$$

### Eq. 9.3.3

where  $P$  (Pa) is the local surface pressure,  $P_{ref}$  (Pa) and  $V_{ref}$  (m/s) are, respectively, the upstream static pressure and free stream velocity (wind), and  $\rho$  (kg/m<sup>3</sup>) is the air density. The values of the

Figure 9.3.12 Total external pressure (Pa) with  $V_{wind} = 3$  m/s

pressure coefficient on the wind catcher and envelope windward side of model 4 were higher than those of all studied models. The highest  $C_p$  conducts to the most efficient natural ventilation. Analysis of the streamline in **Figure 9.3.13** shows the existence of a recirculation zone in the leeward side of the wind catcher device in all studied models. An additional recirculation zone exists in the middle wind catcher, which can reduce the airflow at the inlet of the device. A small recirculation zone is created above the air channel that connects the traditional wind catcher and the envelope, resulting thus an additional negative pressure in the windward of the envelope as well as in the ventilated spaces.

#### 9.3.5.5.1 Analysis of the Internal Airflow in Ventilated Spaces

The airflow inside the ventilated area is widely influenced by the external airflow around it. The thermal comfort in building occupants is directly related to the internal pressure and airflow velocity. The following values of wind speed, namely: 1, 2, 3, 5, 6, and 10 m/s, are chosen based on the weather conditions of the region (south-west of Algeria). For further details, the envelope was divided into nine equal sub-zones as illustrated in (Figure 16; not shown here – please refer to [Sakhri et al.])<sup>127</sup>). The total internal pressure and airflow velocities are discussed. The analysis of the internal pressure has given the following results:

High pressure was observed in front and Takhtabush models in five zones: A, C, D, F, and G. The most elevated total pressure of 37 Pa existed in the Takhtabush model, especially in the G zone. As observed in **Figure 9.3.14**, the highest values of pressure were located in G, H, and I zones due to the air density and internal airflow. For the middle tower model, the highest value of total pressure exists in zone B due to the discharge opening.

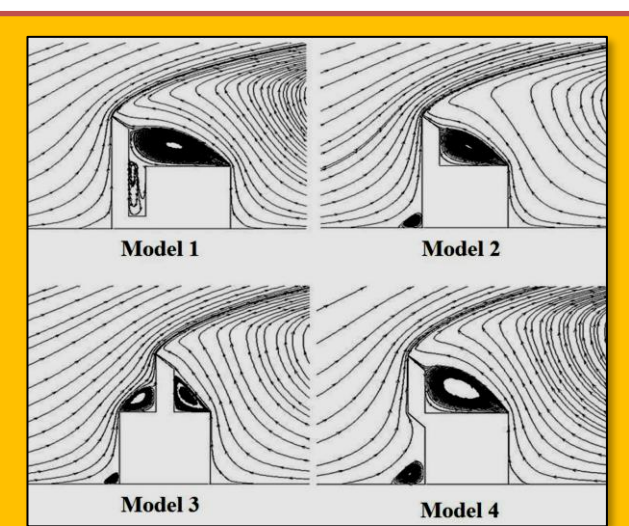


Figure 9.3.13 External streamline of airflow around the structures (tower and house)

A	B	C
D	E	F
G	H	I

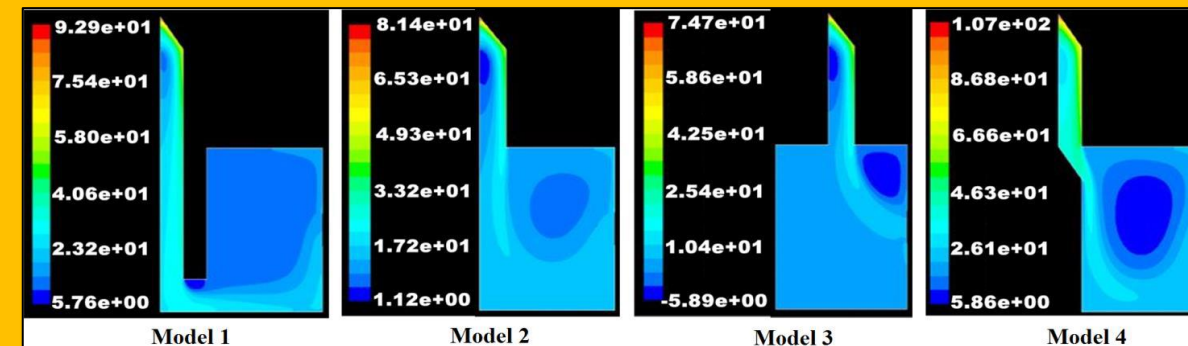


Figure 9.3.14 Total internal pressure (Pa) with  $V_{wind} = 3$  m/s

<sup>127</sup> N. Sakhri, Y. Menni, H. Ameur, A. J. Chamkha, N. Kaid, M. Bensafi, G. Lorenzini and O. D. Makinde, "Investigation of the natural ventilation of wind catchers with different geometries in arid region houses", DOI: <https://doi.org/10.15282/jmes.14.3.2020.12.0557>

However, the lowest value is observed in zone C, which presents a dead fluid or a stagnation zone where the airflow is recirculated. The middle tower model offers the lowest values of total pressure among all models, because of the existence of a short loop of airflow between the discharge orifice and window (Not shown here – please refer to [Sakhri et al.])<sup>128</sup> - Figure 18).

The traditional wind tower with A, B, C zones and the middle tower with D and E zones present a uniform pressure zones, and the high values exist in G, H, and I zones. The high pressure in these zones is the result of discharge or injection orifice from the catcher outlet to the ventilated space. Air pressures in zone F are probably the same (between 18 and 22 Pa) in all models. This is due to the existence of the window, where the airflow leaves the envelope.

For the velocity magnitude, the highest values were observed at the discharge opening (or the tower outlet that is connected directly with the envelope). These maximum values were 4.9, 4.5, 4.4, and 4.2 m/s for *Takhtabush*, front model in zone A, middle tower at zone C, and traditional wind catcher at zone G, respectively. The lowest velocities characterize zone E, and the central recirculation zone is located at the center region of the space, which can cause a flow stagnation area (**Figure 9.3.15** and Table 3 – Note ; Table 3 not shown here – please refer to [Sakhri et al.])<sup>129</sup>. Airflow velocities in zone F are very close, and they vary between 3.85 and 3.36 m/s. These values present the outflow velocities of the internal air leaving the ventilated space.

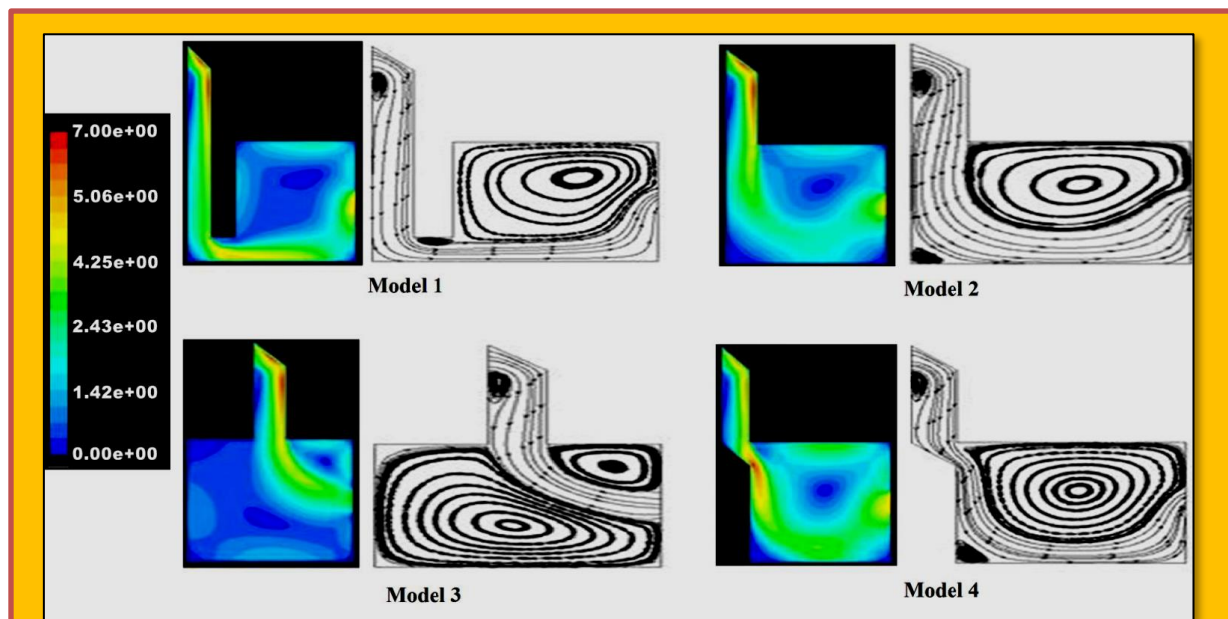


Figure 9.3.15 Internal airflow velocities and streamlines for the four studied models with  $V_{wind} = 3\text{m/s}$

The occupants of the ventilated space or the house occupied half of the area as showed in (Not shown here - please refer to Figure 20 [Sakhri et al.])<sup>130</sup>. Figure 20, with hos presents  $\frac{1}{2}H$  house equal to 2.5 m. For a wind speed varying between 1 and 10 m/s, the obtained figures give an idea about the internal airflow velocity from the tower outlet (air discharge orifice) through the occupied area until leaving the envelope by the window (exist opening). The obtained results in **Table 9.3.3** show that

<sup>128</sup> N. Sakhri, Y. Menni, H. Ameur, A. J. Chamkha, N. Kaid, M. Bensafi, G. Lorenzini and O. D. Makinde, "Investigation of the natural ventilation of wind catchers with different geometries in arid region houses", DOI: <https://doi.org/10.15282/jmes.14.3.2020.12.0557>

<sup>129</sup> N. Sakhri, Y. Menni, H. Ameur, A. J. Chamkha, N. Kaid, M. Bensafi, G. Lorenzini and O. D. Makinde, "Investigation of the natural ventilation of wind catchers with different geometries in arid region houses", DOI: <https://doi.org/10.15282/jmes.14.3.2020.12.0557>

<sup>130</sup> See Previous

the internal airflow velocities increase with the rise of wind speeds for all models.

	$V_{wind}$ (m/s)	1	2	3	5	6	10
Model 1	Tower outlet	1.05	2.88	3.65	5.96	7.7	14.43
	Occupied space	0.48	1.25	2.41	4.33	5.01	9.43
	Window	1.05	2.98	4.13	7.41	9.62	16.74
Model 2	Tower outlet	1.05	2.20	3.35	5.45	7.18	12.63
	Occupied space	0.48	1.34	1.91	4.11	4.88	8.90
	Window	0.57	2.77	3.82	7.65	9.67	16.56
Model 3	Tower outlet	1.17	2.21	3.46	5.82	7.36	12.61
	Occupied space	0.14	0.73	0.95	2.28	4.05	3.97
	Window	1.17	2.28	3.16	5.01	6.11	10.75

Table 9.3.3 Airflow velocities (m/s) inside the ventilated space with different wind speeds:  $V_{wind} = 1, 2, 3, 5, 6$  and 10 m/s

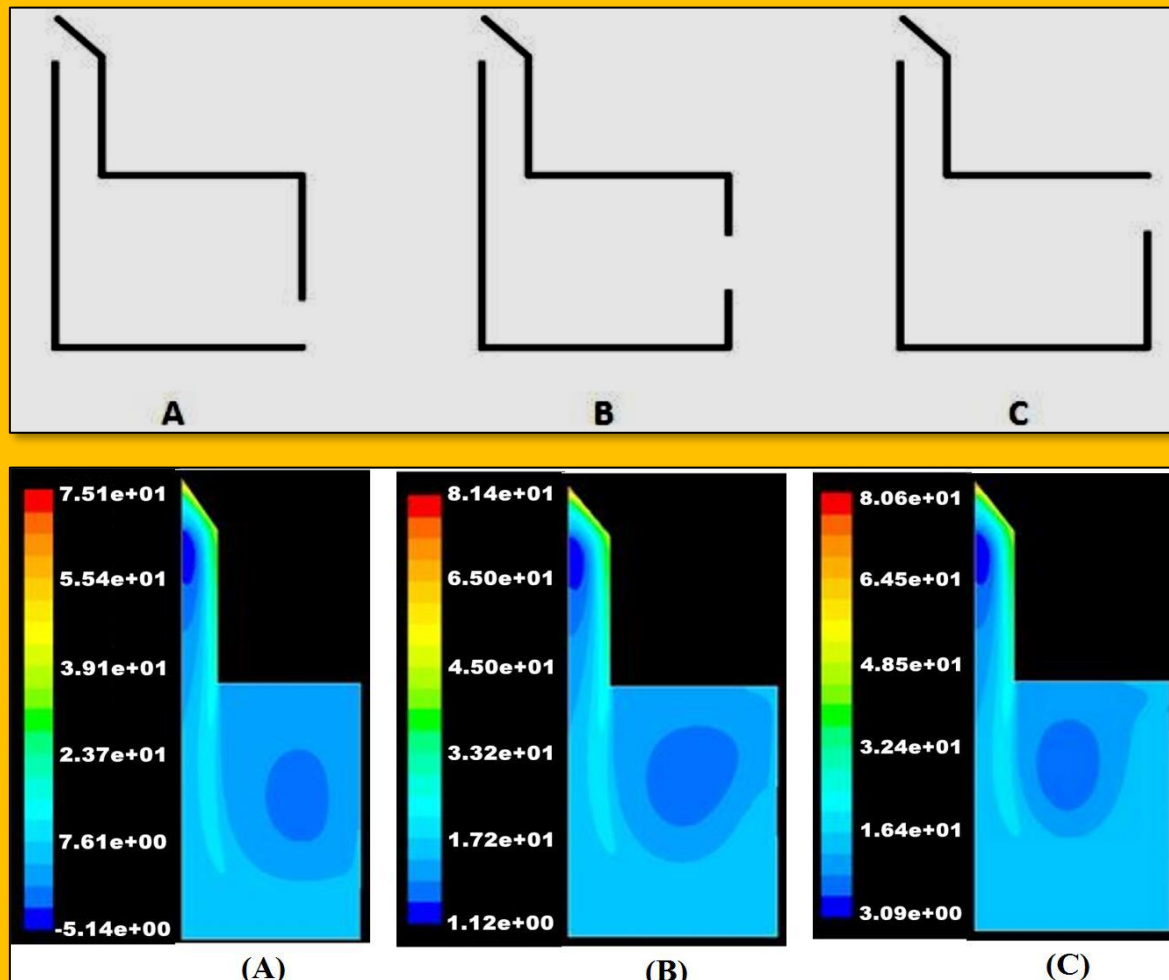


Figure 9.3.16 Internal total pressure (Pa) for three window positions: (a) down, (b) middle and (c) top ( $V_{wind} = 3$  m/s)

Internal airflow velocity is reduced from the air discharge orifice to the occupied area by 33, 72, 42, and 36% for the front tower, middle tower, *Takhtabush* tower, and traditional wind catcher models, respectively. This velocity increases after leaving this area to the window opening for all four models. A sharp edge at the outlet of the *Takhtabush* tower model yields a high air velocity in comparison with the other studied models. The lowest airflow velocities in the occupied space occur in the middle tower model and very satisfactory results are reached for the three other models.

### 9.3.5.2 Effect of the Opening Position on Internal Airflow

The third part of the study is dedicated to the outflow opening or window position, as shown in **Figure 9.3.16**. Two additional locations are studied and compared with the usual window position that is generally located in the middle of the opposite wall of the structure. An upper window is located directly under the roof, and a lower position window is located directly above the envelope base. The front wind catcher was selected as a natural ventilation device. The distribution of the total air pressure shows a uniform pressure field in the upper window model, compared with the middle and lower windows by a difference of 23 Pa. The same result was obtained for the airflow velocity magnitude with 2.65 m/s, which can reduce the internal temperature of the ventilated space by 4 to 5 °C [53]. The streamline analysis of the three configurations was compared in (Not shown here - please refer to [Sakhri et al.]<sup>131</sup> on Figure 23). The size of the airflow stagnation zone of the occupied space equipped with a front tower model was 55, 46, and 35% for the lower window (case A), middle window (case B), and upper window (case C), respectively. The upper window or opening configuration is the most appropriate to reduce the central recirculation area and provide more airflows for the ventilated space occupants. Furthermore, the stagnation area is reduced with the increased height of the window position.

### 9.3.5.6 Conclusion

The natural ventilation is taking more and more important in designing bioclimatic buildings due to thermal efficiency and cost-saving advantages. Naturally ventilated buildings must be well studied and dimensioned. Besides, the natural ventilation strategy and device choices must take into consideration the weather conditions of the region. Wind catchers have been employed for a very long time to nowadays because of their efficiency and variety of use (with Qanat, Yakhchal, solar chimney, courtyard, etc.). It is a technology that never stops development. The performance of four one-sided wind catchers was studied to demonstrate the influence of the device position on natural ventilation. These models were: the Iranian traditional wind catcher, Mulkaf, modern wind catchers placed in the middle of the ventilated space. The last model was inspired from the Egyptian technique *Takhtabush*. The obtained results showed the importance of the device position on the system performance. The external airflow around the tower-house system indicated that front and *Takhtabush* models create the maximum pressure difference  $\Delta P$  and pressure coefficient  $C_p$  between the windward and leeward of the system, compared to the traditional and middle towers, which lead to the best wind-driven natural ventilation. The second part of the study was a comparison of internal airflow properties inside the ventilated envelope equipped with the four studied models. The wind speed varied between 1, 2, 3, 5, 6, and 10 m/s based on the weather conditions of the South-West of Algeria (Bechar, Tindouf, Adrar). The results analysis has given the following conclusions:

- 1) The airflow velocities inside the building increased with the increase of wind speed in all models.
- 2) Front and *Takhtabush* models were able to create more airflow inside the ventilated space, in comparison with the middle and traditional catchers.
- 3) A reduction of internal airflow velocities from the tower outlet to the occupied space occupants by 72, 42, 36, and 33% was observed for the middle tower, *Takhtabush* tower, traditional tower, and front model, respectively.

---

<sup>131</sup> See Previous

- 4) The positions of Front and *Takhtabush* models against the ventilated space geometry are highly recommended in comparison with the middle tower position. The results of the traditional wind catcher are also very satisfactory.
- 5) The third part of the study clarified the effect of window position in the opposite wall on internal airflow stagnation or air recirculation area, and therefore on the wind-driven natural ventilation. The upper window was able to reduce the stagnation area by 20 and 11%, compared with the lower and middle window positions, respectively. The use of the upper window with the wind catcher technique allows the best natural ventilation by decreasing the stagnation zone, which also improves the IAQ inside the ventilated space. The wind catcher is a very promising technique for the wind-driven natural ventilation in residential houses that are located in windy and arid regions like the Southwest of Algeria.
- 6) For future works, the authors will study by experiments the effects of the new models in arid regions.

### **Acknowledgments**

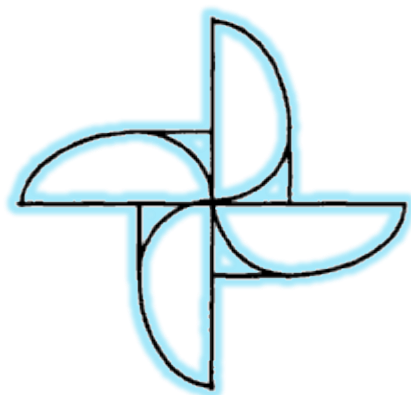
*The authors are grateful to Mr. Nairi Abdelkarim for providing the site for the study.*

#### **9.3.5.7 References**

- [1] C. Siew, A. Che-Ani, N. Tawil, N. Abdullah, and M. Mohd-Tahir, "Classification of natural ventilation strategies in optimizing energy consumption in Malaysian office buildings," *Procedia Engineering*, vol. 20, pp. 363-371, 2011.
- [2] G. Evola and V. Popov, "Computational analysis of wind driven natural ventilation in buildings," *Energy and Buildings*, vol. 38, pp. 491-501, 2006.
- [3] E. H. Moghaddam, S. Amineldar, and A. Besharatizadeh, "New approach to natural ventilation in public buildings inspired by Iranian's traditional windcatcher," *Procedia Engineering*, vol. 21, 2011.
- [4] M. Mansor, U. Rahman, M. Z. Abidin, M. M. Zain, and M. M. Yusof, "Variation of car cabin temperature influenced by ventilation under direct sun exposure," *Journal of Mechanical Engineering and Sciences*, vol. 6, pp. 1014-1023, 2014.
- [5] M. Nawi, A. Mamat, and H. Ismail, "Numerical heat transfer analysis of waste heat exchanger for exhaust gas energy recovery," *Journal of Mechanical Engineering and Sciences*, vol. 8, 2015.
- [6] M. Ashham, S. Raheemah, and K. Salman, "Numerical investigation on enhancement of heat transfer using rod inserts in single pipe heat exchanger," *Journal of Mechanical Engineering and Sciences*, vol. 13, pp. 6112-6124, 2019.
- [7] D. Sahel, H. Ameur, and M. Mellal, "Effect of tube shape on the performance of a fin and tube heat exchanger," *Journal of Mechanical Engineering and Sciences*, vol. 14, pp. 6709-6718, 2020.
- [8] A. Hajjar, S. Mehryan, and M. Ghalambaz, "Time periodic natural convection heat transfer in a nano-encapsulated phase-change suspension," *International Journal of Mechanical Sciences*, vol. 166, p. 105243, 2020.
- [9] M. Ghalambaz, S. Mehryan, A. Hajjar, and A. Veismoradi, "Unsteady natural convection flow of a suspension comprising Nano-Encapsulated Phase Change Materials (NEPCMs) in a porous medium," *Advanced Powder Technology*, vol. 31, pp. 954-966, 2020.
- [10] M. Ghalambaz, T. Groşan, and I. Pop, "Mixed convection boundary layer flow and heat transfer over a vertical plate embedded in a porous medium filled with a suspension of nano-encapsulated phase change materials," *Journal of Molecular Liquids*, vol. 293, p. 111432, 2019.
- [11] M. Ghalambaz, A. J. Chamkha, and D. Wen, "Natural convective flow and heat transfer of nano-encapsulated phase change materials (NEPCMs) in a cavity," *International journal of heat and mass transfer*, vol. 138, pp. 738-749, 2019.
- [12] M. J. Al-Dulaimi, F. A. Kareem, and F. A. Hamad, "Evaluation of thermal performance for natural and forced draft wet cooling tower," *Journal of Mechanical Engineering and Sciences*, vol. 13, 2019.

- [13] M. Zafirah and A. Mardiana, "Experimental investigation on the performance of an air-to-air energy recovery for building applications in hot-humid climate," *Journal of Mechanical Engineering and Sciences*, vol. 10, pp. 1857-1864, 2016.
- [14] N. Sakhri, Y. Menni, and H. Ameur, "Experimental investigation of the performance of earth-to-air heat exchangers in arid environments," *Journal of Arid Environments*, vol. 180, p. 104215, 2020.
- [15] L. Kolsi, A. Abidi, M. Borjini, N. Daous, and H. Ben Aïssia, "Effect of an external magnetic field on the 3-D unsteady natural convection in a cubical enclosure," *Numerical Heat Transfer, Part A: Applications*, vol. 51, pp. 1003-1021, 2007.
- [16] L. Kolsi, H. F. Oztop, A. Alghamdi, N. Abu-Hamdeh, M. N. Borjini, and H. B. Aïssia, "A computational work on a three dimensional analysis of natural convection and entropy generation in nanofluid filled enclosures with triangular solid insert at the corners," *Journal of Molecular Liquids*, vol. 218, 2016.
- [17] M. N. Borjini, L. Kolsi, N. Daous, and H. B. Aïssia, "Hydromagnetic double-diffusive laminar natural convection in a radiatively participating fluid," *Numerical Heat Transfer, Part A: Applications*, vol. 48, pp. 483-506, 2005.
- [18] L. Kolsi, K. Kalidasan, A. Alghamdi, M. N. Borjini, and P. R. Kanna, "Natural convection and entropy generation in a cubical cavity with twin adiabatic blocks filled by aluminum oxide–water nanofluid," *Numerical Heat Transfer, Part A: Applications*, vol. 70, pp. 242-259, 2016.
- [19] A. Abidi, L. Kolsi, M. N. Borjini, and H. B. Aïssia, "Effect of radiative heat transfer on three-dimensional double diffusive natural convection," *Numerical Heat Transfer, Part A: Applications*, vol. 60, pp. 785-809, 2011. N. Sakhri et al. | Journal of Mechanical Engineering and Sciences | Vol. 14, Issue 3 (2020) 7123 journal.ump.edu.my/jmes
- [20] C. Maatki, L. Kolsi, H. F. Oztop, A. Chamkha, M. N. Borjini, H. B. Aïssia, and K. Al-Salem, "Effects of magnetic field on 3D double diffusive convection in a cubic cavity filled with a binary mixture," *International Communications in Heat and Mass Transfer*, vol. 49, pp. 86-95, 2013.
- [21] S. M. H. Zadeh, S. Mehryan, E. Izadpanahi, and M. Ghalambaz, "Impacts of the flexibility of a thin heater plate on the natural convection heat transfer," *International Journal of Thermal Sciences*, vol. 145, p. 106001, 2019.
- [22] S. Mehryan, M. Ghalambaz, R. K. Feeoj, A. Hajjar, and M. Izadi, "Free convection in a trapezoidal enclosure divided by a flexible partition," *International journal of heat and mass transfer*, vol. 149, p. 119186, 2020.
- [23] S. Mehryan, E. Izadpanahi, M. Ghalambaz, and A. Chamkha, "Mixed convection flow caused by an oscillating cylinder in a square cavity filled with Cu-Al 2 O 3/water hybrid nanofluid," *Journal of Thermal Analysis and Calorimetry*, vol. 137, pp. 965-982, 2019.
- [24] E. Jamesahar, M. Sabour, M. Shahabadi, S. Mehryan, and M. Ghalambaz, "Mixed convection heat transfer by nanofluids in a cavity with two oscillating flexible fins: A fluid–structure interaction approach," *Applied Mathematical Modelling*, vol. 82, pp. 72-90, 2020.
- [25] A. Alsabery, F. Selimefendigil, I. Hashim, A. Chamkha, and M. Ghalambaz, "Fluid-structure interaction analysis of entropy generation and mixed convection inside a cavity with flexible right wall and heated rotating cylinder," *International journal of heat and mass transfer*, vol. 140, 2019.
- [26] M. J. Mendell, W. J. Fisk, J. A. Deddens, W. G. Seavey, A. H. Smith, D. F. Smith, A. T. Hodgson, J. M. Daisey, and L. R. Goldman, "Elevated symptom prevalence associated with ventilation type in office buildings," *Epidemiology*, pp. 583-589, 1996.
- [27] G. Gualtieri, "Development and application of an integrated wind resource assessment tool for wind farm planning," *International Journal of Renewable Energy Research (IJRER)*, vol. 2, 2012.
- [28] N. Sakhri, Y. Menni, A. Chamkha, M. Salmi, and H. Ameur, "Earth to air heat exchanger and its applications in arid regions—an updated review," *TECNICA ITALIANA Ital J Eng Sci*, vol. 64, 2020.
- [29] J. Seifert, Y. Li, J. Axley, and M. Rösler, "Calculation of wind-driven cross ventilation in buildings with large openings," *Journal of Wind Engineering and Industrial Aerodynamics*, vol. 94, 2006.
- [30] D. Etheridge, "A perspective on fifty years of natural ventilation research," *Building and Environment*, vol. 91, pp. 51-60, 2015.

- [31] B. R. Hughes, J. K. Calautit, and S. A. Ghani, "The development of commercial wind towers for natural ventilation: A review," *Applied energy*, vol. 92, pp. 606-627, 2012.
- [32] G. Soltani, A. Nazari, and N. Ghanavati, "Energy Management in Iranian Sustainable Ancient Architecture" Introducing Ice Houses and Cisterns in Yazd City," *Canadian Journal on Environmental, Construction and Civil Engineering*, vol. 3, pp. 173-178, 2012.
- [33] A.-m. El-Shorbagy, "Design with nature: windcatcher as a paradigm of natural ventilation device in buildings," *International Journal of Civil & Environmental Engineering IJCEE-IJENS*, vol. 10, 2010.
- [34] H. Okhovat, N. Almasifar, and M. Reza Bemanian, "A research on historical and cultural buildings in Iranian vernacular architecture," *ACE: architecture, city and environment*, vol. 6, pp. 37-58, 2011.
- [35] M. Dehghani-Sanij, "Wind Towers: Architecture, Climate and Sustainability," Ed: Taylor & Francis, 2018.
- [36] A. Mostafaeipour, B. Bardel, K. Mohammadi, A. Sedaghat, and Y. Dinpashoh, "Economic evaluation for cooling and ventilation of medicine storage warehouses utilizing wind catchers," *Renewable and Sustainable Energy Reviews*, vol. 38, pp. 12-19, 2014.
- [37] J. K. Calautit, B. R. Hughes, and S. S. Shahzad, "CFD and wind tunnel study of the performance of a uni-directional wind catcher with heat transfer devices," *Renewable Energy*, vol. 83, pp. 85-99, 2015.
- [38] S. Suleiman and B. Himmo, "Direct comfort ventilation. Wisdom of the past and technology of the future (wind-catcher)," *Sustainable Cities and Society*, vol. 5, pp. 8-15, 2012.
- [39] A. M. Salama, "A typological perspective: the impact of cultural paradigmatic shifts on the evolution of courtyard houses in Cairo," *METU Journal of the Faculty of Architecture*, vol. 23, 2006.
- [40] A. Petersen, *Dictionary of Islamic architecture*: Psychology Press, 1996.
- [41] T. Yang, "CFD and field testing of a naturally ventilated full-scale building," University of Nottingham, 2004.
- [42] J. Revuz, "Numerical simulation of the wind flow around a tall building and its dynamic response to wind excitation," University of Nottingham, 2011.
- [43] Y. Tominaga and T. Stathopoulos, "CFD simulation of near-field pollutant dispersion in the urban environment: A review of current modeling techniques," *Atmospheric Environment*, vol. 79, 2013.
- [44] H. Montazeri and R. Azizian, "Experimental study on natural ventilation performance of one-sided wind catcher," *Building and Environment*, vol. 43, pp. 2193-2202, 2008.
- [45] A. Dehghan, M. K. Esfeh, and M. D. Manshadi, "Natural ventilation characteristics of one-sided wind catchers: experimental and analytical evaluation," *Energy and Buildings*, vol. 61, 2013.
- [46] Y. Gao and W. Chow, "Numerical studies on air flow around a cube," *Journal of Wind Engineering and Industrial Aerodynamics*, vol. 93, pp. 115-135, 2005.
- [47] M. H. Ghadiri, M. F. Mohamed, and N. L. N. Ibrahim, "CFD analysis of natural ventilation behavior in four sided wind catcher," in *Proceedings of World Academy of Science, Engineering and Technology*, 2012, p. 704. N. Sakhri et al. | Journal of Mechanical Engineering and Sciences | Vol. 14, Issue 3 (2020) 7124 journal.ump.edu.my/jmes
- [48] A. R. Vempati, "Computational Fluid Dynamics Investigation of Air Velocity and Temperature Distribution in a Room Equipped with Active Chilled Beam Air-conditioning," University of Florida, 2011.
- [49] S. Murakami, "Current status and future trends in computational wind engineering," *Journal of Wind Engineering and Industrial Aerodynamics*, vol. 67, pp. 3-34, 1997.
- [50] C. M. Mak, "Application of computational fluid dynamics to the study of designed green features for sustainable buildings," *Computational Fluid Dynamics*, p. 173, 2010.
- [51] A. A. Elmualim, "Effect of damper and heat source on wind catcher natural ventilation performance," *Energy and Buildings*, vol. 38, pp. 939-948, 2006.
- [52] F. Chellali, A. Khellaf, A. Belouchni, and A. Reciou, "A contribution in the actualization of wind map of Algeria," *Renewable and Sustainable Energy Reviews*, vol. 15, pp. 993-1002, 2011.
- [53] R. Vittone, *Bâtir: manuel de la construction*: PPUR Presses Polytechnique, 2010.



## 10 Cooling Data Centers

### 10.1 Preliminaries

Data centers are an integral part of our society, and those who work in the industry know that cooling has been and will always be an important part of this ecosystem. Computers in a data center work 24/7 at tremendously high rates that they get exceptionally hot. Sophisticated cooling systems need to be applied for these computers to continue working without overheating. Cooling systems have evolved over the years, and in this article, we will discuss data center cooling options, methods, and the best practices for your data center. We will also discuss new innovations that may be ahead in the coming years<sup>132</sup>. Traditionally, there are two ways of cooling a data center: ***air-based*** and ***liquid-based*** cooling.

#### 10.1.1 Air-Based Cooling

The first and most common, method within the realm of air-based cooling is what's called 'cold aisle/hot aisle.' The idea is to separate the cold air from the hot air. This is done by facing the cold sides of each cabinet away from the hot sides of each cabinet, which creates a sort of convection system where the cabinets cool themselves. But this does not always work, and the data center managers have to pump a larger amount of cold air in. This older, inefficient method has limitations, which is why many data centers are moving towards new innovations. A similar process is called 'cold or hot air containment' focused on improving the older cold aisle/hot aisle method by physically isolating and containing the servers so the hot and cold air does not mix. Driving the air directly from the ***Computer Room Air Conditioning (CRAC)*** unit helps achieve this. (see [Figure 10.1.1](#)). This method works fairly well, but it does have the issue of hot spots.

The last method in the territory of air-based cooling is in-rack heat extraction. This method tries to achieve the same end goal of removing hot air but is done so by having compressors and chillers built into the rack itself. According to Schneider Electric, both Hot Aisle Containment (HACS) and Cold Aisle Containment (CACS) can provide savings. Hot aisle containment can provide 40% more savings than the Cold Aisle Containment. CACS traps the cold air within the system letting the rest of the data center become a hot-air return. While the HACS traps hot air and lets it leave through an exhaust system.

#### 10.1.2 Liquid-Based Cooling

Water-cooled racks and servers are the first methods in liquid-based cooling. In this method, water is used to cool the hot side of the cabinet to bring the temperature down. Because water conducts electricity, the water never touches the actual components. The water is contained in basins, which then flows through pipes through cooling tower pumps. The water then runs alongside the server behind a barrier. The cold water helps bring down the temperature of the components inside. This method works well, but the risk of leaks scares many data center managers from using it. The next liquid-based cooling method is liquid immersion cooling. In this method, liquid coolant flows across the hot components of a server cooling it down. The servers are fully emerged into the fluid. The way this is done is by using a dielectric fluid. This type of fluid does not conduct electricity but can damage components if not used properly. If this sparks your interest. (see [Figure 10.1.2](#)).

#### 10.1.3 Evaporative Cooling

Evaporative cooling is an old technology that is being incorporated to cool machines in data centers. It is also known as swamp cooling. This type of cooling system is fairly simple. Evaporative cooling takes the process of water evaporation and applies it to cool data centers. These swamp coolers have a wet pad or a wet filter. Excess heat is dissipated in the water of these pads or filters, which then cools the data center. This type of cooling works best in low humidity climates, like Los Angeles. The

---

<sup>132</sup> Michael Isberto, *Data Center News*, 2018.

only power that evaporative cooling needs are for the fan and the water pump. It doesn't need a compressor that most other cooling systems use. Evaporative cooling or swamp cooling is so simple

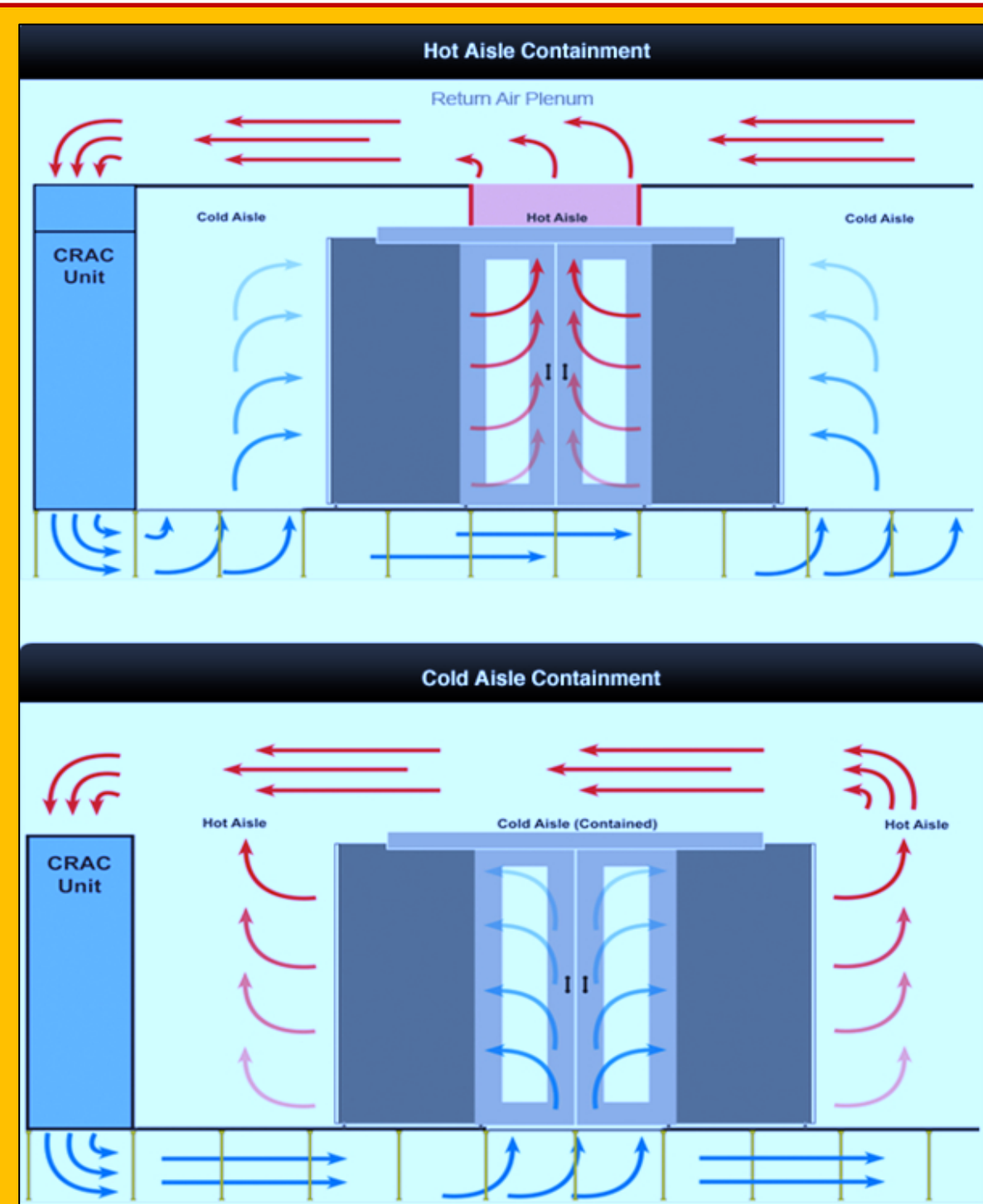


Figure 10.1.1 Cold or Hot Air Containment - Source: Submer

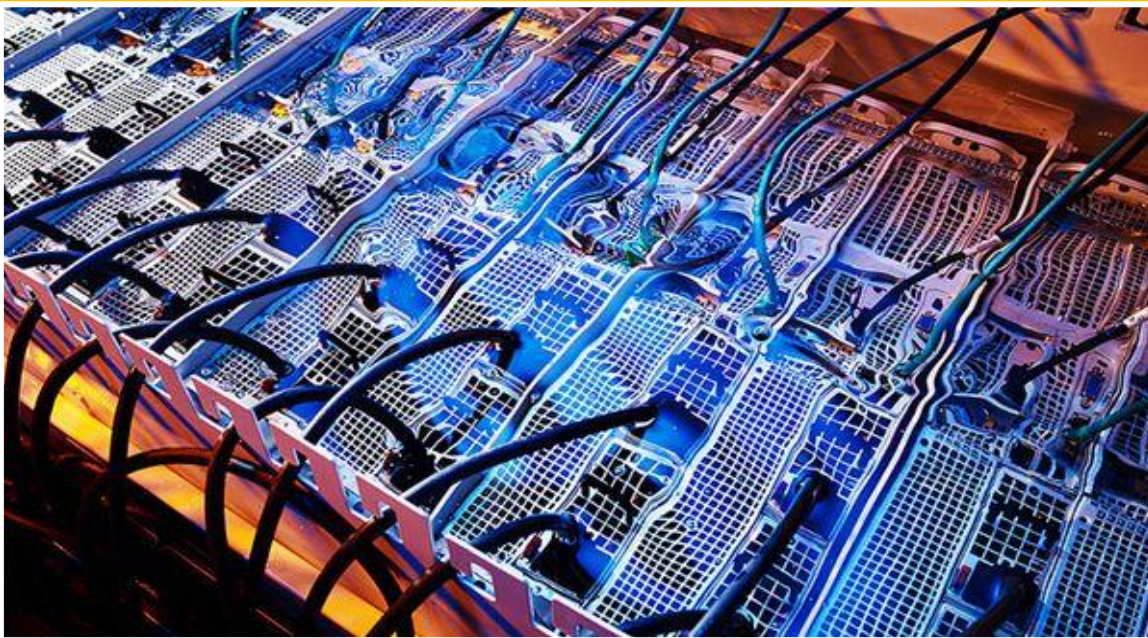


Figure 10.1.2 Liquid Based Cooling - Source: data center frontier

and needs so little power that it also has the nickname “free cooling” as well. Although the cost of evaporative cooling is more affordable than the most data center cooling systems, it is far from free. The average cost of evaporative cooling is 25% of traditional HVAC systems. Also, evaporative or swamp cooling comes at other costs. The term swamp cooling is not by accident. This type of system brings higher humidity levels into the data center, which typically isn’t good for any computer equipment. This is why evaporative cooling works best in dry climates or low

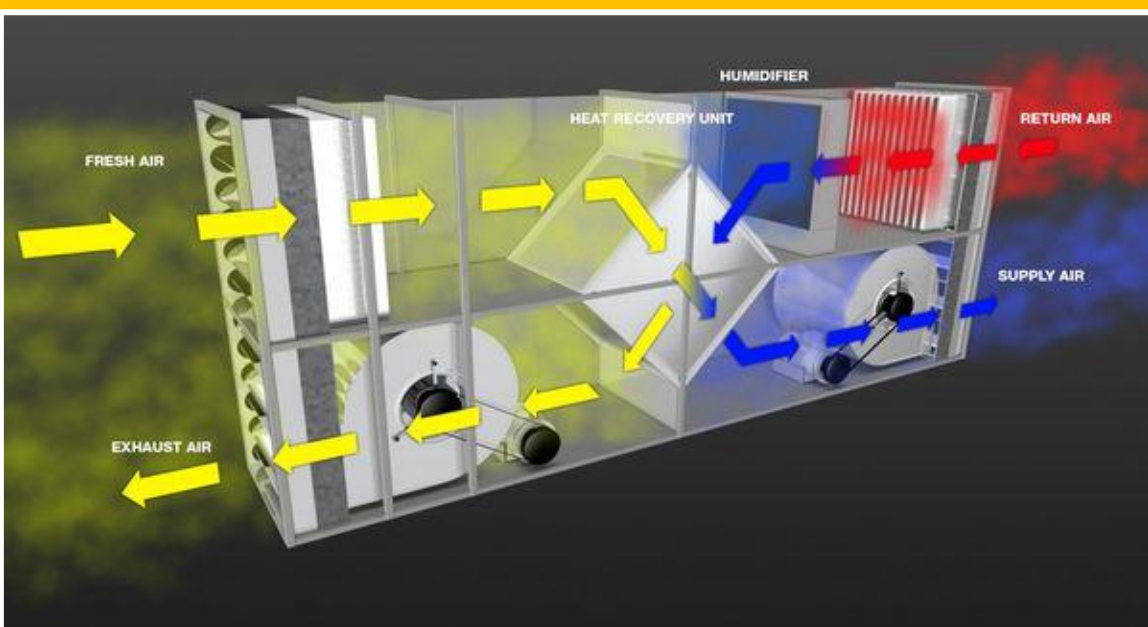


Figure 10.1.3 An Evaporated Cooling - Source: Condair

humidity environments so the humidity levels even out. Evaporative cooling is a great way for data centers to decrease their overall power usage significantly. (see [Figure 10.1.3](#)).

#### 10.1.4 What Are Some New Data Center Cooling Systems and Innovations?

There are many innovations from different companies that are changing the landscape of data center cooling. One notable mention is [Google's environmentally friendly data center](#). The search engine company is using seawater to cool one of their data centers in Hamina, Finland. This system doesn't need to burn any carbon but instead uses the cold water to cool the mechanism. In this system, Facebook also uses captured rainwater to do the same. [Data center smart assistant](#) and AI technology is also an important innovation when it comes to cooling a data center. It is reported that data centers use 75 percent more cooling than needed. According to [datacenterknowledge.com](#) (linked above), cooling a data center is there for risk management, but the amount of money spent on cooling is more than required. A smart assistant like [AdeptDC](#) helps data centers save on costs because it lets you know the data center manager know when and how much cooling is needed. It uses smart cooling and machine learning to [read CPU and GPU temperatures](#) and processes that data in real time. This software will help data centers become more cooling efficient.

Another new innovation is a [data center cooling robot](#) that monitors the temperature and humidity levels of the server from the inside of the cabinet. The [OneNeck](#) robot sensor is placed on the bottom of the cabinet and moves to the top and back down again scanning for heat and humidity levels. The robot is able to detect hot spots within the rack. One can check these levels from their smart device never having to open up the cabinet. This technology is smarter and more efficient allowing managers to cool only areas that need cooling. Instead of wasting energy cooling the entire data center. Facebook and Nortek Air Solutions have also collaborated on an indirect cooling system called [State Point Liquid Cooling \(SPLC\)](#). One of the main differences between SPLC and evaporative cooling is the SPLC uses cold water to cool the air instead of using cold air to cool the water. Through a membrane separation layers, the system can use both cold weather and hot and humid weather to produce water, which it then uses to cool the air inside the data center. Facebook estimates this system can [cut water usage by 20 percent](#). For additional information, please consult the posting in 2019 Colocation America Inc.

## 10.2 Case Study 1 - Smart Cooling of Data Centers

**Authors :** Chandrakant D. Patel, Cullen E. Bash, Ratnesh Sharma, Monem Beitelmal, Rich Friedrich  
**Citation :** Patel, CD, Bash, CE, Sharma, R, Beitelmal, M, & Friedrich, R. "Smart Cooling of Data Centers." Proceedings of the ASME 2003 International Electronic Packaging Technical Conference and Exhibition. 2003 International Electronic Packaging Technical Conference and Exhibition, Volume 2. Maui, Hawaii, USA. July 6–11, 2003. pp. 129-137. ASME. <https://doi.org/10.1115/IPACK2003-35059>

The data center of tomorrow is characterized as one containing a dense aggregation of commodity computing, networking and storage hardware mounted in industry standard racks (Patel, et al, 2003)<sup>133</sup>. In fact, the data center is a computer. The walls of the data center are akin to the walls of the chassis in today's computer system. The new slim rack mounted systems and blade servers enable reduction in the footprint of today's data center by 66%. While maximizing computing per unit area, this compaction leads to extremely high power density and high cost associated with removal of the dissipated heat. Today's approach of cooling the entire data center to a constant temperature sampled at a single location, irrespective of the distributed utilization, is too energy inefficient. We propose a smart cooling system that provides localized cooling when and where needed and works in conjunction with a compute workload allocator to distribute compute workloads in the most energy efficient state. This paper shows a vision and construction of this intelligent data center that uses a combination of modeling, metrology and control to provision the air conditioning resources and workload distribution. A variable cooling system comprising variable capacity computer room air conditioning units, variable air moving devices, adjustable vents, etc. are used to dynamically allocate air conditioning resources where and when needed. A distributed metrology layer is used to sense environment variables like temperature and pressure, and power. The data center energy manager redistributes the compute workloads based on the most energy efficient availability of cooling resources and vice versa. The distributed control layer is no longer associated with any single localized temperature measurement but based on parameters calculated from an aggregation of sensors. The compute resources not in use are put on "standby" thereby providing added savings.

### 10.2.1 Motivation

In examining the motivation behind the need for smart cooling of data centers, we must begin by reviewing the state of the art in data center design and control<sup>134</sup>. The **computer room air conditioning (CRAC)** units are sized by adding up the heat loads and matching the capacity. The control of the cooling resources in today's data center takes the form of setting the "set point" temperature on the CRAC units qualitatively and moving or opening the supply vent tiles by intuition. Typically, distributed sensing in a data center is availed by a person walking around the data center or through an ad hoc distribution of sensors. Based on the sensed temperature qualitative decision is made on "set point" temperatures of individual CRAC units and on adjusting or moving the supply vent tiles. The set point in today's data center is the return air temperature to the individual CRAC. No information is obtained about the local conditions making it difficult to properly set the optimum operating points of the CRAC units. Furthermore, the air flow distribution in the data center is conducted through manual and qualitative changing of air supply openings. This type of approach, one that maintains the temperature based on return air set point to the CRAC units and strives to

<sup>133</sup> Chandrakant D. Patel, Cullen E. Bash, Ratnesh Sharma, Monem Beitelmal, Rich Friedrich, "Smart Cooling of Data Centers", Proceedings of IPACK'03 International Electronic Packaging Technical Conference and Exhibition July 6–11, 2003, Maui, Hawaii, USA.

<sup>134</sup> Schmidt, R, Shaukatullah, H, Computer and Telecommunications Equipment Room Cooling: A Review of Literature, Eighth Intersociety Conference on Thermal and Thermomechanical Phenomena in Electronic Systems" San Diego, California, 2002.

keep a constant mixed air temperature in a data center, is very energy expensive<sup>135</sup>. A 10,000 square foot data center, with hundreds of 10KW racks, requires hot zones and cold zones, also called hot aisles and cold aisles in a data center. In fact, there is universal agreement on the need to maintain hot and cold aisles. Indeed, we believe there needs to be a fluidic separation of hot and cold streams. The hot return air stream to the CRAC units must return at the highest possible temperature, typically exhaust temperature from the racks. However, in the highly complex thermo-fluids data center environment, this vision can only be realized with numerical analysis and maintained with dynamic quantitative control.

Previous papers have noted that for the high power density data center of tomorrow, one with heat load reaching 2700 W/m<sup>2</sup> (ratio of gross heat load to gross floor area), designing the air conditioning system using a simple energy balance is no longer adequate<sup>136</sup>. Indeed, energy balance is the first necessary step, but using it alone leads to average provisioning of the air conditioning resources e.g. for a data center with a heat load of 1 MW, and ten CRAC units with 100 KW sensible heat removal, the assumption is that all the units are provisioned appropriately when the data center is in operation. However, it has been shown by [Patel et. Al]<sup>137</sup> that the thermo-fluids behavior is very complex for a high power density data center and the actual provisioning depends on the geometry of racks, air vents, and the heat load distribution. The authors note that it is necessary to model the air flow and temperature distribution in the data center through computational fluid dynamics modeling to provision the air conditioning resources. We term the provisioning of the air conditioning resources through numerical modeling for a given distribution of heat load as static provisioning and “static smart cooling”.

### 10.2.2 Static Smart Cooling

**Figure 10.2.1** shows a typical raised floor data center. The modular CRAC units sized for the overall heat load are located in the data center. The exhaust hot air from the racks is pulled into the CRACs and cooled to approximately 12oC to 20oC by direct expansion or chilled water coils. A typical 3 m by 0.9 m by 1.8 m modular AC unit has a maximum sensible heat removal capacity of 95 KW. The cool air is recirculated back to the racks through vented tiles in the raised under-floor plenum. The air movers in a modular AC unit have a typical volumetric

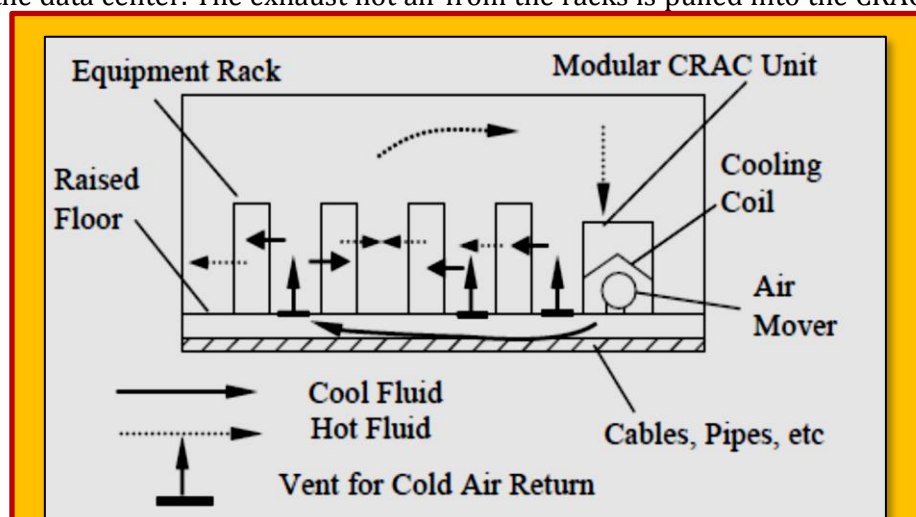


Figure 10.2.1 Typical Data Center Configuration

<sup>135</sup> Bash, C.E., Patel, C.D. and Sharma, R.K., "Efficient Thermal Management of Data Centers – Immediate and Long-Term Research Needs", J. HVAC&R Res., April, 2003.

<sup>136</sup> Patel, C.D., Bash, C.E., Belady, C., Stahl, L., Sullivan, D., July 2001, Computational fluid dynamics modeling of high compute density data centers to assure system inlet air specifications, Proceedings of IPACK'01 – The Pacific Rim/ASME International Electronics Packaging Technical Conference and Exhibition, Kauai, Hawaii.

<sup>137</sup> Patel, C.D., Sharma, R.K, Bash, C.E., Beitelmal, A, Thermal Considerations in Cooling Large Scale High Compute Density Data Centers," 8<sup>th</sup> Intersociety Conference on Thermal and Thermomechanical Phenomena in Electronic Systems" San Diego, California, 2002.

delivery of approximately 5.7 m<sup>3</sup>/sec (~12,000 CFM). The air movers pressurize the plenum with cool air. The cool air enters the data center through vented tiles near the inlet of the racks. As the CRACs are sized for the overall load in the data center, the average provisioning is anticipated. However, the actual provisioning depends on the distribution of air flow devices and the heat load.

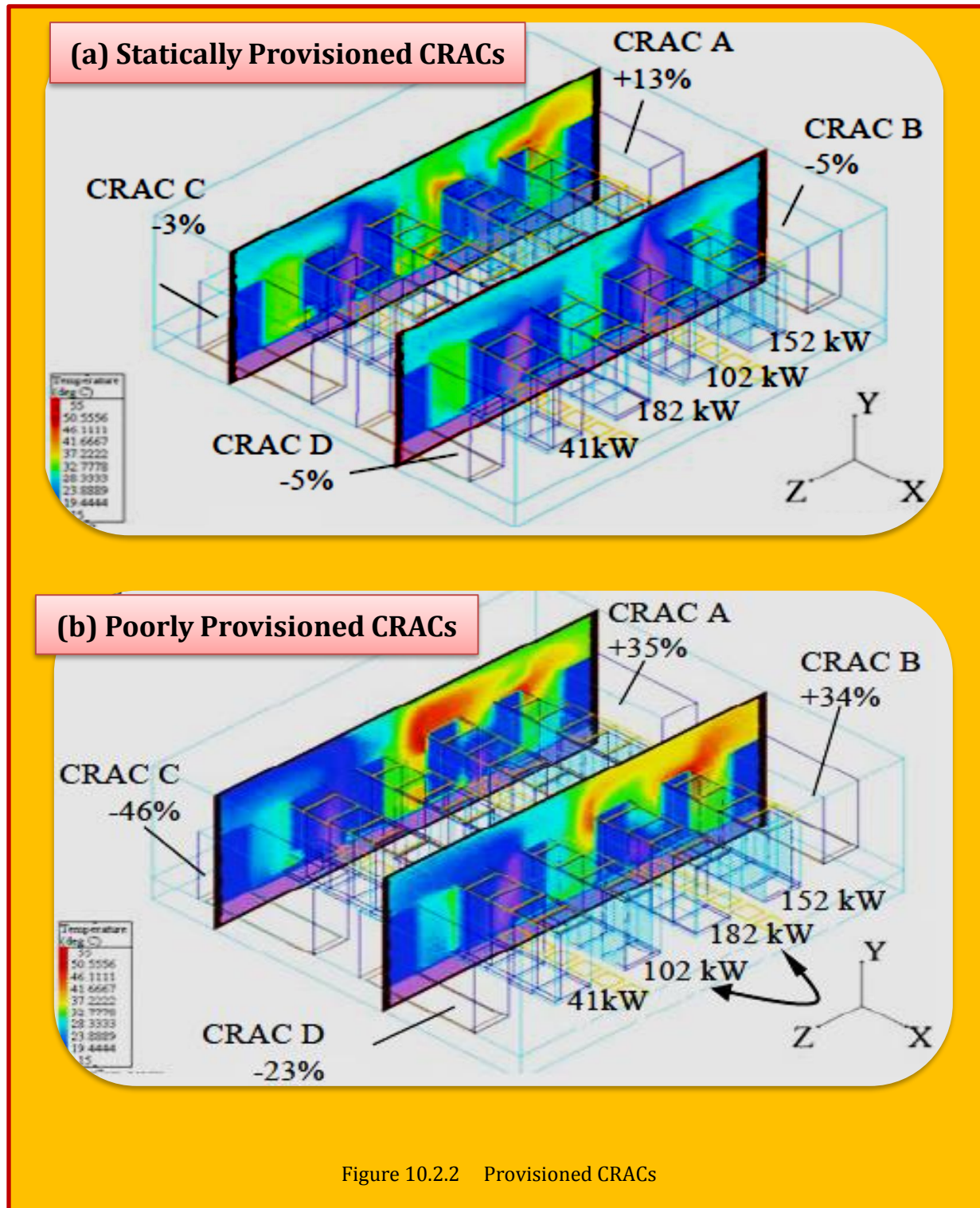


Figure 10.2.2 Provisioned CRACs

**Figure 10.2.2 (a)** shows a row-wise distribution of heat load for a combination of compute, storage and networking equipment and a given distribution of inlet vent tiles. The computational fluid dynamics modeling shows the CRACs are provisioned to within 15% of their capacity. **Figure 10.2.2 (b)** shows the same geometry in the data center, but with a swapped row-wise (102 KW and 182 KW row) distribution of heat loads. The provisioning in this case is completely out of balance. The CRACs on one side are grossly under provisioned for the data center, and are undersized by 35%. Therefore, for any data center, for various distributions of heat load and given air conditioning resources, one has to determine the statically balanced provisioned state. A data center would have many statically provisioned states built through the modeling of the type shown by [Patel et. al]<sup>138</sup>. While the raised floor infrastructure is a common approach used in data center cooling, the details presented herein apply to other approaches e.g. ceiling based heat exchangers<sup>139</sup> and office type cooling distribution.

### 10.2.3 Dynamic Smart Cooling

A smart-cooled data center must contain a feedback control system that continually provisions the cooling resources based on given distribution of workloads. Indeed, a modern data center must further schedule compute workloads in the data center in a way that minimizes the energy use for cooling purposes. In the context of utility computing, it is assumed that compute resources will not be dedicated to a particular user. Rather, compute resources will be allocated dynamically when the need arises. Therefore, in the context of this modern paradigm, dynamic smart cooling is envisioned as one that apportions its cooling and workloads with the objective of minimizing energy use by the cooling resources. It provides just the right amount of cooling where and when it is needed i.e. dynamically provisions cooling in a data center based on heat loads. And, it redistributes the workload based on the most energy efficient availability of cooling resources. Implicit in the workload distribution proposal is that there exist some elasticity in power draw by machines. In our characterization of slim 1U (44 mm high) servers running Windows, we observed a ranging of power from 120 W to 180 W from idle to running fully busy. Furthermore, as the world moves to utility computing, it will be necessary to have a “standby” or “off” functionality on machines and the ones not in use will be required to be powered off. Running the systems at “busy” anticipating loads that only occur at a given time during the day, as some systems of today do, is prohibitively expensive. While a modern house can manage energy using multiple zones, a data center presents a much more complex picture. A house has walls, low heat load and very slim air movement. However, a data center, especially one at 2700 W/m<sup>2</sup>, has high air flow movement and in order to facilitate proper thermal management and minimize energy use, fluidic boundaries separating hot zones and cold zones are required. The hot fluid Q from the exhaust of racks must make its way back to the CRAC units with minimal infiltration into cold aisles or zones as such infiltration increases the temperature of the cold supply air. The prediction of the level of infiltration, and its impact on provisioning of CRAC units, is complex. Sharma et. al. proposed dimensionless data center figures of merit based on the characterization of heat infiltration [8][8]. The figures of merit, called RHI (return heat index) and SHI (supply heat index) are indicators of the degree of provisioning and infiltration in a data center. Denoting actual heat load by Q, Supply Heat Index (SHI) for the data center is given by:

---

<sup>138</sup> Patel, C.D., Sharma, R.K, Bash, C.E., Beitelmal, A, *Thermal Considerations in Cooling Large Scale High Compute Density Data Centers*, " 8<sup>th</sup> Intersociety Conference on Thermal and Thermomechanical Phenomena in Electronic Systems" San Diego, California, 2002.

<sup>139</sup> Patel, C.D., Bash, C.E., Belady, C., Stahl, L., Sullivan, D., July 2001, *Computational fluid dynamics modeling of high compute density data centers to assure system inlet air specifications*, Proceedings of IPACK'01 – The PacificRim/ASME International Electronics Packaging Technical Conference and Exhibition, Kauai, Hawaii.

$$SHI = \frac{\delta Q}{Q + \delta Q} = \frac{\text{aisle cold in on infiltration due to rise Enthalpy}}{\text{exhaust rack at the rise EnthalpyTotal}}$$

#### Eq. 10.2.1

The numerator ( $\delta Q$ ) denotes the sensible heat gained by the air in the cold aisle before entering the racks while the denominator represents the total sensible heat gain by the air leaving the rack exhausts. Since the mass flow rates at the inlet and outlet of each rack are equal,  $SHI$  can be rewritten as a function of rack inlet, rack outlet and CRAC outlet temperatures.

$$SHI = \left[ \frac{\sum_j \sum_i (T_{in}^r)_{ij} - T_{ref}}{\sum_j \sum_i (T_{out}^r)_{ij} - T_{ref}} \right]$$

#### Eq. 10.2.2

$SHI$  can be calculated for individual servers, racks or data centers. Conversely,  $RHI$  denotes the mixing of the cold air with the return hot air to the CRAC units. It has been shown that  $SHI$  represents the thermodynamic irreversibility in the data center due to mixing of hot and cold air in the cold aisle. Therefore, in order to provide data center control, we draw upon this research in data center fluid flow.  $RHI$  and  $SHI$  are proposed as control parameters for data centers built with variable air conditioning resources. The ability to vary air flow and cooling coil temperature to stay in a dynamically provisioned state for a given load would allow us to reduce energy associated with flow work (work done to distribute cool air) and thermodynamic work (work done to extract heat from the hot exhaust air). If the data center with flexible cooling resources has the proper distributed metrology and a control system, we would have the makings of a smart data center. Thus, dynamic smart cooling is availed by building a data center with the following salient attributes:

- Distributed sensing
  - Temperature sensors on the racks measuring supply and exhaust air temperature to the systems.
  - Temperature sensors in the aisles measuring three dimensional temperature distribution in the data center.
  - Temperature sensors at the CRAC return and supply.
  - Pressure sensors in the air distribution plenum.
  - Power drawn by machines (if available).
- Variable air conditioning resources
  - Variable air flow devices to modulate flow work.
  - Variable cooling coil temperature in the CRACs to modulate thermodynamic work.
- Data aggregation system
  - Collect sensed data from thousands of locations.
  - Present visually the real time power draw.
  - Calculate data center figure of merit control parameters e.g.  $RHI$  and  $SHI$ .
- Control system
  - Modulate the variable air conditioning resources through a control algorithm for a given distribution of workloads (heat loads).
- Data Center Manager (Computer Science Element)
  - Workload scheduler that uses thermal policies to distribute workloads in the data center.

#### 10.2.4 Smart Cooled Data Center Concept

The sketch, Error! Reference source not found., shown below is the holistic concept we envision for a smart data center. Our driving motivation behind the entire approach is to get a combined energy savings, through air conditioning and work load placement, of approximately 50% over today's

energy use for cooling purposes. For an example data center which draws 5 MW of power for compute resources, this would imply 1.25 MW of electricity draw for cooling resources instead of the ~2.5 MW required by conventional designs. At \$100 per MWh, this would result in annual savings of approximately a million dollars. shows the concept of a data center, containing the key attributes noted in the previous section.

With reference to variable air conditioning resources, shows a CRAC with variable frequency drive for control of blower speed. A three way valve controls the mass flow of chilled water through the CRAC units. The vent tile shown is a "smart tile" - an actuated tile that can be commanded to vary its resistance to fluid flow. Power meters in the plenum sense the power distribution to the racks. The temperature at rack level,  $T_{ij}$ , are sensed by static sensors at the rack exhaust and supply. The return air temperature,  $T_r$ , is sensed at the CRAC return vent. The room temperatures are sensed by an autonomous mobile robot traversing the aisles with temperature sensors attached to a pole at various heights. The UDC (utility data center) controller<sup>140</sup> is the data center collection and evaluation engine. The controller changes  $T_{set}$ , the CRAC set point, in response to the local need. The roof top external condenser shown on the sketch is the heat exchanger (cooling tower) that rejects the heat to the environment. Rejecting the heat at a night time ambient of 20°C at New Delhi will result in a lower lift from evaporator to the condenser<sup>141</sup>. Thus, with respect to the vapor compression cycle, a better cycle efficiency will be availed over a Phoenix day time ambient of 45°C. Global workload, therefore, is placed according to the most energy efficient location in the world with reference to

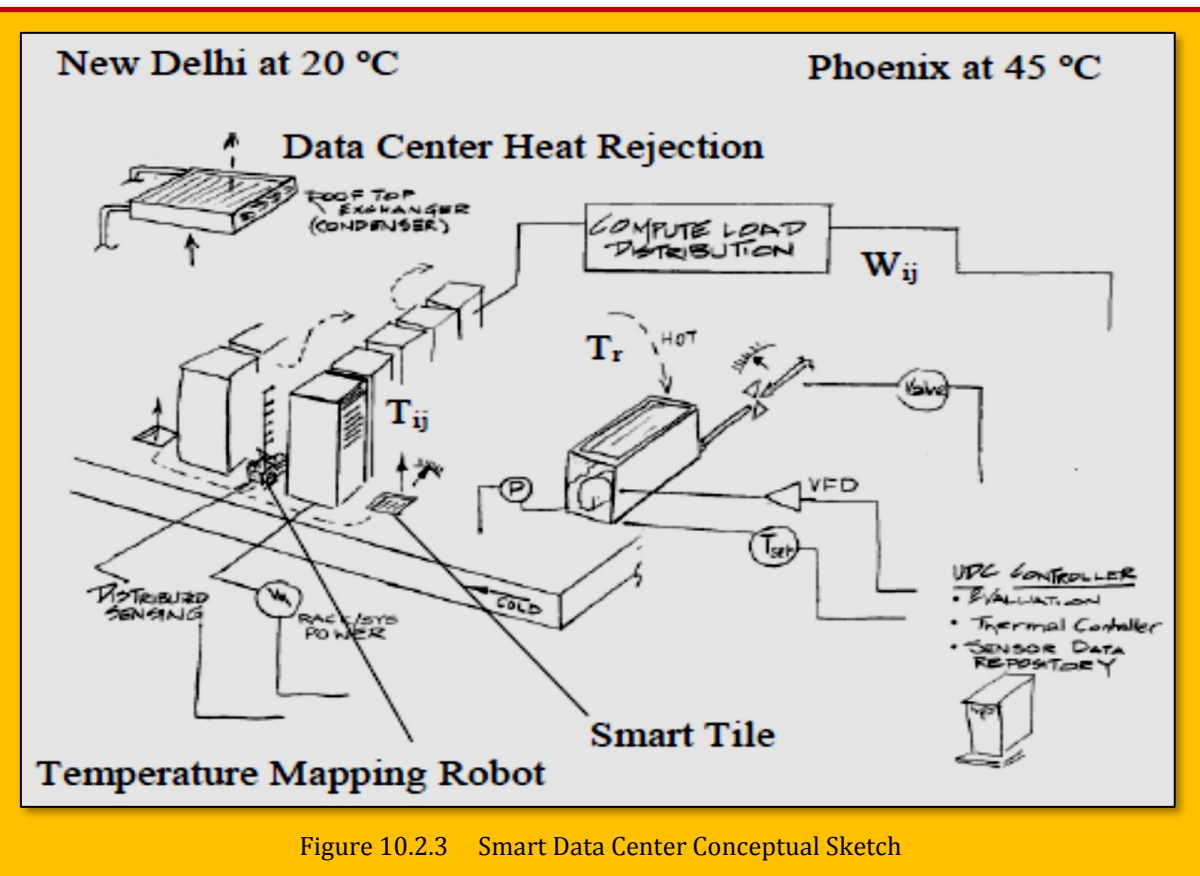


Figure 10.2.3 Smart Data Center Conceptual Sketch

<sup>140</sup> J. Rolia, S. Singhal, R. Friedrich, "Adaptive Internet Data Centers," SSGRR 2000, European Computer and eBusiness Conference, L'Aquila, Italy, July 2000.

<sup>141</sup> Engineering Thermodynamics, by Reynolds, W.C., and Perkins, H.C., McGraw Hill Inc., 1977.

GRID based computing<sup>142-143-144</sup>.

### 10.2.5 Construction of The Smart Data Center

To investigate this concept of smart cooling of data centers, we have constructed a data center at Hewlett-Packard Laboratories in Palo Alto, California that serves the dual purposes of providing a production information technology (IT) environment while serving as a test vehicle for air conditioning and workload placement research. The IT department is using the HP Utility Data Center core for the computer, networking and storage farm. Besides the production racks, rack thermal loads are employed to allow a controlled study. The first three key attributes noted in the previous section under dynamic smart cooling have been implemented and experimental work has begun. **Figure 10.2.3** shows the sketch of the implementation. A return air plenum, not shown in **Figure 10.2.4**, provides an alternate return path for the hot air. The return air can be routed through the exhaust air ceiling plenum or through the room or a combination of the two paths. For complete information, please consult the work by [Patel, et al]<sup>145</sup>.

Thermistors are used as fixed sensors to measure the temperature at the exhaust and supply to the racks. shows the robotic sensing device with a data acquisition unit for temperature mapping. It carries a pole with sensors at various heights and an onboard computer for data acquisition. The computer is on a wireless local area network. The robot is to be event driven and designed to determine the temperature distribution in the aisles when required. It has an onboard laser for ranging and obstacle avoidance. The laser is also used to map the data center. The robot is then programmed to follow the shortest path to given goals – locations from where temperatures are to be reported measured.

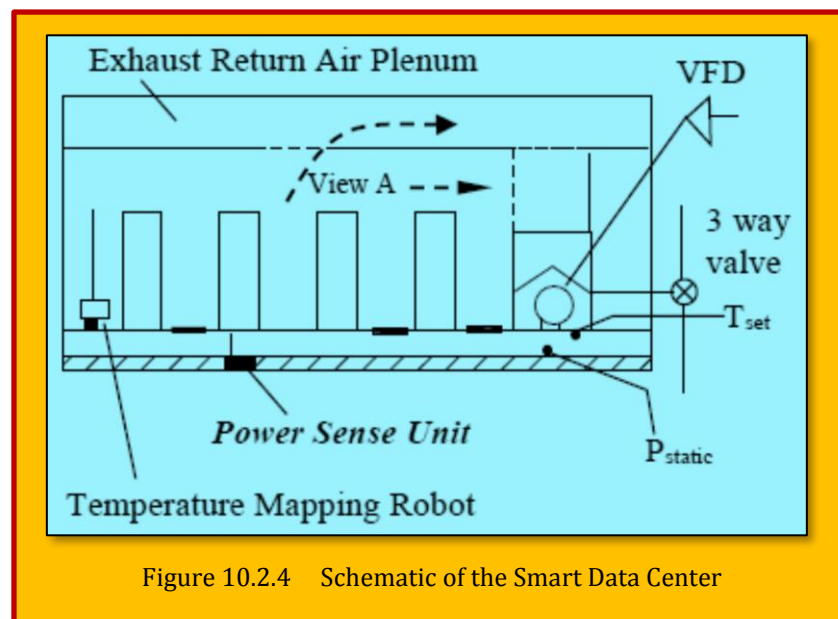


Figure 10.2.4 Schematic of the Smart Data Center

<sup>142</sup> Thilmany, J., Mar 2003, "Getting on the Grid", Mechanical Eng., No.3, Vol. 125, pp46-48.

<sup>143</sup> Ian Foster, Carl Kesselman (Eds.): *The Grid: Blueprint for a New Computing Infrastructure*, Morgan Kaufmann Publishers, 1999.

<sup>144</sup> Patel, C.D., Sharma, R.K, Bash, C.E. and Graupner, S., "Energy Aware Grid: Global Workload Placement based on Energy Efficiency", Hewlett-Packard Laboratories Technical Report: HPL-2002-329

<sup>145</sup> Chandrakant D. Patel, Cullen E. Bash, Ratnesh Sharma, Monem Beitelmal, Rich Friedrich, "Smart Cooling of Data Centers", Proceedings of IPACK'03 International Electronic Packaging Technical Conference and Exhibition July 6-11, 2003, Maui, Hawaii, USA.

### 10.2.6 Work Underway To Develop The Control Systems

The evaluation algorithms are currently under investigation and will be described in a subsequent report. There are two primary classes of control systems that are being considered as shown in **Figure 10.2.5**, classical multi-input, multi-output feedback control, and agent based control. The primary differences among the approaches is lie in the distribution of the decision making decision-making. Feedback control is a centralized control structure with control decisions throughout the system made from a single algorithm. Agent based systems (e.g. market-based control systems), by contrast, are distributed systems where local agents can make limited control decisions based on local data collection. More sophisticated systems can employ a hierarchy of agents through which data can be shared to enable decision making at the local (e.g. smart tiles) and global (e.g. CRAC supply temperatures and air flow rates) levels. An appropriate data center control system will have the following attributes:

- Stability;
- Response time on the order of 30 seconds;
- Flexibility and adaptation to changes in boundary conditions – especially changes in computer equipment layout;
- Minimization of zonal and local SHI.

As previously discussed, SHI is a measure of heat infiltration into cold aisles. Minimization of SHI implies a minimization of rack inlet air preheat. While other parameters may also contribute to the control algorithm, SHI should be used as the primary control parameter to insure inlet air specifications are met by using the least amount of energy. While developing the control system is critical, the first step of the work is focused on static smart cooling for varying conditions and determination of savings in energy consumption. The experiments are focused on achieving statically achieving statically provisioned states for various changes introduced into the system e.g. changes in workload distribution, change to air flow by shutting off the ceiling return, etc. Experiments also include use of “thermal policies” developed by thermo-fluids modeling and metrology to migrate and allocate workloads.

### 10.2.7 Summary & Conclusions

The availability of slim servers enables tremendous reduction in data center footprint. In financial districts of the world, such as London and New York with real estate at \$100 per square foot per year, the reduction in data center overall area is an attractive option. Furthermore, with pervasive computing, data centers are expected to have a global presence. As these data centers present a

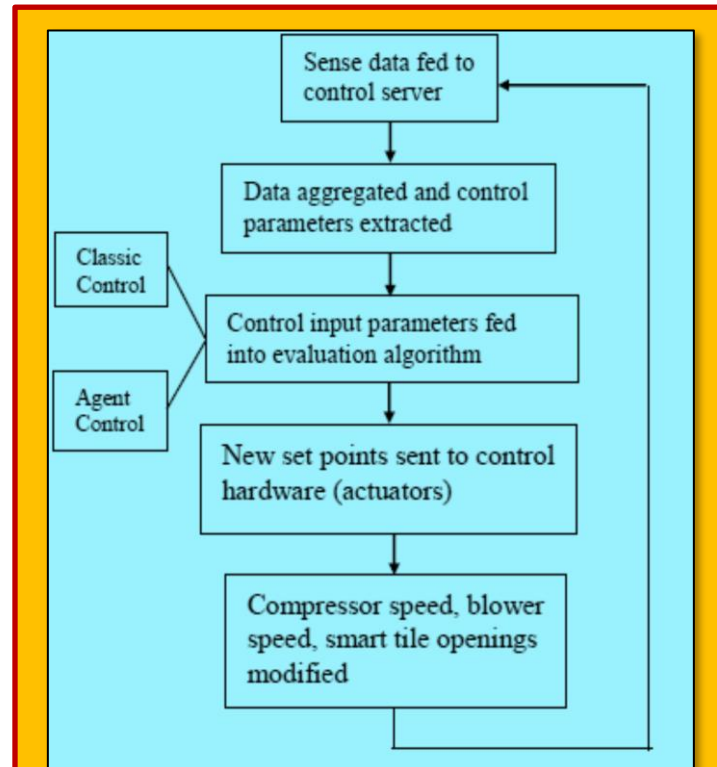


Figure 10.2.5 Data Center Control Diagram

challenge in power delivery and cooling, we propose an intelligent data center that manages energy as a resource. However, these data centers cannot be designed by intuition alone due to the complex thermo-fluids behavior. To that end, we propose use the principles of heat transfer and fluid flow to define dimensionless numbers that can be used as control points to allocate compute workloads and cooling with the intent of minimizing energy use.

### 10.3 Case Study 2 - Performance Assessment of Cooling Systems for Data Centers with New Thermal Metric

**Citation :** Behzad Norouzi-Khangah, Mohammd Bagher Mohammadsadeghi-Azad, Seyed Morteza Hoseyni, Seyed Mohsen Hoseyni, *Performance assessment of cooling systems in data centers; Methodology and application of a new thermal metric*, *Case Studies in Thermal Engineering*, Volume 8, 2016, Pages 152-163, ISSN 2214-157X, <https://doi.org/10.1016/j.csite.2016.06.004>. (<https://www.sciencedirect.com/science/article/pii/S2214157X1630034X>)

(Norouzi-Khangah et al., 2016)<sup>146</sup> introduces a comprehensive cooling index to assess performance of cooling systems in data centers and demonstrates its application on a real case by using CFD method. The proposed methodology provides a metric for comparing and ranking of the cooling efficiency of the air distribution configurations among available designs alternatives.

#### 10.3.1 Introduction

Data center is a facility containing computer equipment and related devices such as storage systems of a tele-communication system. These devices consist of power supply, air conditioner, fire-fighting devices and security systems<sup>147</sup>. Air conditioner of data centers should work full time all over the year to remove the heat added to the system by operation of different devices. Development of telecommunication industry, therefore, made data center a common element for either general or dedicated usage<sup>148</sup>. Heat propagation increases the temperature and causes damage to rackservers; therefore protection of system and prolonging their life by cooling the inherent devices is of crucial importance. In other words, it's very significant to design an appropriate air conditioner to protect data center from destruction caused by heating. For proper operation of devices, they should be held on a certain and proper temperature. Each IT server should receive certain amount of cool air enough for the removal of the produced heating<sup>149</sup>. Appropriate operation of equipment depends on proper distribution of cool air on data center and the response of supply air to the demand of components. CFD is an assisting tool to configure the hall of devices. Some indexes are used for quantitative assessment of efficient performance of cooling systems. In practice, influence of the design factors is quantified using cooling indexes such as **SHI**, **RHI**, **RCI** and **RTI** (described in detail later) for different models where each index indicates specific aspect of operation in the cooling systems; however in some cases the mismatch among existing approaches might end up with irrelevant results which makes decision making process a challenge. To overcome the deficiencies of this area, herein, we propose a new framework for the quantification and ranking of the performance of cooling systems in data centers by using the results of CFD analysis. In the sequel, first we will review the existing cooling indexes and the theory behind them. Then a new cooling index is proposed for more efficient estimation of the cooling performance of the data center and finally, its application will be elaborated on a real case in Iran considering different configurations for the design of cooling system.

<sup>146</sup> Behzad Norouzi-Khangah, Mohammd Bagher Mohammadsadeghi-Azad, Seyed Morteza Hoseyni, Seyed Mohsen Hoseyni, "Performance assessment of cooling systems in data centers; Methodology and application of a new thermal metric", <http://dx.doi.org/10.1016/j.csite.2016.06.004>.

<sup>147</sup> N.M.S Hassan, M.M. K.Khan, M.G. Rasul, *Temperature monitoring and CFD analysis of data center*, (2013).

<sup>148</sup> J.Cho ,B.S.Kim, *Evaluation of air management system's thermal performance for superior cooling efficiency in high-density data centers*, *J. Energy Build.* (2014)2145–2155.

<sup>149</sup> J. Priyadumkol, C. Kittichaikarn, *Application of the combined air conditioning systems for energy conservation in data center* *J. Energy Build.*(2014).

### 10.3.2 Indexes for Assessing Data Center Cooling

[Shrivastava et al.]<sup>150</sup> introduced a dimensionless parameter that is a norm of cooling performance in rack level. [Noh et al.]<sup>151</sup> used three different methods to design data center with 5–6 KW racks. In communication equipment centers three states 'horizontal air supply and return flow system model', 'underfloor air supply and overhead return flow system model', and 'overhead air supply and underfloor return flow system model' were investigated and results showed that 'underfloor air supply and overhead return flow system model' state has better performance. [Cho et al.]<sup>152</sup> assessed the performance of air distribution system to reduce energy consumption in high-density data centers. 46 models for air distribution were studied and results showed that temperature of output air of package has the most pronounced effect on flow efficiency. In addition, it stated that closing the chamber of aisle can increase the temperature of output air of package up to 22 °C (without decreasing the efficiency).

#### 10.3.2.1 Return Heat Index (RHI) and Supply Heat Index (SHI)

[Sharma et al.]<sup>153</sup> introduced two dimensionless parameters called supply heat index (SHI), and return heat index (RHI) which are used to assess the temperature performance of data center. These indexes can be used for investigation of convective air flow in equipment room with raised-floor. Energy efficiency depends not only on the type of cooling system but also on the configuration of equipment room that influences the mixing of cold and hot air. [Herrlin]<sup>154</sup> studied the return heat index (RHI) that is a measure of net level of by-pass air or net level of recirculation air in data center. Both of them have deficient effects on total energy and temperature efficiency of air in that area. RHI and SHI indicate the mixing of input cool air flow to the rack and output hot air flow from the rack. These indexes are formulated as follows:

$$\text{SHI} = \frac{\delta Q}{Q + \delta Q} , \quad \text{RHI} = \frac{Q}{Q + \delta Q}$$

#### Eq. 10.3.1

where  $Q$  is the total heat propagation of racks and indicates the amount of cool air enthalpy increase before its entering to the rack, i.e.:

$$Q = \sum_j \sum_i m_{ij}^r C_p [(T_{out}^r)_{ij} - (T_{in}^r)_{ij}]$$

#### Eq. 10.3.2

where  $m_{ij}^r$  is the entrance flow to the  $i$ th rack in the  $j$ th row. The relation between RHI and SHI is shown below:

$$\text{SHI} + \text{RHI} = 1$$

#### Eq. 10.3.3

<sup>150</sup> S.K. Shrivastava, J.W. VanGilder, B.G. Sammakia, *Prediction of cold aisle end air flow boundary conditions using regression modeling*, IEEE (2009).

<sup>151</sup> H.Noh ,K.Song, S.K.Chun, *The cooling characteristic con the air supply and return flow system in the telecommunication cabinet room*, Proceedings of International Telecommunications Energy Conference (INTELEC), Vol.33,No.2,1998.

<sup>152</sup> J.Cho,J.Yang, W.Park, *Evaluation of air distribution system's airflow performance for cooling energy savings in high-density datacenters*, Energy Build. 68(2014)270–279.

<sup>153</sup> R.K. Sharma, C.E. Bash, C.D. Patel, *Dimensionless parameters for evaluation of thermal design and performance of large scale data centers*, AIAA (2002)3091–3101.

<sup>154</sup> M.K. Herrlin, *Rack cooling effectiveness in data centers and telecom central offices: the rack cooling index (RCI)*, ASHRAE Transactions, 2005.

As much RHI increases, SHI will decrease and the design will approach to the ideal design of cooling system for data center. This condition shows less mixing of cool air with the output hot air from the rack. Usually RHI (80%) is acceptable.

### 10.3.2.2 Rack Cooling Index (RCI)

Rack cooling index has been introduced by [Herrlin]. RCI is a measure of rack cooling and consists of two equations; one indicates allowable area for low rack temperature ( $RCI_{LO}$ ) and the other for high rack temperature ( $RCI_{HI}$ ). As it implies,  $RCI_{HI}$  more than 95% is desirable (see [Norouzi-Khangah et al.]<sup>155</sup>). Current index deals with temperature of cool air, in other words, the condition that cooled racks need to keep up their operation. When the inlet temperature of racks becomes more than maximum allowable temperature, the over temperature of the devices will occur. Summation of over temperature of each rack is called total over temperature. Under temperature appears on the other hand when the inlet temperature of racks becomes less than minimum recommended temperature. The limitation of recommended temperatures depends on the instruction that is used, usually provided by the standards and regulations. An efficient measurement of rack cooling can be depicted using graphical presentation. RCI indexes should be shown by understandable numbers which alter between 0% and 100%. The 100% value shows that all racks have cooled by a specific guide or standard. The criterion of a harmful condition should be defined. These indexes must be independent of measurement units and also be matched with each standard which recommended minimum and maximum temperature. In this case the indexes can be used in conjunction with standards. RCI consists of two parts which illustrates the safety of server room in both sides of temperature limitation.  $RCI_{HI}$  is defined by:

$$\begin{aligned} RCI_{HIGH} &= \left[ 1 - \frac{\text{Total Over Temperature}}{\text{Max Allowable Over Temperature}} \right] \times 100\% \\ &= \left[ 1 - \frac{\sum(T_i - T_{max-rec})_{T_i > T_{max-rec}}}{n \times (T_{max-all} - T_{max-rec})} \right] \times 100\% \end{aligned}$$

**Eq. 10.3.4**

$RCI_{HI}$  is a scale of over temperature absence. 100% value represents that over temperature does not occur. As much as it decreases, the probability of over temperature increases. The interpretation of this index is shown in **Table 10.3.1**. Similar index can be defined considering low temperatures.  $RCI_{LO}$  is the complement of  $RCI_{HI}$ , especially when the temperature of supply is lower than what is recommended. In this situation the indexes can be used as alternate of each other. As the low temperature is less harmful for the system, the concentration should be on  $RCI_{HI}$ .  $RCI_{LO}$  is defined by:

$$\begin{aligned} RCI_{LOW} &= \left[ 1 - \frac{\text{Total Under Temperature}}{\text{Max Allowable Under Temperature}} \right] \times 100\% \\ &= \left[ 1 - \frac{\sum(T_{min-rec} - T_i)_{T_i < T_{min-rec}}}{n \times (T_{min-rec} - T_{min-all})} \right] \times 100\% \end{aligned}$$

**Eq. 10.3.5**

---

<sup>155</sup> Behzad Norouzi-Khangah, Mohammd Bagher Mohammadsadeghi-Azad, Seyed Morteza Hoseyni, Seyed Mohsen Hoseyni, "Performance assessment of cooling systems in data centers; Methodology and application of a new thermal metric", <http://dx.doi.org/10.1016/j.csite.2016.06.004>.

$RCI_{HI}$  is the most significant index in designing the plant of data center and other indexes would not be studied if this index is not in the appropriate range. Increasing the rate of input air to the racks improves this index and raises the energy consumption as is inferred from **Eq. 10.3.5**.

### 10.3.2.3 Return Temperature Index (RTI)

RTI indicates the output air flow rate from the cooling package to the equipment such as racks. Also return temperature index shows the existence of re-circulation or by-passed air. RTI is defined by Eq.

$$RTI = \left[ \frac{T_{return} - T_{supply}}{\Delta T_{equipment}} \right] \times 100$$

#### Eq. 10.3.6

the return temperature index is more than 100%, it indicates re-circulation and if the RTI is less than 100% the flow is by-passed. Therefor the ideal percentage for this index is 100%. RCI never achieves 100% in practice; however the desired value would be feasible by enclosing the chamber of aisle.

### 10.3.3 Introducing a New Index for Assessment of Data Center Cooling

CRAC devices are used in data center hall for transferring cool air to the racks and IT equipment by using duct or the perforated raised floor vent tiles. Main application of ADS (air distribution system) in data center is preventing the increase of temperature in IT equipment, therefore it's significant to ensure if the cool and hot air in the entrance and exit of the equipment are mixed or not. Most of the practical users of data centers do not pay enough attention to the by-passed air that is provided by the CRAC and returns to the device without use. By-passed air makes a distance between produced air temperature in CRACs and entrance air to the servers. CRACs are designed to provide low temperature and prevent the return of hot air from servers back to the inlet of them. Also by-passed air causes lack of supply air to the servers and increases re-circulation of hot air (**Figure 10.3.1**). Management of air is to prevent the hot air re-circulation and cool air by-passing in the data centers that not only improves the energy consumption but also makes better temperature condition. If the air flow in the server room is managed optimally, the efficiency of system will be improved. But because of lack of information, most of the data centers cannot increase cooling performance and energy efficiency. Therefore to overcome heating problem, adding more cooling equipment is preferred instead of improving the cooling operation. Air management of server room consist of all steps of transferring cool air provided by CRAC to the IT servers and returning hot air to the CRAC after neutralizing the heat production. The factors which inhibit the air flow such as re-circulation and by-pass (as shown in [Error! Reference source not found.](#)) decrease the cooling efficiency and produce defective cycle of local temperature raise. Main goal of this paper is to offer the optimum state of investigated hall not only by comparing several parameters such as thermal contour, outlet and inlet temperature of packages and racks but also by studying the coefficients of **RCI**, **RTI**, **RHI**, **SHI** and appropriate air flow. All these indexes assess only a limited aspect of cooling operation; therefore it is not possible to have a comprehensive study of the system. A new index should be introduced to indicate the results of whole indexes. In this paper a new index is presented which is called **CCI** (Comprehensive Cooling Index). This index includes not only previous indexes but also average temperature of cool and hot aisles between racks. **Eq. 10.3.7** is suggested for CCI index.

$$CCI = (2 \times SHI) + \left( \frac{100 - RCI_{HI}}{100} \right) + \left( \frac{100 - RCI}{100} \right) + \left( \frac{ATA - T_{out}}{ATA} \right)$$

#### Eq. 10.3.7

All the indexes should be dimensionless and not in percentage form to balance the indexes. As the summation of SHI and RHI is one, 2 times of SHI is used. As much as  $RC_{HI}$  and RTI are close to 100 and also average temperature of aisles (ATA) is close to outlet temperature of package, ideal condition will be achieved. Therefore the lower the CCI values the better the design performance. Finally by calculating the number of CCI and comparing them, the models are sorted by operation and optimum state.

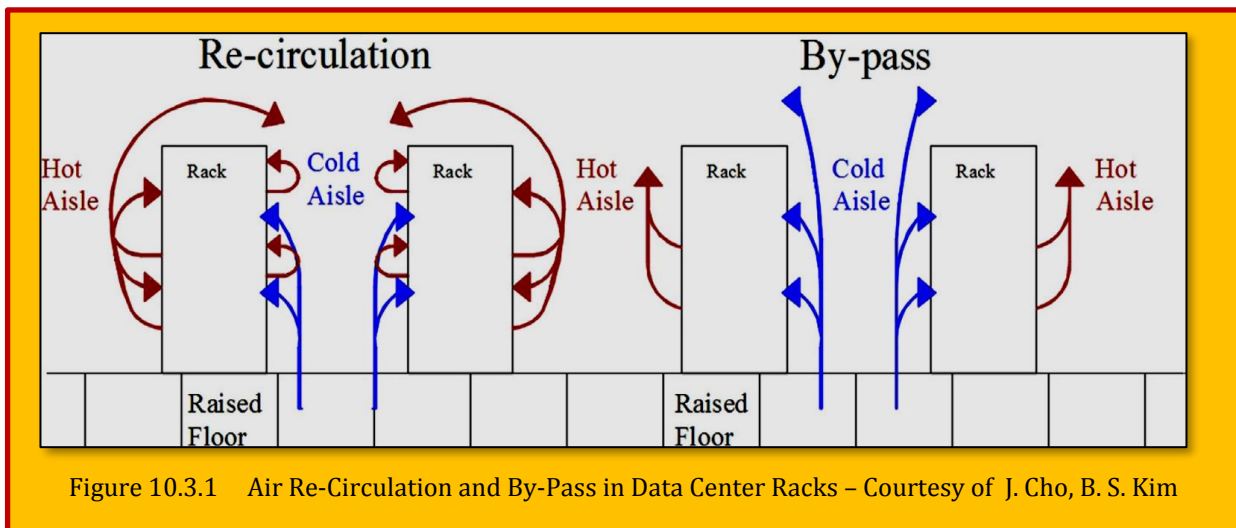


Figure 10.3.1 Air Re-Circulation and By-Pass in Data Center Racks – Courtesy of J. Cho, B. S. Kim

#### 10.3.4 Development of Numerical Model and Calculation of CCI for Different Configuration of Data Center

In this paper, CFD method is used for analyzing and modeling of data center. Primary data center of *Marand* is selected and simulated as a sample of telecommunication data centers. The design factors affect the efficiency of data center air flow, therefore several physical conditions based on standard modulus of design and architecture variables are investigated. Air flow in data center is turbulent and an appropriate turbulent model should be selected for simulation. Previous investigations indicated that  $k-\epsilon$  turbulent model has better performance and produce results in good agreement with experimental data in comparison to the  $k-\omega$ , SST, RSM and RNG  $k-\epsilon$  models.

##### 10.3.4.1 Governing Equations

Data center is simulated by SIGMA DC 6 package software where basic equations are solved in a steady-state, turbulence and incompressible 3D field. Considering the turbulence air flow on data center, for numerical modeling of in-compressible flow on aisle of it, not only the equation of state of gas and equations of conservation of mass, momentum and energy but also a turbulence model must be used. The 3D equations of flow field for conservation of mass, momentum and energy is provided in the following:

$$\begin{aligned} \frac{\partial}{\partial x_i} (\rho u_j) &= 0 \\ \frac{\partial}{\partial x_j} (\rho u_i u_j) &= -\frac{\partial p}{\partial x_i} + \frac{\partial}{\partial x_j} \left[ \mu \left( \frac{\partial u_i}{\partial x_j} + \frac{\partial u_j}{\partial x_i} - \frac{2}{3} \delta_{ij} \frac{\partial u_k}{\partial x_k} \right) \right] + \frac{\partial}{\partial x_j} (-\bar{\rho} \bar{u}'_i \bar{u}'_j) \\ \frac{\partial}{\partial x_j} \left[ \rho u_i h + \frac{1}{2} u_j u_j \right] &= \frac{\partial}{\partial x_i} \left[ K_{eff} \frac{\partial T}{\partial x_j} + u(\tau_{ij})_{eff} \right] \quad \text{where } K_{eff} = K + \frac{c_p \mu_t}{Pr_t} \end{aligned}$$

**Eq. 10.3.8**

And also the ideal gas model is used for simulation since air is used as working fluid. Data center has low temperature air flow and small value of Mach number; therefore incompressible, non-viscous and irrotational air flow is expected. This assumption is becoming less accurate around the racks and walls because of thick boundary layer but a precise model is achieved. Finite volume method is employed to solve above equations. For accurate calculation, discretization of the continuity, momentum and energy equations is done by second order method. In addition because of incompressible working fluid, SIMPLE algorithm is employed to make the velocity and pressure dependent. Segregated Solver algorithm is employed to solve the equations.

#### 10.3.4.2 Boundary Condition and Inlet

According to the thermal architecture of data center are presented hall, following assumptions for definition of the systems:

1. Location and amount of inlet flow is known and measurable. According to the catalog of blower fan of CRAC, flow rate is about 7000 CFM, outlet section of blower is  $8 \text{ ft}^2$  and the velocity of outlet air in blower is about  $875 \text{ ft/min}$  ( $4.4 \text{ m/s}$ ).
2. Velocity boundary condition for each rack in data center is to consider the velocity of air flow in cool and hot aisle as inlet and outlet velocity respectively (see **Figure 10.3.3**).
3. Location and amount of return flow to each CRAC is following the steady state condition.
4. Location and amount of cooling load in the room is known and measurable.
5. Walls of data center hall are isolated, therefore it is assumed to be adiabatic and the effect of radiation is not considered.

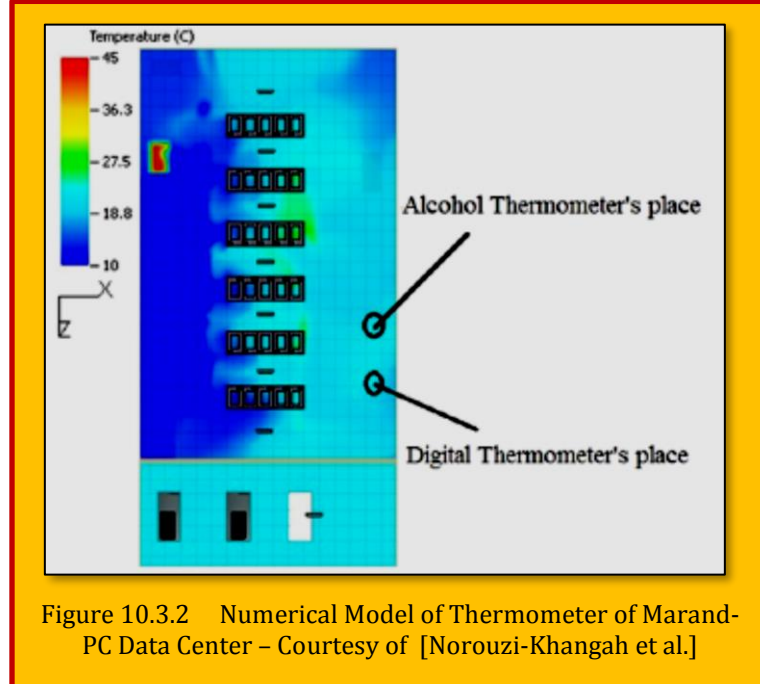


Figure 10.3.2 Numerical Model of Thermometer of Marand-PC Data Center – Courtesy of [Norouzi-Khangah et al.]

#### 10.3.4.3 Validation of the Model

Numerical results of temperature are validated by comparing them to the measured values of 2 diverse thermometers located in data center, depicted schematically by two circles in the graphs of **Figure 10.3.2**. Measured values of the PC data center are compared with the computational results obtained by CFD calculations. The result shows a very good agreement between calculated and measured values.

#### 10.3.4.4 Modeling and Problem Description

Channeling, downward or upward blowing of packages, closing the chamber of cool aisle and partitioning underfloor are some design alternatives for the architecture of data center hall. Number of meshes in the current models is about  $3 \times 10^6$ . This is achieved through a number of sensitivity analyses to show the independence of the results from the number of nodes. First of all, geometry of model is simulated according to the location and dimension of racks, dimension of saloon, location and power of electrical equipment (**Table 10.3.1**). The heat load is calculated by the software and suitable package is selected. The type of package (upward or downward blower) is selected considering the saloon and the location of racks. Finally the momentum, energy and conservation equations are solved and the outlets of equations are obtained including velocity, temperature, pressure, humidity and operation indexes (RCI, RTI, SHI and RHI). Values of indexes (such as RTI and SHI) for different mesh dimensions and maximum size of 5 cm, 10 cm, 15 cm, and 25 cm that makes mesh numbers more than  $2.9 \times 10^6$ , is approximately constant; therefore the results are independent of mesh numbers.

#### 10.3.4.5 Detailed Room

##### Summary of Marand PC Data Center and Introducing Alternative Models

One of the modeled data centers is shown in **Figure 10.3.3**. Dimension, thermal load of used equipment in the hall is presented below. A general method for specifying the CRAC capacity is to sum the 1.3 times of cooling load of data center and every other extra load. In current data center the whole load is 85.27 Kw; therefore a CRAC package by the capacity of 87.92 KW (from catalog) is selected. In the

<b>96 m<sup>2</sup></b>	<b>Area of Hall</b>
<b>4 m</b>	Height of Hall
<b>0.64 m</b>	Height of Under Floor
<b>20</b>	Number of Racks
<b>3 KW</b>	Thermal Load of each Rack
<b>5.59 KW</b>	Thermal Load of Cooling System
<b>65.59 KW</b>	Total Thermal Load
<b>87.92 KW</b>	Cooling Capacity of Package

Table 10.3.1 Dimensions of Hall and Thermal Load of Equipment – Courtesy of Norouzi-Khangah et al.]

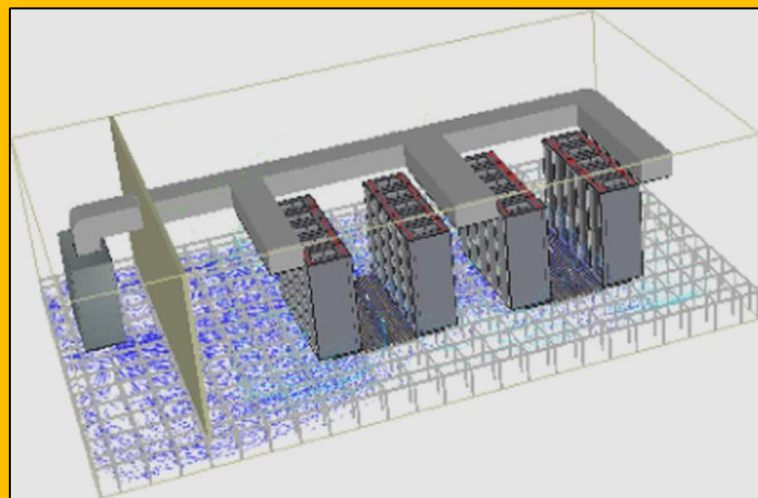


Figure 10.3.3 A Sample of Modeled Data Center – Courtesy of [Norouzi-Khangah et al.]

practical data center an 80 KW CRAC is used and in investigated model the same capacity is simulated. Optimum rack layout and cooling distribution are studied. Different configuration of channeling and also putting the cool aisles in closed chamber (see [Norouzi-Khangah et al.]<sup>156</sup>) with their detailed explanation provided as:

<sup>156</sup> Behzad Norouzi-Khangah, Mohamm Bagher Mohammadsadeghi-Azad, Seyed Morteza Hoseyni, Seyed Mohsen Hoseyni, "Performance assessment of cooling systems in data centers; Methodology and application of a new thermal metric", <http://dx.doi.org/10.1016/j.csite.2016.06.004>.

**Model 1** - Downward flooded package blowing from the front of aisle and recirculate the air to the front of package

**Model 2** - Downward flooded package blowing from the front of aisle and recirculate the air to the top of the package using local duct to the hot aisles

**Model 3** - Upward package blowing from the front of aisle using local duct to the cool aisles and recirculate the air to the top of the package using local duct to the hot aisles

**Model 4** - Upward package blowing from the front of aisle using local duct to the cool aisles and recirculate the air to the front of the package

**Model 5** - Downward flooded package from package room and recirculate the air to the front of package by recirculation chamber of package room (2.5 m height)

**Model 6** - Downward flooded package from package room and recirculate the air to the top of the package using local duct to the hot aisles

**Model 7** - Upward flooded package blowing from the exit chamber of package room and recirculate the air to the front of package by recirculation chamber of package room (1 m height)

**Model 8** - Upward flooded package blowing from the exit chamber of package room and recirculate the air using recirculation chamber of package room (2.5 m height) by local duct to the hot aisles

**Model 9** - Upward blowing package with local duct to the cool aisle and recirculate the air to the front of package by recirculation chamber of package room (1 m height)

**Model 10** - Upward blowing package with local duct to the cool aisle and recirculate the air using recirculation chamber of package room (2.5 m height) by local duct to the hot aisles

**Model 11** - Downward flooded package blowing from the front of aisle (cool aisle with enclosed chamber) and recirculate the air to the front of package

**Model 12** - Downward flooded package blowing from the front of aisle (cool aisle with enclosed chamber) and recirculate the air to the top of the package using local duct to the hot aisles

**Model 13** - Downward flooded package from package room (cool aisle with enclosed chamber) and recirculate the air to the front of package by recirculation chamber of package room (2.5 m height)

**Model 14** - Downward flooded package from package room (cool aisle with enclosed chamber) and recirculate the air to the top of the package using local duct to the hot aisles

**Model 15** - Downward flooded package blowing from the front of aisle (with partitioning underfloor) and recirculate the air to the front of package.

### 10.3.5 Results

#### 10.3.5.1 Investigated Temperature Points

For better thermal analyses of cool and hot aisles, a number of points (at the beginning, middle and end of aisle) are selected in 3 different heights (0, 1 and 2 m from floor) and their associated temperatures were calculated by the simulated sensors, **Figure 10.3.4**. The inlet and outlet temperature of package are sensed as well as selected points.

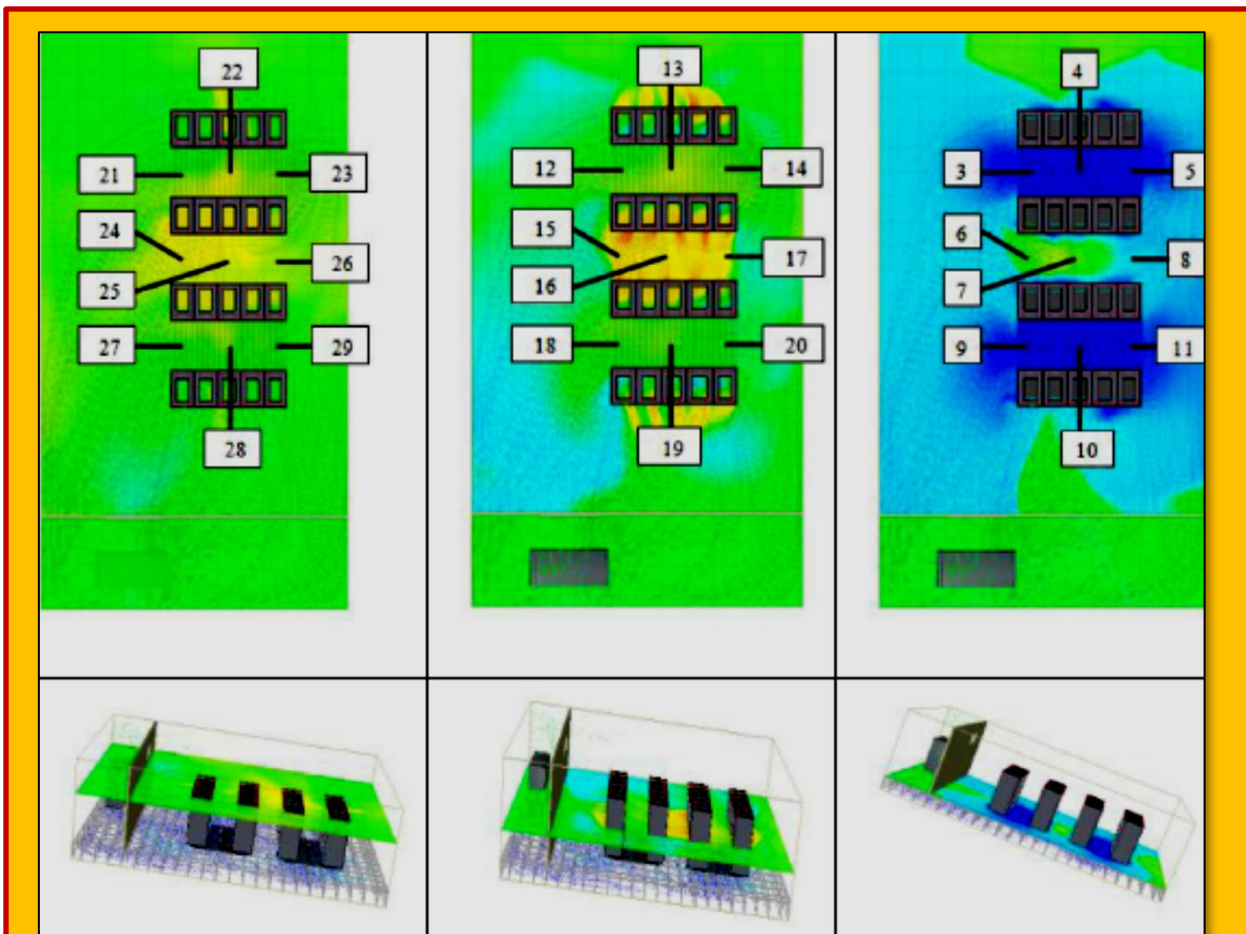


Figure 10.3.4 Thermal Assessed Points of Model – Courtesy of [Norouzi-Khangah et al.]

### 10.3.5.2 Assessing the Performance and Cooling Efficiency

Among all the models some of them have the same configuration and they can be classified in same groups, so that these groups can be investigated separately. We categorized them in 3 groups as described in the following.

#### 10.3.5.2.1 Group 1: Models 11–14

Current models have cool aisle with closed chamber and downward blowing packages (cooling from the floor). Model 12 and 14 which contain local channeling to return to the hot aisles have better conditions in comparison to the other models of this group. Also number 14 that has a separated package room and cool air blowing is perpendicular to the aisle direction has better results in average temperature of corridors and separation of

Rank 4	Rank 3	Rank 2	Rank 1	
13 (0.1513)	11 (0.1444)	12 (0.1439)	14 (0.1428)	SHI
-	-	-	11,12,13,14 (100)	RCI-hi
-	-	11,13,14 (115.3)	12 (115.2)	RTI
13 (17.477)	11 (17.296)	12 (17.180)	14 (17.014)	ATA

Table 10.3.2 Comparing 11, 12, 13 and 14 Models – Courtesy of [Norouzi-Khangah et al.]

hot and cools air in comparison to the model 12. But in re-circulation of hot air, number 12 is better than 14. Same RTI is obtained for number 11 and 13 that have no local channeling. And also model 11 has better results for SHI and average temperature of aisle in comparison with model 13. It's noticeable that all the models do not have overheating (RCIHI) and also RTI is almost the same (**Table 10.3.2**).

#### 10.3.5.2.2 Group 2: Models 5–10

Models number 5 and 6 have downward blowing packages, other ones have upward blowing and in whole models the blowing is perpendicular to the aisles direction. Number 10 has local channeling and results are close to the ideal condition while re-circulation is more than others (**Table 10.3.3**).

Number 9 is the second model that has acceptable operation whereas it performs weakly at re-circulation of hot air in aisles. The other model that has desirable operation is number 6. It includes only local returning channel that has the most RTI. Number 5 that is the real sample of problem comes after number 6. Both 7 and 8 configurations have the worst results in RCIHI (r100%) that indicates the overheating of racks. It's noticeable that number 7 is in the first rank of hot air re-circulation (RTI) because of distance of return air chamber from air supply channel.

#### 10.3.5.2.3 Group 3: Models 1–4 and 15

Number 3 and 4 have upward blowing packages, other ones have downward blowing and in whole models the blowing is across to the aisles direction.

Number 3 contains local channeling for supplying and returning to the aisles and is in the first rank. Second rank is number 4 that only have return local channel to the hot aisle. Number 2 comes after number 4 that only has return local channeling and gets the most re-circulation. In number 15 cool air flow is limited by partitioning the aisles that avoids the wasting in the floor. The worst operation is for number 1 that has not any channeling or partitioning where all the data centers has this configuration (**Table 10.3.4**).

Rank 6	Rank 5	Rank 4	Rank 3	Rank 2	Rank 1	
8 (0.5414)	7 (0.5396)	5 (0.406)	6 (0.399)	9 (0.3759)	10 (0.3405)	SHI
-	-	-	7 (98.82)	8 (99.63)	5,6,9,10 (100)	RCI-hi
6 (116)	10 (115.7)	9 (115.6)	5 (115.5)	8 (115.2)	7 (115.1)	RTI
7 (25.521)	8 (24.392)	5 (22.178)	6 (19.774)	9 (17.873)	10 (15.525)	ATA

Table 10.3.3 Comparing 5–10 Models – Courtesy of [Norouzi-Khangah et al.]

Rank 5	Rank 4	Rank 3	Rank 2	Rank 1	
1 (0.4419)	15 (0.4156)	2 (0.398)	4 (0.3979)	3 (0.3845)	SHI
-	-	1 (97.46)	15 (98.91)	2,3,4 (100)	RCI-hi

Table 10.3.4 Comparing 1, 2, 3, 4 and 15 Models – Courtesy of [Norouzi-Khangah et al.]

### 10.3.6 Numerical Calculation of CCI

As mentioned before, among the entire indexes high temperature rack cooling index (RCI<sub>HI</sub>) should be studied first. RCI<sub>HI</sub> shows that whether the temperature of racks is less than the universal maximum standard temperature or not. If the RCI is exactly equal to 100%, the racks are in an ideal temperature. As shown in **Table 10.3.5**, most of the models are in ideal situation however models number 1, 7, 8 and 15 have acceptable results that can be improved by either supplying more cool air or decreasing temperature of supply air. Except these 4 models, no overheating happened in the IT data center equipment.

Low temperature rack cooling index (RCI<sub>LO</sub>) presents the difference between the temperatures of racks and equipment. This index is not a noticeable parameter because if the temperature becomes less than standard, it will be controlled by reducing flow rate. Energy efficiency in air management system is presented by RTI. This index indicates the existence of re-circulation or by-pass air flow. As results show, in all the models RTI is more than 100%, therefore by-pass air flow does not exist and re-circulation happens. Model 7 has the least amount of RTI and re-circulation air flow that causes better cooling performance.

In spite of this, model 6 has the biggest RTI and the least efficiency.

As mentioned before, RHI and SHI are the indexes for the separation rate of hot and cool air. According to the **Figure 10.3.4**, only 11, 12, 13 and 14 models have suitable conditions regarding this index.

By using the results shown in **Table 10.3.6** and **Eq. 10.3.7** comprehensive cooling indexes are calculated and the models are ranked. As is apparent from this table, the calculated values for CCI fall between 1 and 2 where number 14 and 7 models are in the best and the worst state respectively. Model 7 has the least amount of RTI and re-circulation air flow that causes better cooling performance. In spite of this, model 6 has the biggest RTI and the least efficiency. As mentioned before, RHI and SHI are the indexes for the separation rate of hot and cool air.

### 10.3.7 Conclusion

A new index is introduced here as comprehensive cooling index (CCI) to identify the best design of data centers. The

ATA	RTI	RCI <sub>hi</sub>	RHI	SHI	Model
23.567	115.6	97.46	0.5583	0.4419	Model 1
20.174	115.6	100	0.6012	0.398	Model 2
15.809	115.2	100	0.614	0.3845	Model 3
17.506	115.3	100	0.6012	0.3979	Model 4
22.178	115.5	100	0.5942	0.406	Model 5
19.774	116	100	0.602	0.399	Model 6
25.521	115.1	98.82	0.4584	0.5396	Model 7
24.392	115.2	99.63	0.4566	0.5414	Model 8
17.873	115.6	100	0.6243	0.3759	Model 9
15.525	115.7	100	0.6591	0.3405	Model 10
17.296	115.3	100	0.8562	0.1444	Model 11
17.180	115.2	100	0.8566	0.1439	Model 12
17.477	115.3	100	0.8495	0.1513	Model 13
17.014	115.3	100	0.8579	0.1428	Model 14
21.632	115.9	98.91	0.5865	0.4156	Model 15

Table 10.3.5 Values of Indexes – Courtesy of [Norouzi-Khangah et al.]

CCI	Model	Rank
1.027	Model 14	1
1.032	Model 12	2
1.037	Model 11	3
1.055	Model 13	4
1.387	Model 10	5
1.478	Model 3	6
1.516	Model 9	7
1.549	Model 4	8
1.604	Model 6	9
1.605	Model 2	10
1.651	Model 5	11
1.678	Model 15	12
1.768	Model 1	13
1.952	Model 8	14
1.968	Model 7	15

Table 10.3.6 Ranking of Models According to the CCI index

verification of the developed method is sought on meaningful case study in where *Marand data center* is assessed in more detail. Different configurations of the data center (15 configurations) were analyzed to find out the most desirable design of the cooling system. Based on the obtained results, the following conclusion is derived:

- 1 Cooling systems by downward blowing have more cooling efficiency in comparison to upward blowing packages.
- 2 Not only closing the chamber of cool aisles but also local channeling of hot aisles improves the efficiency of cooling system.
- 3 Closed chamber cooling system has better performance than cooling system with normal under floor.
- 4 Conducting cool air to the IT equipment by either channeling or partitioning is useful for improving the efficiency of cooling system where channeling is more effective than partitioning.
- 5 If the cool air flow is across the aisle direction better results are obtained than perpendicular configuration.

## 10.4 Case Study 3 - Load Capacity and Thermal Efficiency Optimization of a Research Data Center Using Computational Modeling

**Authors :** Joseph R.H. Schaadt<sup>1</sup>, Kamran Fouladi<sup>2</sup>, Aaron P. Wemhoff<sup>3</sup>, and Joseph G. Pigeon<sup>4</sup>

**Affiliations :** <sup>1-3</sup>Department of Mechanical Engineering Villanova University, Villanova, PA, USA

<sup>4</sup>Department of Mathematics and Statistics Villanova University Villanova, PA, USA

**Title of Paper :** Load Capacity and Thermal Efficiency Optimization of a Research Data Center Using Computational Modeling

**Adapted From :** ASME 2015 International Technical Conference and Exhibition on Packaging and Integration of Electronic and Photonic Microsystems collocated with the ASME 2015 13th International Conference on Nanochannels, Microchannels, and Mini channels, July 6–9, 2015

San Francisco, California, USA

**Citation :** Schaadt, JRH, Fouladi, K, Wemhoff, AP, & Pigeon, JG. "Load Capacity and Thermal Efficiency Optimization of a Research Data Center Using Computational Modeling." Proceedings of the ASME 2015 International Technical Conference and Exhibition on Packaging and Integration of Electronic and Photonic Microsystems collocated with the ASME 2015 13<sup>th</sup> International Conference on Nanochannels, Microchannels, and Mini channels. Volume 1: Thermal Management. San Francisco, California, USA. July 6–9, 2015.

**Source :** <https://doi.org/10.1115/IPACK2015-48364>

Data centers are most commonly cooled by air delivered to electronic equipment from centralized cooling systems. The research presented here is motivated by the need for strategies to improve and optimize the load capacity and thermal efficiency of data centers by using computational fluid dynamics (CFD). Here, CFD is used to model and optimize the **Villanova Steel Orca Research Center (VSORC)**. VSORC, presently in the design stages, will provide a testing environment as well as the capability to investigate best practices and state of the art strategies including hybrid cooling, IT load distribution, density zones, and hot aisle and cold aisle containment. The results of this study will be used in the overall design and construction of the aforementioned research data center. The nomenclatures are provided in **Table 10.4.1**.

The objective of this study is to find the optimal operating points and design layout of a data center while still meeting certain design constraints. A focus is on finding both the ideal total supply flow rate of the air conditioning units and the ideal chilled water supply temperature (CHWST) setpoint under different data center design configurations and load capacities. The total supply flow rate of the air conditioning units and the supply temperature setpoint of the chilled water system are varied as design parameters in order to systematically determine the optimal operating points. The study also examines the influence of hot aisle and cold aisle containment strategies in full containment, half containment, and no containment configurations on the determined optimal operating conditions for the modeled research data center.

COP Coefficient of Performance	
P <sub>chiller</sub>	Chiller Work (kW)
P <sub>fan1</sub>	Power at State 1 (kW)
P <sub>fan2</sub>	Power at State 2 (kW)
P <sub>Total</sub>	Total Power (kW)
PUE	Power Usage Effectiveness
Q"	Heat Load (kW)
T <sub>max</sub>	Maximum Inlet Temperature (°C)
T <sub>supply</sub>	CRAH Supply Temperature (°C)
V' <sub>1</sub>	Total Supply Flow Rate at State 1 (cfm)
V' <sub>2</sub>	Total Supply Flow Rate at State 2 (cfm)
V' <sub>Total</sub>	Total Supply Flow Rate (cfm)

Table 10.4.1 Nomenclature

#### 10.4.1 Introduction and Literature Survey

In 2007, data centers consumed 1.5% of U.S. electricity consumption, of which one-third to one-half was used for cooling of these centers<sup>157-158</sup>. Additionally, it is has been estimated that the data center power consumption is to grow 15% annually. The National Science Foundation Industry/University Cooperative Research Center (I/UCRC) for Energy Smart Electronic Systems (ES2) has been established in part to thwart this growth by developing new methods for energy consumption reduction in data centers. These methods focus on designing data centers with a focus on energy minimization while averting detrimental conditions for the electronic equipment in the facility. The present study is focused on finding the optimal operating points and design layout of a data center while still meeting certain design constraints. In support of this goal, the authors utilize 3D (CFD) simulations to analyze the airflow, temperature, and relative humidity distributions in the data center model. The results of CFD simulations are then used for optimization of the modeled data center by calculating the optimal thermal loads and airflow rates.

CFD has been extensively to simulate airflow patterns in a data center<sup>159</sup>. [Hassan et al.]<sup>160</sup> applied CFD to examine airflow recirculation in a data center from hot aisle to cold aisle. In addition, [Ahuja]<sup>161</sup> used CFD to model the impact of installing a containment system, showing how installing hot aisle and cold aisle containment systems can produce power savings. CFD has also been used to analyze the airflow, temperature, and pressure distribution of a data center to monitor the effect of varying design parameters and determine the proper cooling layout to improve energy efficiency through the inclusion of thermal mass. [Khalil et al.]<sup>162</sup> modeled the airflow and temperature distribution of a data center in CFD.

Cruz et al. showed that turbulence models can be used to determine air flow patterns within a data center for a CFD model. Turbulence models, through comparison to experimental temperature and flow field data, are able to determine the reliability of the model and ultimately the accuracy of optimization<sup>163</sup>. Turbulence modeling is actively incorporated in the 6SigmaDC<sup>®</sup> software<sup>164</sup>. [Arghode and Joshi] used CFD to model the perforated tiles in order to view the overall data center flow field. The modeling of perforated tiles allows the software to create a sophisticated CFD model capable of calculating the fluid and thermal properties within the data center airspace. Applying energy modeling to thermodynamic models can produce significant energy savings in enclosed aisle containment configurations by reducing the total power needed to move air through the data center and bypass recirculation rather than focusing on energy savings in the refrigeration system<sup>165</sup>.

<sup>157</sup> Brown, R., et al. (2008). *Report to Congress on Server and Data Center Energy Efficiency: Public Law 109-431*.

<sup>158</sup> Greenberg, S., et al. (2006). *Best Practices for Data Centers: Lessons Learned from Benchmarking 22 Data Centers*. 2006 ACEEE Summer Study on Energy Efficiency in Buildings, 76-87.

<sup>159</sup> Schmidt, R. R., Cruz, E. E., and Iyengar, M. K.. "Challenges of data center thermal management," IBM Journal of Research and Development, **2005**.

<sup>160</sup> Hassan, N. M. S., Khan, M. M. K., and Rasul, M. G., (2013). "Temperature monitoring and CFD analysis of data center," 5th Bangladesh Society of Mechanical Engineers (BSME) International Conference on Thermal Engineering, pp. 551-559.

<sup>161</sup> Ahuja, N., (2012). "Datacenter power savings through high ambient datacenter operation: CFD modeling study," 28th Annual IEEE Semiconductor Thermal Measurement and Management Symposium, pp. 104-107.

<sup>162</sup> Khalil, E. E., and Aziz, M. H., (2013). "On the computations of flow regimes and thermal patterns in large scale high compute density data centers," ASME International Mechanical Engineering Congress and Exposition.

<sup>163</sup> Cruz, E., Joshi, Y., Iyengar, M., Schmidt, R., (2010). "Comparison of numerical modeling to experimental data in a small data center test cell," Proceedings of the ASME InterPack Conference 2009, pp. 953-961.

<sup>164</sup> "6SigmaRoom - Data Center Design CFD Simulation Software" [Online]. Available: <http://www.futurefacilities.com/software/room/6SigmaRoom.php>. [Accessed: 8-Aug-2014].

<sup>165</sup> Demetriou, D.W., Khalifa, H.E., (2011). "Energy modeling of air-cooled data centers: Part I the optimization of enclosed aisle configurations," ASME 2011 Pacific Rim Technical Conference and Exhibition on Packaging and Integration of Electronic and Photonic Systems, pp. 385-394.

CFD can provide flow field details that can be used to estimate the energy consumption of data centers based on equipment layout. However, the use of CFD becomes more powerful when used in conjunction with optimization tools. This approach enables the determination of the optimal layout that minimizes energy consumption. One such optimization approach is through the regression modeling methodology, where the input parameters to the CFD simulations are varied based on an established algorithm<sup>166</sup>.

This study provides a framework to design data centers based on minimizing power consumption to meet a known constraint. The results from this approach will be applied to an actual data center configuration to validate the method proposed here, and this data center is scheduled to be in operation within the next couple of years. The data center to be modeled is part of the Villanova-Steel Orca Research Center (VSORC), a proposed 10,000 square foot research data center in Princeton,

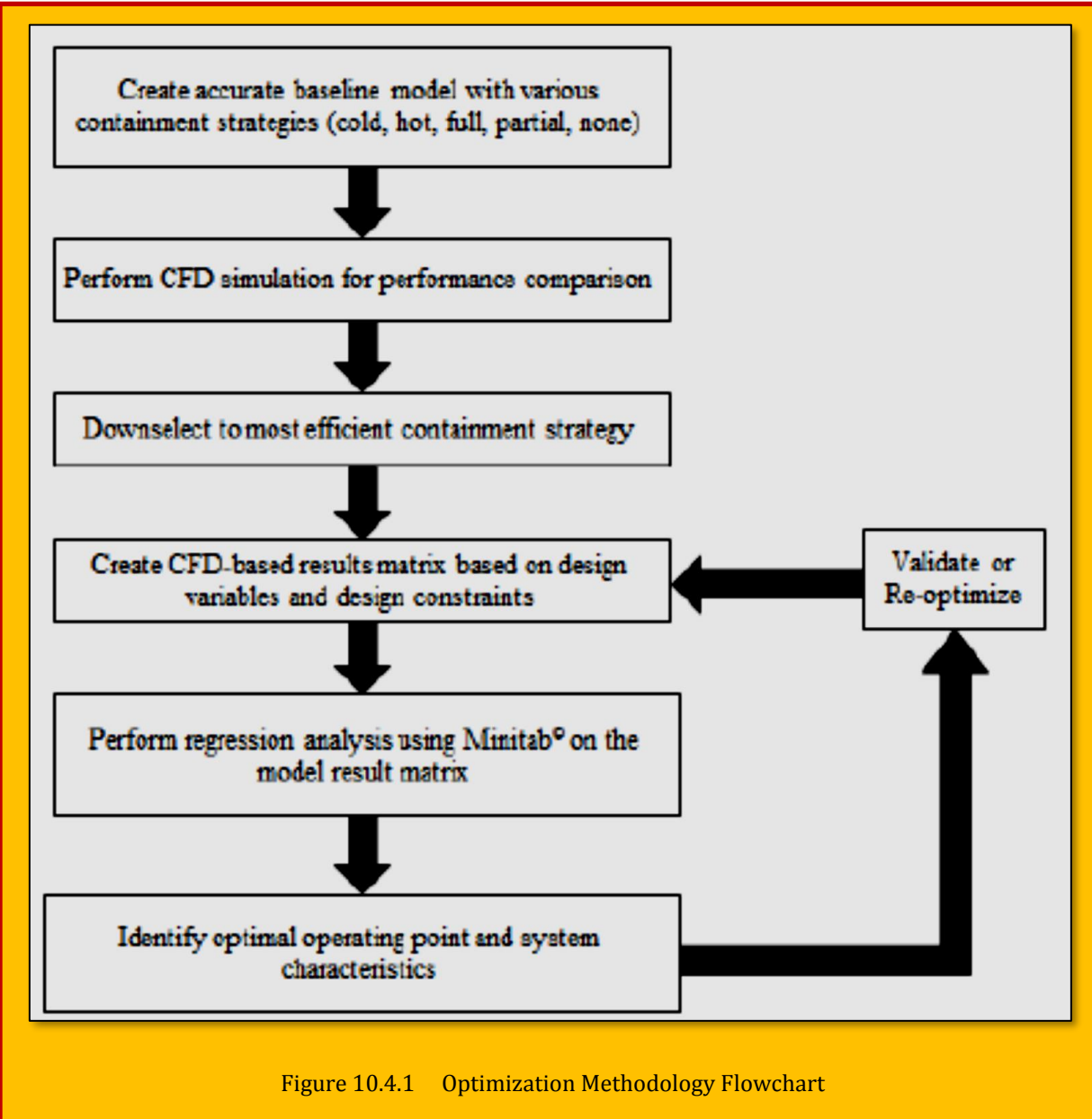


Figure 10.4.1 Optimization Methodology Flowchart

<sup>166</sup> Karadas, M., et al. (2015). "Multiple regression analysis of performance parameters of a binary cycle geothermal power plant," *Geothermics*, 54, pp. 68–75.

New Jersey. VSORC will have the capability to investigate the viability of a variety of data center configurations.

This study combines CFD simulations using the software package 6SigmaDC<sup>©</sup> with DOE and factorial analysis to aid in the design of the data center within VSORC. The present study aims to improve the efficiency of data centers accomplished through the analysis of a data center model's response under different conditions including hot aisle and cold aisle containment, fan speed modulation, and CHWST setpoint regulation. The results of this research will allow for better characterization of hot aisle and cold aisle containment techniques, accurate data center design parameters, and an improved method for the design layout and arrangement of a data center.

#### 10.4.2 Method

The optimization methodology is based on a sequential procedure utilizing sophisticated CFD and statistical software. The design optimization variables of the methodology are the flow rate and air supply temperature of the air conditioning units (ACUs), while the chiller supply temperature varies with ACU supply temperature. The maximum temperature entering the computer cabinets (racks) serves as the design constraint and is not to exceed 85°F (29.4°C). This temperature value is chosen as between the ASHRAE recommended value and the allowable value.

The CRAH supply air flowrate is varied within the model, but the server air flowrate is left unchanged. In contained systems, the amount of air to the servers will be affected by the change in CRAH flow rate, but it is assumed in this study that the changes in resultant server flow rate is negligible on server operation. In reality, the server flow rates may be inconsistent with the CRAH supply flow rate for contained aisles.

**Figure 10.4.1** shows a flowchart depicting the optimization methodology where the minimum system energy consumption is determined while maintaining the 85°F (29.4°C) constraint. The method begins with the creation of the baseline model created based on industry modeling standards such as proper equipment gaps, containment leakages, and the placement of supply and return tiles. These industry modeling standards are important in being able to extend results of this study for improvement of actual working data center facilities.

Next, the baseline model was modified to produce the different configurations needed for analysis. VSORC was modelled in hot aisle and cold containment with full, partial and no containment configurations.

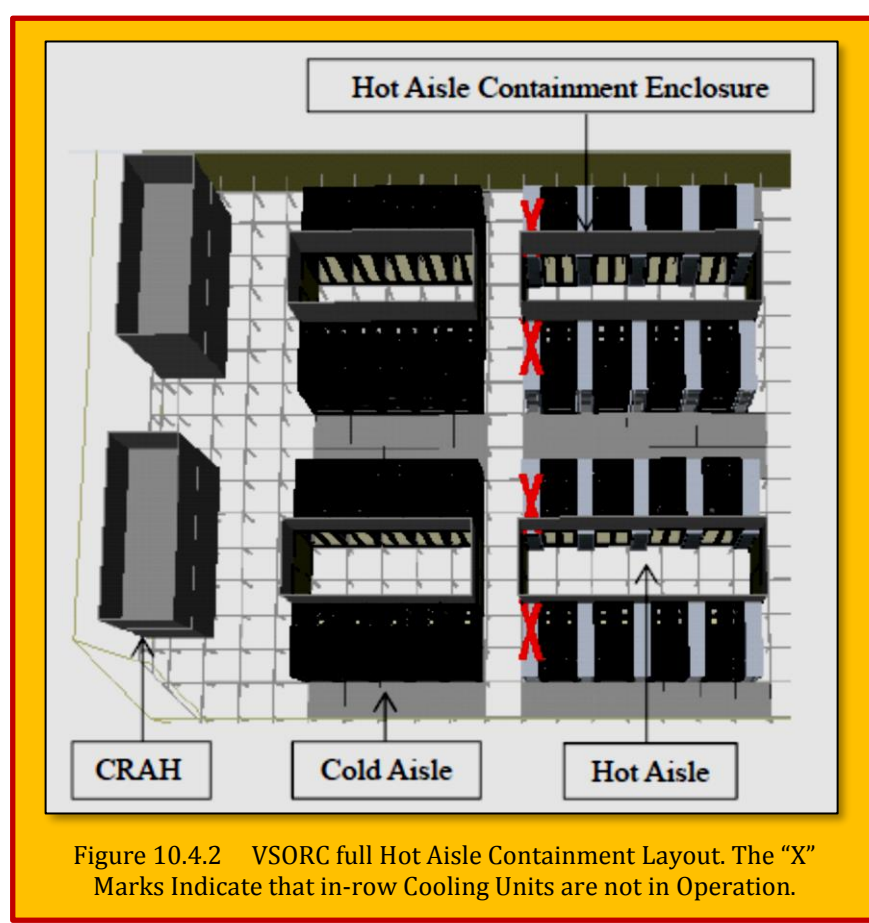


**Figure 10.4.2** displays the full hot aisle containment configuration. There are 8 rows in the data center and 36 racks. The total IT power is 550 kW and split between 2 rows of 5 kW racks, 2 rows of 10 kW racks, and 4 rows of high density 40 kW racks. The fan power consumption is calculated using the Fan Affinity Law<sup>167</sup>

$$\frac{p_{fan2}}{p_{fan1}} = \left( \frac{\dot{V}_2}{\dot{V}_1} \right)^3$$

#### Eq. 10.4.1

where P and V' are the fan power in kW and supply flow rate in cfm, respectively. Energy efficiency is also gained by increasing the supply temperature setpoint of the chilled water system. As the chiller consumes the largest amount of electricity in the data center, there are large opportunities for improvement in energy efficiency. An increase in the CHWST setpoint leads to an increase in the chiller coefficient of performance (COP), causing a decrease in chiller power consumption. The COP is calculated as<sup>168</sup>

$$COP = 0,0068T_{supply}^2 + 0,0008T_{supply} + 0.458$$

#### Eq. 10.4.2

where  $T_{supply}$  is the CHWST setpoint in °C. The chiller power is calculated using the standard equation

$$p_{chiller} = \frac{Q}{COP}$$

#### Eq. 10.4.3

Where Q' is the heat load. The combined power consumption of the cooling system is defined in the present study as :

$$p_{Total} = p_{fan} + p_{chiller}$$

#### Eq. 10.4.4

Special care was placed into creating these configurations using industry's best practices. For the partial containment configurations, the high density zones were contained while the sever cabinets closest to the computer room air handlers (CRAHs) were placed without containment. In partial hot aisle containment, the containment enclosures were removed from the two left hot aisles. In this experiment, the total flow rate and the chilled water supply temperature setpoint values were the parameters of interest used as design variables to improve energy efficiency. A range of reasonable values for these parameters were also created based on industry recommendations<sup>169</sup>.

It should be noted that inclusion of containment system does not directly play into calculation of energy efficiency of a data center. However, containment systems eliminates the premature mixing of hot and cold air streams, resulting in a reduced cooling load and subsequently lower air flow rate requirement. The "X" marks indicate that in-row cooling units are not in operation. The results of each aisle containment configuration were compared, and the most efficient containment strategy was then selected as the basis for further optimization. Leaks in contained aisles have been removed from the simulations, resulting in all CRAH supply air being used by the servers. It is assumed that the amount of CRAH supply air provides adequate cooling for the servers, but this assumption must be tested in practice.

<sup>167</sup> Fox, R. W., (2011). *Fox and McDonald's introduction to fluid mechanics*, Wiley, Hoboken, NJ.

<sup>168</sup> Samadiani, E., et al. (2010). "Coordinated optimization of cooling and IT power in data centers," Journal of Electronic Packaging, Transactions of the ASME, 132(3).

<sup>169</sup> Wu, T., (2014). Applications Engineer at Future Facilities Ltd., U.S.A., private communication.

An analysis matrix was then created based on the most important input variables (CRAH flow rate and supply temperature) and constraints (maximum server inlet temperature) present in the system. Regression modeling was then applied through the use of the software *Minitab*®. The optimal operating points and the viable operating range were found for the total flow rate and the chilled water supply temperature. The prediction equations for maximum inlet temperature and total power were found in order to characterize the system and find their values for prospective flow rates and supply temperatures. The *Minitab*® software provides a means for calculation of a predictive equation that relates the inlet parameters directly to the objective function (cooling equipment power) and the constraint (maximum server inlet temperature).

The first stage of optimization involved the selection of input parameter combinations using a factorial design approach within a design of experiments methodology. Various combinations of parameters were chosen such that an optimal CRAH based on the limited of number of input combinations. In general, factorial analysis varies input parameter values using combinations of finite levels of values in order to ascertain the sensitivity of the output parameters on each of the input parameters. Details of the factorial analysis, performed using *Minitab*®, can be found in standard texts such as [Saltelli et al.]<sup>170</sup>. The second phase of optimization involved creating the run result matrix, which after analysis characterized the data to determine the data was reasonable. The matrix was then combined with the advanced graphical capabilities of *Minitab*® to create an over layer contour plot. The over layer contour plot of the developed fit curve relations allowed for the relation of both total supply flow rate and CHWST temperature setpoint to the total power and maximum inlet temperature. This was used to identify the optimal operating point and system characteristics.

#### 10.4.3 Results

**Figure 10.4.3** shows the influence of cold and hot aisle containment on the maximum inlet temperature entering racks in the data center when the flowrate is varied. The figure clearly shows that full hot aisle containment provides the minimum entering temperature into the servers. The maximum inlet temperatures of the full hot aisle containment configuration are all below the constraint temperature, whereas all other configuration contained some elevated maximum inlet temperatures at lower flowrates. The figure also shows that the maximum inlet temperature decreased with increasing flowrate as expected. The “without hot aisle containment” and “without

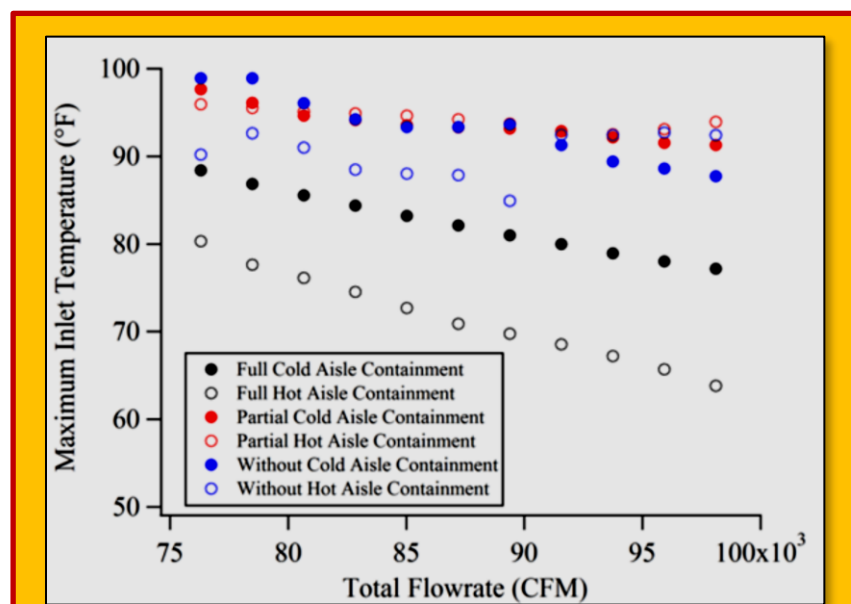


Figure 10.4.3 Flow Rate Effect on Max Inlet Temperature

<sup>170</sup> Saltelli, A., Chan, K., and Scott, E. M., eds., (2000). *Sensitivity analysis*, Wiley, Chichester ; New York.

"cold aisle containment" scenarios refer to the removal of the containment enclosures but leaving the perforated tile cold air

delivery and air return paths. The difference between "without cold aisle containment" and "without hot aisle containment" is in the way the air is delivered to the room due to the different locations of the cold aisle. In "without cold aisle containment", the cold aisle where the cold air is delivered into the room is located in between the racks. In "without hot aisle containment", the cold aisle is located along the perimeter of the outside of the racks. This placement of the cold aisle may be the cause of the unusual trend for the "without hot aisle containment" data, which might be attributed to an increase in the maximum inlet temperature due to an increase in warm air recirculation.

**Figure 10.4.4** displays the effect of installing containment systems on the maximum inlet temperature when the supply side control temperature is varied. The figure shows that the constraint temperature increases with increasing CHWST as expected. Again, full hot aisle containment is seen as the most effective configuration layout. The other configurations were significantly less thermally-efficient with some maximum inlet temperatures close to 100°F (37.8°C) at higher CHWST values. The full hot aisle containment scenario produced temperatures below the constraint maximum inlet temperature for the given data range, which no other containment configuration accomplished. The agreement of the two figures led to the selection of full hot aisle containment as the strategy to proceed with.

Using

**Eq.**

**10.4.1-**

**Eq. 10.4.4**, the regression analysis leads to predictive equations of the total system power consumption in kW and maximum server inlet temperature  $T_{max}$  in °F as

$$p_{Total} = 1609 + 0.00223\dot{v}_{Total} - 22.913T_{supply}$$

$$T_{max} = 80.076 - 0.000681\dot{v}_{Total} + 0.992656T_{supply}$$

**Eq. 10.4.5**

where  $\dot{v}_{Total}$  in units of cfm and  $T_{supply}$  is in units of °F. It should be noted that **Eq. 10.4.5** is used in the calculation of data center power of because of the equation's simplicity, but the combination of **Eq.**

**10.4.1-**

**Eq. 10.4.4** could also have been used. **Eq. 10.4.5** is necessary as  $T_{max}$  only be related to the flowrate and supply temperature using CFD modeling. These equations provided good estimates of total system power and the maximum server inlet temperature through interpolation of data points from the factorial analysis. The R-squared values for total power and maximum inlet temperature were

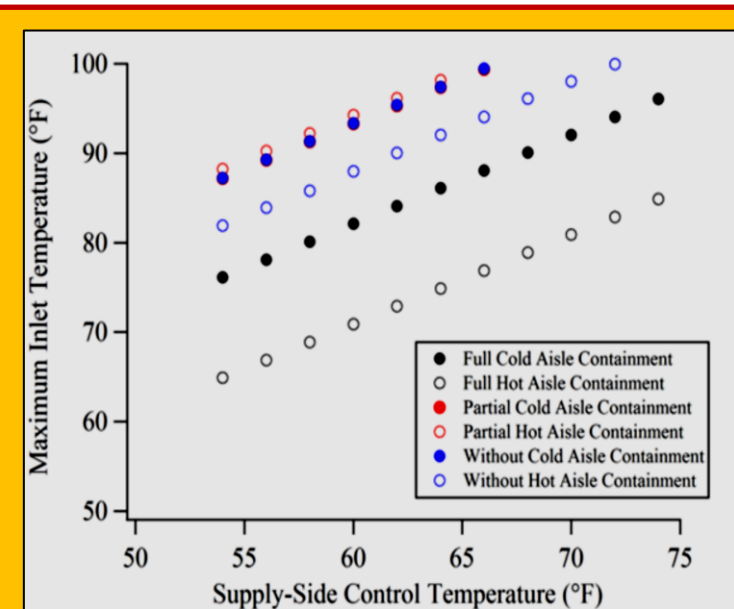


Figure 10.4.4 Supply Temperature Effect on Maximum Inlet Temperature.

calculated to be 94.17% and 99.89%. Therefore, these equations were then used to provide the viable operating range for the data center cooling system as well as determine the operating point that minimizes the total system power consumption.

**Figure 10.4.5** applies Eq. 10.4.5 to determine the influence of CHWST and flow rate on the energy consumption and maximum server inlet temperature. The predictive equations agree with **Figure 10.4.2** and **Figure 10.4.3** in that the max inlet temperature decreases as the total supply flow rate is increased when a full hot aisle containment configuration is used.

Furthermore, an increase in the supply temperature results in an increased max inlet temperature with full hot aisle containment as the most effective configuration in reducing the max inlet temperature. **Table 10.4.2** provides details of the optimal design point, marked with an X in **Figure 10.4.5**, determined as the operating point with the minimum energy consumption that satisfies the system constraints. The white region in **Figure 10.4.5** refers to the efficient operating range that satisfies the maximum inlet temperature constraint and is within the region of low, highly efficient energy consumption. The lower bound of the maximum inlet temperature is declared as 80°F since any lower maximum server inlet temperature is considered an output of an over-cooled configuration. In a similar manner, the upper limit for power consumption is set at 325 kW, which defines a boundary between efficient and inefficient cooling.

#### 10.4.4 Conclusions

The study here suggests that full hot aisle containment is the most efficient configuration for VSORC, and that factorial analysis can be used to define the optimal combination of CHWST setpoint and total flow rate. This methodology enables the savings of a significant amount of energy in data centers while minimizing the number of model runs necessary, and that CFD programs can be effectively used to identify optimal operating points of total supply flow rate and chilled water supply temperature setpoint for a data center. However, this study requires validation, which will occur when the VSORC data center is constructed. The next stages of this research also involves the use of

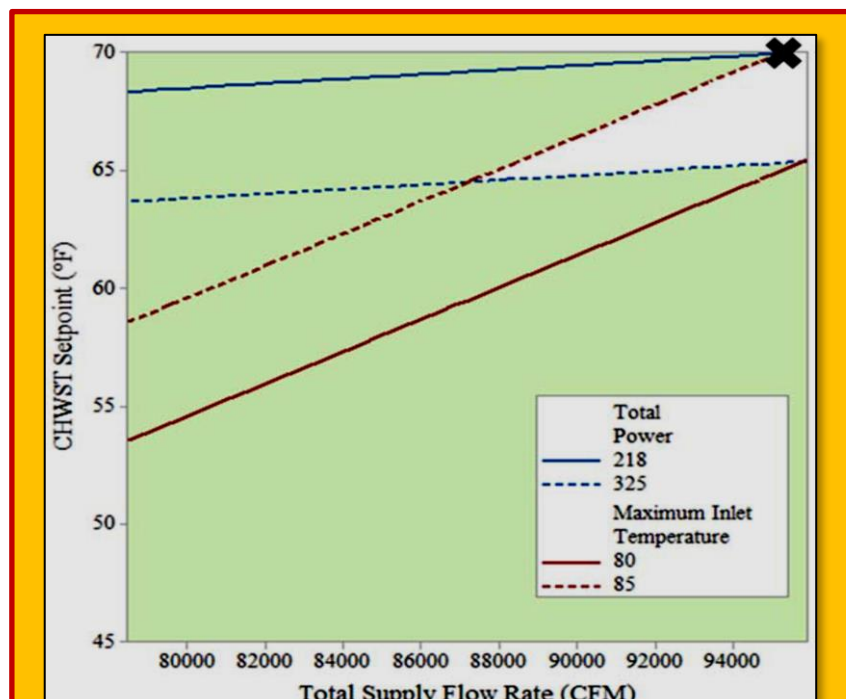
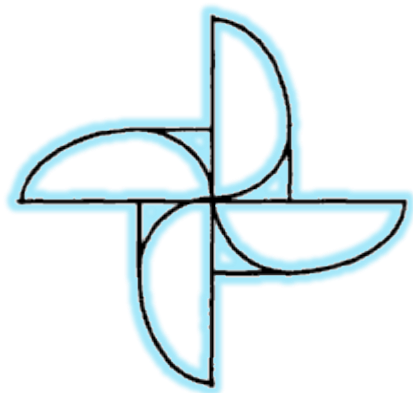


Figure 10.4.5 Minimization of Total Power Using Factorial Analysis.  
The "X" indicates the Optimal Design Operating Point, and  
White Region Indicates Feasible Operation.

Parameter	Value
<b>Total Supply Flow Rate, cfm</b>	95200
<b>CHWST, °F (°C)</b>	70(21)
<b>Total Power Consumption, kW</b>	218
<b>Maximum Inlet Temperature, °F</b>	85 (29.4)

Table 10.4.2 Optimal Design Operating Point

three-dimensional CFD modeling to explore steady state behavior of various VSORC designs including an abbreviated model data center using various hybrid cooling systems (e.g., in-row, rear-door, and overhead heat exchange systems) with and without containment strategies. This will include exergy based analysis in the optimization strategy and will explore how containment configurations affect the influence of various hybrid cooling strategies.



## 11 Heat Transfer in Semiconductor Industry

As with most of the technologies, one can know its applications only when it is invented<sup>171</sup>. Today CFD is being used to help in designing in every area where Fluid is involved. CFD has found its application with semiconductor industry as well. CFD solution can help immensely in reducing the number of experiments required to design various chip manufacturing equipment's. After validation with experiments, one can find finer details more easily from CFD than with experiment e.g. temperature distribution over the surface, deposition rate, rate of desorption. Various semiconductor industries have started using CFD calculation to help their design engineers. But it still has a long way to go and gain confidence from everybody to its results. CFD (Computational Fluid Dynamics) could be used to model the thermal system at a board level as well as within a semiconductor chip, so that efficient heat-dissipation mechanisms and sufficient cooling systems could be designed around these systems. CFD could hold interesting possibilities given that we are now looking at three-dimensional (3D) transistor dies as well as multi-die two-dimensional (2D) packages. Heat dissipation is critical for the long-term reliability of semiconductor devices

### 11.1 Brief Description of Semiconductor Devices

Semiconductor devices are electronic components that exploit the electronic properties of semiconductor materials, principally silicon, germanium, and gallium arsenide, as well as organic semiconductors. Semiconductor devices have replaced thermionic devices (vacuum tubes) in most applications. They use electronic conduction in the solid state as opposed to the gaseous state or

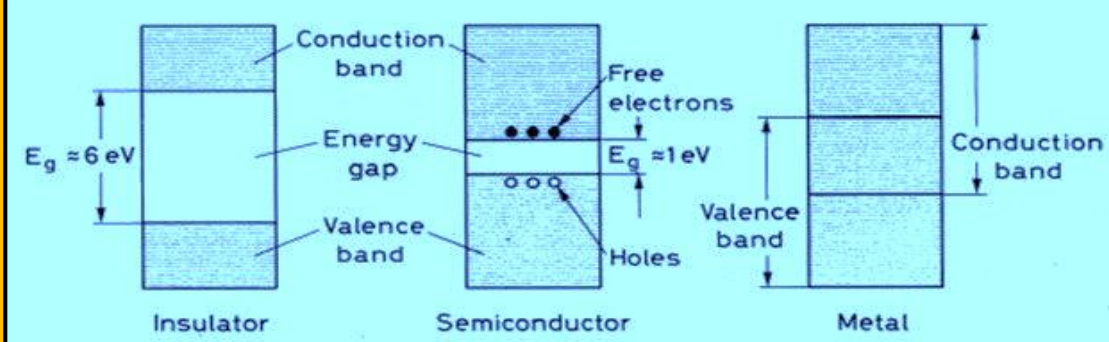


Figure 11.1.1 Illustrates the various classes of conductors

thermionic emission in a high vacuum. In layman terms, semiconductor is the category of conductors which besides being a conductor of current is also an insulator. As evident from the diagram (see **Figure 11.1.1**), the energy band gap between valence band and conduction band is:

- large in case of Insulator
- overlap in case of Metal
- moderate in case of Semiconductor

What are they you ask?

1. Valence Band - Band in which electrons reside.
2. Conduction Band - Band to which electrons jump and conduct electricity.
3. Energy Band - Band which does nothing!

<sup>171</sup> CFD online.

Similarly for an electron to jump to conduction band, it requires energy. Such an amount of energy is almost impossible to provide to insulators but easily achievable in case of metals. In case of semiconductors energy can be tuned so as to make it work like metal or an insulator. The energy provided must be greater than the energy of band gap ( $>1\text{eV}$ ). This feature enables semiconductors to be used as *Switch*. For switching ON the circuit you just need to provide energy greater than  $1\text{eV}$  to the semiconductor device. **Figure 11.1.2** demonstrates a semiconductor electronics.



Figure 11.1.2 Modern Semiconductor

## 11.2 Thermal Management in Semiconductors

There are at least ten good reasons to include thermal measurements as a routine step in any electronic component or system design process<sup>172</sup>. Amid all the promotion of solid-state superlatives ranging from data rate to feature size to LED light output, one characteristic is never touted: *Junction Temperature*. That's because Junction Temperature (JT) is an undesired but unavoidable side-effect of high currents and/or switching speeds. A p-n junction, whether it is one of millions on a CPU chip or the only one within a power LED, generates heat. In the past two decades the industry has seen heat dissipation increase by orders of magnitude. Faster is better, but faster is also hotter. This trend is not without consequences. A  $10^\circ$  increase in JT can cause a 50% reduction in a semiconductor device's life expectancy. In LEDs, both brightness and color can suffer as JT increases. And of course the twin issues of safety and cooling can impact the design of an entire system, not just the semiconductor device producing the heat. All these facts point toward the need for a thorough grasp of thermal behaviors at the chip level, and beyond. True understanding comes with physical measurements performed on actual devices. This is especially true in the world of semiconductors. You see heat dissipation in semiconductor packages is one of the limiting factors in miniaturization. One of the biggest concerns of circuit designers is reducing power that is continuously increasing due to bandwidths. As a result, the chip temperature increases. This change first modifies and then later destroys the operation of the circuit if the heat is not correctly led out of the device. Being able to understand the true thermal characteristics of a chip that will go inside an enclosure which is jam packed with other heat generating equipment can be very helpful. While most manufacturers publish thermal metrics for their chips, unfortunately not every manufacturer knows how to conduct an appropriate thermal characterization of their devices. So you can't always rely on published metrics<sup>173</sup>. (see **Figure 11.2.1**).

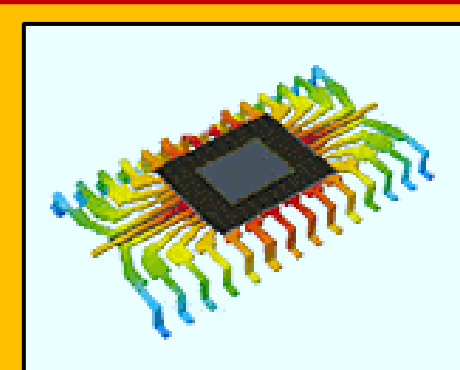


Figure 11.2.1 Thermal Management of Semiconductor (courtesy of Mentor CFD)

<sup>172</sup> From Mentor CFD Blogs.

<sup>173</sup> From Mentor CFD Blogs.

### 11.2.1 Can You Really Fry an Egg on a CPU?

An interesting question arises whether you can really fry an egg in CPUs. Believe or not, somebody already tried that<sup>174</sup>. Solving complex thermal models with computational fluid dynamics (CFD) requires a lot of processing power, and a central processing unit (CPU) under full load generates a fair amount of heat. But can you cook an egg on it? This article describes the model, simulations, and the ultimate conclusion. Solving complex thermal models with CFD requires a lot of processing power and a CPU under full load generates a fair amount of heat. But can you cook an egg on it? Before you throw away your conventional heatsink and fan in favor of a multifunctional omelet, we'll investigate what CFD to predict about the fate of your PC if you do so. (see **Figure 11.2.2**). Unfortunately, the CPU junction temperature exceeds 90°C within 6 seconds, at which point the CPU clock would throttle down to reduce the thermal power and prevent damage to the system; less than ideal for a cooling solution. The egg would also burn and catch fire. The central location of the CPU on the board and the large obstacles to air flow in the neighboring memory DIMMs and I/O ports mean limited cold air can passively flow over the hot egg by natural convection. The passive cooling of the egg cannot match the forced convection of the stock cooler. An egg-based cooling solution would only keep the CPU below the maximum 90°C if the CPU performance were throttled down so there are only possible applications in lower power environments with plenty of ventilation. With the requirement of frequently swapping out the egg, it can't be this catching on. If the aim is to cook eggs though, CPUs certainly produce enough heat to do so; with thermal throttling, the processor acts as a thermostatically controlled surface at around 90°C, sufficient to cook on. If you value your computer, maybe consider buying a frying pan instead.

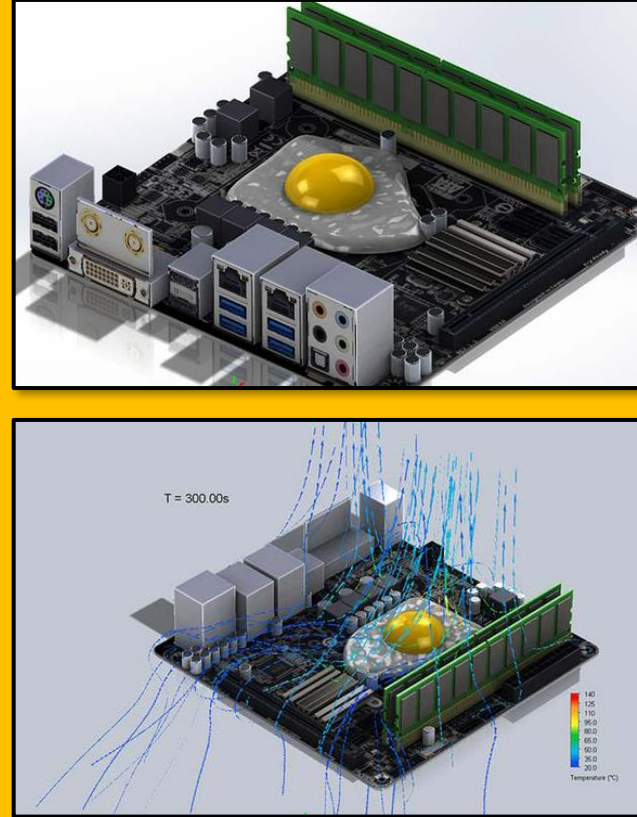


Figure 11.2.2 An Example of an Egg Frying on a CPU

<sup>174</sup> James Forsyth, System-Level Design, Semiconductor engineering.

### 11.3 Case Study 1 - Thermal Analysis on Micro-Electronic Heat Sink by CFD using Rectangular and Trapezoidal Fin Arrays

#### Article Information

**Authors :** B. Jayalakshmi<sup>1</sup>, P. S. Kishore<sup>2</sup> & J. Ramesh Naidu<sup>3</sup>

**Affiliation :** <sup>1</sup>Assistant Professor(M.E) Avanthi Institute of Engineering and Technology

<sup>2</sup>Professor Andhra University, Vishakapatnam

<sup>3</sup>Associate Professor Avanthi Institute of Engineering and Technology

**Title of Paper :** Thermal Analysis On Microelectronic Heat Sink By CFD Using Rectangular And Trapezoidal Fin Arrays

**Citation :** (Jayalakshmi, Kishore, & Naidu, 2017)

**Bibliography :** Jayalakshmi, B., Kishore, P. S., & Naidu, J. R. (2017). Thermal Analysis On Microelectronic Heat Sink By CFD Using Rectangular and Trapezoidal Fin Arrays. International Journal of Engineering Sciences & Management Research (IJESMR), pp. 120-131.

#### 11.3.1 Abstract

The concern about thermal performance of micro-electronics cooling is on the increase due to recent overheating induced failures which have led to product recalls. Removal of waste heat from these systems with the use of heat sinks could improve thermal efficiency of the system. The present work investigates the effect of change in aluminum heat sink geometry on thermal performance. Sinks with two models with rectangular and trapezoidal fins are taken. Heat transfer analysis were conducted to investigate the thermal performance of air cooling through heat sink rectangular cross section with dimensions of 55mm × 1mm × 20mm and the other of trapezoidal with dimension of 55mm × 0.25mm × 20mm. Nine channels of each configuration are modeled on aluminum base. The measurements were performed under steady state with air velocity of 2 m/s, and at temperatures varying from 60°C-110°C in steps of 10°C. Theoretical results are compared with numerical analysis with *Fluent15.0®*. Graphs are drawn, to show the performance of array of rectangular and trapezoidal fins using CFD.

**Keywords :** trapezoidal array of fins, rectangular array of fins, electronics cooling, heat sink

#### 11.3.2 Introduction

##### 11.3.2.1 Optimal Heat Sink in Micro-Electronic Cooling System

In all the electronic systems available in the present market, a heat sink is acting as passive heat exchanger which cools the device by dissipating heat into the surroundings. In computer applications, heat sinks **Figure 11.3.1** are used to cool different units such as central processing units (CPU) or graphic processors (GPU). The heat sink is used with high-power semiconductor devices such as opto-electronics such as light emitting diodes (LEDs). Power transistors and lasers where the heat dissipation ability of the device is insufficient in order to moderate its attacking temperature. The heat sink was designed in such a way in maximizing its applicable surface area which is in contact with the considering cooling medium placed surrounding it, such as the atmosphere. The factors that affect the ambient performance of a heat sink are protrusion design, choice of material, surface treatment and air velocity. The integrated

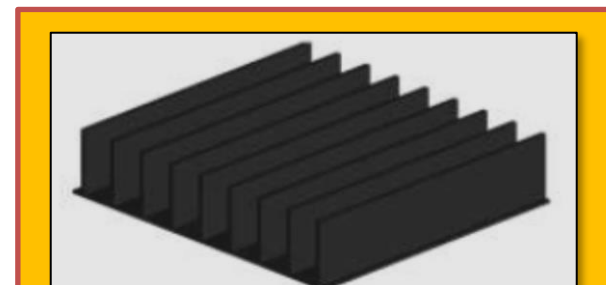


Figure 11.3.1 Rectangular Heat Sink Model

circuit temperature is also affected due to the effect of the thermal interface materials. Adhesives which have good thermal properties such as thermal grease improve the heat sink's performance by filling the air gaps between the sink and the heat spreader on the electronic device.

Sukumar et al. [1] in their study described that heat indulgence techniques are the prime concern to remove the waste heat produced by electronic devices, to keep them within permitted operating temperature limits. Heat indulgence techniques include heat sinks, fans for air cooling, and other forms of cooling such as liquid cooling. The choice of an optimal heat sink depends on a number of geometric parameters such as fin height, fin length, fin thickness, number of fins, base plate thickness, space between fins, fin shape or profile, material etc. Therefore for an optimal heat sink design, initial studies on the fluid flow and heat transfer characteristics of standard continuous heat sinks of different designs have been carried through CFD simulations. It is observed from the results that optimum cooling is achieved by the heat sink design which contains interrupted fins with holes. These heat sink design promises to keep electronic circuits cooler than standard heat sinks and reduction in cost due to reduction in material.

Teertstra et al. [2]. in their study said that analytical models are developed for the average heat transfer rate in forced convection-cooled, slotted fin heat sinks. These models for the upper and lower bounds can be used to investigate the effects of slot size and placement on heat sink performance. Experimental measurements are performed for a variety of slot configurations over a range of Reynolds numbers, the data is compared with the proposed analytical models. In this thesis, Approximate model is proposed that predicts the experimental results for the average heat transfer rate to within 12% RMS difference.

Sane et al. [6]. in their thesis analyzed the thermal properties by varying geometry, material and thickness of cylinder fins. They also said that transient thermal analysis determines temperatures and other thermal quantities that vary over time. The variation of temperature distribution over time is of interest in many applications such as in cooling. The accurate thermal simulation could permit critical design parameters to be identified for improved life Sandhya and Kishore [8]. in their paper conducted heat transfer analysis by putting rectangular and triangular fins on periphery of engine cylinder. They found enhancement in heat transfer by varying length and base temperature on fins..Balanna and Kishore [9]. in their article took automotive radiator with coolant in vertical tubes and air in a wavy arch which resembles a fin. They have found heat transfer enhancement using this fin. (Mounika et al. [10]). in their paper done performance analysis on an automobile radiator treating it to be a heat exchanger. The fins are in a radiator which ultimately shows increase in heat transfer. (Jayalakshmi [11]). In her thesis investigated thermal performance of air cooling through heat sink using rectangular and trapezoidal fin arrays.

### 11.3.2.2 Need of Optimization

For novice users, there are basically three types of cross-sectional fins as described in **Figure 11.3.2**. There are **Rectangular** (RFA), **Trapezoidal** (TPFA) and **Concave Parabolic** profiles (which is not included in this study).

The fins has to be designed in a such a way that the TPFA's and RFA's

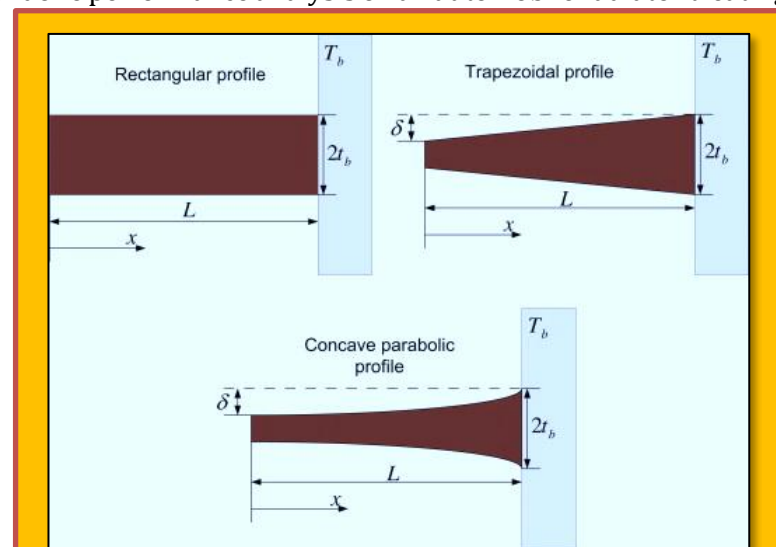


Figure 11.3.2 Cross-Section of Three Types of Fins

should have approximately same surface area and the dimensions of the TPFA's have to be determined in such a way that for various temperatures and the combination of them to have same surface area and to calculate heat transfer rate for each combination of TPFA and RFA. The trial and error approach to calculate these dimensions is at tough task and it involves time.

### 11.3.3 Numerical Analysis

The experimental analysis involves consumption of resources like material, time and hence it becomes expensive to do. In order to do theoretical calculations, they involve solving of many complex equations like continuity, mass and energy equations which is a time taking process and the accuracy of the results also decreases. This comes up with a solution of numerical analysis by using software's developing from decades. As the fast running computers have been developed, which reduces the time required to calculate the solution and many differential equations have been easily solved using software's, this provoked the present work to solve in CFD using *ANSYS FLUENT 15*.

### 11.3.4 Methodology

Methodology of the present work involves the problem identification and then the optimization of the problem by the reduction of material and modification of fin geometry. The fins are modeled using *CREO PARAMETRIC* by considering dimensions. These models are then analyzed in CFD by using *ANSYS FLUENT 15*. Along with the TPFA's, RAF is also analyzed in order to compare the performance of RAF and TPFA's for various temperatures in forced convection cases. The RFA modified geometry as TPFA to improve the heat transfer rate in forced convection case. Then the results are compared with the fins theoretical results and then the present work is concluded.

#### 11.3.4.1 Design Procedure for Rectangular Array of Fin Heat Sink Model

We have designed this model in *Creo parametric 2.0* The steps involved to create this model are as follows:

- 1 Click on File → New → Part → Select the system of units in mm
- 2 Enter the file name
- 3 Click on extrude to create the feature by entering the dimensions 61, 2thk and enter depth value as 55 as shown in the drawing
- 4 Click on extrude to create the fin by entering the width as 1 and position from one end as 6 and enter the height as 18.
- 5 Right click on extrude → click on pattern → select the direction pattern option to create the pattern by entering the number of instances as 9 and distance between the fins as 6.
- 6 Click on file → prepare → model properties and select the Aluminum 6061 material to apply on the model to know the mechanical properties like density, volume and surface area etc.
- 7 Click on file → save. The model is as shown in the **Figure 11.3.3**.

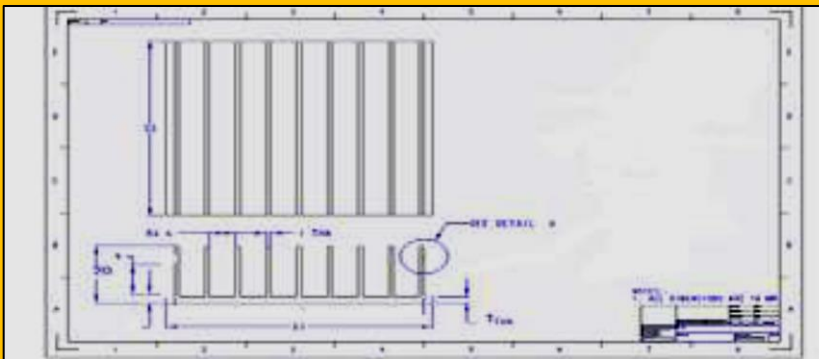


Figure 11.3.3 Design for Rectangular array of fin heat sink model

#### 11.3.4.2 Design Procedure for Trapezoidal Array of Fin Heat Sink Model

We have designed this model in *CREO PARAMETRIC 2.0*. The steps involved to create this model are as follows:

- 1 Click on file New → part → select the system of units in mm.
- 2 Enter the file name as Trapezoidal.
- 3 Click on extrude to create the feature by entering the dimensions 61, 2thk and enter depth value as 55 and also add the draft as  $2^\circ$  as shown in the drawing.

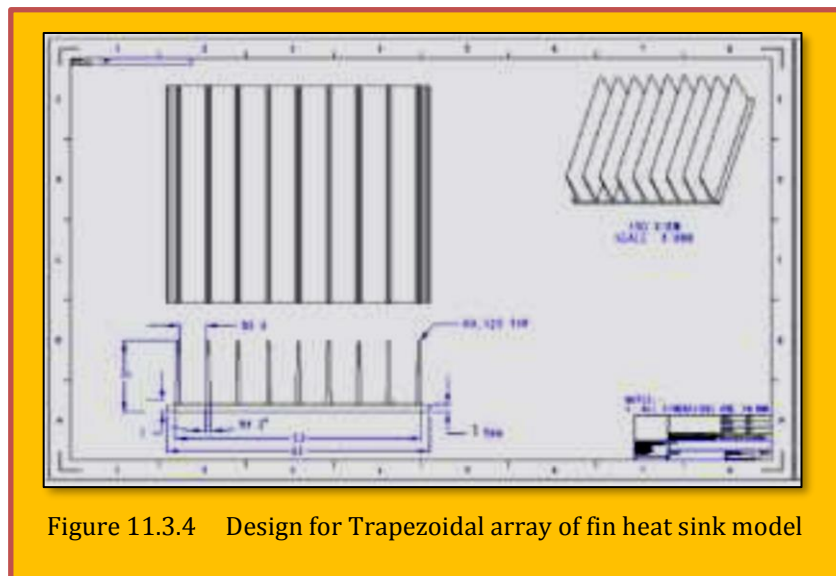


Figure 11.3.4 Design for Trapezoidal array of fin heat sink model

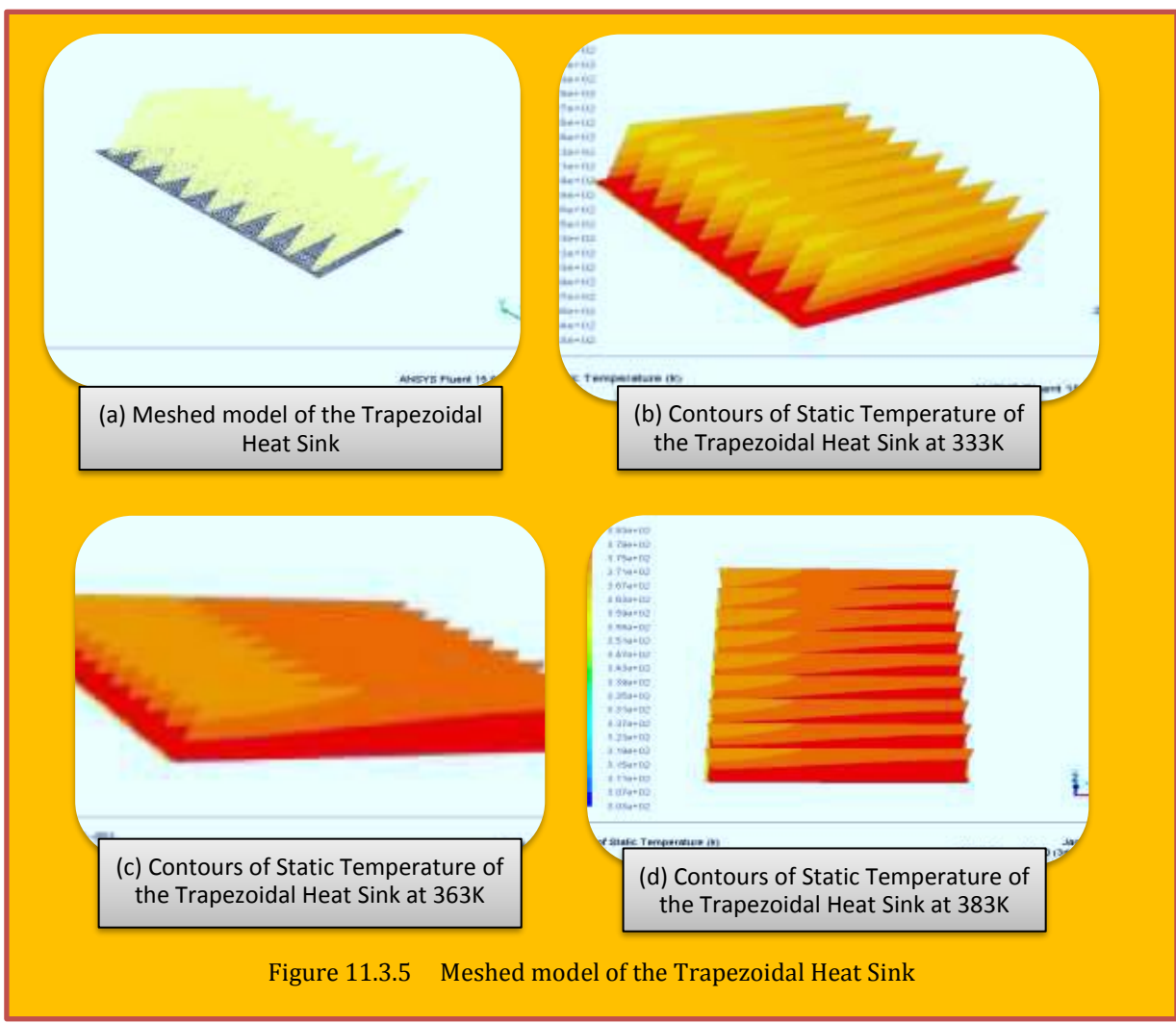


Figure 11.3.5 Meshed model of the Trapezoidal Heat Sink

- 4 Click on extrude to create the fin by entering the width as 1 and position from one end as 6 and enter the height as 18.
- 5 Right click on extrude → click on pattern → select the direction pattern option to create the pattern by entering the number of instances as 9 and distance between the fins as 6.
- 6 Click on file → prepare → model properties and select the Aluminum 6061 material to apply on the model to know the mechanical properties like density, volume and surface area etc.
- 7 Click on file → save. The model is as shown in the **Figure 11.3.4**.

### 11.3.5 Governing Equations

On the subject of G.Es., please refer to the source (Jayalakshmi, Kishore, & Naidu, 2017), for further information. Also, please consult the same source for the results regarding to Rectangular fins.

### 11.3.6 Results and Discussion

#### 11.3.6.1 Trapezoidal Heat Sink

The meshed and three contours of static temperature at different levels are distribution are shown in **Figure 11.3.5**

#### 11.3.6.2 Graphical Representation of Temperature

##### 11.3.6.2.1 Heat Transfer Coefficient (H)

**Figure 11.3.6-a** shows the variation of heat transfer coefficient with the temperature. The results shows that with the increase of temperature ,the heat transfer coefficient decreases gradually because of decrease in air Reynolds number and increase in thermal conductivity and decrease in Nusselt number. Heat transfer coefficient of rectangular profile heat sink more than the trapezoidal profile.

##### 11.3.6.2.2 Nusselt Number

**Figure 11.3.6-b** shows the variation of Nusselt number with the temperature. The results shows that with the increase of temperature ,Nusselt number decreases gradually because of decrease in air Reynolds number and decrease in Prandtl number . Nusselt number of trapezoidal profile less than rectangular profile because of the small change in the geometry of rectangular profile. For all the three cases Nusselt number decreases with the increase in temperatures.

##### 11.3.6.2.3 Heat Transfer Rate

**Figure 11.3.6-c** shows the variation of heat transfer rate with the temperature. The results shows that with the increase of temperature, the heat transfer rate increases gradually because of decrease in Reynolds number of air and increase in thermal conductivity and increase in temperature difference. In the above analyses absorbed that heat transfer rate for trapezoidal profile approximately equal the rectangular profile even increases in surface area. While absolving theoretical rectangular profile and numerical analyses of rectangular profile results are almost coincides.

##### 11.3.6.2.4 Temperature vs. Efficiency

**Figure 11.3.6-d** shows the variation of efficiency of fin with the temperature. as the temperature increases efficiency also efficiency is not maximize with respect to the fin length, but generally with respect to te volume and weight of the material, which also has cost implications. near the fin base fin efficiency is high and it goes on increasing as we moves towards the end of the fin; this is because, the surface temperature of fin falls as we move away from the base towards end. For more info, please consult the (Jayalakshmi, Kishore, & Naidu, 2017).

### 11.3.7 Conclusions

The performance of the rectangular array of fin heat sink and trapezoidal array of fin heat sink is evaluated using CFD analysis by varying temperatures on the surface of the fin. Validation from 60C

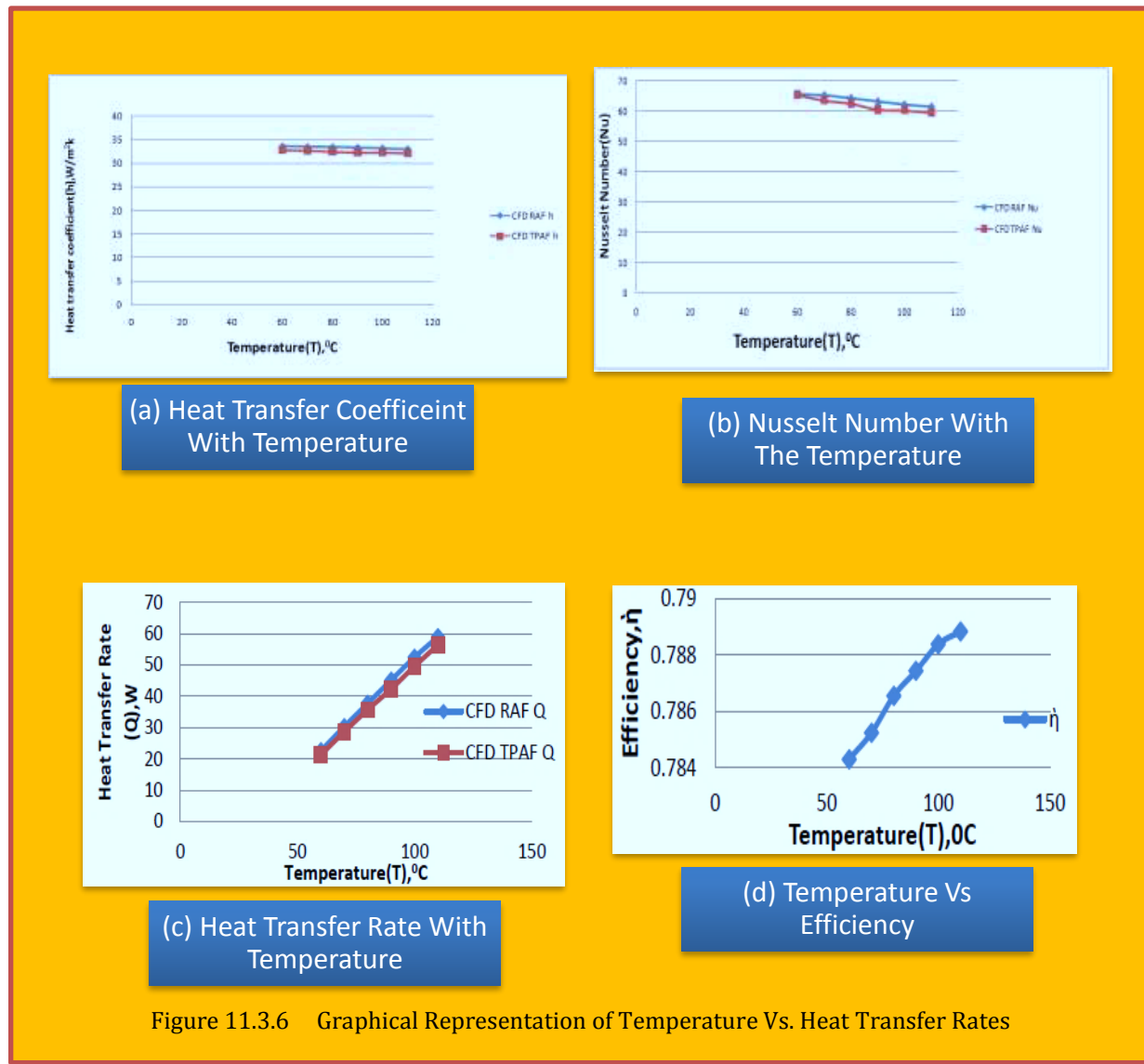


Figure 11.3.6 Graphical Representation of Temperature Vs. Heat Transfer Rates

to  $110^{\circ}\text{C}$  in steps of  $10^{\circ}\text{C}$ . The fins are modeled in *CREO PARAMETRIC 2.0* and are meshed in *ICEM CFD* and analysis is made in *ANSYS FLUENT 15.0*. From this analyses the results concluded that

- CFD analysis of rectangular heat sink array compared with theoretical calculations found to have deviation of 15%
- Heat transfer coefficient calculated for rectangular heat sink is found to be more than 3% compare to trapezoidal array fin
- Nusselt number for array of rectangular heat sink is found to more than 2% compare to trapezoidal array fin
- Heat transfer rate of an array of rectangular heat sink is found to be more than 2% compare to trapezoidal array fin
- Even though the above factors are more for rectangular array of fins, when weight factor is considered the rectangular array fins is replaced with trapezoidal array fin.

### Acknowledgements

I express my sincere gratitude to my guide P. S. Kishore, professor and Head of the department, Mechanical Engineering Department and other faculty members for encouraging and guiding me to undertake this Project work.

### 11.3.8 References

1. R. Sam Sukumar, G. Sriharsha, S. Bala Arun, P. Dilip kumar and Ch. Sanyasi Naidu, Modelling and Analysis of Heat Sink With Rectangular Fins Having Through Hole, Journal of Engineering Research and Applications , Vol. 3, No.2, pp.1557-1561,March /April 2013.
2. P. Teertstra, J. R. Culham and M.M. Yovanovich, Analytical Modeling of Forced Convection in Slotted Plate Fin Heat Sinks, Microelectronics Heat Transfer Laboratory, University of Waterloo, Canada, pp.34 - 41. March 2011
3. S. P. Chuhan and S. Singh steady and unsteady state thermal analysis of fins using CFD, vol. 2, No.5, pp. 519-526, May 2013.
4. Deepak Gupta, Vignesh Venkataraman and Rakesh Nimje, CFD and Thermal Analysis of Heat Sink and its application in CPU, International Journal of Emerging Technology And Advanced Engineering, Vol. 4, No. 8,pp.1381-1385, 2014.
5. Mr. N. Phani Raja Rao and Mr. T. Vishnu Vardhan, Thermal Analysis Of Engine Cylinder Fins By Varying its Geometry And Material”, International Journal of Engineering Research and Technology , Vol. 2, No.8,pp.404-412,2013
6. S. S. Sane, N. K. Sane and G. V. Parishwad, Computational Analysis of Horizontal Rectangular Notched Fin Arrays Dissipating Heat by Natural Convection”, 5<sup>th</sup> European Thermal-Sciences Conference, Netherlands, 2008
7. Nocedal J and Wright , Numerical Optimization. New York: Springer.
8. Sandhya Mirapalli, Kishore P. S. , “Heat Transfer Analysis on a Triangular Fin”, Published in International Journal of Engineering Trends and Technology, Vol.19, No.5, pp. 279-284, Jan., 2015.
9. K.Balanna, P.S.Kishore, “Evaluation of Heat Transfer and Friction Factor on Wavy Fin Automotive Radiator”, Published in International Journal for Scientific Research and Development, Vol.3, No.8, pp. 144-147, October, 2015.
10. P. Mounika, Rajesh K.Sharma, P.S.Kishore, “Performance Analysis of Automobile Radiator”, Published in International Journal of Recent Technologies in Mechanical and Electrical Engineering, Vol.3, No.5, pp. 35-38, May 2016.
11. Bangari Jayalakshmi, “Heat Transfer of Rectangular and Trapezoidal Fin Array on Microelectronic Heat Sink using CFD”, M.E. Thesis, Andhra University, 2016.

## 11.4 Case Study 2 - CFD Analysis of Convective Heat Transfer from Inverted Trapezoidal Plate Fin Array

### Article Information

**Authors :** S. G. Chavan<sup>1</sup>, S. Y. Bhosale<sup>2</sup> and H. N. Deshpande<sup>3</sup>

**Affiliation :** <sup>1,3</sup>Department of Mechanical Engineering, PES's Modern College of Engineering, Shivaji Nagar Pune, 5 Savitribai Phule Pune University, Pune, Maharashtra, India

**Title of Paper :** CFD Analysis of Convective Heat Transfer from Inverted Trapezoidal Plate Fin Array

**Citation :** (Chavan, Bhosale, & Deshpande, 2018)

**Bibliography :** Chavan, S. G., Bhosale, S. Y., & Deshpande, H. N. (2018). CFD Analysis of Convective Heat Transfer from Inverted Trapezoidal Plate. International Science and Technology Journal, ISSN NO: 1632-2882, pp. 189-198.

### 11.4.1 Abstract

Heat sinks with plate fins are widely used for surface cooling purpose in various heat transfer applications. Plate fin geometry affects the performance of heat sinks. In this work numerical study has been performed for **Rectangular Plate Fins**, **Trapezoidal Plate Fins** and **Inverted Trapezoidal Plate Fins**. For numerical study software used was *Ansys Fluent* ©. Velocity are 0.44, 0.88, 1.31 and 1.75 m/s. Heat supplied was 125 W. Average Heat Transfer Coefficient, Nusselt No. Pressure Drop are calculated and compared. Inverted Trapezoidal plate fins type II (ITPF-II) gives better performance and % enhancement of 7.57 was observed over RPF and 4.94 % over TFHS. Further pressure drop also calculated and it was observed that as Reynolds No increases pressure drop also increases and it is almost linear with small difference in case of Rectangular, Trapezoidal and Inverted Trapezoidal fins of type I but Inverted Trapezoidal fins of type II shows higher deviation in pressure drop at higher Reynolds No. that is greater than 12000 in comparison with other geometries.

**Keywords** - Heat Transfer Coefficient, Nu, Pressure Drop, Trapezoidal plate Fins (TPF) and Inverted Trapezoidal Plate Fins (ITPF-I and II).

### 11.4.2 Introduction

Convective heat transfer augmentation in heat sinks with plate fins is very challenging now a days. Many researchers worked on rectangular fins with different parameters. Parameters include use of pin fins in the passages between fins by varying diameters of fin pins. Some researchers worked on geometrical parameters like fin spacing, aspect ratio, angle of attack of working fluid. Some work also has done using Trapezoidal shape plate fins. A numerical study was done using rectangular, Trapezoidal and parabolic shaped heat sink for comparing their performance and convective heat transfer coefficient was found to be maximum in case of trapezoidal heat sink [1].

Design of fin for heat dissipation in natural convection was studied using rectangular, Trapezoidal and Inverted trapezoidal fins having heat load varies from 3 to 20 W and it was found that conventional rectangular fin gives better performance than trapezoidal fins but in case of inverted trapezoidal fins heat transfer coefficient is 25 % higher than trapezoidal fins and 10 % higher than conventional rectangular fins [2]. Performance of rectangular plate fins was studied to analyze heat transfer on vertical base experimentally and numerically at different inclinations and results shows that 0° staggered fins gives better performance than 300° staggered fins and this enhancement is about 17 %. Staggered fins shows enhancement as there is more turbulence in flow compared to inline fins [3].

Experimental and numerical analysis of rectangular plate fins with circular pin fins accommodated between gap of two plate fins was carried out under forced convection over vertical base and about 20 % enhancement was found for heat Sink with Plate Pin Fin over Heat Sink with Plate Fin [4]. A numerical study for shape optimization of flat plate fins was done with geometry defined linear functions [5]. An inverted trapezoidal fins are analyzed using 2-D analytical method. Here in this method heat loss from fin was represented as a function of fin shape factor, fin base thickness. It was observed that heat loss decreases and fin efficiency increases linearly with increase in shape factor [6]. A comparative experimental and numerical study of Heat Sink with Plate pin fin and Heat Sink Plate Fin was done and form numerical analysis it was observed that thermal resistance for PPFHS 30 % lower than that of PFHS [7].

To Optimize fin spacing an experimental analysis in rectangular fin array to maximize the heat transfer rate in natural and forced convection was done. Aim of this work was to fin optimum fin spacing which gives maximum enhancement [8]. Rectangular fins with perforation under natural convection was investigated [9]. Heat transfer enhancement using porous fin can also be achieved [12].

In present study a comparative numerical study has been done using flat plate, Rectangular Plate Fins, Trapezoidal Plate Fins and Inverted Trapezoidal Plate Fins type I and Inverted Trapezoidal Plate Fins type II under forced convection. Reynolds No. Selected as 4000, 8000, 12000 and 16000 with corresponding velocities are 0.44, 0.88, 1.31 and 1.75 m/s and heat input is 125 W. Simulation has been done using *Ansys CFD* software and solver used is *Fluent* ©.

#### 11.4.3 Numerical Analysis

the basic three steps in Numerical Analysis. (1) Pre Processing (2) Solver execution and (3) Post processing. Pre-processing in CFD include preparation of geometrical models, computational domain, computational meshing etc. Solver execution includes selection of models, application of suitable boundary conditions, selection of suitable material and fluid, selection of convection schemes, cell zone condition etc. In this step different governing equations are solved as per models selected till the solution gets converged. CFD post processing consists of plotting the various property counters, such as temperature counters, Pressure contours, velocity counters, vector plots, velocity stream lines etc.

<i>Sr. No.</i>	<i>Geometry Type</i>	<i>Mesh Details</i>
1	RPF	Mesh Type: Hexahedral + Prisms Total Mesh Count: 1,036,390 First Prism Layer Thickness: 0.075 mm Total Prism Layer Height: 0.1555 mm Number of Layers: 5
2	TPF	Mesh Type: Hexahedral + Prisms Total Mesh Count: 3,534,516 First Prism Layer Thickness: 0.075 mm Total Prism Layer Height: 0.1555 mm Number of Layers: 5
3	ITPF	Mesh Type: Hexahedral + Prisms Total Mesh Count: 2,608,752 First Prism Layer Thickness: 0.075 mm Total Prism Layer Height: 0.1555 mm Number of Layers: 5

**Figure 11.4.1-a** shows

*Rectangular Plate Fins*, **Figure**

**11.4.1-b** shows *Trapezoidal*

*Plate Fins*, and **Figure 11.4.1-c** shows *Inverted Trapezoidal Plate Fins*.

##### 11.4.3.1 Computational Mesh

All meshing details are shown in **Table 11.4.1**. In this work Hexahedral mesh is selected with prismatic layers.

Table 11.4.1 Meshing Details

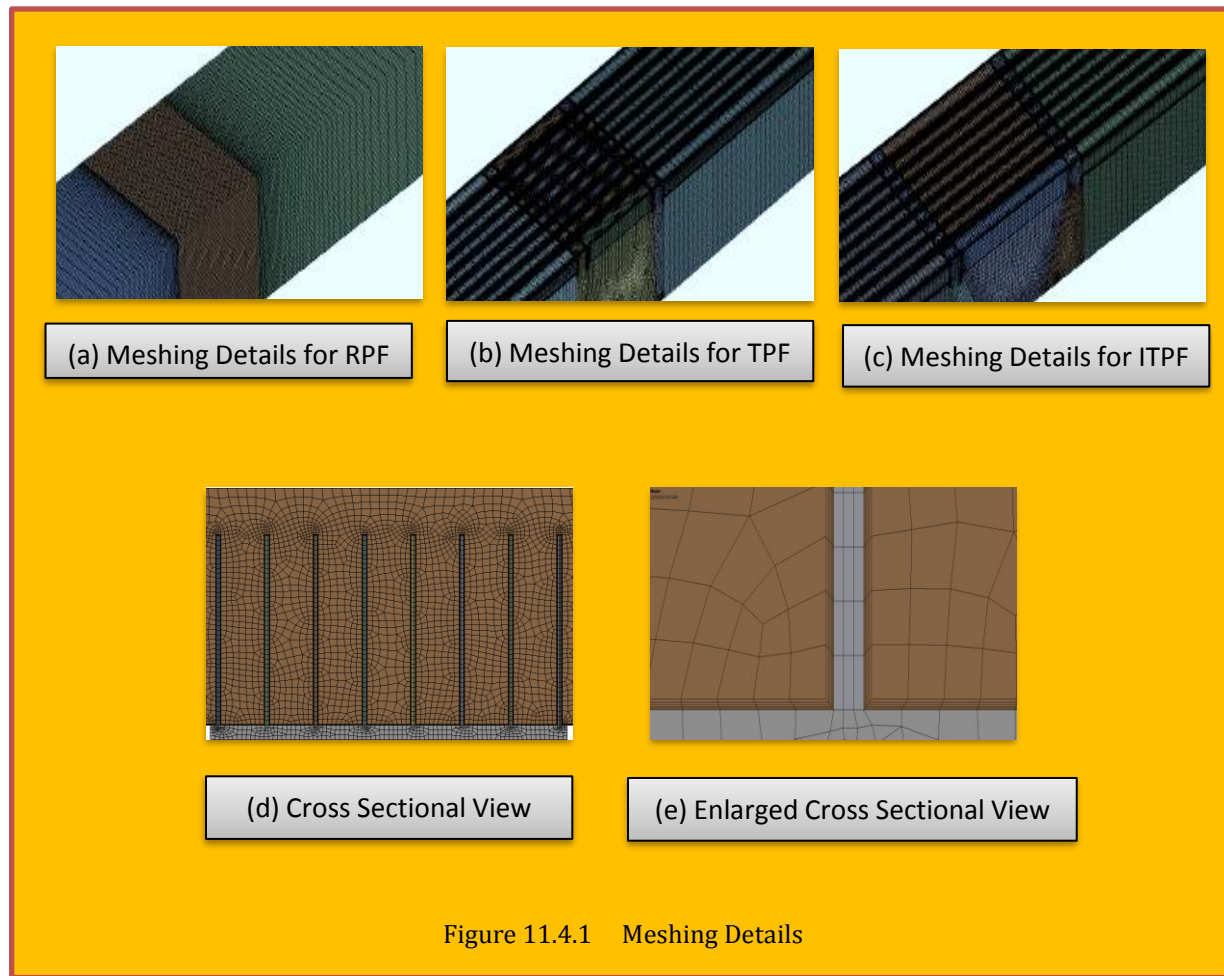


Figure 11.4.1 Meshing Details

#### 11.4.3.2 CFD Simulation Approach

- The mesh file was imported in to *ANSYS FLUENT* for simulation set-up.
- The pressure-based CFD solver was selected for the simulations.
- The flow turbulence was resolved using Reynolds Averaged Navier Stokes (RANS) approach using the two equation model Realizable k-epsilon with Enhanced wall functions.
- Air with material properties at standard conditions was assigned for the simulations.

#### 11.4.3.3 Boundary Conditions

- The flow inlet was modeled using the ‘velocity-inlet’ boundary condition with velocity based on the Reynolds number
- The heat input of 125 Watt is applied to the flat plate was specified using the ‘constant wall heat flux’ boundary conditions
- ‘Pressure-Outlet’ boundary condition was assigned for the Duct outlet
- The remaining surfaces - top, bottom and sides of the duct – were modeled as adiabatic, Stationary, No-Slip wall boundary condition.

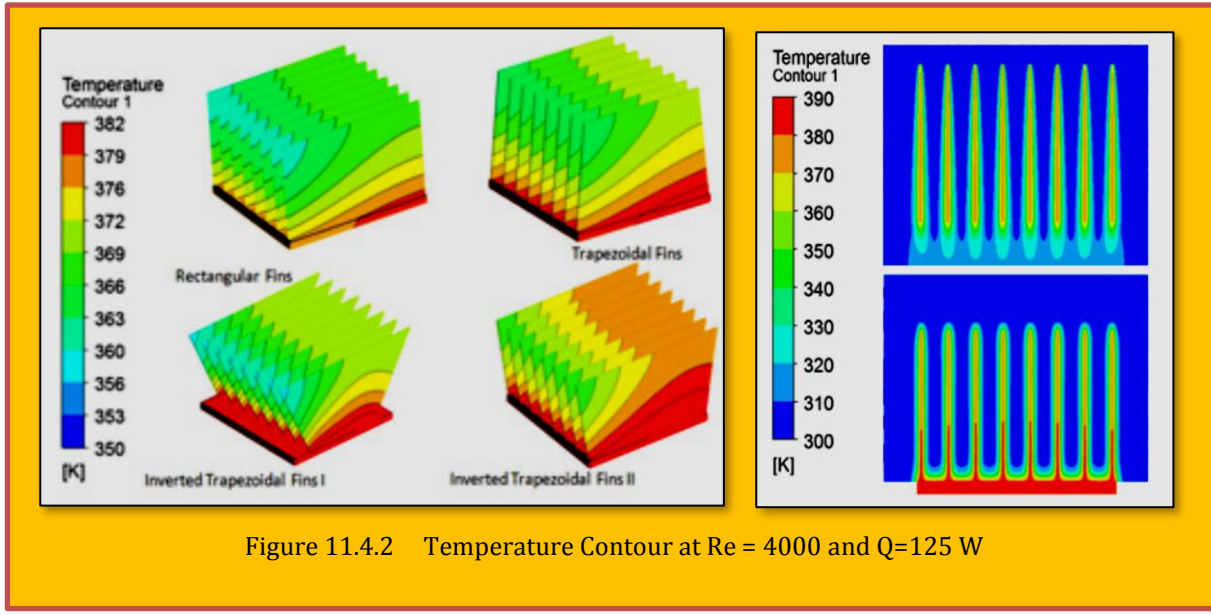


Figure 11.4.2 Temperature Contour at  $Re = 4000$  and  $Q=125$  W

#### 11.4.3.4 CFD Post Processing

**Figure 11.4.2** shows planer and side view of temperature contours for *Rectangular*, *Trapezoidal*, *Inverted Trapezoidal* plate fin array at Reynolds No. 4000 and heat input is 125 W. From these temperature contours is observed that maximum surface temperature is 382°C. For more details regarding  $Re = 8000, 12000, 16000$  please see (Chavan, Bhosale, & Deshpande, 2018). It can be concluded that at  $Re= 4000$  surface temperature is higher and Inverted trapezoidal fins shows higher surface temperature than Rectangular and Trapezoidal fins but as Reynolds No. increased to 8000 and so on maximum surface temperature get lowered in case of Inverted trapezoidal fins in comparison with rectangular and trapezoidal fins. [see (Chavan, Bhosale, & Deshpande, 2018)].

#### 11.4.4 Result and Discussion

##### 11.4.4.1 Variation of Heat Transfer Coefficient with Re

**Figure 11.4.3** shows variation of heat transfer coefficient with respect to Reynolds No. It was found that as Reynolds No. increases convective heat transfer coefficient also increases. Average increase in heat transfer coefficient of RPF, TPF, ITPF-I, and ITPF-II over Flat plate was 22.5 %, 24.6%, 25.89 % and 28.66 % respectively.

##### 11.4.4.2 Variation of Nu with Re

**Figure 11.4.4** shows variation of Nu with respect to Re. It was observed that as Re increases Nu also increases. Average increase in Nu of RPF, TPF, ITPF-I, and ITPF-II over Flat plate was 22.5 %, 24.6%, 25.89 % and 28.66 % respectively. There was an increase observed in TFHS and it was around 2.75 %. Also an enhancement of 4.28 % of ITPF-I over RPF and 7.57 % of

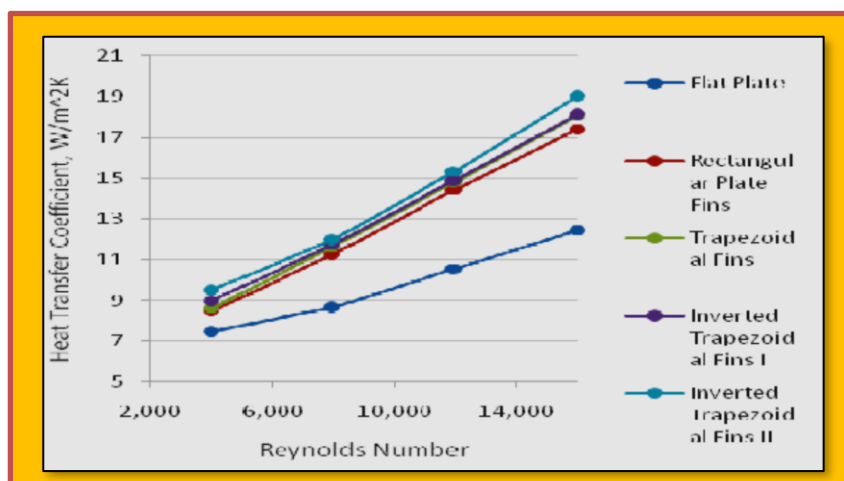


Figure 11.4.3 Heat Transfer coefficient vs. Reynolds No. at  $Q = 125$

ITPF-II over RPF. Further an enhancement of 4.94 % of ITPF-II over TPF was observed via numerical analysis.

#### 11.4.4.3 Variation of Pressure Drop with Re

**Figure 11.4.5** shows variation of Pressure drop with respect to  $Re$ . As  $Re$  increases pressure drop also increases. Pressure drop is directly proportional to friction between fluid and solid walls. Increase in pressure drop also leads to increase in Pumping Power. From graph it was observed that ITPF-II has higher pressure drop in comparison with Flat plate, and Array with RPF, TPF and ITPF-I.

#### 11.4.5 Conclusions

After doing a numerical analysis using Flat Plate, RPFHS, TPFHS, ITPFHS at 125 W and for the selected range of  $Re$  (4000 , 8000, 12000 and 16000) following conclusions are made.

- As Reynolds No. increases  $Nu$  also increases in case of all geometries.
- ITFHS-II gives better performance and % increase of 7.57 was over RFHS and 4.94 % over TFHS.
- Pressure drop is higher in case of ITFHS-II in comparison with other geometries.

#### 11.4.6 References

- [1] Ambeprasad. S .Kushwaha, Prof. Ravindra Kirar, "Comparative Study of Rectangular, Trapezoidal and Parabolic Shaped Finned Heat sink "IOSR Journal of Mechanical and Civil Engineering,(2013).
- [2] Roody Charles,Chi-Chuan Wang "A novel heat dissipation fin design applicable for natural convection augmentation "International Communications in Heat and Mass Transfer,(2014).
- [3] Harshal Patil, Prof. S. V. Dingare," Experimental and Numerical Investigation of Forced Convection Heat Transfer in Heat Sink with Rectangular Plates on Vertical Base" International Journal of Current Engineering and Technology,2016.

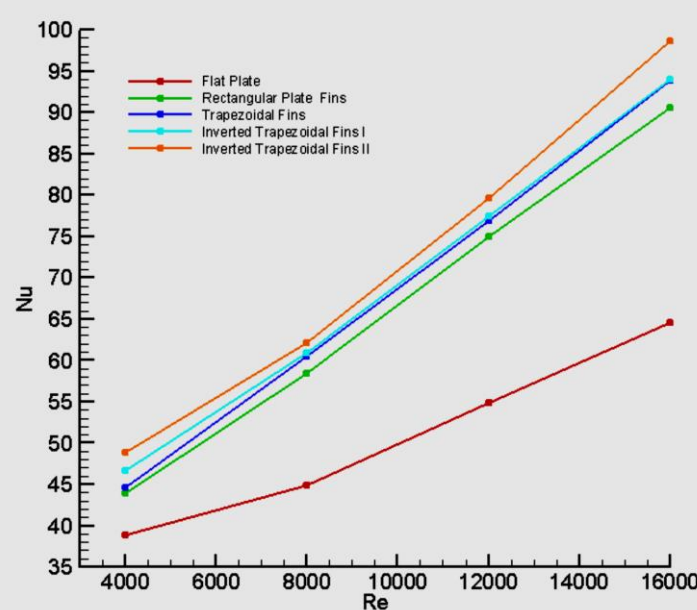


Figure 11.4.4 Nusselt No. Vs Reynolds No. at  $Q= 125$  W

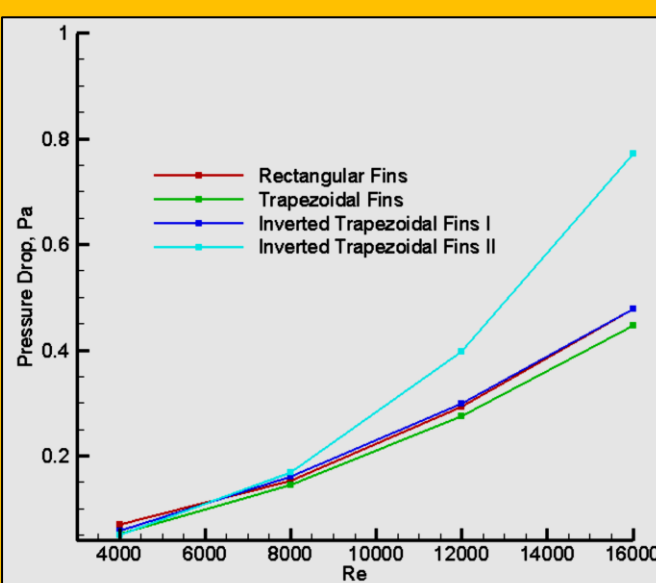


Figure 11.4.5 Pressure drop Vs Reynolds's No. at  $Q= 125$  W

- [4] Gaurav Kamde, Sunil Dingare, "Experimental and computational investigation of forced convection analysis of plat circular pin fin heat sinks over vertical base "Journal of Mechanical Science and Technology,2015.
- [5] Julian D. Osorio, Alejandro Rivera-Alvarez, Juan C. Ordóñez, "Shape optimization of thin flat plate fins with geometries defined by linear piecewise functions "Applied Thermal Engineering , 2016.
- [6] Hyung Suk Kang "Analysis of Reversed Trapezoidal Fins using a 2-D Analytical Method," Universal Journal of Mechanical Engineering,(2015).
- [7] Xiaoling Yu, Jianmei Feng, Quanke Feng, Qiuwang Wang, "Development of a plate-pin fin heat sink and its performance comparisons with a plate fin heat sink", Applied Thermal Engineering (2005).
- [8] Lohar, S.G.Taji, "Experimental Investigation for Optimizing Fin Spacing in Horizontal Rectangular Fin Array for Maximizing the Heat Transfer under a Natural and Forced Convection "International Journal of Engineering Research & Technology,(2014).
- [9] J.S. Chavan, R.D. Shelke , H.N. Deshpande, "Experimental & Numerical Investigation of Heat Transfer from Horizontal Interrupted Fins with Perforations under Natural Convection" International Journal for Research in Technological Studies,(2017).
- [10] H. N. Deshpande , S. G. Taji," Experimental Study of Heat Transfer from Perforated Horizontal Rectangular Fins for Richardson Number Less than 0.1" International Journal of Engineering and Management Research (IJEMR),(2015), 29-34.
- [11] S.M. Ramnani, S. Y Bhosale , "Optimization of Heat Transfer Rate by Forced Convection Process on Perforated Fin" International Engineering Research Journal (2015), 295-298.
- [12] S. Y Bhosale "Experimental Investigation of Heat Transfer using Porous Fins" Proceedings 21st national and 10<sup>th</sup> ISHMTASME , Heat and Mass Transfer, Conference ,( 2011), 28-30.

## 11.5 Case Study 3 - The Optimal Design of Heat Sinks: A Review

### Article Information

**Authors :** Hussein T. Dhaiban and Maha A. Hussein

**Affiliation :** Department of Refrigeration and Air-Conditioning Techniques Engineering, Dijlah University, Baghdad, Iraq

**Title of Paper :** The Optimal Design of Heat Sinks: A Review

**Citation :** (Dhaiban & Hussein, 2020)

**Bibliography :** Dhaiban, H. T., & Hussein, M. A. (2020). The Optimal Design of Heat Sinks: A Review. *Journal of Applied and Computational Mechanics*, Vol. 6, No. 4, 1030-1043.

### 11.5.1 Abstract

Heat sinks are used in industrial equipment to dissipate the excess heat from their heat-generating parts to the ambient. In the last few years, efforts on manufacturing electronic or mechanical devices with less weight, space, and lower cost were spent. Heat dissipation from the heat sink is stalling a big problem which many researchers are trying to solve. The aim of this study is to brief the previous investigation attempted enhancing the heat sinks thermal performance and to provide help to understand the cooling ability of their specific geometries. The various enhancement techniques used for optimizing the hydrothermal design of a pin fin, flat fin, micro-channel, and topology optimized heat sinks were summarized. The way in which the heat sinks' thermal performance is affected by orientation, shapes, perforation, slot, interruption, and space between fins and their arrangement under free and forced convection condition also reviewed.

**Keywords:** Heat sink, Optimal design, Pin and plate fin, Natural and forced convection.

### 11.5.2 Introduction

With the rapid development in electronic and mechanical devices (such as conditioning equipment, turbines, and electronic equipment), the need for efficient heat sinks with less size and weight has increased. The excess heat generated by these devices becomes a major problem which can cause damages in their parts. Furthermore, traditional cooling methods have become ineffective due to their limitations. The demand for developing effective ways to dissipate heat turns into a serious challenge. Therefore, researchers have been developing new effective techniques to solve the problem of high temperature.

The heat transfer enhancement focuses on increasing the heat transfer rate between the hot surfaces with surrounding by raising the heat transfer coefficients or increasing the heat transfer area. Using extended surfaces (fins) is considered as a good technique which is widely used to enhance the heat transfer in various types of heat sinks [1, 2]. Different designs have been investigated in order to obtain optimized fin geometry. Interruption, slots, and perforation are examples of geometrical modifications that have been improved the thermal performance of fins or to reduce their weight or cost [3, 4]. A heat sink with working fluid which is called micro-channel heat sink is another technique in which the flow characteristics have an impact on the thermal performance. The fluid that fills the heat sink channels has a great influence on the heat removal rate [5, 6].

Various geometries have been utilized to increase the heat transfer rate in micro-channel heat sinks such as using circular, rectangular and trapezoidal cross-sections. Because the surface area of the microchannel is small, different modifications were used in order to maximize the heat transfer efficiency such as using rough surfaces, twisted tap and rib [7, 8, 9, 10]. Moreover, many researchers reported different shapes by using waves, zigzag and curves structures in which structures affect the flow characteristics in micro-channel heat sink [11, 12].

Another approach that introduces optimizing the geometry of a heat sink without predefining the shape or configuration of the final design is topology optimization [13, 14, 15]. Topology optimization can be defined as a mathematical science approach which has been used in designing a heat sink due to its geometric freedom. In this approach, the computational domain is divided into a large number of elements. Each element has a relative density that determines whether the element is occupied by solid material or not. Therefore, the distribution of the relative density within the computational domain determines the heat sink geometries. In fact, there are many review articles that summarize the work previously performed by other researchers like [16, 17, 18, 19]. This paper mainly illustrates various designs of heat sinks and their geometrical parameters which have been designed by previous researchers during the last five years. It mainly focuses on the pins and flat surface fins heat sinks under free and forced convection due to their wide range of applications in industry and the modern design of microchannel heat sink. Besides, the effective topology optimization methods which are used in designing heat sinks.

### 11.5.3 Heat Sink Classification

A heat sink is a device, made of conductive metal, used to absorb heat from high-temperature parts and dissipate it to the surrounding. Heat sinks are commonly used in many industrial devices such as computer processors and air conditioning systems. Copper and aluminum are common metal used in manufacturing the heat sink. Most of the heat sinks designed with fins which are attached to the heat sink base to increase the heat dissipation area. There are two main techniques for heat transfer enhancement active and passive [20, 21]. Heat sinks vary in their shapes and applications, in this work heat sinks classified into four categories as follows:

#### 11.5.3.1 Pin Fin Heat Sink

Due to their excellent heat transfer performance, pin fins have a wide range of applications in industries [22, 23]. Cylindrical, square, triangular and elliptical pin fins are examples of shapes used by many researchers to investigate their performance with the aim of increasing their efficiency [24 -28]. The previous works which used pin fins heat sink under free and forced convection along with the enhancement made with those pin fins are summarized below:

##### 11.5.3.1.1 Optimal Pin Fin Heat Sink under Natural Convection

Mao-Yu and Cheng-Hsiung [29] examined experimentally and numerically the heat transfer rate for two different pin fin heat sinks under natural convection. The first was flat and solid heated base, while, the other had a hole in its heated base. The influence of the base plate, fin height, holes diameter in the base plate and the heat sink porosity on the heat transfer performance was also studied. The heat sink made of aluminum and the heated element was fitted into a copper block while attached to the heat sink. **Figure 11.5.1** displays a schematic of a pin heat sink.

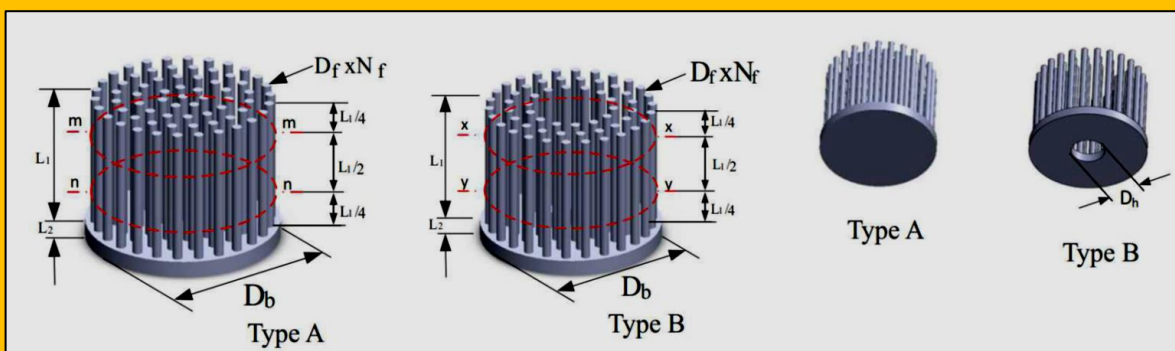


Figure 11.5.1 Schematic of a pin fin configuration [29]

The results showed that the heat transfer coefficient for hallow heated base heat sink is higher than that of the unhallow one due to greater acceleration and velocity in the circulation region. As the fin height, holes inside-outside diameter and input heat increases, the thermal performance increases. Finally, the hollow heat sink has a higher heat transfer coefficient than the solid heat sink when its porosity is  $\leq 0.262$ .

Sing [30], analyzed the thermal performance of a heat sink under natural convection by designing a model with ANSYS software. The ordinary circular pin fin with 32mm length was used then the

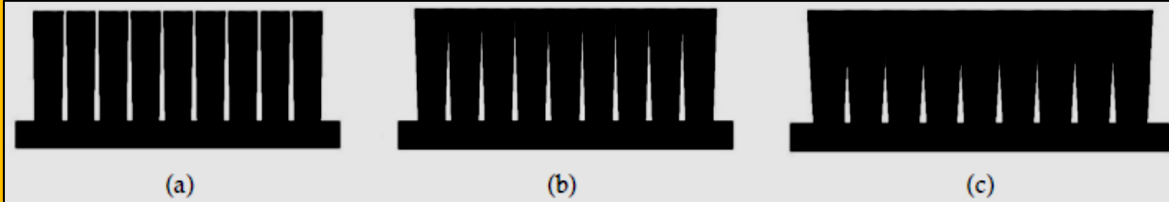


Figure 11.5.2 The modified pin fin heat sinks with (a) 1 degree (b) 2 degree and (c) 3 degree of expansion [30]

diameter of the pin was modified by an angle of expansion of 1 degree, 2 degrees and 3 degrees outward as shown in **Figure 11.5.2**. In this work, it was found that the 2 degree of expansion is the best modification as it dissipates more heat from the heat sink than other geometries.

Effendi et al. [31], predicted Nusselt number correction for a heat sink with round hollow hybrid fin (HHFHSs) under natural convection.

CFD software has been used to generate a 3D-thermal model as shown in **Figure 11.5.3**. 108 cases were studied, which include 36 arrangements with a different base temperature (50, 70 and 90°C). The numerical results have been experimentally validated. The developed Nusselt number correlation which is based on the fin height, Raleigh number, fin wall thickness, and external fin diameter, was shown to have reasonable

accuracy with less than 20% difference compared to the complicated numerical correlation. Baldry et al [32] adapted a numerical 3D model by using *COMSUL CFD* program to design a heat sink that is used in thermoelectric cooling cap under natural convection. This study examined 19 configurations of pin fin heat sink with 6 different pin fin parameters which are number, diameter, height, wetted area, center to center spacing and arrangements. The results were experimentally validated with the traditional pin fin heat sink. This research developed a pin fin heat sink with base temperature equals 44.4 C and 10.9 kW-1 thermal resistance which meets the efficiency requirement for dissipation the waste heat from the cooling cap.

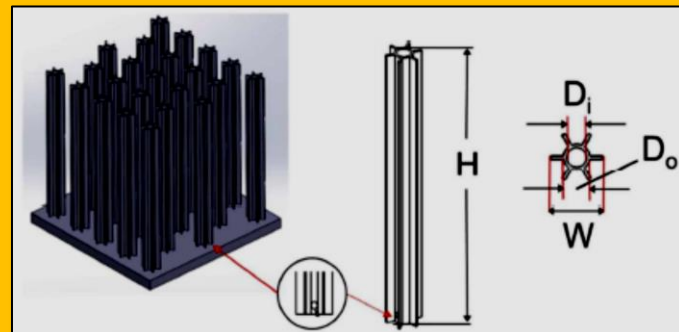


Figure 11.5.3 The structure and design of the heat sink [31]

### 11.5.3.1.2 Optimal Pin Fin Heat Sink under Forced Convection

Al-Damook et al. [33], investigated experimentally and computationally the effect of perforation on the pin fin thermal performance and the pressure drops across a heat sink under forced convection with different flow rates. Two aluminum heat sinks were designed; the first with solid pin fin while the second with perforated pin fin (the same work done by [34]). The pin is 12 mm long with 2 mm diameter fitted with a regular array into a base plate with 6.5mm spacing between each two-pin

centers. The perforated pins have holes with 1mm diameters with different locations as can be seen in **Figure 11.5.4**. The results showed that the Nusselt number (Nu) for the perforation pin is 11% higher than that in the corresponding solid. As the perforation increases, the pressure drop increases to reach its maximum value when using 5 perforations. In contrast, the location of the perforation was shown to have a less enhancing influence on the thermal performance in the heat sink.

Mao-Yu and Cheng [35] conducted simulation studies by using *COMSOL* multi-physics software to examine the thermal performance under forced convection for the heat sink designed in their

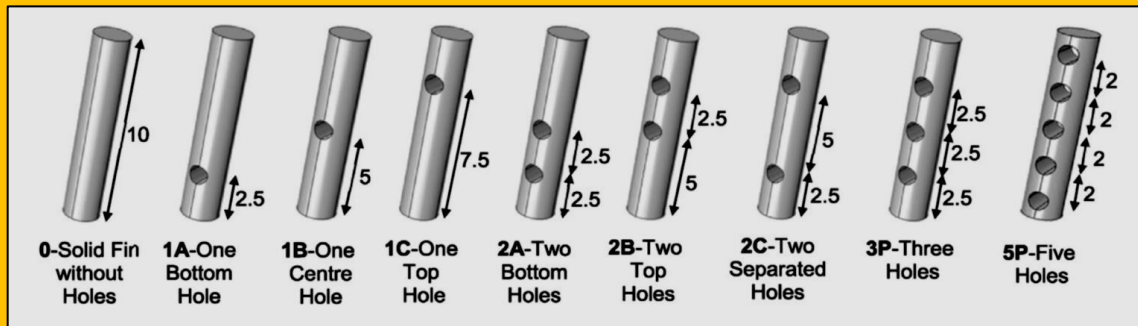


Figure 11.5.4 The various numbers and locations of perforation in pin fin heat sink [33]

previous research [29]. Reynolds number (Re) range from 6468 to 45919 was studied and data obtained were compared with experimental data from other investigators. The results showed the

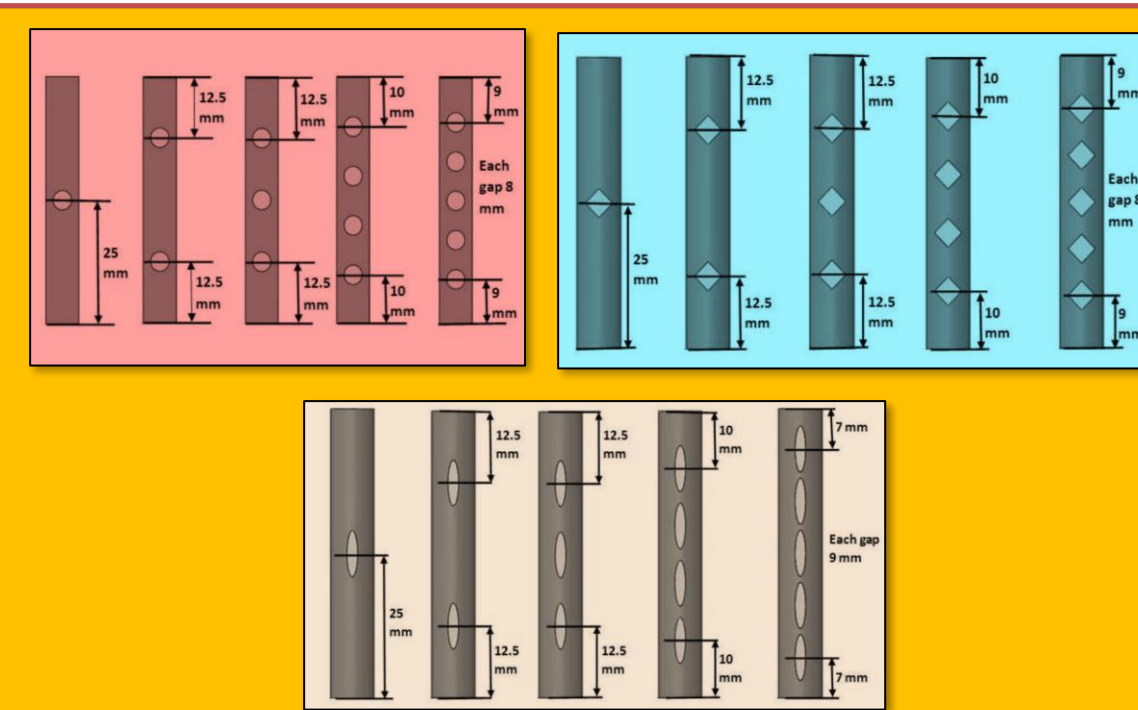


Figure 11.5.5 Fins with circular, diamond and elliptical perforation shapes [36]

highest heat transfer performance gained when a small hollow ( $D_h/D_b < 0.15$ ) is used in the base plate heat sink. Maji et al. [36] studied numerically the heat transfer through a pin fin with different

numbers, shapes, and sizes of perforation under forced convection by using inline and staggered arrangements. All the perforated fin heat performance and pressure drop were compared with the corresponding solid fin under the same conditions. ANSYS 14 fluent software was used to design the system models. Heat flux of  $5903 \text{ W/m}^2$  was applied at the bottom of the base plate which has an area of  $(0.1 \times 0.1) \text{ m}^2$  and a thickness of 3mm, where the fins are mounted either in inline or staggered.

**Figure 11.5.5** shows the different perforations geometries used and their numbers.

The results showed that all perforated fins had higher thermal performance than the solid fins, especially with a staggered arrangement. The Nu number increases and the pressure drop decreases as the perforation number and size increase. The maximum heat transfer rate obtained by using elliptical fins with elliptical perforation is higher by 40.5 % than that of the solid circular fin.

Maiti and Prasad [37], carried out a computational study on the heat transfer performance and the pressure drop in a fin heat sink under forced convection. Solid cylinder, slotted cylindrical, and kidney fin geometries were designed as shown in **Figure 11.5.6**. Reynolds number ranged from 2000 to 11000. The results obtained were validated with experimental results from previous work, and they found that the higher heat transfer rate acquired by using slotted kidney fin shapes with a staggered arrangement. Moreover, the decrease in pressure drop associated with the slotted fin was higher than that associated with the solid fin for both geometries, cylindrical and kidney.

Khonsue [38], conducted an experimental study to calculate the heat transfer rate and pressure drop

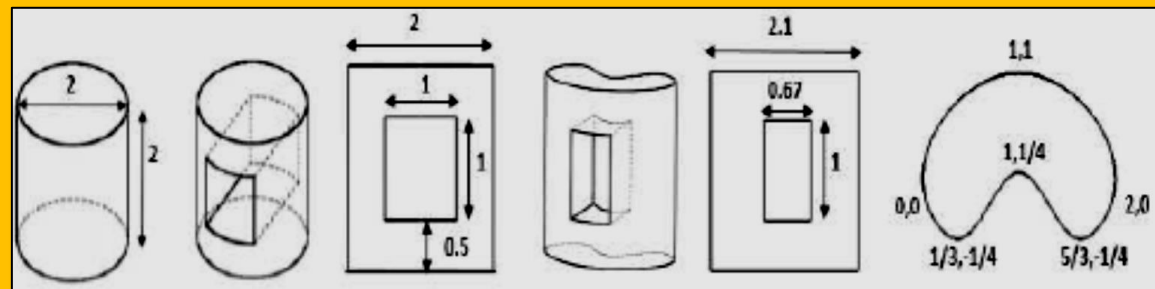


Figure 11.5.6 Geometries and dimensions of the different fins [37]

of mini pin-fin heat sink under forced convection to make a guide for the design and development of electronic devices. They used 63 aluminum pin fins with three different configurations, Rectangular, cylindrical and spiral pin-fin configurations. The experiments were carried out under a constant heat flux ranging from  $9.132$  to  $13.698 \text{ kW/m}^2$  and the air Reynolds number range was from 322 to 1982. The results showed that the spiral pin fins had the highest heat transfer coefficient and Nusselt number compared to the other configurations. On the other hand, the minimum pressure drop was obtained when the rectangle pin fin was used. Tijani and Jaffri [39], investigated numerically and experimentally the influence of circular configuration on thermal performance, pressure drop and temperature distribution of two finned heat sink geometries under forced convection. The experiments were performed with a constant heat flux of 50 W. The heat sink was placed inside a channel where air flowed through with a velocity range from 1 m/s to 3 m/s. solid and perforated pin fin and flat plate were designed together and compared in this work. The results showed that perforated pin and flat fin enhanced the heat transfer coefficient by 8.3% and 6.3% more than the corresponding solid fins respectively. Also, the Nusselt number was increased by 2% to 4% when perforated pin fin was used instead of a solid pin fin. The perforated fin had a smaller pressure drop in the experiment.

### 11.5.3.2 Flat Fin Heat Sink

The flat fin is one of the popular augmentation design used in a heat sink. Many researchers enhanced flat fin heat transfer performance by making holes, interrupted and rough surface, etc. [40]. The following are some of the enhancements made to flat fin in previous work.

#### 11.5.3.2.1 Optimal Flat Fin Heat Sink under Natural Convection

Awasarmol and Pise [41], carried out an experimental study to investigate the thermal performance of a perforated fin in a heat sink with different holes diameters and angles of inclination under natural convection. The perforations diameters ranged from 4 to 12 mm, the input powers supplied ranged from 15 to 35 W, and the angles of inclination ranged from  $0^\circ$  to  $90^\circ$ . The effect of these parameters was studied and the results are compared with the corresponding solid fins under the same conditions. The results obtained showed that the fins with 12 mm perforation diameter and  $45^\circ$  angle of inclination had a higher heat transfer coefficient with 32% enhancement over the solid fin. Also, perforation fins saved about 30% in the material by mass. Shitole and Arkirimath [42], presented an experimental work to calculate the heat transfer rate of a heat sink by using a vertical perforated plate under natural convection. Aluminum fins with dimensions of  $(200 \times 200 \times 20)$  mm and with different shapes (circular, square and triangular) and perforation size were used and compared with the non-perforated fin. The area of perforation was varied from ( $33.2$  to  $176.8$  mm $^2$ ) and the heat input was varied from (60 to 120 W) to investigate their influence on the heat transfer coefficient. The results showed that the heat transfer increases by increasing the heat input supply as well as perforation area. Moreover, the circular perforation had a higher heat transfer coefficient than the triangular perforation. Prasad et al. [43], carried out an experimental study to investigate the effect of a number of perforation on the heat transfer rate for a cylindrical heat sink under natural convection (the same work done by [44, 45]). The voltage supplied to the heat sink was ranged from 100 to 220 V. The perforation diameter was constant but their number ranged from 24 to 60.

The experimental results were compared with results obtained from computational analysis using the ANSYS program. The results showed that the heat dissipation increases by 20% to 70% as the perforation number increases from 24 to 60. Venkitaraj and Sanooj [46], investigated numerically the heat transfer enhancement by using fins with different perforation shapes under natural convection. Circular, square, elliptical and triangular perforations with a variety of diameters are designed. The heat input supplied to the heat sink ranged from 15 to 30 watt. The results obtained were compared with that obtained when using solid fin under the same conditions. It was found that the perforation fin dissipates more heat than solid fin [47] and the maximum heat transfer coefficient (9 W/m $^2$ .K) was achieved by using perforation area equivalent to 12 mm diameter. In addition, circular and elliptical perforation shapes nearly have the same characteristics [48]. Triangular perforation had the lowest heat transfer coefficient among the other shapes. Feng et al. [49], investigated experimentally and numerically the heat transfer enhancement by using cross fins heat

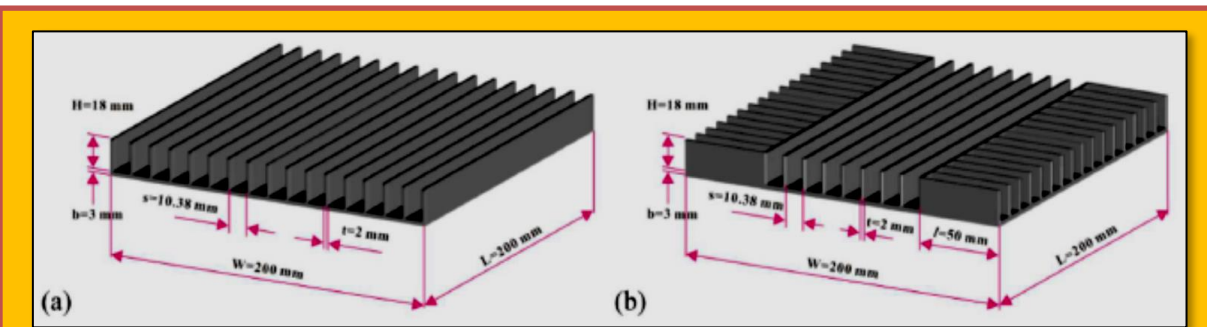


Figure 11.5.7 Design and dimensions of (a) plate-fin heat sink and (b) cross-fin heat sink [49]

sink under natural convection. The thermal efficiency of the cross fin heat sink was compared with the corresponding plate fin heat sink in a horizontal orientation.

The plate fin heat sink dimensions were 200mm length, 21mm height, and 2mm thickness. The cross fin heat sink has the same dimensions, but the length of the short fin was 50 mm as shown in **Figure 11.5.7**. The heat supplied ranged from 20 to 60 watt. The results showed that cross fin heat sink enhanced the heat transfer coefficient by 15% with the same volume and materials used in reference plate fin and without more cost.

Hussein [50], performed an experimental study to investigate the effect of v-corrugated perforation and non-perforation fin on the thermal performance of a heat sink under natural convection. The heat input to the heat sink was varied by varying the voltage supplied from 110 to 200 V. the fins were made from aluminum with 250 mm length, 250 mm width and, 2 mm thickness. The first fin is v-corrugated solid while the second fin is v-corrugated with inline arrangement circular perforation; the third fin is v-corrugated with staggered arrangement circular perforation.

The results obtained were validated with empirical results from previous literature [51]. The heat transfer coefficient and the heat dissipation for V-corrugated solid fin are greater than the flat [52, 53]. The heat transfer coefficient for a v-corrugated perforated fin was improved by 20% and 27% more than the corresponding solid for the inline and staggered arrangement respectively. Also, the results showed that perforation fin with staggered arrangement dissipated more heat than the inline arrangement by 22%.

Mousavi et al. [54], estimated numerically the heat transfer performance for 10 various configurations vertical finned heat sink under natural convection. 3D simulation by CFD software fluent 6.3 was made and compared with the previous experimental and theoretical investigation [55]. The vertical finned heat sink is of 305 mm length and 101 mm width. The fine configurations used in that work was shown in **Figure 11.5.8**.

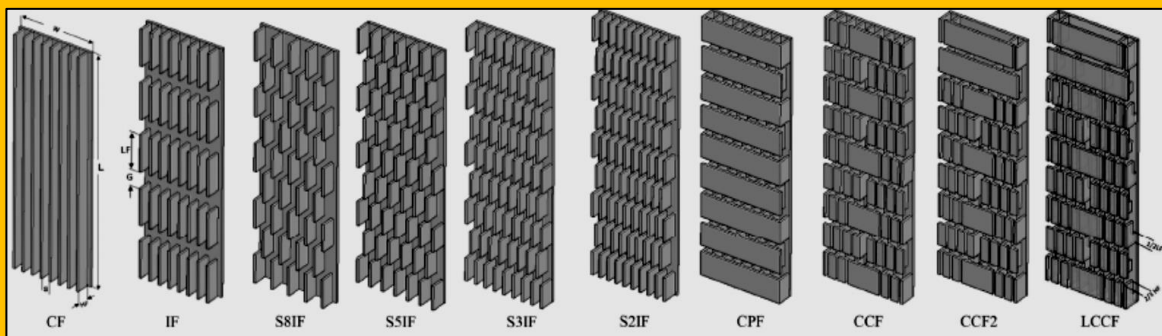


Figure 11.5.8 Schematics configurations of the heat sinks [54]

The results showed that decreasing the space between interrupted fins did not improve the cooling process. The capped fins enhanced the heat transfer rate but they have a higher weight than a continuous fin. In contrast, L-shape and cut-capped fins have less weight with higher heat transfer performance than other fins. Haghghi et al. [56], conducted an experimental investigation to study the thermal performance of a plate-cubic pin fin heat sink under natural convection. Six fins were designed with different configurations; fin numbers and fins spacing. The heat supplied was varied from 10 W to 120 W. The results showed that the plate cubic pin fin enhanced the heat transfer by 10 - 41.6 % and have lower thermal resistance compared to the normal plate fin. Also, the thermal performance improved as the fins spaces and fin numbers increased. The results of that work demonstrated that the optimal design was by using plate-cubic pin fin heat sink with 7 fins and 8.5mm spacing.

### 11.5.3.2.2 Optimal Flat Fin Heat Sink under Force Convection

Shadlaghani et al. [57], studied numerically the optimal fin designed to get a higher heat transfer rate for a heat sink under forced convection. First, triangular, rectangular and trapezoidal fins with constant volume were examined as shown in **Figure 11.5.9**. They found that the triangular shape had a greater heat transfer rate than other shapes. Second, the cross-section of the triangular fin was investigated and the results showed that when the ratio of fin height to its thickness increases, the heat transfer rate increases. Third, the convection enhanced by using longitudinal different shape perforation with different locations as can be seen in **Figure 11.5.10**. Results also showed that rectangular perforation with 0.3 ( $H_c/H$ ) location is the optimal design which gave the higher heat transfer rate.

Singh et al [58], analyzed computationally the heat transfer coefficient, Reynolds number (Re) and Nusselt number (Nu) for perforated fin heat sink under forced convection. CFD program was used to design the fins with circular, rectangular and slotted perforation with the same surface area. Reynolds number was varied from 8000 to 35000 with a constant heat input of 100 W. The results showed that fin with circular perforation dissipated more heat than the other configurations.

Besides, other perforation shapes were also shown to have a high heat transfer coefficient and Nusselt number [59].

Anish and Kanimozhi [60] determined experimentally the heat transfer coefficient of rectangular fins with the circular notch, triangular notch and without notch under forced convection. The test section was made of aluminum plates with  $190 \times 110 \times 1$  mm dimensions. These plates were modified by making a circular and triangular notch at their centers with 20 % notch area as can be seen in **Figure 11.5.11**. Experiments were carried under different heat flux values that ranged from 200 to 360 W and with various airflow rates. The results indicated that fins with circular notch have a heat transfer coefficient range from 10.34 to 10.55  $\text{W/m}^2 \text{ }^\circ\text{C}$ , compared to 10.08 to 10.29 for triangular notch and 9.6 to 9.76 for fin without a notch.

Salam et al. [61], carried out an experimental analysis to compare the performance of solid fins and perforation fins under forced convection. Three aluminum fins with a 10 cm length, 5 cm width, and a 3 cm thickness were used. The first fin was solid; the second was drilled along the lateral axis of the

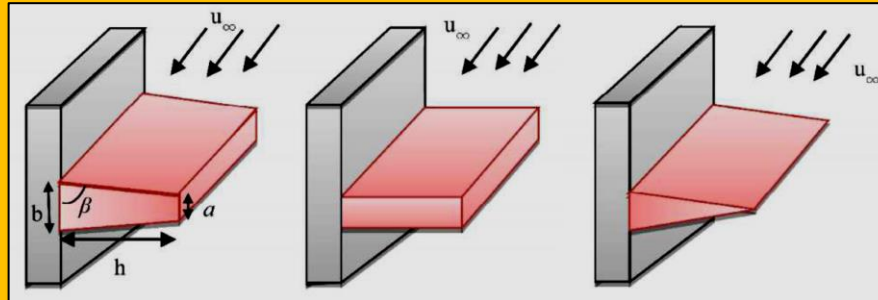


Figure 11.5.9 Fins with different geometries: (a) trapezoidal, (b) rectangular and (c) triangular [57]

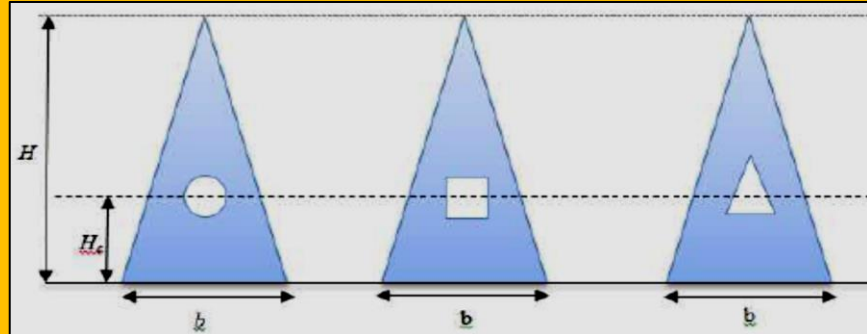


Figure 11.5.10 Triangular fin with different perforations shapes [57]

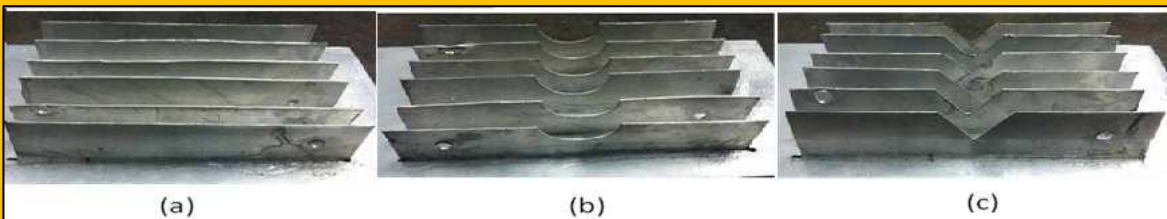


Figure 11.5.11 Plat fin (a) without notch (b) with circular notch (c) with triangular notch [60]

fin with 6mm diameter of circular perforation, and the third with 9mm diameter of circular perforation. The results showed that the perforated fin had a higher Nusselt number ( $Nu$ ) with a lower pressure drop and more weight reduction than the solid fin. Yadav et al. [62], modeled numerically a fin heat sink with different holes configurations to study their effects on heat transfer rate under force convection by using the COMSOL program. The heat sink was  $(13 \times 13 \times 1)$  mm dimensions and the fin was a 20 mm length, 15 mm width, and a 12 mm height. Circular and rectangular perforations were used with the same surface area of 25.13 mm and this was achieved by changing the size and number of perforation. The results showed that the perforation fins dissipate 3.5 – 5.5 % more heat than the solid fin with 34 – 40 % reduction in the wetted area. Al-Sallami et al. [63], studied numerically the optimal design of a finned heat sink under forced convection. They explored and compared the effect of longitudinal circular, notch and slot perforation on the heat transfer rate and pressure drop with a corresponding solid fin. Aluminum heat sink with base plate dimensions  $(50 \times 50)$  mm and a 2 mm thickness was used.

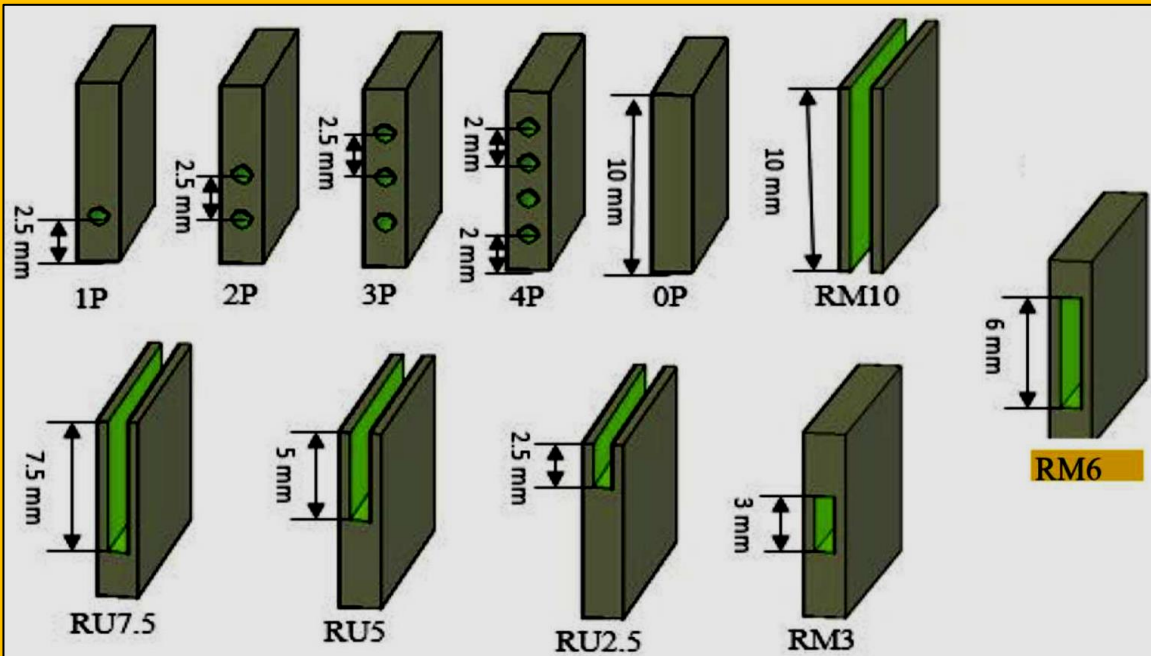


Figure 11.5.12 Designs and dimensions of the fins [63]

The fin height and thickness were the same in all cases and equal 10 mm and 2 mm, respectively. The first fin geometry was solid while the second fin was with 1, 2, 3 and 4 circular perforations with 1mm diameter. The third geometry was three fins with rectangular notches with 1mm width and different heights (2.5, 5 and 7.5 mm). The last geometry was three slotted fins with slot width equal

1mm and different heights (3, 6 and 10 mm) as shown in **Figure 11.5.12**. The result showed that the fins with notch perforation exhibit a significant advantage compared to the other perforations in terms of heat transfer and pressure drop. The notch perforation fin reduced the temperature of the heat sink base below its critical temperature with less fan power and less material.

Ibrahim et al. [64], investigated experimentally and numerically the heat transfer performance of a heat sink by using perforated and non-perforated fins under forced convection. The heat sink was an aluminum plate with a 195 mm length, 120 mm width, and 15mm thickness. Four fin geometries were chosen in this experiment; all of them were  $(120 \times 85)$  mm dimensions. One of them was solid while the other was perforating with circular, rectangular and triangular perforation. The air velocity used was varying from 1.8 to 2.8 m/s with 0.2 steps. The results showed that the perforated fins have a heat transfer coefficients 35.8% to 51.29% higher than that of the solid fin according to perforation shapes.

Patil and Dingare [65], investigated experimentally and numerically the heat transfer performance of a rectangular plate fin heat sink at varying orientation and arrangement under force convection. Three fins inclinations  $0^\circ$ ,  $30^\circ$  and  $60^\circ$  degree with inline and staggered arrangement were studied as shown in **Figure 11.5.13**. The experiments were carried out with Reynolds number ranged from 4000 to 18,000 and

different heat supplies (50, 80, 100 and 125 W). The results showed that the maximum heat transfer coefficient was obtained at  $30^\circ$  inclination with inline arrangement whereas at  $0^\circ$  for the staggered arrangement. The heat transfer associated with the  $0^\circ$  inclination with the staggered arrangement was 17 % higher than that associated with the  $30^\circ$  inclination with the inline arrangement and 76 % higher than that for flat plate fin.

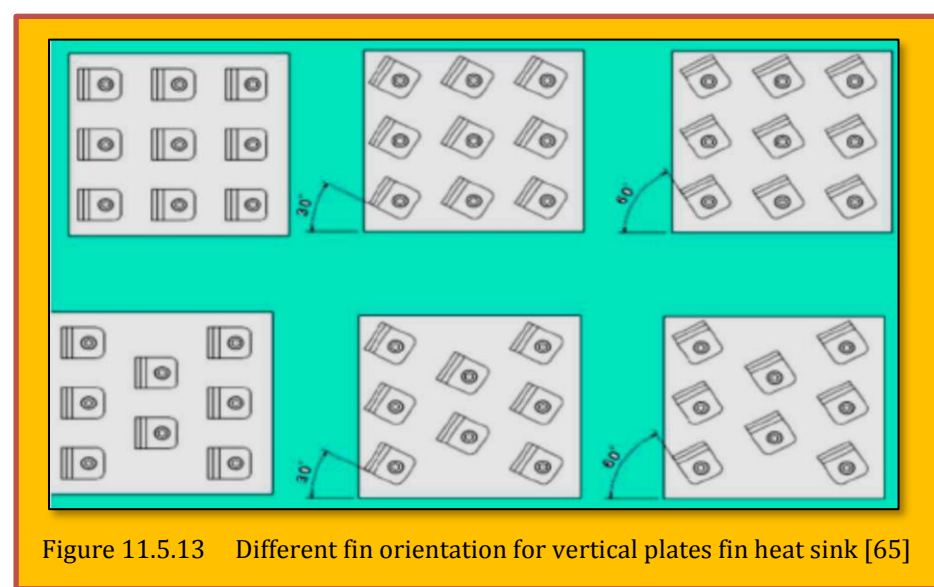


Figure 11.5.13 Different fin orientation for vertical plates fin heat sink [65]

Gupta et al. [66], investigated experimentally the heat transfer performance of a heat sink by using dimples and protrusions plate fin under forced convection condition. The plate fin was made of aluminum with 180 mm width and 80 mm height. The effect of dimples depth and pitch for inline and staggered arrangement on the Nusselt number and friction factor was also indicated. The experiments were carried out under Reynolds number range from 6800 – 15200 while the heat flux and dimples diameter was constant. Results showed that using the heat sink with dimples fins enhances the heat transfer, friction, and the fin performance compared to that of a smooth fin. The heat transfer rate and flow performance increase by developing the depth of the dimples. The maximum Nusselt number was obtained by using dimples fin with the staggered arrangement with dimple pitch and depth ratio of 2.5 and 0.5 respectively.

Bouchenafa et al [67] investigated numerically the effect of wavy plate fins on the heat sink performance under forced convection. The influence of the wave amplitude and numbers of waves on the Nusselt number and pressure drop was also analyzed are compared with the flat fin heat sink. By comparing the two heat sink configurations, higher heat transfer rate and pressure drop obtained from the wavy fin heat sink. Moreover, the wavy plate with a higher number of waves and amplitude

had a lower thermal resistance. Hoi et al. [68] optimized numerically the design of flat plate heat sink with fractal grid-induced turbulence under forced convection by using *CFD ANSYS fluent* program. The grid fin separation, fractal thickness ratio, and inter fin distance were studied numerically at Reynolds number equal  $2 \times 10^4$ .

The results obtained were validated with previous work by [69, 70] and showed that maximum Nusselt number was 3661 which was obtained by using 9.77, 0.005 mm and 0.01 mm for thickness ratio, inter fin distance and grid fin distance respectively. This value of Nusselt number was increased by 6.1% as compared to the reference case, and by 16.3% for the other configuration used in this study. Hussain et al. [71] investigated numerically the effect of fillet profile and flow direction on the heat sink thermal performance under forced convection. Two heat sink configurations were designed, the first one was with fillet profile and subjected to parallel flow, while the other one was without a fillet and subjected to impinging flow as can be seen in **Figure 11.5.14**. The radius of the fillet fin is 1.5 mm and the heat sink base dimensions were the same in both cases ( $40 \times 39.7 \times 1.5$  mm). The results showed that the heat sink with fillet fin profile had base temperature and thermal resistance that are 7.5% and 18% respectively lower than the non-fillet one.

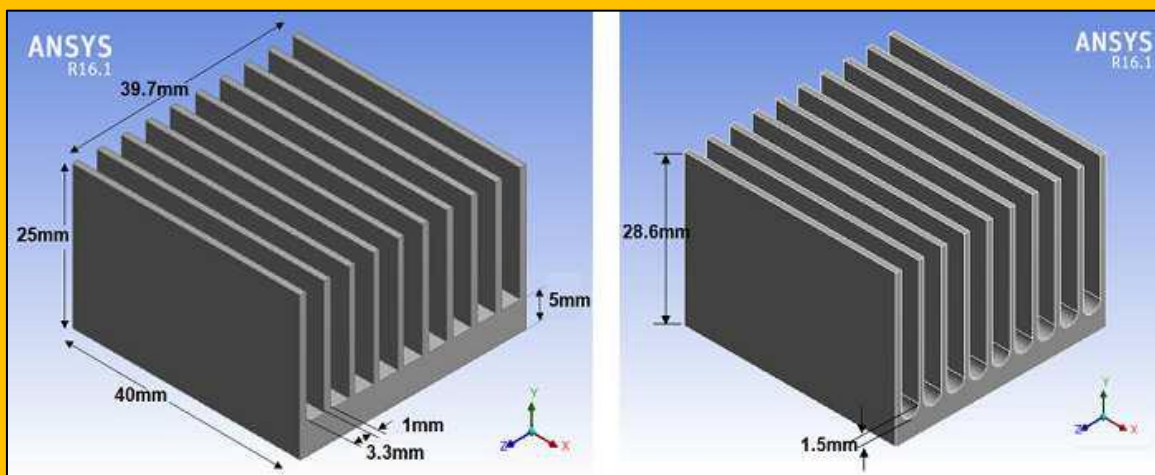


Figure 11.5.14 The geometrical model (a) non-fillet profile (b) fillet profile [71]

Taimoor et al. [72] examined experimentally the thermal performance of a heat sink with hexagonal perforated fin under forced convection. The Nusselt number, heat transfer coefficient, thermal resistance, fin efficiency and fin effectiveness for a perforated fin were calculated and compared with the non-perforated fin. The results demonstrated that Nusselt number, heat transfer coefficient, fin efficiency and fin effectiveness for a perforated fin are greater than those for non-perforated fin. Meanwhile, the thermal resistance and pressure drop for a perforated fin are smaller than solid one under the same conditions.

### 11.5.3.3 Micro-channel Heat Sink

Microfluidic devices are being widely used in different heat transfer applications and, thermal performance in microchannels become a serious challenging issue. As a solution, different geometries of micro-channel heat sinks have been employed to enhance the heat transfer. Khan et al. [73] analyzed numerically the effect of ribbed channels on the performance of a micro-channel heat sink by using three dimensional Navier-Stokes analysis. Six rib shapes were used in laminar flow with Reynolds number ranged from 100 to 500. The ribs dimensions were fixed and the results obtained with the traditional channel. From the results, it was found that using ribs in micro-channel improves the heat transfer rate and reduces the thermal resistance. Also, the Nusselt number and pressure

drop in ribbed channel increased gradually as Reynolds number increased. Those results also proved by other researchers [74, 75].

Among the various configurations of the ribs, the triangular rib showed the smallest thermal resistance while the rectangular rib resulted in the highest pressure drop. Xia et al. [76] studied experimentally and analytically the heat transfer performance and fluid flow characteristics in a micro-channel heat sink with complex corrugation channels. The thermal resistance and amount of enhancement were determined and compared with the smooth rectangular channel. The dimensions of the two channels were the same and the max/min widths of corrugation were 0.2/0.1 mm with 0.2 mm pitch.

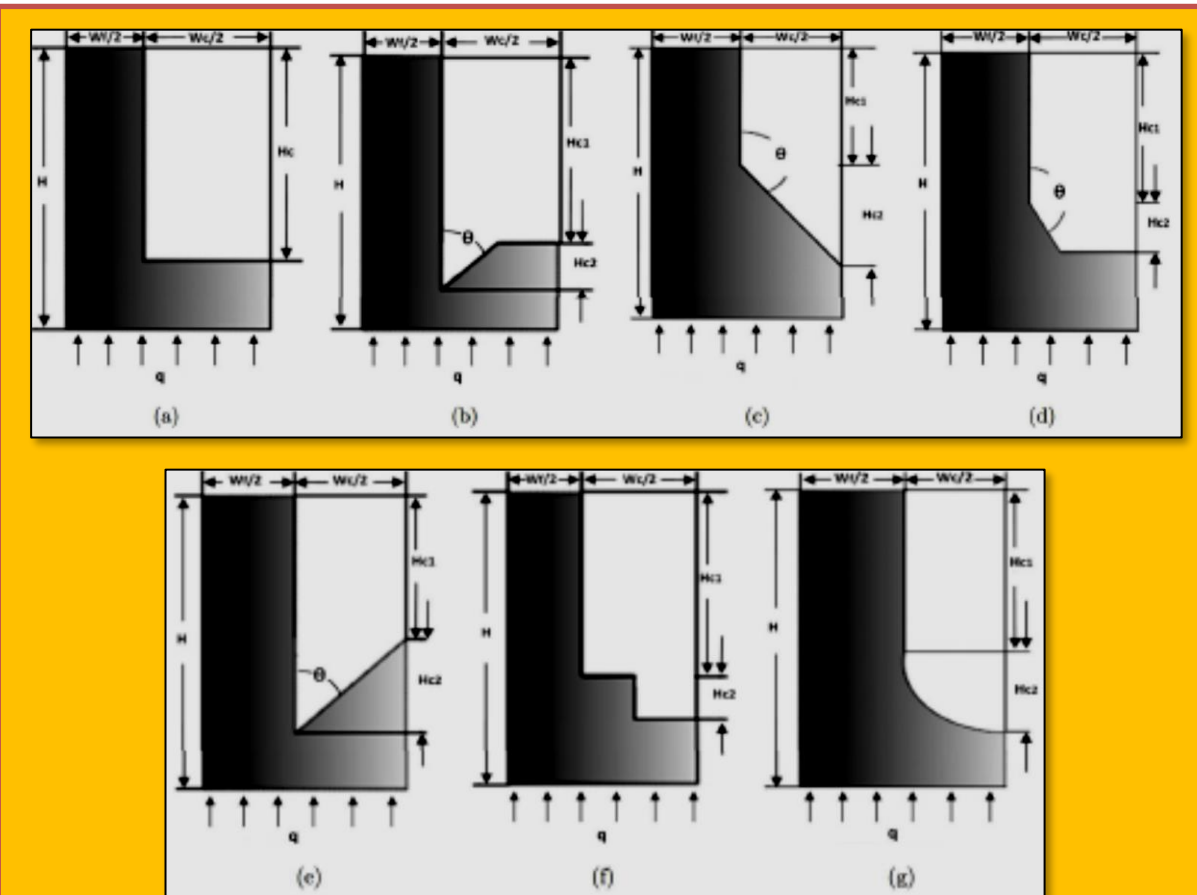


Figure 11.5.15 Various Geometrical cross-sections for micro-channel heat sink. (a) Rectangular, (b) inverse trapezoidal, (c) triangular bottom, (d) trapezoidal bottom, (e) W shape, (f) varied width rectangular, and (g) semi-oval [77]

The results indicated that thermal performance for the corrugated channel was enhanced by 1.24 for Reynolds number equal 611 and the thermal resistance was reduced by 18.99% than the regular rectangular channel. Khan and Kim [77] investigated numerically the thermal and hydraulic performance of various configuration micro-channel heat sinks by using the ANSYS CFD program. The design of the seven geometries used in this research can be seen in **Figure 11.5.15**. Nusselt number, friction factor, and thermal resistance were studied with a Reynolds number ranged from 50 to 500. The results showed that the inverse trapezoidal configuration introduced the best thermal performance and highest Nusselt number with the lowest increasing rate in the thermal resistance. Those results were also proved by [78] who investigated the thermal performance and resistance of

micro-channel heat sink with three different configurations of the channel cross-section area (Trapezoidal, square and semi-circular).

The design with trapezoidal cross-section provided the least thermal resistance Osanloo et al. [79] evaluated numerically the thermal, bottom wall temperature and pressure drop of a double layer microchannel heat sink with tapered lower and upper channel. Different flow rates of coolant fluid and convergence angles were studied. The results showed that the pressure drop and thermal resistance were significantly increased and the temperature of the bottom wall was reduced by increasing the volumetric flow rate and the convergence angle from  $0^\circ$  to  $6^\circ$ , in this cases the pumping power also increased [80].

The research showed that the optimal convergence angle was  $4^\circ$  which introduces the best temperature distribution with less thermal resistance. Ansari et al. [81] analyzed numerically the effect of randomly hotspots on the performance of a double layer microchannel heat sink by using 3D Navier

Stock equations. Two double-layer microchannel heat sink was designed with the same dimensions. The first one with parallel channels and the other with cross channels design, as shown in **Figure 11.5.16**. Eleven hotspots were introduced with three different schemes.

These hotspots distributed randomly depending on the design of the experimental techniques. The numerical analysis carried out with Reynolds number ranging from 400 to 933. The model was validated with experimental results from kinds of literature [82, 83]. From the results of that work, it can be concluded that the heat sink with the transverse flow and multiple hotspots is considered the best choice for cooling due to its lowest temperature variation and thermal resistance among the other schemes.

Jing and He [84] studied numerically the thermal performance of a staggering double-layer microchannel heat sink (DLMCHS). The influence of inlet velocity, geometrical parameters such as the offset between the lower and upper layer of micro-channels and vertical rib thickness on thermal resistance also investigated. The results showed that the geometrical parameters highly affected the thermal performance of the DLMCHS. This statement completely agrees with [85] who showed that hydraulic resistance and heat transfer of fluid flow in a micro-channel is strongly dependent on the geometric parameters of the channel. Deng et.al [86] studied numerically the hydraulic and thermal performance of double-layer microchannel heat sink (DL-MCHS) with various cross-sectional geometries. Five DL-MCHS were designed with triangular, trapezoidal, rectangular, circular and reentrant as can be seen in **Figure 11.5.17**. The thermal resistance, pressure drop, and wall temperature distribution were compared for all these configurations and the single layer (MCHS). The results showed that DL-MCHS decreases the wall temperature with a 27% reduction in thermal resistance. Among the five geometries of DL-MCHS, the rectangular shape was shown to be the best choice for the best thermal performance, whereas the reentrant shape required the least pumping power. While, the trapezoidal shape showed the worst pressure drop, thermal resistance, and pumping power.

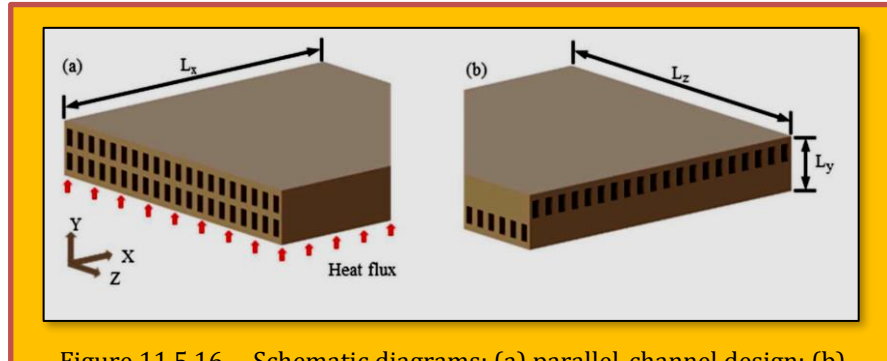


Figure 11.5.16 Schematic diagrams: (a) parallel-channel design; (b) cross-channel design [81]

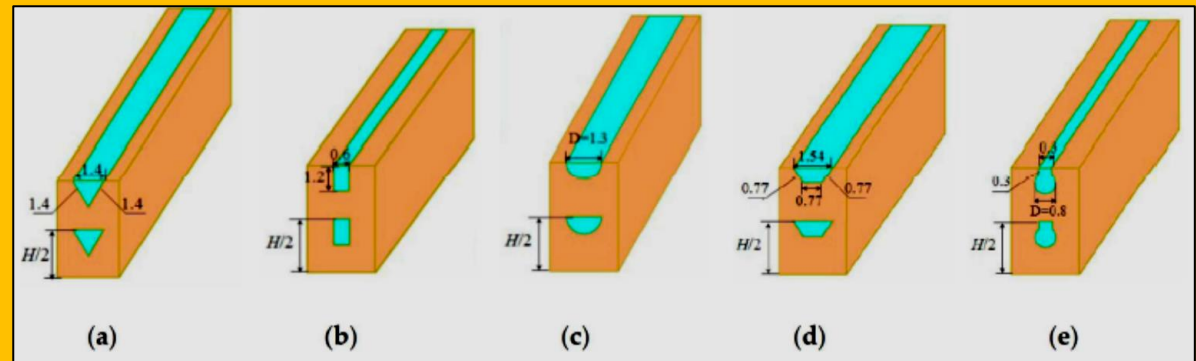


Figure 11.5.17 Schematic of the DL-MCHS with different micro-channel cross-sectional shapes: (a) triangular; (b) rectangular; (c) circular; (d) trapezoidal; (e) reentrant shaped [86]

#### 11.5.3.4 Topology Optimized Heat Sink

Topology optimization is a new method used by some researchers for thermal optimization of heat sink configurations without specifying a fin shape. Dede et al. [87] presented a topology optimization method for steady-state conduction with side convection to design a 3D air-cooled heat sink. In this research, the additive layer manufacturing (ALM) approach was used to fabricate the optimized heat sink. The benefit of using the ALM approach is to design complex geometries or external profiles that cannot be designed by using the conventional manufacturing method. The thermal resistance and pressure drop for optimized heat sink versus different airflow rates were studied (numerically and experimentally) and compared with heat sink designs that have straight plat, radial plate, stepped straight plate and staggered pin fin arrangement which is fabricated by using conventional machining techniques in kinds of literature.

The results showed that the optimized heat sink had lower thermal resistance and pressure drop than the other heat sink geometries. Alexandersen et al. [88] applied the density-based topology optimization method to design a 3D heat sink cooled by natural convection by using a fully coupled non-linear thermofluidic model. Various optimized designs are implemented in laminar flow conditions with Grashof number ranged from  $10^3$  to  $10^6$ . The methodology used in this work is capable of avoiding problems with the formation of non-physical internal cavities, recovers interesting physical effects and insights and length-scale effects and artificial convection assumptions. The results were verified with the results obtained from the finite element analysis method performed by the *COMSOL* program and showed good agreement. The results showed that the branches of the designed heat sink increase as the Grashof number increase. In addition,

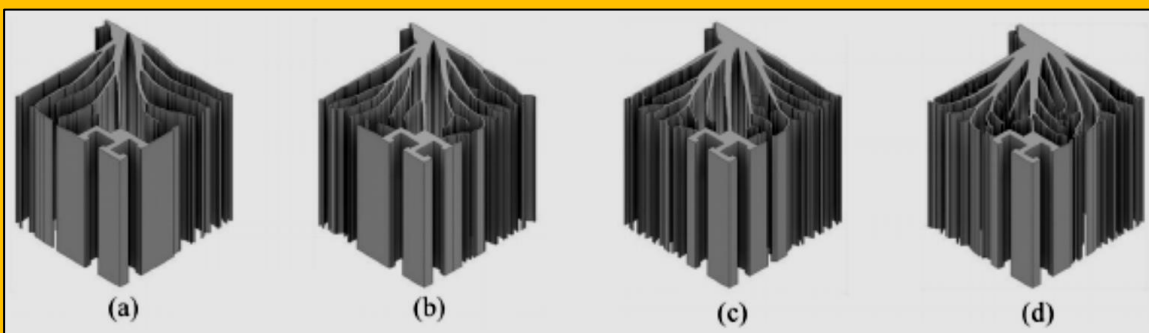


Figure 11.5.18 3D topology optimized heat sink with volume fraction (a) 0.19 (b) 0.23 (c) 0.27 (d) 0.31 [89]

complex geometries can notably enhance the cooling behavior compared to the simple fin geometry. Joo et al. [89] optimized the thermal performance of a heat sink in natural convection by using topology optimization method.

In order to predict the shape-dependent influence of the heat sink, a surrogate model that is applicable to arbitrarily shape structures was used with the effective channel spacing. The thermal performance of the optimized heat sink was compared to that of a plate-fin heat sink from the numerical correlations. To determine the thermal performance of the optimized heat sink, the finite volume method was used and implemented in the ANSYS software program. The four volume fractions used in this work can be seen in [Figure 11.5.18](#). The results obtained showed that the thermal resistance of the optimized heat sink is 15% lower than that of the conventional heat sink with 26% material saving.

Maradiaga et al. [90] designed and modeled a topology optimized heat sink to enhance the thermal management of the tablet by using the *COMSOL* optimization module. Three aluminum heat sinks were designed, the first one as L shape heat sink and the others were topology optimized by using the robust and non-robust approach as can be seen in these sharp edges have no zones with intermediate densities. Therefore, they are easy to manufacture. The results showed that the non-robust heat sink has the lowest average temperature and the highest heat transfer coefficient in experimental and numerical modeling. Zeng and Lee [91] designed a 3D liquid-cooled micro-channel heat sink (MCHS) by using the topology optimization method. The model was implemented depending on the derived accurate 2D model with considering minimum pressure drop and average temperature. The optimized MCHS was performed for different velocities on the conventional straight channels. The results indicated that the optimized MCHS saves about 50% of pumping power with high thermal performance.

#### 11.5.4 Conclusions

The optimal design of a heat sink aims to enhance the heat removal process with less mass, size, frictional losses, cost and weight with better performance. In the present paper, the techniques implemented in previous researches to increase the thermal efficiency of heat sinks for the last 5 years are reviewed. For plate and pin fin heat sink, the shapes, orientation, perforation, slot interrupted fins dimensions; space between fins and their arrangement under free and forced convection conditions are examined. The Micro-channel heat sinks with different sizing, geometries, and cross sections, using turbulators, single- and double-layers, and topology optimized heat sinks are also reviewed. The following conclusions can be drawn:

- 1 For forced convection, as the Reynolds number increases the Nusselt number, heat transfer rates and pressure drop also increases. Fins with perforation, slot, corrugated, dimples, notch, and interruption for either free or forced conditions showed a better heat transfer rate than the solid fins. Staggered arrangement for a pin fin, flat fin, perforations, and slots showed good enhancement in heat transfer coefficient compared to the inline arrangement. The spacing between fins had a significant influence on the heat sink performance. As the space increases, the heat performance increases. The amount of heat removal from the heat sink is largely affected by the orientation and inclination angle of the fins. Two basic considerations are used in optimizing the heat transfer performance, the amount of heat removal and the heat removal per unit weight. When the total heat dissipation is the basic demand, the optimal plate-fin heat sink is more efficient than the optimal pin fin heat sink. In contrast, the optimal pin fin heat sink dissipates more heat per unit weight than the optimal plate-fin heat sink in many practical applications.
- 2 The thermal performance of a micro-channel heat is significantly enhanced by using a double layer, different channel geometry, turbulators and ribs between channels. Nevertheless,

using augmentations can result in a high pressure drop in some applications and need more pumping power than a smooth single layer microchannel heat sink.

- 3 Topology optimization is a powerful method for designing heat sinks capable of maintaining a low operating temperature in limited space. The topology optimization designing approach leads to branching, tree-shaped flow network designs. This type of fins shapes create more complex flow phenomena in forced convection conditions like secondary flow, boundary initiation, flow mixing and participating in the enhancement of thermal and hydraulic performance. However, more experimental validation is needed to improve and confirm the topology optimization method.

### **Author Contributions**

*H.T. Dhaiban planned the scheme, collected the previous literatures and suggested the review classifications. M.A. Hussein initiated and wrote the research; all authors discussed the conclusions, reviewed and approved the final version of the manuscript.*

### **Conflict of Interest**

*The authors declared no potential conflicts of interest with respect to the research, authorship and publication of this article.*

### **Funding**

*The authors received no financial support for the research, authorship and publication of this article.*

### **11.5.5 References**

- [1] Kraus A.D., Abdul Aziz, J.W., *Extended surface heat transfer*, 1st edition, John Wiley and Sons, U.S.A, 2001.
- [2] Holman J.P., *Heat Transfer*, 10th edition, McGraw-Hill Book Company, New York, 2010.
- [3] Ahmadi M., Mostafavi G., Bahrami M., Natural convection from rectangular interrupted fins, *International Journal of Thermal Sciences*, 82, 2014.
- [4] Huang G., Wong S., Pei L.C., Enhancement of natural convection heat transfer from horizontal rectangular fin arrays with perforations in fin base, *International Journal of Thermal Sciences*, 2014.
- [5] Wang Y., Zhu K., Cui Z., Li H., Wei J., Evaluation of Water Cooling Heat Sink Performance and Dynamic flow effect, *10th International Conference on Applied Energy (ICAE2018)*, Hong Kong, 2018.
- [6] Yang D., Wang Y., Ding G., Jin Z., Zhao J., Wang G., Numerical and experimental analysis of cooling performance of single-phase array micro-channel heat sinks with different pin-fin, *Applied Thermal Engineering*, 112, 2017, 1547-1556.
- [7] Bello-Ochende T., Liebenberg L., Meyer J.P., Constructed cooling channels for micro-channel heat sinks, *International Journal of Heat and Mass Transfer*, 50, 2007, 4141–4150.
- [8] Hao P.F., Yao Z.H., He F., Zhu K.Q., Experimental Investigation of Water Flow in a Smooth and Rough Silicon Micro-channels, *Journal of Micromechanics and Microengineering*, 16(7), 2006.
- [9] Sharma D., Singh P.P., Garg H., Numerical analysis of trapezoidal shape double layer micro-channel heat sink, *International Journal of Mechanical and Industrial Engineering*, 3, 2013, 10–15.
- The Optimal Design of Heat Sinks: A Review Journal of Applied and Computational Mechanics, (2020).
- [10] Chai L., Xia G., Zhou M., Li J., Qi J., Optimum thermal design of interrupted micro-channel heat sink with rectangular ribs in the transverse microchambers, *Applied Thermal Engineering*, 51, 2013.
- [11] Sui Y., Teo C.J., Lee, P.S., Chew Y.T., Shu C., Fluid Flow and Heat Transfer in Wavy Micro-channels, *International Journal of Heat and Mass Transfer*, 53(13–14), 2010, 2760- 2772.
- [12] Mohammed H.A., Gunnasegaran P., Shuaib N.H., Numerical simulation of heat transfer enhancement in wavy micro-channel heat sink, *International Communications in Heat and Mass Transfer*, 38, 2011, 63–68.
- [13] Bendsoe M.P., Sigmund O., *Topology Optimization – Theory, Methods and Applications*, Springer Verlag, 2003.

- [14] Subramaniam V., Dbouk T., Harion1 J., Thermal Measurements in Conductive Heat Transfer Tree-Like Structures Obtained by Topology Optimization, *the 3rd World Congress on Momentum, Heat and Mass Transfer (MHMT'18)*, Budapest, Hungary, 2018.
- [15] Zhou M., Alexandersen J., Sigmund O., Pedersen C., Industrial application of topology optimization for combined conductive and convective heat transfer problems, *Structural and Multidisciplinary Optimization Journal*, 54(4), 2016, 1045–1060.
- [16] Ahmed H. E., Salman B.H., Kherbeet A.Sh., Ahmed M.I., Optimization of thermal design of heat sinks: A review, *International Journal of Heat and Mass Transfer*, 118, 2018, 129–153.
- [17] Khattak Z., Ali H. M., Air cooled heat sink geometries subjected to forced flow: A critical review, *International Journal of Heat and Mass Transfer*, 130, 2019, 141–161.
- [18] Dbouk T., A review about the engineering design of optimal heat transfer systems using topology optimization, *Applied Thermal Engineering*, 112, 2017, 841-854.
- [19] Wang C.C., A Quick Overview of Compact Air-Cooled Heat Sinks Applicable for Electronic Cooling—Recent Progress, *Inventions Journal*, 2(5), 2017, 1-26.
- [20] Jadhav M., Awari R., Bibe D., Bramhane A., Mokashi M., Review on Enhancement of Heat Transfer by Active Method, *International Journal of Current Engineering and Technology*, 6, 2016, 221-225.
- [21] Sonawane T., Patil P., Chavhan A., Dusane B.M., A Review on heat transfer enhancement by passive methods, *International Research Journal of Engineering and Technology*, 3(9), 2016.
- [22] Shen Q., Sun D., Ya Xu, Jin T., Zhao X., Zhang N., Wu K., Huang Z., Natural convection heat transfer along vertical cylinder heat sinks with longitudinal fins, *International Journal of Thermal Sciences*, 100, 2016, 457-464.
- [23] Jang D., Yook S., Lee K., Optimum design of a radial heat sink with a fin-height profile for high-power LED lighting applications, *Applied Energy*, 116, 2014, 260–268.
- [24] Tomar Y.S., Sahu M.M., Comparative Study of Performance of Pin Fin under Forced Convection Heat Transfer, *International Journal of Engineering Research & Technology*, 2(9), 2013, 364-374.
- [25] Muthukumarn R., Rathnasamy R., Karthikeyan R., Experimental Study of Performance of Pin Fin Heat Sink under Forced Convection, *International Journal of Mechanical Engineering and Information Technology*, 4(10), 2016, 1791-1796.
- [26] Cuce E., Oztekin E.K., Cuce P.M., Heat transfer enhancement in cylindrical fins through longitudinal parabolic perforations, *International Conference on Advanced Engineering Technologies*, Turkey, 2017.
- [27] Muhammad E.H., A Comparison of the Heat Transfer Performance of a Hexagonal Pin Fin with Other Types of Pin Fin Heat Sinks, *International Journal of Science and Research*, 4(9), 2015.
- [28] Usman H., Ali H.M., Arshad A., Ashraf M.J., Khushnood S., Janjua M.M., Kazi S.N., An experimental study of PCM based finned and un-finned heat sinks for passive cooling of electronics, *Heat and Mass Transfer*, 54(12), 2018, 3587–3598.
- [29] Mao-Y W., Cheng-Hsiung Y., Natural convective performance of perforated heat sinks with circular pin fins, *Journal of Heat and Mass Transfer*, 51, 2015, 1383-1392.
- [30] Singh G., Natural convection heat transfer from modified 1degree 2 degree and 3 degree outward expansion of pin fins, *International Journal of Engineering Science and Computing*, 7, 2017.
- [31] Effendi N.S., Severianus S.G., Putra R., Kim K.J., Prediction methods for natural convection around hollow hybrid fin heat sinks, *International Journal of Thermal Sciences*, 126, 2018, 272–280.
- [32] Baldry M., Timchenko V., Menictas C., Optimal design of a natural convection heat sink for small thermoelectric cooling modules, *Applied Thermal Engineering*, 160, 2019, 1-13.
- [33] Al-Damook A., Kapur N., Summers J.L., Thompson H.M., An experimental and computational investigation of thermal air flows through perforated pin heat sinks, *Journal of Applied Thermal Engineering*, 89, 2015, 365–376.
- [34] Abdullah S.M., Autee A.T., Experimental Analysis Of Heat Transfer From Square Perforated Fins In Staggered Arrangement, *International Journal of Engineering Research and Applications*, 2015.

- [35] Mao-Y W., Cheng-Hsiung Y., Numerical study of thermal performance of perforated circular pin fin heat sinks in forced convection, *Journal of Heat and Mass Transfer*, 53, 2017, 2031-2044.
- [36] Maji A., Bhanja D., Patowari P.K., Numerical investigation on heat transfer enhancement of heat sink using perforated pin fins with inline and staggered arrangement, *Journal of Applied Thermal Engineering*, 125, 2017, 596-616.
- [37] Maiti A., Prasad S.S., Alternative Heat Sink to Enhance Thermo-Hydraulic Behavior of an Array of Short Pin Fins, *3rd World Congress on Mechanical, Chemical, and Material Engineering*, Italy, 2017.
- [38] Khonsue O., Enhancement of the forced convective heat transfer on mini pin fin heat sinks with micro spiral fins, *Journal of Heat and Mass Transfer*, 54, 2017, 563-570.
- [39] Tijani A.S., Jaffri N.B., Thermal analysis of perforated pin-fin heat sink under force convection conditions, *Procedia H.T. Dhaiban and M.A. Hussein*, Vol. 6, No. 4, 20xx *Journal of Applied and Computational Mechanics*, Vol. 6, No. 4, (2020).
- [40] Singh P., Patil A.K., Experimental Investigation of Heat Transfer Enhancement through Embossed Fin Heat sink under Natural Convection, *Experimental Thermal and Fluid Science*, 61, 2015.
- [41] Awasarmol U.V., Pise A.T., An experimental investigation of natural convection heat transfer enhancement from perforated rectangular fins array at different inclinations, *Experimental Thermal and Fluid Science*, 68, 2015, 145-154.
- [42] Shitole A.S., Arkirimath R.R., Experimental study and heat transfer analysis of effect of various perforations on vertical heated plates in natural convection, *International Engineering Research Journal*, 1, 2016, 45-50.
- [43] Prasad L., Tewari S., Kumar A., An experimental study of heat transfer enhancement in the perforated rectangular fin, *Journal of Integrated Science & Technology*, 4(1), 2016, 5-9.
- [44] Sudheer M., Shetty A., Somayaji S., Finite Element Investigations of Temperature Distribution in Fins with Circular Perforations, *American Journal of Materials Science*, 5(3), 2015, 157-161.
- [45] Kaushik S., Sati V., Gupta A., Puri K., Experimental Analysis between Rectangular Solid Fins with Different Circular Perforated Rectangular Fins under Natural Convection, *International Journal of Engineering Research & Technology*, 4(5), 2015, 1299-1306.
- [46] Venkitaraj K.P., Sanooj S., natural convection heat transfer enhancement from rectangular fin arrays with diverse geometrical perforations, *International Conference on Energy Efficient Technologies for Sustainability*, IEEE, 2016.
- [47] Patil M.H., Patil, S.V., Deore E.R., Chaudhari G.A., Design & Analysis of Perforated Rectangular Fin Array with Varying Percentage of Perforation, *International Advanced Research Journal in Science, Engineering and Technology*, 3(9), 2016, 26-31.
- [48] Shirjose P.P., Numerical Investigation of Elliptical and Triangular Perforated Fins under Forced Convection, *International Journal of Scientific Research Engineering & Technology*, 5(4), 2016, 232-235.
- [49] Feng S., Shi M., Yan H., Sun S., Li F., Jian Lu T., Natural Convection in a Cross-Fin Heat Sink, *Journal of Applied Thermal Engineering*, 132, 2018, 30-37.
- [50] Hussein M.A., The Effect of Circular Perforation on a V-Corrugated Fin Performance under Natural Convection, *Journal of Engineering*, 24(7), 2018, 19-34.
- [51] Muthuraja C.S., Kumar A., Hanoca P., Experimental Study Of The Perforated Rectangular Fins By Natural Convection, *International Journal of Advanced Technology in Engineering and Science*, 3(1), 2015, 303-307.
- [52] Solanki M., Vedpathak M., Modelling and Analysis of Heat Sink with V Shaped Fin Arrays, *Journal of Material Science and Mechanical Engineering*, 2(4), 2015, 292-297.
- [53] Wani S.A., Shrotri A.P., Dandekar A.R., Experimental Investigation of Natural Convection Heat Transfer from a Fin Array- A Review, *International Journal of Modern Studies in Mechanical Engineering*, 2(1), 2016, 46-50.
- [54] Mousavi H., Darzi A.A., Farhadi M., Omidi M., A novel heat sink design with interrupted, staggered and capped fins, *International Journal of Thermal Sciences*, 127, 2018, 312-320.

- [55] Ahmadi M., Mostafavi G., Bahrami M., Natural convection from rectangular interrupted fins, *International Journal of Thermal Sciences*, 82, 2014, 62 -71.
- [56] Haghghi S.S., Goshayeshi H.R., Safaei M.R., Natural convection heat transfer enhancement in new designs of plate-fin based heat sinks, *International Journal of Heat and Mass Transfer*, 125, 2018.
- [57] Shadlaghani A., Tavakoli M.R., Farzaneh M., Salimpour M.R., Optimization of triangular fins with/without longitudinal perforate for thermal performance enhancement, *Journal of Mechanical Science and Technology*, 30(4), 2016, 1903-1910.
- [58] Singh H., Singh H., Sehgal S.S., Computational analysis on performance of heat sink with different configurations of fins array, *Indian Journal of Science and Technology*, 9(36), 2016, 1-4.
- [59] Vyas A., Gupta S., Gupta S., Determining relation among Shape of Perforation and Convective Heat transfer from Lateral fin arrangement using Simulation by Computational Fluid Dynamics, *International Refereed Journal of Engineering and Science*, 5(4), 2016, 24-31.
- [60] Anish M., Kanimozhi B., Experimental Investigation and Heat Transfer Process on Longitudinal Fins With Different Notch Configuration, *International Journal of Ambient Energy*, 39, 2018, 34-37.
- [61] Salam N., Rahmatullah K., Faizanurrahman, Salman A., Tohid A., Khan T., Heat transfer enhancement through perforated fin, *Journal of Mechanical and Civil Engineering, RDME*, 2017.
- [62] Yadav S., Das K., Pandey K.M., A comparative analysis of heat transfer in extended surfaces with and without holes, *Fluid Mechanics and Fluid Power-Contemporary Research*, 2017.
- [63] Al-Sallami W., Al-Damook A., Thompson H.M., A numerical investigation of the thermal-hydraulic characteristics of perforated plate fin heat sinks, *International Journal of Thermal Sciences*, 121, 2017.
- [64] Ibrahim T.K., Mohammed M.N., Mohammed M.K., Najafi G., Sidik N.A., Basrawi F., Abdalla A.N., Hoseini S.S., Experimental study on the effect of perforations shapes on vertical heated fins performance under forced convection heat transfer, *International Journal of Heat and Mass Transfer*, 118, 2018, 832-846.
- [65] Patil H.B., Dingare S.V., Experimental and Numerical Investigation of Forced Convection Heat Transfer in Heat Sink with Rectangular Plates at Varying Inclinations on Vertical Base, *Journal of the Institution of Engineers India: Ser. C*, 100(3), 2019, 461-471.
- [66] Gupta A., Kumar M., Patil A.K., Enhanced heat transfer in plate fin heat sink with dimples and protrusions, *Heat and Mass Transfer*, 55, 2019, 2247-2260.
- [67] Bouchenafa R., Mohammed H.A., Saim R., Numerical study of the thermal and hydraulic performances of heat The Optimal Design of Heat Sinks: A Review Journal of Applied and Computational Mechanics, Vol. 6, No. 4, (2020), 1030-1043 1043 sink made of wavy fins, *Mechanics and Mechanical Engineering*, 23, 2019, 150-161.
- [68] Hoi S.M., Teh A.L., Ooi E.H., Chew I.M., Foo J.J., Forced convective heat transfer optimization of plate-fin heat sink with insert-induced turbulence, *Applied Thermal Engineering*, 160, 2019, 1-15.
- [69] Mazellier N., Vassilicos J.C., Turbulence without Richardson-Kolmogorov cascade, *Physics of Fluids*, 22(7), 2010, 075101.
- [70] Shiva S., Yeoh C.V., Chin W.M., Foo J.J., Forced convective heat transfer and flow characteristics of fractal grid heat sinks, *International Journal of Thermal Science*, 125, 2018, 176-184.
- [71] Hussain A.A., Freegah B., Khalaf B.S., Towsyfyan H., numerical investigation of heat transfer enhancement in plate-fin heat sinks: Effect of flow direction and fillet profile, *Case Studies in Thermal Engineering*, 13, 2019, 1-14.
- [72] Taimoor I., Rahman M.L., Aankhy N.S., Bin Khalid M., Thermal performance analysis of plate fin arrays with hexagonal perforations under turbulent flow regime, *8th BSME International Conference on Thermal Engineering, AIP Conference Proceeding*, 2121, 2019.
- [73] Khan A.A., Kim S., Kim K., Performance Analysis of a Micro-channel Heat Sink with Various Rib Configurations, *Journal of Thermophysics and Heat Transfer*, 40(3), 2016, 1-9.
- [74] Chai L., Xia G.D., Wang H.S., Laminar flow and heat transfer characteristics of interrupted micro-channel heat sink with ribs in the transverse microchambers, *International Journal of Thermal Sciences*, 110, 2016, 1-11.

- [75] Chai L., Xia G.D., Wang H.S., Numerical study of laminar flow and heat transfer in micro-channel heat sink with offset ribs on sidewalls, *Applied Thermal Engineering*, 92, 2016, 32-41.
- [76] Xia G., Ma D., Zhai, Y., Li Y., Liu R., Du M., Experimental and numerical study of fluid flow and heat transfer characteristics in micro-channel heat sink with complex structure, *Energy Conversion and Management*, 105, 2015, 848-857.
- [77] Khan A.A, Kim K., Evaluation of Various Channel Shapes of a Micro-channel Heat Sink, *International Journal of Air-Conditioning and Refrigeration*, 24(3), 2016, 1-9.
- [78] Vinoth R., Kumar D.S., Experimental investigation on heat transfer characteristics of an oblique finned microchannel heat sink with different channel cross sections, *Heat and Mass Transfer*, 2018.
- [79] Osanloo B., Mohammadi-Ahmar A., Solati A., Baghani M., Performance enhancement of the double-layered micro-channel heat sink by use of tapered channels, *Applied Thermal Engineering*, 102, 2016, 1345-1354.
- [80] Wong K., Ang M., Thermal hydraulic performance of a double-layer micro-channel heat sink with channel contraction, *International Communications in Heat and Mass Transfer*, 81, 2016, 1-7.
- [81] Ansari D., Kim K., Performance Analysis of Double-Layer Micro-channel Heat Sinks under Non-Uniform Heating Conditions with Random Hotspots, *Micromachines*, 8(2), 2017, 1-20.
- [82] Wei X., Joshi Y., Patterson M.K., Experimental and numerical study of a stacked micro-channel heat sink for liquid cooling of microelectronic devices, *Journal of Heat Transfer*, 129, 2007, 1432.
- [83] Qu, W., Mudawar, I., Experimental and numerical study of pressure drop and heat transfer in a single-phase microchannel heat sink, *International Journal of Heat and Mass Transfer*, 45, 2002, 2549-2565.
- [84] Jing D., He L., Thermal Characteristics of Staggered Double-Layer Micro-channel Heat Sink, *Entropy*, 20(7), 2018, 537.
- [85] Jing D., Song S., Pan Y., Wang X., Size dependences of hydraulic resistance and heat transfer of fluid flow in elliptical micro-channel heat sinks with boundary slip, *International Journal of Heat and Mass Transfer*, 119, 2018, 647-653.
- [86] Deng D., Pi G., Zhang W., Wang P., Fu T., Numerical Study of Double-Layered Micro-channel Heat Sinks with Different Cross-Sectional Shapes, *Entropy*, 21(1), 2019, 1-16.
- [87] Dede E.M., Joshi S.N., Zhou F., Topology Optimization, Additive Layer Manufacturing, and Experimental Testing of an Air-Cooled Heat Sink, *Journal of Mechanical Design*, 137, 2015, 1-9.
- [88] Andersen J., Sigmund O., Aage N., Large scale three-dimensional topology optimization of heat sinks cooled by natural convection, *International Journal of Heat and Mass Transfer*, 100, 2016.
- [89] Joo Y., Lee I., Kim S.J., Topology optimization of heat sinks in natural convection considering the effect of shape dependent heat transfer coefficient, *International Journal of Heat and Mass Transfer*, 109, 2017, 123-133.
- [90] Maradiaga D., Damonte A., Manzo A., Haertel J.H.K., Engelbrecht K., Design and testing of topology optimized heat sinks for a tablet, *International Journal of Heat and Mass Transfer*, 142, 2019.
- [91] Zeng S., Lee P.H., Topology optimization of liquid-cooled micro-channel heat sinks: An experimental and numerical study, *International Journal of Heat and Mass Transfer*, 142, 2019, 1-20.

